



**HAL**  
open science

# Spectroscopic and Structural Properties of Iron in Silicate Glasses

Vincent Vercamer

► **To cite this version:**

Vincent Vercamer. Spectroscopic and Structural Properties of Iron in Silicate Glasses. Material chemistry. Université Pierre et Marie Curie - Paris VI, 2016. English. NNT : 2016PA066077 . tel-01458771

**HAL Id: tel-01458771**

**<https://theses.hal.science/tel-01458771>**

Submitted on 7 Feb 2017

**HAL** is a multi-disciplinary open access archive for the deposit and dissemination of scientific research documents, whether they are published or not. The documents may come from teaching and research institutions in France or abroad, or from public or private research centers.

L'archive ouverte pluridisciplinaire **HAL**, est destinée au dépôt et à la diffusion de documents scientifiques de niveau recherche, publiés ou non, émanant des établissements d'enseignement et de recherche français ou étrangers, des laboratoires publics ou privés.



Université Pierre et Marie Curie

Thèse de doctorat présentée par :

**Vincent Vercamer**

Pour obtenir le grade de :

**DOCTEUR de l'UNIVERSITÉ PIERRE ET MARIE CURIE (PARIS)**

Spécialité : Physique et chimie des matériaux

Propriétés spectroscopiques et structurales  
du  
fer dans les verres silicatés

Soutenue le 5 février 2016 devant le jury composé de :

Dr Yusuke ARAI	AGC Research Center	Examineur
Pr Paul BINGHAM	Sheffield Hallam University	Rapporteur
Dr Maurits HAVERKORT	Max Planck Institute	Examineur
Dr Philippe LEGRAND	AGC	Invité
Dr Gérard LELONG	Université Pierre et Marie-Curie	Directeur de thèse
Pr Pierre LEVITZ	Université Pierre et Marie-Curie	Président du jury
Pr Akira TAKADA	University College London	Rapporteur

*École doctorale Physique et chimie des matériaux – ED 397*

*Institut de Minéralogie, de Physique des Matériaux et de Cosmochimie – UMR 7590*





Spectroscopic and Structural Properties  
of  
Iron in Silicate Glasses





FOR THOSE WHO LOVE GLASS A BIT TOO MUCH...



© HMain 2010 hmainillustrations.blogspot.com



# Remerciements

## Acknowledgements

Cette thèse est issue de la collaboration entre l'équipe PALM (Propriétés des Amorphes, Liquides et Minéraux) de l'IMPMC (Institut de minéralogie, de physique des matériaux et de cosmochimie) et l'entreprise AGC. Elle a en partie été financée grâce à l'Association Nationale de la Recherche et de la Technologie (ANRT) par la convention industrielle de formation par la recherche (CIFRE) n°2012/0640. Je remercie AGC pour avoir financé cette thèse et pour les nombreux échanges constructifs que nous avons eus autour de ce travail. Je remercie l'IMPMC au travers de ses deux directeurs, Bernard Capelle et Guillaume Fiquet, pour leur accueil bienveillant, leur écoute et leurs conseils.

Je remercie tous les membres du jury d'avoir examiné ce travail. En particulier, Pierre Levitz pour avoir présidé le jury, ainsi que Paul Bingham et Akira Takada qui m'ont fait le plaisir de relire attentivement mon manuscrit et d'accepter d'en être les rapporteurs. J'ai été très heureux de pouvoir bénéficier de leur expertise, de leurs remarques et de leurs réflexions. Je remercie vivement, Yusuke Arai, Maurits Haverkort et Philippe Legrand de m'avoir fait l'honneur de juger mon travail.

Mes remerciements infinis s'adressent ensuite à mon directeur de thèse, Gérald Lelong, qui a magnifiquement dirigé cette recherche et qui m'a guidé tout au long de mon travail. Merci pour les bilans intermédiaires et réguliers qui m'ont permis de me remettre en question et d'améliorer mes méthodes de travail. Merci pour ta bienveillance, ton immense pédagogie, mais aussi pour ta disponibilité, la confiance et l'autonomie que tu m'as accordées et qui m'ont permis de présenter mon travail lors de nombreuses conférences. Merci pour ces discussions entrecoupées de contradictions et de rires. Tu as été un génial capitaine qui m'a bien remonté le moral quand il m'arrivait de me retrouver au creux de la vague afin de mieux surfer dessus.

Je remercie les membres d'AGC qui ont grandement contribué au succès de cette recherche :

本研究を進めるにあたり、旭硝子株式会社の多くの方々にお世話になりました。また、2012年には旭硝子中央研究所に研究生としてお招き頂きました。美しい日本で過ごした貴重な時間は、生涯に渡り忘れ得ぬものとなりました。ここに深く感謝の意を表します。

研究活動全般に渡り、格別なるご指導とご高配を賜りました、旭硝子中央研究所の近藤裕己氏、中島哲也氏に甚大なる謝意を表します。

本論文をご精読頂き、様々に有用なコメントを頂き、また博士論文最終審査会には審査員としても参加して下さった、高田章氏に深く感謝致します。

旭硝子中央研究所の荒井雄介氏には、研究指導およびディスカッションのために多大なる時間を割いていただきました。博士論文最終審査会に日本よりお越しくださ

り、質疑応答においては、そのコメントに大いなる刺激とご厚意を頂きました。心より感謝申し上げます。

また、同研究所の土屋博之氏、藤田早苗氏には本研究の要である硝子実験に際して、多大なるご協力を頂きました。両氏の実験資料や計算結果のご提供、ならびに種々のご助言、またその好意に対し最大の感謝を致します。

研究活動費の調達および共同研究を円滑に進めるために、貴社、横塚俊亮氏、船津志郎氏ならびに留野暁氏に多大なるご援助を頂きました。深く感謝申し上げます。

Je remercie aussi Bérangère Joumel d'AGC pour le formidable suivi administratif de mon dossier tout au long de cette thèse.

Un immense merci aux MIAM (mangeurs insatiables et anticonformistes de multiplet) : Marie-Anne Arrio, Amélie Juhin, Christian Brouder qui m'ont fait découvrir le monde enivrant des calcools (un mélange de calculs, de cool et d'alcool ?). Merci pour votre patience et votre disponibilité, pour le temps passé à m'expliquer les différents codes de calculs multiplet et pour vos réponses à mes nombreuses questions quantiques. Merci de m'avoir permis d'aller apprendre à utiliser le code de DFT ORCA au Wigner Research Center à Budapest.

Je remercie grandement les personnes de l'équipe PALM : Georges Calas, Laurence Galois, Laurent Cormier pour les discussions et réunions régulières que nous avons eues tout au long de cette thèse.

J'adresse un remerciement spécial à Jean-Louis Robert pour son aide à la synthèse des phosphates de fer, pour la relecture minutieuse qu'il a faite de ma prose et pour ses nombreux conseils qu'il a distillés tout au long de ces trois ans.

J'exprime toute ma gratitude à Jean-Claude Bouillard, François Farges et Didier Nectoux pour les minéraux qu'ils ont donnés afin de réaliser les nombreuses mesures de cette thèse et pour leur expertise inestimable en minéralogie et gemmologie.

I am infinitely grateful to Maurits Haverkort for his revolutionary code `Quanty`, which is a 30-year jump forward compared to `TTMULT`. Thank you for the time spend to explain me how to use this code and implement all sort of new features. I am very thankful to György Vankó and Mátyás Pápai for their warm welcome at the Wigner Research Center of Budapest, and thank you for the time spent to train me for using ORCA.

Merci à ma binôme de thèse, Myrtille Hunault, d'avoir supporté mes diverses incursions et perturbations dans son travail, merci pour son infailible collaboration qui nous a permis de faire converger nos travaux vers de super résultats.

Merci aux experts de l'IMPMC : Maxime Guillaumet pour son aide avec les spectroscopies optique et RPE, Guillaume Morin, Étienne Balan et Thierry Allard pour la RPE, Agnès Elmaleh pour le temps qu'elle m'a accordé pour la mesure et l'interprétation des expériences de magnétisme, Ludovic Delbes et Benoit Baptiste pour la DRX, Jessica Brest et Sylvain Locati pour la chimie, Delphine Cabaret, Guillaume Ferlat, Guillaume Radtke et Philippe Sainctavit pour les inestimables discussions sur la théorie et les calculs numériques.

Un très grand merci aux experts qui ne sont pas du laboratoire, mais dont l'aide a été tout aussi précieuse et décisive : Michel Fialin du service CAMPARIS de l'UPMC pour son

aide à la microsonde, Dominique Bonnin pour son expertise multi-spectroscopiques et les fructueuses discussions que nous avons eues et le temps passé à relire mon manuscrit, Jürgen Von Bardeleben de l'INSP pour son incroyable savoir-faire et expertise concernant cette délicate technique qu'est la RPE à basse température, Melanie Escudier et Michelle Jacquet de l'atelier d'optique cristalline de l'INSP pour leur inestimable expertise du polissage des verres, Emrick Briand de l'INSP pour les mesures RBS qu'il a accepté de réaliser à Namur, Pieter Glatzel et Mauro Rovezzi de la ligne ID26 du synchrotron ESRF de Grenoble pour le support technique et les discussions scientifiques instructives que nous avons eues, Brigitte Leridon et Armel Descamps Mandine du LPEM de l'ESPCI Paris de m'avoir permis de réaliser des mesures de magnétisme avec un SQUID.

Un grand merci à Marie-Louise Saboungi pour sa bonne humeur et tous ses conseils !

Je souhaite remercier toutes les générations de doctorants, stagiaires et postdocs que j'ai côtoyées et plus particulièrement : Mathieu Chassé, Louisiane Verger, Benjamin Cochain, Flora Boekhout, Lucas Poirier. Merci aussi à mes co-bureaux et co-bagnards respectifs de leur thèse : Nicolas Dupuy, Nith Cam, Thibault Sohier, on a bien rigolé !

Special thanks to Holly Main, Illustrator and Cartoonist, Toronto, Ontario, for the use of her *For Those Who Love Glass A Bit Too Much* comic in the dedication. For more comics and illustrations, visit [www.hollymain.com](http://www.hollymain.com).

Enfin, je souhaite remercier du fond du cœur mes parents ainsi que Cécile et Rémi pour m'avoir encouragé dans cette voie. On oublie trop souvent de remercier les mamies pour le calme, la quiétude et le soutien logistique qu'elles apportent dans les moments difficiles de la rédaction. . .

Pour finir, je souhaite remercier Judith pour son soutien quotidien et indéfectible durant ces quelques années mouvementées.



# Table of contents

<b>Introduction</b>	<b>17</b>
<b>1 Iron in glass: an heterovalent ion in a complex medium</b>	<b>21</b>
1.1 What is a glass?	21
1.2 Iron redox in glass	22
1.3 Iron environment in glass	23
1.3.1 Fe <sup>2+</sup> coordination number in glass	23
1.3.2 Fe <sup>3+</sup> coordination number in glass	24
1.3.3 The question of [5]-fold coordinated iron in glasses	25
1.3.4 From iron coordination number to site geometry	26
1.3.5 Group theory to describe the local environment	27
1.4 Conclusion & Thesis statement	28
<b>2 Samples and experimental methods</b>	<b>29</b>
2.1 Glasses	29
2.1.1 Choice of the glass set	29
2.1.2 Sample preparation	30
2.1.3 Characterization	33
2.1.4 Summary	35
2.2 Optical absorption spectroscopy	35
2.2.1 Transmission measurements	35
2.2.2 Background correction	36
2.3 X-ray Absorption Spectroscopy (XAS)	39
2.3.1 Principle	39
2.3.2 Experiment	40
2.3.3 Data processing	41
2.4 RIXS and HERFD	42
2.4.1 Principle	42
2.4.2 Experiment	43
2.4.3 Data processing	43
2.4.4 Why HERFD and RIXS can be useful?	43
2.5 SQUID-VSM	44
2.5.1 Approach	44
2.5.2 SQUID data acquisition	45



2.6	Electron Paramagnetic Resonance (EPR) . . . . .	46
2.6.1	EPR principles . . . . .	46
2.6.2	EPR data acquisition and data processing . . . . .	48
2.6.3	EPR example and interpretation elements . . . . .	49
<b>3</b>	<b>Ligand Field Multiplet Theory applied to the calculation of XAS and optical absorption spectra</b>	<b>51</b>
3.1	Historical introduction to Ligand Field Multiplet Theory (LFMT) . . . . .	51
3.2	From mono-electronic picture to multiplet states . . . . .	52
3.3	Spectroscopic terms and ground state . . . . .	52
3.4	The importance of geometry . . . . .	53
3.5	Crystal field parameters . . . . .	54
3.6	Tanabe-Sugano diagrams . . . . .	56
3.7	Hamiltonian describing the multielectronic configuration . . . . .	58
3.8	Intensities – absorption cross-section . . . . .	58
3.9	Transition rules in optics . . . . .	59
3.10	Quanty – a quantum many body script language . . . . .	61
3.11	Summary . . . . .	62
<b>4</b>	<b>Investigation of a reference set of crystalline compounds: determination and interpretation of spectral signatures</b>	<b>63</b>
4.1	The case of $O_h$ – octahedral $^{6}Fe^{2+}$ in siderite . . . . .	65
4.1.1	XAS . . . . .	65
4.1.2	Optical absorption spectroscopy . . . . .	66
4.1.3	Effect of the different parameters . . . . .	67
4.1.3.1	Hybridization . . . . .	67
4.1.3.2	Crystal field . . . . .	69
4.1.3.3	Nephelauxetic ratio $\beta$ . . . . .	70
4.1.3.4	Spin-orbit coupling on the $3d$ levels . . . . .	71
4.2	The case of $O_h$ – octahedral $^{6}Fe^{3+}$ in andradite . . . . .	72
4.2.1	XAS . . . . .	72
4.2.2	Optical absorption spectroscopy . . . . .	73
4.2.3	Effect of the different parameters . . . . .	74
4.2.3.1	Crystal field . . . . .	74
4.2.3.2	Nephelauxetic ratio $\beta$ . . . . .	76
4.2.3.3	Spin-orbit coupling on the $3d$ . . . . .	77
4.3	The case of $D_{4h}$ – square planar $^{4}Fe^{2+}$ in gillespite . . . . .	77
4.3.1	Model used for the calculation of gillespite . . . . .	78
4.3.2	Comparison experimental data/LFM calculation . . . . .	79
4.4	The case of $T_d$ – tetrahedral $^{4}Fe^{2+}$ in staurolite . . . . .	80
4.4.1	Comparison of experimental spectra/LFM calculation . . . . .	80
4.4.2	Effect of the different parameters . . . . .	82
4.4.2.1	Crystal field . . . . .	82

4.4.2.2	Nephelauxetic ratio $\beta$ . . . . .	83
4.4.2.3	Effect of ground state hybridization . . . . .	84
4.5	The case of $T_d$ – tetrahedral $^{[4]}\text{Fe}^{3+}$ in ferriorthoclase . . . . .	85
4.5.1	Comparison experimental data/LFM calculation . . . . .	86
4.5.2	Effect of the different parameters . . . . .	88
4.5.2.1	Crystal field . . . . .	88
4.5.2.2	Nephelauxetic ratio $\beta$ . . . . .	89
4.6	The case of $D_{3h}$ – trigonal bipyramidal $^{[5]}\text{Fe}^{2+}$ in grandidierite . . . . .	89
4.6.1	XAS . . . . .	89
4.6.2	Optical absorption spectroscopy . . . . .	90
4.7	The case of $C_{3v}$ – trigonal bipyramidal $^{[5]}\text{Fe}^{3+}$ in yoderite . . . . .	93
4.7.1	XAS $K$ pre-edge . . . . .	93
4.7.2	Optical absorption spectra . . . . .	94
4.8	Summary . . . . .	95
<b>5</b>	<b>Iron local environment in a soda-lime-silicate glass</b>	<b>97</b>
5.1	Introduction to the optical absorption spectrum of iron in silicate glass . . .	98
5.2	Structure–spectroscopy analysis of $\text{Fe}^{2+}$ . . . . .	99
5.2.1	Spectroscopic origins of $\text{Fe}^{2+}$ optical bands . . . . .	99
5.2.2	The contribution of XAS to the analysis of $\text{Fe}^{2+}$ optical bands . . . .	101
5.2.3	LFM calculations of $\text{Fe}^{2+}$ spectroscopic signature in glasses . . . . .	104
5.2.4	Influence of redox on the $\text{Fe}^{2+}$ local environment . . . . .	106
5.2.5	Evidence of $\text{Fe}^{2+}$ spin-forbidden bands in reduced glass . . . . .	109
5.3	Structure–spectroscopy analysis of $\text{Fe}^{3+}$ . . . . .	110
5.3.1	Study of the OMCT bands in the UV range . . . . .	110
5.3.2	Evidence of [5]-fold ferric iron ( $^{[5]}\text{Fe}^{3+}$ ) in glasses . . . . .	111
5.3.3	The contribution of XAS experiments and LFM calculations to the analysis of $\text{Fe}^{3+}$ optical bands . . . . .	115
5.3.4	Study of the impact of redox on $\text{Fe}^{3+}$ site distortion . . . . .	116
5.4	Site partitioning: isolated vs. clustered iron . . . . .	119
5.4.1	Introduction . . . . .	119
5.4.2	X-ray absorption spectroscopy (XAS) . . . . .	120
5.4.3	Electron paramagnetic resonance (EPR) . . . . .	120
5.4.4	SQUID magnetometry . . . . .	122
5.4.5	Conclusions . . . . .	123
<b>6</b>	<b>Influence of chemical composition on iron local environment in glasses</b>	<b>125</b>
6.1	Absence of sodium, what are the effects? . . . . .	125
6.1.1	Effects on $\text{Fe}^{3+}$ : DIO vs NCS . . . . .	125
6.1.2	Effects on $\text{Fe}^{2+}$ : DIO vs. NCS . . . . .	128
6.2	Influence of the alkaline earth nature: Ca vs. Mg . . . . .	130
6.2.1	The opposite effect of Ca:Mg ratio on the $\text{Fe}^{2+}$ and $\text{Fe}^{3+}$ UV-edge .	131
6.2.2	Ca:Mg effects on ferric iron ( $\text{Fe}^{3+}$ ) optical signatures in glasses . . .	132

6.2.3	Evolution of Fe <sup>3+</sup> distortion when Mg substitute Ca . . . . .	134
6.2.4	Ca:Mg effects on ferrous iron (Fe <sup>2+</sup> ) optical signatures in glasses . .	136
6.2.5	Are there more Fe-clusters in Mg-rich glass? . . . . .	138
6.2.6	Calcium or magnesium who is the favorite neighbor? . . . . .	140
<b>Conclusions and suggestions for future work</b>		<b>143</b>
<b>References</b>		<b>147</b>
<b>Appendix A Crystalline references data</b>		<b>163</b>
<b>Appendix B Optical absorption spectroscopy</b>		<b>203</b>
B.1	Perkin-Elmer <sup>®</sup> Lambda 1050 . . . . .	203
B.2	How to convert $\alpha$ to $\varepsilon$ . . . . .	203
B.3	Beer lambert verification for reduced glasses . . . . .	204
B.4	Data processing of weak Fe <sup>3+</sup> signals . . . . .	205
B.4.1	Removing the UV-edge to extract Fe <sup>3+</sup> <i>d-d</i> transitions . . . . .	206
B.4.2	Separation of Fe <sup>2+</sup> /Fe <sup>3+</sup> . . . . .	207
B.4.3	Gaussian fit of the Fe <sup>3+</sup> bands . . . . .	209
B.4.4	Low-iron glasses . . . . .	209
<b>Appendix C SQUID-VSM</b>		<b>211</b>
C.1	Magnetic units . . . . .	211
C.2	Correction for the diamagnetism of the glassy matrix . . . . .	212
<b>Appendix D X-ray absorption spectroscopy</b>		<b>213</b>
D.1	Temperature effect - Boltzmann distribution . . . . .	213
D.2	Spectral broadening . . . . .	213
D.3	Beam damage . . . . .	214
D.4	Sum rules . . . . .	217
<b>Appendix E Theoretical developments with LFMT</b>		<b>219</b>
E.1	Isotropic resonant inelastic X-ray scattering – the powder formula . . . . .	219
E.2	Geometrical factor of the Kramers-Heisenberg formula . . . . .	221
E.3	Angular dependence of RIXS. E1-E2 interference term . . . . .	223
E.3.1	General expression . . . . .	223
E.3.2	Angular terms . . . . .	223
E.3.3	Matter tensors . . . . .	226
E.3.4	$9j$ -symbols . . . . .	226
E.3.5	Final formulas . . . . .	227
E.3.6	Conclusion . . . . .	228
E.4	The absolute absorption cross-section $\sigma(\omega)$ in $\text{\AA}^2$ . . . . .	229
E.5	Crystal field Hamiltonian in $D_{3h}$ geometry . . . . .	230
<b>Appendix F Curriculum Vitae</b>		<b>233</b>

<b>Résumé de la thèse en français</b>	<b>235</b>
1 Introduction à la problématique du fer dans les verres : un ion hétérovalent dans un milieu complexe . . . . .	235
1.1 Contexte . . . . .	235
1.2 Redox . . . . .	235
1.3 Le verre . . . . .	235
1.4 Relation structure-propriétés . . . . .	236
1.5 Intérêt des cristaux pour l'étude des verres . . . . .	236
1.6 L'environnement du fer dans les verres . . . . .	237
1.7 La théorie des groupes pour décrire l'environnement local . . . . .	237
1.8 Problématique . . . . .	238
2 Échantillons et méthodes expérimentales . . . . .	238
2.1 Compositions et synthèses . . . . .	238
2.2 Spectroscopie d'absorption optique . . . . .	239
2.3 Spectroscopie d'absorption des rayons X (XAS) . . . . .	239
2.4 Spectroscopie RIXS et HERFD . . . . .	240
2.5 SQUID . . . . .	241
2.6 Résonance Paramagnétique Électronique (RPE) . . . . .	242
3 La théorie des multiplets en champ de ligands appliquée au calcul des spectres d'absorption X et d'absorption optique . . . . .	242
4 Étude d'un jeu de références cristallines : détermination et interprétation des signatures spectrales . . . . .	243
5 Environnement local du fer dans un verre sodo-calcique . . . . .	245
5.1 Analyse structure-spectroscopie du $\text{Fe}^{2+}$ . . . . .	245
5.2 Analyse structure-spectroscopie du $\text{Fe}^{3+}$ . . . . .	246
5.3 Fer en cluster vs. fer isolés . . . . .	247
6 Conclusions et perspectives . . . . .	247
<b>Résumé</b>	<b>249</b>
<b>Abstract</b>	<b>250</b>



# Introduction

Iron is the fourth most abundant element in Earth's crust (after oxygen, silicon and aluminum); 11 times more abundant than titanium (the second most abundant transition element). It is, therefore, present as an impurity in raw materials used by industry to manufacture millions of metric tonnes of glass each year. Beyond this constant presence, iron impurities play a major role for many advanced applications (e.g. automotive, solar panels, construction) and can be used to control glass coloration, thermal insulation, and energy transmission.

These latter properties are all related to optical absorption, which is one of the main spectroscopic properties considered in the glass industry to improve the technical characteristics of glasses. Understanding the influence of Fe on glass properties may then help to develop innovative functional glasses. For example, the absorption of UV light by iron is an annoying side effect for solar panel applications; high-energy photons are absorbed by the protective glass containing iron instead of being converted into electricity by the photovoltaic materials. Another problematic consequence of this UV absorbing properties is for photolithography during microfabrication of electronic components such as CPU. UV photons have to pass through several lenses equivalent to one meter of glass without being absorbed, in order to etch the billions of transistors present on the chip. On the other hand, the control of UV absorption is useful for glasses manufactured to protect from degradation of plastics inside cars, or the pigments of photos and paintings, but visible light has to be transmitted. Concerning the infrared range, the control of the absorption is crucial to optimize solar and heat transfer through glass windows.

In amorphous materials such as glasses, but also in minerals and chemical complexes, iron usually occurs under two oxidation states  $\text{Fe}^{2+}$  (ferrous) and  $\text{Fe}^{3+}$  (ferric), whose relative proportion defines the redox state of iron. The redox depends on synthesis conditions such as chemical composition, temperature or atmospheric conditions. Ferrous and ferric ions are localized in specific environments within the glass structure. They give to diluted glasses a blue ( $\text{Fe}^{2+}$ ), yellow ( $\text{Fe}^{3+}$ ) or green (mixed oxidation states) color. The amorphous character of glass and the heterovalent nature of iron are two reasons explaining that even after 80 years of active scientific research, the comprehension of iron local environment in glass is still partial.

Through spectroscopy, the interactions of radiation with matter can be used to probe the structure-property relationships in glass. For example, Ultraviolet–Visible–Near-Infrared (UV–Visible–NIR) spectroscopy provides a correlation between the colorimetric properties of

glasses containing transition metals, and the redox state and structural surrounding of these transition elements. To complete the knowledge brought by optical absorption spectroscopy (OAS), complementary techniques presenting such as X-ray absorption spectroscopy (XAS) and electron paramagnetic resonance (EPR), can be used.

In order to deduce structural properties from spectroscopic analysis, crystalline compounds, in which the local structure is known, are useful references. Signatures of tetrahedral and octahedral sites were widely studied and characterized. However, [5]-fold species, especially in the case of iron, are not always considered for the interpretation of the spectral signature, which is very sensitive to the local geometry and site coordination. Interpretations can be sustained by coupling experimental results with calculations of the electronic structure and spectroscopy in order to interpret the structure-property relationships. The complex problem of optical spectra simulations of  $3d$  elements can be addressed using group theory to describe the local geometry. Thus, the ligand field multiplet (LFM) approach is used to take into account the point group symmetry of the iron site in order to evaluate the multi-electronic effects of the neighboring atoms on the central transition metal electrons. These simulations help to extract tendencies from the calculation of iron minerals in order to extrapolate them for the understanding iron in glasses.

Among the infinite possibilities of glass compositions, this thesis focused on soda-lime silicates representing 90% of the glass production. Specific glasses with extreme redox, reduced or oxidized, were synthesized to isolate the respective  $\text{Fe}^{2+}$  and  $\text{Fe}^{3+}$  spectroscopic signatures that are usually mixed due to the heterovalent nature of iron. A multi-spectroscopic study was performed by coupling experimental measurements with simulations. Therefore, it is possible to cross the results from multiple points of view to improve the comprehension of the local structure around iron in order to interpret the optical properties of iron in glasses.

**The first chapter** presents a brief state of the art about the glass material, the iron redox and the local environment of both  $\text{Fe}^{2+}$  and  $\text{Fe}^{3+}$  in glasses. The thesis statement that will be developed in the next chapters is presented after this review.

**Chapter 2** justifies the choice of glass samples, their preparation and characterization. The experimental methods used in this work are details (optical absorption spectroscopy (OAS), X-ray absorption spectroscopy (XAS), Resonant Inelastic X-ray Scattering (RIXS), High-Energy Resolution Fluorescence Detected X-ray Absorption Spectroscopy (HERFD-XAS), Superconducting Quantum Interference Device with a Vibrating Sample Magnetometer (SQUID-VSM) and Electron Paramagnetic Resonance (EPR)).

**Chapter 3** presents the ligand field multiplet theory that is used to describe the local environment of iron. At the end of this chapter, the implementation of this theory using **Quanty** software for the calculation of the spectra of minerals is presented.

**Chapter 4** investigates the spectroscopic signature of both  $\text{Fe}^{2+}$  and  $\text{Fe}^{3+}$ , in [4]-, [5]- and [6]-fold geometries using crystalline reference compounds. The aim of this chapter is to improve the understanding of structure-spectroscopy relationships using both optical absorption and X-ray absorption spectroscopies coupled with ligand field multiplet calculations of these two techniques.

**Chapter 5** studies the structure-spectroscopy links for  $\text{Fe}^{2+}$  and  $\text{Fe}^{3+}$  in a soda-lime glass as function of the redox state. The tendencies highlighted by calculations for minerals are transposed to glasses. This chapter is also the occasion to discuss Fe-Fe interaction and the site partitioning between isolated iron and Fe-clusters.

**Chapter 6** develops the analysis of the previous chapter by considering composition change of the glassy matrix. The effect of sodium-lack and calcium-magnesium substitution on glass structure are evaluated using Fe as a local probe using the spectroscopic method developed in this thesis.





## Chapter 1

# Iron in glass: an heterovalent ion in a complex medium

### 1.1 What is a glass?

Glass is a non-crystalline solid, also described by Scholze [1980] as a “frozen supercooled liquid”, according to its usual synthesis process by quenching a melt. Compared to crystals, which show a precise melting temperature, glass exhibits a “glass transition” spanned in temperature (Figure 1.1) [Shelby, 2005]. As opposed to crystals, glasses do not have a long-range order nor periodic atomic arrangements. To schematically describe the complexity of glass structure, Zachariasen [1932] introduced the *random network theory* with the notions of network former and network modifier. This model was later modified by Greaves [1985] that introduced percolation path containing mobile alkaline and alkaline earth cations. Despite the amorphous nature of glass, experimental studies suggest a medium-range ( $\sim 15 \text{ \AA}$ ) order with local inhomogeneities of enriched domains [Neuville et al., 2013].

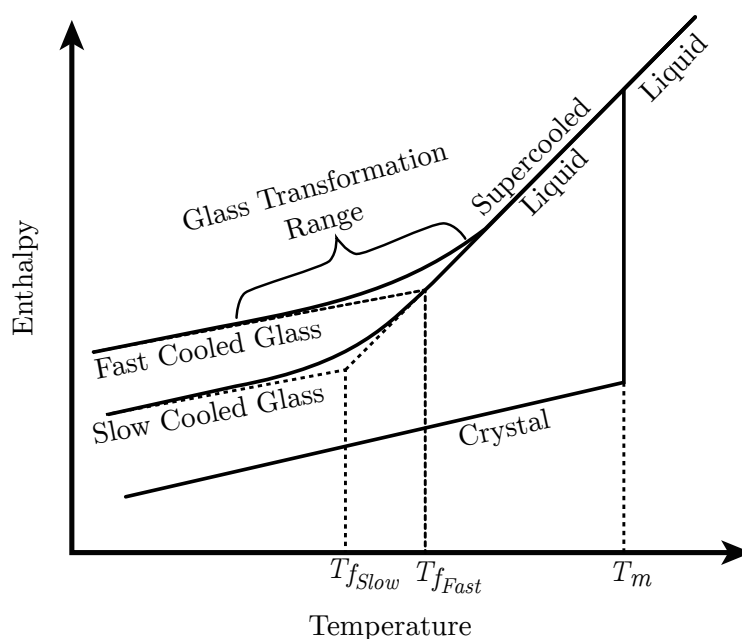


**Figure 1.1** – Temperature effect on the enthalpy of a glass forming melt (based on Shelby [2005]).

The main problem with characterization of glass structure remains in the fact that experimental spectroscopies only give an average picture of the heterogeneous local environments and do not reflect the variety of sites. Glass is then a complex system in which local environment around impurities can vary for a given matrix composition.

## 1.2 Iron redox in glass

$\text{Fe}^{2+}$  and  $\text{Fe}^{3+}$  are the two valence states of iron usually observed in glasses. The partition of iron in these two valence states is characterized by the redox state, defined as:

$$R = \frac{[\text{Fe}^{2+}]}{[\text{Fe}^{2+}] + [\text{Fe}^{3+}]} \quad (1.1)$$

$R = 0\%$  for a fully oxidized glass and  $R = 100\%$  for a fully reduced glass. When an iron-bearing glass is reduced, it is also possible to form metallic  $\text{Fe}^0$  by reducing  $\text{Fe}^{2+}$  [Schreiber et al., 1982]. Iron redox depends on several factors [Paul, 1990; Schreiber, 1986], such as:

- oxygen partial pressure [Johnston, 1964]
- temperature [Johnston, 1964; Kress and Carmichael, 1991]
- matrix composition [Duffy, 1996; Schreiber et al., 1994]
- interactions between redox pairs [Chopin et al., 2002]
- total iron content [Rüssel and Wiedenroth, 2004; Uchino et al., 2000]
- heating rate [Yamashita et al., 2008]

The final bulk redox is an important experimental parameter because of its major effect on the glass mechanical, spectroscopic or structural properties. Among others, glass redox is correlated to color: reduced glasses with only  $\text{Fe}^{2+}$  are blue and oxidized one with only  $\text{Fe}^{3+}$  are yellow [Bamford, 1977]. Thermal properties such as near infrared absorption (NIR) [Sakaguchi and Uchino, 2007] or ultraviolet (UV) absorption [Uchino et al., 2000] also depend on redox, and lead to industrial consequences for NIR/UV protective glass or black-body absorption in furnaces. Redox also plays a role on other properties not studied in this thesis, but important to keep in mind such as melt viscosity [Mysen and Richet, 2005], nucleation and crystallization processes [Sørensen et al., 2005] or surface redox variations within the first microns [Flank et al., 2011].

Another key factor is time, during synthesis, it is crucial to control the redox kinetics in order to achieve or avoid thermodynamic equilibrium. Time and redox kinetics have been studied in several papers [Densem and Turner, 1938], [Paul and Douglas, 1965], [Goldman and Gupta, 1983], [Pyare and Nath, 1984], [Paul, 1990], [Cochain, 2009], [Pigeonneau and Muller, 2013].

### 1.3 Iron environment in glass

The characterization of iron local environment is a crucial question, since it is interrelated with spectroscopic and chemical properties. The modification of structure has an effect on the physical and chemical properties (Figure 1.2). Therefore, the understanding of iron local environment can help to interpret, simulate, and predict the optical properties, such as color or the behavior in UV and NIR domains.

Structural information, such as Fe–O distances or coordination number can be obtained from neutron scattering or extended X-ray absorption fine structure (EXAFS). Other methods can bring indirect structural information on iron, such as Electron Paramagnetic Resonance (EPR, only Fe<sup>3+</sup> not Fe<sup>2+</sup>), X-ray Absorption Near Edge Structure (XANES), Mössbauer and optical absorption spectroscopies. These methods do not give direct structural information, however, it is possible to relate spectroscopic signals with site of specific coordination number using fingerprint analysis with minerals in which the local environment is known [Burns, 1993]. In addition, numerical calculations of glass structure coupled with experimental data, such as Reverse Monte Carlo (RMC), Empirical Potential Structure Refinement (EPSR) or Molecular Dynamics (MD) methods, are valuable tools to extract structural information about the local environment [Weigel et al., 2008a].

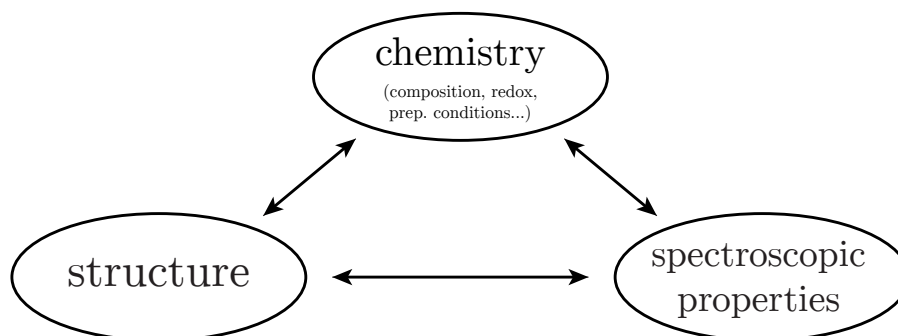


**Figure 1.2** – Schematic relationships between chemical properties, structure and spectroscopic properties.

#### 1.3.1 Fe<sup>2+</sup> coordination number in glass

Within the framework of industrial glass, this study is focused on silicate glasses containing alkali and alkaline earth ions doped with transition metal, more precisely iron. The role of ferrous iron is considered as a network-modifier [Goldman and Berg, 1980]. It has been historically described to be exclusively in tetrahedral and octahedral geometries [Bates, 1962, p. 245], with less than 15% of <sup>[4]</sup>Fe<sup>2+</sup> and more than 85% of <sup>[6]</sup>Fe<sup>2+</sup> [Calas and Petiau, 1983a], which is in contradiction with optical spectroscopy results estimating the <sup>[4]</sup>Fe<sup>2+</sup> content to be lower than 1% [Nolet, 1980]. More recently, the presence of [5]-fold coordinated Fe<sup>2+</sup> has been evidenced in silicate glasses containing a significant (~20 mol% of FeO) using XAS and magnetic circular dichroism [Brown et al., 1995; Jackson et al., 2005]. Mössbauer studies of CaO–FeO–2SiO<sub>2</sub> glass indicate an average coordination number between [4] and [5] and a maximum coordination number lower than [6] [Rossano et al., 1999,

2008]. Using EXAFS, Rossano et al. [2000c] found that the distribution of Fe–O distances is too wide to only correspond to a simple mix of [4]-fold and [6]-fold, in CaO–FeO–2SiO<sub>2</sub> glass. By comparing these experimental EXAFS data with MD calculations, they suggested a continuous distribution of the O–Fe–O angles between the oxygens of [4]-fold and [5]-fold ferrous iron (Figure 1.3). They found 70% of [4]-fold coordinated Fe<sup>2+</sup> and 30% of [5]-fold coordinated Fe<sup>2+</sup>. It can be noticed the angular distributions are not centered around the angles of the regular polyhedra (tetrahedron or trigonal bipyramid), which demonstrate the presence of a variety of possible sites. Moreover, concerning the trigonal bipyramid, there are almost no polyhedra with a 180° Fe–O–Fe angle, which means that the regular trigonal bipyramid with the apical oxygens aligned with the transition metal ion (forming the  $C_3$  axis) is not representative of the [5]-fold coordinated irons. In low-iron content glasses, the combined results, from a multi-spectroscopic study by Jackson et al. [2005], suggest that Fe<sup>2+</sup> predominantly occupies [4]-fold and [5]-fold coordinated sites, with ratios differing with the composition. This study also suggests that small amounts of [6]-fold coordinated Fe<sup>2+</sup> are possible.

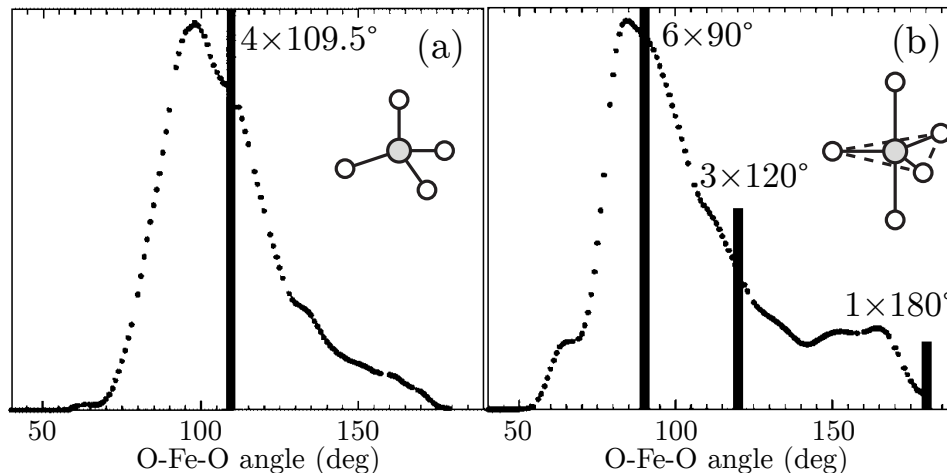


**Figure 1.3** – Angular distribution around central iron in [4]-fold (a) and [5]-fold (b) coordinated sites for a cut-off radius of 2.6 Å. The bars correspond to the distribution expected for a perfect tetrahedron (a) and a regular bipyramid (b). From: Rossano et al. [2000c].

### 1.3.2 Fe<sup>3+</sup> coordination number in glass

Several studies suggested that the largest fraction of Fe<sup>3+</sup> (50 to 70%) is present as network forming [4]Fe<sup>3+</sup> in tetrahedra and that the remaining Fe<sup>3+</sup> are higher coordinated species ([5]-fold or [6]-fold) and plays a network modifying role in the glass matrix [Calas and Petiau, 1983a; Weigel et al., 2008b; Wright et al., 2014].

Weigel et al. [2008b], using neutron diffraction with Fe isotopic substitution combined with Empirical Potential Structure Refinement (EPSR) simulations on NaFeSi<sub>2</sub>O<sub>6</sub> with a 22% redox, pointed out the predominance of Fe<sup>3+</sup> in tetrahedra (60%), while 36% are Fe<sup>2+</sup> and Fe<sup>3+</sup> in [5]-fold, and only 4% of total iron are [6]-fold coordinated. On the other hand, Wright et al. [2014], proposed that Fe<sup>2+</sup> and Fe<sup>3+</sup>, when present as network modifying cations, are predominantly octahedrally coordinated by oxygen atoms, rather than in [5]-fold coordination. The difficulty in concluding on the coordination number of

$\text{Fe}^{3+}$  present as network modifying cations is due to the poor resolution of experimental data, highlighting the necessity of numerical simulations [Weigel et al., 2008a]. Nevertheless, from the interatomic distance distribution, both studies concluded that a higher coordinated  $\text{Fe}^{3+}$  acting as a network modifier is needed to interpret experimental data.

By combining XANES and MD, Farges et al. [2004] found evidence of  $^{[5]}\text{Fe}^{3+}$  in a soda-lime silicate glass doped with 0.2 wt%  $\text{Fe}_2\text{O}_3$ . In addition, a recent study [Bingham et al., 2014], on oxidized silicate glasses doped with  $\sim 1$  wt%  $\text{Fe}_2\text{O}_3$ , points out an average  $\text{Fe}^{3+}$  coordination number varying from [4] to [6] depending on the nature of the alkali and alkaline earth used in the glass composition.  $^{[4]}\text{Fe}^{3+}$  are stabilized by larger alkali and smaller alkaline earth, while  $^{[5,6]}\text{Fe}^{3+}$  are stabilized by smaller alkali and larger alkaline earth. These opposing effects of alkali and alkaline-earth ions on  $\text{Fe}^{3+}$  coordination cannot be explained with a simple bond-valence model, and the nature and local environment of all second neighbors of  $\text{Fe}^{3+}$  have to be considered.

### 1.3.3 The question of [5]-fold coordinated iron in glasses

The existence of [5]-fold coordinated iron in glasses, has been debated for the last 20 years since the work of Brown et al. [1995]. Despite the average coordination around 5 in glasses, its existence was contradicted by the rare presence of [5]-fold coordination in crystals and complexes. Evidence of [5]-fold coordinated transition metals were found in glasses for nickel and titanium. Galois and Calas [1991] showed evidence of  $^{[5]}\text{Ni}^{2+}$  in a trigonal bipyramidal site, which opened the search of other transition metals in [5]-fold coordination in glasses. Cormier et al. [1998] confirmed the presence of [5]-fold coordinated Ti within a square-based pyramid in a silicate glass studied by neutron diffraction with isotopic substitution.

Concerning coordination complexes, Ciampolini [1969] reviewed numerous transition metals [5]-fold coordinated complexes, including iron. Some silicate minerals also exhibit [5]-fold coordinated  $\text{Fe}^{2+}$  in both square-based pyramid or trigonal bipyramid such as grandidierite, joaquinite [Rossman and Taran, 2001], vesuvianite [Wilke et al., 2001], hibonite, rhodonite, pyroxmangite [Seifert and Olesch, 1977] or eudialyte [Pol'shin et al., 1991]. However, in these exotic minerals, the structural interpretation is challenging because only a part of the total iron is [5]-fold coordinated, and often in a distorted site or  $5 + 1$ , i.e. a strongly deformed octahedron.

As for complex reviewed by Ciampolini [1969], [5]-fold  $\text{Fe}^{3+}$  are less frequent than  $^{[5]}\text{Fe}^{2+}$  in silicate minerals but exist in yoderite or in non-silicate minerals such as  $\text{FeAsO}_4\text{-I}$ ,  $\text{Fe}_3\text{PO}_7$  (Berthet et al. [1988, 1989]) and  $\text{Fe}_3^{2+}\text{Fe}_4^{3+}(\text{AsO}_4)_6$  [Weil, 2004].

In addition to the existence of [5]-fold coordinated iron in complexes and minerals and to the presence of other transition metals in glasses, several studies on Fe-bearing glasses lead to confirm the existence of [5]-fold coordinated iron in glass. Rossano et al. [1999] first showed evidence of [5]-fold  $\text{Fe}^{2+}$  in tektites, natural impact glasses, by Mössbauer, that have been enhanced by an EXAFS and MD study in a  $\text{CaO-FeO-2SiO}_2$  silicate glass Rossano et al. [2000c]. Complementary to these conclusions, [5]-fold iron was later confirmed by Guillot and Sator [2007] for both valence states by another MD study in high iron-content

silicate melts (Figure 1.4). They found that  $\text{Fe}^{3+}$  is mainly [4]-fold (55%) but an important amount is [5]-fold (30%), while  $\text{Fe}^{2+}$  is mainly [5]-fold (35%) and partly [4]-fold and [6]-fold (25% each). The conclusions of these studies on highly Fe-concentrated glasses tend to prove that both  $\text{Fe}^{2+}$  and  $\text{Fe}^{3+}$  exist in [5]-fold coordinated sites.

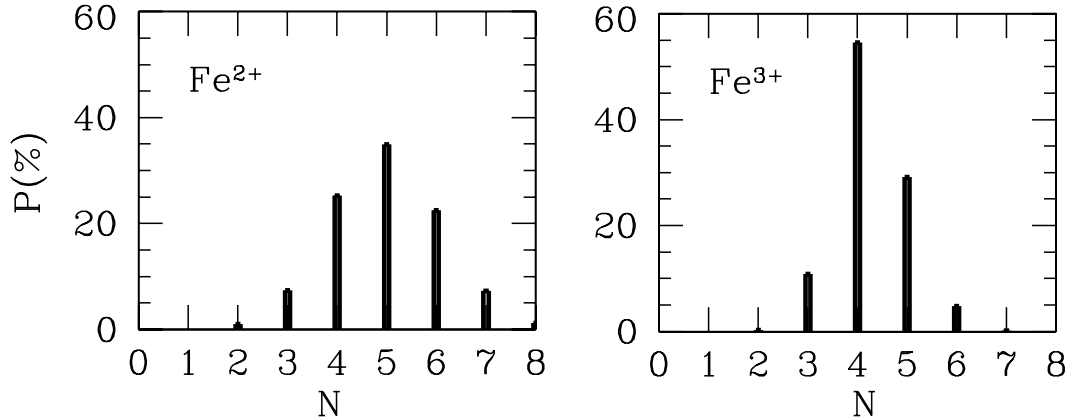


**Figure 1.4** – Population analysis of  $\text{Fe}^{2+}$  and  $\text{Fe}^{3+}$  coordination numbers in a mid-ocean ridge basalt (MORB) from *Guillot and Sator [2007]*.

However, there is no evidence in previous studies that even if the average coordination of iron is around [5], the majority of iron is [5]-fold coordinated. For example, several scenarios that give an average value of [5] can be considered: a mix of [4]-fold and [6]-fold; a mix of [4]-fold and [6]-fold with a minority of [5]-fold and a distribution of coordination number centered around [5] with the highest proportion of iron in [5]-fold coordination (such as in Figure 1.4); a distribution of centered around [5] with the majority of iron [5]-fold coordinated (more than all other coordination numbers together). It is also important to keep in mind that there is no unique geometry associated to [5]-fold coordination, and that several kind of geometries are possible (such as trigonal bipyramid and square-based pyramid). Moreover, several distortions of the regular geometries can coexist in glasses (as previously detailed with Figure 1.3) leading to a broad variety of [5]-fold sites. Finally, non-bonding oxygens and second neighbors can also influence the spectroscopic signatures in addition to the coordination number of iron.

### 1.3.4 From iron coordination number to site geometry

The understanding of iron optical spectra on their interpretation is still a matter of research, despite the knowledge on Fe local environment, the comprehension of the origins of optical band remains complicated. For example, the correlation of the asymmetrical shape of the  $\text{Fe}^{2+}$  band in the near infrared with the chemical composition remains hard to explain. Difficulties are enhanced by the vitreous nature of glasses, the disordered structure necessary leading to a distribution of the glass environment and indirectly to variations of the coordination number.

To interpret the iron spectroscopic signatures, lots of work focused on iron coordination but we must go further in the description of iron sites and use angles, distances, coordination number, nature of the second neighbors... Because the optical absorption depends on the local geometry, ligand field theory is an adapted tool to study and characterize iron

coordination local environment, by using group theory to describe the geometry of the ligands around iron and parameters to quantify the effect of neighbors.

### 1.3.5 Group theory to describe the local environment

The coordination number is an interesting parameter but its simplicity overrides the complexity of the local environment. The geometry of the site, determined by the surrounding ligands, rules the spectroscopic properties. The characterization of the relationships between spectroscopic and structural properties brings valuable information to the understanding of iron behavior in glasses. Group theory\* is used to describe the site geometry formed by an iron cation and its first coordination shell of oxygens (see Ludwig and Falter [1988] for a full introduction to group theory and Altmann and Herzig [1994] for point group tables).

In general, different coordination numbers lead to different point group symmetries, for example, an isolated atom will be in the spherical geometry ( $O_3$ ), a regular octahedron is described by the  $O_h$  group, and a regular tetrahedron by the  $T_d$  group. However, there is no bijective relation between coordination number and point group symmetry. For example, a triangular bipyramid ([5]-fold coordination) and a trigonal plane ([3]-fold coordination) have the same point group symmetry  $D_{3h}$  (see Figure 1.5-a).

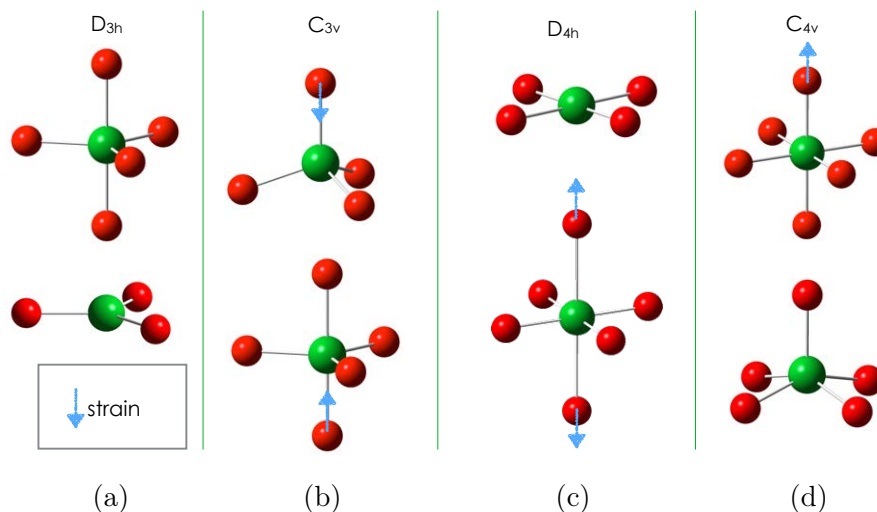


**Figure 1.5** – Coordination polyhedra and their associate point groups. The blue arrows represent strains leading to atomic shifts.

When a polyhedron is strained, the point group symmetry is lowered, which is characterized by a lower number of symmetry elements. In a regular tetrahedron or a trigonal bipyramid, when a ligand is moved along a  $C_3$  axis from its position in the regular geometry, both sites can be represented in  $C_{3v}$  (Figure 1.5-b).  $D_{4h}$  can be likewise related to a square plane or an octahedron compressed or stretched along a  $C_4$  axis (Figure 1.5-c). The last example is the  $C_{4v}$  geometry, which is associated to the square-based pyramidal geometry but could also be related to a distorted octahedron (Figure 1.5-d). The displacement of the central cation along a  $C_4$  axis also leads to the  $C_{4v}$  geometry. In conclusion, the coordination number is an interesting but incomplete information. On the contrary, a point group can

\*Schönflies notation is preferred to Hermann–Mauguin notation for point group naming (e.g.  $D_{4h}$  is preferred to  $4/mmm$ )



be associated with two or more coordination polyhedra, which can be discerned using the sign and magnitude of the crystal field parameters, as we will see in the Chapter 3.

## 1.4 Conclusion & Thesis statement

We saw that the study of iron in glass does not come without difficulties. Distortion and distribution of iron in a broad variety of sites complicate the definition of the environment. Moreover, the complexity of the problem is increased by the presence of iron in two redox states  $\text{Fe}^{2+}$  and  $\text{Fe}^{3+}$ , each with a proper distribution into more or less regular/distorted [4]-fold, [5]-fold and [6]-fold coordinated sites that could potentially segregate to form Fe-rich clusters instead of being isolated by their random distribution into the glass matrix.

Generally speaking, the links between chemical composition, redox, iron local environment (structure), and spectroscopic properties remain misunderstood. In order to simplify this complex question, we have chosen to study few simple silicate glass compositions, synthesized under different redox conditions, and measured with a broad panel of spectroscopic methods to extract information about the local environment around iron in soda-lime glasses.

Along this manuscript, a special focus is made on crossing and comparing the results from the different spectroscopies to improve the comprehension of the origins of optical absorption bands of iron in glass. A particular attention has been paid to the study of the valence  $3d$  orbitals of iron, which are involved in the chemical bond with its neighboring ligands and, thus, reflecting the Fe local environment.

Optical Absorption Spectroscopy (OAS) is an appropriate method since the energy range of optical photons is similar to the energy transitions between the different  $3d$  levels of iron. Electron Paramagnetic Resonance (EPR) has proven to be a sensitive technique to probe the environment of  $\text{Fe}^{3+}$  in iron-doped glasses, the absence of  $\text{Fe}^{2+}$  resonance is an asset to extract specific information about  $\text{Fe}^{3+}$  site-distortion and site-distribution. Results from X-ray Absorption Spectroscopy (XAS) will be presented such as X-ray Absorption Near Edge Structure (XANES), which is widely known to be chemically selective to specifically study one element (here iron). But other XAS methods that have never been used for glass will bring new grist to the mill: Resonant Inelastic X-ray Scattering (RIXS) and High Energy Resolution Fluorescence Detection (HERFD).

Theoretical calculations are powerful complementary tools to interpret spectroscopic data. We used the Ligand Field Multiplet (LFM), which is particularly adapted to the study of localized final states with multielectronic interactions as in  $3d$  orbitals. Strong efforts were made to improve LFM calculations in order to reproduce and interpret experimental data with this multielectronic simulation method, which is particularly adapted to probe transition metal valence  $d$ -electrons. LFM brings indirect structural information since it is intimately related to the point group symmetry of the iron site. Emphasis will be done on finding a unique set of parameters that enables to calculate all spectroscopic data.

## Chapter 2

# Samples and experimental methods

## 2.1 Glasses

### 2.1.1 Choice of the glass set

90% of manufactured glass is soda-lime silicate glasses, especially, 40% of the production is float glass, mainly used in construction (80%), automotive (15%), and solar (5%) industries\*. In 2009, flat glass production was about 52 million metric tonnes per year<sup>†</sup>, therefore, every optimization of the production has an important economic impact.

Authentic industrial glasses are complex systems using about 10 to 15 oxides in various proportions depending on the desired application, but the number of glass compositions is infinite. Nevertheless, for float glass, 98 mol% of the constituents are SiO<sub>2</sub>, MgO, CaO and Na<sub>2</sub>O. Model compositions, made of these four oxides and close to industrial soda-lime glasses will be studied in details in this manuscript. Their nominal molar compositions are: 16Na<sub>2</sub>O–10RO–74SiO<sub>2</sub>, where R is an alkaline-earth ion. The absence of magnesium in glass, is empirically known to improve the optical transmission window in the visible, which is a key property for float glass applications. The amount of silicon and sodium oxides was kept constant in the soda-lime glass and part of the calcium was replaced by magnesium. Particular attention will be devoted to the effect of alkaline earth nature on iron behavior.

To study the effect of sodium, we looked at an alkali-free glass based on diopside mineral (CaMgSi<sub>2</sub>O<sub>6</sub>) with the composition: 50SiO<sub>2</sub>–25CaO–25MgO in molar proportion. The corresponding glass exhibits singular properties and iron-doped diopside gives exotic optical absorption spectra due to different local environments around iron [Calas and Petiau, 1983b].

The total iron content was maximized to optimize the signal to noise ratio from the different analytical methods and spectroscopies, an upper limit of ~0.5 wt% of Fe<sub>2</sub>O<sub>3</sub> (5000 ppm) was chosen to stay close to industrial glass compositions and properties.

To limit the side effects on properties due to the presence of other chemical compounds, all the presented glasses are free from aluminum, potassium and boron that are often used

---

\*<http://www.glassforeurope.com/>

<sup>†</sup>Pilkington and the Flat Glass Industry 2010, NSG Group

in industrial float glass. These glasses are also free from other coloring elements, especially other transition metals that could interact with iron such as titanium [Burns, 1981], [Taran and Koch-Müller, 2011].

### 2.1.2 Sample preparation

Glasses listed in Table 2.1 were synthesized in AGC research center, Yokohama, Japan, using reagent-grade materials ( $\text{Fe}_2\text{O}_3$ ,  $\text{SiO}_2$ ,  $\text{Na}_2\text{CO}_3$ ,  $\text{MgO}$  and  $\text{CaCO}_3$ ). The major component is silica (silicon dioxide:  $\text{SiO}_2$ ).  $\text{Na}_2\text{O}$  is added using soda (sodium carbonate:  $\text{Na}_2\text{CO}_3$ ),  $\text{CaO}$  is added using lime (calcium carbonate:  $\text{CaCO}_3$ ),  $\text{MgO}$  is added using magnesium oxide ( $\text{MgO}$ ). Iron(III) oxide ( $\text{Fe}_2\text{O}_3$ ) was used to intentionally add iron. However, raw materials contain iron as an impurity leading to contamination of about 100 ppm of  $\text{Fe}_2\text{O}_3$  (0.01 wt%).

**Table 2.1** – Nominal compositions of the silicate glasses set with and without iron. mol% and wt% are expressed as oxides (e.g.  $\text{Na}_2\text{O}$ ), at% are expressed as atomic percent (e.g. Na). Oxides percentages are aligned to the left while atomic percentages are aligned to the right.

#### Sodium Calcium Silicate (NCS) or Soda-Lime (SL)

name		$\text{SiO}_2$ / Si	$\text{Na}_2\text{O}$ / Na	$\text{CaO}$ / Ca	$\text{MgO}$ / Mg	$\text{Fe}_2\text{O}_3$ / Fe	- /	O	Total
<b>NCS00</b>	(mol%)	74	16	10	-	-	-		100
	(wt%)	74.12	16.53	9.35	-	-	-		100
	(at%)	25.52	11.03	3.45	-	-	-	60.00	100
<b>NCS05</b>	(mol%)	73.86	15.97	9.98	-	0.1884	-		100
	(wt%)	73.75	16.45	9.30	-	<b>0.5000</b>	-		100
	(at%)	25.43	11.00	3.44	-	0.1298	-	60.00	100

#### Sodium Calcium Magnesium Silicate (NCMS) or Soda-lime-magnesium (SLM)

name		$\text{SiO}_2$ / Si	$\text{Na}_2\text{O}$ / Na	$\text{CaO}$ / Ca	$\text{MgO}$ / Mg	$\text{Fe}_2\text{O}_3$ / Fe	- /	O	Total
<b>NCMS00</b>	(mol%)	74	16	5	5	-	-		100
	(wt%)	75.11	16.75	4.74	3.40	-	-		100
	(at%)	25.52	11.03	1.72	1.72	-	-	60.00	100
<b>NCMS05</b>	(mol%)	73.86	15.97	4.99	4.99	0.1859	-		100
	(wt%)	74.73	16.67	4.71	3.39	<b>0.5000</b>	-		100
	(at%)	25.44	11.00	1.72	1.72	0.1281	-	60.00	100

#### Sodium Magnesium Silicate (NMS) or Soda-magnesium (SM)

name		$\text{SiO}_2$ / Si	$\text{Na}_2\text{O}$ / Na	$\text{CaO}$ / Ca	$\text{MgO}$ / Mg	$\text{Fe}_2\text{O}_3$ / Fe	- /	O	Total
<b>NMS00</b>	(mol%)	74	16	-	10	-	-		100
	(wt%)	76.12	16.98	-	6.90	-	-		100
	(at%)	25.52	11.03	-	3.45	-	-	60.00	100
<b>NMS05</b>	(mol%)	73.86	15.97	-	9.98	0.1835	-		100
	(wt%)	75.74	16.89	-	6.87	<b>0.5000</b>	-		100
	(at%)	25.44	11.00	-	3.44	0.1264	-	60.00	100

#### Diopside (DIO): $\text{CaMgSi}_2\text{O}_6$ or Alkali-free (AF)

name		$\text{SiO}_2$ / Si	$\text{Na}_2\text{O}$ / Na	$\text{CaO}$ / Ca	$\text{MgO}$ / Mg	$\text{Fe}_2\text{O}_3$ / Fe	- /	O	Total
<b>DIO00</b>	(mol%)	50	-	25	25	-	-		100
	(wt%)	55.49	-	25.90	18.61	-	-		100
	(at%)	20.00	-	10.00	10.00	-	-	60.00	100
<b>DIO05</b>	(mol%)	49.92	-	24.96	24.96	0.1701	-		100
	(wt%)	55.21	-	25.77	18.52	<b>0.5000</b>	-		100
	(at%)	19.93	-	9.97	9.97	0.1358	-	60.00	100

Figure 2.1 shows an example of the total iron content effect in diopside glass. With 0.5 wt% the coloration is already intense and can be easily studied by optical absorption spectroscopy.



**Figure 2.1** – Effect of iron content on diopside glass at 0.01, 0.1 and 0.5 wt% Fe<sub>2</sub>O<sub>3</sub> (size: ~2 cm, thickness: 5.5 mm).

In all protocols, powders were weighted to obtain the desired amount of batch and mechanically mixed without grinding. No decarbonation step was done in order to enhance bubble mixing during melting.

For a given composition, it is possible to adjust the synthesis conditions in order to change the properties of a glass. The iron redox ( $R = \frac{[Fe^{2+}]}{[Fe^{2+}] + [Fe^{3+}]}$ ) has a major effect on the glass properties (see Section 1.2). Figure 2.2 illustrates the impact of redox on color; for glasses with the same soda-lime composition (NCS): the color evolves from yellow (pure ferric) to blue (pure ferrous) with intermediate green color for a mixture of both valence states.



**Figure 2.2** – Soda-lime silicate glasses (NCS) at three different redox states (oxidized, air synthesized, reduced), sample thickness: 2.5 mm.

To control the redox state, two parameters were mainly modified, the atmospheric composition and the temperature. It is known that oxygen-rich and lower temperature favors oxidation of glass [Johnston, 1964; Kress and Carmichael, 1991]. Regarding these properties, three synthesis conditions were developed.

- oxidizing conditions, to make “Ox” glasses with a redox  $R \sim 5\%$ ;
- ambient conditions, i.e. under air atmosphere, to make medium “Med” glasses with a redox  $R \sim 25\%$ ;
- reducing conditions, to make “Red” glasses with a redox  $R \sim 99\%$ .

**Oxidizing conditions: synthesis under oxygen atmosphere**

The aim of this treatment proposed by Johnston [1964] is to make a glass sample with only ferric iron (0% Fe<sup>2+</sup>) without using any oxidizing agent, such as arsenic (As<sub>2</sub>O<sub>3</sub>), antimony (Sb<sub>2</sub>O<sub>3</sub>) or cerium (CeO<sub>2</sub>) [Stålhandske, 2000].

A tubular furnace under oxygen atmosphere (O<sub>2</sub> flux: 1 L/min) set to 1200°C was used to melt 5 g of batch in a Pt crucible during at least 24 h and up to 72 h. A long melting

time is necessary to reach thermodynamic equilibrium due to the slow oxygen diffusion process into the glass matrix [Pigeonneau and Muller, 2013]. The heating was performed at 200°C/h and the cooling at 150°C/h. Glasses were not annealed to avoid any reduction. Traces of O–H groups are detected in the samples because the furnace is not isolated from the atmosphere containing water.

The oxidized diopside glass was not synthesized due to crystallization problems, this composition does not melt under 1450°C and can easily devitrify. Below 1200°C, glasses are not homogenous and a higher temperature favors reduction process [Paul, 1985]. It was not possible to avoid remaining  $\text{Fe}^{2+}$ , and redox are at least 4% without using a refining agent such as cerium oxide ( $\text{CeO}_2$ ) [Bingham et al., 2014].

#### **Ambient conditions: synthesis under air atmosphere**

Glasses synthesized under air atmosphere have an intermediary redox and are therefore named “medium” glasses. The furnaces were not air-controlled, the partial pressures of water, carbon dioxide and oxygen could slightly vary from one synthesis to another.

400 g of batch was melted in three times to avoid foam overflow, then stirred at 1500°C for 1 h in a Pt crucible under air atmosphere. The glass was rapidly cooled by quenching onto a carbon plate edged with steel, preheated at 120°C to avoid intense thermal shock stress. Right after this cooling, the glass was annealed at 480°C (below  $T_g$ , see Table 2.2) for 1 h to relieve internal stress. Finally, the glass was slowly cooled down to room temperature at 1°C/min.

#### **Reducing conditions: synthesis under nitrogen atmosphere**

This process was used to obtain 5 g of glass with only ferrous iron (redox state close to 100%  $\text{Fe}^{2+}$ ). The oven was located in a glove box under nitrogen atmosphere (only  $\text{N}_2$  without additional  $\text{H}_2$ ). Samples were melted without stirring in graphite crucibles at 1550°C during 1 h, then progressively cooled down to 1200°C in 1 h. At 1200°C, the crucible was removed from the oven and cooled down under  $\text{N}_2$  without quenching. Glasses were not annealed to avoid any oxidation. No carbon powder or reducing agent was added to the batch.

For the diopside composition, due to the low viscosity of this glass, all tested melting temperatures lead to opaque black glasses. This side-effect of carbon crucibles constrains the synthesis of alkali-free glass (AF) in a platinum crucible, thereby the redox of this glass is not so high than soda-lime glasses set (see Table 2.2).

**Sample naming conventions:**

The three sodium-silicate glasses are named sodium-calcium-silicate (NCS) or soda-lime (SL), sodium-magnesium-silicate (NMS) or soda-magnesium (SM) and sodium-calcium-magnesium-silicate (NCMS) or soda-lime-magnesium (SLM) regarding their Ca:Mg ratio (respectively 100:0, 0:100 and 50:50). The diopside (DIO) glass is also named alkali-free (AF) due to its lack of sodium.

wt%  $\text{Fe}_2\text{O}_3$  is used to express the total iron content, and glass samples are named using this percentage. For example, the diopside glasses (DIO) with 0.01, 0.1 and 0.5 wt% are respectively named DIO00, DIO01 and DIO05.

Samples are named regarding their synthesis conditions, for example, glasses of the soda-lime composition with 0.5 wt%  $\text{Fe}_2\text{O}_3$  (NCS05) are respectively named NCS05Ox, NCS05Med and NCS05Red for oxidized ( $R \sim 5\%$ ), medium ( $R \sim 25\%$ ) and reduced ( $R \sim 99\%$ ).

**2.1.3 Characterization**

This section presents basic properties of glass bulk, i.e. chemical composition, refractive index, density and iron redox.

**Composition and homogeneity (EMPA, XRD)**

Composition and homogeneity were checked using electron microprobe analyzers (EMPA), CAMECA SXFive and SX100, at the Camparis Facility (Université Pierre et Marie Curie, Paris, France). Analyses were performed with a 15 kV accelerating voltage and a 4 nA sample current. All results and nominal compositions were converted in wt% of oxides. A good agreement was observed between nominal and experimental compositions. With a number of data points from 10 to 50 with EMPA, low standard deviations suggest a good sample homogeneity.

X-ray diffraction (XRD) was used to confirm the vitreous nature of the glasses, which do not exhibit any Bragg peaks, characteristic of crystalline phases.

**Redox measurement (wet chemistry)**

The amount of FeO and total iron was determined by wet chemical analysis based on a standard test method [C14 Committee, 2011]. To summarize, the glass is dissolved with hydrofluoric acid (HF) and  $\text{Fe}^{2+}$  forms a complex with o-phenanthroline. The FeO and total iron content are estimated using the optical absorption band of the complex at 510 nm as described in Fortune and Mellon [1938].

Table 2.2 presents the measured redox of the 11 samples. The uncertainty is  $\pm 3\%$ . These results will be discussed in light of X-ray absorption spectroscopy, optical absorption spectroscopy and EPR along Chapter 5 and in Appendix B.4.2 that presents a method, developed during this thesis, to estimate the  $\text{Fe}^{2+}/\text{Fe}_{\text{tot}}$  ratio using the separation of  $\text{Fe}^{2+}$  and  $\text{Fe}^{3+}$  optical contributions.

	SiO <sub>2</sub>	Na <sub>2</sub> O	CaO	MgO	Fe <sub>2</sub> O <sub>3</sub>	Total	wet chem redox (%)	density (kg/L)	refractive index	optical basicity	Tg(°C)
NCS05Med	73.89 (0.73)	15.73 (0.37)	9.47 (0.23)	0.01 (0.01)	0.52 (0.02)	99.61 (0.56)	27.8	2.4888	1.519		
NCS05Ox	75.43 (0.50)	15.99 (0.40)	8.26 (0.31)	0.00 (0.00)	0.54 (0.004)	100.23 (0.43)	6.4		1.515		
NCS05Red	74.32 (0.80)	15.61 (0.44)	9.35 (0.33)	0.00 (0.00)	0.51 (0.02)	99.79 (0.58)	96.8		1.517		
Nominal	73.75	16.45	9.3	0	0.5	100				0.6392	495
NCMS05Med	75.78 (1.18)	16.05 (0.51)	4.54 (0.23)	3.31 (0.31)	0.52 (0.03)	100.17 (0.84)	25.3	2.4569	1.511		
NCMS05Ox	77.32 (0.56)	15.89 (0.10)	4.43 (0.17)	2.84 (0.10)	0.52 (0.003)	100.99 (0.59)	4.9		1.510		
NCMS05Red	74.50 (0.68)	16.37 (0.65)	4.97 (0.16)	3.67 (0.16)	0.55 (0.04)	100.05 (0.61)	96.1		1.511		
Nominal	74.73	16.67	4.71	3.39	0.5	100				0.6282	515
NMS05Med	75.62 (0.96)	16.77 (0.43)	0.01 (0.01)	7.03 (0.21)	0.51 (0.03)	99.93 (0.88)	23.9	2.4194	1.503		
NMS05Ox	75.69 (0.47)	17.61 (0.28)	0.00 (0.00)	7.00 (0.16)	0.56 (0.01)	100.87 (0.46)	6.5		1.505		
NMS05Red	75.45 (0.91)	17.04 (0.37)	0.02 (0.03)	7.19 (0.20)	0.52 (0.02)	100.19 (0.88)	96.4		1.502		
Nominal	75.74	16.89	0.0	6.87	0.5	100				0.6172	535
DIO05Med	54.26 (0.55)	0.02 (0.02)	24.92 (0.30)	20.45 (0.46)	0.47 (0.01)	100.17	45.7	2.8450	1.617		
DIO05Red	55.25 (0.62)	0.00 (0.00)	25.37 (0.51)	18.54 (0.30)	0.45 (0.01)	99.36	79.5		1.611		
Nominal	55.21	0	25.77	18.52	0.5	100				0.6850	730

**Table 2.2** – EMPA measurements (in wt%) and nominal composition (converted in wt%), standard deviations of each element are in parenthesis. Redox measurements:  $\text{Fe}^{2+}/\text{Fe}_{\text{tot}}$  (in %) from wet chemical analysis (incertitude of 3%). Density ( $\rho$  in kg/L) were measured for the 3 sodium-silicate glasses, diopside density is taken from Richet et al. [1986]. Experimental refractive indexes ( $n$ ) averaged for all glasses with the same composition (precision  $\pm 0.001$ ). Theoretical optical basicity are calculated according to Duffy and Ingram [1976]. Glass transition temperatures ( $T_g$ ) are averaged over measured values with a TGA-DSC device and published  $T_g$  values.

## Refractive indexes

Refractive indexes were measured at INSP (Université Pierre et Marie Curie, Paris, France) using an Abbe refractometer with diiodomethane  $\text{CH}_2\text{I}_2$ , a liquid with high refractive index ( $n = 1.741$ ), at the interfaces with the prisms. Measures were performed with a sodium lamp at the wavelength  $\lambda = 589.3$  nm. There was no significant variation of the refractive index within a set of glasses with the same composition and different small total iron amounts ( $< 0.5$  wt%) or redox. Precision of  $\pm 0.001$  on the refractive index value is estimated from standard deviation of the bench of six measures and compared with results from AGC obtained using a V-block refractometer and a prism coupler refractometer.

### 2.1.4 Summary

Table 2.2 summarized the chemical compositions, redox states, refractive indexes, densities and optical basicities of the 11 glasses studied. The present set of samples composed with three similar sodium-alkaline earth silicate glasses (NCS, NCMS and NMS) and an alkali-free (AF) glass with the diopside (DIO) composition will be used in the next chapters to study the influence of composition on the local environments of  $\text{Fe}^{2+}$  and  $\text{Fe}^{3+}$ . Especially, the influence of magnesium and sodium on iron in sodium-silicate glasses. The extreme redox values obtained for these glasses will be helpful for studying the effect of redox state. However, we have to keep in mind that changing synthesis conditions can modify the  $\text{Fe}^{2+}:\text{Fe}^{3+}$  ratio, but could also change the speciation of  $\text{Fe}^{2+}$  and  $\text{Fe}^{3+}$ .

## 2.2 Optical absorption spectroscopy

Optical properties of iron have been widely studied, especially the coloring properties as explained in a recent review on the question [Rossman, 2014]. The interpretation of optical absorption signatures is related to electronic transitions between  $d$ -levels split by the ligand field. Since the energy splittings of the  $3d$  orbitals by the surrounding ligands have the same order of magnitude than energies of optical photons, optical absorption spectroscopy is a suitable probe to understand the local environment and speciation of transition metal ions.

Optical absorption spectroscopy, also named “UV-Visible\*-NIR” spectroscopy, measures the absorption of light as a function of wavelength ( $\lambda$  in nm), wavenumber ( $\bar{\nu}$  in  $\text{cm}^{-1}$ ) or electron-volt (eV)<sup>†</sup> in the energy range 0.5–6 eV (i.e. 4000–50 000  $\text{cm}^{-1}$ ).

### 2.2.1 Transmission measurements

Optical absorption measurements presented here have been carried out on a Perkin-Elmer<sup>®</sup> Lambda 1050 UV-Visible-NIR spectrophotometer in transmission mode using three detectors and two light sources (see Appendix B.1 for more details) to cover a wide wavelength ( $\lambda$ ) range with a 1 nm step. The measured spectral range is spanned from ultraviolet (180 nm) to near-infrared (3300 nm) region.

---

\*energy range of visible photons: 380–750 nm, 27 000–13 000  $\text{cm}^{-1}$ , 3.3–1.6 eV

<sup>†</sup>nm are used for experimental setup, but “energy” unit  $\text{cm}^{-1}$  or eV are used for results (1 eV = 8066  $\text{cm}^{-1}$ )



The experimental transmission  $T$  is the ratio between the intensity  $I$  passing through the sample and the intensity  $I_0$  of a reference beam.

$$T = \frac{I}{I_0} \quad (2.1)$$

Transmittance  $\%T$  (in %) is related to absorbance by these relations:

$$\%T = 100 \cdot 10^{-A} \quad \text{and} \quad A = \log_{10} \left( \frac{100}{\%T} \right) \quad (2.2)$$

Absorbance  $A$  is usually preferred to transmittance since it is directly proportional to the intrinsic capacity of a material to absorb light, characterized by the molar absorption coefficient  $\varepsilon$  in  $\text{L}\cdot\text{mol}^{-1}\cdot\text{cm}^{-1}$ . The measured absorbance  $A$  is related to  $\varepsilon$  by the Beer-Lambert law:

$$A(\lambda) = bkg(\lambda) + \alpha(\lambda) \cdot l = bkg(\lambda) + \varepsilon(\lambda) \cdot c \cdot l \quad (2.3)$$

where  $\alpha$  is the linear absorption coefficient ( $\text{cm}^{-1}$ ),  $\varepsilon$  the molar absorption coefficient ( $\text{L}\cdot\text{mol}^{-1}\cdot\text{cm}^{-1}$ ),  $bkg$  is the background signal,  $l$  the path length (cm) and  $c$  the molar concentration ( $\text{mol}\cdot\text{L}^{-1}$ ) of absorbing species in the material. Optical absorption spectrum resulting from light beam passes throughout the transparent sample is the sum of the intrinsic properties of the sample  $\varepsilon$  and of the physical phenomena disturbing the measurement  $bkg(\lambda)$ .

### 2.2.2 Background correction

The origin of the optical absorption background in the optical spectrum can be due to several physical processes, such as:

- scattering processes
- specular reflection on the surface
- tail of the charge transfer band in the UV

Scattering can be caused by volume defects (bubbles, composition inhomogeneities, impurities...) or surface defects (scratches, polishing imperfections...). To eliminate the scattering defects of  $bkg(\lambda)$ , sample homogeneity and surface roughness have been controlled by a careful synthesis and polishing process. In the present study, the particular care devoted to the sample preparation allowing us to neglect this phenomenon.

However, there is always specular reflection of the beam on the faces  $r(\lambda)$  due to the difference of refractive index between air and glass. By using parallel faces and normal incidence, the transmission coefficient is given by the following equation:

$$t(n) = 1 - r(n) \quad (2.4)$$

where  $t(n)$  is the transmittance and  $r(n)$  is the reflectance. Using Fresnel equations for

normal incidence, the reflectance is directly linked to the refractive index  $n(\lambda)$ :

$$r(n) = \left( \frac{n - 1}{n + 1} \right)^2 \quad (2.5)$$

For a soda-lime silicate glass, the refractive index at  $\lambda = 589.3 \text{ nm}$  is  $n = 1.52$  (see Table 2.2), reflection coefficient  $r$  is therefore around 4.26% and transmission coefficient  $t$  is 95.74%.

Considering a parallel-sided glass plate with multiple internal reflections, total transmittance can be expressed as:

$$\%T = \frac{t}{2 - t} \quad (2.6)$$

For a soda-lime silicate glass, the resulting transmitted energy is found equal to 91.83%. Using absorbance scale (Equation 2.2), the fraction of the absorption signal due to reflection is estimated to be 0.037.

In a first approximation, this constant can be subtracted to the absorption spectra in order to calculate the molar absorption coefficient. However, following Equation 2.3, glass is a dispersive medium, which means that the refractive index varies with wavelength.

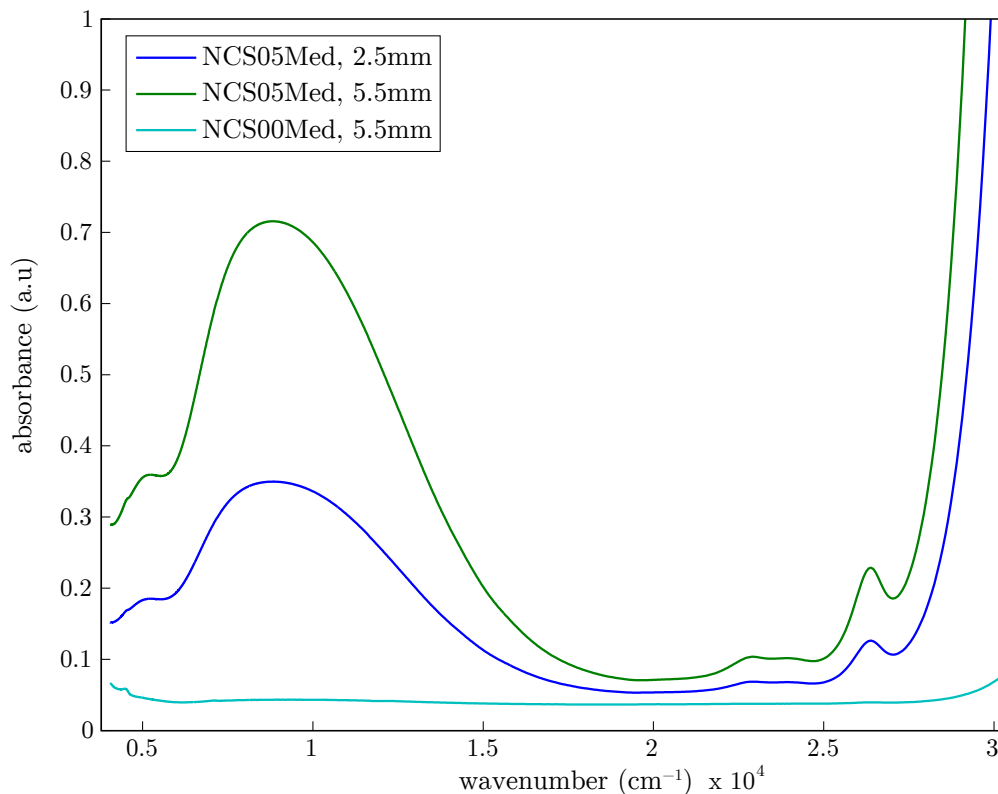


**Figure 2.3** – Absorbance of NCS05Med and NCS00Med before background subtraction.

Since background correction depends on the wavelength, the following experimental approach was used to estimate the absorption background. For each composition (here results for soda-lime (NCS) are presented), two glasses were considered, they were of different

thickness (respectively 2.5 mm and 5.5 mm), from the same piece of glass, NCS05Med, which contains 0.5 wt% of  $\text{Fe}_2\text{O}_3$  and intermediate redox (Med).

The absorption difference between the two equally doped samples of 2.5 and 5.5 mm-thick gives the equivalent spectrum of a 3 mm-thick sample corrected from surface defects and part of the volume defects (see Equation 2.7). If the volume defects such as scattering phenomena are considered insignificant, the remaining signal corresponds to the reflection background.

$$y = y_{NCS05Med_{2.5mm}} - (y_{NCS05Med_{5.5mm}} - y_{NCS05Med_{2.5mm}}) * \frac{2.5}{3} \quad (2.7)$$

Figure 2.4 shows the optical absorption spectrum of NCS05Med accompanied by the absorbance of the extracted background in green that was fitted from  $15\,000\text{ cm}^{-1}$  to  $25\,000\text{ cm}^{-1}$  with a linear function of the wavenumber (yellow curve).

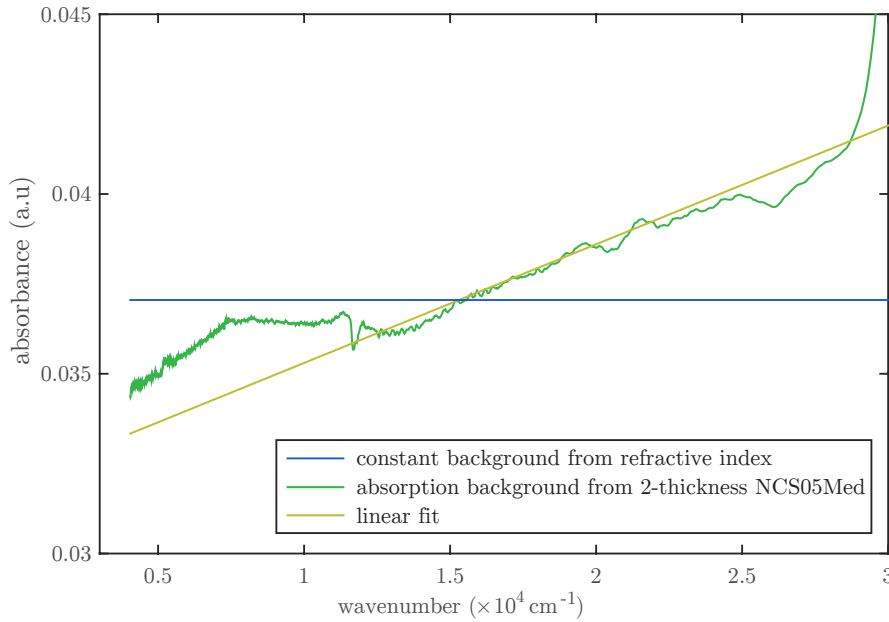


**Figure 2.4** – Background estimation of NCS05Med.

A linear function of the wavenumber with only two parameters is an adequate choice to represent the spectral background regarding the variability induced by the samples and experimental setup. This signal (Table 2.3) was subtracted from the three redox samples (Red, Med and Ox) of the same composition.

**Table 2.3** – Parameters of the linear function of the wavenumber ( $y = a\bar{\nu} + b$ ) used to correct the background of glasses containing 0.5 wt%.

Sample	a (cm)	b ( $\text{cm}^{-1}$ )
NCS05	$2.136 \cdot 10^{-7}$	$3.416 \cdot 10^{-2}$
NCMS05	$3.256 \cdot 10^{-7}$	$3.134 \cdot 10^{-2}$
NMS05	$1.279 \cdot 10^{-7}$	$3.352 \cdot 10^{-2}$
DIO05	0	$4.587 \cdot 10^{-2}$

## 2.3 X-ray Absorption Spectroscopy (XAS)

### 2.3.1 Principle

X-ray Absorption Spectroscopy (XAS) is a core-shell spectroscopy used in this thesis at the Fe  $K$  edge to study the  $1s \rightarrow 3d$  or  $1s \rightarrow (3d, 4p)$  transitions of the absorbing element. This method\* is chemically selective and can bring information on the local environment (i.e. distances, symmetry, structural disorder, nature and numbers of neighbors in a radius of 4–5 Å) and the electronic structure (i.e. redox state, inter- or intra-site hybridization between  $p$  and  $d$  orbitals).

The principle is to excite a core-electron ( $1s$ ) to the first empty states with an incident X-ray photon of a given energy  $E_{in}$ . Depending on  $E_{in}$ , different physical events lead to different structures in the measured absorption spectrum (Figure 2.5).

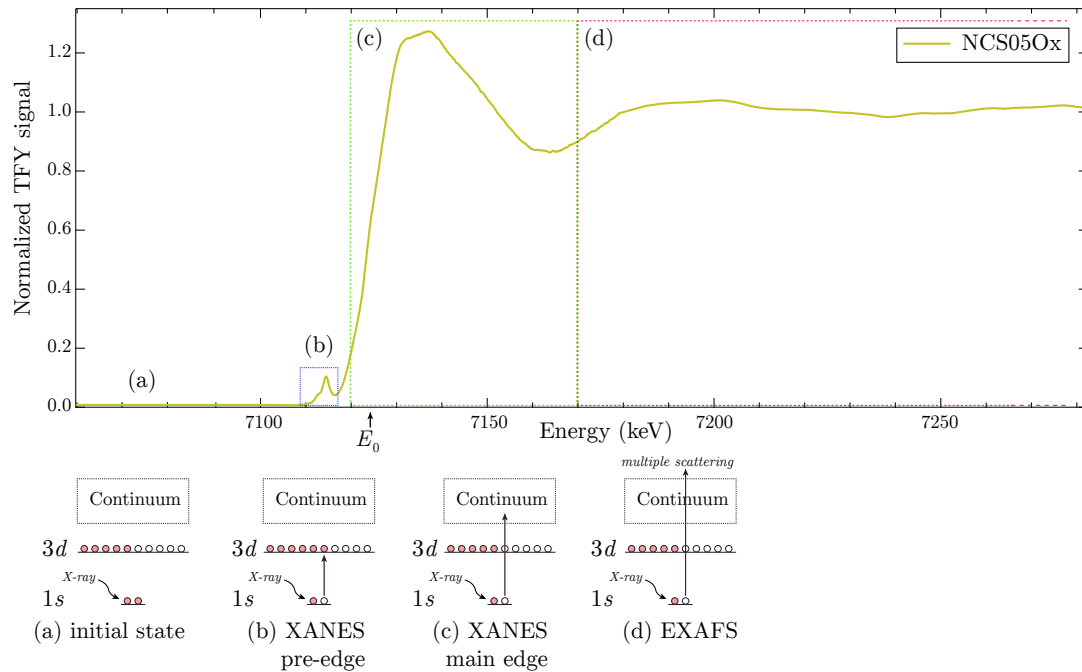


**Figure 2.5** – The different regions of a XAS spectrum (here, the Fe  $K$  edge spectrum of NCS05Ox glass).

#### $K$ pre-edge

In the pre-edge range (Figure 2.5-b), the energy of the incident photon  $E_{in}$  is lower than the main edge energy ( $E_0 \sim 7123$  eV). However, this energy is sufficient to transfer a  $1s$  core-electron to the first open shells because the incident photon energy is higher than the  $1s$  binding energy (7112 eV for the Fe  $K$  edge).  $3d$  levels are localized on the absorbing element. The pre-edge is essentially described by two phenomena: (i) the local electric quadrupole transitions  $1s \rightarrow 3d$ ; (ii) the local electric dipole transitions  $1s \rightarrow 4p$ , where the  $4p$  levels of the absorbing element are hybridized with the empty  $3d$  states [Arrio et al., 2000]. The  $3d$ – $4p$  mixing<sup>†</sup> is only allowed for a non-centrosymmetric site in absence of inversion center [Brouder, 1990; Westre et al., 1997] or by the atomic displacement of the

\*For a full introduction to XAS, the reader can refer to Calvin [2013].

<sup>†</sup>Do not confuse the local (*on-site*) electric dipole transitions,  $1s \rightarrow 4p$ , with the non-local (*off-site*) electric

absorbing element induced by vibrations [Cabaret et al., 2010]. Therefore, as in optical absorption spectroscopy, these transitions are sensitive to the valence state, coordination number, symmetry and orbital hybridization.

### **XANES at $K$ edge**

The  $K$  edge range or XANES (X-ray Absorption Near Edge Structure) corresponds to an incident energy in the first 50 eV above the ionization energy  $E_0$ . A  $1s$  electron is ejected to the continuum with a low kinetic energy. Therefore, the mean free path of the electron is large enough for the electron to be involved in multiple scattering processes with neighboring atoms.

However, to analyze the rich but complex information of XANES spectra the support of XANES calculation is often needed. In the case of glasses, the extraction of information from the medium-range structure remains a challenging step. In the framework of this thesis, XANES spectra above the  $K$  edge will be interpreted using a simple fingerprint analysis.

### **EXAFS**

The EXAFS (Extended X-ray Absorption Fine Structure) region corresponds to an incident energy larger than 50 eV above the edge energy. The core electron is ejected in the continuum with a large kinetic energy. Therefore, its mean free path is small and the electron is essentially involved in simple scattering process with neighboring atoms. The oscillations are visible in this energy range on experimental data due to interferences between the electronic wave from the absorber ion and the waves backscattered by neighboring atoms. The analysis of these EXAFS oscillations allows extracting average information about the nature and number of neighbors, the first absorber-neighbors distances and the structural disorder around the absorber atom in the sample. EXAFS have not been performed during this thesis; however, results from previous papers will be used for the interpretation of spectroscopic data.

## **2.3.2 Experiment**

Measurements have been performed on ID26 beamline at the European Synchrotron Radiation Facility (ESRF) in Grenoble (France), during two sessions of 4 days in February 2013 and February 2015.

All the data have been collected with a Si(311) monochromator and detection was performed in fluorescence mode with an angle of  $90^\circ$  between incident beam and fluorescence beam (Figure 2.6). The polarization of the incident beam was always linear and horizontal.

In this thesis, the Total Fluorescence Yield (TFY) is considered equal to the XAS measured in transmission when the concentration of the absorbing element is low [Jaklevic et al., 1977]\*. Above a threshold of  $\sim 1$  wt%, samples were ground into a fine powder and mixed with boron nitride or cellulose to reach a  $\sim 1$  wt% dilution. Otherwise, self-absorption phenomenon can happen in fluorescence mode, which could compress the first

---

dipole transitions,  $1s \rightarrow p$ , in which the empty  $4p$  levels of the absorber are mixed with those of the nearest-neighbor metal atoms, via the  $2p$  orbitals of the ligands [Glatzel and Juhan, 2013, p. 126].

\*This assumption, is not true for the  $L_{2,3}$  edges due to the opening of inelastic decay channels as explained by Kurian et al. [2012] or Tröger et al. [1992].

XANES oscillations decrease the whiteline intensity leading to a more intense measured pre-edge intensity than expected (but with the same shape). The absence of self-absorption phenomenon was verified with *ATHENA* (fluo package) and *PyMca* (XAS self-attenuation correction). And XANES spectra of crystalline compounds have been compared with results from Wilke et al. [2001] and Jackson et al. [2005] when available. In this study, none of the glass were ground because they are considered as diluted and only crystalline compounds were prepared as powders.

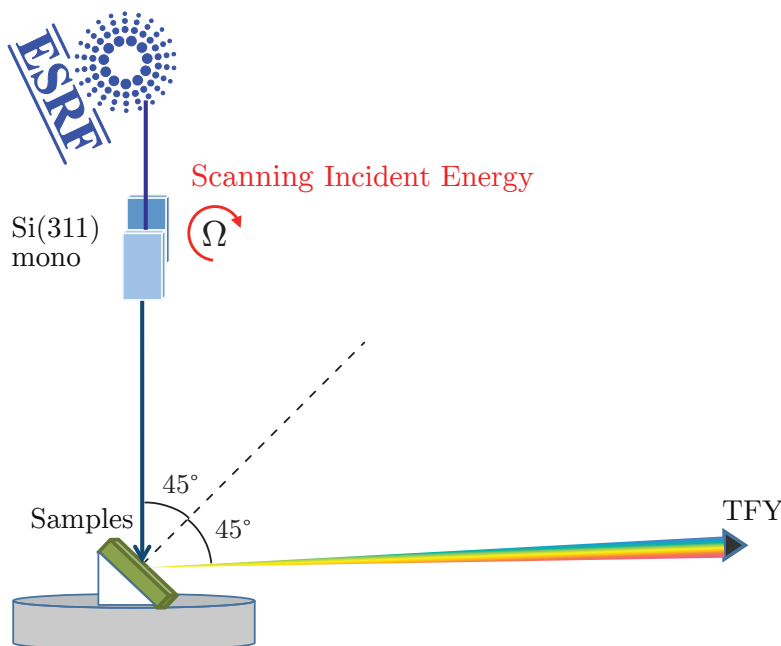


**Figure 2.6** – Setup of XAS experiment.

For each sample, several spectra were measured:

- in the pre-edge region with a 0.05 eV step from 7108 to 7123 eV, 1 minute duration each (~60 spectra)
- in the XANES region with a 0.05 eV step from 7105 to 7180 eV, 2 minutes duration each (2 to 5 spectra)
- in the EXAFS region with a 1 eV step, 7000 to 7550 eV, 1 minute duration each (1 or 2 spectra)

### 2.3.3 Data processing

Spectra were extracted with *PyMca* software [Solé et al., 2007]. Using *Matlab*<sup>®</sup>, all spectra of the same kind were averaged, then the pre-edge spectra were merged onto the XANES and the XANES onto the EXAFS. A Savitzky-Golay noise reduction was applied. Spectra were then normalized to the edge jump using *ATHENA* software [Ravel and Newville, 2005]. The pre-edge was extracted by subtracting an arctangent function used to fit the edge tail.

## 2.4 RIXS and HERFD

### 2.4.1 Principle

In order to improve the XAS measurement and obtained high-resolution data, the fluorescence signal can be monochromatized using analyzer crystals. This method is called Resonant Inelastic X-ray Scattering (RIXS) spectroscopy\*, in which both incident  $\Omega$  and emitted  $\omega$  energies are simultaneously scanned. This two-photon process is illustrated in Figure 2.7, and resulting measures are plotted as 3D graph (see an example below, Figure 2.9). There are the two ways to represent RIXS maps:  $(\Omega, \omega)$  or  $(\Omega, \Omega - \omega)$ , where the x-axis is the incident energy, the y-axis is the emitted energy  $\omega$  or the energy transfer  $\Omega - \omega$ , respectively, and the z-axis is the intensity relatively to the number of emitted photons [Glatzel and Bergmann, 2005]. The representation adopted here, will be the second one  $(\Omega, \Omega - \omega)$ .

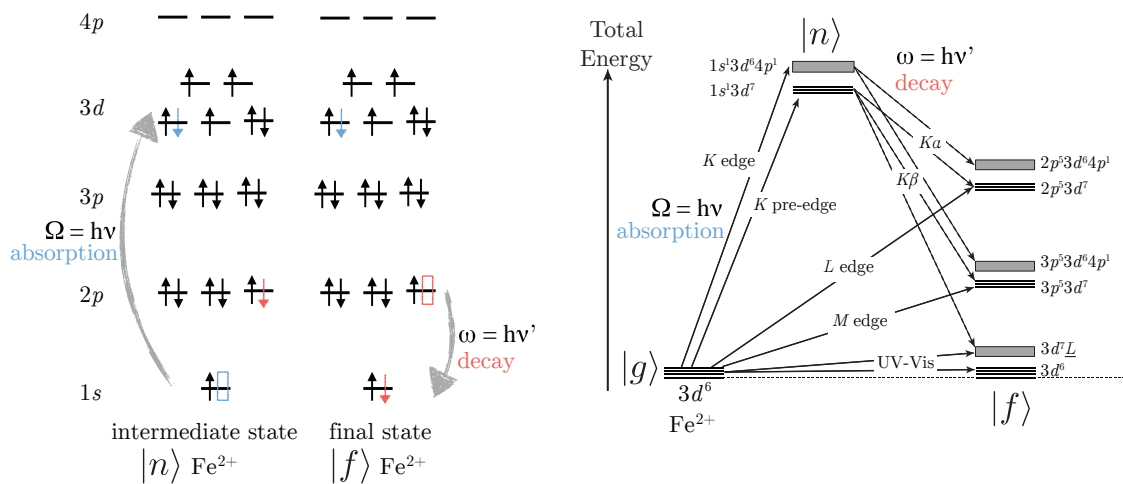


**Figure 2.7** – Mono-electronic picture (left) and multi-electronic picture (right) of  $\text{Fe}^{2+}$  electronic transitions involved in the RIXS spectroscopy.  $\Omega$  is the absorption energy,  $\omega$  the emitted energy and  $\Omega - \omega$  the energy transfer.

A 1D cut of the RIXS plane (at a given emitted energy) is called a High-Energy Resolution Fluorescence Detected X-ray Absorption Spectroscopy (HERFD-XAS or simply HERFD). HERFD-XAS differs from TFY-XAS, i.e. conventional X-ray absorption spectroscopy of the total fluorescence yield, because the peak broadening is smaller and the number of peaks and the intensity ratios may vary.

\*More information can be found in these reviews: Rovezzi and Glatzel [2014]; de Groot [2001]; Bauer [2014]; Rueff and Shukla [2013].

### 2.4.2 Experiment

XAS and HERFD spectra were collected simultaneously (Figure 2.8). The fluorescence was analyzed at the  $K\alpha$  line (about 6404 eV) using 4 Ge(440) crystal to diffract the emitted light. Each HERFD line of the RIXS takes about 1 minute and is focused on the  $K$  pre-edge with a 0.05 eV step from 7108 to 7123 eV for the incident beam and with a 0.2 eV step from 6395 to 6408 eV for the emitted beam. About 60 spectra were collected per hour of experiment, the evolution of XAS data can inform about sample alteration due to beam-damage (details are given in Appendix D.3).

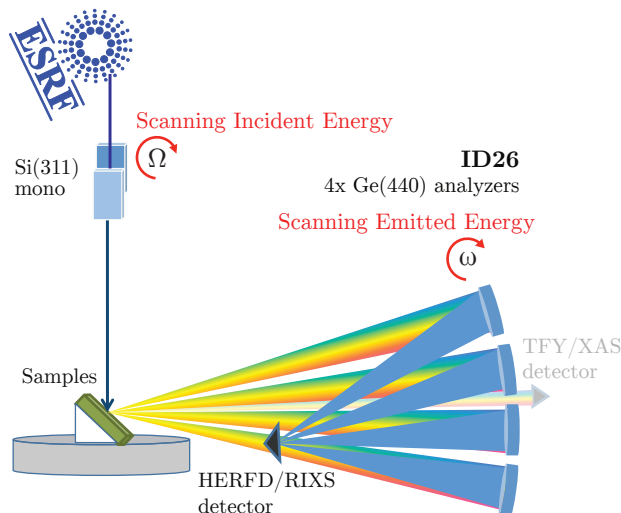


Figure 2.8 – Setup of RIXS experiment.

### 2.4.3 Data processing

HERFD-XAS individual spectra were processed and merged in the same way than the TFY-XAS spectra (see above). RIXS map was plotted using the 60 HERFD spectra. The HERFD-XAS spectrum corresponding to the maximum of the  $K\alpha$  line was normalized with ATHENA in the same way than the TFY-XAS spectra. The pre-edge RIXS map was normalized by proportionality with this HERFD-XAS spectrum.

### 2.4.4 Why HERFD and RIXS can be useful?

TFY-XANES is the measure of the total fluorescence yield (TFY) while HERFD-XAS is the recording of only one fluorescence energy at constant emitted energy (CEE) represented by a diagonal cut in the RIXS map in Figure 2.9-a. The average spectrum obtained by summing along y-axis for a range of emitted energies is called partial fluorescence yield (PFY).

Figure 2.9-b shows the potentialities of the HERFD-XAS measurements. A better resolution and signal to noise ratio with a lower background signal on the  $K$  pre-edge are good arguments in favor of this method. Especially to identify overlapping transitions. Nevertheless, one shall keep in mind that the HERFD can be interpreted only from the RIXS and should not be compared directly to the TFY. In particular, different peak intensity ratios are often observed between TFY and HERFD.



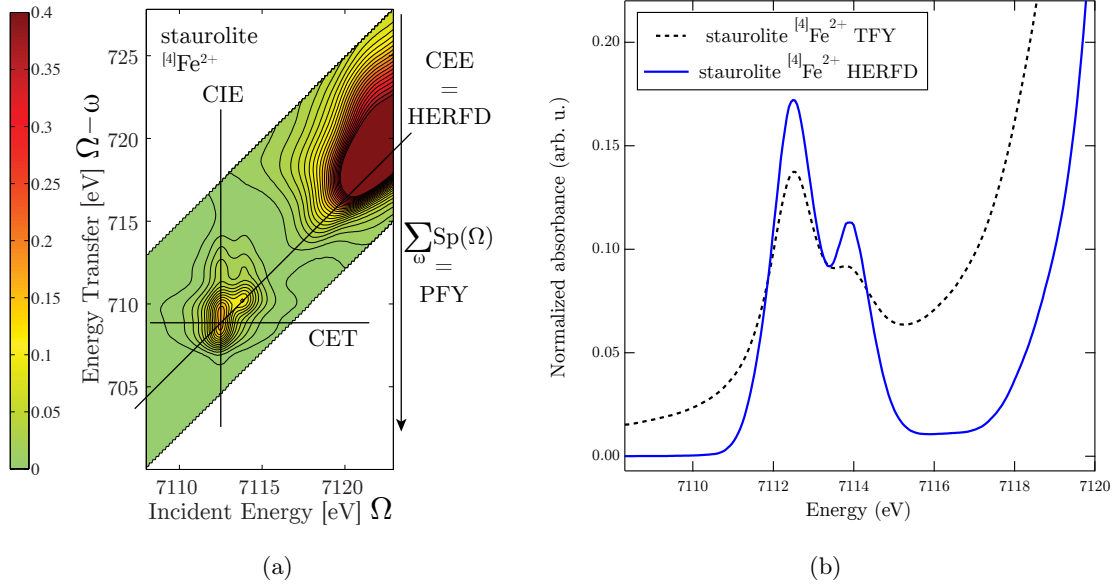


**Figure 2.9** – (a) Experimental RIXS map of staurolite ( $^{[4]}\text{Fe}^{2+}$ ). The diagonal cut results in the constant emitted energy (CEE) line plot, which is the HERFD spectrum. The normalized spectral intensities in the RIXS plane are given in the shaded bar. The peaks present in the Energy Transfer direction correspond to the multiplet split final states. Horizontal and vertical cuts give the constant energy transfer (CET) and constant incident energy (CIE) line plots, respectively. (b) Experimental Fe  $K$  edge TFY and HERFD spectra of staurolite after normalization to the main edge.

## 2.5 SQUID-VSM

### 2.5.1 Approach

Iron in doped-glasses is usually considered as isolated and paramagnetic species in a diamagnetic matrix\*. When a paramagnetic material is subject to a magnetic field  $H$ , the magnetization  $M$  (total magnetic moment per unit volume) is given by:

$$M_J = NgJ\mu_B B_J(\alpha), \quad (\alpha = Jg\mu_B H/k_B T) \quad (2.8)$$

where  $N$  is the spin number per volume unit,  $g = 2.0023$  is called the Landé  $g$ -factor for the electron,  $J$  is the total angular momentum quantum number,  $\mu_B$  is the Bohr magneton and  $B_J(\alpha)$  is the Brillouin function. For  $3d$  elements, due to the crystal field the orbital angular momentum is quenched, therefore  $L$  is reduced to 0 and  $J$  is approximated by  $S$ , thus only the spin contributes to the magnetization process.

For low magnetic field,  $\alpha \ll 1$ ,  $M(H)$  is linear and the first term of the expansion in Taylor series of Equation 2.8 is the Curie law for paramagnetic materials:

$$\chi = \frac{M}{H} = \frac{C}{T} \quad (2.9)$$

where  $C = N\mu_{\text{eff}}^2/3k_B$  is the Curie constant and  $\mu_{\text{eff}} = g\sqrt{J(J+1)}\mu_b = g\sqrt{S(S+1)}\mu_b$  is

\*For short introduction to magnetic materials the reader can consult Spaldin [2010] and of course [Kittel, 2004] for a detailed introduction

the effective magnetic moment of the atom. The magnetization  $M$  is therefore directly proportional to the applied magnetic field  $H$ , and the magnetic susceptibility  $\chi$  is a constant ( $\chi > 0$  for paramagnetic ions and  $\chi < 0$  for diamagnetic ions).

For iron, the calculated  $g\sqrt{S(S+1)}$  and measured  $\mu_{\text{eff}}$  values of the effective magnetic moment, expressed in Bohr magneton, are given in Table 2.4.

**Table 2.4** – Effective magnetic moment for iron ions, adapted from Kittel [2004, Chap. 11].

ion	configuration	total spin	$g\sqrt{S(S+1)}$	$\mu_{\text{eff}}$
$\text{Fe}^{2+}$	$3d^6$	$S = 2$	4.90	5.4
$\text{Fe}^{3+}$	$3d^5$	$S = 5/2$	5.92	5.9

The purpose of the SQUID-VSM experiment is to measure the static magnetic properties of glasses and to look for any deviation from the ideal, paramagnetic behavior. Any deviation from the ideal could bring to light iron-iron interactions due to iron-clustering.

### 2.5.2 SQUID data acquisition

Superconducting Quantum Interference Device (SQUID) with a Vibrating Sample Magnetometer (VSM) measurements were performed on a Quantum Design’s Magnetic Property Measurement System (MPMS<sup>®</sup>3). Samples are machined to be cylindrical with a diameter of 5.5 mm and a 2.5 mm thickness, corresponding to a mass  $m \simeq 150$  mg (see Figure 2.10). They are put in a plastic straw fixed on the sample holder. The sample holder is vertically oscillating along the z-axis in the cavity. Measurement temperatures vary from 2.5 K to 300 K. All measurements with doped iron glass (0.5 wt% of  $\text{Fe}_2\text{O}_3$ ) were duplicated with almost iron-free samples (<100 ppm of  $\text{Fe}_2\text{O}_3$ ) to evaluate the diamagnetic contribution of the matrix.

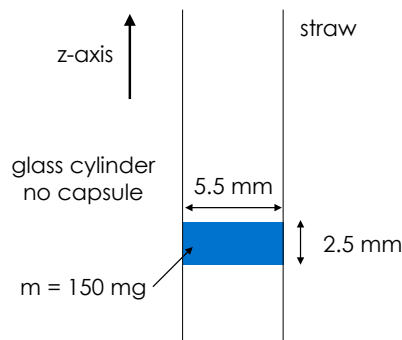


**Figure 2.10** – Sample shape for SQUID experiments.

In magnetic measurements, the initial state of the system is very important. We performed all the measurements after a zero field cooling, in order to avoid magnetic relaxation effects which would occur in the case of a clustering of the iron ions. However, the superconducting magnet of the MPMS traps magnetic fields in their windings after being charged at high fields. Therefore, we evaluated and canceled the remnant field using palladium as a paramagnetic reference prior to each measurement.

Using the SQUID-VSM, the total magnetic moment of the sample was measured. The magnetization of the material was then deduced by dividing the moment by the mass\*.

Two kinds of experiments were performed:

### Measure of $M$ vs $T$ under low magnetic fields

Objective: estimating the variations of the magnetic susceptibility vs  $T$  and check whether or not it follows the Curie law.

The sample was cooled down from room temperature to 2.5 K without applied magnetic field.  $\mu$  was measured as a function of temperature with a magnetic induction  $B = 10$  mT. In the range, 0-300 K, the linearity of  $M(H)$  was verified for our glasses, therefore, it is possible to approximate  $\chi$  by  $M/H$  for this small magnetic field.  $\mu$  was corrected with the diamagnetism of the matrix (see Appendix C.2).  $\chi_{\text{mol}}$  is calculated with formula C.2.  $\frac{1}{\chi_{\text{mol}}}$  was fitted with a linear curve  $a.T + b$  for different temperature ranges. In the case of material that follows a Curie's Law:  $a = 1/C$  and  $b = 0$ . Instead, if the material presents magnetic interaction and becomes ordered below some characteristic temperature  $\theta$ , it can follow Curie-Weiss law:  $\chi = \frac{C}{T - \theta}$ , therefore  $a = 1/C$  and  $b = -\theta/C$  where  $\theta$  is the Curie-Weiss temperature. The effective moment  $\mu_{\text{eff}}$  was obtained with equation C.3 for the same temperature ranges.

### Measure of $M$ vs $H$

Objective: verifying the scaling of  $M$  as a function of  $H/T$  for different temperature and compare with the theoretical Brillouin function (Equation 2.8).

The sample was cooled down to 3 K without applied magnetic field.  $\mu$  was measured as a function of magnetic field  $H$  from 0 to 7 T at different temperature  $T = 2.5, 5, 10, 20, 35, 50, 65, 100, 135, 200$  and 300 K. No hysteresis was observed for the measured samples.

## 2.6 Electron Paramagnetic Resonance (EPR)

### 2.6.1 EPR principles

Since the pioneering work of Castner et al. [1960], Electron Paramagnetic Resonance (EPR), also named Electron Spin Resonance (ESR), has proven to be a sensitive technique to probe  $\text{Fe}^{3+}$  in glasses. Especially to study clustering, site distortion and to quantify  $\text{Fe}^{3+}$  content [Balan et al., 1999, 2000; Griscom, 1980]. The high sensibility of EPR can also be used to confirm the absence of paramagnetic impurities (only those that could be observed with EPR, such as  $\text{Mn}^{2+}$ ).

EPR is a chemically selective method, and lots of paramagnetic species are silent and do not give any signal. Elvers and Weissmann [2001] list the oxidation states of 3d transition metals that can be analyzed by EPR:  $\text{Ti}_{\text{RT}}^3$  ( $d^1$ ),  $\text{V}_{\text{RT}}^{4+}$  ( $d^1$ ),  $\text{Cr}_{\text{RT}}^{3+/5+}$  ( $d^3/d^1$ ),  $\text{Mn}_{\text{RT}}^{2+}$  ( $d^5$ ),  $\text{Fe}_{\text{RT}}^{3+}$  ( $d^5$ ),  $\text{Co}_{\text{LT}}^{2+}$  ( $d^7$ ),  $\text{Ni}_{\text{LT}}^{2+}$  ( $d^8$ ),  $\text{Cu}_{\text{RT}}^{2+}$  ( $d^9$ ). The species marked by RT can usually be detected at room temperature. To analyze the LT-indexed elements, low temperature measurements have to be carried out. For transition metals, an empirical rule (that is not always true) is that only paramagnetic ions with unpaired electrons give a signal.

\*See Appendix C, Table C.1 presents the useful units for magnetism in both CGS and SI systems.

For the case of ferric and ferrous iron, conventional EPR (magnetic fields  $B_0 \leq 1.5$  T and microwave frequencies  $\nu \leq 35$  GHz) is only sensitive to  $\text{Fe}^{3+}$  and  $\text{Fe}^{2+}$  is a silent species. The short spin-lattice relaxation time and the large zero-field splitting of  $\text{Fe}^{2+}$  preclude the direct observation of  $\text{Fe}^{2+}$  with conventional EPR in glasses. However,  $\text{Fe}^{2+}$  can be observed with high-frequency EPR, pulse EPR or below helium temperature (4 K). It can also affect the  $\text{Fe}^{3+}$  signals with  $\text{Fe}^{3+}$ - $\text{Fe}^{2+}$  coupling effects.

For a free electron with the energy  $E_0$ , the spin is  $s = \pm\frac{1}{2}$ . If this electron is in a static magnetic field  $H$ , the energy levels are split in  $2s + 1$  levels due to Zeeman effect. Each level is characterized by the magnetic spin quantum number  $m_s$  (here  $m_s = \pm\frac{1}{2}$ ) and the energy is  $E_0 \pm m_s g \mu_B H$ , where  $\mu_B$  is Bohr magneton and  $g$  is the Landé  $g$ -factor\*. The energy difference between the two levels is  $\Delta E = g \mu_B H$ . (see Fig 2.11)

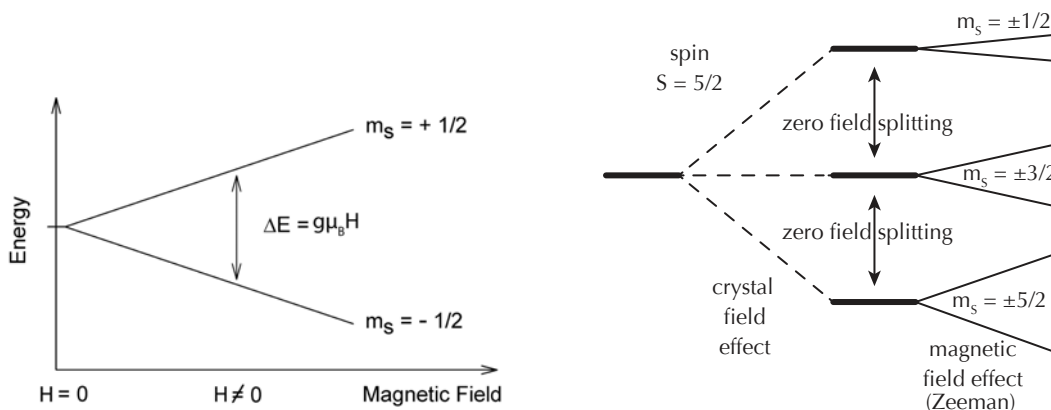


**Figure 2.11** – Zeeman effect: under a magnetic field there is a splitting of the levels.

**Figure 2.12** – Fine-structure splitting of a  $d^5$  ion ( $\text{Fe}^{3+}$ ). Dashed lines represent zero-field splitting due to crystal field, while plain line indicate the Zeeman splitting due to applied magnetic field. Inspired from Griscom [1980].

An electromagnetic field with the microwave frequency  $\nu$  (9.5 GHz for X-band, 34 GHz for Q-band) is superimposed to this static magnetic field. If the energy  $h\nu$  of a microwave photon is equal to the level splitting, there is resonance and the photon is absorbed by the electron. It is the resonance condition:

$$h\nu = g\mu_B H \tag{2.10}$$

The different common  $g$ -factor values at X- and Q-band are listed in Table 2.5.

For an ion such as  $\text{Fe}^{3+}$  ( $d^5$ ), there are three levels known as Kramers doublets corresponding to  $m_s = \pm\frac{1}{2}$ ,  $\pm\frac{3}{2}$  and  $\pm\frac{5}{2}$ . They are represented in Figure 2.12 and they are already split at zero magnetic field by the ligand field or electronic repulsions. This zero-field splitting (ZFS) is characterized in EPR with the fine-structure parameters  $D$  and  $E$  (or  $B_2^0 = D/3$  and  $B_2^2 = E$  with Stevens operators). Resonance can be observed between levels respecting the selection rule  $\Delta m_s = \pm 1$

\*The effective  $g$ -factor  $g_{\text{eff}}$ , will be simply noted  $g$ .

**Table 2.5** – Conversion table between magnetic field and  $g$ -factor, for X-band frequency of 9.5 GHz and Q-band frequency of 34 GHz.

$g$ -factor	X-band field (mT)	Q-band field (mT)
2	340	1210
4.3	160	560
6	110	400
8	85	305
10	70	240
13	50	190

### 2.6.2 EPR data acquisition and data processing

EPR spectra were measured using a Bruker ESP300 spectrometer at X-band (9.5 GHz) and Q-band (34 GHz), with a field modulation of 100 kHz and an amplitude modulation of 1 mT. Low-temperature measurements were carried out using helium Oxford cryostats allowing measurements down to 4K.

Due to the amorphous nature of glass, there is no need to grind the samples to obtain powder spectra averaged on all orientations. On the contrary, it is better to keep the bulk samples intact to avoid contamination of the tube with the powders and to minimize the impact of surface defects in spectra when samples are ground into fine powders. Samples were machined to have a cylindrical form: 15 mm long by about 2 mm diameter for X-band and 2 mm long by 1.5 mm diameter for Q-band. Samples were placed in pure silica tubes (Suprasil) for X-band or stuck on a pure silica rod for Q-band.

The measurements were performed at different microwave power to adjust a convenient signal to noise ratio without saturation phenomena. EPR X-band spectra were normalized to sample mass, gain, amplitude modulation and square root of power (in mW). Q-band was used for qualitative analysis, therefore, spectra were not normalized and are displayed in arbitrary units along the y-axis.

The magnetic field\*, generated by an electromagnet, is varying slowly compared to the microwave frequency, thus it is considered as a static field. The measured EPR signal is the derivative signal because an alternative magnetic (using a Helmholtz coil) field is added to improve the signal to noise ratio (with an amplitude of 1 mT at the frequency 100 kHz).

These are the typical parameters for the measurement:

- Frequency: 9.5–9.9 GHz (X-band) and  $\sim$ 34 GHz (Q-band)
- Microwave power: 20 mW to 200 mW (attenuation: 10 to 0 dB) at room temperature.
- modulation amplitude: 1 mT (smaller values do not narrow the signals for glasses)
- Time constant: 164 ms (of the low-pass filter)
- Conversion time: 240 ms (time per point)
- Temperature: room temperature (298 K) to liquid helium temperature (4 K)

For low temperature measurements another similar Bruker spectrometer was used. Thus, the magnetic field values are corrected to take into account the frequency differences between

\*spectra are expressed with magnetic units in SI unit: mT instead of CGS gauss units (1 mT = 10 G)

the two spectrometers. Therefore, the x-axis values were divided by the measured frequency in GHz and multiplied by 9.5 GHz.

The cavity signal can be removed, especially for samples with low  $\text{Fe}^{3+}$  content. The cavity was measured without sample, and the signal was subtracted to obtain the flattest signal around 800 mT (where there is no resonance).

### 2.6.3 EPR example and interpretation elements

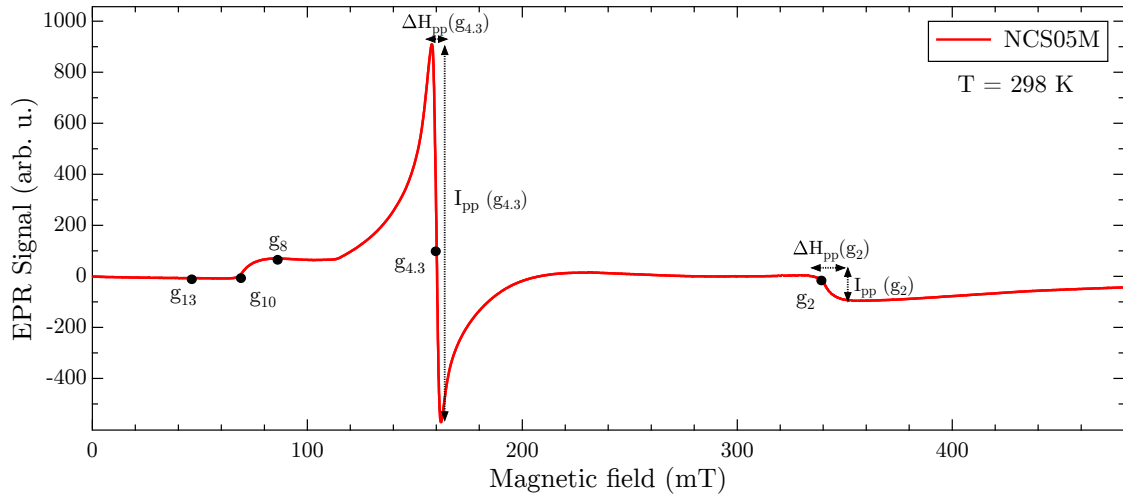


**Figure 2.13** – Example of a typical EPR spectrum (NCS05Med).

Soda-lime-silicate (NCS05Med) glasses with 0.5 wt% of  $\text{Fe}_2\text{O}_3$  synthesized under atmospheric conditions (intermediate redox) gives a typical X-band EPR spectrum of  $\text{Fe}^{3+}$ -doped silicate glasses, presented in Figure 2.13.

The X-band EPR spectrum of  $\text{Fe}^{3+}$  in silicate glasses is characterized by an intense asymmetric signal at  $g = 4.3$ , accompanied by two weaker features near  $g = 8$  and  $g = 2$ . The resonances at  $g = 4.3$  and  $g = 8$  originate from paramagnetic transitions of isolated  $\text{Fe}^{3+}$  ions in rhombic ( $E/D \sim 1/3$ ) and axially ( $E/D \sim 0$ ) distorted sites, respectively [Dowsing and Gibson, 1969; Kurkjian and Sigety, 1968; Montenero et al., 1986]. This peak is due to the three transitions  $xx$ ,  $yy$  and  $zz$ . The more the peak is thin and the more the site is distorted. If the site is distorted the three bands are superimposed; if the site is regular, the three bands are separated. The signal at  $g = 4.3$  has been also attributed to tetrahedral or octahedral sites with rhombic distortions [Kurkjian and Sigety, 1968; Montenero et al., 1986]. There are several types of distortions, for example, Figure 2.14 shows some distortions of an octahedron.

The attribution of the feature at  $g = 2$  is less clear [Dunaeva et al., 2012]. Different scenarios have been proposed: (i) a signal due to exchange-coupled pairs or clusters of more than two atoms [Rüssel, 1993] involving edge- or face-sharing  $\text{Fe}^{3+}$  sites [Griscom, 1980; Montenero et al., 1986; Moon et al., 1975]. These clusters could be trimers [Boudalis et al., 2006] up to nano-clusters as in ferritine [Aime et al., 1997], nanoparticles [Koksharov et al., 2000] or obsidian glasses [Calas and Petiau, 1983b; Duttine et al., 2003]; (ii) a paramagnetic

signal due to  $\text{Fe}^{3+}$  in axially distorted sites ( $E/D \sim 0$ ) [Griscom, 1980], this signal is enhanced by dipole-dipole interactions [Abragam and Bleaney, 1970, §9.8].

1. Regular  
all distances are equivalent
2.  $C_4$  axial distortion  $a \neq b$
3. Rhombic distortion  $a \neq b \neq c$
4. Trigonal distortion  $a \neq b$

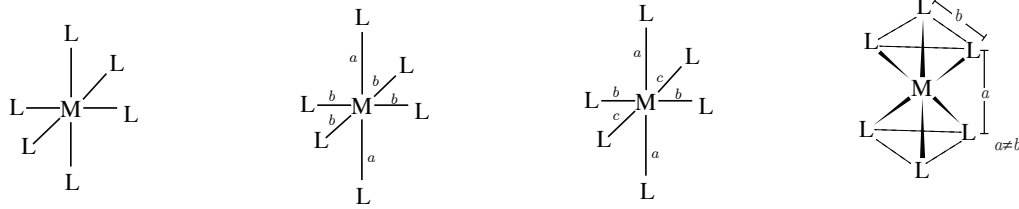


**Figure 2.14** – Distortions of an octahedron

The proportion of these two overlapping contributions depends on glass composition and Fe-redox state [Elvers and Weissmann, 2001; Montenero et al., 1986]. The  $g = 2$  signal can also be assigned to  $\text{Fe}^{3+}$  in regular site with high symmetry, e.g. tetrahedral or octahedral [Camara, 1982; Kurkjian and Sigety, 1968]. However, the latter interpretation is not coherent with the long tail above 350 mT that goes back to 0 around 600 mT. Low-temperature EPR measurements have shown the presence of paramagnetic clusters in Fe-doped borate glasses, because small clusters exhibit antiferromagnetic behavior with a broader EPR line, whereas the EPR signal of diluted  $\text{Fe}^{3+}$  exhibits paramagnetic behavior with a more intense EPR signal [Berger et al., 1995]. Thus, the disappearance of the  $g = 2$  signal when temperature decreases is used as evidence of the presence of  $\text{Fe}^{3+}$  containing clusters, as observed in [Aime et al., 1997] or nanoparticles [Koksharov et al., 2000].

The linewidth is the peak to peak value in mT, it is proportional to  $1/t$  (lifetime) and linked to the dipole-dipole interaction of  $\text{Fe}^{3+}$  ions [Elvers and Weissmann, 2001]. In Figure 2.13, the linewidth of the  $g = 4.3$  and  $g = 2$  signals are defined with  $\Delta H_{pp}(g = 4.3)$  and  $\Delta H_{pp}(g = 2)$ . The intensities of these bands are named  $I_{pp}(g = 4.3)$  and  $I_{pp}(g = 2)$ .

## Chapter 3

# Ligand Field Multiplet Theory applied to the calculation of XAS and optical absorption spectra

This chapter presents Ligand Field Multiplet Theory (LFMT) that is used by **Quanty** to interpret the spectroscopic properties, especially optics of iron in crystals and glasses. LFM calculations performed during this thesis are focused on the interpretation of the iron  $3d$  orbitals probed by X-ray absorption and optical spectroscopy in order to understand the relationships with Fe local environment.

### 3.1 Historical introduction to Ligand Field Multiplet Theory (LFMT)

To describe the chemical bond, crystal field theory was developed in the 1930's by Bethe and Van Vleck [Bethe, 1929; Van Vleck and Sherman, 1935]. It was used to interpret the crystal field potential created by the neighboring atoms and its effects on the electronic states of the central ion. In coordination chemistry, one of the fundamental questions is how to describe the chemical bond by considering interactions with the neighboring anions, named *ligands*. The valence-bond theory, proposed by Pauling in 1929, gave a first representation of the chemical bonding, with the concepts of electronegativity, bond-length, ionic radius and coordination number. Gibbs et al. [2014] recently revisited this concept and the definition of atomic/ionic radii in crystals; the authors underlined that the electronic density is highly distorted around atoms and this asphericity shows all the complexity to define the ionic radius, which depends on site geometry, nature and number of ligands and interactions with surrounding atoms. To take into account the chemical bonding and hybridization with neighbors, crystal field theory was completed by ligand field theory [Ballhausen, 1962; Jørgensen, 1971]. Tanabe and Sugano [1956] did quantitative calculations of the electronic levels using Racah parameters to characterize covalency and consider multielectronic interactions. Ligand Field Multiplet Theory (LFMT) was born. This chapter presents basic notions necessary for the comprehension of this manuscript,



for further details, the reader can refer to these books: Ballhausen [1962]; Bates [1962]; Jørgensen [1971]; Cowan [1981]; Lever [1984]; Burns [1993]; Figgis and Hitchman [2000].

### 3.2 From mono-electronic picture to multiplet states

Electron configurations of ferrous and ferric ions are  $\text{Fe}^{2+}$ :  $[\text{Ar}]3d^6$  and  $\text{Fe}^{3+}$ :  $[\text{Ar}]3d^5$  respectively, where  $[\text{Ar}]$  is the electron configuration of argon:  $1s^22s^22p^6 3s^23p^6$ . The mono-electronic approach, based on hydrogen-like model, predicts five degenerated  $d$  orbitals for the free ion ( $d_{xy}$ ,  $d_{yz}$ ,  $d_{xz}$ ,  $d_{x^2-y^2}$ ,  $d_{z^2}$ ), each can accept 2 electrons with spin  $\pm\frac{1}{2}$ . Thus, with  $n$  electrons to put in 10 spin orbitals, there are  $\binom{10}{n}$  possible combinations, corresponding for  $\text{Fe}^{2+}$  ( $d^6$ ) to 210 microstates and for  $\text{Fe}^{3+}$  ( $d^5$ ) to 256 microstates. The simplest scenario would be the absence of electron interactions where all microstates are degenerated. However, electronic repulsions raise the degeneracy by splitting the electronic levels. Microstates are not equivalent depending on their fillings, and some arrangements are energetically more favorable than others. To understand multielectronic effects, the simple mono-electronic vision is inappropriate to the study of transition metals, and a nomenclature using spectroscopic terms is suitable.

### 3.3 Spectroscopic terms and ground state

Spectroscopic terms are symbols used to describe electronic states. In absence of spin orbit coupling, split levels, named *multiplets*, are labeled with terms (such as  $^5D$  or  $^6S$ ) regarding their  $L$  (total atomic orbital angular momentum) and  $S$  (resultant spin quantum number) values. They are written as  $^{2S+1}L$ , with  $L = S, P, D, F, G, H, I$  (where  $S = 0$ ,  $P = 1$ ,  $D = 2\dots$ ) The number of microstates is the product of *orbital multiplicity* ( $2L + 1$ ) by the *spin multiplicity* ( $2S + 1$ ).

Ground state can be guessed with Hund's rules (find the term that maximized  $S$ , then maximized  $L$ ), which is the one that has the lowest energy by minimizing the repulsions. Other spectroscopic terms representing all excited states are listed in Table 3.1 without energy ordering. For  $d^6$  and  $d^5$  ions, no excited state has the same spin multiplicity as the ground state.

For  $\text{Fe}^{2+}$ , the ground state is  $^5D$  and other spectroscopic terms are triplets ( $^3P$ ,  $^3D$ ,  $^3F\dots$ ) or singlets ( $^1I$ ,  $^1G$ ,  $^1F\dots$ ). Triplet states are more likely to be involved in a transition than the singlets (due to selection rules that will be presented in the next section).

For  $\text{Fe}^{3+}$ , the ground state is a sextet  $^6S$  and other spectroscopic terms are quadruplets ( $^4G$ ,  $^4P$ ,  $^4D$ ,  $^4F$ ) or doublets ( $^2I$ ,  $^2H$ ,  $^2D\dots$ ). For the same reason as for  $\text{Fe}^{2+}$ , quadruplet states of  $\text{Fe}^{3+}$  are lead to higher intensity of transition.

**Table 3.1** – Spectroscopic terms of ferrous iron ( $\text{Fe}^{2+}$ ) and ferric iron ( $\text{Fe}^{3+}$ ) in spherical geometry (from p. 53 of Burns [1993]).

Configuration	Ground state	Excited states
$\text{Fe}^{2+}$ ( $d^6$ )	$^5D$	$^3H, ^3G, ^3F, ^3F, ^3D, ^3P, ^3P, ^1I, ^1G, ^1G, ^1F, ^1D, ^1D, ^1S, ^1S$
$\text{Fe}^{3+}$ ( $d^5$ )	$^6S$	$^4G, ^4F, ^4D, ^4P, ^2I, ^2H, ^2G, ^2G, ^2F, ^2F, ^2D, ^2D, ^2D, ^2P, ^2S$

Racah parameters are energies, expressed in  $\text{cm}^{-1}$  or eV, used to characterize the strength of multielectronic repulsions, they are named  $A$ ,  $B$  and  $C$ , relatively to the values  $A_0$ ,  $B_0$  and  $C_0$  of the free ion. In  $O_h$  or  $T_d$  geometries without spin-orbit coupling, all electronic states energies can be expressed as a linear combination of the Racah parameters (For example see Griffith [1961, Table 4.6]). Since  $A$  is only related to the average energy of an electronic configuration, it can be disregarded for comparison of relative energies. For metal ions surrounded by ligands, electrons of the central metal ion are influenced by their neighboring atoms. The overlapping of metal orbitals with ligand orbitals, which forms the chemical bond, leads to delocalize the electrons of the metal, thus, Racah parameters have to be reduced to take this effect into account.

The nephelauxetic ratio  $\beta$  characterizes this reduction, it is defined by  $\beta = B/B_0$  where  $B$  is the Racah parameter of the compound and  $B_0$  the value of the free ion. Therefore,  $\beta = 1$  corresponds to a fully ionic bonding and a lower value of  $\beta$  means that the bond is more covalent. In oxide compounds, such as minerals or glasses studied in this work, bonds are ionocovalent with  $\beta$  commonly about 60~80% [Arrio et al., 2000; Burns, 1993; de Groot and Kotani, 2008; Lever, 1984; Westre et al., 1997]

For the  $d$ -shell, Racah parameters  $A$ ,  $B$  and  $C$  are related to Slater-Condon parameters  $F^0$ ,  $F^2$  and  $F^4$  (direct Slater integrals). The former are often used for experimental interpretation of the chemical bond while the later are used to characterize electronic repulsions. They are related by these relations [Lever, 1984, p. 103]:

$$A = F^0 - \frac{49}{441}F^4 \quad (3.1a)$$

$$B = \frac{1}{49}F^2 - \frac{5}{441}F^4 \quad (3.1b)$$

$$C = \frac{35}{441}F^4 \quad (3.1c)$$

### 3.4 The importance of geometry

The surrounding ligands that determine the site geometry create an electric field, the *crystal field*, that raises the degeneracy of the  $3d$ -levels and splits the spectroscopic terms. Split terms are relabeled using group theory regarding the point group geometry of the site. The naming convention is to use small letters for mono-electronic states (e.g.  $d_{xy}$  or  $t_{2g}$ ) and capital letters for multielectronic states (multiplet states coupling all electrons), e.g.  ${}^5D$  or  ${}^5T_{2g}$ .

Figure 3.1 shows the high-spin and low-spin states of a  $\text{Fe}^{3+}$  ion in the center of a regular octahedron ( $O_h$ ). In this symmetry, the five mono-electronic  $3d$  orbitals are split into  $t_{2g}$  and  $e_g$  which are linear combinations of the atomic  $3d$  orbitals,  $t_{2g}:(d_{xy}, d_{yz}, d_{xz})$  and  $e_g:(d_{x^2-y^2}, d_{z^2})$ . In a multielectronic model, the ground state  ${}^6S$  gives  ${}^6A_{1g}$ , and, for example, the excited term  ${}^4F$  is split into  ${}^4A_{2u} \oplus {}^4T_{1u} \oplus {}^4T_{2u}$ . The spin multiplicity 4 remains unchanged, and the dimension of the initial state is equal to the sum of split states dimensions (here  $\dim(F) = \dim(A_{2u}) + \dim(T_{1u}) + \dim(T_{2u})$  with  $\dim(F) = 7$ ,  $\dim(A_{2u}) = 1$ ,  $\dim(T_{1u}) = \dim(T_{2u}) = 3$ ).

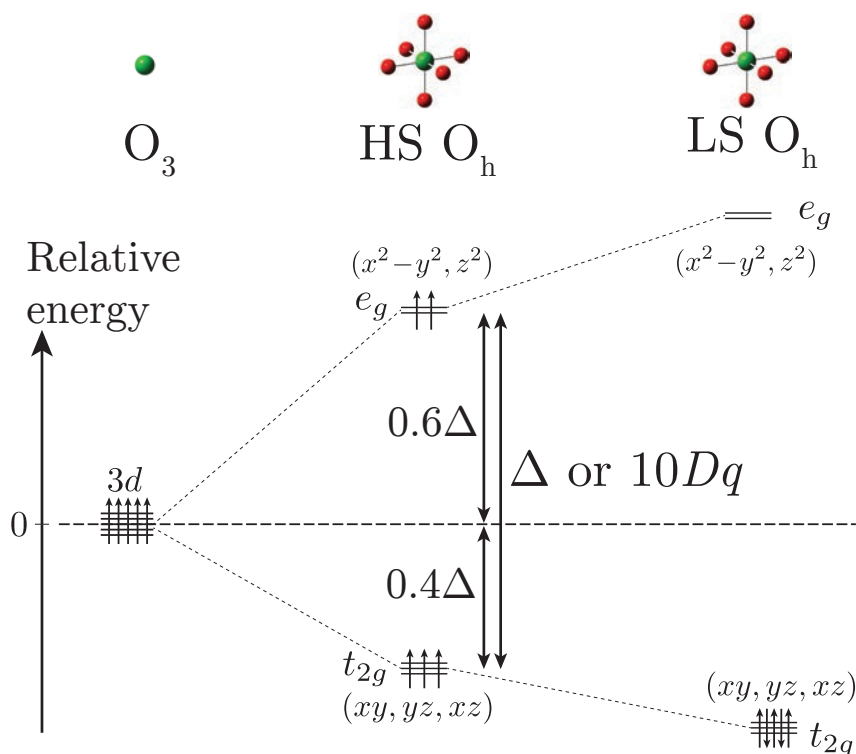


**Figure 3.1** – Crystal field splitting of Fe<sup>3+</sup> 3d orbitals in O<sub>h</sub> geometry, Fe<sup>3+</sup> is in the center of a regular octahedron. A weak-field leads to a high-spin (HS) ground state and a strong-field leads to a low-spin (LS) ground state. To simplify, only one microstate has been represented. The represented filling of the degenerated orbitals with spins is a single particle picture of a multielectronic state.

### 3.5 Crystal field parameters

Crystal field parameters are semi-empirical energies used to quantify the splittings induced by the crystal field potential. The number of parameters depends on geometry: the more the geometry is regular, the fewer parameters there are. In the case of O<sub>h</sub> geometry, there is only one parameter, named 10Dq or Δ, in D<sub>3h</sub> there are 2 parameters (Dμ, Dν) and in D<sub>4h</sub> there are 3 parameters (Dq, Ds, Dt).

For a strong crystal field (10Dq) compared to electronic repulsions (Racah B parameter), it is better to minimize the energy of the system by having paired electrons than maximizing the total spin by putting electrons in the e<sub>g</sub> orbital. Figure 3.1 illustrates the evolution of the Fe<sup>3+</sup> ground state with increasing crystal field 10Dq, Fe<sup>3+</sup> changes from <sup>6</sup>A<sub>1g</sub> high-spin (HS) to <sup>2</sup>T<sub>2g</sub> low-spin (LS) ground state. In oxides and glasses, Fe<sup>3+</sup> and Fe<sup>2+</sup> are generally both in HS state. To summarize:

$$\begin{aligned} \text{High-spin} &= \text{weak-field } (10Dq \searrow) \text{ with ionic behavior } (\beta \rightarrow 1) \\ \text{Low-spin} &= \text{strong-field } (10Dq \nearrow) \text{ with covalent behavior } (\beta < 1) \end{aligned}$$

The crystal field potential has the same symmetry as the site formed by the metal ion and its first neighbors. Usually different coordination numbers lead to different point group symmetries, but sometimes two distinct polyhedra with different coordination numbers can have the same point group geometry. In such case, it can be discerned by the sign and magnitude of the crystal field parameters.

Figures 3.2 and 3.3 respectively show the evolution with the site geometry of mono-electronic  $3d$  orbitals and multielectronic spectroscopic terms. Depending on the number and positions of the ligands the point charge model illustrates by Figure 3.2 explain the following situations:

- orbitals of an ion in regular octahedral (b) and tetrahedral (g) geometries have the similar splittings between the two groups of orbitals, which are respectively  $\Delta_O$  and  $\Delta_T$ , with  $\Delta_O = -\frac{4}{9}\Delta_T$ .
- ions in  $T_d$  (g) and  $D_{4h}$  (d) are both [4]-fold coordinated, however, the resulting energy splittings are different ( $e$  and  $t_2$  for  $T_d$ ;  $a_{1g}$ ,  $e_g$ ,  $b_{2g}$  and  $b_{1g}$  for  $D_{4h}$ ).
- same remark can be done for the square pyramidal  $C_{4v}$  (e) and the trigonal bipyramidal (f) geometries that are both [5]-fold coordinated with different energy splittings ( $e$ ,  $a_1$ ,  $b_2$  and  $b_1$  for  $C_{4v}$ ;  $e''$ ,  $e'$  and  $a_1'$  for  $D_{3h}$ )
- 6 -fold octahedron with weak tetragonal distortion along  $z$ -axis (c) and [6]-fold octahedron strong tetragonal distortion (d) or [4]-fold square-planar environment (when axial ligands are at infinite distance) both belong to the  $D_{4h}$  point group but their respective orbitals have different energies and not the same energy order, especially the ground states are respectively  $e_g$  and  $a_{1g}$ .

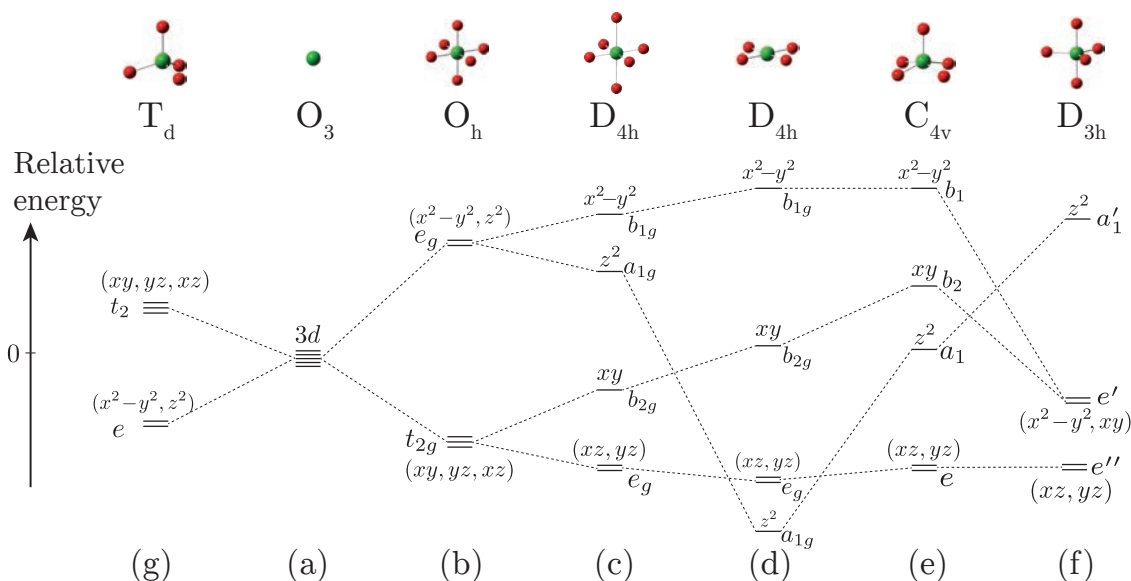


**Figure 3.2** – Single particle representation of energy level diagrams in the point charge approximation of the  $d$  orbitals of a transition metal compiled from [Lever, 1984]. (a) Spherical geometry, (b) [6]-fold regular octahedron, (c) [6]-fold octahedron with weak tetragonal distortion along  $z$ -axis, (d) [6]-fold octahedron strong tetragonal distortion or [4]-fold square-planar environment, (e) [5]-fold square pyramid (f) [5]-fold trigonal bipyramid (g) [4]-fold tetrahedron.

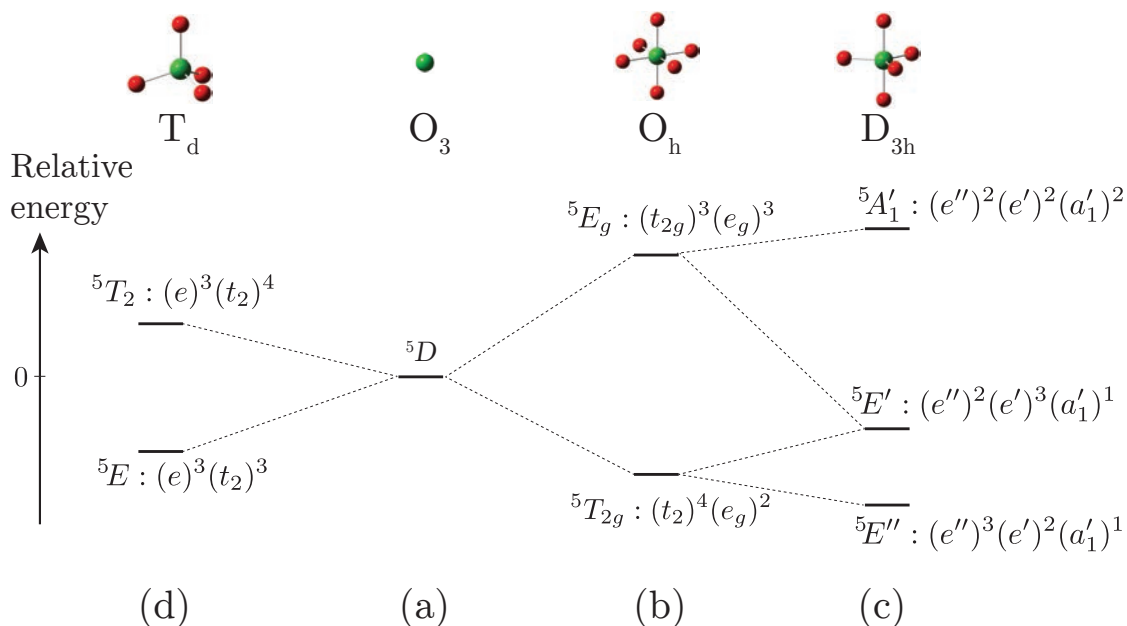


**Figure 3.3** – Evolution of the multielectronic ground state term of high-spin  $Fe^{2+}$  with local geometry.

### 3.6 Tanabe-Sugano diagrams

Tanabe-Sugano diagrams [Tanabe and Sugano, 1954a,b, 1956], have been widely used as an approximation to analyze the effect of crystal field on the spectroscopic terms of a transition metal ion in a specific geometry without spin-orbit coupling\*. Energy levels are plotted as a function of a crystal field parameter (e.g.  $10Dq$  for  $O_h$ ) with the ground state taken as energy reference†.

Tanabe-Sugano diagrams are calculated for a given  $C/B$  ratio (generally  $\sim 4$ ), and represent  $E/B$  as a function of  $10Dq/B$  [Tanabe and Sugano, 1954a]. Figure 3.4 shows the well-known Tanabe-Sugano diagrams of  $Fe^{2+}$  ( $d^6$ ) and  $Fe^{3+}$  ( $d^5$ ) ions in ideal  $O_h$  geometry for given  $\beta$ ,  $C/B$  and  $B_0$  values. In this case, the high-spin/low-spin transition of  $Fe^{2+}$  happens at 1.4 eV, and ground state  ${}^5T_{2g}$  is replaced by  ${}^1A_{1g}$ . For the glasses and minerals studied in this work, crystal field is known to be weak (lower than  $\sim 1$  eV for  $Fe^{2+}$  and  $\sim 1.5$  eV for  $Fe^{3+}$ ) and samples only exhibit high-spin ground state.

\*In addition to original Tanabe-Sugano diagrams [Tanabe and Sugano, 1954a], König and Kremer [1977] present in their book an extensive set of Tanabe-Sugano diagrams for all  $d^n$  orbitals with different ligand field parameters in tetragonal, trigonal and cylindrical geometries.

†With optical absorption spectroscopy we are only concerned by relative energies, for the same reason that Racah A parameter is ignored, we can choose to take the energy centroid as reference (as in Figure 3.2) or to express the energies relatively to the ground state (as in Tanabe-Sugano diagrams).

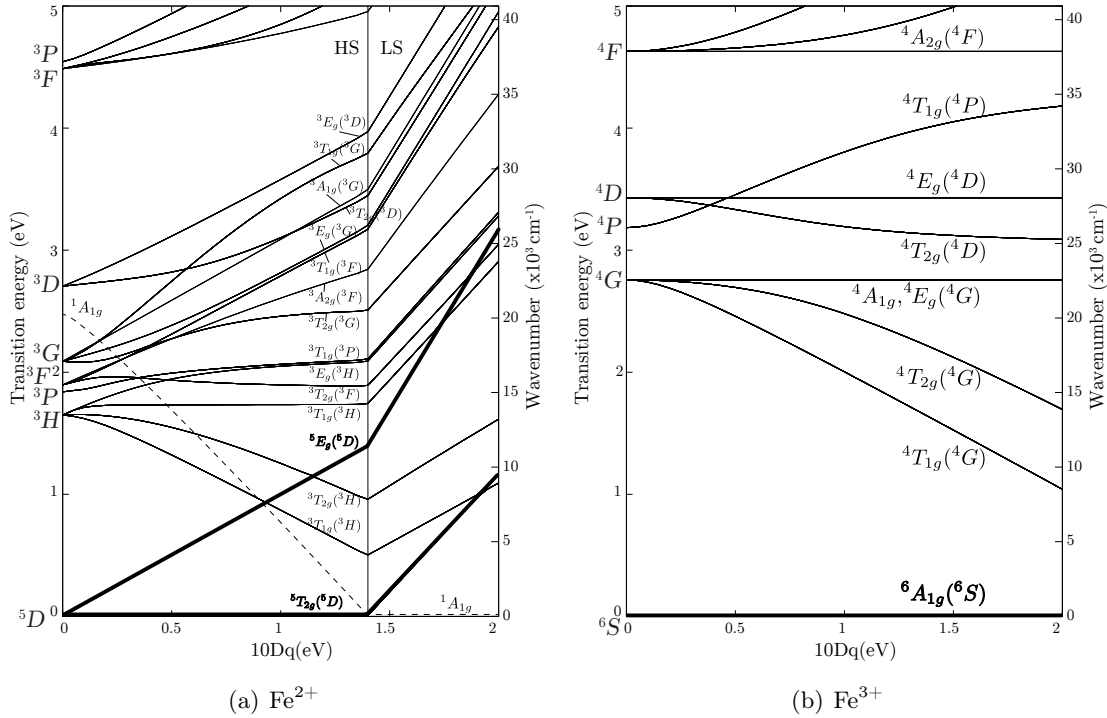


**Figure 3.4** – Tanabe-Sugano diagrams of octahedral Fe<sup>2+</sup> and Fe<sup>3+</sup> (*O<sub>h</sub>* geometry) as a function of crystal field parameter 10Dq with  $\beta = 0.6$  and without spin-orbit coupling. Atomic values of  $B_0$  and  $C_0$  are calculated with Cowan’s code, and spectroscopic terms are calculated with **Quanty** software. (a) Fe<sup>2+</sup> spectroscopic terms are plotted without singlet states of spin multiplicity 1 with  $B_0 = 1280.4 \text{ cm}^{-1}$  and  $C/B = 3.69$  (b) Fe<sup>3+</sup> spectroscopic terms are plotted without doublet states of spin multiplicity 2 with  $B_0 = 1381.6 \text{ cm}^{-1}$  and  $C/B=3.73$ .

Levels are experimentally broadened by several factors, such as sample inhomogeneities. The spectroscopic signals are indeed an average over all iron sites of the structure. Therefore, a repartition of iron into different crystalline sites distributes the crystal field parameters around average values and leads to level broadening. Ligand field energy dependent levels, which are function of  $10Dq$  (not horizontal in Tanabe-Sugano diagram), yield to broader spectral bands than levels whose energy is independent of the crystal field, for example,  ${}^4T_{2g}(G)$  vs.  ${}^4E_g(D)$  in the Tanabe-Sugano diagram of Fe<sup>3+</sup> ( $d^5$ ). The stronger is the slope, the broader is the band. A distribution of bond covalency (Racah B) also leads to level broadening.

Spin-orbit coupling is another origin for the broadening effect of  $d$ -levels, it is related to the magnetic interactions between the spin and the magnetic dipole created by the electron motion in their orbit [Ballhausen, 1962]. The spin-orbit coupling on the  $3d$  electrons is denoted  $\zeta_{3d}$  and is however one or two order of magnitude smaller than electronic repulsions. For example,  $\zeta_{3d}(\text{Fe}^{2+}) = 0.052 \text{ eV}$ , while  $F_{3d3d}^2(\text{Fe}^{2+}) = 10.966 \text{ eV}$  and  $F_{3d3d}^4(\text{Fe}^{2+}) = 6.815 \text{ eV}$ ; or  $\zeta_{3d}(\text{Fe}^{3+}) = 0.059 \text{ eV}$ , while  $F_{3d3d}^2(\text{Fe}^{3+}) = 12.043 \text{ eV}$  and  $F_{3d3d}^4(\text{Fe}^{3+}) = 7.535 \text{ eV}$ . When added, the degeneracy of the levels is slightly lifted, which increases the level broadening and lowers the energy resolution of experimental spectra [Lever, 1984, p. 187].

Jahn-Teller effect also broadens the bands and changes the spectral intensities [Lever, 1984, p. 189]. To keep it simple, energy minimization can be achieved by lowering ideal

regular geometries (such as  $O_h$  and  $T_d$ ), this distortion spontaneously split the energy levels to raise the degeneracy, which stabilizes the atom [Burns, 1993]. For the compounds studied in this work, iron is often in a low symmetry site, which leads to adjust many crystal field parameters. However, it is possible to work with higher geometry as an approximation to get similar spectral data with fewer parameters. In conclusion, the goal is to find the smallest number of parameters in the most regular environment that reproduces the experimental data.

### 3.7 Hamiltonian describing the multielectronic configuration

In term of quantum mechanics formalism the Hamiltonian describing the multielectronic configuration of the ion is noted  $\hat{H}_{ion}$ . The initial states  $|i\rangle$  and final states  $|f\rangle$  are the eigenvectors of  $\hat{H}_{ion}$  describing the initial and final configurations, respective energies are  $E_i$  and  $E_f$ , eigenvalues of  $\hat{H}_{ion}$ .

Without magnetic field, the Hamiltonian  $\hat{H}_{ion}$  can be written as the sum of several terms:

$$\hat{H}_{ion} = \hat{H}_{kin} + \hat{H}_{e^-/N} + \hat{H}_{e^-/e^-} + \hat{H}_{SO} + \hat{H}_{CF} + \hat{H}_{hybrid} \quad (3.2)$$

where  $\hat{H}_{kin}$  is the kinetic energy of the electrons,  $\hat{H}_{e^-/N}$  the electrostatic interaction of the electrons with the nucleus,  $\hat{H}_{e^-/e^-}$  the electron-electron repulsion,  $\hat{H}_{SO}$  is the spin-orbit coupling interaction,  $\hat{H}_{CF}$  is the crystal field Hamiltonian, which takes into account the local environment around the absorbing atom and  $\hat{H}_{hybrid}$  is the hybridization Hamiltonian.

$\hat{H}_{hybrid}$  describes the *on-site*  $3d-4p$  mixing. As  $\hat{H}_{CF}$ , it depends on parameters regarding the site geometry and the point group symmetry [Arrio et al., 2000; Hunault, 2014]. The possible *off-site* transitions from the  $3d$  orbitals of the transition metal to the  $2p$  orbitals of the ligands are not taken into account in this work but the effect of the mixing with the  $2p$  is taken into account through  $\beta$  that characterizes the ionocovalency of the bond (see p. 52).

### 3.8 Intensities – absorption cross-section

The intensity of absorption bands is ruled by the probability of an absorption process between two energy states. The process can be of several natures, for example, electric dipole, electric quadrupole or magnetic dipole transitions. Table 3.2 details the nature of the transition depending on the spectroscopic method. In our case, we only have electric dipole and quadrupole transitions.

The intensity is proportional to the absorption cross-section which is given by Fermi's "Golden rule":

$$\sigma(\hbar\omega) = 4\pi^2\alpha\hbar\omega \sum_{i,f} \frac{1}{d_i} |\langle f|\hat{O}|i\rangle|^2 \delta(E_f - E_i - \hbar\omega) \quad (3.3)$$

where  $\hbar\omega$  is the energy of incident photons,  $\alpha = e^2/4\pi\epsilon_0\hbar c$  the fine structure constant ( $\alpha \simeq 7.297 \cdot 10^{-3}$ ) and  $d_i$  the degeneracy of the initial state  $|i\rangle$ . The Dirac function  $\delta(E_f - E_i - \hbar\omega)$  ensures the conservation of the energy.  $\hat{O}$  is the transition operator, this Hamiltonian is related to the nature of the transitions. For example, electric dipole and electric quadrupole transitions operators are respectively defined by:  $\hat{O}_{dip} = \hat{\epsilon} \cdot \mathbf{r}$  and

$\hat{O}_{quad} = \frac{i}{2}(\hat{\varepsilon} \cdot \mathbf{r})(\hat{\mathbf{k}} \cdot \mathbf{r})$ , with  $\hat{\varepsilon}$  and  $\hat{\mathbf{k}}$ , the unit vectors for polarization of the light and wave vector, respectively [Brouder, 1990].

**Table 3.2** – Nature of the different transitions depending on the spectroscopic method

Spectroscopic method	Transition	Operator nature	Initial configuration	Final configuration
XAS $K$ pre-edge	$1s \rightarrow 3d$	quad	$3d^n$	$1s^1 3d^{n+1}$
XAS $K$ pre-edge	$1s \rightarrow 4p$	dip	$3d^n$	$1s^1 3d^n 4p^1$
XAS $L_{2,3}$ edge	$2p \rightarrow 3d$	dip	$3d^n$	$2p^5 3d^{n+1}$
Optics (UV-Vis)	$(3d,4p) \leftrightarrow (3d,4p)$	dip	$(3d,4p)^n$	$(3d,4p)^n$
$K\alpha$ XES	$2p \rightarrow 1s$	dip	$1s^1 (3d,4p)^{n+1}$	$2p^5 (3d,4p)^{n+1}$
$K\beta$ XES	$3p \rightarrow 1s$	dip	$1s^1 (3d,4p)^{n+1}$	$3p^5 (3d,4p)^{n+1}$
V2C XES*	$(3d,4p) \rightarrow 1s$	dip+quad	$1s^1 (3d,4p)^{n+1}$	$(3d,4p)^n$

\*XES V2C: valence to core X-ray emission spectroscopy

Without coupling between the electric dipole and quadrupole terms,  $\sigma(\hbar\omega)$  is simply the sum of electric dipole  $\sigma_{dip}(\hbar\omega)$  and electric quadrupole  $\sigma_{quad}(\hbar\omega)$  contributions:

$$\sigma(\hbar\omega) = \sigma_{dip}(\hbar\omega) + \sigma_{quad}(\hbar\omega) \quad (3.4)$$

This condition is fulfilled if the system is either centrosymmetric or if, at the same time, the system is nonmagnetic (no net magnetic moment on the absorbing ion) and one uses exclusively linear polarization [Juhin et al., 2008]. This second condition is verified for all XANES measurements. The cross-section calculation is detailed in Appendix E.4.

### 3.9 Transition rules in optics

The energy of photons used in optical spectroscopy is of the same order of magnitude than the energy difference between valence levels. Therefore, optical absorption spectroscopy is a suitable and powerful tool for the study of the chemical bond and local environment. Extensive work has been done to understand the position of energy levels, which is related to energy level differences and thus refers to crystal field theory, quantum mechanics and group theory.

However, the complexity remains in the understanding of their intensities, its computer calculation requires a fine modeling to reproduce the spectra of this very sensitive and accurate method. Unfortunately, the interpretation is limited by the absence of a theory that correctly simulates optical spectra. An interesting preliminary work has been done by Rossano et al. [2000a] proving that optical transitions are electric dipole (and not magnetic dipole or electric quadrupole) and one of the rare calculated absorption spectra has been made by Watanabe et al. [2009] for chromium  $\text{Cr}^{3+}$  in ruby ( $\text{Cr}^{3+}:\alpha\text{-Al}_2\text{O}_3$ ) and alexandrite ( $\text{Cr}^{3+}:\text{BeAl}_2\text{O}_4$ ).

Due to the parity selection rule (Laporte rule), the so-called “ $d-d$  transitions” are theoretically forbidden because initial and final states have the same parity, whereas  $p-d$  or  $d-f$  transitions are allowed. However, “ $d-d$  transitions” are observed in optics because



Laporte rule is weakened, or relaxed, by several factors. The absence of a center of symmetry allows, for example in a tetrahedral symmetry, the  $3d$  orbitals to mix with the  $4p$  orbitals, which possess opposite parities. Another mechanism by which Laporte-forbidden transitions may occur, even in cations located in centrosymmetric sites (e.g. regular octahedron), is through *vibronic* coupling, which involves coupling of *vibrational* and *electronic* wave functions with opposite parities [Ballhausen, 1962].

When the spin multiplicity of the initial and final state remains unchanged ( $\Delta S = 0$ ), transitions are known as “spin-allowed”. As written in Table 3.1, in absence of ligand field potential, for  $d^5$  and  $d^6$  ions there is no other state that has the same spin multiplicity as the ground state (opposite to  $d^2$  ( $V^{3+}$ ),  $d^3$  ( $Cr^{3+}$ ,  $Mn^{4+}$ ),  $d^7$  ( $Co^{2+}$ ,  $Ni^{3+}$ ) and  $d^8$  ( $Ni^{2+}$ ) [Burns, 1993, p. 53]). However, for  $Fe^{2+}$  the degenerated ground state  $^5D$  can be split by ligand field, leading to spin-allowed transitions, while the  $Fe^{3+}$  ground state  $^6S$  is a singlet. For example, in the  $Fe^{2+}$  “ $d-d$  transitions”  $^5T_{2g} \rightarrow ^5E_g$  (octahedral site) or  $^5E \rightarrow ^5T_2$  (tetrahedral or trigonal bipyramid sites) cause the broad signals from 4000 to 19 000  $cm^{-1}$ . In the case of  $Fe^{3+}$ , transitions are “spin-forbidden” and only sextuplet to quartet transitions are possible. However, spin-orbit coupling modifies the *spin selection rule* by allowing the mix of states of different spin multiplicities, leading to weak “spin-forbidden” transitions. For example,  $^6A_{1g} \rightarrow ^4E_g, ^4A_{1g}(G)$  occurring around 22 000  $cm^{-1}$ , but intensities for  $Fe^{3+}$  are generally one or two orders of magnitude weaker than the spin-allowed transitions of  $Fe^{2+}$  ions.

In the case of heterovalent compounds with a mix of both  $Fe^{2+}$  and  $Fe^{3+}$  ions, intense electronic transitions (100 times higher than  $d-d$  transitions), named *intervalence charge transfer* (IVCT), can occur between two neighboring metal ions of different valency. For example, it commonly happens when they are located in edge-sharing coordination polyhedron [Burns, 1993]. For iron doped glasses, bands appear in the range: 11 000~18 000  $cm^{-1}$ \* [Amthauer and Rossman, 1984], which indicates clustering of iron ions [Ookawa et al., 1997].

In the UV range ( $\bar{\nu} > 28\,000\,cm^{-1}$  or  $\lambda < 360\,nm$ ), the intensity is dominated by broad and intense bands, three orders of magnitude higher than the crystal field bands. These spin-allowed and Laporte-allowed bands are due to an electronic transition between the  $2p$  of the nearest-neighbor oxygen ligand and the  $3d$  of the central transition metal ion. They are therefore named *ligand to metal charge transfer* (LMCT) or *oxygen to metal charge transfer* (OMCT) in the case of oxides. The diversity of optical transitions is summarized in Table 3.3.

---

\*11 000~18 000  $cm^{-1}$ ; 900~550 nm; 1.4~2.2 eV

**Table 3.3** – Selection rules and intensity ( $\varepsilon$  in  $\text{L}\cdot\text{mol}^{-1}\cdot\text{cm}^{-1}$ ) of different types of optical absorption bands [Burns, 1993, p. 72]

Transitions	$\varepsilon$	Rules
$\text{Fe}^{3+}$ in regular octahedral site $\text{Fe}^{2+}$ (except ${}^5T_{2g} \rightarrow {}^5E_g$ ) in regular octahedral site	<0.1	Laporte-forbidden and spin-forbidden transitions for a centrosymmetric ion
$\text{Fe}^{3+}$ in tetrahedral site $\text{Fe}^{2+}$ (except ${}^5T_2 \rightarrow {}^5E$ ) in distorted octahedral site	1	Laporte-forbidden and spin-forbidden transitions for a non-centrosymmetric ion
$\text{Fe}^{2+}$ ( ${}^5T_{2g} \rightarrow {}^5E_g$ ) in regular octahedral site	1	Laporte-forbidden but spin-allowed transition for a centrosymmetric ion
$\text{Fe}^{2+}$ ( ${}^5T_2 \rightarrow {}^5E$ ) in distorted octahedral site $\text{Fe}^{2+}$ ( ${}^5T_2 \rightarrow {}^5E$ ) in tetrahedral site	10	Laporte-forbidden but spin-allowed transition for a non-centrosymmetric ion
Intervalence Charge Transfer (IVCT) $\text{Fe}^{2+} \rightarrow \text{Fe}^{3+}$	100	Spin-allowed transitions between two different Fe sites
Charge transfer $\text{O}^{2-} \rightarrow \text{Fe}^{2+}$ Charge transfer $\text{O}^{2-} \rightarrow \text{Fe}^{3+}$	1000 10000	Spin- and Laporte allowed transitions of electrons from the oxygen ligands

### 3.10 Quanty – a quantum many body script language

In the case of strongly correlated electronic levels localized on the absorbing atoms, multiplet calculation has proven to be an efficient method to reproduced the XAS  $K$  pre-edge and the  $L_{2,3}$  edge [Thole et al., 1985], [Briois et al., 1995], [Westre et al., 1997], [Arrio et al., 2000], [de Groot, 2001], [de Groot et al., 2005], [Vankó et al., 2008], [Haverkort et al., 2012]. The first step uses atomic values from Hartree-Fock calculations of the free ion using the code developed by Cowan [1981].

At the beginning of this thesis, we were using Thole’s code TTMULT [Thole et al., 1985] with the formalism of Butler [1981]. However, problems were limiting the calculations of some systems. For low symmetries, configuration interaction for  $\text{Fe}^{3+}$ , which has an unpaired number of  $d$  electrons, led to complex reduced matrix elements when using the sub-program TTRCG. These complex values were not usable by TTRAC to calculated spectra. Moreover, TTRAC was not able to do transitions between level of the same electronic configuration as in optical spectra. Other technical issues, have incited us to use another multiplet software. For example, the impossibility to perform parallel computing in order to reduce the calculation time of complicated spectra of iron in a lower geometry than  $O_h$  and  $T_d$ . All these complications were intrinsic to TTMULT development, which started in the 1980’s and was not maintained since 1997.

In the last year of my thesis, a collaboration with Maurits W. Haverkort was initiated.

During two stays in Dresden (Germany), I learned how to use his program **Quanty**\* and I have implemented the character table of the 32 point groups to use other geometries than the ones already implemented.

**Quanty** is a Lua based script language developed by Maurits W. Haverkort and co-workers. It allows the user to program quantum mechanical problems in second quantization, using creation and annihilation operators to describe and analyze quantum many-body systems. This formalism is different but can be related to the one of **TTMULT**. Cross-section is calculated as Green function, and the output transitions have therefore a linewidth, while **TTMULT** outputs Dirac transitions called sticks. The idea of **Quanty** is that the user can focus on the model and its physical or chemical meaning while **Quanty** takes care of the mathematics.

As all Hamiltonian, the crystal field potential is expanded on spherical harmonics. The idea is that any potential can be written as a sum over spherical harmonics:

$$V(r, \theta, \phi) = \sum_{k=0}^{\infty} \sum_{m=-k}^k A_{k,m} C_{k,m}(\theta, \phi) \quad (3.5)$$

with the expansion coefficients  $A_{k,m}$  depending on the given symmetry and  $C_{k,m}(\theta, \phi)$  are the renormalized spherical harmonics.

**Quanty** is still in its infancy, but growing fast. The code developed from the need to calculate core level spectroscopy (X-ray absorption, resonant diffraction, ...) of correlated transition metal and rare earth compounds. So these areas are the best developed or documented, but many more examples in different fields are regularly added. During the last year, I was able to reproduce **TTMULT**  $K$  pre-edge and  $L_{2,3}$  calculations of isotropic powders. Promising results have been obtained with the help of Amélie Juhin, Marie-Anne Arrio and Christian Brouder concerning the calculation of RIXS spectra, but further developments are still needed to fully implement RIXS powder formulas of Juhin et al. [2014], which are necessary to extract the HERFD-XAS spectra.

### 3.11 Summary

Ligand field multiplet theory is interesting to study the valence orbitals with several spectroscopic methods. We saw that  $3p-4d$  mixing of the transition metal orbitals increases the intensity of transitions, nevertheless, to interpret and simulate optical spectra we have to quantify these intensities. In particular, the intensity of transitions as a function of symmetry and their energy dependence with the crystal field needs a deeper understanding. Which transitions are weak or strong? Which species are “silent” and do not absorb light?

A multi-spectroscopic approach is necessary to probe  $3d$  orbitals and extract qualitative and quantitative information on the structure and the local environment. With such an approach, different electronic configuration of the same ion can be studied through different experimental methods, which increases the accuracy and strengthens the interpretation.

---

\*<http://quanty.org>

## Chapter 4

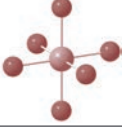




# Investigation of a reference set of crystalline compounds: determination and interpretation of spectral signatures

We saw in the previous chapter that optical absorption spectroscopy (OAS) and X-ray absorption spectroscopy (XAS) at Fe  $K$  pre-edge probe the localized  $3d$  orbitals, which allows us to extract information on the local environment of transition metals. In order to determine the relationships between the electronic/crystallographic structure and the spectral signature, I studied, with OAS and XAS, a set of crystalline compounds in the following geometries:  $O_h$ ,  $T_d$ ,  $D_{3h}/C_{3v}$  and  $D_{4h}$ . Comparison with the calculated spectral signatures enables to interpret the experimental evolution of spectra and describes the geometry as a function of crystal-field and  $4p$ - $3d$  mixing parameters. For this reason, new theoretical developments, detailed in Appendix E, were needed.

In order to study glasses, we first have to understand what contributions can be expected from the different site geometries. We saw in Section 1.3 that, in glasses, angles and distances between iron and its ligands are distributed, which complicates the separation of the different contributions. A possible alternative to study the relationships between the structure and the spectroscopic properties is to look at crystals. Differently than in amorphous materials, there exist crystals in which iron is found to occupy only one crystallographic site and the local environment around iron can be determined by X-ray diffraction (XRD) or EXAFS. The presence of well-defined crystallographic sites makes crystals an interesting model for the determination of structural-spectroscopic relationships, with the intention of extrapolating the results to glasses.

In the following, I will present in parallel the OAS and XAS  $K$  pre-edge spectra obtained from experiments and then calculated data for selected  $Fe^{2+}$ - and  $Fe^{3+}$ -bearing crystalline references: siderite ( $[^6, O_h]Fe^{3+}$ ), andradite ( $[^6, C_{3i}]Fe^{2+}$ ), gillespite ( $[^4, D_{4h}]Fe^{2+}$ ), staurolite ( $[^4, T_d]Fe^{2+}$ ), ferriorthoclase ( $[^4, T_d]Fe^{3+}$ ), grandidierite ( $[^5, C_{3v}]Fe^{2+}$ ) and yoderite ( $[^5, C_{3v}]Fe^{3+}$ ).

**Table 4.1** – List of theoretical crystal field and hybridization parameters related to the point group symmetries studied. The ground states for high-spin  $\text{Fe}^{2+}$  and  $\text{Fe}^{3+}$  ions are listed for the considered geometries, with the degeneracy given in parenthesis.

Point group symmetry	Crystal field parameters	$p$ - $d$ hybridization parameters	Ground state (dim)	
			$d^6$ - $\text{Fe}^{2+}$	$d^5$ - $\text{Fe}^{3+}$
$O_h$ 	$10Dq$	–	${}^5T_{2g}$ (15)	${}^6A_{1g}$ (6)
$D_{4h}$ 	$Dq$ $Dt$ $Ds$	–	${}^5A_{1g}$ (5)	${}^6A_{1g}$ (6)
$T_d$ 	$10Dq$	$V_{pd}$	${}^5E$ (10)	${}^6A_1$ (6)
$C_{4v}$ 	$Dq$ $Dt$ $Ds$	$V_{pd}^e$ $V_{pd}^{a_1}$	${}^5E$ (10)	${}^6A_1$ (6)
$D_{3h}$ 	$D\mu$ $D\nu$	$V_{pd}$	${}^5E''$ (10)	${}^6A_1'$ (6)

In order to extract quantitative information from the pre-edge, we performed LFM calculations using the method developed by Thole et al. [1985] in the framework established by Cowan [1981] and Butler [1981]. Here, this approach is implemented in the code `Quanty`, in which operators are defined using second quantization, and spectra are calculated using Green’s functions, as explained in Section 3.10. It takes into account all the  $3d$ - $3d$  and  $1s$ - $3d$  electronic Coulomb interactions, as well as the spin-orbit coupling on every open shell of the absorbing atom. For all sites, we applied a reduction factor of  $\beta = 0.6$  to the Slater integrals calculated for an isolated ion and spin-orbit coupling is considered at 100% of its free ion value\*. Iron is considered as an isolated ion and its geometrical environment is treated through a parameterized crystal-field potential defined by the point group symmetry of the absorbing site. These parameters, summarized in Table 4.1 were fitted in agreement with the optical spectra of the compounds. For non-centrosymmetric sites, hybridization is allowed between  $3d$  and  $4p$  orbitals of iron and is described by a hybridization Hamiltonian. The  $p$ - $d$  hybridization Hamiltonian depends on the energy difference  $\Delta$  and  $\Delta'$  between the average energies of the two electronic configurations in the initial and final states, respectively. Figure 4.1 explains the configuration interaction between the different electronic configurations involved in the LFM calculation. The  $\Delta$  and  $\Delta'$  values were fixed to the difference between the Hartree-Fock energies of the electronic configurations obtained from Cowan’s code “RCN” (atomic). For  $\text{Fe}^{2+}$ :  $\Delta = 12.6$  eV and  $\Delta' = 13.8$  eV; for  $\text{Fe}^{3+}$ :  $\Delta = 21.2$  eV and  $\Delta' = 22.9$  eV (Figure 4.1). We observe that  $\Delta'$  of the excited state after a  $1s \rightarrow 3d$  transition is about 10% larger than  $\Delta$  of the initial state.

\*Slater integrals for  $\text{Fe}^{2+}$  free ion:  $F_{3d,3d}^2 = 10.966$  eV,  $F_{3d,3d}^4 = 6.815$  eV and  $\zeta_{3d} = 0.052$  eV and for  $\text{Fe}^{3+}$  free ion:  $F_{3d,3d}^2 = 12.043$  eV,  $F_{3d,3d}^4 = 7.535$  eV and  $\zeta_{3d} = 0.059$  eV.

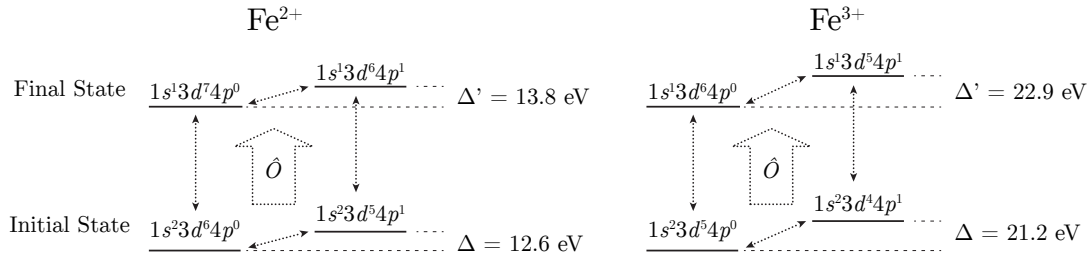


**Figure 4.1** – Scheme of configuration interaction for  $\text{Fe}^{2+}$  and  $\text{Fe}^{3+}$  that takes into account  $p$ - $d$  hybridization in the framework of ligand field multiplet theory (LFMT).

Depending on the symmetry, the hybridization Hamiltonian is described by one ( $T_d$  and  $D_{3h}$ ) or two ( $C_{4v}$ )  $V_{pd}$  parameters. The hybridization Hamiltonian mixes  $d$  and  $p$  orbitals of same symmetry:  $t_2$  for  $T_d$ ,  $e'$  for  $D_{3h}$ ,  $a_1$  and  $e$  for  $C_{4v}$ . For each point group symmetry, the hybridization parameters were adjusted in order to reproduce the experimental intensity of the  $K$  pre-edge, which determines the respective contributions of dipole and quadrupole transitions to the pre-edge (the sum is explained in Appendix E.4). The absolute intensities were calculated at  $T = 300$  K and the population of the ground-state levels is given by the Boltzmann law (see Appendix D.1). The use of Green's function in the calculation (see Appendix E.4) prevents from finding sticks corresponding to Dirac function at the position of the transitions. However, “sticks” can be approximated by calculating the spectrum with a small Lorentzian broadening ( $L_{\text{FWHM}} = \Gamma = 0.01$  eV) and no Gaussian broadening. For plotting convenience, the intensities of “sticks” were divided by 100 because they were too intense due to the conservation of the area by the convolution. As explained by Arrio et al. [2000], to obtain the calculated isotropic spectrum of a powder that we can compare with the experimental data, the sticks were convoluted by a Lorentzian line (full width half maximum,  $L_{\text{FWHM}} = \Gamma = 2\gamma = 1.12$  eV) and a Gaussian line ( $G_{\text{FWHM}} = 2\sqrt{2 \ln 2} \sigma = 0.35$  eV), which respectively account for the  $1s$  core-hole lifetime of Fe and for the instrumental resolution (see Appendices D.2 and E.4). Finally, the transitions are normalized by the edge jump at the Fe  $K$  edge, calculated for Fe on atom as  $3.3 \cdot 10^{-4} \text{ \AA}^2$  [Gullikson, 2010]. Hence, the calculated spectra can be directly compared to the normalized experimental ones. Concerning the calculated optical spectra, they were convoluted by a Lorentzian line with  $L_{\text{FWHM}} = 0.01$  eV ( $80 \text{ cm}^{-1}$ ) and a Gaussian line with  $G_{\text{FWHM}}$  from  $0.09$  eV ( $726 \text{ cm}^{-1}$ ) to  $0.15$  eV ( $1210 \text{ cm}^{-1}$ ) in order to be compared with experimental optical spectra.

#### 4.1 The case of $O_h$ – octahedral $^{61}\text{Fe}^{2+}$ in siderite

Siderite has a simple chemical formula  $\text{FeCO}_3$  with 100% of  $\text{Fe}^{2+}/\text{Fe}_{\text{tot}}$ .  $\text{Fe}^{2+}$  ions occupy the center of a regular  $O_h$  octahedral site (See Appendix A for more details). In this particular case, there is only one crystal field parameter  $10Dq$  and no  $3d$ - $4p$  hybridization parameter  $V_{pd}$ .

##### 4.1.1 XAS

Figure 4.2 shows the experimental Fe  $K$  pre-edge XAS spectrum of siderite. After removing the main edge using an arctangent fit, the pre-edge intensity is only 2% of

the main edge, which is consistent with pure electric quadrupole transitions as expected in  $O_h$ . **Quanty** was used to calculate the spectrum (quadrupole contribution only), parameters were adjusted to best match the experimental data:  $10Dq = 0.98$  eV ( $7900$   $\text{cm}^{-1}$ ) and  $\beta = 0.6$  (corresponding to Racah parameters  $B = 0.0879$  eV =  $709.2$   $\text{cm}^{-1}$  and  $C = 0.3245$  eV =  $2617.7$   $\text{cm}^{-1}$ ).

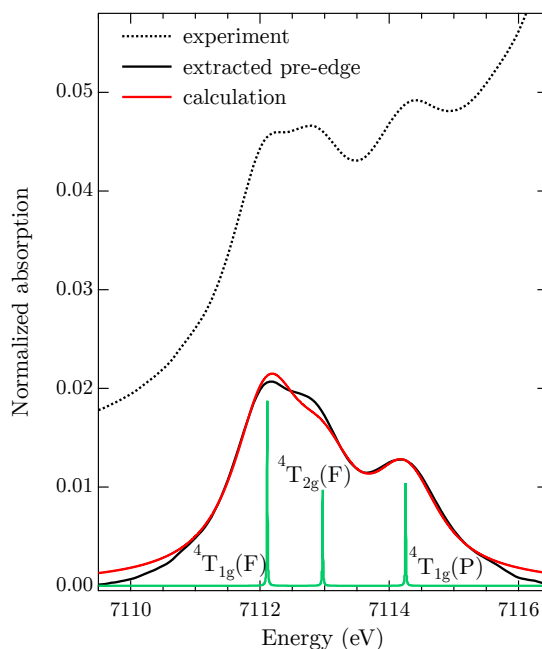


**Figure 4.2** – Experimental Fe  $K$  pre-edge XAS of siderite before (black dashed line) and after (black solid line) edge subtraction, and the calculated pre-edge (red).

In comparison with the experiment, the ratio of intensities between the first and the second peak is slightly different. The tail of the experimental pre-edge is lower than the calculated one, which is probably due to the pre-edge extraction. LFM calculation performed in this thesis does not accurately reproduce the main edge, which is due to transitions to delocalized levels\*. Nevertheless, a good overall agreement is found between multiplet calculations and the experimental data.

From the calculation, the ground state is the high-spin level  ${}^5T_{2g}(D)$ , which is conformed to Hund's rule.  $10Dq = 0.98$  eV is close to the  $10Dq$  value deduced from OAS experiment in Fe-bearing minerals with  $O_h$  geometry [Burns, 1993, p. 229-230]. The  $K$  pre-edge intensity only comes from the weak electric quadrupole transitions  $1s \rightarrow 3d$ , as confirmed by our calculation in the absence of  $p$ - $d$  mixing. By analogy with the  $d^7$  configuration (without the core-hole), the three peaks can be attributed to the transitions  ${}^5T_{2g}(D) \rightarrow {}^4T_{1g}(F)$ ,  ${}^5T_{2g}(D) \rightarrow {}^4T_{2g}(F)$  and  ${}^5T_{2g}(D) \rightarrow {}^4T_{1g}(P)$  because the  $1s$  core-hole has a weak influence on the  $3d$  [Calas and Petiau, 1983a; Westre et al., 1997].

#### 4.1.2 Optical absorption spectroscopy

For centrosymmetric geometries such as  $O_h$ , the difficulty of calculating optical spectra remains in the fact that optical electric dipole transitions between  $d$  levels are theoretically

\*For the  $K$  edge XANES region, a single particle approach, such as DFT, is more adapted.

forbidden. Due to the presence of an inversion center, the  $p$  and  $d$  orbitals cannot mix because they are not of the same parity:  $p$  orbitals are *ungerade* or odd (e.g.  $e_u, t_{2u}$ ), while  $d$  orbitals are *gerade* or even (e.g.  $e_g, t_{2g}$ ).

To solve this problem of forbidden transitions, a small hybridization potential has been added in order to mix the  $3d$  orbitals with a small fraction of  $4p$  orbitals, allowing the computation of transition intensities that are not zero. The  $C_{4v}$  potential was used with  $V_{pd}^e = V_{pd}^{a_1} = 0.1$  eV, I have verified that the energies of the electronic states remain unchanged. From a physical point of view, the loss of the inversion center can be explained by two processes: the presence of a static distortion, which breaks the regularity of the geometry, or vibrations that are dynamic effects, which temporarily break the geometry.

Experimental and calculated OAS spectra are compared in Figure 4.3. The experimental spectrum is the combination of a transmission measurement from the GIA gem database\* (solid line) and a reflectance measurement from this study (dashed line). The spin-forbidden signals obtained around  $15\,000\text{ cm}^{-1}$  and  $20\,000\text{ cm}^{-1}$  are 100 times weaker than the spin-allowed transition  ${}^5T_{2g}(D) \rightarrow {}^5E_g(D)$ , as expected by the transitions rules (see Section 3.9, Table 3.3). However, as it can be noticed on the experimental spectrum, the spin-allowed transition is split in two contributions, which suggests that the Fe site is distorted. For  $\text{Fe}^{2+}(\text{H}_2\text{O})_6$ , Burns [1993] explained this splitting by a dynamic Jahn-Teller effect. But a lower geometry can indeed explain the splitting of the  ${}^5T_{2g}(D) \rightarrow {}^5E_g(D)$  transition.

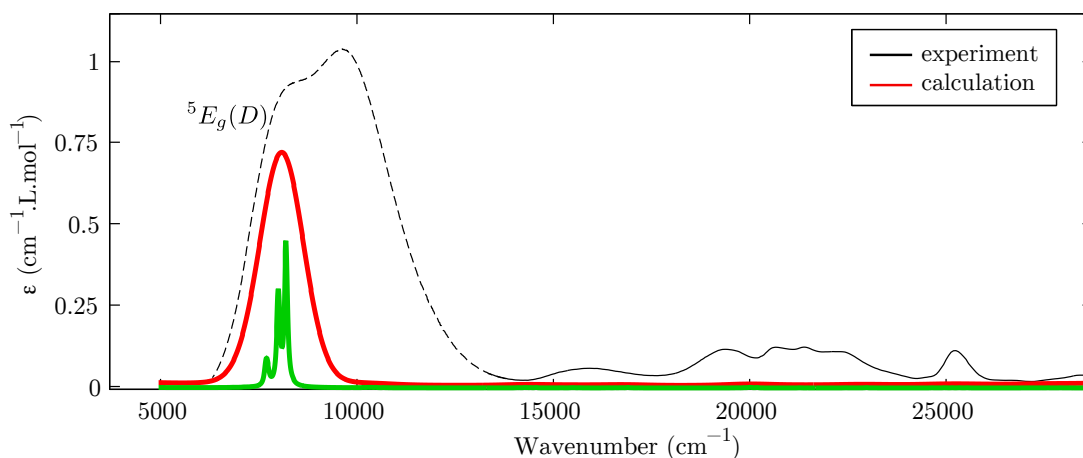


**Figure 4.3** – Experimental optical absorption spectrum (black solid and dashed line) of siderite, and the LFM calculated spectrum (red).

### 4.1.3 Effect of the different parameters

The purpose of this section is to understand the impact on spectra of the different physical parameters considered in the LFM calculation.

#### 4.1.3.1 Hybridization

In order to calculate optical spectra caused by electric dipole transition, a  $p$ - $d$  hybridization was considered in order to get a non-null intensity in the calculated spectra. In the

\*Gemological Institute of America, collection number 35506



case of centrosymmetric geometry such as  $O_h$ , a hybridization Hamiltonian of the  $C_{4v}$  sub-group was considered and the  $p$ - $d$  mixing was quantified using the parameters  $V_{pd}^e$  and  $V_{pd}^{a_1}$ . Figure 4.4 shows the effect of  $V_{pd}^e$  and  $V_{pd}^{a_1}$  on the XAS and optical absorption spectra.

One can note that a slight background growing with increasing wavenumber is visible on the calculated spectrum. This artifact is due to the use of Green's functions, since calculated transitions are not discrete values but a Lorentzian function with an intrinsic linewidth. In this case, this background signal is due to the tail of fully authorized  $3d \rightarrow 4p$  electric dipole transitions present above 12 eV ( $\sim \Delta$ ) with an intensity, that is five orders of magnitude higher than Laporte-forbidden optical transitions.

If  $V_{pd}$  is smaller than a threshold of around 1 eV, the evolution of intensity is proportional to the square value of  $V_{pd}$  and the energy positions of transitions are not modified. Above this value of 1 eV, the shape of spectra is modified because the mixing between  $d$  and  $p$  levels results in new multiplet levels with modified energies.

Regarding the iron  $K$  pre-edge XAS, if  $V_{pd} < 1$  eV the pre-edge intensity of a centrosymmetric site is not modified, and the dipole contribution induced by this small hybridization is negligible when compared to the electric quadrupole intensity. For  $V_{pd}^e = V_{pd}^{a_1} = 0.1$  eV, the electric dipole area only represents 1.9% of the total area. Calculations give the number of  $p$  electrons  $N_p = 1.7 \cdot 10^{-4}$ , which is small compared to the number of  $d$  electrons,  $N_p = 5.9998$ . Therefore, the  $p$ -character of the ground state, defined by  $N_p/(N_p+N_d)$ , is  $2.8 \cdot 10^{-5}$ .

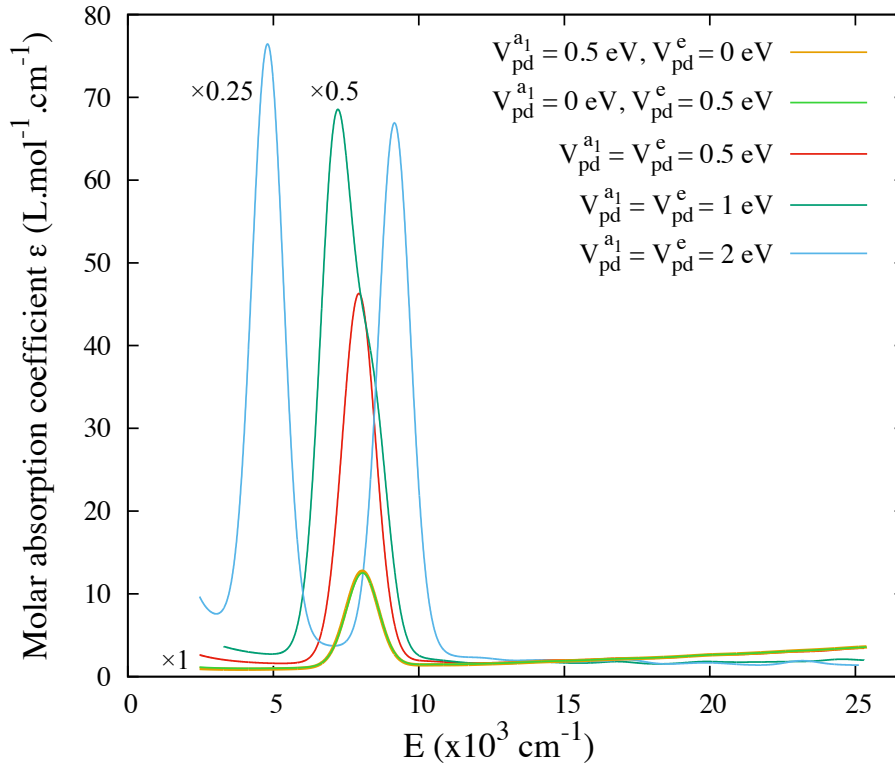


Figure 4.4 – Effect of  $V_{pd}$  on the calculated optical spectra of  $Fe^{2+}$  in  $O_h$ .

### 4.1.3.2 Crystal field

In the case of  $O_h$  geometry there is only one crystal-field parameter  $10Dq$ , therefore it is simple to represent the effect on spectra as a function of this parameter using a Tanabe-Sugano diagram. Thanks to the  $p-d$  mixing, it is now possible to calculate both the positions and the intensities of optical transitions. A third dimension (color bar) representing the intensity of optical transitions can be added to the conventional Tanabe-Sugano diagram calculated without spin-orbit coupling and hybridization.

#### Effect of $10Dq$ on optical bands

Figure 4.5 (left) is a 3D map composed of multiple optical spectra with  $10Dq$  varying from 0 to 1.4 eV that has been calculated with 100% of the spin-orbit coupling value and a hybridization parameters of 0.5 eV. This color map overlaid with the classical Tanabe-Sugano diagram (black lines) allows the attribution of multiplet levels. Each absorption band matches with a transition given by the Tanabe-Sugano diagram. Additional bands related to singlet states (not represented on the Tanabe-Sugano diagram) are also visible on the 3D map. These levels with a spin multiplicity of 1, give optical bands due to spin-orbit coupling when they are nearby triplet or quintet levels.

The calculated optical spectra for three values of  $10Dq$ , centered on the best  $10Dq$  value found in the previous section are shown in Figure 4.5 (right). By increasing  $10Dq$  by 10%, the spin allowed transition is shifted by 10% to higher energies, accompanied by an 10% increase of the molar absorption coefficient.

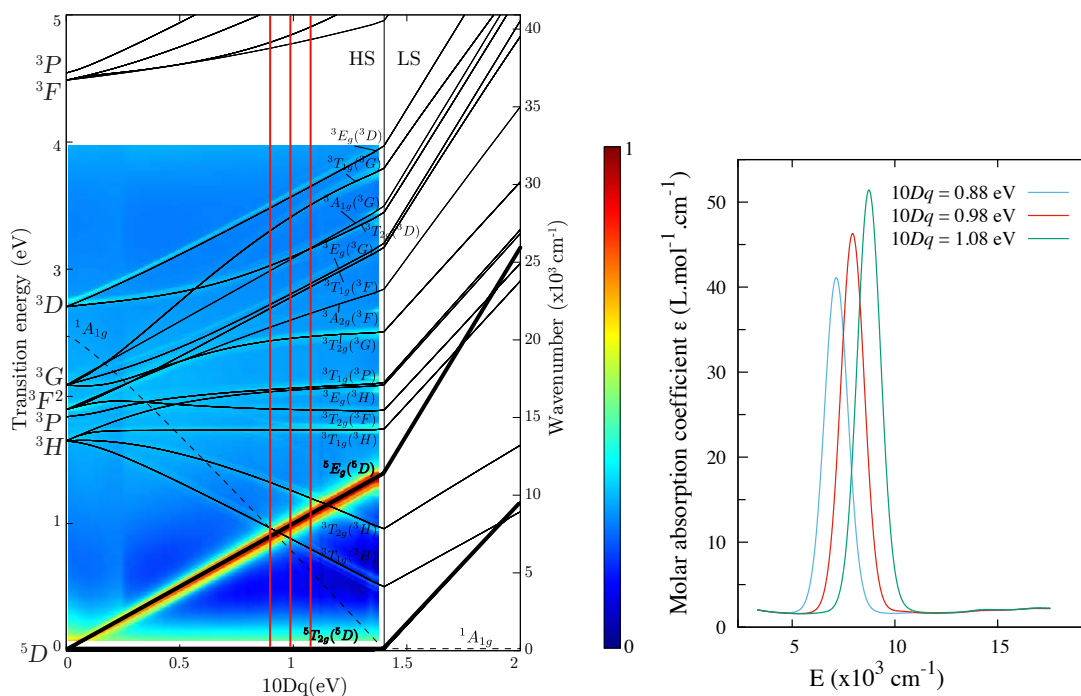


**Figure 4.5** – (Left) Calculated Tanabe-Sugano diagram (black lines) of  $Fe^{2+}$  in  $O_h$  without spin-orbit coupling, singlet levels are not shown, except the low-spin state  $^1A_{1g}$  that becomes the ground state at high  $10Dq$ . The color map shows the respective calculated OAS spectra with spin-orbit coupling and a small (0.5 eV) hybridization parameter. (Right) Calculated optical absorption bands for the three values of  $10Dq$  corresponding to the three lines of the left figure.

Figure 4.6 shows the effects of  $10Dq$  on the Fe  $K$  pre-edge XAS spectrum. With  $10Dq$  varying from 0 eV to 2 eV, the signal is split in three peaks, which shift relatively to each other when  $10Dq$  increases. It can be noticed that the second and third peaks keep a constant splitting energy. By comparing with the experiment, it appears that the  $10Dq$  range seems limited from 0.6 eV ( $4800\text{ cm}^{-1}$ ) to 1.4 eV ( $11\,300\text{ cm}^{-1}$ ).

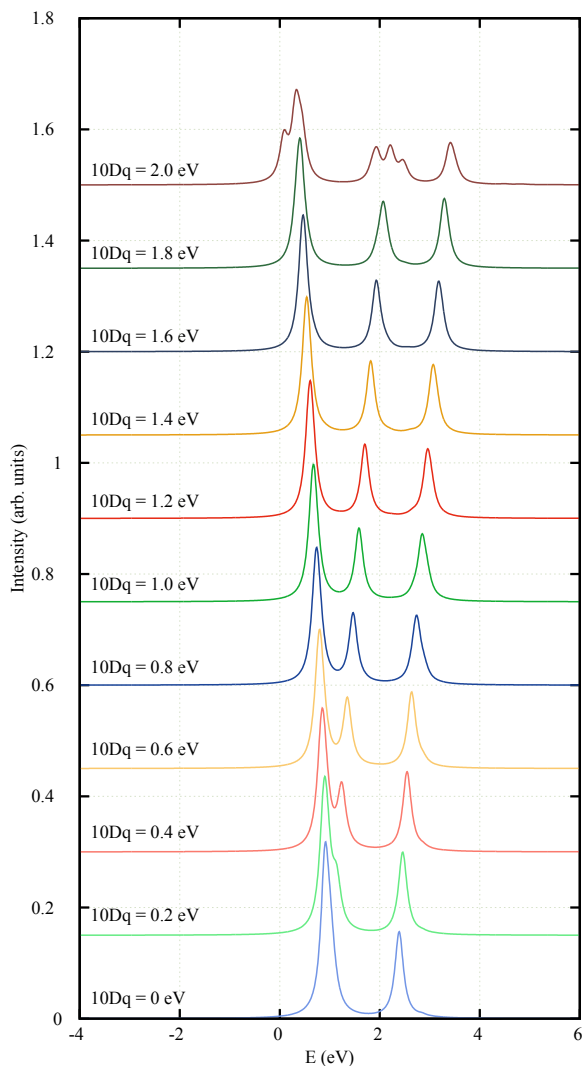


**Figure 4.6** – Effect of  $10Dq$ , from 0 to 2 eV, on the calculated Fe  $K$  pre-edge XAS of  $\text{Fe}^{2+}$  in  $O_h$ , with  $\beta = 60\%$  and a Lorentzian broadening  $\Gamma = 0.2\text{ eV}$ .

Finally, these calculations show that both spectroscopies (XAS and OAS), are sensitive to the  $10Dq$  parameter.

#### 4.1.3.3 Nephelauxetic ratio $\beta$

The effect of nephelauxetic ratio  $\beta$  is the same than Racah  $B$  parameter ( $\beta = B/B_0$ ). For  $\beta = 0.6, 0.7$  or  $0.8$ , the position of the main spin-allowed band at  $0.98\text{ eV}$  ( $7900\text{ cm}^{-1}$ ) remains identical for a given  $10Dq$  (Figure 4.7-left). This confirms the interpretation of the Tanabe-Sugano diagram for  $\text{Fe}^{2+}$  in  $O_h$ , since the band position energy normalized by Racah  $B$  parameter,  $E/B$ , is a linear function of  $10Dq/B$  crossing the origin. In the meantime, a slight increase of  $\varepsilon$  is observed by changing the bond covalency.

For  $\beta = 0.6, 0.7$  or  $0.8$ , modifications of the XAS spectra are noticed on the shoulder visible around  $7115 \text{ eV}$  (Figure 4.7). The energy splitting remains constant between the first and second peak, while the third peak becomes more separated due to a stronger high-energy shift.

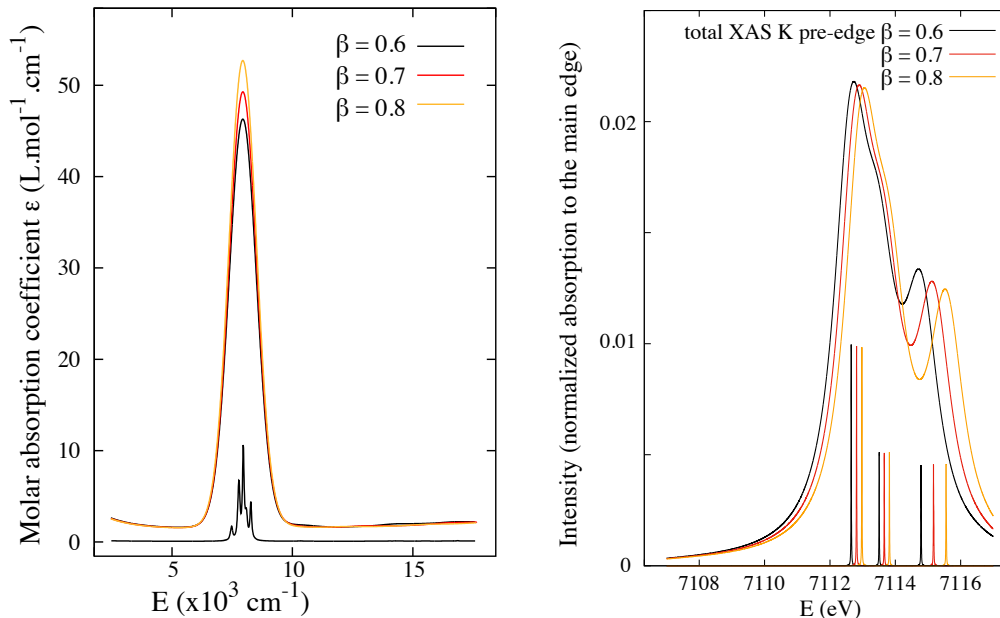


**Figure 4.7** – Effect of nephelauxetic ratio  $\beta$  on the calculated OAS (left) and XAS (right) spectra for  $\text{Fe}^{2+}$  in  $O_h$ .

#### 4.1.3.4 Spin-orbit coupling on the $3d$ levels

The spin-orbit coupling slightly splits the levels by removing part of the ground state degeneracy. This energy splitting is about  $0.05 \text{ eV}$  which is of the same order of magnitude than the spin-orbit coupling value ( $\zeta_{3d} = 0.052 \text{ eV}$  for  $\text{Fe}^{2+}$ ).

As it can be noticed in Figure 4.8-right, spin-orbit coupling slightly splits the XAS transitions but it has no effect on the convoluted pre-edge. The low-energy resolution of XAS leads to a signal broadening about  $1 \text{ eV}$ , which is too large to observe the spin-orbit effect on the  $3d$  orbitals. Therefore, no change is observed in the relative intensities of the broadened calculated XAS spectrum.

On the contrary, spin-orbit coupling change the shape of optical bands (Figure 4.8-left) because the energy resolution of optical spectroscopy is of the same order of magnitude that spin-orbit coupling.

Because spin-orbit coupling does not depend on geometry, the same conclusion can be done whatever the symmetry. Therefore, spin-orbit coupling on the  $3d$  electron can be dismissed for XAS calculations at  $K$  pre-edge but has to be considered for OAS in the UV-Vis-NIR range.

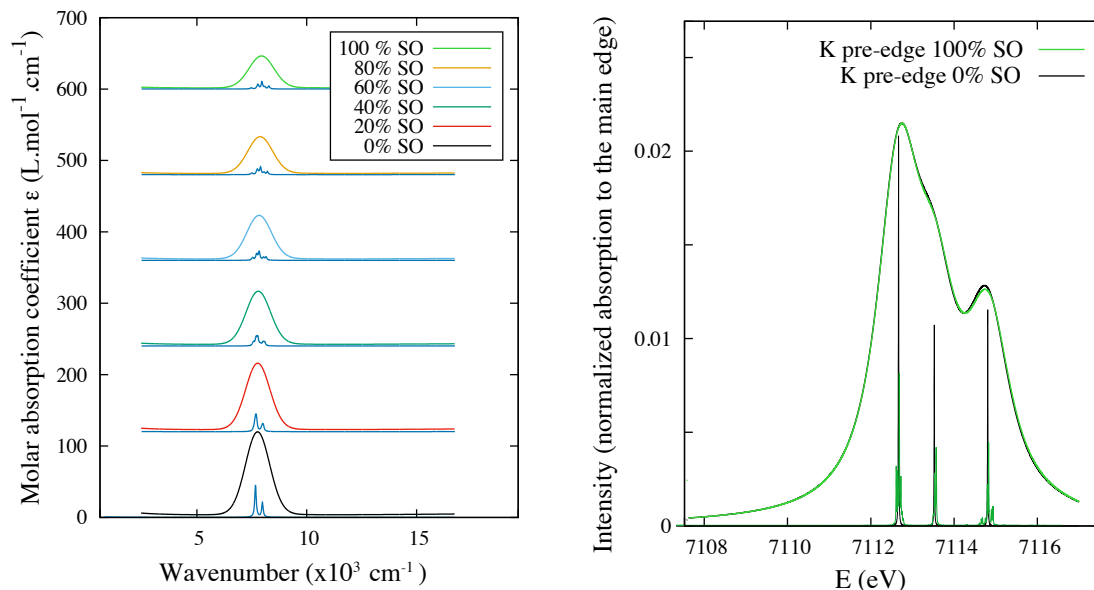


**Figure 4.8** – Effect of spin-orbit coupling  $\zeta_{3d}$  on the calculated OAS (Left) and  $K$  pre-edge XAS spectra (Right) for  $\text{Fe}^{2+}$  in  $O_h$ .

## 4.2 The case of $O_h$ – octahedral $[\text{Fe}^{3+}]_6$ in andradite

Andradite garnet ( $\text{Ca}_3\text{Fe}_2\text{Si}_3\text{O}_{12}$ ) is a silicate mineral with only ferric iron ( $d^5$ ) in the center of a quasi-regular octahedron (all Fe–O distances are equal but the angles are not exactly  $90^\circ$ , see Appendix A for more details). The site geometry is  $C_{3i}$  ( $S_6$ ), and will be approximated to  $O_h$  in this study.

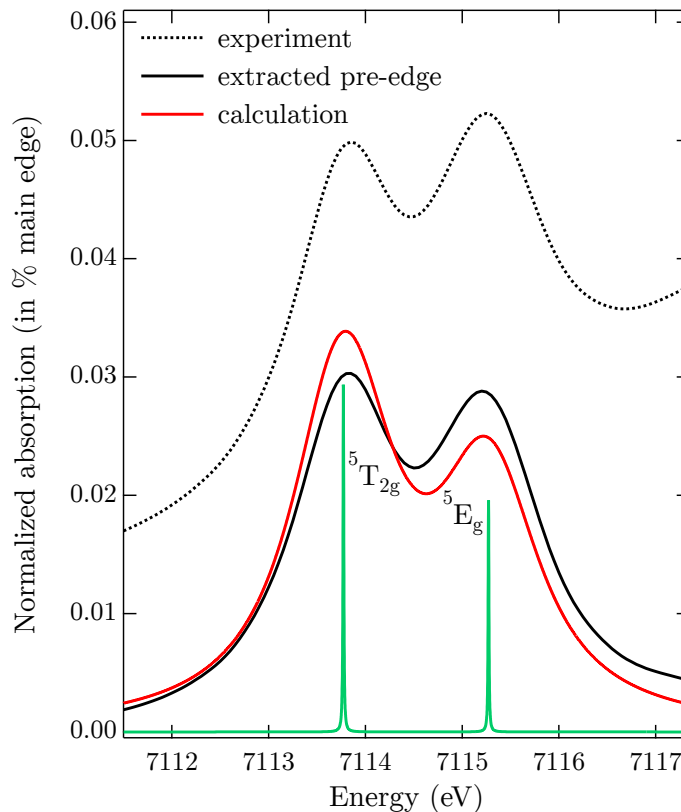
### 4.2.1 XAS

Figure 4.9 shows the experimental Fe  $K$  pre-edge XAS spectrum of andradite composed of two bands. After an arctangent fit of the main edge, the pre-edge intensity is only 3% of the main edge, which is consistent with pure electric quadrupole transitions. Parameters of the calculation were adjusted to best match the experimental spectrum:  $10Dq = 1.5$  eV ( $12100\text{ cm}^{-1}$ ) and  $\beta = 0.6$ .

A good overall agreement has been found between multiplet calculations and experiment. The ground state is the high-spin level  ${}^6A_{1g}(S)$ , which is conformed to Hund’s rule and the value of  $10Dq$  (1.5 eV;  $12100\text{ cm}^{-1}$ ) is consistent with the experimental value of andradite from OAS [Burns, 1993, p. 224]. By analogy with the  $d^6$  configuration, the two peaks at 7113.8 eV and 7115.3 eV can be attributed to the transitions  ${}^6A_{1g}(S) \rightarrow {}^5T_{2g}(D)$  and  ${}^6A_{1g}(S) \rightarrow {}^5E_g(D)$ , respectively [Westre et al., 1997]. In this particular case, the energy difference between the two peaks is equal to  $10Dq$  and does not depend on  $\beta$  [Lever, 1984, p. 126].

The experimental ratio between both intensities is 1.05:1, while the calculated ratio is 1.5:1. The first peak represents 0.6 of the total area, which is equal to the value found for more regular octahedral systems [Westre et al., 1997]. The intensity difference, between experimental and calculated spectra, is probably related to some slight differences in the

site geometry, which is not a pure  $O_h$  but rather a  $C_{3i}$  symmetry. Further adjustment trials of the calculation parameters ( $10Dq$ ,  $\beta$ ) did not improve significantly the relative intensity between both peaks. The point group symmetry has to be lowered to take into account the real symmetry of the crystal.



**Figure 4.9** – Experimental Fe  $K$  pre-edge XAS of andradite before (black dashed line) and after (black solid line) edge subtraction, and the calculated pre-edge (red).

#### 4.2.2 Optical absorption spectroscopy

Compared to the previous section, where  $C_{4v}$  was used for the hybridization Hamiltonian in siderite, the optical intensities were calculated here using a  $C_3$  hybridization potential\* with a small  $V_{pd}$  of 1 eV.  $C_3$  is sub-group of both  $O_h$  and  $C_{3i}$  without inversion center that conserves the  $C_3$  axis characteristic of  $C_{3i}$   $Fe^{3+}$  site in andradite.

Figure 4.10 shows both the experimental spectrum and the calculated one for  $\beta = 0.62$  and  $10Dq = 1.6$  eV. It can be noticed that the calculated intensities obtained for the band around  $12000\text{ cm}^{-1}$  and  $17000\text{ cm}^{-1}$  are stronger than the experimental intensities. This is due to the choice of the sub-group used for hybridization, which is particularly difficult for centrosymmetric point groups such as  $O_h$  because the geometry has to be lowered into a non-centrosymmetric but several possibilities are available.

The signal around  $23000\text{ cm}^{-1}$  is too broad meaning that the experimental broadening ( $G_{FWHM} = 0.15$ ) used in the calculation has been overestimated.

\*The different coefficients for  $p-d$  mixing in  $C_3$  can be further optimized to improve the relative intensities.

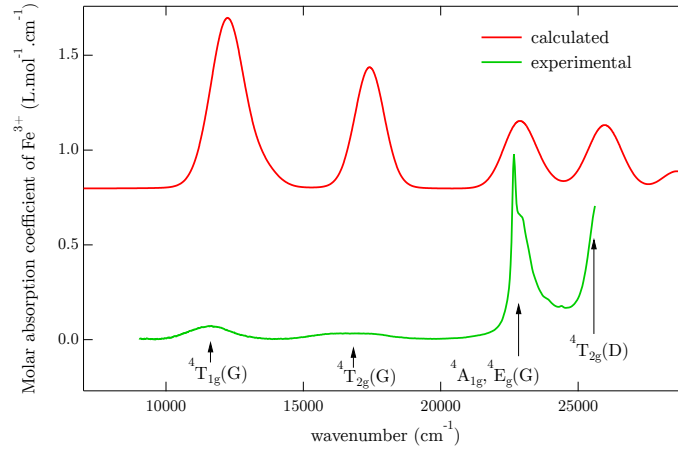


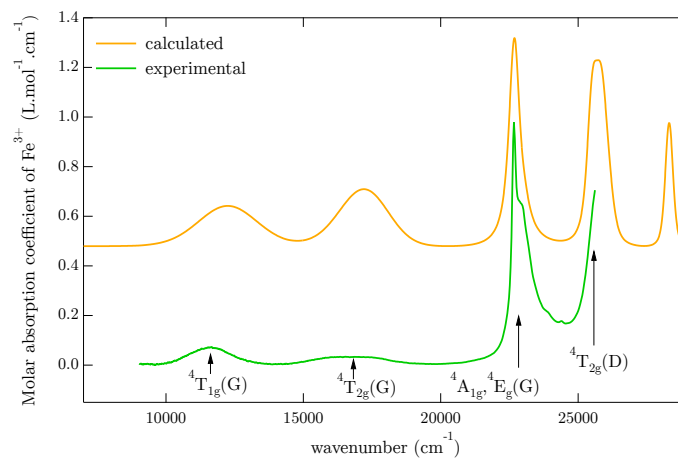
**Figure 4.10** – Calculated and experimental (transmission) optical spectra of andradite. The calculated spectrum is done for  $\beta = 0.62$ ,  $10Dq = 1.6$  eV and Gaussian broadening  $G_{FWHM} = 0.15$

### 4.2.3 Effect of the different parameters

The conclusions on the effects of hybridization on spectra of  $Fe^{2+}$  in  $O_h$  symmetry are transferable to the present case of  $Fe^{3+}$ . Below a threshold of about  $V_{pd} = 1$  eV, there is no effect on the band positions and the band intensities increase with the square value of  $V_{pd}$ .

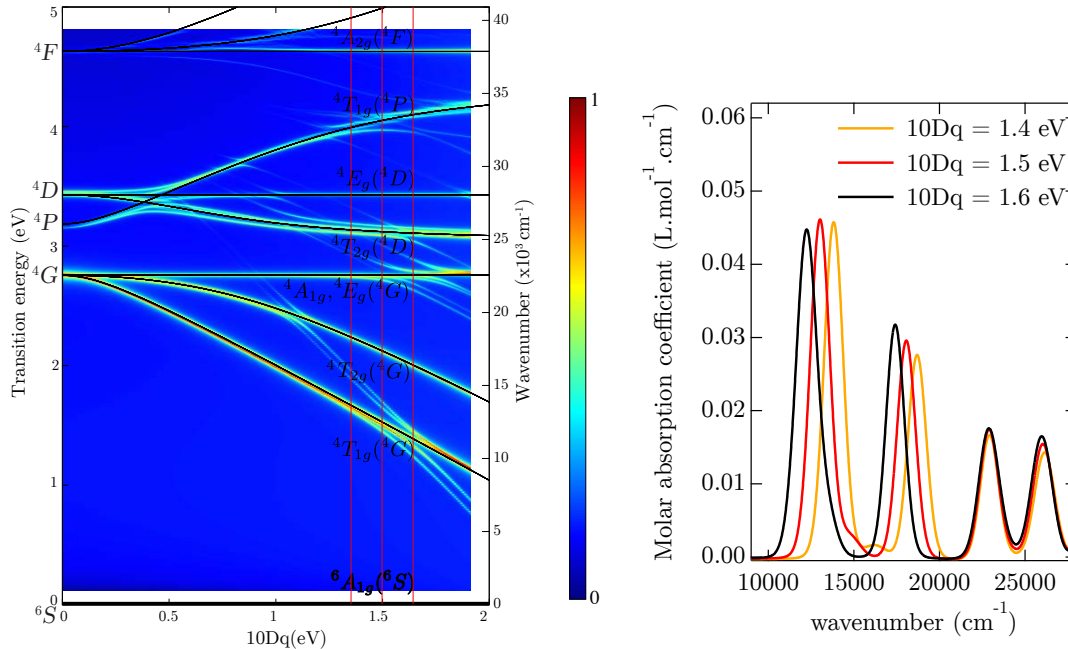
#### 4.2.3.1 Crystal field

Figure 4.11 shows both the experimental spectrum and the calculated one for  $\beta = 0.62$  and an average  $10Dq$  of 1.6 eV without Gaussian broadening. Instead of using a spectral broadening for the optical absorption spectrum, a Gaussian distribution has been applied on  $10Dq$  with a FWHM of 0.3 eV. The use of a  $10Dq$  distribution is a method to reproduce the broad value of the two ligand field dependent transitions  ${}^6A_{1g}(S) \rightarrow {}^4T_{1g}(G)$  and  ${}^6A_{1g}(S) \rightarrow {}^4T_{2g}(G)$  around  $12\,000\text{ cm}^{-1}$  and  $17\,000\text{ cm}^{-1}$ . As opposed to the calculated spectrum of Figure 4.10, with a  $10Dq$  distribution there is no strong broadening of the ligand field independent transitions  ${}^6A_{1g}(S) \rightarrow [{}^4A_{1g}, E_g(G)]$  and  ${}^6A_{1g}(S) \rightarrow {}^4T_{2g}(D)$  around  $23\,000\text{ cm}^{-1}$  and  $26\,000\text{ cm}^{-1}$ .



**Figure 4.11** – Calculated and experimental (transmission) optical spectra of andradite. The calculated spectra was done for  $\beta = 0.62$ , an average  $10Dq = 1.6$  eV and no gaussian broadening. However, a Gaussian distribution has been applied on  $10Dq$  with a FWHM of 0.3 eV.

Figure 4.12-left shows the 3D map of optical spectra using a  $C_3$  hybridization overlaid by the classical Tanabe-Sugano diagram of  $\text{Fe}^{3+}$  in  $O_h$ . Figure 4.12-right shows three OAS spectra for  $10Dq$  values of 1.4, 1.5 and 1.6 eV marked on the 3D map. We see clearly that the two first bands are sensitive to  $Dq$  and the last three bands are crystal field independent (intensity and position).

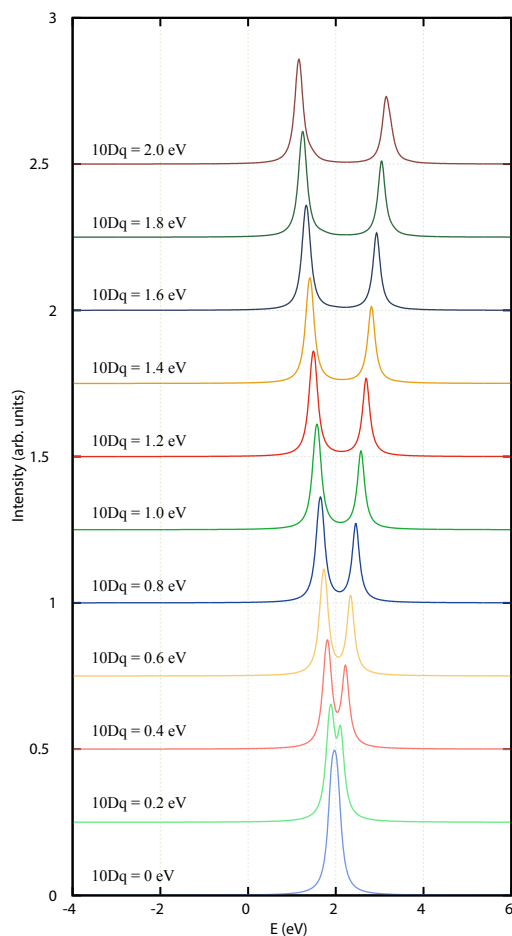


**Figure 4.12** – (Left) Calculated Tanabe-Sugano diagram (black lines) of  $\text{Fe}^{3+}$  in  $O_h$  without spin-orbit coupling, doublet levels are not shown. The color map shows the respective calculated OAS spectra with spin-orbit coupling and a small (1 eV) hybridization parameter. (Right) Calculated optical absorption bands for the three values of  $10Dq$  corresponding to the three lines of the left figure.

When  $10Dq$  increases the  ${}^4T_{1g}(G)$  and  ${}^4T_{2g}(G)$  bands shift in position to lower energy value. In the meantime the intensity of  ${}^4T_{1g}(G)$  is kept unchanged and the intensity of  ${}^4T_{2g}(G)$  increases with  $10Dq$ . As we have seen in the previous section for siderite, optical absorption is sensitive to site geometry through transition intensity. Therefore, the relative intensities of the different optical transitions will depend on the non-centrosymmetric sub-group chosen to get intensity in the OAS spectrum (here it is  $C_3$  with  $V_{pd} = 1$  eV). Nevertheless, the present results are already satisfying but the use of a crystal field Hamiltonian in  $C_{3i}$  point group could eventually reproduce the splitting of the  $[{}^4A_{1g}, {}^4E_g(G)]$  level.

Figure 4.13 shows the effects of  $10Dq$  on the Fe  $K$  pre-edge XAS. For  $10Dq$  varying from 0 eV to 2 eV, the two levels  ${}^5T_{2g}$  and  ${}^5E_g$  are split by an energy of exactly  $10Dq$ , as expected by theory for a  $d^6$  ion [Lever, 1984].

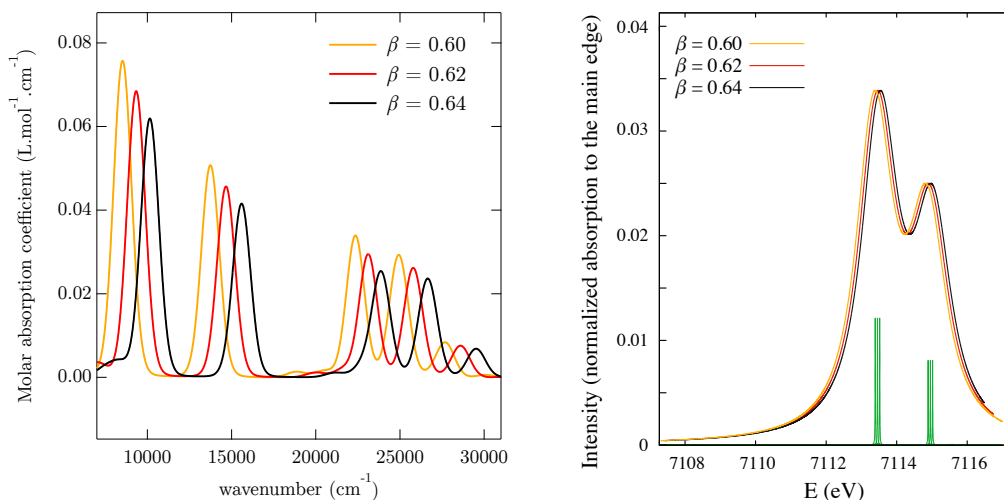




**Figure 4.13** – Effect of  $10Dq$ , from 0 to 2 eV, on the calculated Fe  $K$  pre-edge XAS of  $\text{Fe}^{3+}$  in  $O_h$ , with  $\beta = 60\%$  and a Lorentzian broadening  $\Gamma = 0.2$  eV.

Finally, these calculations show that both spectroscopies (XAS and OAS), are sensitive to the  $10Dq$  parameter.

#### 4.2.3.2 Nephelauxetic ratio $\beta$



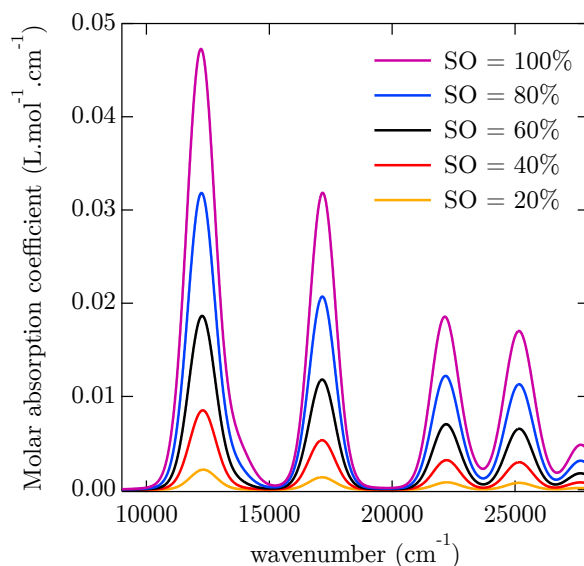
**Figure 4.14** – Effect of nephelauxetic ratio  $\beta$  on the calculated OAS (Left) and XAS (Right) spectra for  $\text{Fe}^{3+}$  in  $O_h$ .

Figure 4.14-right shows the XAS spectra for  $\beta = 0.6, 0.62$  and  $0.64$ . It can be noted that the whole  $K$  pre-edge is slightly shifted. No change is visible on the intensities and relative positions between the two transitions. Since the splitting between these two peaks is  $\beta$ -independent and the absolute position of the theoretical Fe  $K$  edge is just not determined with accuracy, the ionocovalent ratio cannot be determined experimentally using XAS.

On the other hand, as shown in Figure 4.14-left, the optical bands are globally shifted to higher energies. Calculation shows that a modification of 2% of the  $\beta$  value induced a  $1200\text{ cm}^{-1}$  shift on the bands. The peak obtained experimentally around  $23000\text{ cm}^{-1}$  is narrow enough to determine the  $\beta$  value with a 1% accuracy. As opposed to  $10Dq$ ,  $\beta$  is a parameter that cannot be distributed, otherwise, it would be impossible to experimentally obtain such a narrow band.

#### 4.2.3.3 Spin-orbit coupling on the $3d$

Without taking into account the effect of spin-orbit coupling (SOC) in the calculation transitions are expected to be null, as shown on the Figure 4.15. When SOC is added, the intensities of spin-forbidden Fe<sup>3+</sup> bands increase with  $\zeta_{3d}$  from 0% to 100% of  $0.059\text{ eV}$ . Then SOC plays a key role in the intensity of calculated spin-forbidden bands.



**Figure 4.15** – Effect of spin-orbit coupling on the calculated OAS spectra for various values of  $\zeta_{3d}$ .

### 4.3 The case of $D_{4h}$ – square planar $^{[4]}\text{Fe}^{2+}$ in gillespite

For systems with centrosymmetric sites in a geometry lower than  $O_h$ , the number of crystal field parameters necessary to describe the energy of the different levels increases. This can be illustrated by the case of Fe<sup>2+</sup> in gillespite ( $\text{BaFeSi}_4\text{O}_{10}$ ), a rare silicate mineral in which ferrous iron is [4]-fold coordinated in the center of a square-plane with  $D_{4h}$  geometry. Even if this geometry is unlikely to exist in glasses, the simplicity of its composition and the presence of an inversion center is interesting to complete our investigation of crystalline compounds.

### 4.3.1 Model used for the calculation of gillespite

Experimentally, resolved optical transitions are observed for gillespite ( $\varepsilon \sim 5 \text{ L.mol}^{-1}.\text{cm}^{-1}$  around  $20\,000 \text{ cm}^{-1}$ ), therefore  $3d$  orbitals are necessarily mixed with  $p$  orbitals from the neighboring oxygens and/or from the transition metal itself. Vibrations could induce a dynamic distortion that generates hybridization. In the present case, we considered the off-plan vibration mode of the central  $\text{Fe}^{2+}$  ion along the  $C_4$  axis around the centrosymmetric equilibrium position, leading to lower the site geometry to  $C_{4v}$  point group (see Figure 4.16). Therefore, a small hybridization of 0.5 eV for both mixing parameters ( $V_{pd}^e$  and  $V_{pd}^{a_1}$ ) has been used to allow the calculation of optical transitions in  $D_{4h}$ .

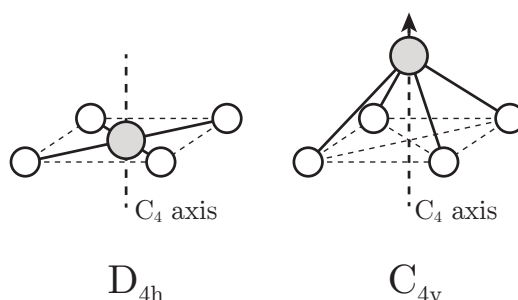


**Figure 4.16** – Square planar [4]-fold geometry and its off-plan distortion along the  $C_4$  axis.

Three crystal field parameters:  $Dq$ ,  $Ds$  and  $Dt$  are required to describe the energy of spectroscopic terms. In the case of a square-planar geometry, the ground state is estimated to be  ${}^5A_{1g}$  using simple point-charge model (see Figure 3.2).

The ground state of  $\text{Fe}^{2+}$  is the same for OAS and XAS, it is therefore described by the same set of parameters. Because the final state of OAS belongs to the same electron configuration  $(3d, 4p)^n$ , no extra parameters are needed for OAS calculation. On the contrary, the final states of XAS are described by a different electron configuration within  $1s^1(3d, 4p)^{n+1}$  that can be described by a second set of parameters.

In order to get a satisfying calculation of the gillespite XAS spectrum the use of two sets of parameters for the initial and final states of XAS was needed. This can be explained by the presence of the core-hole in the excited state that modifies the electronic structure of the transition metal. In comparison with Westre et al. [1997], where the authors systematically used  $\sim 80\%$  of the ground state values to describe the XAS excited state, I had to release this constraint to adjust the calculation parameters to match with both spectroscopic data sets. For  $\text{Fe}^{2+}$  in  $D_{4h}$  geometry, the number of parameters of the calculation is one of the limits of this semi-empirical ligand field multiplet method; especially, when dissimilar sets of parameters between the ground and excited states are used, the number of fitting parameters is doubled. The risk of over-parameterizing could lead to the possibility for an experimental spectrum to be reproduced by several sets of parameters. However, the careful attention to reproduce the experimental data from different spectroscopies with a compatible set of parameters gives confidence in our model.

### 4.3.2 Comparison experimental data/LFM calculation

The calculation of the Fe  $K$  pre-edge XAS using the parameters listed in Table 4.2 reproduces the experimental features. The application of a  $D_{4h}$  crystal field on  $\text{Fe}^{2+}$  lead to a more important raise of degeneracy than in  $O_h$ . Five transitions are found (Table 4.3)

**Table 4.2** – Crystal field parameters  $Dq$ ,  $Ds$  and  $Dt$  used for the calculation of the initial state ( $3d^6$ ) and the final state of XAS ( $1s^13d^7$ ). Source: Table 2 of [Schofield et al., 1998].

State	$Dq$ (eV)	$Ds$ (eV)	$Dt$ (eV)	$\beta$	$V_{pd}$ (eV)
Initial $3d^6$	0.143	0.450	0.110	0.6	0.5
Final $1s^13d^7$	0.161	0.236	0.149	0.6	0.5

**Table 4.3** – Attribution of the XAS Fe  $K$  pre-edge transitions of gillespite.

transition	position (eV)
${}^5A_{1g}(D) \rightarrow {}^4A_{2g}(F)$	7112.5
${}^5A_{1g}(D) \rightarrow {}^4E_g(F)$	7112.6
${}^5A_{1g}(D) \rightarrow {}^4E_g(F)$	7113.4
${}^5A_{1g}(D) \rightarrow {}^4A_{2g}(F)$	7114.1
${}^5A_{1g}(D) \rightarrow {}^4A_{2g}(F)$	7114.8

The total area of the calculated pre-edge is  $A_{sum} = 6.6 \cdot 10^{-2}$  is similar the experimental value  $A_{exp} = 5.6 \cdot 10^{-2}$ . The difference of 15% comes from to the tails of the pre-edge, which is probably due to main-edge subtraction. The calculated area of the dipole part of the spectrum is  $A_{dip} = 0.4 \cdot 10^{-2}$  and of the quadrupole part is  $A_{quad} = 6.2 \cdot 10^{-2}$ .

The electric dipole contribution represents less than 6% of the total pre-edge area, which confirms the quasi-exclusive electric quadrupole character of the XAS transitions characteristic of a centrosymmetric geometry (Figure 4.17-right).

Despite the use of  $C_{4v}$  point group instead of  $D_{4h}$ , the presence of  $3d-4p$  hybridization in the ground state and final states descriptions does not change the XAS spectrum because the  $V_{pd}$  values (0.5 eV) are two small to obtain a significant dipole contribution to the pre-edge.

The experimental OAS spectrum measured in diffuse reflectance (Figure 4.17-left) is very similar to the transmission spectrum from Rossman and Taran [2001] (see Appendix A). LFM calculations confirm that the ground state is  ${}^5A_{1g}(D)$  and reproduce the three bands at  $7900 \text{ cm}^{-1}$  ( ${}^5A_{1g}(D) \rightarrow {}^5B_{2g}(D)$ ),  $9000 \text{ cm}^{-1}$  ( ${}^5A_{1g}(D) \rightarrow {}^3E_g(H)$ ) and  $19300 \text{ cm}^{-1}$  ( ${}^5A_{1g}(D) \rightarrow {}^5B_{1g}(D)$ ). The  ${}^3E_g(H)$  multiplet level comes from the splitting of the  ${}^3T_{1g}(H)$  in  $O_h$  and the  ${}^5E_g(D)$  level is at lower energy, in the infrared region. The calculated positions and the relative intensities of the three bands agree with the experimental data confirming the appropriate choice of  $C_{4v}$  sub-group for hybridization Hamiltonian.

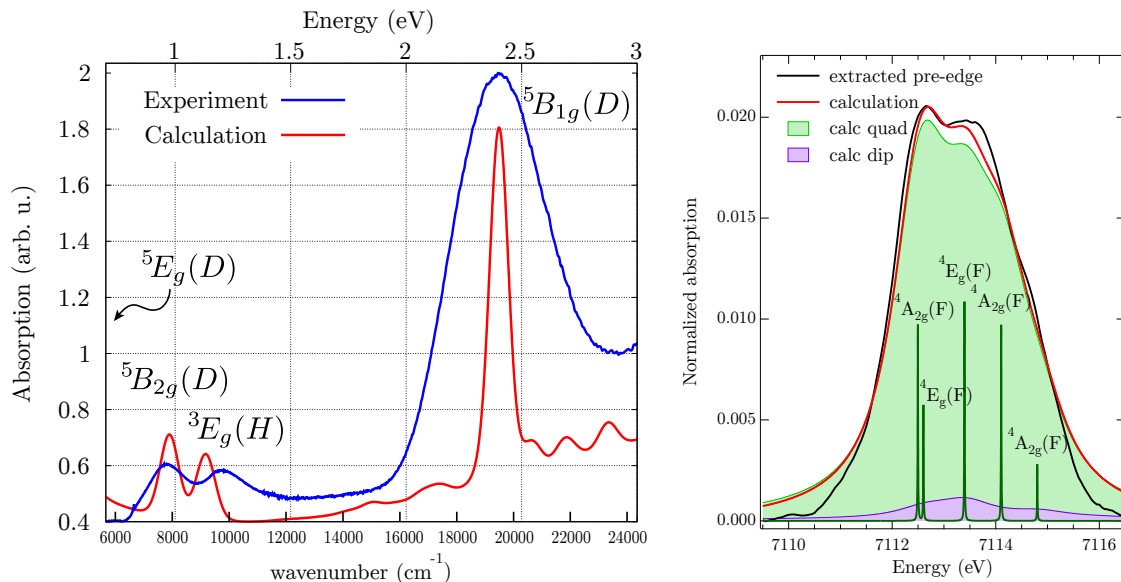


**Figure 4.17** – (Left) Calculated and experimental (diffuse reflectance) OAS of gillespite. (Right) Experimental  $K$  pre-edge XAS spectrum of gillespite and calculated spectrum of  $\text{Fe}^{2+}$  in  $D_{4h}$ . The calculated spectrum is the sum of the electric quadrupole and the electric dipole contributions.

#### 4.4 The case of $T_d$ – tetrahedral $[\text{Fe}^{2+}]$ in staurolite

Without inversion center,  $3d$  and  $4p$  orbitals can mix, therefore an intense electric dipole contribution participates in the  $K$  pre-edge intensity, in addition to the weak electric quadrupole transitions. As detailed in the previous chapter, electric dipole transitions within these multiplet levels are allowed and explain the greater optical intensity of non-centrosymmetric sites as compared to centrosymmetric sites. Here, we will study the case of  $\text{Fe}^{2+}$  in staurolite showing a non-regular tetrahedral site (see Appendix A for more details). In the following, the iron site will be approximated to a regular tetrahedron, characterized by the  $T_d$  point group symmetry, in which there is one crystal field parameter  $10Dq^*$  and one  $p$ - $d$  mixing parameter  $V_{pd}$ .

##### 4.4.1 Comparison of experimental spectra/LFM calculation

Figure 4.18-right shows the comparison between calculated and experimental XAS spectra. The parameters used for the calculation are listed in Table 4.4. The Fe  $K$  pre-edge is composed of four peaks at 7111.6 eV, 7112.4 eV, 7113 eV and 7114 eV related to the transitions  ${}^5E(D) \rightarrow {}^4A_2(F)$ ,  ${}^5E(D) \rightarrow {}^4T_2(F)$ ,  ${}^5E(D) \rightarrow {}^4T_1(F)$  and  ${}^5E(D) \rightarrow {}^4T_1(P)$ , respectively.

The total area of the calculated pre-edge is  $A_{sum} = 29.4 \cdot 10^{-2}$ , this value is 26% higher than the total experimental area  $A_{exp} = 23.3 \cdot 10^{-2}$  because the second peak around 7114 eV has a stronger intensity in the calculation than in the measurement. The calculated area of the dipole part of the spectrum is  $A_{dip} = 23.6 \cdot 10^{-2}$  and of the quadrupole part is  $A_{quad} = 5.8 \cdot 10^{-2}$ . Despite the small  $4p$ -character (1.33%), 80% of the pre-edge area is due to electric dipole transitions, highlighting the importance of the  $3d$ - $4p$  mixing on electronic transitions.

\*In  $T_d$  and  $O_h$ , the Hamiltonian describing the crystal field on  $3d$  orbitals is the same. For  $10Dq > 0$  the crystal field is octahedral and for  $10Dq < 0$  it is tetrahedral. The convention is here to give the absolute value  $|10Dq|$  in  $T_d$ , but the value used in the code is negative.

**Table 4.4** – Parameters used for the calculation of OAS and XAS spectra of staurolite at 300 K

Electronic state	$10Dq$ (eV)	$V_{pd}$ (eV)	$\beta$	$\langle N_p \rangle$	$p$ -character
Ground state $(3d, 4p)^6$	0.7	3.0	60%	$8.6 \cdot 10^{-3}$	0.14%
Excited state $1s^1(3d, 4p)^7$	1.4	12	60%	$9.3 \cdot 10^{-2}$	1.33%

The same methodology than Arrio et al. [2000] has been applied for  $\text{Fe}^{2+}$  in  $T_d$ . However, the present values of parameters are different for two reasons. First, our experimental data have been measured with a better resolution. Second, the supplementary constraints due to the intention of calculating both OAS and XAS spectra with only one set of parameters imply further adjustments to obtain a satisfying agreement with experimental data. With the same parameters than Arrio et al., we reproduced their calculations but the spin-allowed optical transition (attributed to  ${}^5E \rightarrow {}^5T_2$ ) was found below  $300 \text{ cm}^{-1}$  instead of  $5000 \text{ cm}^{-1}$ . The multiplet parameters used in our calculations are of the same order of magnitude, but with two exceptions: (i) the value of  $V_{pd}$  (used in **Quanty**) for the ground state is smaller than for the excited state (3 eV instead of 13 eV), otherwise, the optical intensity is too strong by several orders of magnitude ; and (ii) the value of  $10Dq$  in the excited state is the double of  $10Dq$  in the ground state (instead of being the same).

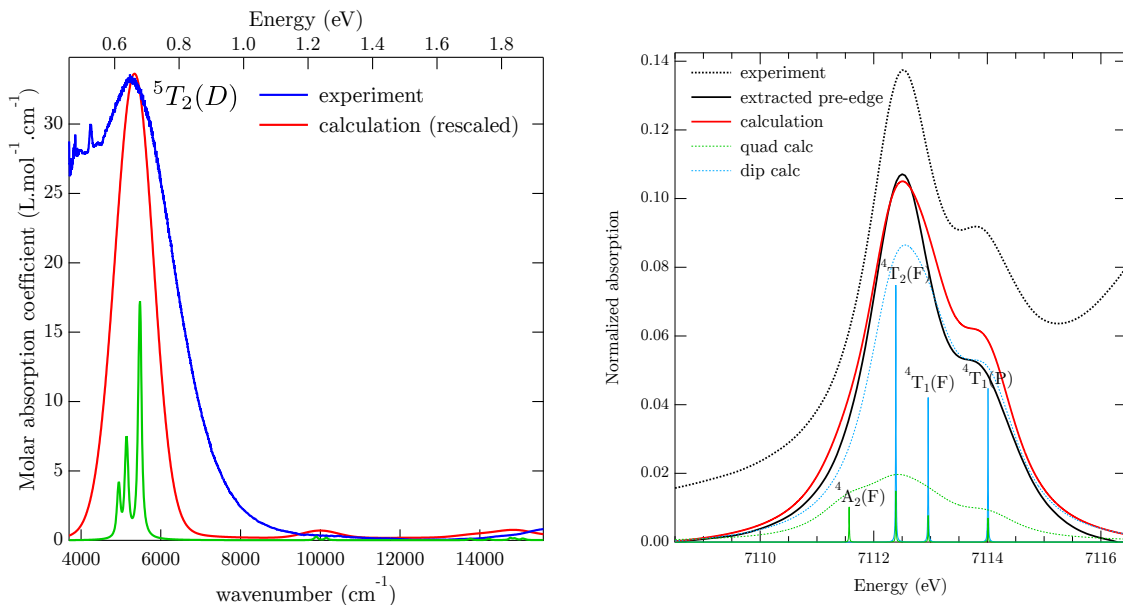


**Figure 4.18** – (Left) Calculated optical absorption spectra for  $\text{Fe}^{2+}$  in  $T_d$  and experimental data for staurolite from Rossman and Taran [2001]. (Right) Experimental  $K$  pre-edge XAS of staurolite before (black dashed line) and after (black solid line) edge subtraction, and the calculated broadened spectrum of  $\text{Fe}^{2+}$  in  $T_d$  (red). The total intensity is the sum of the electric dipole (dashed blue) and the electric quadrupole (dashed green) components.

For the OAS, we found a broad band located around  $5000 \text{ cm}^{-1}$  corresponding to the  ${}^5E(D) \rightarrow {}^5T_2(D)$  transition. This intense band seems to be in good agreement with the experimental isotropic spectrum. However, polarized OAS spectra from Rossman and Taran [2001] (see Appendix A) show that the band around  $5000 \text{ cm}^{-1}$  is experimentally split in three bands located at  $3800 \text{ cm}^{-1}$ ,  $4600 \text{ cm}^{-1}$  and  $5500 \text{ cm}^{-1}$ . By applying 100% of the spin-orbit coupling, the  ${}^5E(D) \rightarrow {}^5T_2(D)$  transition is split by  $500 \text{ cm}^{-1}$ , which is not enough to reproduce the experimental data. Moreover, experimental spectra differ with

polarization, which is not possible for cubic system as  $T_d$ . Then the  $T_d$  approximation is probably too strong, and  $C_{2v}$  point group symmetry should be considered in order to take into account the distortion of the  $\text{Fe}^{2+}$  tetrahedron.

## 4.4.2 Effect of the different parameters

### 4.4.2.1 Crystal field

Figure 4.19-left shows the 3D map of optical spectra overlaid by the Tanabe-Sugano diagram of  $\text{Fe}^{2+}$  in  $T_d$  using a  $T_d$  hybridization parameter of 1 eV. Figure 4.19-right shows three OAS spectra for  $10Dq$  values of 0.6, 0.7 and 0.8 eV marked on the 3D map. The optical spectra are plotted in logarithmic scale to see the effects on the weak spin-forbidden bands.

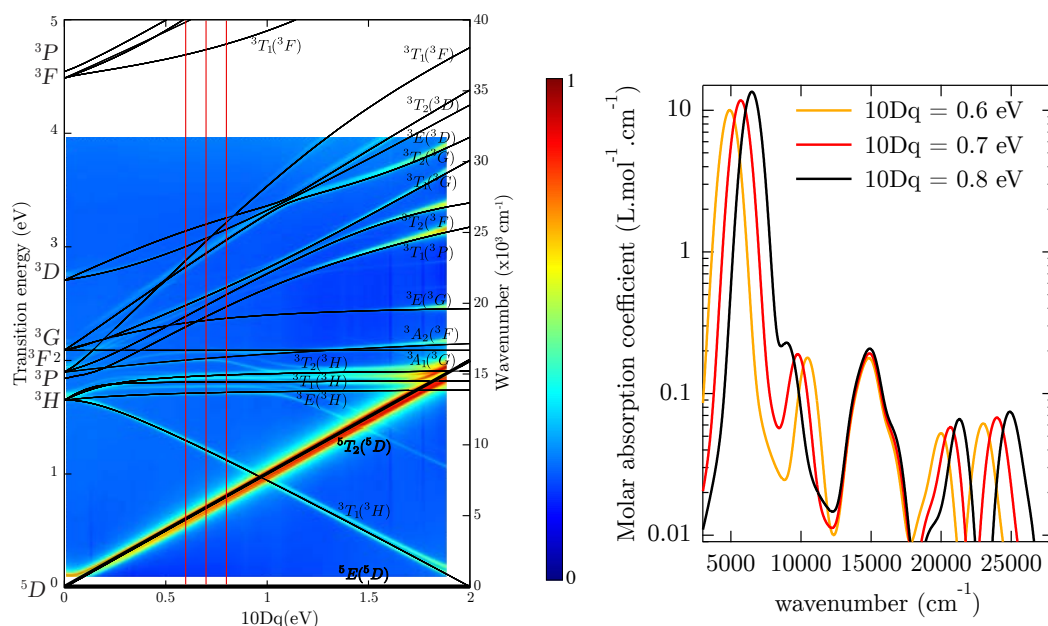


**Figure 4.19** – (Left) Calculated Tanabe-Sugano diagram (black lines) of  $\text{Fe}^{2+}$  in  $T_d$  without spin-orbit coupling, singlet levels are not shown. The color map shows the respective calculated OAS spectra with spin-orbit coupling and a small (1 eV)  $T_d$  hybridization parameter. (Right) Calculated OAS spectra with absorption in logarithmic scale for the three values of  $10Dq$  corresponding to the three lines of the left figure.

When  $10Dq$  increases, the intense spin-allowed band  $5T_1(D)$  shifts to higher energies and becomes more intense. The other bands, which are hardly discernible in the experimental spectrum, remain weak on the simulated spectra, but slightly increase in intensity with  $10Dq$ . However, the variation of their energy positions depend on the spectroscopic term. For example, transitions around  $15\,000\text{ cm}^{-1}$  are kept unchanged, while those around  $20\,000\text{ cm}^{-1}$  and  $25\,000\text{ cm}^{-1}$  shift to higher energies.

Figure 4.20 shows the effects of  $10Dq$  on the Fe  $K$  pre-edge XAS spectra (sum of dipole and quadrupole contributions) based on the staurolite parameters of Table 4.4. With  $10Dq$  of the ground state varying from 0.2 eV to 1.8 eV, it appears that the pre-edge signal is split in two, three or four three peaks, whose positions and relative intensities depend on  $10Dq$ . By comparing with the experiment, it appears that the  $10Dq$  range seems limited from 0.4 eV ( $3200\text{ cm}^{-1}$ ) to 1.2 eV ( $9700\text{ cm}^{-1}$ ).

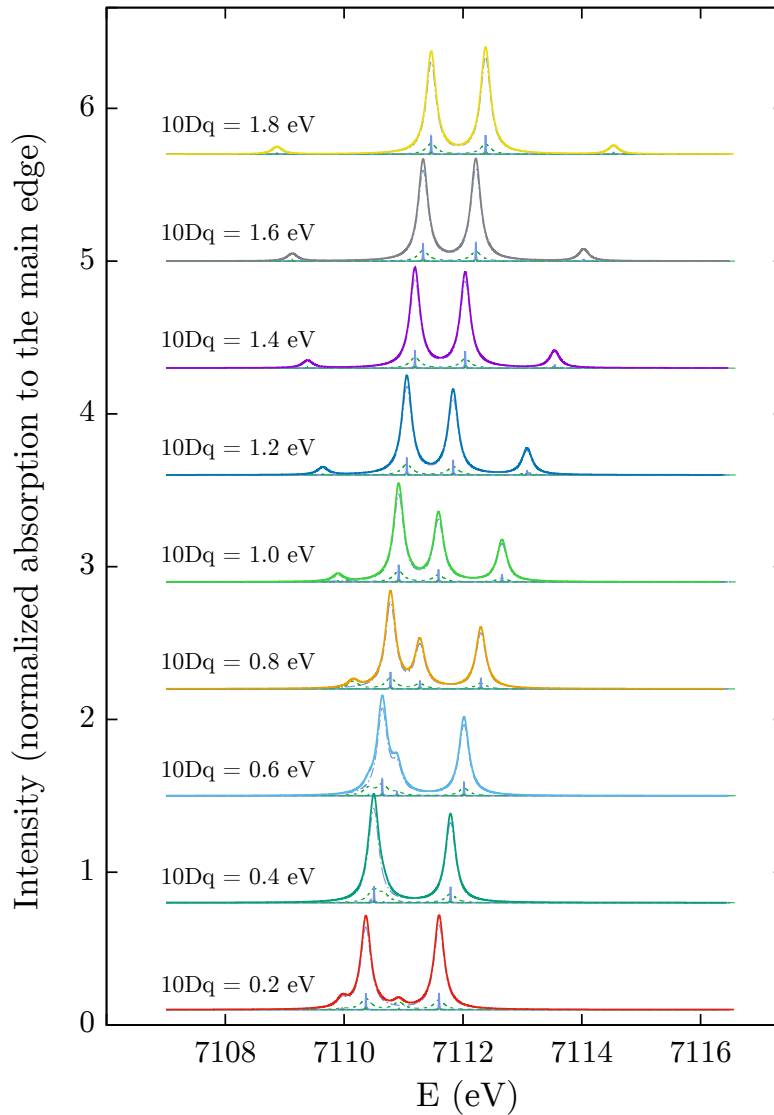


**Figure 4.20** – Effect of  $10Dq^{GS}$ , from 0 to 2 eV, on the calculated Fe  $K$  pre-edge XAS of  $\text{Fe}^{2+}$  in  $T_d$ , with  $V_{pd}^{GS} = 3$  eV and  $V_{pd}^{ES} = 17$  eV,  $10Dq^{ES} = 2 \times 10Dq^{GS}$ ,  $\beta = 60\%$  and a Lorentzian broadening  $\Gamma = 0.2$  eV.

#### 4.4.2.2 Nephelauxetic ratio $\beta$

For  $\beta > 30\%$ , the  $K$  pre-edge quadrupole part is composed of four distinct peaks. By omitting the overall energy shift (which is related to the change in the average energy of the configuration), the first three peaks are  $\beta$ -independent. However, the split of the fourth peak ( ${}^5E(D) \rightarrow {}^4T_1(P)$ ) depends on  $\beta$  (Figure 4.21). As we have previously seen (Figure 4.18), dipole transitions are allowed from the ground state to the three levels of higher energy, only the transition  ${}^5E(D) \rightarrow {}^4A_2(F)$  is forbidden. Consequently, in the present case of  $\text{Fe}^{2+}$  in  $T_d$ , it is possible to extract  $\beta \sim 60\%$  from XAS data using LFM calculations.



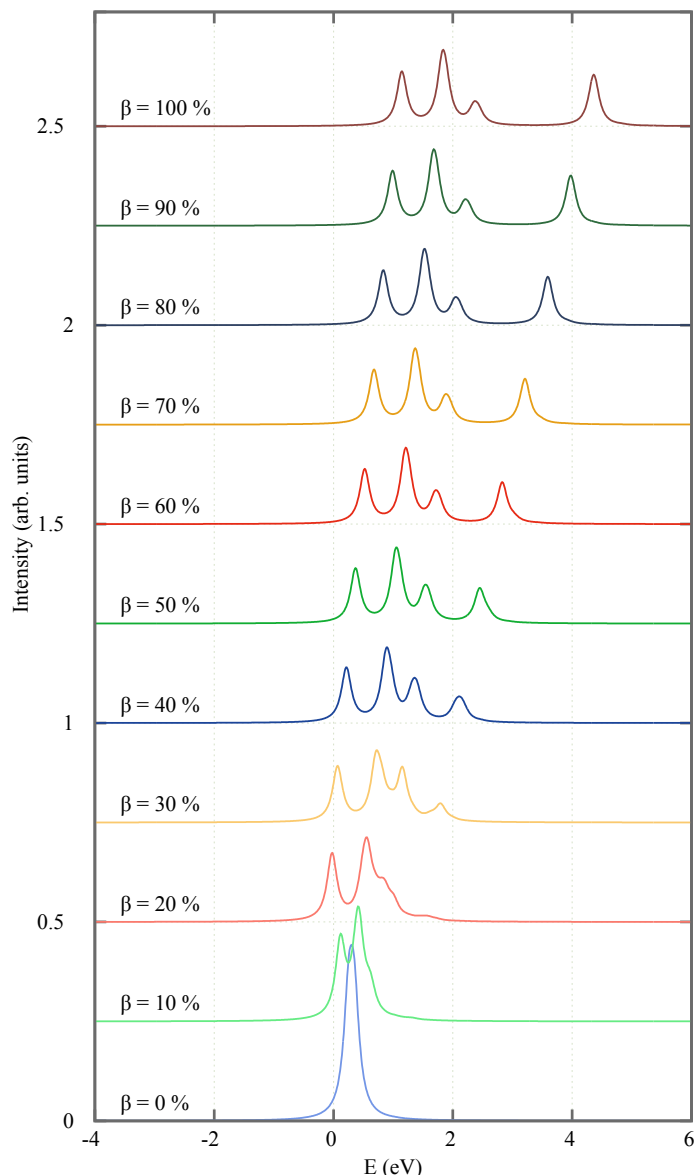


**Figure 4.21** – Effect of nephelauxetic ratio  $\beta$  on the calculated Fe  $K$  pre-edge XAS of  $\text{Fe}^{2+}$  in  $T_d$ , for  $\beta$  varying from 0% to 100%,  $10Dq = 0.7$  eV and a Lorentzian broadening  $\Gamma = 0.2$  eV. These calculations only represent the quadrupole transitions.

#### 4.4.2.3 Effect of ground state hybridization

In tetrahedral geometry, there is only one hybridization parameter,  $V_{pd}$ , mixing the  $t_2$  levels from  $3d$ -orbitals with the  $t_2$  levels from  $4p$  orbitals\*. However, there is a different definition of  $V_{pd}$  between **Quanty**, used here, and **TTMULT**, used by Arrio et al.. **Quanty** uses a development of the Hamiltonian on spherical harmonics while Thole's code uses a basis adapted to the considered point group symmetry using the formalism of Butler [1981]. I calculated the relationship between the two definitions of the mixing parameter by using the Wigner-Eckart theorem that leads to  $V_{pd}(\text{Quanty}) = \alpha V_{pd}(\text{TTMULT})$  with  $\alpha = \frac{\sqrt{5 \times 7}}{4\sqrt{3}} \simeq 0.854$ . Same results can be therefore obtained with both **Quanty** and Thole's code **TTMULT**.

\*  $O_h$  and  $T_d$  are very similar point groups (both are cubic point groups), except that in  $O_h$  the  $t_{2g}$  from  $3d$  orbitals and  $t_{2u}$  from  $4p$  orbitals cannot mix since they do not have the same symmetry.

To quantify the  $4p$ -character of multiplet states, the expectation value  $\langle N_{4p} \rangle$  of the number of electrons in the  $4p$  shell is used. We limit the maximum value to one electron in the  $p$  shell to avoid the contribution from the  $(3d)^{n-2}(4p)^2$  electronic configuration, which is anyway very weak. For example, if the  $\text{Fe}^{2+}$  ground state has  $\langle N_{3d} \rangle = 5.9$  and  $\langle N_{4p} \rangle = 0.1$ , it means that the ground state,  $(e(3d))^3(t_2(3d))^{2.9}(t_2(4p))^{0.1}$ , is composed from 90% of  $3d^n$  and 10% of  $3d^{n-1}4p^1$ , i.e. 1.7% of the six  $3d$  electrons are in the  $4p$  shell (left of Figure 4.22-a).

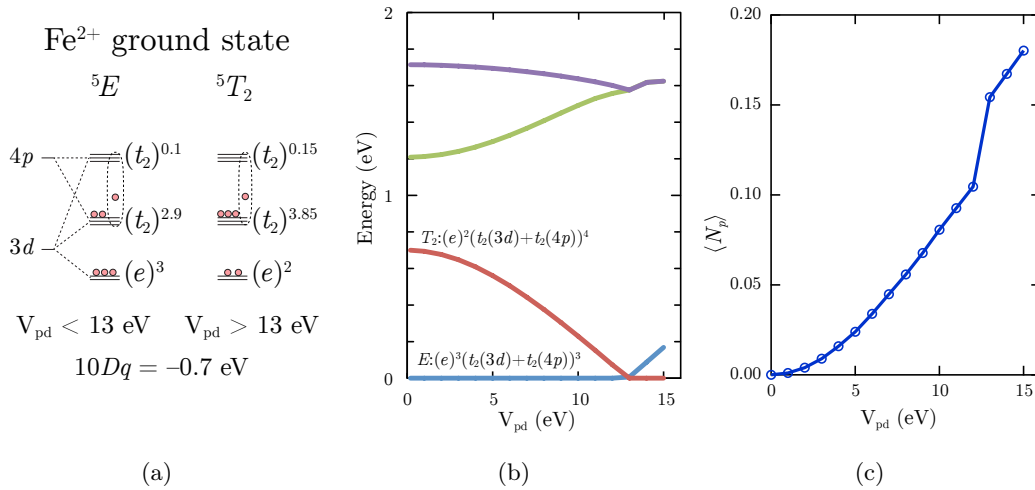


**Figure 4.22** – Evolution of the  $\text{Fe}^{2+}$  ground state in  $T_d$  with the hybridization parameter  $V_{pd}$  for  $10Dq = 0.7$  eV. (a) Schematic electronic representation of the ground state. (b) Energy level diagram: energy of the multiplet states as a function of  $V_{pd}$ . (c) Expectation value  $\langle N_{4p} \rangle$  of the number of electrons in the  $4p$  shell as a function of  $V_{pd}$ .

For a fixed value of the crystal field parameter  $10Dq$ , the  $4p$ -character increases with  $V_{pd}$  (Figure 4.22-c). Thus, the electric dipole intensity of the  $K$  pre-edge progressively increases, while the electric quadrupole intensity remains almost constant. By using the sum rules (see Appendix D.4), the value of the  $K$  pre-edge area due to electric quadrupole transition can be estimated\*. This area does not depend on the geometry or the crystal field parameters. Thus,  $V_{pd}$  is increased until finding the adequate value that reproduces the total pre-edge area. The crystal field parameters are modified in a second time to adjust the shape of the spectrum (relative intensities and separation between peaks).

It has to be noticed that hybridization modifies the nature of the ground state. For high-spin  $\text{Fe}^{2+}$  in  $T_d$  with  $10Dq = 0.7$  eV, the ground state is initially  ${}^5E: (e)^3(t_2)^3$ , when the  $V_{pd}$  parameter increases, the ground state changes from  ${}^5E: (e)^3(t_2(3d))^{2.9}(t_2(4p))^{0.1}$  to  ${}^5T_2: (e)^2(t_2(3d))^{2.85}(t_2(4p))^{0.15}$  at about 13 eV (Figure 4.22-b and -c). It is therefore important to adjust the hybridization parameter such as there is no change in the ground state.

#### 4.5 The case of $T_d$ – tetrahedral $[\text{Fe}^{3+}]$ in ferriorthoclase

Compared to staurolite in which ferrous iron is a major element, ferriorthoclase is an interesting mineral because ferric iron is present in a tetrahedral site as an impurity (0.5 wt%)

\*With the spectral energy in eV and the spectrum normalized to the edge jump,  $A(\text{Fe}^{2+}) = 6.79 \cdot 10^{-2}$  and  $A(\text{Fe}^{3+}) = 9.66 \cdot 10^{-2}$

substituting Al in the orthoclase crystalline matrix with a composition similar to silicate glasses ( $\text{KAlSi}_3\text{O}_8$ ).  $\text{Fe}^{3+}$  environment is not a regular tetrahedral geometry, but it has been approximated to  $T_d$ .

#### 4.5.1 Comparison experimental data/LFM calculation

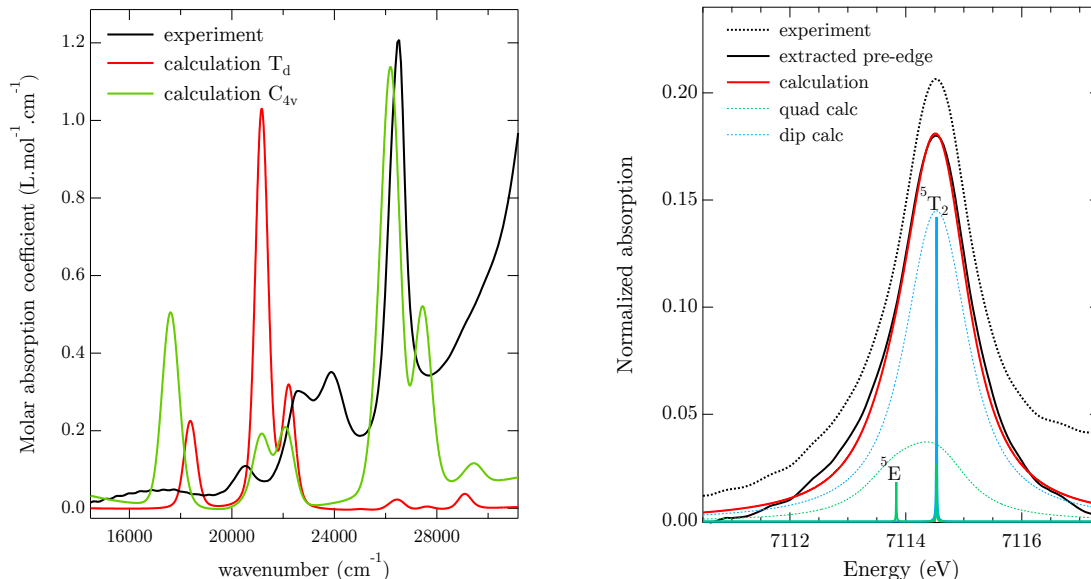


**Figure 4.23** – (Left) Calculated optical spectra in  $T_d$  and  $C_{4v}$  symmetry compared to the experimental transmission of ferriorthoclase. (Right) Experimental  $K$  pre-edge XAS of ferriorthoclase before (black dashed line) and after (black solid line) edge subtraction, and the calculated spectrum (red). The total intensity is the sum of two components: electric dipole (dashed blue) and electric quadrupole (dashed green).

The experimental pre-edge (Figure 4.23-right) is well reproduced by the simulation using  $T_d$  geometry using the parameters given in Table 4.5. However, the  ${}^5E$  band is too close and weak to the  ${}^5T_2$  transition contributing to 90% of the spectrum, which complicates the determination of the crystal field parameter  $10Dq$  using only XAS spectral shape.

The total area of the calculated pre-edge  $A_{sum} = 34.5 \cdot 10^{-2}$  is close to the total experimental area  $A_{exp} = 34.3 \cdot 10^{-2}$ . The calculated area of the dipole part of the spectrum is  $A_{dip} = 26.2 \cdot 10^{-2}$  and  $A_{quad} = 8.28 \cdot 10^{-2}$  for the quadrupole part (close to the estimation from the sum rule  $A(\text{Fe}^{3+}) = 9.66 \cdot 10^{-2}$ , see Appendix D.4). Despite the small  $4p$ -character (1.2%), 76% of the pre-edge area is due to electric dipole transitions.

**Table 4.5** – Parameters used for the  $T_d$  calculation of staurolite at 300 K

Electronic state	$10Dq$ (eV)	$V_{pd}$ (eV)	$\beta$	$\langle N_p \rangle$	$p$ -character
Ground state $(3d, 4p)^5$	0.71	1.5	60%	$7.9 \cdot 10^{-4}$	0.02%
Excited state $1s^1(3d, 4p)^6$	1.42	17.0	60%	$7.2 \cdot 10^{-2}$	1.2%

Experimental and calculated OAS spectra of ferriorthoclase (Figure 4.23-left) exhibit transitions in the same energy range (15 000–30 000  $\text{cm}^{-1}$ ) with similar absolute values for the intensities. However, the relative intensities between peaks for transitions calculated

with a  $T_d$  hybridization Hamiltonian do not reproduce the experiment. This could suggest a wrong assignment of the classical band attribution in the considered site symmetry.

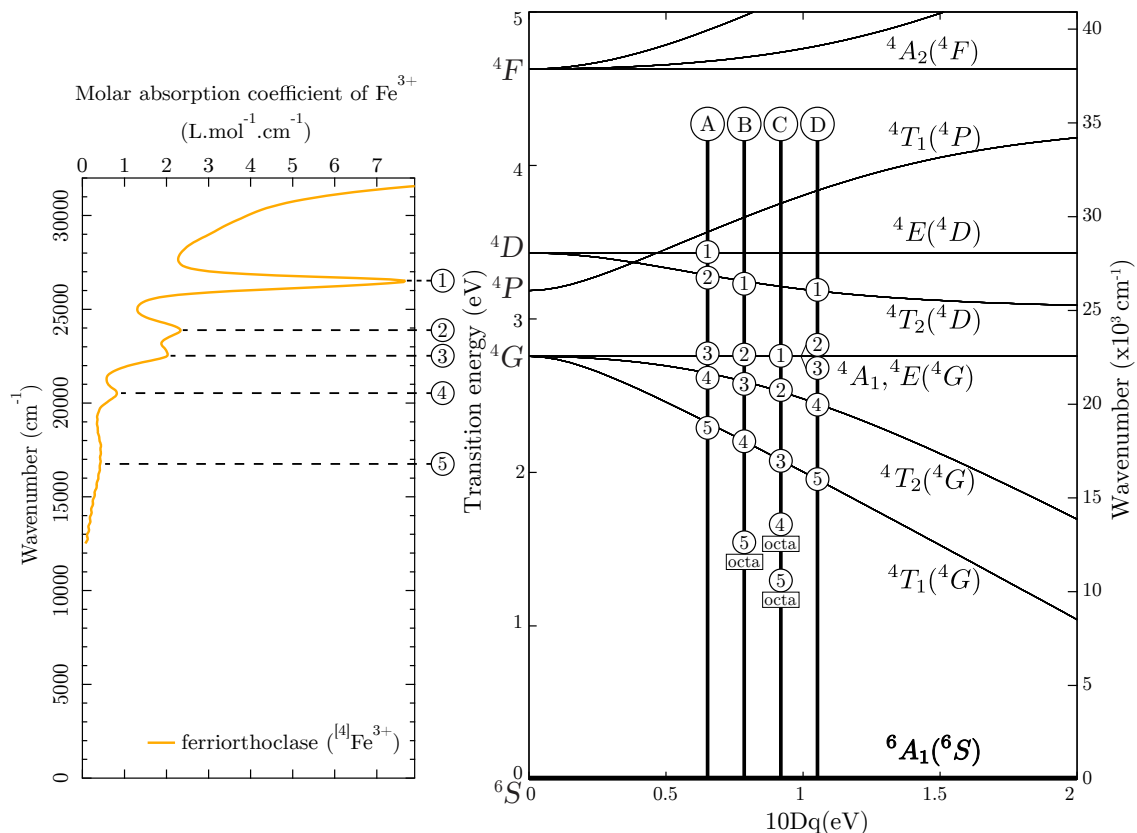


**Figure 4.24** – Left: optical spectrum of ferriorthoclase ( $[{}^4]Fe^{3+}$ ). Right: Tanabe-Sugano diagram for  $Fe^{3+}$  in  $T_d$ , A, B, C and D are the different possible band attribution for ferriorthoclase.

Figure 4.24 compares the optical spectrum of ferriorthoclase (Left) with the calculated Tanabe-Sugano energy level diagram in the  $T_d$  symmetry (Right). The attribution marked “A” is commonly used to interpret tetrahedral  $Fe^{3+}$  bands [Bingham et al., 2014; Burns, 1993; Volotinen et al., 2008]. However, three other attributions of the same bands have also been suggested: “B” [Faye, 1969; Kurkjian and Sigety, 1968], “C” [Faye, 1969] and “D” [Miché, 1985].

For a calculation in  $T_d$ , the attribution marked “A” could not match the experiment because the transitions  ${}^6A_1 \rightarrow {}^4E(D)$  and  ${}^6A_1(S) \rightarrow {}^4T_2(D)$  that should happen around  $26\,300\text{ cm}^{-1}$  are both very weak and the  ${}^6A_1(S) \rightarrow {}^4T_2(G)$  is too intense. The use of  $C_{4v}$  geometry, as an approximation to the  $C_{2v}$  geometry (because  $C_{2v}$  was not implemented in **Quanty**) using the same crystal field parameters than in  $T_d$  ( $D_s = D_t = 0$ ) and the hybridization Hamiltonian of  $C_{4v}$ ,  $V_{pd}^e = V_{pd}^{a_1} = 1.5\text{ eV}$  gives the same  $\langle N_p \rangle$  but totally different optical spectra than in  $T_d$  symmetry (Figure 4.23-left).

Transitions are around the same energies but the relative intensities are different and closer to the experimental spectrum. However, some discrepancies remain in the intensities and positions of bands, for example at  $17\,000\text{ cm}^{-1}$  and in the splitting of the bands around  $24\,000\text{ cm}^{-1}$  and  $26\,000\text{ cm}^{-1}$ . The results in  $C_{4v}$  symmetry are not fully satisfying because the calculated spectra do not explain the experimental shape.

One way to solve this problem is to use a lower point group such as  $C_{2v}$ , because when the working point group contains too many symmetry elements, some transitions are symmetry-forbidden. However, as soon as the symmetry is decreased the intensities immediately become of the same order of magnitude than the bands that were already allowed. Unfortunately, the use of a low-symmetry point group implies the adjustment of several crystal field and hybridization parameters explaining the difficulty to reproduce optical spectra with appropriate positions and intensities.

## 4.5.2 Effect of the different parameters

### 4.5.2.1 Crystal field

Figure 4.25-left shows the 3D map of optical spectra overlaid by the Tanabe-Sugano diagram of  $\text{Fe}^{3+}$  in  $T_d$  using a  $C_{4v}$  hybridization. Figure 4.25-right shows three OAS spectra for  $10Dq$  values of 0.6, 0.7 and 0.8 eV marked on the 3D map. We see clearly that the bands  ${}^4T_1(G)$ ,  ${}^4T_2(G)$  and  ${}^4T_2(D)$  are sensitive to  $10Dq$  and the two bands  $[{}^4A_1, {}^4E(G)]$  and  ${}^4E(D)$  are crystal field independent (intensity and position).

When  $10Dq$  increases the  ${}^4T_1(G)$  and  ${}^4T_2(G)$  bands shift in position to lower energy value. In the meantime the intensities slightly increase with  $10Dq$ . The use of a crystal field Hamiltonian in a lower point group such as  $C_{2v}$  could eventually split the  ${}^4T_2(D)$  or the  $[{}^4A_1, {}^4E(G)]$  levels in order to reproduce the experimental splitting of the band around  $23\,000\text{--}24\,000\text{ cm}^{-1}$ .

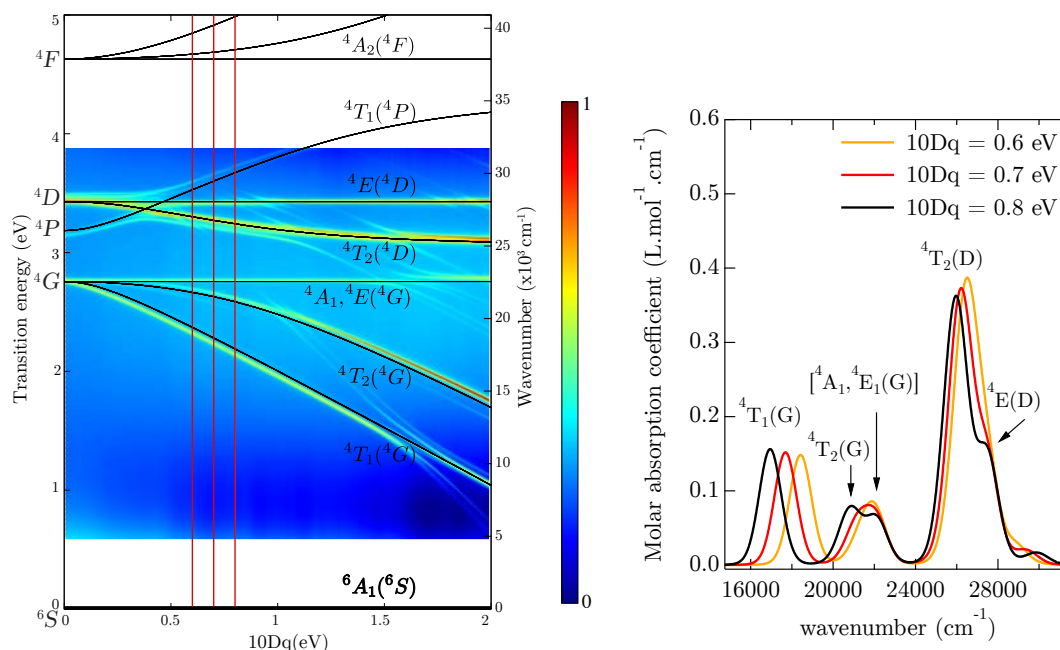


**Figure 4.25** – (Left) Calculated Tanabe-Sugano diagram (black lines) of  $\text{Fe}^{3+}$  in  $C_{4v}$  without spin-orbit coupling,  $10Dq = 0.7\text{ eV}$  and  $Ds = Dt = 0\text{ eV}$ , singlet levels are not shown. The color map shows the respective calculated OAS spectra with spin-orbit coupling and a small hybridization parameter ( $V_{pd}^e = V_{pd}^{a_1} = 1.5\text{ eV}$  in  $C_{4v}$ ). (Right) Calculated OAS spectra for the three values of  $10Dq$  corresponding to the three lines of the left figure.

#### 4.5.2.2 Nephelauxetic ratio $\beta$

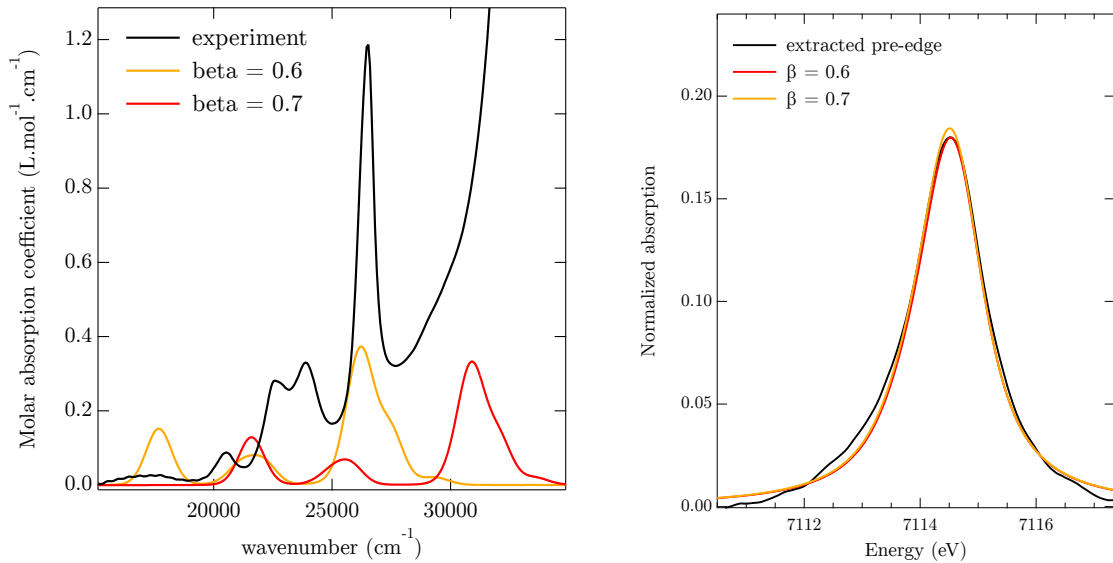


**Figure 4.26** – Effect of the nephelauxetic ratio  $\beta$  for  $\text{Fe}^{3+}$  in tetrahedral site on the calculated OAS (Left) and  $K$  pre-edge XAS (Right) spectra. The black lines are experimental spectra.

In the case of  $\text{Fe}^{3+}$  in  $T_d$  geometry, the pre-edge is mainly constituted of one transition, therefore  $\beta$  has no effect on the calculated spectrum (Figure 4.26-b). Using only XAS, it is not possible to determine  $\beta$ . The optical bands are globally shifted to higher energies and have weaker intensities, the energy splitting between the transitions is also modified.

### 4.6 The case of $D_{3h}$ – trigonal bipyramidal $[\text{Fe}^{2+}]$ in granddierite

This section presents the case of granddierite, a silicate mineral in which iron is [5]-fold coordinated in a distorted trigonal bipyramidal geometry (See Appendix A for more details). The site geometry is first approximated by the  $D_{3h}$  geometry, characteristic of regular trigonal bipyramidal [5]-fold coordinated ions. The crystal field of  $D_{3h}$  geometry can be described by two parameters  $D\mu$  and  $D\nu$  [König and Kremer, 1977, p. 21].

In  $D_{3h}$ , the decomposition of  $d$  orbitals into irreducible representation is  $a'_1 \oplus e' \oplus e''$  and the decomposition of  $p$  orbitals into irreducible representation is  $a''_2 \oplus e'$ . Thus, the  $3d$  ( $x^2 - y^2, xy$ ) and  $4p$  ( $x, y$ ) orbitals belonging to the representation  $e'$  can mix. The intensity of this mixing is described by the parameter  $V_{pd}$  of the  $D_{3h}$  hybridization Hamiltonian that we theoretically determined and implemented in **Quanty** (see Appendix E.5).

#### 4.6.1 XAS

The experimental  $K$  pre-edge spectrum has been corrected of small self-absorption effects (Figure 4.27). It is partially reproduced by the simulation for the parameters listed in Table 4.6. The total intensity of the experimental pre-edge  $A_{exp} = 11.8 \cdot 10^{-2}$  is similar to the calculation ( $A_{sum} = 11.2 \cdot 10^{-2}$ ). Simulations show that dipole transitions contribute to 45% of the spectrum with  $A_{dip} = 5.0 \cdot 10^{-2}$ , and quadrupole transitions contribute to 55% with  $A_{quad} = 6.2 \cdot 10^{-2}$ .

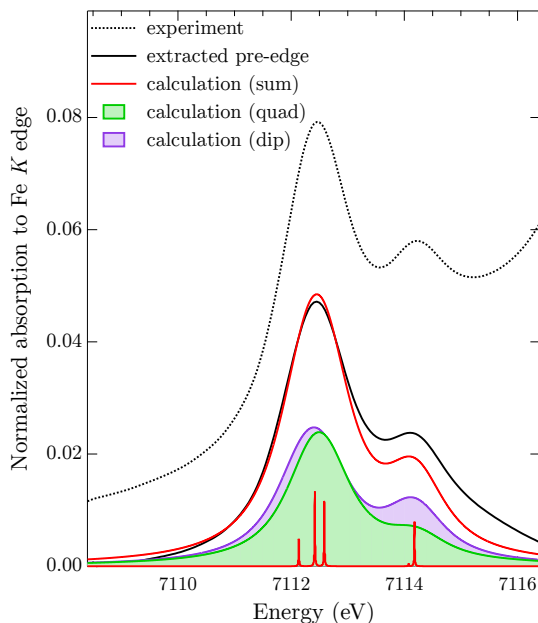


**Figure 4.27** – Experimental  $K$  pre-edge XAS of grandidierite before (black dashed line) and after (black solid line) edge subtraction, and the calculated broadened spectrum (red). The total intensity is the sum of the electric dipole (dashed blue) and the electric quadrupole (dashed green) components.

Concerning the shape of the spectrum, the second transition, around 7114 eV, is underestimated by the calculation, because its intensity is smaller in the electric dipole spectrum than in the electric quadrupole spectrum of because of the pre-edge extraction. It has to be noted that the quadrupole transition reproduces the shape of experimental spectrum but its intensity is twice as less intense. Therefore, to increase the pre-edge intensity, hybridization has to be taken into account.

**Table 4.6** – Parameters used for the calculation of grandidierite at 300 K

Electronic state	$D\mu$ (eV)	$D\nu$ (eV)	$V_{pd}$ (eV)	$\beta$	$\langle N_p \rangle$	$p$ -character
Ground state $(3d, 4p)^6$	0.025	-0.095	1.0	60%	$9.3 \cdot 10^{-4}$	0.02%
Excited state $1s^1(3d, 4p)^7$	0.025	-0.095	4.8	60%	$2.0 \cdot 10^{-2}$	0.29%

### 4.6.2 Optical absorption spectroscopy

Two Tanabe-Sugano diagrams were calculated in  $D_{3h}$  as a function of  $D\mu$  and  $D\nu$  parameters (Figure 4.28) to illustrate the complexity of the interpretation of optical transitions. The diagrams contain many spin-forbidden transitions (thin lines) explaining the numerous optical transitions found by optical absorption spectroscopy in the range 13 000–30 000  $\text{cm}^{-1}$  [Schmetzer et al., 2003]. However, there are only two spin-allowed transitions:  ${}^5E''(D) \rightarrow {}^5E'(D)$  and  ${}^5E''(D) \rightarrow {}^5A'_1(D)$ , occurring respectively around 5000  $\text{cm}^{-1}$  and in the range 10000–15000  $\text{cm}^{-1}$  (bold lines).

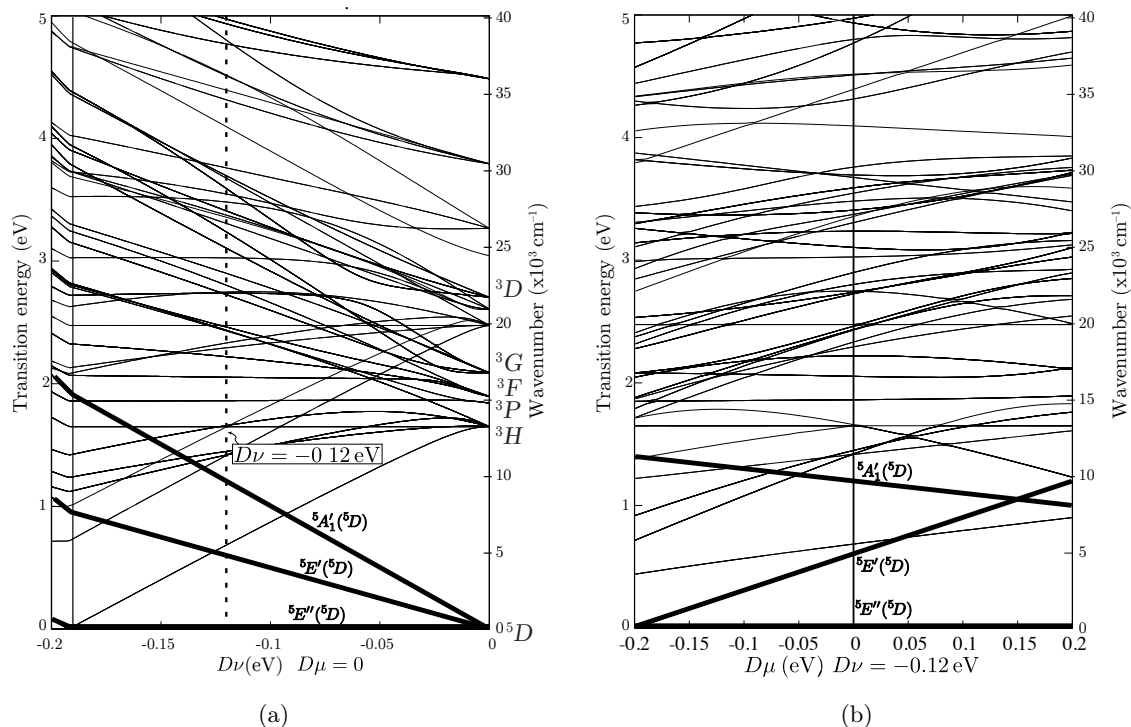


**Figure 4.28** – Calculated Tanabe-Sugano diagram (black lines) of  $\text{Fe}^{2+}$  in  $D_{3h}$  as a function of  $D\mu$  (a) and  $D\nu$  (b), without spin-orbit coupling. Bold levels have a spin multiplicity of 5 (spin-allowed transitions), others are singlets or triplets. The dashed line on diagram (a) indicate the starting point of diagram (b).

There is no known mineral with Fe in a [5]-fold site with a regular trigonal bipyramidal geometry, and they are all distorted. Depending on the distortions, the site symmetry is decreased to  $C_{3v}$ ,  $C_{2v}$ , or even  $C_s$  (Figure 4.29). To simplify the calculation of granddierite ( $^{55}\text{Fe}^{2+}$ ), the geometry was first approximated to  $D_{3h}$  but crystallographic data show that iron is in a  $C_s$  site.

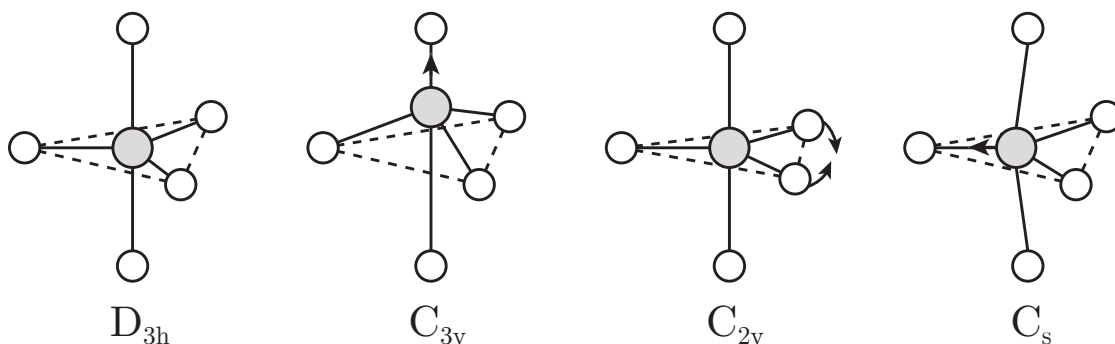


**Figure 4.29** – Point group of the distorted bipyramid trigonal [5]-fold geometries.

The calculated optical spectrum of  $\text{Fe}^{2+}$  in  $D_{3h}$  (Figure 4.30-left) shows one of the two spin-allowed transitions at  $5000\text{ cm}^{-1}$ . The second transition is symmetry-forbidden in  $D_{3h}$  point group. The hybridization Hamiltonian has to be adapted to allow this transition and a decrease in symmetry is therefore necessary to reproduce the granddierite data taken from Rossman and Taran [2001]. Because  $C_s$  and  $C_{2v}$  were not implemented in **Quanty**, the  $C_{3v}$  point group was used instead of  $D_{3h}$  for  $\text{Fe}^{2+}$  in granddierite. In  $C_{3v}$ , the irreducible decomposition of  $3d$  orbitals is  $a_1 \oplus 2e$  and the irreducible decomposition of  $p$  orbitals is



$a_1 \oplus e$ . Thus, the  $3d$  ( $x^2 - y^2, xy$ ), ( $xz, yz$ ) and  $4p$  ( $x, y$ ) orbitals with the representation  $e$  can mix, and the  $3d$   $z^2$  and  $4p$   $z$  orbitals with the representation  $e_1$  can mix.

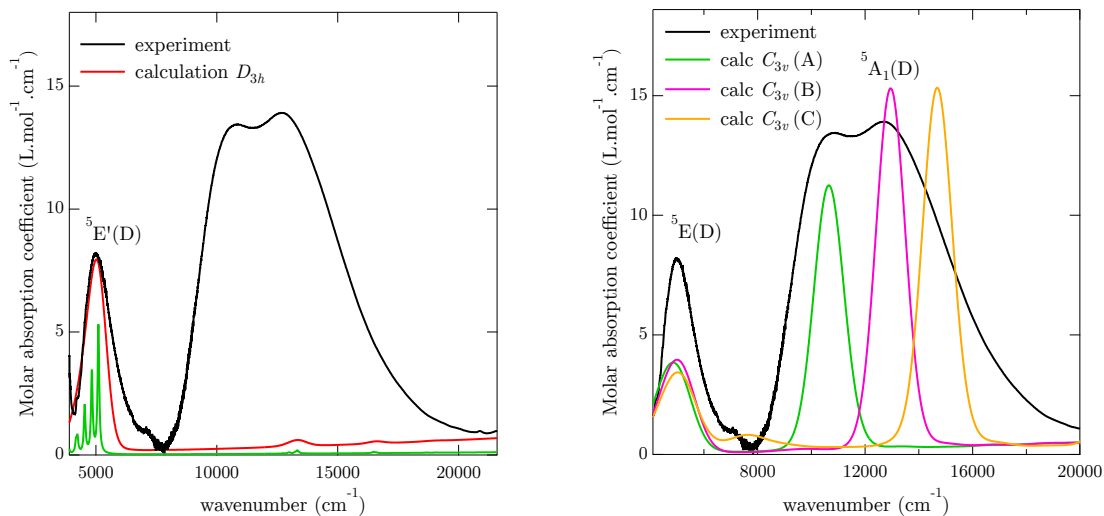


**Figure 4.30** – Experimental optical absorption spectrum of grandidierite (from [Rossman and Taran, 2001]) compared to the calculated spectra of  $\text{Fe}^{2+}$  in  $D_{3h}$  (left) and  $C_{3v}$  (right – for three different sets of ligand field parameters: A, B and C).

This effect is illustrated in Figure 4.30-right by an example of calculation using three sets of parameters in the  $C_{3v}$  geometry (Table 4.7). The three  $C_{3v}$  optical spectra give an optical band around  $5000 \text{ cm}^{-1}$ . The use of  $C_{3v}$  is more satisfying than  $D_{3h}$  geometry, in particular, the second transition to the  ${}^5A_1$  level ( ${}^5A'_1$  level in  $D_{3h}$ ) around  $10\,000 \text{ cm}^{-1}$ – $13\,000 \text{ cm}^{-1}$  is now allowed. However, two sets are necessary to reproduce the splitting of the signal of the experimental spectra around  $10\,000 \text{ cm}^{-1}$ – $13\,000 \text{ cm}^{-1}$  and a third one for the tail around  $15\,000 \text{ cm}^{-1}$ .

**Table 4.7** – Sets of parameters used for  $C_{3v}$  calculation of grandidierite.

name	$D\mu$ (eV)	$D\nu$ (eV)	$V_{pd}$ (eV)	$\beta$
A	−0.025	−0.120	1.0	60%
B	−0.06	−0.155	1.0	60%
C	−0.09	−0.175	1.0	60%

Because this transition around  $13\,000 \text{ cm}^{-1}$  is due the transition towards level  $A_1$ , the splitting cannot be reproduced using only one set of  $C_{3v}$  parameters or by decreasing the symmetry. Two sets representative of two different populations are required and the existence of multiple, non-equivalent  ${}^5\text{Fe}^{2+}$  sites in the grandidierite mineral could be at the origin of these two bands, as suggested by Rossman and Taran [2001]. By looking closely at the structural data of grandidierite, the two  $\text{Fe}^{2+}$ –O distances with apical oxygens are  $2.179 \text{ \AA}$  and  $2.057 \text{ \AA}$  [Stephenson and Moore, 1968]. An analogy can be done with the relation  $\Delta \propto R^{-5}$  between Fe–O distance and crystal field splitting often used by mineralogists [Burns, 1993]. The ratio of the two Fe–O distances at the fifth-power is equal to 1.33, which is not far from the ratio between  $13\,000 \text{ cm}^{-1}$  and  $10\,000 \text{ cm}^{-1}$  equal to 1.3. Moreover, the  ${}^5A_1$  levels are related to the  $z^2$  orbital, which is orientated in the direction of the apical ligands forming the  $C_3$  axis when they are aligned with then central  $\text{Fe}^{2+}$ .

## 4.7 The case of $C_{3v}$ – trigonal bipyramidal $^{55}\text{Fe}^{3+}$ in yoderite

The yoderite mineral is a rare example of  $\text{Fe}^{3+}$ -bearing mineral presenting a [5]-fold coordinated Fe site with a triangular bipyramidal geometry (See Appendix A for more details). I studied the yoderite using  $C_{3v}$  geometry to approximate the Al(3) site occupied by iron according to XRD analysis, which has a point group symmetry  $C_s$  [Higgins et al., 1982]. In the  $C_{3v}$  point group there are the two ligand field parameters of  $D_{3h}$  ( $D\mu$  and  $D\nu$ ), plus an additional ligand field mixing parameters between the  $d$  levels of symmetry  $e$  taken here to 0 eV, in order to keep a  $D_{3h}$  crystal field potential. Concerning  $p$ - $d$  hybridization, a  $V_{pd}$  was taken to 1.5 eV in the ground state to obtain optical intensities without modification of the energy positions as calculated in the case  $V_{pd} = 0$ .

### 4.7.1 XAS $K$ pre-edge

The experimental  $K$  pre-edge spectrum (Figure 4.31) presents a broad band around 7114 eV with a shoulder around 7115.4 eV. The shape and intensity of the spectrum is different from the experimental spectrum of yoderite measured by Wilke et al. [2001]. This experimental variability comes from the diversity of natural samples. For a given mineral, the proportion of  $\text{Fe}^{3+}$  between several possible sites can vary as the amount of  $\text{Fe}^{2+}$  or other transition metal impurities. In the particular case of yoderite, the presence of manganese leads to an oscillating signal from Mn  $K$  edge (around 6539 eV) that overlaps the Fe  $K$  pre-edge and increases the uncertainty on the extracted pre-edge intensity.

Calculations in the  $C_{3v}$  geometry, with the parameters listed in Table 4.8, reproduce the experimental pre-edge with a shoulder around 7115.4 eV that is smaller in the calculated spectrum, and that is due to quadrupole transitions because the dipole part is composed by a single peak at 7114.4 eV. The main experimental band around 7114.2 eV is reproduced by the calculation with two transitions at 7113.8 eV and 7114.4 eV. However, these two bands are not separated because the splitting (0.6 eV) is too small to be resolved by the experiment.

**Table 4.8** – Parameters used for the calculation of yoderite at 300 K

Electronic state	$D\mu$ (eV)	$D\nu$ (eV)	$V_{pd}$ (eV)	$\beta$	$\langle N_p \rangle$	$p$ -character
Ground state $(3d, 4p)^5$	-0.03	-0.16	1.5	60%	$4.7 \cdot 10^{-3}$	0.09%
Excited state $1s^1(3d, 4p)^6$	-0.03	-0.16	4.5	60%	$2.2 \cdot 10^{-2}$	0.36%

The total intensity of the pre-edge ( $A_{exp} = 11.2 \cdot 10^{-2}$ ) is close (7%) to the calculated value  $A_{sum} = 12.0 \cdot 10^{-2}$ , which is composed of  $A_{dip} = 2.4 \cdot 10^{-2}$  and  $A_{quad} = 8.8 \cdot 10^{-2}$ . A dipole contribution corresponding to 21% of the pre-edge area is observed, this value is lower than for  $^{55}\text{Fe}^{2+}$  in grandidierite. The  $p$ -character is smaller than in  $T_d$ . The total area observed in our sample is also smaller than  $A_{exp} = 19 \cdot 10^{-2}$  found by Wilke et al. [2001] for  $^{55}\text{Fe}^{3+}$  in yoderite. In order to reproduce the experimental spectrum,  $V_{pd}$  has to be increased to 9 eV in order to get a dipole contribution about 55% of the total area.

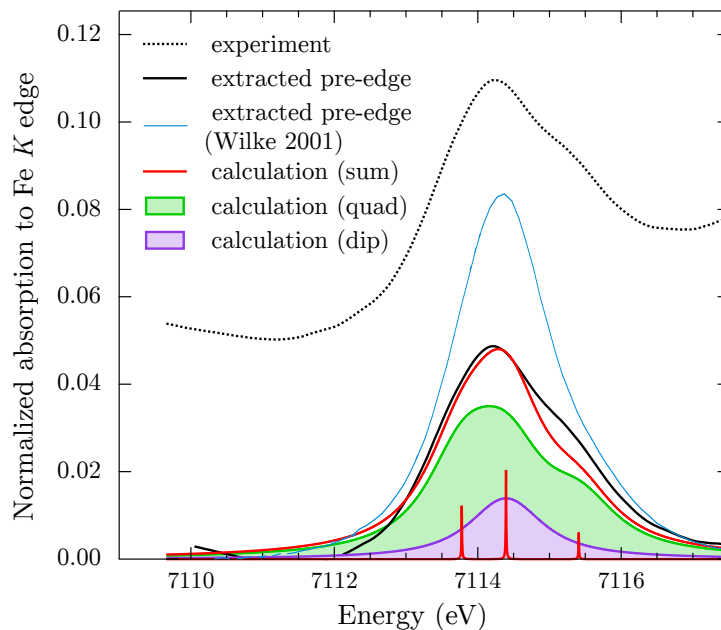


**Figure 4.31** – Experimental XAS spectrum of yoderite (dotted black line), extracted XAS pre-edge (plain black line), compared to the calculated XAS absorption spectrum of  $\text{Fe}^{3+}$  in  $C_{3v}$  geometry with dipole and quadrupole transitions. The extracted XAS pre-edge of yoderite from [Wilke et al., 2001] has been reproduced (blue line).

#### 4.7.2 Optical absorption spectra

Yoderite is a monoclinic mineral. Therefore, three measurements with different incident polarization ( $\alpha$ ,  $\beta$  and  $\gamma$ ) enhance different transitions (Figure 4.32). Unfortunately, the purple color of yoderite comes from manganese impurities. The intense spin-allowed transitions of  $\text{Mn}^{3+}$  ions overlap the spin-forbidden transitions of  $\text{Fe}^{3+}$ , especially in the range  $15\,000\text{--}20\,000\text{ cm}^{-1}$ . However, several weak bands at  $20\,700\text{ cm}^{-1}$ ,  $21\,500\text{ cm}^{-1}$ ,  $25\,500\text{ cm}^{-1}$  and  $28\,200\text{ cm}^{-1}$  (Figure 4.32) were attributed by Abu-Eid et al. [1978] and Langer et al. [1982] to  $[\text{Fe}^{3+}]$  spin-forbidden transitions. The calculation performed for  $\text{Fe}^{3+}$  in  $C_{3v}$  symmetry with the ligand field parameters, listed in Table 4.8, shows several bands in the range  $20\,000\text{--}28\,000\text{ cm}^{-1}$  that could correspond to the experimental signals. Moreover, an additional signal visible on the experimental  $\gamma$  polarized spectrum can correspond to the calculated signal around  $12\,500\text{ cm}^{-1}$ . Except this weak band, it seems that no  $\text{Fe}^{3+}$  bands are expected below  $20\,000\text{ cm}^{-1}$  in the spectral range usually attributed to  $\text{Fe}^{2+}$ . Some transitions calculated around  $24\,000\text{ cm}^{-1}$  could be attributed to  $\text{Fe}^{3+}$  transitions.

In conclusion, these first OAS calculations for [5]-fold  $\text{Fe}^{3+}$ -bearing mineral are promising but isotropic experimental spectra are needed to conclude on the relative intensities of the calculations. Further calculations with various parameters and lower symmetries could help in the attribution of the transitions.

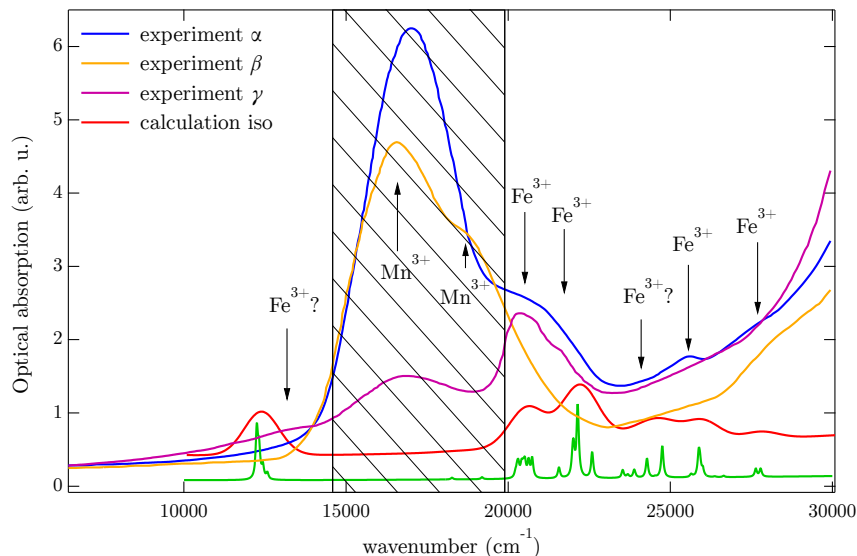


**Figure 4.32** – Experimental polarized transmission spectra of yoderite in the UV-Vis range [Langer et al., 1982] compared to the calculated optical absorption spectrum of  $\text{Fe}^{3+}$  in  $C_{3v}$  geometry. The central part of the spectrum ( $15\,000\text{ cm}^{-1}$ – $20\,000\text{ cm}^{-1}$ ) is dominated by  $\text{Mn}^{3+}$  transitions.

## 4.8 Summary

These results confirm that LFM calculations can reproduce two different spectroscopies probing the  $3d$  levels (valence to valence for OAS and core to valence for XAS). The use of a common set of crystal field parameters for the ground state improved the description of the studied site. For the first time, optical absorption spectra of iron could be calculated, by taking into account the  $3d$ – $4p$  mixing, for a wide range of Fe-bearing crystals representative of various geometries. It proves that the electric dipole contribution are the main origin of the optical absorption as suggested by Rossano et al. [2000a]. The Fe  $K$  pre-edge XAS have been interpreted for both centrosymmetric and non-centrosymmetric sites in  $\text{Fe}^{2+}$ - and  $\text{Fe}^{3+}$ -bearing minerals. Calculations not only reproduce the relative energies of transitions but also the absolute intensities of the X-ray absorption spectra in most compounds. Concerning hybridization, 0.1% of  $3d$  electrons delocalized on the  $4p$  orbitals are sufficient to obtain optical intensities and a significant dipole contribution to the XAS pre-edge.

The proportion of electric dipole and quadrupole contributions to the total  $K$  pre-edge XAS area has been estimated (Table 4.9). Calculations confirmed that electric dipole transitions can be neglected in the case of centrosymmetric geometries ( $O_h$  and  $D_{4h}$ ). For both iron valences ( $\text{Fe}^{2+}$  and  $\text{Fe}^{3+}$ ), tetrahedral sites give the strongest pre-edge intensities with 80% of the area due to dipole transitions. As intermediary geometries, [5]-fold compounds give an intermediate value between  $O_h$  and  $T_d$ , which is different for the  $\text{Fe}^{2+}$ - and  $\text{Fe}^{3+}$ -bearing minerals. The first one, grandidierite, has an equivalent contribution from dipole and quadrupole transitions, while, the pre-edge of yoderite, is mainly due to quadrupole transitions.

**Table 4.9** – Normalized integrated intensities of the  $K$  pre-edge XAS spectrum from dipole electric and quadrupole electric transitions for different geometries. The areas are multiplied by 100 and correspond to the integral of the pre-edge spectrum with energy in eV and its intensity normalized to the main edge. All the extracted  $K$  pre-edge XAS are plotted in the same figure at the end of Appendix A.

Geometry	Mineral	LFM calculations			Experiment
		Quad	Dip	Total	Total
$[6]Fe^{2+}$ ( $O_h$ )	siderite	6.1	0.1	6.2	5.9
		(98%)	(2%)	(100%)	
$[4]Fe^{2+}$ ( $D_{4h}$ )	gillespite	6.2	0.4	6.6	5.6
		(94%)	(6%)	(100%)	
$[5]Fe^{2+}$ ( $D_{3h}$ )	grandidierite	6.0	5.2	11.2	11.8
		(54%)	(46%)	(100%)	
$[4]Fe^{2+}$ ( $T_d$ )	staurolite	5.8	23.6	29.4	23.3
		(20%)	(80%)	(100%)	
$[6]Fe^{3+}$ ( $O_h$ )	andradite	8.6	0.2	8.8	9.7
		(98%)	(2%)	(100%)	
$[5]Fe^{3+}$ ( $C_{3v}$ )	yoderite	8.8	2.4	11.2	12.0
		(79%)	(21%)	(100%)	
$[4]Fe^{3+}$ ( $T_d$ )	ferriorthoclase	8.3	26.2	34.5	34.3
		(24%)	(76%)	(100%)	

More than the possibility of calculating and reproducing an experimental spectrum, calculations shed light on the spectral sensitivity to site geometry and to the different crystal field and hybridization parameters used to describe the local environment in a given point group. The different behavior of the two experimental methods in reaction to the variations of parameters and geometries help to find which parameters are significant and those that do not affect significantly the shape, intensity or position of transitions in order to improve the accuracy of crystal field parameters determination.

Thanks to this new kind of calculations, it is now possible to simulate realistic optical spectra. The sensitivity of optical spectra to the calculation parameters and to the point group symmetry combined with the structural knowledge (XRD) of the iron local environment in minerals, will be useful to analyze the effects of a distribution of the parameters ( $10Dq$ ,  $\beta$ ...) on the OAS and XAS spectra. Despite that local environment of iron in crystals is not representative of the one in glasses\* and that some iron environments in crystals are unlikely to exist in glasses†, this approach offers a new method to estimate the distortion and site distribution of TM in glasses. The study of glass spectroscopic signatures in order to extract tendencies on the parameters characterizing iron local environment will be detailed in the next chapter.

\*For example, it has been proven in highly concentrated glasses that many  $Fe^{2+}$  and  $Fe^{3+}$  ions are [5]-fold coordinated while almost all minerals are [4]- or [6]-fold coordinated [Weigel et al., 2008a, 2006].

†For example, almandine garnet ( $Ca_{0.3}Fe_{1.5}Mg_{1.2}Al_2Si_3O_{12}$ ) a pink silicate mineral where iron is present as  $[8]Fe^{2+}$  in an 8-fold coordinated site [Wilke et al., 2001] is not considered as a good candidate to describe the iron environment in glasses.

## Chapter 5

# Iron local environment in a soda-lime-silicate glass

As we have seen in the previous chapter, a broad variety of iron environment exists in silicate minerals. This diversity of iron environment is increased in the case of amorphous materials such as glass, as introduced in Section 1.3. The purpose of this chapter is to discuss the relationships of iron environment and spectroscopic properties of iron in silicate glasses for both existing valences  $\text{Fe}^{2+}$  and  $\text{Fe}^{3+}$ . This chapter is built around optical absorption spectroscopy, which is a key property for industrial applications.

I will focus on the case of the sodium-calcium-silicate glass composition (NCS), also called soda-lime silicate, that have been introduced and characterized in Chapter 2. Among the different glass compositions studied in this thesis, this one is the most representative of industrial float glass. The studied set consists of three NCS glasses (NCS05Ox, NCS05Med and NCS05Red) doped with 0.5 wt% of  $\text{Fe}_2\text{O}_3$  at three redox ratio ( $R = \text{Fe}^{2+}/\text{Fe}_{\text{tot}}$ ): oxidized ( $R \sim 6\%$ ), medium ( $R \sim 28\%$ ) and reduced ( $R \sim 99\%$ ) glasses, respectively.

The aim is here to cross the optical absorption spectroscopy results with the other spectroscopic methods presented in Chapter 2: XAS, RIXS, EPR, SQUID-VSM. Each method brings a specific insight on the iron environment by enhancing different aspects of the problem. The advantage of X-ray absorption spectroscopy has been shown in the previous chapter with the study of several minerals with characteristic Fe sites. The tendencies highlighted using ligand field multiplet calculation will be extended to the analysis of Fe in glass. The complementary RIXS and HERFD-XAS methods will be used to emphasize the differences between glass and mineral environments. EPR will be mainly dedicated here to the study of  $\text{Fe}^{3+}$  distortion and clustering using the interpretation elements of Section 2.6.3. SQUID-VSM will be used at the end of the chapter to investigate the presence of iron clusters in glass.

I will show that a multi-spectroscopic analysis is useful to get new information on the origins of  $\text{Fe}^{2+}$  and  $\text{Fe}^{3+}$  optical bands, the distortion of  $\text{Fe}^{3+}$  sites and the clustering of iron, in order to have a better understanding of iron speciation and its impact on spectroscopic features as a function of redox state.

## 5.1 Introduction to the optical absorption spectrum of iron in silicate glass

The optical absorption of iron in the NCS glass will be introduced by energy range using an experimental optical absorption spectrum of the most common glass sample: NCS05Med (Figure 5.1).

Silicon dioxide ( $\text{SiO}_2$ ) is the main component of all the glasses studied in this thesis. Experimentally, the transmission window of pure silica glass ( $2000$  to  $50\,000\text{ cm}^{-1}$ ;  $5000\text{ nm}$  to  $200\text{ nm}$ ) defines an intrinsic limitation of the spectral range.

In the near-infrared (NIR) below  $2700\text{ cm}^{-1}$ , the tail of Si–O vibration bands set the lower limit of the optical spectrum. Unfortunately, below  $4000\text{ cm}^{-1}$ , the spectral range is limited by very intense absorption bands due to O–H vibrations of hydroxyl groups. Adsorption of water by the glass during the synthesis under air atmosphere is at the origin of these O–H groups. As we will see later, these bands are not visible on reduced samples synthesized under nitrogen. The most intense bands are situated below  $4000\text{ cm}^{-1}$ , but several weak O–H bands can also be found from  $4000$  to  $7200\text{ cm}^{-1}$  [Boulos et al., 1997; Davis and Tomozawa, 1996; Glebov and Boulos, 1998]. These weak bands, only visible on non-doped glasses (e.g. NCS00Med, DIO00Med), are negligible for glasses with more than  $0.1\text{ wt}\%$  of  $\text{Fe}_2\text{O}_3$ .

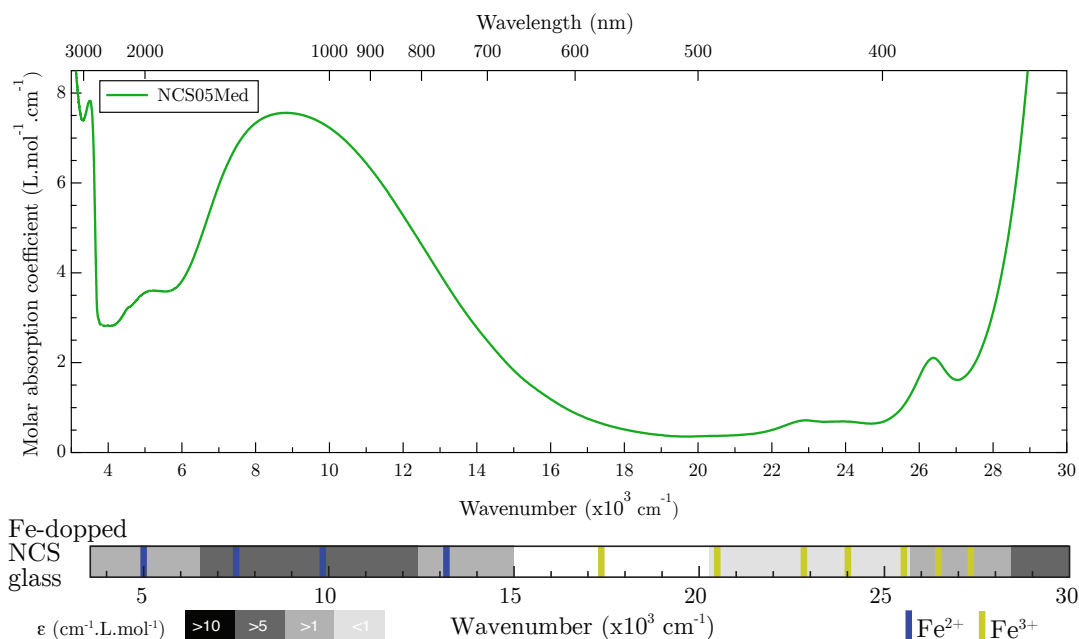


**Figure 5.1** – Top: optical absorption spectrum of the medium sodium-calcium-silicate glass (NCS05Med,  $\text{Fe}^{2+}/\text{Fe}_{\text{tot}} \sim 28\%$ ). Bottom: sticks representing the absorption bands of  $\text{Fe}^{2+}$  (blue) and  $\text{Fe}^{3+}$  (yellow), molar absorption coefficients in grey scale are calculated separately for  $\text{Fe}^{2+}$  and  $\text{Fe}^{3+}$  (see note p.203).

The upper limit in the UV range,  $50\,000\text{ cm}^{-1}$ , is determined by the oxygen to silicon charge transfer. However, in Figure 5.1, the UV-edge happens from  $\bar{\nu} > 28\,000\text{ cm}^{-1}$  ( $\lambda < 360\text{ nm}$ ). The UV range above  $28\,000\text{ cm}^{-1}$  is in fact dominated by broad and intense transition metal bands, three orders of magnitude higher than the crystal field bands. These

spin-allowed and Laporte-allowed bands are due to an electronic transition between the 2p of the nearest-neighbor oxygen ligand and the 3d of the central transition metal ion. They are therefore named *ligand to metal charge transfer* (LMCT) or *oxygen to metal charge transfer* (OMCT) in the case of oxides.

Between these two edges, NIR (4000) and UV (28 000 cm<sup>-1</sup>), are the iron crystal field bands or so-called “*d–d* transitions”. They can be separated into two energy ranges [Fox et al., 1982]:

- Fe<sup>2+</sup> range from 4000 to 19 000 cm<sup>-1</sup>
- Fe<sup>3+</sup> range from 19 000 to 28 000 cm<sup>-1</sup>

## 5.2 Structure–spectroscopy analysis of Fe<sup>2+</sup>

This section presents the results about local environment of Fe<sup>2+</sup> in glasses. Given the low iron content (0.5 wt% of Fe<sub>2</sub>O<sub>3</sub>) of the studied glass, we can reasonably expect that the majority of Fe<sup>2+</sup> are isolated (e.g. no magnetic coupling) from other iron ions. However, some low levels of clustering can also be expected, as suggested by Bogomolova and Henner [1980] and Berger et al. [1995], this will be discussed in Section 5.4.

### 5.2.1 Spectroscopic origins of Fe<sup>2+</sup> optical bands

Regarding the spectrum of Figure 5.1, the Fe<sup>2+</sup> range seems to be composed with only two bands at 5000 cm<sup>-1</sup> and around 10 000 cm<sup>-1</sup> in soda-lime glasses. The signal of the main band is going from 6000 cm<sup>-1</sup> to 17 000 cm<sup>-1</sup> with a maximum around 9000–10 000 cm<sup>-1</sup>. Its characteristic asymmetrical shape is supposed to be due to overlapping of different transitions with various intensities. At least three contributions around 7500 cm<sup>-1</sup>, 10 000 cm<sup>-1</sup> and 13 000 cm<sup>-1</sup> are usually necessary for the interpretation of this band [Ehrt et al., 2001]. The asymmetry and broadness were attributed to octahedral distortion splittings of the <sup>5</sup>E and <sup>5</sup>T<sub>2</sub> [Edwards et al., 1972] or to dynamic Jahn-Teller effect [Ookawa et al., 1997].

Figure 5.2 presents the NCS05Red optical spectrum compared with optical spectra of selected Fe-bearing minerals taken from Rossman’s website\* and Rossman and Taran [2001]. A first method named “fingerprinting” is to analyze spectral features of iron in glass by analogy with optical bands of iron in minerals. In crystalline compounds, the local environment is easier to define and spectral similarities suggest structural similarities. With this fingerprint method, it is possible to find where the bands relative to a given geometry are expected to occur.

For example, the asymmetrical shape of the glass spectrum from 8000 to 17 000 cm<sup>-1</sup> presents some analogies with [5]-fold Fe<sup>2+</sup> in grandidierite, especially the high-energy part, which absorbs in the visible with a gentle slope from 10 000 to 17 000 cm<sup>-1</sup>. However, to explain the signal from 6000 to 9000 cm<sup>-1</sup>, the comparison with distorted tetrahedral sites such as found in pellyite and gehlenite [Rossman and Taran, 2001] could explain the left part of the asymmetrical shape with a steep slope from 6000 to 8000 cm<sup>-1</sup>.

---

\*<http://minerals.gps.caltech.edu>



The shoulder around  $5000\text{ cm}^{-1}$ , is a band twice as less intense and traditionally attributed to a small amount of  $\text{Fe}^{2+}$  in tetrahedral sites [Bingham, 2000, p. 54] such as observed in staurolite, a [4]-fold Fe-bearing mineral. This attribution is convenient to interpret the glass spectra with only octahedral and tetrahedral geometries, because the positions of the bands verifies the relation  $\Delta_T = \frac{4}{9}\Delta_O$ . However, if all and only  ${}^{[4]}\text{Fe}^{2+}$  ions participate to this shoulder, the intensity should be more intense due to the higher molar absorption coefficient of non-centrosymmetric sites ( $p-d$  hybridization). Moreover, the small amount of tetrahedral sites is not compatible with the  $\text{Fe}^{2+}$  average coordination number in soda-lime glasses\*; and several [5]-fold or [6]-fold Fe-bearing minerals also exhibit a secondary band around  $5000\text{ cm}^{-1}$  such as grandidierite, hypersthene or joaquinite. The possibility that this band is being caused by an octahedral site distortion has also been discussed [Fox et al., 1982; Goldman and Berg, 1980]. But the different contributions of the  $\text{Fe}^{2+}$  signal are still not clearly identified on the Tanabe-Sugano diagram of octahedral  $\text{Fe}^{2+}$  (see Figure 4.5).

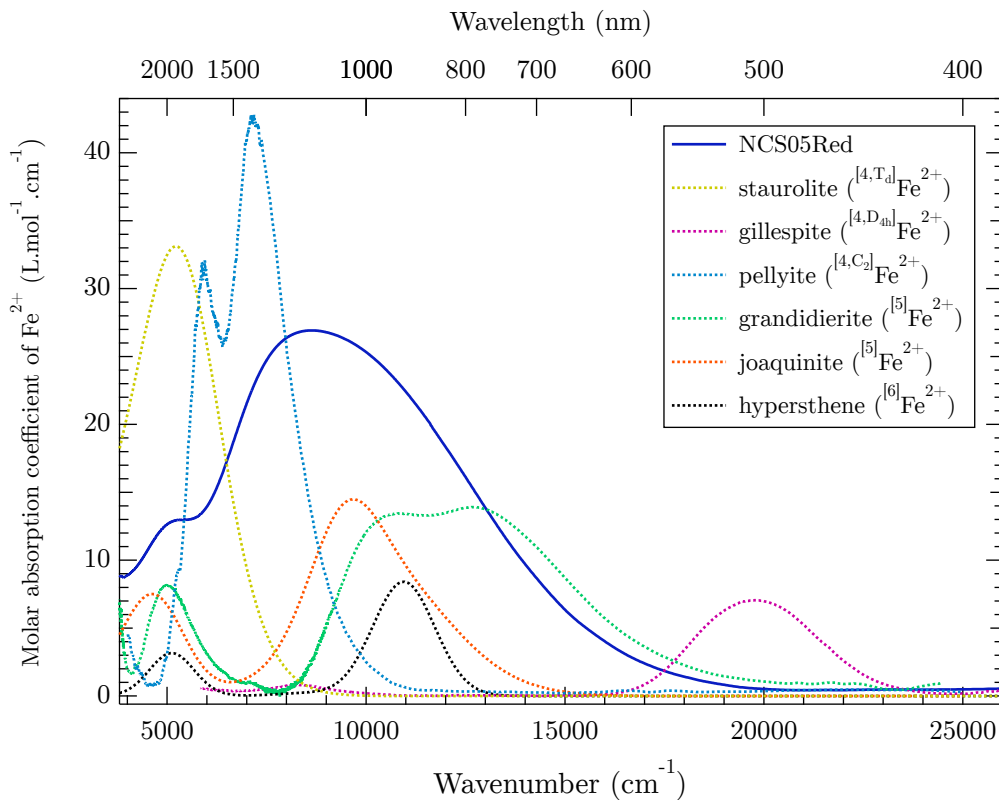


**Figure 5.2** – Optical spectra ( $\epsilon$  molar absorption coefficient) of a reduced glass (NCS05Red) with selected  $\text{Fe}^{2+}$  crystalline references: staurolite ( ${}^{[4,T_d]}\text{Fe}^{2+}$ ), gillespite ( ${}^{[4,D_{4h}]}\text{Fe}^{2+}$ ), pellyite ( ${}^{[4,C_2]}\text{Fe}^{2+}$ ), grandidierite ( ${}^{[5]}\text{Fe}^{2+}$ ), joaquinite ( ${}^{[5]}\text{Fe}^{2+}$ ) and hypersthene ( ${}^{[6]}\text{Fe}^{2+}$ ).

The vision adopted in this thesis is in the continuity with the works of Rossano et al. [2000c], Jackson et al. [2005] and Weigel et al. [2008b], in which  $\text{Fe}^{2+}$  site geometries are considered distributed between several distorted [4]- and [5]-fold sites leading to the characteristic asymmetrical  $\text{Fe}^{2+}$  bands. However, the iron content in our glass is considerably lower (around 0.2 mol% compared to more than 10 mol% in these studies), which may lead to different behaviors. MD calculations did not show significant evidence for [6]-fold  $\text{Fe}^{2+}$

\*4.6 in [Farges et al., 2004], see also Section 1.3.

or  $\text{Fe}^{3+}$  [Farges et al., 2004]. Anyway, centrosymmetric geometry slightly absorb light and transitions are weak, therefore octahedra have to be distorted in order to lose their inversion center to significantly absorb light.

### 5.2.2 The contribution of XAS to the analysis of $\text{Fe}^{2+}$ optical bands

To analyze in details the origins of the  $\text{Fe}^{2+}$  optical bands in glasses, X-ray absorption spectroscopy (XAS) in fluorescence-yield detection mode is a chemically selective method particularly adapted in the case of low iron-content samples. It is a powerful experimental method giving information on both oxidation state and local environment of iron [Calas and Petiau, 1983a], [Waychunas et al., 1983], [Henderson et al., 1984], [Brown et al., 1995], [Galoisy et al., 2001], [Petit et al., 2001], [Farges et al., 2004], [Jackson et al., 2005], [Henderson et al., 2014].

Compared to these studies, in which the total fluorescence yield was measured, this section presents the first RIXS and HERFD measurements performed on iron-doped glasses. As explained in Section 2.4, RIXS and HERFD-XAS allow finely analyzing the fluorescence beam in order to bring new information from the emitted photons.

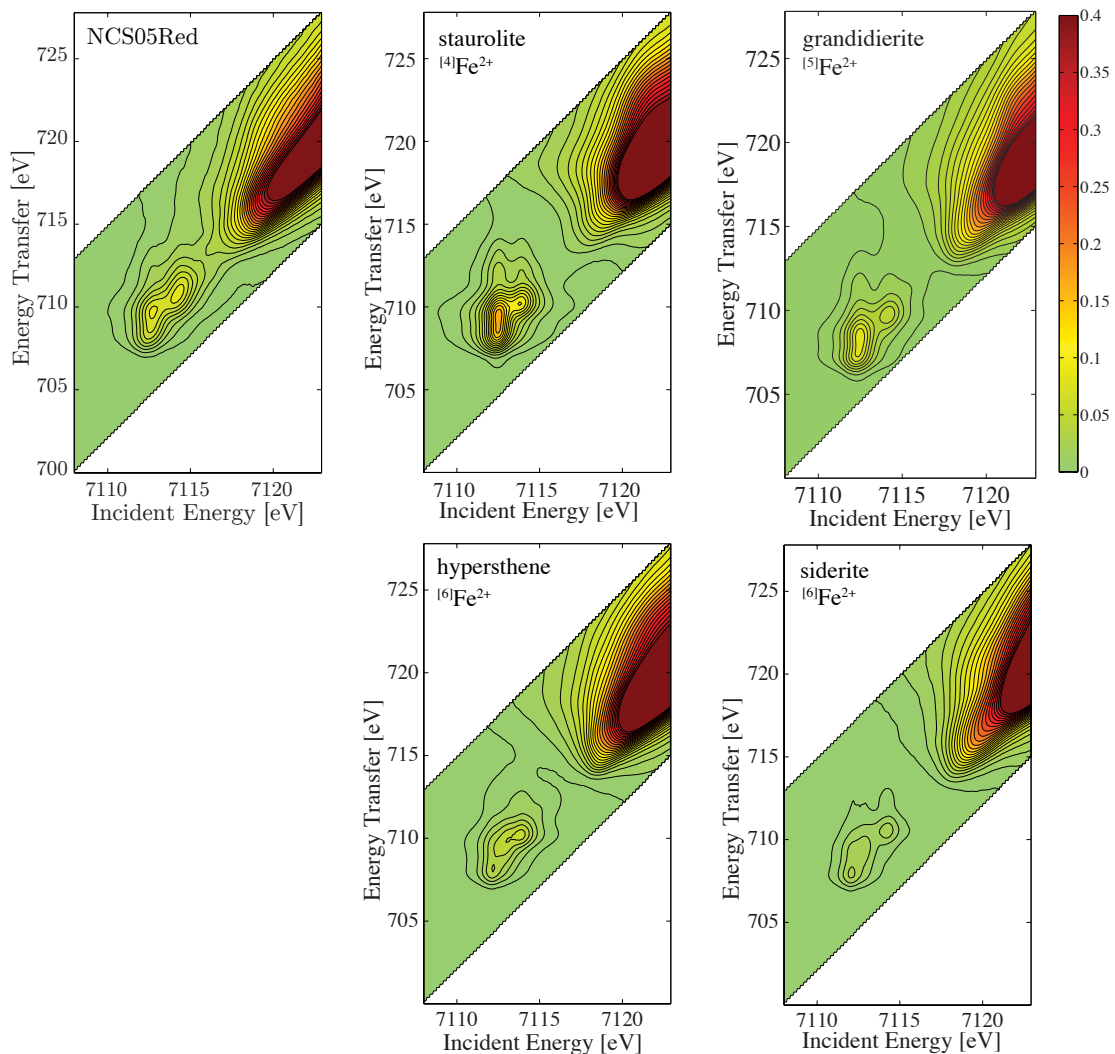


**Figure 5.3** – Normalized RIXS  $K\alpha$  spectra at the Fe  $K$  pre-edge for a reduced glass (NCS05Red) and selected [4]-, [5]-, and [6]-coordinated  $\text{Fe}^{2+}$  model compounds.

In order to study  $\text{Fe}^{2+}$  environment, the RIXS spectrum of the NCS05Red glass is compared with reference compounds (Figure 5.3). NCS05Red show a similar shape with staurolite ( $^{[4]}\text{Fe}^{2+}$ ) and grandidierite ( $^{[5]}\text{Fe}^{2+}$ ) compared to other crystalline reference compounds such as hypersthene or siderite ( $^{[6]}\text{Fe}^{2+}$ ) (RIXS data for all  $\text{Fe}^{2+}$ - and  $\text{Fe}^{3+}$ -bearing mineral reference compounds can be found in Appendix A). This assumption was confirmed by a linear decomposition of the RIXS pre-edge of NCS05Red as a function of the different minerals; staurolite and grandidierite obtained the highest score of similarity.

To confirm this tendency, a cut along the diagonal of the RIXS spectrum, that corresponds to a scan at constant emission energy (CEE) or HERFD spectrum (see Section 2.4.4), is shown in Figure 5.4 for the same five samples. One can notice that it is almost possible to decompose the glass pre-edge with the staurolite ( $^{[4]}\text{Fe}^{2+}$ ) and grandidierite ( $^{[5]}\text{Fe}^{2+}$ ) minerals. Of course, the XANES oscillations just after the main edge are stronger in crystals than in glass regarding the periodic arrangements of crystals compared to the amorphous nature of glass. Two other details can be shed in light, the first one is that NCS05Red spectrum also contains features associated to the presence of  $\text{Fe}^{3+}$ : the pre-edge is more intense than expected around 7114.5 eV and the main edge is at higher energy than expected. This effect, due to beam damage photooxydation, studied in details in Appendix D.3, changes the redox ratio,  $\text{Fe}^{2+}/\text{Fe}_{\text{tot}}$ , from 99 to 85% in the glass, leading to the raise of a  $\text{Fe}^{3+}$  component around 7114.5 eV. The other point is the intensity between the pre-edge and the main edge, which is almost zero in the crystalline compounds and not in the glass, this effect is attributed to delocalized states of iron involved in Fe-clusters and will be detailed later (see Section 5.4).

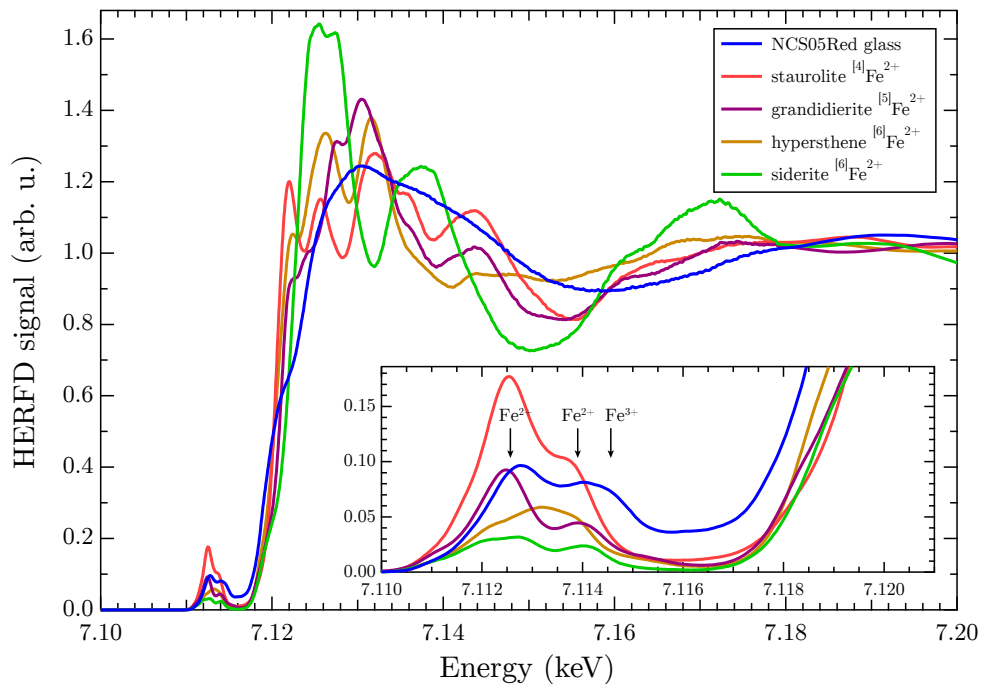


**Figure 5.4** – Cut of the RIXS map at constant emitted energy (CEE), i.e. HERFD spectra, for Fe  $K$  pre-edge spectra of NCS05Red glass and selected [4]-, [5]-, and [6]-coordinated  $\text{Fe}^{2+}$  model compounds.

Concerning the two [6]-fold  $\text{Fe}^{2+}$ -bearing minerals (siderite and hypersthene), their respective pre-edge shapes are not characteristic of the glass pre-edge. In addition, despite the strongly distorted [6]-fold  $\text{Fe}^{2+}$  site of hypersthene, whose intensity is increased by electric dipole transitions due to  $p$ - $d$  mixing, its area remains lower than the glass pre-edge with a maximum at the same position than the local minimum of the glass pre-edge.

These discrepancies are even more visible in Figure 5.5, representing the spectra of the glass and the four minerals as a function of energy transfer for a constant incident energy (CIE) fixed at 7112.5 eV (maximum of the glass pre-edge). The black lines represent three main components of the glass spectrum, however, the first component in the [6]-fold minerals is weaker and at lower energy than in glass, while grandidierite and staurolite approximately match in position. Of these two minerals, only grandidierite exhibits similar intensities with the glass; staurolite is too intense.

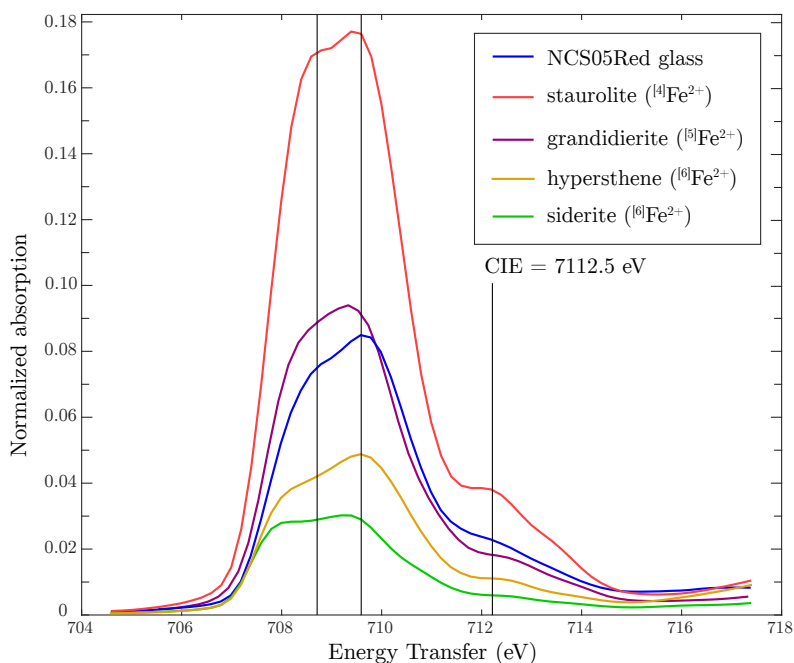


**Figure 5.5** – Cut of the RIXS map at constant incident energy (CIE) for Fe  $K$  pre-edge spectra of NCS05Red glass and selected [4]-, [5]-, and [6]-coordinated  $\text{Fe}^{2+}$  model compounds.

The analysis of  $\text{Fe}^{2+}$  RIXS and HERFD spectra, especially in reduced glasses, agrees with the vision presented at the end of the previous section regarding the predominant role of [5]-fold iron in the  $\text{Fe}^{2+}$  spectroscopic signature of glass. Even if [4]-fold and [6]-fold  $\text{Fe}^{2+}$  could exist in glasses, experimental data suggest that they remain in low proportion compared to [5]-fold geometries.

The accuracy of this “fingerprint” method is however limited by the variability of natural mineral samples, exemplified by the work of Farges [2001] on eight grandidierite samples from different locations. The author concluded that the possible presence of an extra contribution related to  $\text{Fe}^{3+}$  can significantly enhance the Fe  $K$  pre-edge area (+40% for 0.1 wt% of  $\text{Fe}^{3+}$ ). This variability underlines one of the “fingerprint” limits, because only few grandidierite mineral samples can be used as a robust structural model in the study of the  $\text{Fe}^{2+}$  coordination in glasses.

Another issue remains in the differences between the amorphous nature of glass in which iron sites are distributed and the crystalline arrangement of minerals. Structural analogies between glass and minerals can be done, but the intrinsic differences between these materials exclude the possibility of deconvoluting a glass by directly using selected minerals characteristic of iron sites in glass.

### 5.2.3 LFM calculations of $\text{Fe}^{2+}$ spectroscopic signature in glasses

The last chapter shows the potentialities of LFM calculations to the analysis of  $\text{Fe}^{2+}$  spectroscopic features of mineral analyzed by optical absorption spectroscopy and X-ray absorption spectroscopy. During this thesis, several theoretical and software developments have been done (see Appendix E) in order to fully calculate the RIXS and HERFD-XAS spectra of powders using `Quanty` and the method described in Chapter 4. In the current situation, further developments are still needed but we are confident on the possibility of reproducing the RIXS and HERFD spectra with the same set of parameters than XAS and OAS spectra.

It is nevertheless possible to use the TFY measurements, which are less resolved than HERFD but can be reproduced using LFM calculation. With the developments achieved in this work for optical spectroscopy calculations, it is now easier to compare these two complementary spectroscopies. It is also possible to extract tendencies from the calculations in order to study variations of the spectra depending on the point group symmetry representing the Fe absorbing site, crystal field parameters ( $Dq$ ,  $Ds$ ,  $Dt$ ,  $D\mu$ ,  $D\nu$ ), hybridization parameters ( $V_{pd}$ ), nephelauxetic ratio ( $\beta$ ) and spin-orbit ( $\zeta_{3d}$ ).

Concerning staurolite ( $^{[4]}\text{Fe}^{2+}$ ), its optical spectrum of (Figure 5.2) exhibits a band around  $5000\text{ cm}^{-1}$  that was reproduced in Section 4.4. The intensities of the optical band and the pre-edge are too intense compared to the glass, which suggests that  $V_{pd}$  should be decreased. Unfortunately, with  $T_d$  geometry it will never be possible of reproducing the optical features from  $9000\text{ cm}^{-1}$  to  $17000\text{ cm}^{-1}$ , except by taking  $10Dq$  higher than 1 eV, which is not representative of NCS05Red glass regarding the  $K$  pre-edge split observed for  $\text{Fe}^{2+}$  in  $T_d$  in the previous chapter (Figure 4.20). Therefore, another geometry has to be considered in order to interpret the OAS and XAS features of  $\text{Fe}^{2+}$  in glass.

On the other hand, it has been shown that grandidierite ( $^{[5]}\text{Fe}^{2+}$ ) and NCS05Red glass exhibit similar OAS (Figure 5.2) and HERFD-XAS (Figure 5.4) spectra. In the case of NCS05Red, LFM calculations of  $\text{Fe}^{2+}$  in  $C_{3v}$  shows optical bands in the same spectral range with coherent intensities (Figure 5.7).

By adapting the previous results of grandidierite, it is possible to obtain two optical bands at  $5000\text{ cm}^{-1}$  and around  $10000\text{ cm}^{-1}$  (set A, B and C in Table 5.1). By changing the values of crystal field parameters  $D\mu$  and  $D\nu$ , it is possible to keep the first band at  $5000\text{ cm}^{-1}$  and sweep the second band from  $10000\text{ cm}^{-1}$  to  $17000\text{ cm}^{-1}$  (Figure 5.7). In order to reproduce the diversity of sites present in the glass, the parameters have to be distributed around the ones used for grandidierite (Table 4.7). That is why, the use of two additional sets of parameters (D and E in in Table 5.1) have permitted to reproduce the signal between  $6000\text{ cm}^{-1}$  and  $9000\text{ cm}^{-1}$ . These calculations show that we could reproduce

the optical spectrum of  $\text{Fe}^{2+}$  in glasses only using the  $C_{3v}$  geometry representative of [5]-fold trigonal bipyramid. The present results show that the key parameter in the interpretation of optical properties of iron in glass is site distribution.

**Table 5.1** – Sets of  $C_{3v}$  calculation parameters representing the variability of [5]-fold  $\text{Fe}^{2+}$  sites.

name	$D\mu$ (eV)	$D\nu$ (eV)	$V_{pd}$ (eV)	$\beta$
A	-0.025	-0.120	0.9	60%
B	-0.06	-0.155	0.75	60%
C	-0.09	-0.175	0.5	60%
D	0.05	-0.125	1.0	60%
E	0.09	-0.12	1.0	60%

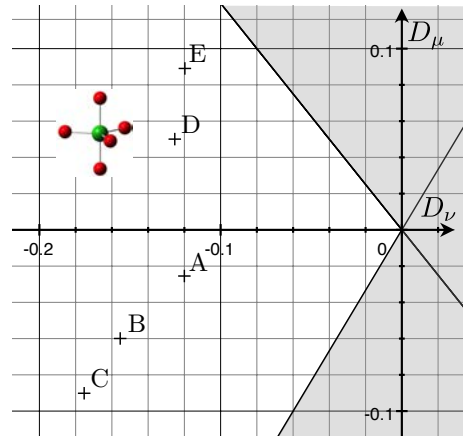


**Figure 5.6** – Crystal field parameters representing a trigonal bipyramid geometry (white area).

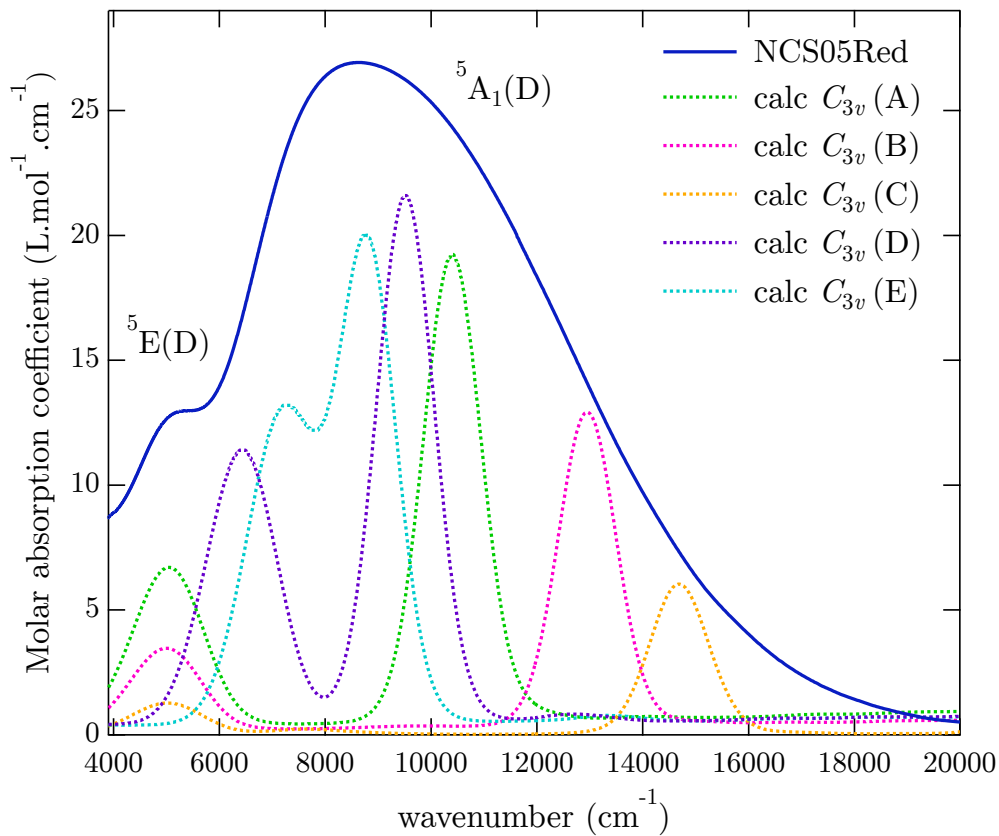


**Figure 5.7** – Optical absorption spectra of NCS05Red glass, and five calculated spectra of  $\text{Fe}^{2+}$  in  $C_{3v}$  geometry (A, B, C, D and E).

In any case, the existence of a simple and unique Gaussian distribution of the crystal field parameters is not probable because at least two sets of parameters were necessary to reproduce the optical spectra of grandidierite (Table 4.7). Therefore, in the eventuality of

a spectroscopic calculation of  $\text{Fe}^{2+}$  in glass, a bimodal or polymodal distribution will be necessary to reproduce the variety of site distortions.

In the hypothesis that [5]-fold ( $C_{3v}$ ) geometries are exclusively used to interpret the origin of the majority of the  $\text{Fe}^{2+}$  optical signal from  $4000\text{ cm}^{-1}$  to  $17\,000\text{ cm}^{-1}$ , the labeling of the two bands should be renamed  ${}^5A_1(D)$  and  ${}^5E(D)$  regarding the irreducible representations of the  $C_{3v}$  point group. Other parameters, such as Racah  $B$  and  $C$  parameters, should also be analyzed in consequence. In the case of grandierite calculation, the value of  $\beta = 0.6$  leads to  $B = 709.2\text{ cm}^{-1}$  and  $C = 2617.7\text{ eV}$ . However,  $\beta$  does not change the positions of the two  $\text{Fe}^{2+}$  spin-allowed transitions (see Section 4.1.3.3). The numerous weak spin-forbidden transitions of grandierite might help to find an adapted value of  $\beta$  using the possibility of easily calculating new Tanabe-Sugano diagrams (Figure 4.28).

### 5.2.4 Influence of redox on the $\text{Fe}^{2+}$ local environment

The atmospheric control used to control the redox is expected to better preserve the iron environment in glass in comparison with a chemical control using a refining agent, which necessarily interacts with iron to exchange electrons, and thus, possibly modifies iron local environment by staying in the vicinity of iron as a second neighbor.

Due to the different synthesis conditions,  $\text{Fe}^{2+}$  represents 100% of iron in the reduced glass (NCS05Red) and only 5% in the oxidized glass (NCS05Ox)..

Figure 5.8-a shows the optical absorption spectra of the three studied soda-lime glasses in the range  $4000\text{--}19\,000\text{ cm}^{-1}$  corresponding to  $\text{Fe}^{2+}$  transitions. The absorbance is maximal for reduced glasses, containing mainly  $\text{Fe}^{2+}$ , and its value ( $\sim 4.2\text{ cm}^{-1}$ ) is one order of magnitude stronger than the oxidized glass ( $\sim 0.3\text{ cm}^{-1}$ ). Therefore, the absorbance was normalized by ferrous iron concentration  $[\text{Fe}^{2+}]$ . (Figure 5.8-b).

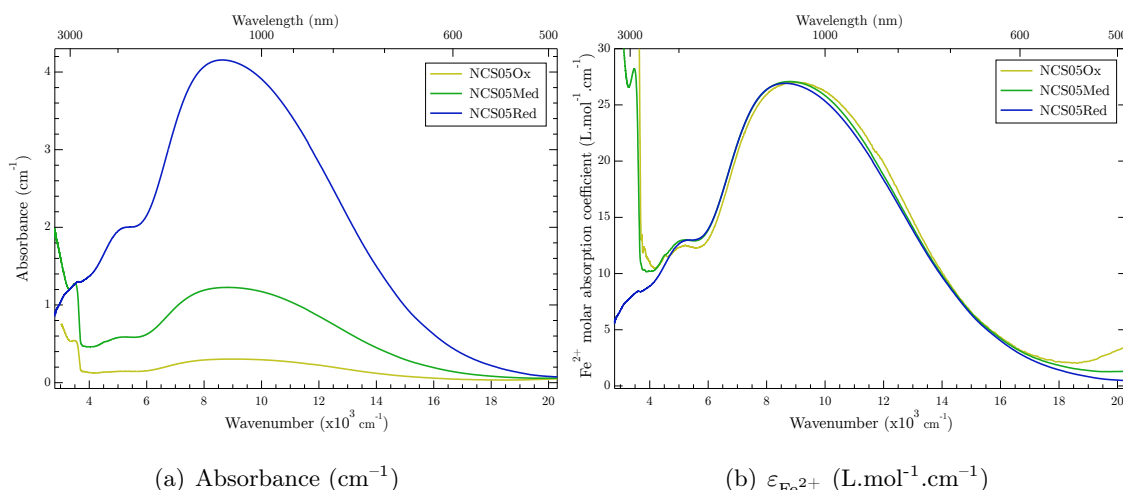


**Figure 5.8** – Optical spectra of the oxidized (NCS05Ox), the intermediate redox (NCS05Med) and the reduced (NCS05Red) soda-lime-silica glasses.

On the NCS05Red spectrum, there are no OH signals below  $4000\text{ cm}^{-1}$ , which is due to the absence of water during reducing synthesis under  $\text{N}_2$ .

Concerning the main signal of  $\text{Fe}^{2+}$  around  $10\,000\text{ cm}^{-1}$ , the band maximum shifts at

lower energy when  $\text{Fe}^{2+}/\text{Fe}_{\text{tot}}$  decreases in the glass. This suggests a change of  $\text{Fe}^{2+}$  local environment, whose proportion of the different sites contributing to the  $\text{Fe}^{2+}$  spectrum evolves with redox. Hannant et al. [2008] also found a similar conclusion concerning the environment dependence of both ferric and ferrous iron with redox by using Mossbauer analysis of high iron-content soda-lime silicate glasses with more complex compositions closer to real industrial glasses.

The band at  $5000\text{ cm}^{-1}$  is more separated from the main band in NCS05Ox than in NCS05Red. In the reduced glass spectrum, this band only shouldered the main band, whereas it presents a local maximum and minimum in the oxidized glass spectrum. This can be analyzed using a Gaussian fit of the  $\text{Fe}^{2+}$  contributions from 4000 to  $16\,000\text{ cm}^{-1}$ . For smaller  $\text{Fe}^{2+}/\text{Fe}_{\text{tot}}$  values, the fit results shown in Table 5.2 exhibit a shift at lower energy of the band #1 (around  $4800\text{ cm}^{-1}$ ) and a shift at higher energy of the component #2 (around  $7800\text{ cm}^{-1}$ ).

In conclusion, the analysis of optical absorption spectra, in the energy range attributed to  $\text{Fe}^{2+}$ , shows a modification of the optical bands suggesting a change of the  $\text{Fe}^{2+}$  local environment with redox.

**Table 5.2** – Fit of  $\text{Fe}^{2+}$  bands with 3 Gaussian functions for NCS05Ox, NCS05Med and NCS05Red glasses

Sample name (peak #)	Position ( $\text{cm}^{-1}$ )	$\sigma$ ( $\text{cm}^{-1}$ )	FWHM ( $\text{cm}^{-1}$ )	Intensity ( $\text{cm}^{-1}$ )	$\varepsilon_{\text{Fe}^{2+}}$ (L/mol/cm)	Area ( $\text{cm}^{-2}$ )
NCS05Red ( $R = 99\%$ )						
#1	4848	492	1159	0.75	4.8	651.6
#2	7812	1277	3007	0.96	6.2	2181.4
#3	9775	3177	7482	3.65	23.7	20 557.5
NCS05Med ( $R = 28\%$ )						
#1	4834	470	1107	0.21	4.6	174.3
#2	7856	1155	2720	0.23	5.1	471.3
#3	9711	3104	7310	1.09	24.0	5988.5
NCS05Ox ( $R = 6\%$ )						
#1	4818	461	1086	0.05	4.5	39.5
#2	7894	1026	2416	0.05	4.4	86.1
#3	9765	3147	7411	0.27	25.0	1510.2

To complement this analysis, we tried to find the best linear combination of the two extreme glasses (NCS05Ox and NCS05Red) that reproduces the RIXS pre-edge of NCS05Med. The linear fit was performed on the region of interest (ROI): Incident energy:  $7111 < x < 7116.5\text{ eV}$ ; Energy transfer:  $707 < y < 716\text{ eV}$ ;  $\Delta x = 5.5\text{ eV}$ ;  $\Delta y = 9\text{ eV}$ .

The RIXS spectra of the three glasses are plotted at the top of Figure 5.9. The spectrum of NCS05Ox is very similar to NCS05Med except that the pre-edge intensity is slightly higher. However, NCS05Red has a different pre-edge shape (lower peak around  $\text{EI} = 7114.5\text{ eV}$  and higher peaks around  $7112.5\text{ eV}$ ) and a more intense main-edge ( $\text{IE} > 7116\text{ eV}$ ).



The best linear combination (LC), corresponding to  $Med \simeq LC = 0.787Ox + 0.192Red$ , is plotted at the bottom right of Figure 5.9. This spectrum is very close to the NCS05Med spectrum. The difference spectrum (bottom left of Figure 5.9), corresponding to  $Resi = Med - LC$ , does not show any difference higher than 2% of the NCS05Med intensity in the ROI range. However, the main-edge is at higher energy in the LC spectrum (red colors values around  $EI = 7120$  eV) and the area between the pre-edge and the main-edge (blue values around  $EI = 7117$  eV) is overestimated (this last point will be discussed in the last Section 5.4 of this chapter).

The small differences obtained for three glasses of the same composition with different redox, confirm the observation of optical spectra suggesting some evolution of iron environment with redox. In particular the sum of coefficient (0.979) is almost equal to 1 (ideal case) but this disparity suggest a change of the iron partition between different sites that do not have the same X-ray molar absorption coefficient.

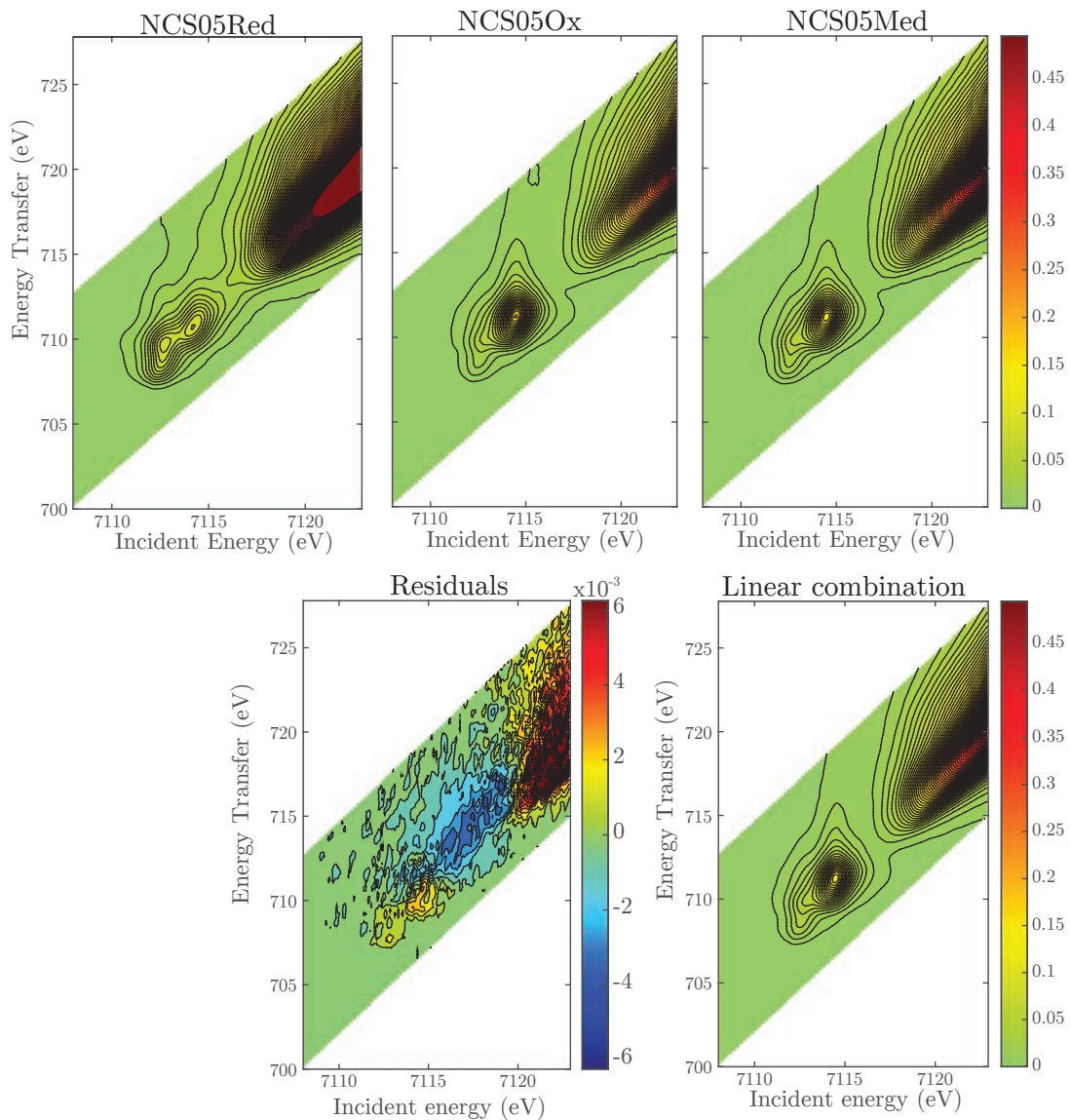


**Figure 5.9** – Top: Fe  $K\alpha$  RIXS pre-edge spectra of three NCS05 glasses (Ox, Red, Med). Bottom-right: best linear combination of Ox and Red to reproduce the Med spectrum ( $LC = 0.787Ox + 0.192Red$ ), Bottom-left: difference between LC and Med spectra ( $Resi = LC - Med$ ).

### 5.2.5 Evidence of $\text{Fe}^{2+}$ spin-forbidden bands in reduced glass

The spectrum of NCS05Red does not show any trace of the  $\text{Fe}^{3+}$  band around  $26\,300\text{ cm}^{-1}$ . Even after removing the UV edge (see Appendix B.4.1), no “ $d-d$ ” transitions are discernible in the spectrum. The absence of  $\text{Fe}^{3+}$  bands confirms the high  $\text{Fe}^{2+}/\text{Fe}_{\text{tot}}$  ratio ( $R = 99\%$ ). In the spectral region of interest for  $\text{Fe}^{3+}$ , i.e. from  $18\,000$  to  $28\,000\text{ cm}^{-1}$ , the background is slightly higher than in NCS05Ox and two weak bands are visible around  $21\,500\text{ cm}^{-1}$  and  $23\,400\text{ cm}^{-1}$ . By using the extracted absorbance of  $\text{Fe}^{2+}$  (See Appendix B.4.2), it appears in Figure 5.10 that a third band is also visible around  $25\,200\text{ cm}^{-1}$ .

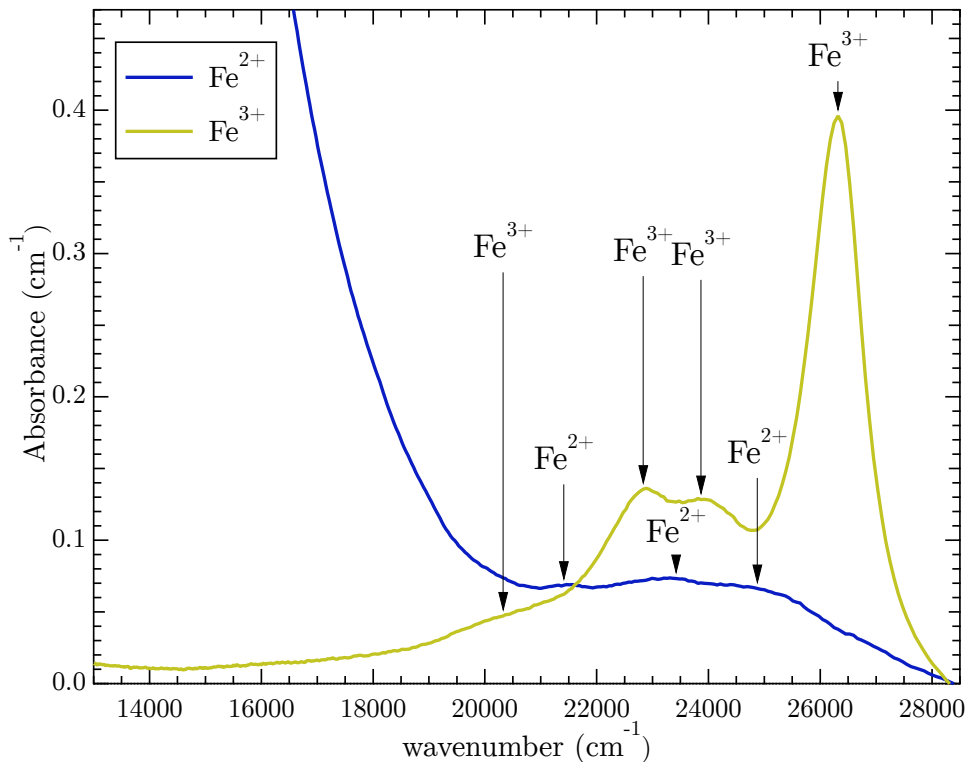


**Figure 5.10** – Estimated signals for 100% of  $\text{Fe}^{2+}$  and 100% of  $\text{Fe}^{3+}$  in NCS05 glasses.

The position of these three weak bands are different from the expected values of  $\text{Fe}^{3+}$  and their intensities are higher than expected intensities for residual  $\text{Fe}^{3+}$  regarding the estimated concentration ( $\sim 50\text{ ppm}$ ). Since, they can not be ascribable to residual  $\text{Fe}^{3+}$ , they can be assigned to the  $\text{Fe}^{2+}$  spin-forbidden transitions  ${}^5T_2(D) \rightarrow {}^3T_1(H)$  and  ${}^5T_2(D) \rightarrow {}^3T_2(H)$  as suggested in  $\text{Fe}^{2+}(\text{H}_2\text{O})_6$  [Burns, 1993] and in a sodium-alkaline earth silicate glass [Glebov et al., 1998]. Grandidierite ( ${}^{[5]}\text{Fe}^{2+}$ ) shows similar weak features from  $20\,000$  to  $25\,000\text{ cm}^{-1}$  Rossman [2014] and Schmetzner et al. [2003]. Our measurements suggest that the background of the optical spectra of reduced silicate glasses containing iron is constituted by a succession of poorly resolved bands with low intensities related to  $\text{Fe}^{2+}$  spin-forbidden transitions accordingly to Tanabe-Sugano diagrams. This band superposition could lead to overestimate the background if the minimum of the spectrum around  $18\,000\text{ cm}^{-1}$  is considered as the background value.

## 5.3 Structure–spectroscopy analysis of Fe<sup>3+</sup>

### 5.3.1 Study of the OMCT bands in the UV range

The UV range\* of optical spectra is commonly dominated by electron transitions from  $2p$ -orbitals of oxygen ligands to metal  $3d$ -orbitals (OMCT) in complexes, minerals or glasses [Burns, 1993]. These Laporte-allowed OMCT bands are 3 orders of magnitude more intense than the weak spin-forbidden  $d-d$  transitions of Fe<sup>3+</sup> (see Table 3.3 p.61). However, they are not widely studied because their intensities often saturate the detectors, bands are very broad and all transition metals have OMCT bands in the UV range leading to overlapping intense signals from impurities.

Concerning iron in soda-silicate glasses, Steele and Douglas [1965] and Sigel and Ginther [1968] showed that both Fe<sup>2+</sup> and Fe<sup>3+</sup> have OMCT bands centered at 47 000 cm<sup>-1</sup> (210 nm) and 42 000 cm<sup>-1</sup> (225–230 nm), respectively. The molar absorption coefficient of Fe<sup>3+</sup>-OMCT ( $\epsilon \sim 7000 \text{ L}\cdot\text{mol}^{-1}\cdot\text{cm}^{-1}$ ) is 2.5 to 6 times higher than Fe<sup>2+</sup>-OMCT. Therefore, Fe<sup>3+</sup> OMCT bands have a dominant effect in the visible range. Ehrt [2002]

Due to their high extinction coefficients, very thin samples ( $\sim 100 \mu\text{m}$ ) with low-doping are needed to resolve the signals. For this reason, two thin sodium-calcium-silicate (NCS) glasses with 0.1 wt% of Fe<sub>2</sub>O<sub>3</sub> were studied:

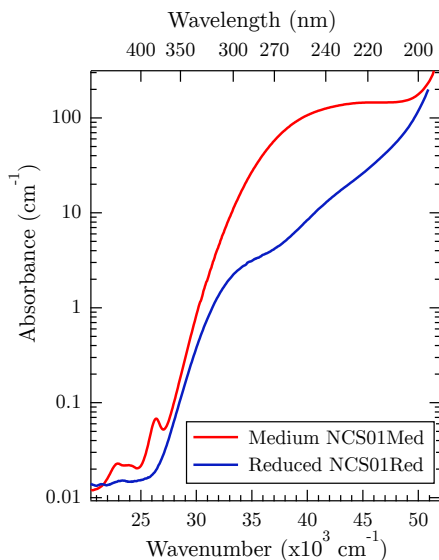
- NCS01Med, with redox  $R \sim 28\%$ , 100  $\mu\text{m}$ -thick
- NCS01Red, with redox  $R \sim 99\%$ , 100  $\mu\text{m}$ -thick

Since that absorbance is extended over several orders of magnitude, logarithmic scale for the y-axis can be useful to emphasize the absorption bands with a low extinction coefficient. According to Beer-Lambert law (Equation 2.3), the absorbance is proportional to concentration. Thus, a vertical translation without any modification of the shape of the absorption band represents a change in the concentration of the absorbing species without any environmental modification.

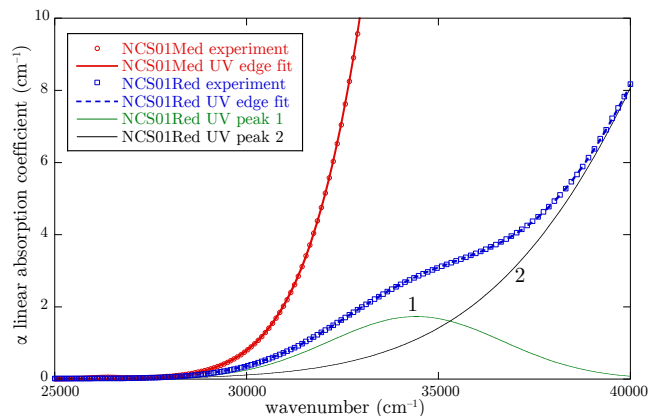
Figure 5.11 in logarithmic scale, shows for the medium glass NCS01Med (in red), the remaining  $d-d$  transitions of Fe<sup>3+</sup> overlapped by the tail of a broad Fe<sup>3+</sup>-OMCT band in the UV, around 42 000 cm<sup>-1</sup>. On the other hand, the NCS01Red spectrum (in blue) probably results from an overlapping of several Fe<sup>2+</sup>- and Fe<sup>3+</sup>-OMCT bands at 34 000, 42 000, maybe 47 000 and over 52 000 cm<sup>-1</sup>, contrasting with NCS01Med showing a wide band at 43 000 cm<sup>-1</sup> and an edge above 52 000 cm<sup>-1</sup>. This suggests that orbitals of iron and its neighboring oxygens have different overlappings due, for example, to the evolution of valence state, Fe–O distances or site geometries.

Figure 5.12 shows that the UV-edge of NCS01Med (in red) is at lower energy than for NCS01Red (in blue). After fitting the reduced glass with two Gaussian curves, it appears that the band #2 attributed to Fe<sup>2+</sup> → O charge transfer has a lower intensity than Fe<sup>3+</sup>-OMCT. This conclusion agrees with Steele and Douglas [1965] and Sigel and Ginther [1968] observations saying that Fe<sup>2+</sup>-OMCT is at higher energy (210nm) with a lower molar absorption coefficient (2.5 to 6 times lower than Fe<sup>3+</sup>-OMCT).

\*28 000~50 000 cm<sup>-1</sup>; 3.5~6.2 eV; 360~200 nm



**Figure 5.11** – logarithmic representation of the optical absorption spectra for the “air” and reduced soda-lime silicate glasses.



**Figure 5.12** – UV-edge fitting of the optical absorption spectra for the “air” and reduced soda-lime silicate glasses.

The band #1 at  $34\,000\text{ cm}^{-1}$  in NCS01Red can be attributed to remaining  $\text{Fe}^{3+} \rightarrow \text{O}$  charge transfer that confirms the high redox of reduced glasses close to 100%  $\text{Fe}^{2+}$ . However, its shape and position differ from observation of medium glasses, suggesting that the remaining  $\text{Fe}^{3+}$  are in a different environment than the “common” or “average”  $\text{Fe}^{3+}$  observed in medium glasses which have the same spectral shape than fully oxidized glasses (not shown in Figure 5.11).

### 5.3.2 Evidence of [5]-fold ferric iron ( $^{[5]}\text{Fe}^{3+}$ ) in glasses

The existence of [5]-fold coordinated  $\text{Fe}^{3+}$  in glasses has been suggested by X-ray absorption spectroscopy, neutron diffraction and numerical simulation studies [Farges et al., 2004; Guillot and Sator, 2007; Jackson et al., 2005; Weigel et al., 2008a], although, their influence on optical absorption spectra in iron-doped glasses is still speculative.

Spin-forbidden transitions of  $\text{Fe}^{3+}$  lead to weaker but more numerous bands than  $\text{Fe}^{2+}$  [Bingham et al., 2007]. As explained in Section 1.3,  $\text{Fe}^{3+}$  is mainly in [4]-fold tetrahedral site but the average coordination number\* ([4.6]–[5.0]) suggests the presence of [5]- or [6]-fold coordination. Iron in non-centrosymmetric geometries (such as [5]-fold or distorted [6]-fold) are therefore expected to take part in the optical absorption to a lesser extent.

In silicate glasses, some  $\text{Fe}^{3+}$   $d-d$  bands can happen below  $19\,000\text{ cm}^{-1}$  and be overlapped by  $\text{Fe}^{2+}$  signals, but  $\text{Fe}^{3+}$  transitions are mainly apparent in the range  $19\,000\text{--}28\,000\text{ cm}^{-1}$ . Band attribution was performed by comparison with  $\text{Fe}^{3+}$ -bearing mineral references. Figure 5.13 shows experimental data of NCS05Ox glass and the example of three minerals: ferriorthoclase ( $^{[4]}\text{Fe}^{3+}$ ), yoderite ( $^{[5]}\text{Fe}^{3+}$ ) and andradite ( $^{[6]}\text{Fe}^{3+}$ ) that reflects the variety of signals observed for  $\text{Fe}^{3+}$  in silicates.

\*[4.6] in [Farges et al., 2004] and [5.0] in [Bingham et al., 2014], see also Section 1.3.

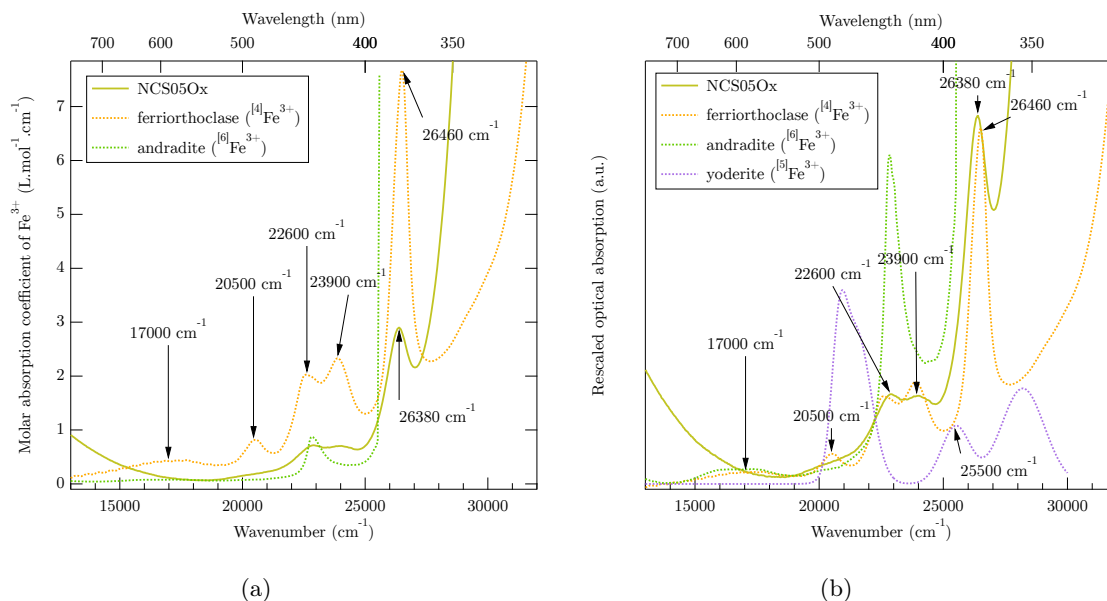


**Figure 5.13** – Optical spectra comparison of an oxidized glass (NCS05Ox) with three Fe<sup>3+</sup> crystalline references: ferriorthoclase ([<sup>4</sup>Fe<sup>3+</sup>]), yoderite ([<sup>5</sup>Fe<sup>3+</sup>]) and andradite ([<sup>6</sup>Fe<sup>3+</sup>]). (a)  $\epsilon_{\text{Fe}^{3+}}$  molar absorption coefficient of Fe<sup>3+</sup> (b) arbitrarily rescaled optical absorption.

Ferriorthoclase and andradite data were measured in transmission mode from natural sample. Yoderite data have been taken from Langer et al. [1982] (molar absorption coefficient was not available). Fe<sup>3+</sup> bands have been fitted to remove the intense Mn<sup>3+</sup> contribution, however, the signals around 21 000 cm<sup>-1</sup> are probably overestimated because of this overlapping of Mn<sup>3+</sup> and Fe<sup>3+</sup>.

Ferriorthoclase and NCS05Ox glass have a similar spectral shape attesting the dominant tetrahedral character usually attributed to Fe<sup>3+</sup> in glasses. For the mineral, the bands are indeed narrower and the signal is lower between each peaks due to site uniformity. On the contrary, the broader bands observed in glass confirm the site distribution and the less defined environment of iron characteristic of amorphous materials. This conclusion is confirmed by the  $\epsilon$  values that are 3 times smaller for glasses than for ferriorthoclase, suggesting that, in addition to site distortion and distribution of tetrahedral geometry, part of Fe<sup>3+</sup> is not in tetrahedral sites but in higher coordinated sites potentially leading to “silent” species.

After a careful subtraction of the UV-edge and an extraction of the Fe<sup>3+</sup> optical signature using linear combinations of several spectra from the same glass composition at different Fe-redox, a fit of Fe<sup>3+</sup> bands has been done between 19 000 and 28 000 cm<sup>-1</sup> (see Appendix B.4 for details on Fe<sup>3+</sup> data processing).

The shapes and positions of the three main Fe<sup>3+</sup> bands, obtained by comparison with Fe<sup>3+</sup>-bearing crystalline references (Table 5.4), were used to fit the Fe<sup>3+</sup> spectrum (Figure 5.14). The bands are near 22 800, 24 000 and 26 300 cm<sup>-1</sup>, however, the residuals (in dashed grey) are not null and present a Gaussian shape. Thus, three additional contributions at around 21 200, 25 500 and 27 200 cm<sup>-1</sup> have to be considered to obtain a good fit.

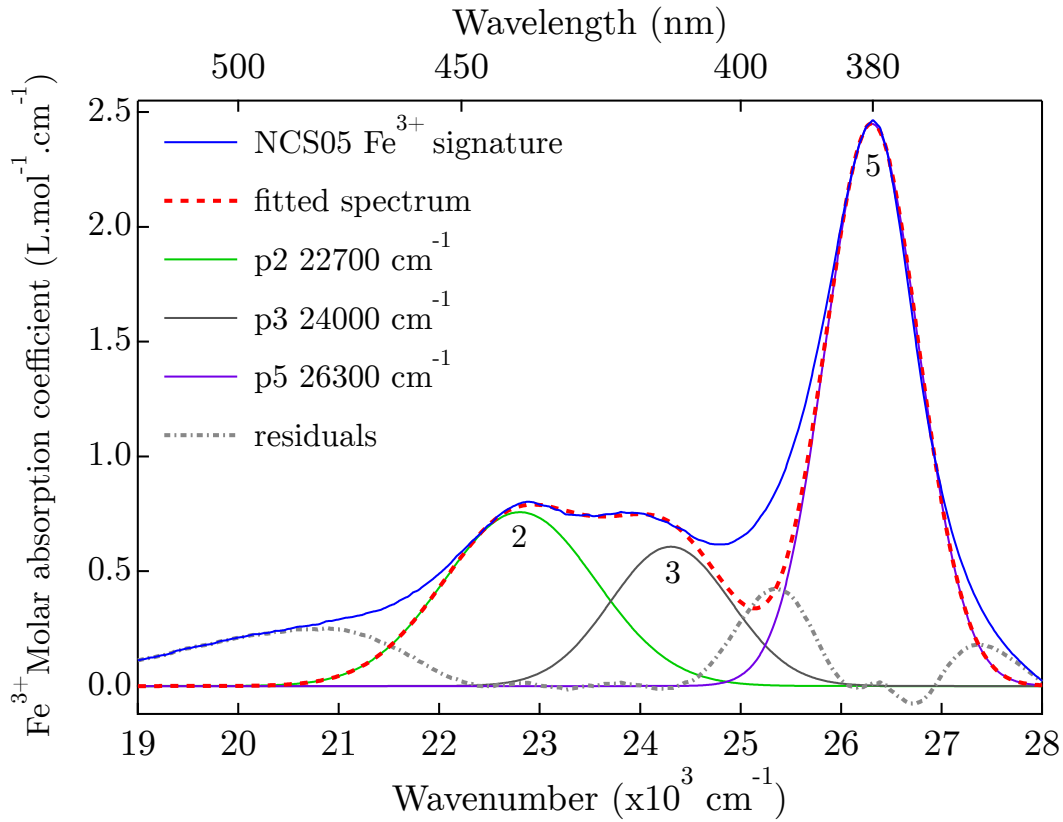


**Figure 5.14** – Molar absorption coefficient of  $\text{Fe}^{3+}$  in the soda-lime oxidized glass (NCS05Ox) after UV-edge removal. Example of  $\text{Fe}^{3+}$  bands fitted with 3 Gaussians.

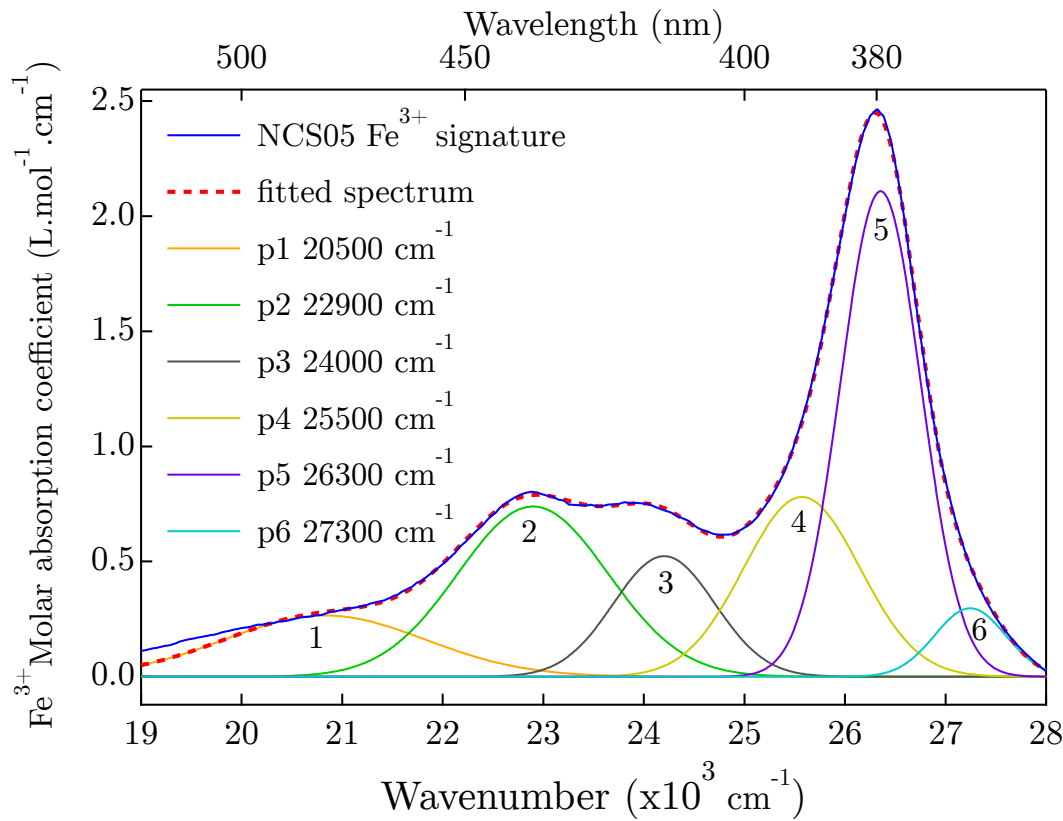


**Figure 5.15** – Molar absorption coefficient of  $\text{Fe}^{3+}$  in the soda-lime oxidized glass (NCS05Ox) after UV-edge removal. Example of  $\text{Fe}^{3+}$  bands fitted with 6 Gaussians.

**Table 5.3** – Fitting parameters and corresponding spin forbidden  $d-d$  transitions attribution for the absorbance peaks of  $\text{Fe}^{3+}$  ions in the NCS05Med glass.

Peak	Position ( $\text{cm}^{-1}$ )	FWHM ( $\text{cm}^{-1}$ )	$\varepsilon_{\text{Fe}^{3+}}$ ( $\text{L.mol}^{-1}.\text{cm}^{-1}$ )	Assignments
p6	$27\,244 \pm 50$	$831 \pm 100$	0.297	$^{[5,6]}\text{Fe}^{3+}$ , $^6A_{1(g)}(S) \rightarrow ^4E_{(g)}(D)$
p5	$26\,353 \pm 10$	$940 \pm 10$	2.109	$^{[4]}\text{Fe}^{3+}$ , $^6A_1(S) \rightarrow ^4E(D)$
p4	$25\,570 \pm 30$	$1359 \pm 75$	0.781	$^{[5]}\text{Fe}^{3+}$ , $^6A_1(S) \rightarrow ^4T_2(D)$
p3	$24\,200 \pm 30$	$1189 \pm 100$	0.524	$^{[4]}\text{Fe}^{3+}$ , $^6A_1(S) \rightarrow ^4T_2(D)$
p2	$22\,896 \pm 40$	$1759 \pm 70$	0.739	$^{[4]}\text{Fe}^{3+}$ , $^6A_1(S) \rightarrow ^4A_1, ^4E(G)$
p1	$20\,826 \pm 200$	$2355 \pm 300$	0.266	$^{[4]}\text{Fe}^{3+}$ , $^6A_1(S) \rightarrow ^4T_2(G)$ $^{[5]}\text{Fe}^{3+}$ , $^6A_1(S) \rightarrow ^4A_1, ^4E(G)$

**Table 5.4** – Spin forbidden  $d-d$  transitions attribution of the absorbance peaks of 3 Fe-bearing minerals with different site symmetry and coordination number (CN). Ferriorthoclase ( $^{[4]}\text{Fe}^{3+}$ ) [Burns, 1993], yoderite\* ( $^{[5]}\text{Fe}^{3+}$ ) [Abu-Eid et al., 1978; Langer et al., 1982] and andradite ( $^{[6]}\text{Fe}^{3+}$ ) [Burns, 1993; Lin, 1981]. The ground state is  $^6A_{1(g)}$ .

Name	CN	Geometry	$^4T_{1(g)}(G)$	$^4T_{2(g)}(G)$	$^4A_{1(g)}, ^4E_{(g)}(G)$	$^4T_{2(g)}(D)$	$^4E_{(g)}(D)$
ferriorthoclase	$^{[4]}\text{Fe}^{3+}$	$T_d$	17000	20000	22600	23800	26460
yoderite	$^{[5]}\text{Fe}^{3+}$	$C_{3v}$			20700 21500	25500	28200
andradite	$^{[6]}\text{Fe}^{3+}$	$C_{3i}(S_6)$	12450	16650	22700 23000	24000	27000

\* Yoderite is a [5]-fold  $\text{Fe}^{3+}$ -bearing mineral with iron in a distorted trigonal bipyramidal site (approximated by a  $C_{3v}$  geometry). The “g” was removed from the name of the energy levels given by Langer et al. [1982], because [5]-fold coordinated site are necessarily non-centrosymmetric.  $\text{Fe}^{3+}$  Band attribution in yoderite was done in literature by analogy with the octahedral geometry. However, Tanabe-Sugano diagrams are different for trigonal geometries and parameters are  $D\mu$  and  $D\nu$  instead of  $10Dq$ , therefore spectroscopic terms should not be the same than for cubic geometries ( $T_d$  or  $O_h$ ).

The adjustment performed with these six Gaussians fits the experimental data (Figure 5.15 and Table 5.3). According to the transitions observed in crystalline references (Table 5.4), the three resolved bands at around 22 800, 24 000 and 26 300  $\text{cm}^{-1}$  are assigned to tetrahedral  $^{[4]}\text{Fe}^{3+}$  [Volotinen et al., 2008]. A weak contribution at around 27 200  $\text{cm}^{-1}$  can hardly be assigned and can be an artifact due to the edge subtraction. The band at around 25500  $\text{cm}^{-1}$ , which has a similar absorbance as the bands at 22 800 and 24 000  $\text{cm}^{-1}$ , is absent from optical spectra of ferriorthoclase ( $^{[4]}\text{Fe}^{3+}$ ) or andradite ( $^{[6]}\text{Fe}^{3+}$ ). Moreover, the important integrated area indicates a non-centrosymmetric site, such as in  $^{[5]}\text{Fe}^{3+}$ , which is consistent with the position and intensity of the  $^6A_1(S) \rightarrow ^4T_2(G)$  transition of  $^{[5]}\text{Fe}^{3+}$  in yoderite (Table 5.4). The correspondence of this band between glass and mineral supports the existence of [5]-fold  $\text{Fe}^{3+}$  in glass.

The weak and broad contribution around 20 500–21 200  $\text{cm}^{-1}$  has been previously assigned to the  ${}^6A_1(S) \rightarrow {}^4T_2(G)$  transition of tetrahedral  $\text{Fe}^{3+}$  [Manning, 1970]. For the glasses under investigation, this band is broader than in ferriorthoclase and no decrease in the absorbance is observed between the local maximums at 20 500  $\text{cm}^{-1}$  and 22 800  $\text{cm}^{-1}$ . This can be explained by the overlapping of absorption bands of higher coordinated  $\text{Fe}^{3+}$ , such as  ${}^{[5]}\text{Fe}^{3+}$ , whose bands at 20 700 and 21 500  $\text{cm}^{-1}$  in yoderite were assigned by Langer et al. [1982] to the transition\*  ${}^6A_1(S) \rightarrow [{}^4A_1, {}^4E(G)]$ . This optical evidence of  ${}^{[5]}\text{Fe}^{3+}$  in glass promotes the idea of a  $\text{Fe}^{3+}$ -site distribution from [4]- to [5]-coordinated sites, as previously shown for  $\text{Fe}^{2+}$  (see Sections 1.3 and 5.2.1).

$\text{Fe}^{3+}$  in octahedral site has been suggested by the study of minerals such as andradite (Table 5.4), which lead to transitions around 10 000–17 000  $\text{cm}^{-1}$ . Therefore, I looked for the two bands observed at 11 200 and 15 600  $\text{cm}^{-1}$  in oxidized soda-lime glass by Hannyoyer et al. [1992] and attributed to crystal field dependent transitions of  ${}^{[6]}\text{Fe}^{3+}$  ( ${}^6A_{1g}(S) \rightarrow {}^4T_{1g}(G)$ ) and  ${}^6A_{1g}(S) \rightarrow {}^4T_{2g}(G)$ . Despite a polynomial fit and a study of the second derivative of the optical spectrum of the oxidized glass (NCS05Ox), there was no significant contribution superimposed to the tail of  $\text{Fe}^{2+}$  absorption band in the range 10 000–17 000  $\text{cm}^{-1}$ . In the range 20 000–26 000  $\text{cm}^{-1}$ , optical absorption bands of [6]-fold  $\text{Fe}^{3+}$  should occur at almost the same positions than [4]- and [5]-fold coordinated  $\text{Fe}^{3+}$ , but they are expected to be less intense due to the centrosymmetric geometry of octahedra. In addition, the presence of  ${}^{[4]}\text{Fe}^{3+}$  and  ${}^{[5]}\text{Fe}^{3+}$  was sufficient to account for the visible transitions in this range, and no evidence of [6]-fold coordinated  $\text{Fe}^{3+}$  has been found in the investigated glasses by EPR or XAS spectroscopies.

### 5.3.3 The contribution of XAS experiments and LFM calculations to the analysis of $\text{Fe}^{3+}$ optical bands

To corroborate these results, the  $K$  pre-edge of the oxidized glass can be compared with the same three mineral references (andradite, yoderite and ferriorthoclase). The normalized HERFD spectra are shown in Figure 5.16.

As for optical spectra (Figure 5.13-a), [4]-fold  $\text{Fe}^{3+}$  in ferriorthoclase is the most intense species in the pre-edge range. Despite a similar shape, NCS05Ox has a lower integrated area. This suggests that non-tetrahedral  $\text{Fe}^{3+}$  species with a lower absorption coefficient also participate to reduce the intensity of this pre-edge.

Regarding the LFM calculations, [4]-fold  $C_{2v}$  (ferriorthoclase) and [5]-fold  $C_{3v}$  (yoderite) give spectroscopic features that are compatible with  $\text{Fe}^{3+}$  signature in glass with both spectroscopies. A decrease of the  $V_{pd}$  parameter in the  ${}^{[4]}\text{Fe}^{3+}$  calculation could explain both OAS and XAS smaller integrated areas. However, smaller  $V_{pd}$  values cannot explain the average coordination number of  $\text{Fe}^{3+}$  in soda-lime glasses  $\sim[4.6]$  (see Section 1.3.2) and a mixture of at least two site geometries should be considered.

---

\*The assignments of this paper is ambiguous, since it use the level symmetry of  $T_d$  and  $O_h$  instead of  $D_{3h}$ , for example there is no  $T_2$  symmetry in  $D_{3h}$  but only  $A'_1$ ,  $A''_1$ ,  $A'_2$ ,  $A''_2$ ,  $E'$  and  $E''$ .



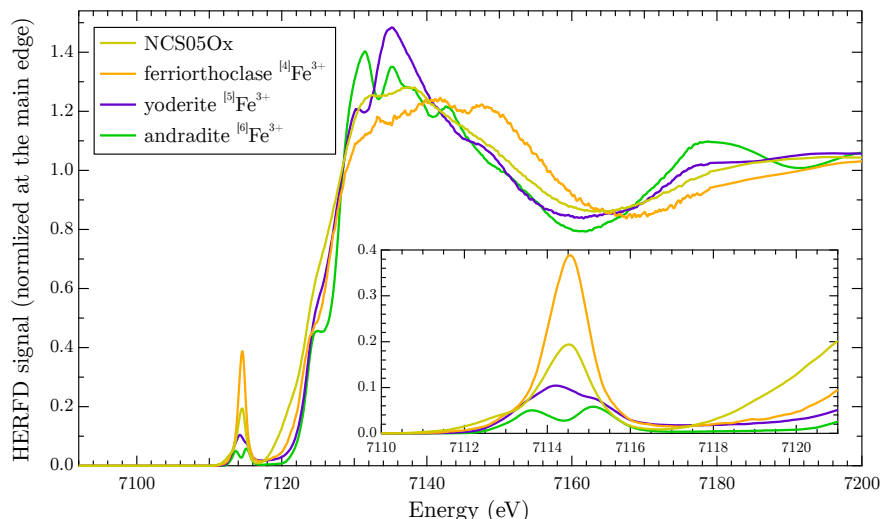


**Figure 5.16** – HERFD spectra for Fe *K* pre-edge spectra of NCS05Ox glass and selected [4]-, [5]-, and [6]-coordinated Fe<sup>3+</sup> model compounds.

With ligand field multiplet calculations it is not easy to consider a distribution of geometries, and only a distribution of calculation parameters can be considered to take into account the amorphous nature of glass. Because the optical absorption peak around  $26\,300\text{ cm}^{-1}$  is relatively well defined, it means that  $\beta$  is not distributed more than  $\pm 1\%$  (see Section 4.5). The broadening of the optical bands, which are less resolved in NCS05Ox glass, can partly be explained by a distribution of  $10Dq$  in a tetrahedral geometry. This supports the fact that [5]-fold Fe<sup>3+</sup> in  $C_{3v}$  should be considered because their optical bands are calculated to be in the same spectral range with compatible intensities. This hypothesis will be further developed in the next chapter by studying the effect on spectroscopic properties of a substitution of Ca by Mg in the glass formula.

### 5.3.4 Study of the impact of redox on Fe<sup>3+</sup> site distortion

As we have seen for ferrous iron in Section 5.2.4, the redox influences the local environment of transition metals. This part uses the selectivity of EPR to focus on the distortion of ferric iron sites.

The X-band EPR spectra of the three NCS05 glasses with different redox (Ox, Med and Red) are shown in Figure 5.17. The general shape of the EPR spectra depends on the redox state of the investigated samples. NCS05Med and Ox glasses give typical EPR signals for a Fe<sup>3+</sup>-bearing glasses with two main lines at 160 mT ( $g = 4.3$ ) and at 340 mT ( $g = 2$ ) characteristic of two kinds of sites: rhombically distorted isolated sites and sites presenting Fe–Fe interactions (see Section 2.6.3 for interpretation elements of X-band EPR glass spectra). However, NCS05Red ( $\sim 50\text{ ppm Fe}^{3+}$ ) gives rise to a peculiar EPR signal (Figure 5.17) with (i) a zero field signal, (ii) a sloping background below 100 mT, (iii) a weak signal at  $g = 8$  (around 80 mT), (iv) appearance of shoulders just before and after the  $g = 4.3$  line (at 130 mT and 170 mT), and (v) a split signal at  $g = 4.3$  (see the inset of the figure). Moreover, two signals are superimposed at  $g = 2$ : a wide signal (marked A) related to clustering of Fe<sup>3+</sup> ions and a sharp one at 350 mT (marked B) related to defects trapped on silicate groups that will not be studied here.

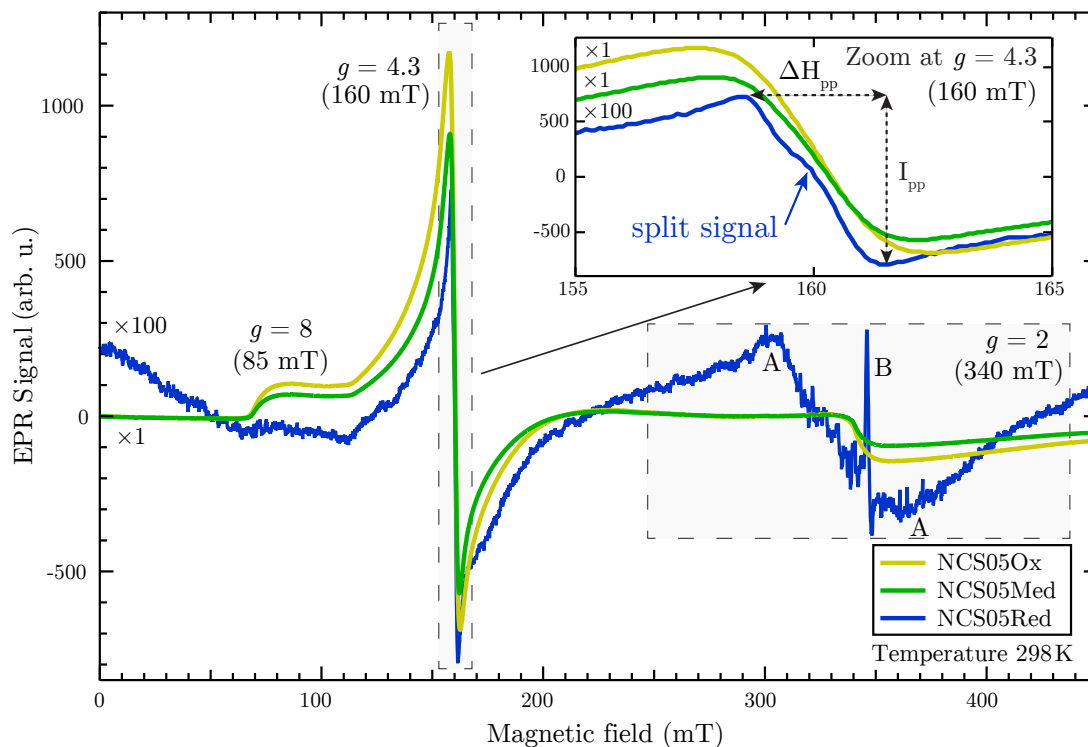


**Figure 5.17** – Room temperature X-band EPR signals of the NCS05 glasses at three different redox: NCS05Ox (yellow/ $R = 6\%$ ), NCS05Med (green,  $R = 28\%$ ) and NCS05Red (blue,  $R = 99\%$ ). The inset zooms on the  $g = 4.3$  line.

Concerning the signal at  $g = 4.3$ , the peak to peak intensity  $I_{pp}$  and peak to peak linewidth  $\Delta H_{pp}$  are both increasing with the oxidation (i.e. lower  $Fe^{2+}/Fe_{tot}$ ). The enhancement of the NCS05Ox intensity is consistent with the increase of  $Fe^{3+}$  concentration, and the enlargement of the  $g = 4.3$  signal of NCS05Ox, which is larger in Ox glasses than Med than Red suggests a lower average distortion of  $Fe^{3+}$  sites in oxidized than reduced glasses. The split of the  $g = 4.3$  signal in the reduced sample is due to the separation of the three EPR Kramer's doublet transitions  $d_{xx}$ ,  $d_{yy}$ ,  $d_{zz}$ , which are not overlapping each other. This splitting, rarely observed in glasses, indicates that the distribution of the isolated rhombic  $Fe^{3+}$  sites is relatively narrow in NCS05Red and does not include sites with a pure rhombic distortion. In contrast, in oxidized samples,  $Fe^{3+}$  ( $> 3500$  ppm) there is no splitting of the  $g = 4.3$  signal, suggesting a broader distribution among sites with different rhombic distortions.

To our knowledge, Q-band EPR spectra have not been investigated in silicate glasses even though higher microwave frequency may help in assessing the rhombic distortion of the  $Fe^{3+}$  site. Q-band (34 GHz) EPR spectra have been investigated for NCS05Med and NCS05Red samples (Figure 5.18). The NCS05Med signal is not constant before and after the  $g = 2$  line, suggesting the presence of a broad signal (dashed line in Figure 5.18) originating from Fe-Fe interactions and overlapping with the isolated  $Fe^{3+}$  signal at  $g = 2$ . The question of Fe-clustering will be discussed in Section 5.4. Regarding the  $g = 4.3$  signal of NCS05Med, there is a weak and split signal.

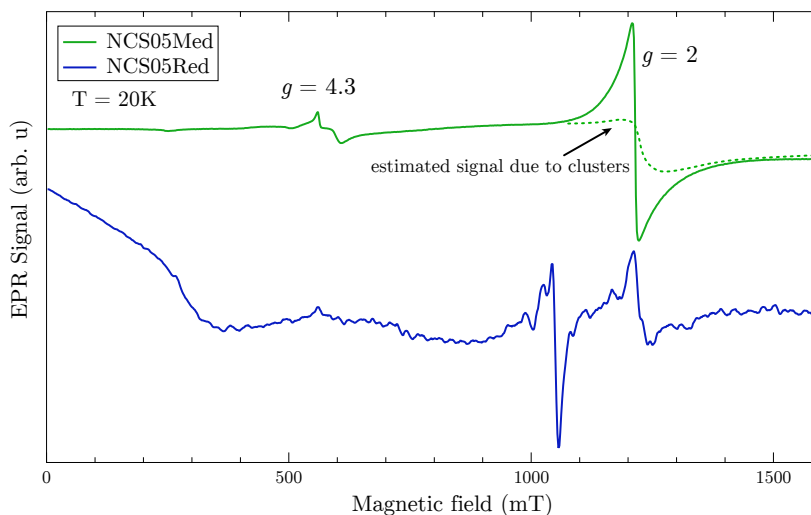


**Figure 5.18** – Low-temperature Q-band EPR signals of NCS05Med (green,  $R = 28\%$ ) and NCS05Red (blue,  $R = 99\%$ ) soda-lime glasses measured at 20 K. The intensities are not normalized. The EPR signal of NCS05Red has been magnified for clarity reasons.

By comparing Q-band to X-band for NCS05Med sample, the intensity proportion between the signals at  $g = 2$  and  $g = 4.3$  are inverted. In Q-band, the dramatic loss of intensity of the  $g = 4.3$  signal is compensated by the presence of a sharp and intense signal at  $g = 2$ . In term of integrated EPR signal of NCS05Med, the  $g = 4.3$  signal participates in less than 10% of the total integrated Q-band signal, while it represents about 60% of the total area in X-band. This change of proportion indicates that rhombic distortions present in the glasses are small relative to the Q-band frequency. As a consequence, the  $g = 2$  signal of isolated paramagnetic species is increased relatively to X-band spectra. The trend of the  $g = 2$  signal to increase at Q-band relatively to X-band, in which the  $g = 4.3$  signal is dominating, agrees with previous observations on borate glasses [Yahiaoui et al., 1994]. However, in our silicate glasses, the lower intensity of the Q-band signal at  $g = 4.3$  relatively to the signal at  $g = 2$  suggests a smaller proportion of rhombically distorted  $\text{Fe}^{3+}$  sites than in the lithium-borate glasses studied by Yahiaoui et al. [1994].

The remaining  $g = 4.3$  weak signal in NCS05Med (Figure 5.18) demonstrates the presence of a small amount of rhombically distorted sites while in the Q-band spectrum of NCS05Red (Figure 5.18), the absence of  $g = 4.3$  signal suggests a less distorted environment for  $\text{Fe}^{3+}$  in the reduced than in the medium sample. The numerous  $\text{Fe}^{3+}$  peaks between 1000 to 1300 mT may be related to a lower site distribution in agreement with the splitting observed at  $g = 4.3$  in X-band (inset of Figures 5.17).

The low-field signal (below 500 mT) is also detected at X-band (see above). The X-band EPR spectrum of NCS05Red at 4 K (Figure 5.21) shows an intense and broad line centered on 60 mT ( $g \sim 13$ ), which follows Curie law ( $I_{\text{pp}}$  is proportional to  $1/T$ ). This signal has been attributed by Montenero et al. [1986] to a ferromagnetic resonance due to traces of metallic Fe. This attribution has to be confirmed but it is at the origin of the zero field signal and the sloping background observed at room temperature X-band EPR (Figure 5.17).

Figure 5.19 summarizes the three conclusions of the above discussion. The average site appears more distorted at X-band for NCS05Red than NCS05Med than NCS05Ox because  $\Delta H_{\text{pp}}$  is smaller. NCS05Med presents sites with a stronger rhombic distortion that generate

a Q-band signal at  $g = 4.3$ , while NCS05Red does not present a  $g = 4.3$  signal. This last point agrees with the lower site distribution deduced from the X-band split  $g = 4.3$  signal of NCS05Red. This confirms that  $\text{Fe}^{3+}$  plays a network former role with a limited distribution of the polarization of the oxygens in polymerized glasses and that only a few sites show a strong rhombic distortion [Calas and Petiau, 1983b, p.46].

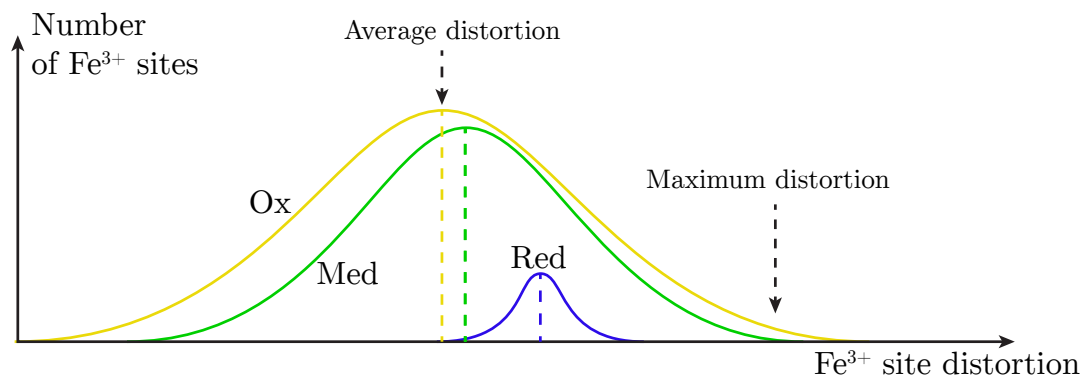


**Figure 5.19** – Schematic vision of the distortion and distribution of  $\text{Fe}^{3+}$  sites in NCS glass depending on the redox.

## 5.4 Site partitioning: isolated vs. clustered iron

### 5.4.1 Introduction

In addition to isolated iron that do not interact with other irons present in the glass. Bingham et al. [1999] have demonstrated, in the case of similar soda-lime-silica glasses that when the  $\text{Fe}_2\text{O}_3$  content is higher than 1 mol%, the fraction of the Fe ions involved in Fe-clusters becomes significant. This clustering causes magnetic or intervalence interactions. Below this concentration, the influence of clustering trends to be negligible. The possible clustering was deduced from changes in the optical spectra of the glasses, interpreted by the authors as due to  $\text{Fe}^{2+}\text{-O-Fe}^{3+}$  and  $\text{Fe}^{3+}\text{-O-Fe}^{3+}$  interactions. Rossano et al. [2000b] confirmed, by EXAFS and MD simulation, the existence of Fe-Fe distances that are characteristic of edge-sharing polyhedra in  $\text{CaFeSi}_2\text{O}_6$  glass. However, they did not find evidence for iron to form aggregates and segregate in small particles in the matrix. The number of clusters was conformed to the random distribution of iron in the glass structure. More recently, using EPSR structural simulations for the same  $\text{CaFeSi}_2\text{O}_6$  glass composition, Weigel et al. [2008b] found that [5]- and [6]-fold  $\text{Fe}^{3+}$  tends to segregate instead of being randomly distributed as a network-former in tetrahedral sites. The duality of iron populations (isolated vs clusterized) was also demonstrated for lower  $\text{Fe}^{3+}$  concentrations by Sakaguchi and Uchino [2007] in alkali alkaline-earth silicate glass system based on a typical float-glass composition, for 0.19 mol% of  $\text{Fe}_2\text{O}_3$ , the authors found clusters of  $\text{Fe}^{3+}$  ions (possibly with  $\text{Fe}^{2+}$  ions). Here we used a combination of X-ray absorption spectroscopy, Electron Paramagnetic Resonance and magnetometry to address the question of iron clustering in soda-lime-silicate glasses containing 0.5 wt% of  $\text{Fe}_2\text{O}_3$ .

### 5.4.2 X-ray absorption spectroscopy (XAS)

We performed X-ray absorption measurements at the Fe  $K$  edge of the three NCS05Red, NCS05Med and NCS05Ox glasses, using two different detection modes, the total fluorescence yield (TFY or classical XANES) and HERFD (or high-resolution XANES) (Figures 5.20). First, with both methods, we observe a shift of the position of the edge among the three samples, which can be attributed to the evolution of the  $\text{Fe}^{2+}/\text{Fe}_{\text{tot}}$  ratio. Second, in the HERFD spectra (Fig. 5.19b) we clearly observe that the reduced glass presents an absorption feature at an intermediate energy between the pre-edge and the main edge, around 7116 eV. This feature is not visible in the case of oxidized glasses. This effect is not clear on the classical XAS measurements (Figure 5.20-a) because the main edge of  $\text{Fe}^{2+}$  is at lower energy in reduced glass than the main edge of  $\text{Fe}^{3+}$  in oxidized glass. However, HERFD spectra of NCS05Ox and Med samples are almost null between the pre-edge and the edge, while the NCS05Red presents a significant broad feature (Figure 5.20-b).

Similar features have been previously observed in hematite, ferrihydrite [Wilke et al., 2001] or on our spectra of maghemite and  $\text{Fe}_3\text{PO}_7$  (see comparison of HERFD spectra in Appendix A). They have been ascribed to delocalized states due to interactions caused by the presence of Fe ion as a second neighbor. I checked with multiplet calculations that no signal is observed above the pre-edge, around 7116 eV. This gives weight to the second-neighbor hypothesis, because the Fe–Fe interactions are not implemented in the mono-atomic calculations performed in the framework of this thesis.

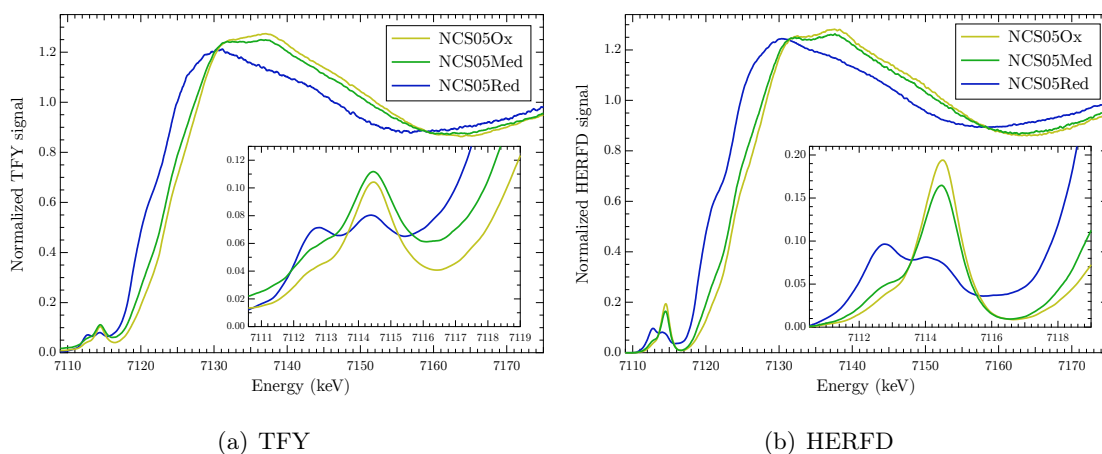


**Figure 5.20** – X-ray absorption spectra of the oxidized (NCS05Ox), the intermediate redox (NCS05Med) and the reduced (NCS05Red) soda-lime-silica glasses using classical XAS (a) and high-resolution XAS (b).

### 5.4.3 Electron paramagnetic resonance (EPR)

In the case of X-band EPR, the low-temperature measurements are used as evidence of the presence of  $\text{Fe}^{3+}$ -containing clusters, which signals are expected to vanish against paramagnetic signal of isolated iron (see EPR interpretation elements in Section 2.6.3). The three same glasses (NCS05Red, NCS05Med and NCS05Ox) measured with X-band EPR at 298 K and presented in Section 5.17, have been studied at helium temperature

(4 K) and are plotted in Figure 5.21. The main alteration of the signal shape is observed for NCS05Red, the  $g = 2$  signal vanished while for both NCS05Med and NCS05Ox, the  $g = 2$  signal keeps the same shape at low temperature but the ratio  $I_{pp}(g = 4.3)/I_{pp}(g = 2)$  is two times higher than at room temperature. These observations confirm a modification of the  $Fe^{3+}$  site repartition as a function of the redox state of the glass. As the intensity of the signal at  $g = 2$  line disappears on the EPR spectra of NCS05Red when temperature is lowered to 4 K, this signal is assigned to the presence of  $Fe^{3+}$ -clusters, with  $Fe^{3+}-Fe^{3+}$  and/or  $Fe^{3+}-Fe^{2+}$  magnetic coupling that becomes insignificant in comparison with the increase of the at  $g = 4.3$  paramagnetic signal from iron in isolated sites [Sakaguchi and Uchino, 2007], [Kurkjian and Sigety, 1968], [Bogomolova and Henner, 1980], [Montenero et al., 1986], [Dunaeva et al., 2012], [Berger et al., 1995], [Yahiaoui et al., 1994], [Reid et al., 1968], [Bart et al., 1982], [Ardelean et al., 1997, 2003].

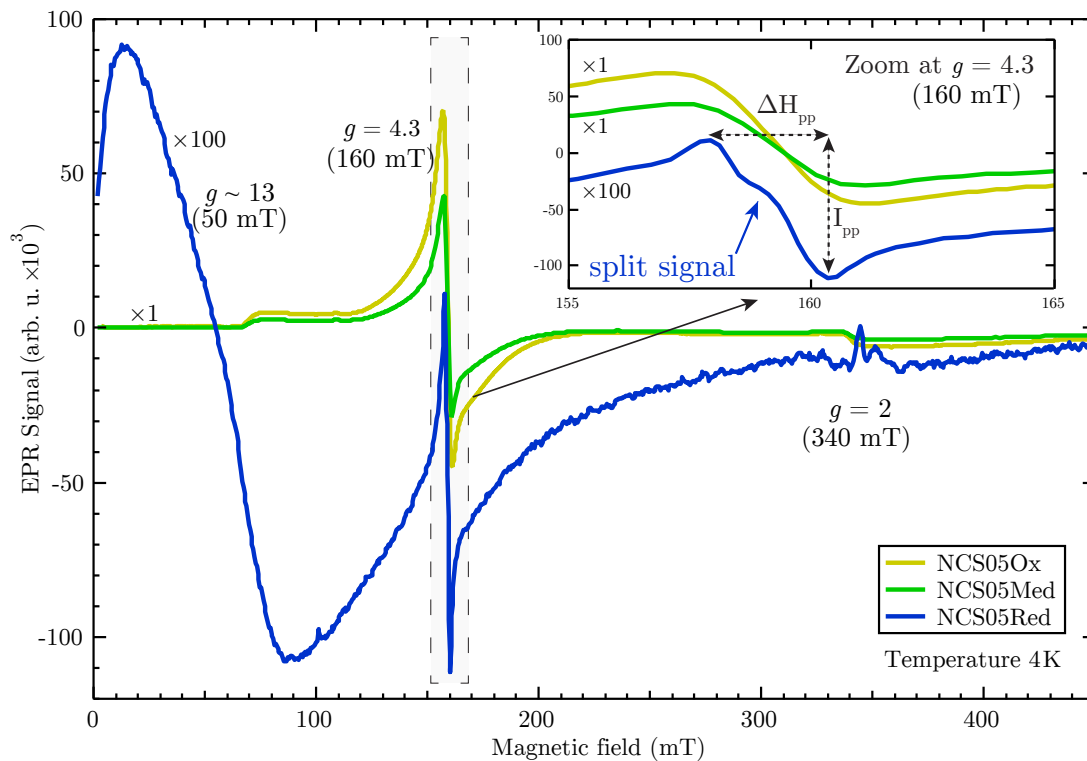


**Figure 5.21** – Low-temperature X-band EPR signals of the NCS05 glasses at three different redox: NCS05Ox (yellow/ $R = 6\%$ ), NCS05Med (green,  $R = 28\%$ ) and NCS05Red (blue,  $R = 99\%$ ). The inset is a zoom on the  $g = 4.3$  line.

In the case of X-band EPR at 298 K shown on 5.17. Clustering effects may be evaluated by the ratio between the intensity of the transitions linked to isolated and clustered  $Fe^{3+}$  at  $g = 4.3$  and  $g = 2$ , respectively. The values for the three glasses are: Med =  $14.9 \pm 0.7$ , Ox =  $12.4 \pm 0.6$  and Red =  $2.7 \pm 1.1$ . The reduced samples have the lowest  $I_{pp}(g = 4.3)/I_{pp}(g = 2)$  ratio, suggesting that they contain a higher proportion of  $Fe^{3+}$  involved in clusters than more oxidized samples (Med and Ox). This interpretation is corroborated by the antiferromagnetic origin of the  $g = 2$  signal in reduced samples (disparition of the  $g = 2$  signal in Figure 5.21). The  $g = 2$  line (marked A in Figure 5.17) is wider in NCS05Red ( $\Delta H_{pp} \sim 60$  mT) than in NCS05Med and NCS05Ox ( $\Delta H_{pp} \sim 25$  mT). According to previous articles studying the effect of total Fe-content in sodium-silicate glasses, the

reduced samples investigated here have a  $g = 2$  signal shape similar to the one observed at higher iron content ( $[\text{Fe}_2\text{O}_3] > 1 \text{ mol}\%$ ) [Dunaeva et al., 2012], [Rüssel, 1993]. In these high Fe-glasses,  $\text{Fe}^{3+}$ -rich clusters have been shown by optical absorption and Mössbauer spectroscopic properties [Bingham et al., 1999] and confirmed by neutron diffraction and numerical simulations [Weigel et al., 2008b].

#### 5.4.4 SQUID magnetometry

The information on Fe–Fe interactions gained by SQUID magnetometry complements that of EPR. Indeed, both  $\text{Fe}^{2+}$  and  $\text{Fe}^{3+}$  contribute to the bulk magnetization. Moreover, the dynamics of magnetization is probed at a different timescale ( $> \text{s}$  for SQUID, as compared to  $10^{-8} \text{ s}$  with EPR). Two glasses, NMS05Ox and NMS05Red, containing magnesium instead of calcium are presented, but we will see in the next chapter that the effect of the alkaline earth nature is negligible compared to the effect of the redox state.

The magnetic susceptibility  $\chi(T)$  can be extracted (Figure 5.22-a) from both measurement protocols presented in Section 2.5.2. Thus, a value of the Curie constant  $C$  and the effective magnetic moment  $\mu_{\text{eff}}$  can be deduced with Equation C.3 (Figure 5.22-b). In the case of NMS05Red, the effective moment is  $5.36 \mu_B/\text{at}$ , for NMS05Ox the measure gives  $5.95 \mu_B/\text{at}$ . These values are close to the expected free spin value:  $5.4 \mu_B/\text{at}$  for  $\text{Fe}^{2+}$  and  $5.9 \mu_B/\text{at}$  for  $\text{Fe}^{3+}$  [Kittel, 2004]. Therefore, within our approximations, there is no evidence for a giant effective moment, which would characterize a superparamagnetic behavior due to isolated, non-interacting, nanoparticles as in ferritine [Kilcoyne and Cywinski, 1995].

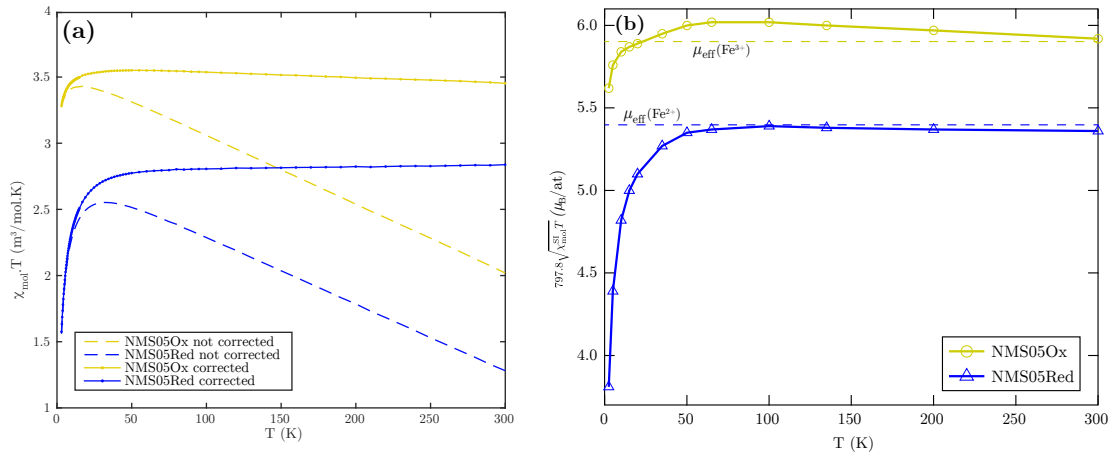


**Figure 5.22** – (a)  $\chi \cdot T \simeq C$  Curie constant obtained from  $M$  vs  $T$ , measured at low field (10 mT). (b) values of  $\chi$  obtained from  $M$  vs.  $H$  measured at low field and plotted as  $797.8 \sqrt{\chi_{\text{mol}}^{\text{SI}} T}$  in order to compare it with the theoretical value  $\mu_{\text{eff}}$  of free  $\text{Fe}^{2+}$  and  $\text{Fe}^{3+}$  (dashed lines).

In the case of NMS05Red, the fit of the magnetic susceptibility with a Curie-Weiss law (see p. 46) gives  $\theta = -2 \text{ K}$ . This Curie-Weiss temperature is very small (dimers, trimers or no more than few atoms) in absolute value and negative, suggesting very weak antiferromagnetic interactions between iron ions and confirm the preponderant paramagnetic behavior. On the other hand, the fit with a Curie-Weiss law of the NMS05Ox gives a null temperature confirming Curie law behavior and the paramagnetic nature of the oxidized glasses. However, for both samples, deviations are observed from the paramagnetic behavior,



below 10 K for NMS05Ox and below 35 K for NMS05Red, confirming stronger, but still weak, interactions in the reduced glass than in its more oxidized counterpart.

A similar conclusion is deduced from the magnetization curves. As shown for NMS05Ox in Figure 5.23-a, the magnetization curves obtained at different temperatures overlap in a graph representing  $M$  vs  $H/T$  down to 10 K. Above 10 K, the magnetization curves agrees with the Brillouin functions of  $\text{Fe}^{3+}$  free-spin within 7%. The small deviation from Brillouin function below 10 K agrees with the susceptibility measurements and suggests a small departure from a paramagnetic behavior. On the other hand, the NMS05Red shown in Figure 5.23-b fits the expected Brillouin function of  $\text{Fe}^{2+}$  from 300 to 35 K (also 7% more intense). However, below 35 K, the magnetization curves fall clearly below the Brillouin curve for  $\text{Fe}^{2+}$  (spin only), strongly than for NMS05Ox (40% instead of 8%), confirming the deviation from the Curie law observed from susceptibility measurements, and suggesting weak but consistent antiferromagnetic interactions in the material.

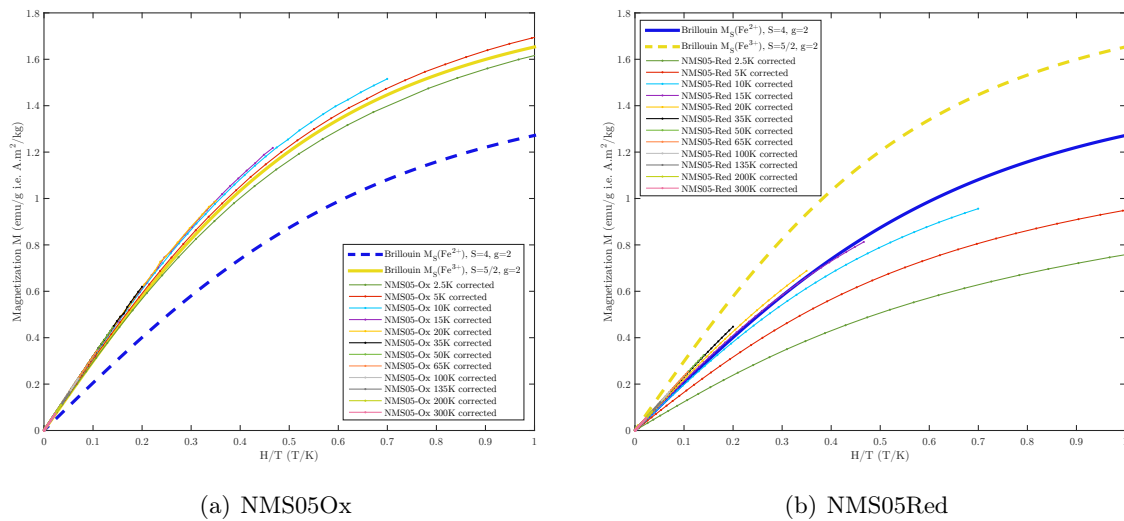


**Figure 5.23** – Magnetization of NMS05Ox and NMS05Red as a function of  $H/T$  compared to the Brillouin function of  $\text{Fe}^{2+}$  and  $\text{Fe}^{3+}$  free spin.

SQUID AC measurements performed at 10 Hz, 100 Hz and 1000 Hz on NMS05Ox and NMS05Red showed null imaginary component  $\chi'' = 0$  and the real component  $\chi$  were equivalent to the DC susceptibility. Therefore, if any, clusters are very small and are only visible with the high frequency of EPR (9.5 GHz).

#### 5.4.5 Conclusions

With the present study, several arguments point out that there are no large Fe-clusters (such as in ferritin with about 1000 Fe atoms) but that there is still some Fe–Fe antiferromagnetic interactions in iron-doped soda-lime silicate glasses with a preponderant effect in reduced samples, in which residual  $\text{Fe}^{3+}$  tends to be in the vicinity of other irons and interact with them leading to similar EPR signatures than in concentrated glasses. However, SQUID measurements did not show evidence of Fe nanoparticles with collective magnetic effect such as superparamagnetism.



In minerals, clusters involve  ${}^{[6]}\text{Fe}^{3+}$  cations preferably to  ${}^{[4]}\text{Fe}^{3+}$  [Burns, 1993]. By analogy, iron clusters in glasses would be favored by  $\text{Fe}^{3+}$  located in [5]-fold or [6]-fold coordinated sites: this could suggest that reduced glasses contain a higher proportion of  ${}^{[5]}\text{Fe}^{3+}$  and/or  ${}^{[6]}\text{Fe}^{3+}$  than the corresponding oxidized glasses. Indeed, the linkage between tetrahedral cation sites is energetically unfavored, as predicted by the Lowenstein exclusion rule [Delaye et al., 2001] leading to the formation of oxygen triclusters.

In conclusion, even if very small Fe-clusters exist in diluted glasses with a preponderance in reduced glasses, their presence have little impact on the optical properties.

## Chapter 6

# Influence of chemical composition on iron local environment in glasses

In the previous chapter, local environments of  $\text{Fe}^{2+}$  and  $\text{Fe}^{3+}$  have been studied in the NCS05 glass as a function of redox state. This chapter presents the results for two kinds of chemical composition variation of the matrix, using the same iron content (0.5 wt%). First, a comparison of NCS with DIO glass, an alkali-free glass of the diopside composition, is presented to study the impact of the presence or absence of sodium. Second, a comparison of NCS with NMS glass, in which the Ca has been substituted by Mg, is done to study the fine effect of the alkaline-earth nature on spectroscopic properties.

### 6.1 Absence of sodium, what are the effects?

To study the effect of sodium, we looked at an alkali-free glass based on diopside mineral ( $\text{CaMgSi}_2\text{O}_6$ ) with the composition:  $50\text{SiO}_2\text{-}25\text{CaO-}25\text{MgO}$ . This composition is one of the few simple alkali-free compositions of the  $\text{SiO}_2\text{-CaO-MgO}$  system that do not crystallize. Thus, the matrix considerably differs between the soda-lime (NCS:  $74\text{SiO}_2\text{-}10\text{CaO-}16\text{Na}_2\text{O}$ ) and alkali-free (DIO:  $50\text{SiO}_2\text{-}25\text{CaO-}25\text{MgO}$ ) glasses, implying a higher melting temperature due to the absence of alkali and a lower viscosity of diopside glass due to the inferior  $\text{SiO}_2$  content [Richet et al., 2006]. This diopside glass easily devitrify and it was therefore impossible to synthesized the DIO05Ox. Concerning, the reduced glasses, the use of a Pt crucible instead of graphite crucible leads to a less reduced DIO05Red ( $R = 80\%$ ) compared to the 99% of NCS05Red. In addition, at the end of the glass synthesis under air atmosphere, the  $\text{Fe}^{2+}/\text{Fe}_{\text{tot}}$  ratio is  $R = 28\%$  for NCS05Med and  $R = 46\%$  for DIO05Med. Despite these differences, this section details new results and interpretations of the iron environment for both  $\text{Fe}^{2+}$  and  $\text{Fe}^{3+}$  thanks to the comparison of the two glass compositions.

#### 6.1.1 Effects on $\text{Fe}^{3+}$ : DIO vs NCS

The extraction of  $\text{Fe}^{3+}$  optical signatures was challenging because the UV-edge of diopside glass overlaps the  $\text{Fe}^{3+}$  bands and is present at lower energy than in soda-lime glass. Figure 6.1 shows the extracted molar absorption coefficient of  $\text{Fe}^{3+}$ , relatively to the

$\text{Fe}^{3+}$  concentration deduced from wet chemical redox measurements, and after UV-edge subtraction (detailed in Appendix B.4.1).

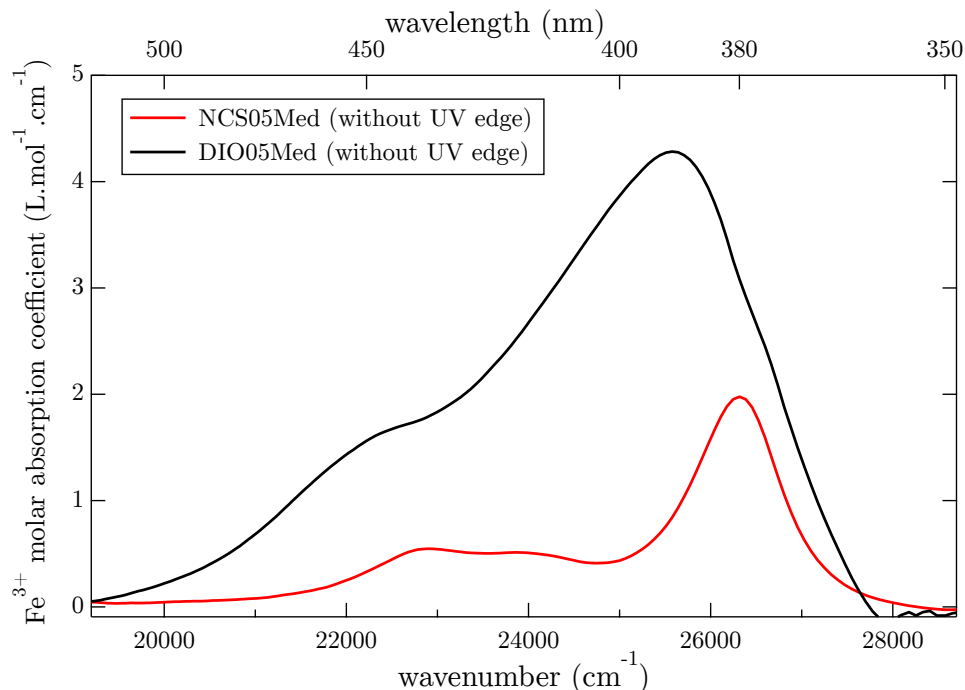


**Figure 6.1** – molar absorption coefficient of  $\text{Fe}^{3+}$  ( $\epsilon_{\text{Fe}^{3+}}$ ) in NCS05Med and DIO05Med after UV-edge subtraction.

The  $\text{Fe}^{3+}$  signals in alkali-free glass are now clearly visible and can be compared with the soda-lime glass. For DIO05Med, the main peak is at  $25\,500\text{ cm}^{-1}$  and there is a shoulder around  $22\,000\text{ cm}^{-1}$ . While in NCS05Med the main peaks are at  $22\,800$ ,  $24\,000$  and  $26\,300\text{ cm}^{-1}$ . Moreover, the spectral shape of DIO05Med is characterized by broader and more intense peaks than in the soda-lime glass. Compared to NCS05Med, for which the  $\text{Fe}^{3+}$  optical signatures have similarities with the tetrahedral  $[\text{Fe}^{3+}]_4$  sites of ferriorthoclase, the  $\text{Fe}^{3+}$  signatures of DIO05Med look more like the  $[\text{Fe}^{3+}]_5$  signals of yoderite with a main signal at  $25\,500\text{ cm}^{-1}$  and weaker bands around  $20\,700$ – $21\,500\text{ cm}^{-1}$ . Regarding calculation results of Chapter 4 about  $\text{Fe}^{3+}$  in  $C_{3v}$  (see Section 4.7) optical spectrum of DIO agrees with a distribution of  $\text{Fe}^{3+}$  among a variety of strongly distorted sites leading to these intense optical transitions. The similarity with yoderite agrees with the average  $\text{Fe}^{3+}$  coordination number of diopside glass estimated by Lefrère [2002] to be around [5]. However, the average coordination is always complicated to define if the value only comes from a pure [5]-fold mixture, from an equal mixture of [4]- and [6]-fold, or from a mixture of [4]-, [5]- and [6]-fold with the possible presence of different site symmetry for each coordination number.

In the previous chapter, EPR has been proven to be a useful tool to complement the analysis of  $\text{Fe}^{3+}$  sites. Figure 6.2 shows the comparison of X-band normalized EPR spectra of NCS05Med and DIO05Med. The different EPR signatures between the two glasses reflect the disparities observed with the optical spectra. The linewidth of the signal at  $g = 4.3$  (around  $160\text{ mT}$ ) is  $\Delta H_{\text{pp}} \sim 40\text{ mT}$  for both samples. However,  $I_{\text{pp}}$  is more intense and the peak is globally narrower for the signal of diopside sample, which is compatible with a greater distortion of  $\text{Fe}^{3+}$  environment than in soda-lime glass. Furthermore, there is almost

no  $g = 2$  signal around 340 mT suggesting the absence of Fe–Fe interactions in DIO05 glass as previously observed by Sakaguchi and Uchino [2007] who found no Fe-clustering in another alkali-free glass (MgO–Al<sub>2</sub>O<sub>3</sub>–SiO<sub>2</sub> system).

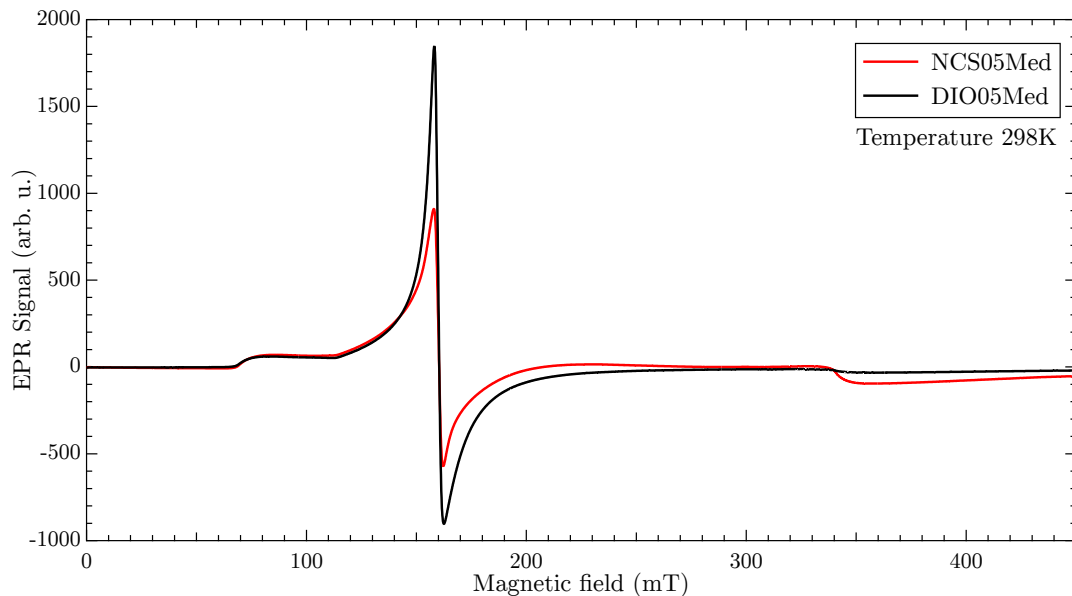


**Figure 6.2** – X-band EPR spectra of NCS05Med and DIO05Med measured at room temperature.

The analysis of X-ray absorption data could help to extract information on the local environment of iron. Figure 6.3 compares the HERFD spectra of NCS05Med and DIO05Med. The main edge is at lower energy for DIO, and the pre-edge has a similar shape than the soda-lime glass with a lower intensity of the tetrahedral Fe<sup>3+</sup> peak at 7114.5 eV.

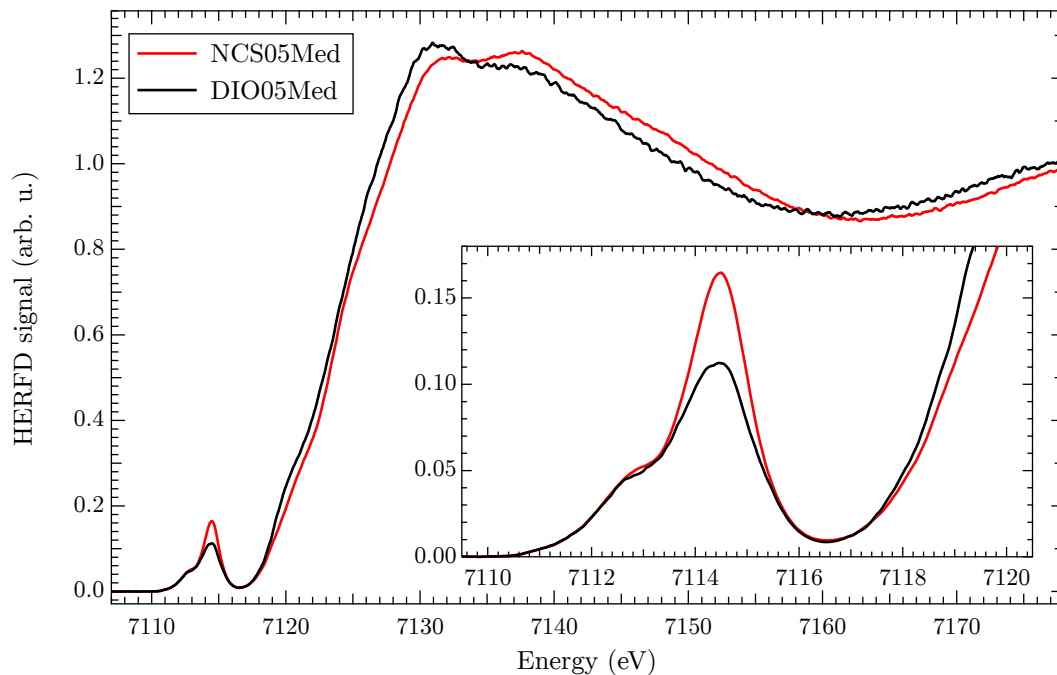


**Figure 6.3** – HERFD spectra at Fe  $K$  edge of NCS05Med and DIO05Med.

The comparison of RIXS maps of NCS05Red and DIO05Med glasses (Figure 6.4), complement the HERFD spectra, which are only diagonal cuts of the RIXS maps. NCS05Med

and DIO05Med have similar appearance, except that the maximal intensity of the pre-edge ( $IE = 7114.5$  eV and  $ET = 711$  eV) is higher for the soda-lime glass. For both compositions the signal between the edge and pre-edge is almost null, which comfort the idea of the absence of significant Fe-clustering in medium glasses for both compositions.

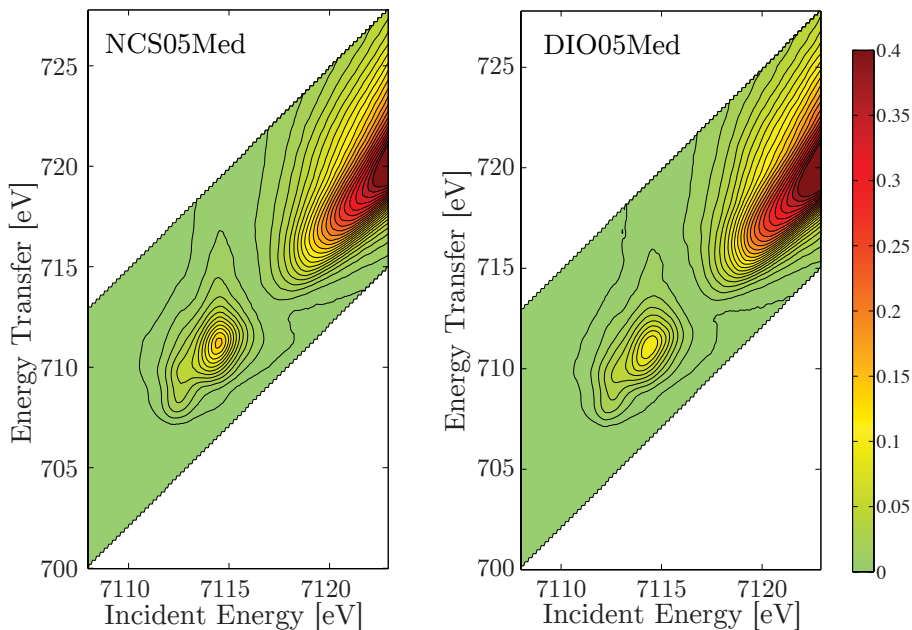


**Figure 6.4** – Fe  $K\alpha$  RIXS spectra of NCS05Med (left) and DIO05Med (right).

These results mainly confirm the wet chemical measurements of the  $Fe^{2+}/Fe_{tot}$  ratio ( $R = 46\%$  for DIO vs.  $R = 28$  for NCS). However, they are also compatible with a higher proportion of tetrahedral sites than suggested by optical spectroscopy. A further study using more glasses with different redox could be useful to extract the signature of  $Fe^{2+}$  and  $Fe^{3+}$  that are mixed in the pre-edge in order to get more structural information by comparing DIO and NCS of the similar redox state.

### 6.1.2 Effects on $Fe^{2+}$ : DIO vs. NCS

By contrast with  $Fe^{3+}$  environment in diopside glass, which have not been previously studied using optical spectroscopy, the study of  $Fe^{2+}$  spectroscopic properties is easier because it does not require a processing of the UV-edge.  $Fe^{2+}$  signatures have been analyzed by Calas and Petiau [1983b] in iron-doped diopside. The authors found a singular optical absorption spectrum, characteristic of a different local environment around iron than in soda-lime glass [Calas and Petiau, 1983b]. To study the impact of sodium on the  $Fe^{2+}$  local environment in glass,  $Fe^{2+}$  content of our glasses has been maximized using reducing synthesis conditions. This section compares two reduced glasses, a soda-lime glass (NCS05Red) and a sodium-free glass (DIO05Red), with a respective  $Fe^{2+}/Fe_{tot}$  ratio  $R = 99\%$  and  $R = 80\%$ .

Optical absorption spectra normalized by glass thickness and  $Fe^{2+}$  concentration are plotted in Figure 6.5 for the two glasses. Globally, the molar absorption coefficient of  $Fe^{2+}$  ( $\epsilon_{Fe^{2+}}$ ) is lower for DIO05Red than NCS05Red. The fact that  $Fe^{2+}$  sites in sodium-free glass

are less absorbent than in sodium-silicate suggests a smaller  $p$ - $d$  mixing and geometries characteristic of higher  $\text{Fe}^{2+}$  coordination numbers.

Moreover, the more symmetric shape of the band around  $10\,000\text{ cm}^{-1}$  in DIO05Red is the signature of a different  $\text{Fe}^{2+}$  local environment than in NCS05Red. The more gentle slope between  $6\,000$  and  $8\,000\text{ cm}^{-1}$  potentially ascribable to the decrease of the absorption band of distorted tetrahedral sites (see Section 5.2.1) also confirm this theory.

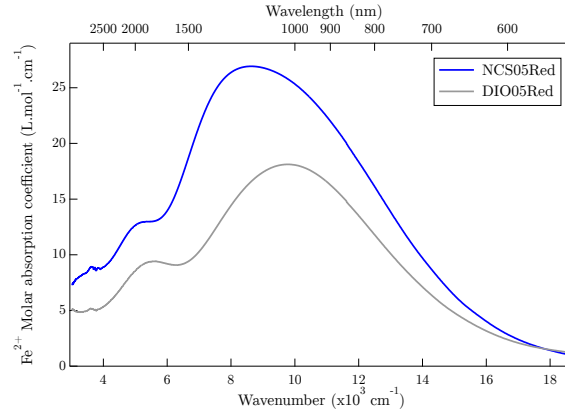


**Figure 6.5** – Molar absorption coefficient of  $\text{Fe}^{2+}$  ( $\epsilon_{\text{Fe}^{2+}}$ ) in a reduced soda-lime glass (NCS05Red) and in a reduced diopside glass (DIO05Red).

Table 6.1 shows the results of a fit performed on the DIO05Red and NCS05Res optical spectra between  $4\,000\text{ cm}^{-1}$  and  $16\,000\text{ cm}^{-1}$  using three Gaussian functions. These results confirm the lower molar absorption coefficient and area of  $\text{Fe}^{2+}$  in sodium-free glass. The only exception is that the signal around  $5\,000\text{ cm}^{-1}$  is broader because of the small contribution around  $8\,000\text{ cm}^{-1}$ . The three bands are shift at higher energy, which agrees with a decrease of the proportion of tetrahedral sites.

**Table 6.1** – Fit of  $\text{Fe}^{2+}$  bands with 3 Gaussian functions for NCS05Red and DIO05Red glasses

	Position ( $\text{cm}^{-1}$ )	$\sigma$ ( $\text{cm}^{-1}$ )	FWHM ( $\text{cm}^{-1}$ )	Intensity ( $\text{cm}^{-1}$ )	$\epsilon_{\text{Fe}^{2+}}$ (L/mol/cm)	Area ( $\text{cm}^{-2}$ )
NCS05Red fit3						
#1	4848	492	1159	0.75	4.8	651.6
#2	7812	1277	3007	0.96	6.2	2181.4
#3	9775	3177	7482	3.65	23.7	20557.5
DIO05Red fit3						
#1	5135	926	2181	0.84	6.7	1384.4
#2	8121	1368	3222	0.42	3.3	1013.5
#3	10296	2499	5885	2.13	16.9	9434.8

Differences can also be noticed in the RIXS spectra (Figure 6.6) and the diagonal cut, corresponding to the HERFD spectra, of the two reduced glasses. In the case of diopside glass, the higher concentration of  $\text{Fe}^{3+}$  should lead to higher pre-edge intensity\*. However,

\* $\text{Fe}^{3+}$  features in the pre-edge are generally more intense than  $\text{Fe}^{2+}$  in crystalline compounds (see Appendix A) and sum rules (Appendix D.4)

the observed DIO05Red pre-edge intensity is lower than NCS05Red, which agrees with a lower amount of  $\text{Fe}^{2+}$  in tetrahedral sites for diopside glass.

In addition, the smaller signal between the pre-edge and main-edge for the alkali-free glass, attributed to a lower amount of Fe-clusters, comforts the previous observations for  $\text{Fe}^{3+}$ .

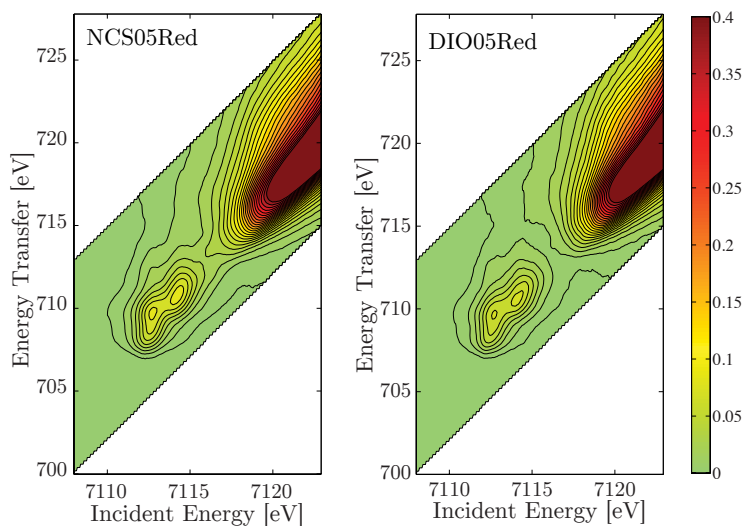


**Figure 6.6** –  $K\alpha$  RIXS spectra at Fe of NCS05Red (Right) and DIO05Red (Left)

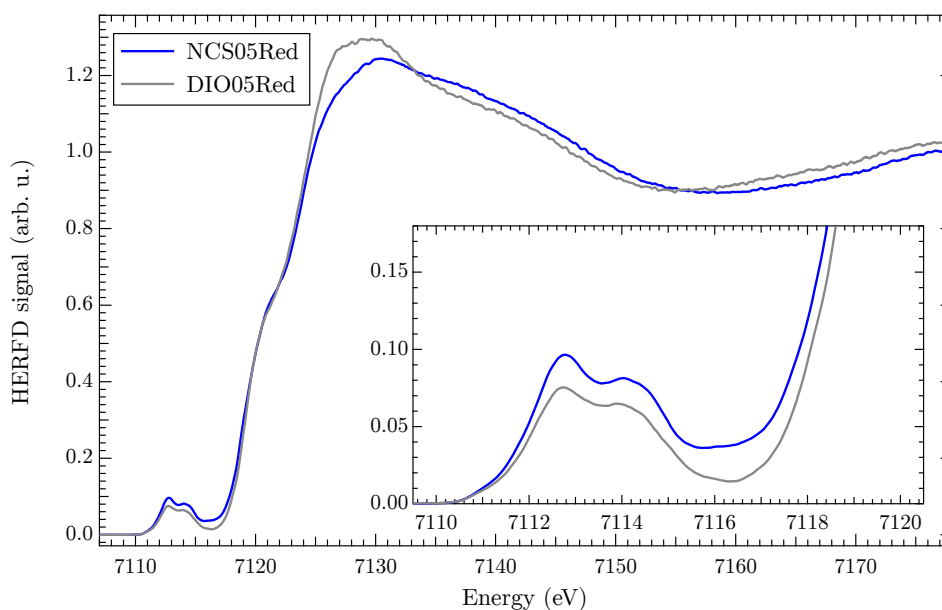


**Figure 6.7** – HERFD spectra at Fe  $K$  edge of NCS05Red (blue) and DIO05Red (grey).

## 6.2 Influence of the alkaline earth nature: Ca vs. Mg

After studying the first order effect of redox in Chapter 5, and the second order effect with the presence or absence of alkali in the previous section, this part is focused on the analysis of spectroscopic properties modifications induced by the substitution of Ca by Mg.

The comparison of iron signatures in response to the alkaline earth nature not only gives information on the iron local environment complementing the previous results, but also enables to discuss the fine effects such as evolution of the transmission window in the visible, which is a key property for industrial float glass applications.

### 6.2.1 The opposite effect of Ca:Mg ratio on the $\text{Fe}^{2+}$ and $\text{Fe}^{3+}$ UV-edge

As we have previously seen, the UV-edge analysis is a preliminary step necessary to the interpretation of  $\text{Fe}^{3+}$  spectroscopic signatures and also bring valuable information on both  $\text{Fe}^{2+}$  and  $\text{Fe}^{3+}$  environments. Given the strong OMCT absorption bands of iron in the UV range, the UV-edge determines the maximum transmitted energy, also called UV cut-off.

Figure 6.8 shows the UV-edge of NCS05 and NMS05 glasses at two different redox states, oxidized and reduced. The UV-edge position is at higher energy in NMS05Ox than NCS05Ox and at lower energy in NMS05Red than NCS05Red. As we have seen in Section 5.3.1, the UV-edge of reduced glasses is dominated by  $\text{Fe}^{2+}$ -OMCT and the one of oxidized glasses by  $\text{Fe}^{3+}$ -OMCT. Therefore, when Mg is used instead of Ca, the opposite effect on the UV-edge for reduced and oxidized glasses highlights a different behavior of  $\text{Fe}^{2+}$  and  $\text{Fe}^{3+}$  in reaction to the modification of the alkaline earth nature. This result could suggest an opposite evolution of the  $\text{Fe}^{2+}$ -O and  $\text{Fe}^{3+}$ -O bond lengths, which show the necessity to separately consider the effect of the alkaline earth nature on  $\text{Fe}^{2+}$  and  $\text{Fe}^{3+}$  local environments.

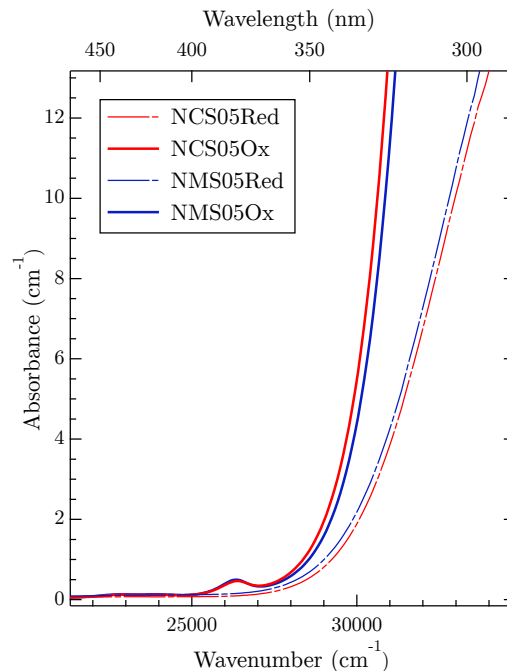


**Figure 6.8** – Optical absorption spectra in the UV range of NCS05 and NMS05, oxidized and reduced glasses.

According to Farges et al. [2004], in which similar NCS and NMS glasses doped with iron were studied, the authors found that when Ca is replaced by Mg, the average coordination number of  $\text{Fe}^{2+}$  increases:  $[4.6] \rightarrow [4.9]$ , while the average coordination number of  $\text{Fe}^{3+}$  decreases:  $[4.6] \rightarrow [4.4]$ . Fe-O bond length increases with the coordination number of iron [Brown et al., 1995], this correlation explains the opposite evolution on the UV-edges



of Ox and Red glasses. It also agrees with Loeffler et al. [1974] in which the UV-edge of [4]-fold  $\text{Fe}^{2+}$  calculated to be at lower energy than [6]-fold  $\text{Fe}^{2+}$ .

### 6.2.2 Ca:Mg effects on ferric iron ( $\text{Fe}^{3+}$ ) optical signatures in glasses

The substitution of Ca by Mg acts on the optical spectral signature of  $\text{Fe}^{3+}$ . This part is focused on the study of the four oxidized and medium glasses, containing the highest amount of  $\text{Fe}^{3+}$ : NCS05 and NMS05, Med and Ox, in order to bring information regarding the influence of alkaline-earth nature on the  $\text{Fe}^{3+}$  local environment.

The optical absorption spectra for medium and oxidized glasses of the two compositions NCS05 and NMS05 are shown in Figure 6.9-a. The first thing to notice is that the four spectra have similar spectral shapes, confirming the fine variations that are studied here. At a given redox (Ox or Med), a similar trend is observed between NCS and NMS glasses. In oxidized glasses, the UV-edge is shifted at lower energy due to the higher  $\text{Fe}^{3+}$  concentration, which increases the  $\text{Fe}^{3+}$ -OMCT intensity according to Beer-Lambert law. In the visible range, the tail of the  $\text{Fe}^{2+}$  main band around  $10\,000\text{ cm}^{-1}$  and the small spin-forbidden contributions overlap the  $\text{Fe}^{3+}$  optical bands when the  $\text{Fe}^{2+}/\text{Fe}_{\text{tot}}$  ratio is higher. These two side effects are not of the same order of magnitude than fine effects caused by the alkaline earth nature on the weak spin-forbidden  $\text{Fe}^{3+}$  bands. Therefore, a necessary processing has been performed using the methodology detailed in Appendix B.4 to extract  $\text{Fe}^{3+}$  signatures from  $d-d$  transitions and complement this extraction by a Gaussian fit of  $\text{Fe}^{3+}$  contributions participating to  $\varepsilon_{\text{Fe}^{3+}}$ .

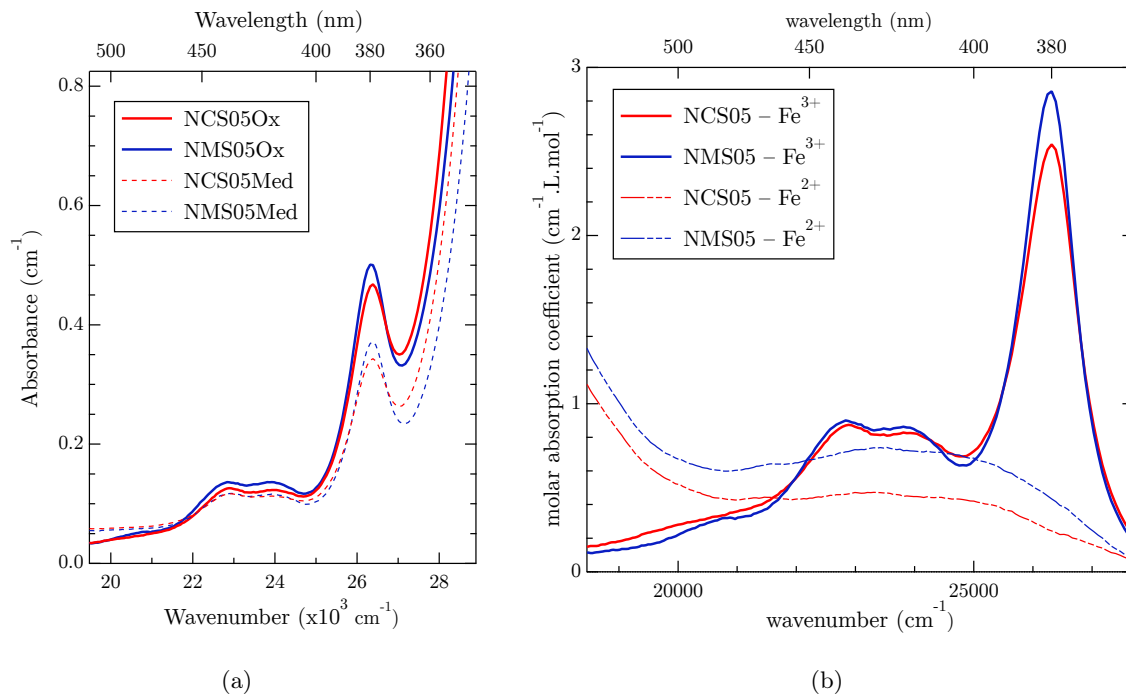


**Figure 6.9** – (a) Optical spectra of the two sodium-silicate glasses respectively containing Ca or Mg as an alkaline earth network modifier. (b) Extracted molar absorption coefficient of  $\text{Fe}^{2+}$  and  $\text{Fe}^{3+}$   $d-d$  transitions in NCS and NMS glass extracted.

Figure 6.9-b presents the extracted molar absorption coefficient  $\varepsilon$  of  $\text{Fe}^{3+}$  and  $\text{Fe}^{2+}$ . The dashed lines represent the separated signal due to  $\text{Fe}^{2+}$  that can disturb the analysis of

$\text{Fe}^{3+}$  signatures. The plain lines, corresponding to the signals of interest in this section, present several changes with the alkaline earth nature.

When Mg is added instead of Ca, the extracted  $\text{Fe}^{3+}$  spectra keep a similar shape, but the main  $\text{Fe}^{3+}$  band at  $26\,300\text{ cm}^{-1}$  is more intense and narrower, while the signal around  $25\,500\text{ cm}^{-1}$  becomes weaker. This change of proportion between these two contributions results in the optical spectra of Mg-containing glasses by a weaker local minimum around  $25\,000\text{ cm}^{-1}$  which makes the band at  $26\,300\text{ cm}^{-1}$  more defined. The two bands between  $22\,800$  and  $24\,000\text{ cm}^{-1}$  do not significantly vary, however, the signal width of the  $21\,000\text{ cm}^{-1}$  band is narrower and the spectrum from NMS glass is better defined.

If we have a look on the high-resolution X-ray absorption  $K$  pre-edge (HERFD), the substitution of Ca by Mg results in a slightly more intense peak around  $7114.5\text{ eV}$  in Figure 6.10. No other change in the shape could be noted.

The change of proportion of the two optical contributions at  $26\,300\text{ cm}^{-1}$  and  $25\,500\text{ cm}^{-1}$  becoming respectively more intense and weaker, suggests an increasing proportion of  $[\text{Fe}^{3+}]_4$  in the Mg-rich samples (NMS) compared to Ca-rich samples (NCS), according to the previous chapter, the  $25\,500\text{ cm}^{-1}$  contribution was attributed to  $\text{Fe}^{3+}$  in [5]-fold coordination, while the signal at  $26\,300\text{ cm}^{-1}$  is mainly due to [4]-fold tetrahedral ferric iron.

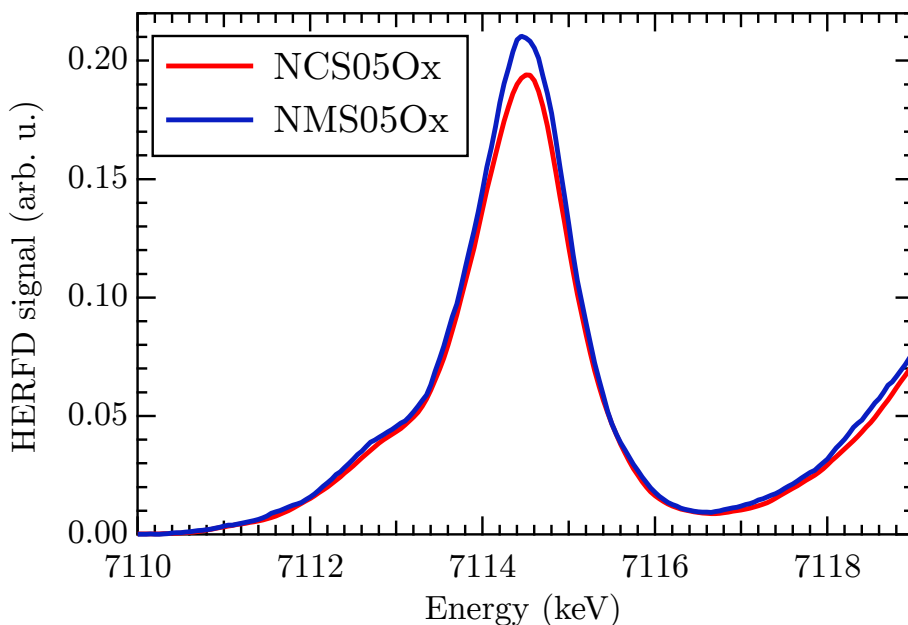


**Figure 6.10** – HERFD spectra at Fe  $K$  edge of NCS05Ox and NMS05Ox.

Due to its broadness, the signal below  $22\,000\text{ cm}^{-1}$  was fitted by a single Gaussian, the refinement of this band observed in NMS could signify a smaller variety of  $\text{Fe}^{3+}$  sites causing a more restricted number of bands in the range  $18\,000$ – $22\,000\text{ cm}^{-1}$ . In the previous chapter, part of the signal around  $21\,500\text{ cm}^{-1}$  was attributed to the presence of weak spin-forbidden bands possibly due to [5]-fold as in yoderite, while [4]-fold of ferriorthoclase happens around  $20\,500\text{ cm}^{-1}$ .

From the structural point of view, the correlations of the two previous paragraph could

be interpreted as an increase of [4]-fold  $\text{Fe}^{3+}$  in the oxidized and medium magnesium-rich glasses (NMS) compared to calcium-rich glasses (NCS). This also agrees with the slight increase of XAS intensity, suggesting that  $\text{Fe}^{3+}$  are lower coordinated in presence of Mg than Ca, i.e. there are more tetrahedral sites.

Regarding LFM calculations of  $\text{Fe}^{3+}$  in  $T_d$  geometry (Section 4.5) these slight differences can also be attributed to a larger distribution of the crystal field  $10Dq$  parameter in NCS glass than in NMS glass.

This conclusion of the decrease of  $\text{Fe}^{3+}$  coordination number by using a smaller alkaline earth ion agrees with Bingham et al. [2002], except that the authors interpreted the  $\text{Fe}^{3+}$  coordinance by only considering tetrahedral and octahedral sites. The vision adopted here is that the average site distribution among a variety of [4]- and [5]-fold sites is modified by the nature of the network modifier.

### 6.2.3 Evolution of $\text{Fe}^{3+}$ distortion when Mg substitute Ca

To continue with this idea, a third glass NCMS with an intermediate composition between NCS and NMS glasses is considered. The band around  $26\,300\text{ cm}^{-1}$  of the three glasses has been fitted alone (without considering the other contributions) and results are plotted in Figure 6.11-c. As it can be noticed, the FWHM decreases with the increase of Mg, which corroborates the previous observation of a more intense and narrower band at  $26\,300\text{ cm}^{-1}$  when Mg replaces Ca. This agrees with an increase of iron in less distributed sites, such as tetrahedral sites. However, given the size of the error bars estimated by the fitting program, the use of another spectroscopic method is necessary to confirm these tendencies.

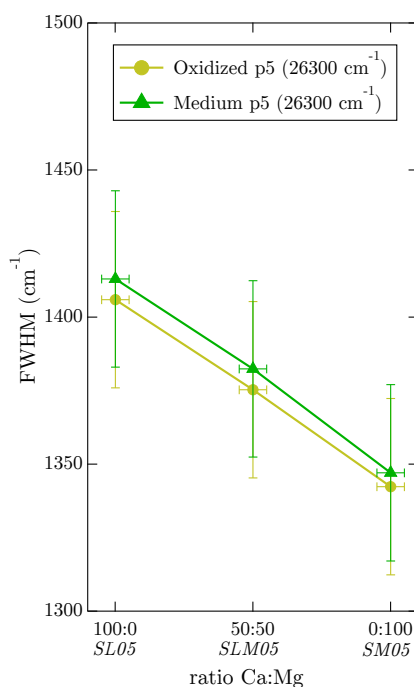


**Figure 6.11** – Extracted FWHM of the optical band at  $26\,300\text{ cm}^{-1}$  from Gaussian fit of NCS, NCMS and NMS Ox and Med glasses.

The use of EPR is particularly well suited in that case, because of its high sensitivity and the chemical selectivity to  $\text{Fe}^{3+}$ . EPR spectra of the three Med glasses are shown in

Figure 6.12. When  $\text{Ca}^{2+}$  is substituted by  $\text{Mg}^{2+}$  in the glassy matrix, EPR spectra show (a) an increase of the  $g = 8$  line, (b) a decrease and broadening of the  $g = 4.3$  line and (c) an increase of the  $g = 2$  line. Concerning the signals at  $g = 4.3$ , these tendencies are summarized in Figure 6.13 for the nine glasses (3 redox states times 3 compositions).

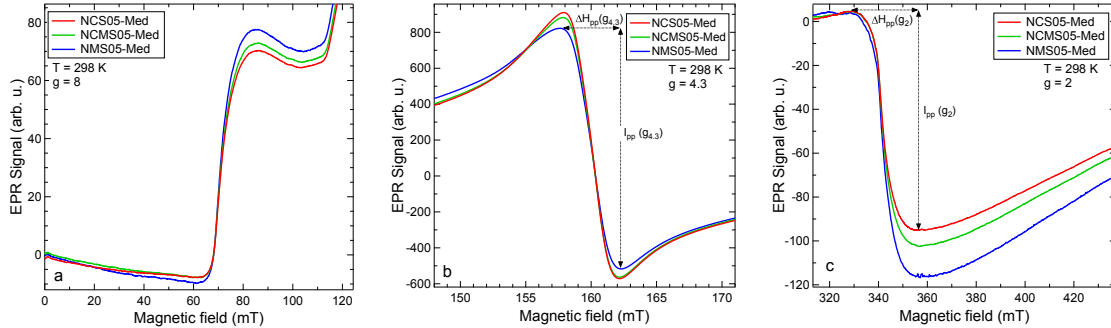


**Figure 6.12** – X-band EPR signals for the three intermediate redox glasses (NCS05Med, NCMS05Med and NMS05Med) at (a)  $g = 8$ , (b)  $g = 4.3$  and (c)  $g = 2$ .

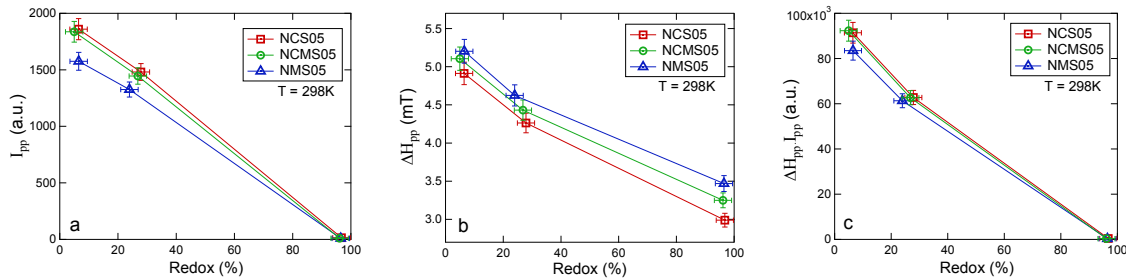


**Figure 6.13** – (a)  $g = 4.3$  peak-to-peak intensity ( $I_{pp}$ ), (b)  $g = 4.3$  peak-to-peak linewidth ( $\Delta H_{pp}$ ) and (c) the product of  $\Delta H_{pp}$  and  $I_{pp}$  as a function of redox  $R = \text{Fe}^{2+}/\text{Fe}_{\text{tot}}$  for the three glass compositions: NCS, NCMS and NMS. The lines are a guide for the eyes.

The nature of the alkaline earth cations has a smaller effect on  $I_{pp}$  and  $\Delta H_{pp}$  than the redox. Nevertheless, Mg-containing samples systematically show a weaker and broader signal at  $g = 4.3$ . Whatever the redox, the larger linewidth of the  $g = 4.3$  signal (Figures 6.12-b and 6.13-b) for NMS samples compared to NCS samples reflects a decrease of the rhombic distortion of  $\text{Fe}^{3+}$  sites (i.e. lower value of  $\lambda = E/D$ ) [Elvers and Weissmann, 2001]. This lower rhombic distortion is supported by the increase of the signal associated to axially distorted sites at  $g = 8$  (Figure 6.12-a) and  $g = 2$  (Figure 6.12-c). Due to smaller coordination numbers, [4]-fold sites are indeed less subject to distortion. This effect is consistent with the increase of the concentration of tetrahedral sites in Mg-bearing glasses compared to Ca-bearing glasses, with lower average coordination number for  $\text{Fe}^{3+}$  in soda-magnesia glasses ( $\sim 4.5$ ) than in soda-lime glasses ( $\sim 5.0$ ) [Bingham et al., 2014]. This is supported by our optical absorption data (Figure 6.9) suggesting an increase of the  $25\,500\text{ cm}^{-1}$  contribution (attributed to [5]-fold  $\text{Fe}^{3+}$ ) and a decrease of the  $26\,300\text{ cm}^{-1}$  contribution (attributed to tetrahedral  $\text{Fe}^{3+}$ ).

Figure 6.13, can be used in addition to the study of the  $g = 4.3$  signal broadening as a function of redox, discussed in Section 5.3.4. The almost linear evolution of  $I_{pp}$  and  $\Delta H_{pp}$  with redox for a fixed total iron content (0.5 wt% of  $\text{Fe}_2\text{O}_3$ ) is similar to the variation obtained by changing the total iron content at a given redox [Elvers and Weissmann, 2001]. This indicates a linear variation of the  $\text{Fe}^{3+}$  concentration as a function of  $\text{Fe}^{2+}/\text{Fe}_{\text{tot}}$ . The

quasi-linearity of the product  $I_{pp} \times \Delta H_{pp}$  (Figure 6.13-c) confirms the Lorentzian shape expected for the  $g = 4.3$  signal of  $Fe^{3+}$  in diluted glasses [Elvers and Weissmann, 2001]. Increasing  $Fe^{3+}$  concentration leads to a broadening of this  $g = 4.3$  EPR signal, which is indicative of a larger distribution including isolated  $Fe^{3+}$  sites with a smaller average distortion. On the contrary, at low  $Fe^{3+}$ -content, site distribution is smaller (discrete EPR transitions at  $g = 4.3$  compared to oxidized sample without split signal) with a predominance of distorted sites (smaller  $\Delta H_{pp}$ ).

In the case of iron-doped silicate glasses, OAS, XAS and EPR spectroscopies suggest a lower coordination, distortion and distribution of  $Fe^{3+}$  local environment in Mg-rich glasses compared to Ca-rich glasses. However, as suggested by the study of the optical UV-edge, the substitution of Ca by Mg implies a different behavior on the  $Fe^{2+}$  local environment.

#### 6.2.4 Ca:Mg effects on ferrous iron ( $Fe^{2+}$ ) optical signatures in glasses

In this section, we focus on the  $Fe^{2+}$  environmental and spectroscopic changes in response to the modification of the alkaline-earth nature ( $Ca \rightarrow Mg$ ) in sodium-silicate glasses. Glasses studied here are the reduced glasses (NCS05Red, NCMS05Red and NMS05Red) that maximized the  $Fe^{2+}$  content.

In glasses, the shape of the main  $Fe^{2+}$  band (around  $10\,000\text{ cm}^{-1}$  strongly depends on the nature of cation modifiers. In the case of alkali modification, the asymmetry increases with the alkali radius and can be related to distortion and distribution of site geometries [Bingham, 2000, p. 74–76]. Section 6.1.2 also that the absence of alkali leads to a particularly symmetric band.

Concerning the effect of the nature of the alkaline-earth, Figure 6.14 shows the optical molar absorption coefficients of  $Fe^{2+}$  for the three glasses of interest. The band around  $10\,000\text{ cm}^{-1}$  is at higher energy for Mg-rich glass but the intensity maximum does not significantly change. On the other hand, signals from  $4000\text{ cm}^{-1}$  to  $9000\text{ cm}^{-1}$  are smaller when magnesium is added.

In order to help in the interpretation of these change a fit of the optical absorption from  $4000\text{ cm}^{-1}$  to  $16\,000\text{ cm}^{-1}$  has been performed with 3 Gaussian functions (Table 6.2). It seems that two simultaneous effects explain the modification of the spectral shape: (i) a shift at high energy of the bands due to an increase of the crystal field (as studied with LFM calculation in Chapter 4); (ii) a decrease of the signals from  $6000\text{ cm}^{-1}$  to  $9000\text{ cm}^{-1}$  mirrored by an increase of the signals above  $9000$ . This last point, can be due to a coordination number evolution with less distorted tetrahedral sites and more non-tetrahedral  $Fe^{2+}$  sites. However, there is no significant evolution of the  $4800\text{ cm}^{-1}$  band, except a slight broadening and shift to lower energies, which could be a possible side effect of the decrease of the  $8000\text{ cm}^{-1}$  contribution.

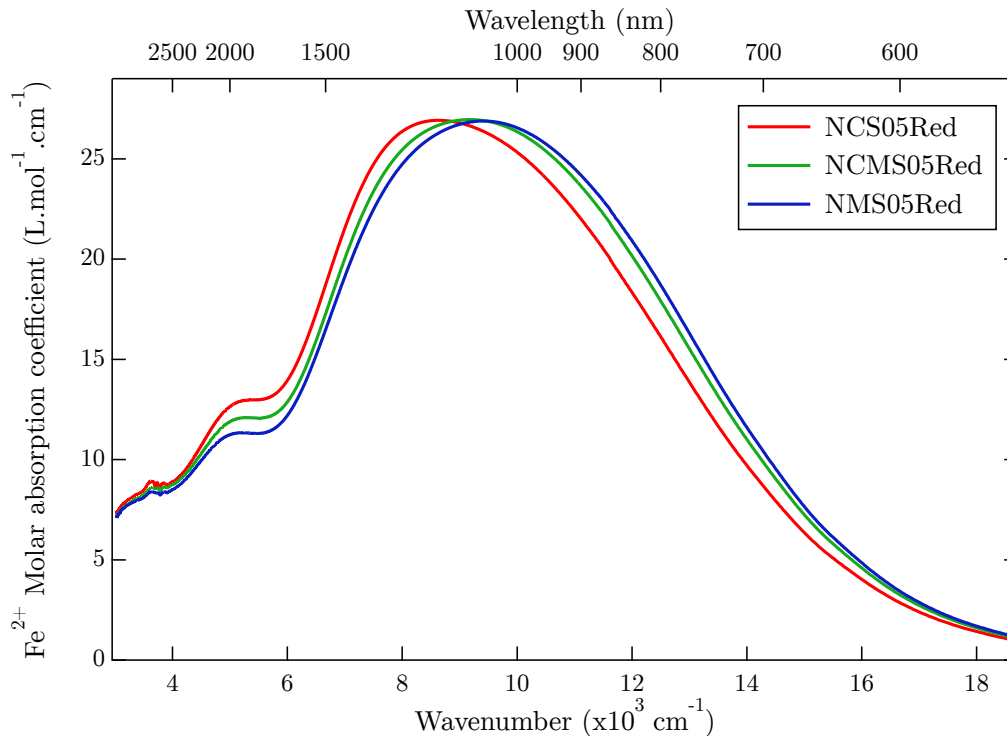


**Figure 6.14** – molar absorption coefficient of  $\text{Fe}^{2+}$  ( $\varepsilon_{\text{Fe}^{2+}}$ ) for the three sodium-alkaline earth silicate glasses with a  $\text{Fe}^{2+}/\text{Fe}_{\text{tot}}$  ratio around 99%: NCS05Red (red), NCMS05Red (green) and NCM05Red (blue).

**Table 6.2** – Fit of  $\text{Fe}^{2+}$  bands with 3 Gaussian functions for NCS05Red, NCMS05Red and NMS05Red glasses

Sample name	Position ( $\text{cm}^{-1}$ )	$\sigma$ ( $\text{cm}^{-1}$ )	FWHM ( $\text{cm}^{-1}$ )	Intensity ( $\text{cm}^{-1}$ )	$\varepsilon_{\text{Fe}^{2+}}$ (L/mol/cm)	Area ( $\text{cm}^{-2}$ )
NCS05Red						
#1	4848	492	1159	0.75	4.8	651.6
#2	7812	1277	3007	0.96	6.2	2181.4
#3	9775	3177	7482	3.65	23.7	20557.5
NCMS05Red						
#1	4825	511	1203	0.77	4.9	701.9
#2	7905	1264	2977	0.82	5.1	1838.9
#3	9994	3157	7435	3.96	24.8	22141.8
NMS05Red						
#1	4787	520	1225	0.72	4.8	666.7
#2	7944	1287	3031	0.73	4.8	1665.3
#3	10129	3144	7404	3.80	25.0	21198.3

To enhance the signal originating from small absorption band, the optical spectra are plotted with a logarithmic scale for the absorbance (Figure 6.15).

There is no evolution of the position of the band around  $21\,500\text{ cm}^{-1}$  and  $23\,500\text{ cm}^{-1}$  bands that have been attributed in Section 5.2.5 to  $\text{Fe}^{2+}$  spin-forbidden transition. This signifies that these bands can be due to transitions independent of the crystal field, which would explain that they emerge from the absorption background.

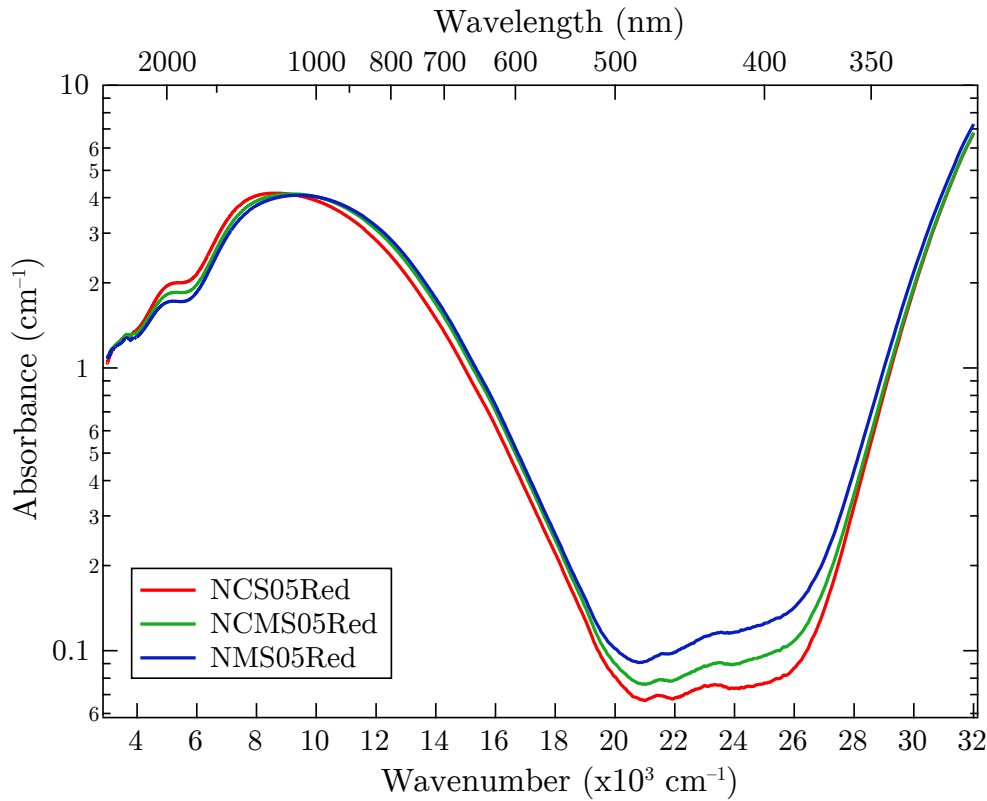


**Figure 6.15** – Optical absorption spectra (y-axis in log scale) for the three sodium-alkaline earth silicate glasses with a  $\text{Fe}^{2+}/\text{Fe}_{\text{tot}}$  ratio around 99%: NCS05Red (red), NCMS05Red (green) and NCM05Red (blue).

This increase of the background signal with Mg-content raises the question of Fe–Fe interactions as a function of the alkaline-earth nature. This question, discussed in Section 5.4 as the function of redox, will be studied in the next paragraph as a function of the Ca:Mg ratio.

### 6.2.5 Are there more Fe-clusters in Mg-rich glass?

In order to check the background origin, the three reduced glasses are compared with an “iron-free” glass (NCS00Med) containing about 75 ppm of  $\text{Fe}_2\text{O}_3$  (compared to 5000 ppm). According to Figure 6.16, representing a zoom on the low absorbance intensities, the signal of reduced glasses is due to iron because the iron-free glass is almost null after the reflection subtraction.

The evolution of the absorption background of silicate glasses doped with 0.5 wt% of  $\text{Fe}_2\text{O}_3$  was only observed for reduced glasses. For Mg-rich glasses, a higher background is observed suggesting the presence of  $\text{Fe}^{2+} + \text{Fe}^{3+} \rightarrow \text{Fe}^{3+} + \text{Fe}^{2+}$  Intervalence charge transfer (IVCT) that are expected in this energy range [Taran et al., 2007]. However, the low temperature measurements down to 10 K with a cryostat, did not evidence any enhancement from a potential intervalence charge transfer (IVCT).

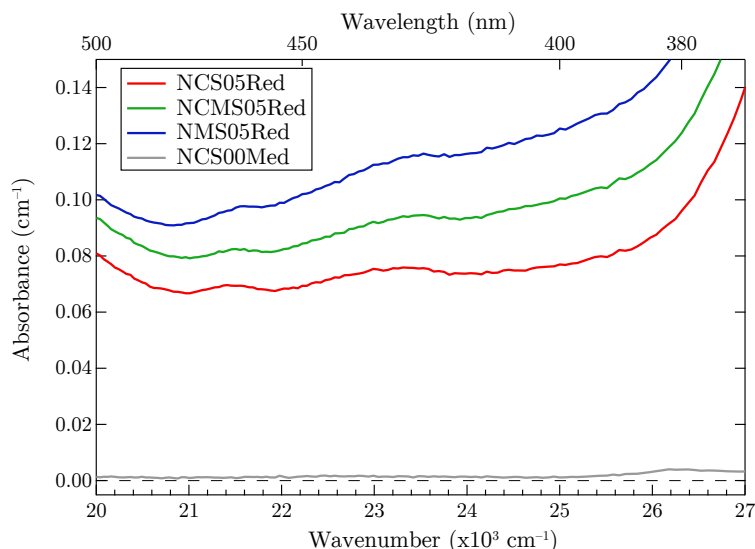


**Figure 6.16** – Optical absorption spectra in  $\text{cm}^{-1}$  for the three sodium-alkaline earth silicate glasses with a  $\text{Fe}^{2+}/\text{Fe}_{\text{tot}}$  ratio around 99%: NCS05Red (red), NCMS05Red (green) and NCM05Red (blue) and an “iron-free” glass NCS00Med (grey) with an intermediate redox.

In the same way, for XAS measurements, only reduced glasses exhibit a difference with magnesium content of the signal between the pre-edge and the main edge. The HERFD-XAS spectra (Figure 6.17) show an increase of this signal with Mg-content. This signal has been interpreted by Vankó et al. as non-local dipole excitation, due to the presence of a neighboring transition metal via the  $\text{M}(4p)\text{-O-M}'(3d)$  intersite hybridization [Vankó et al., 2008].

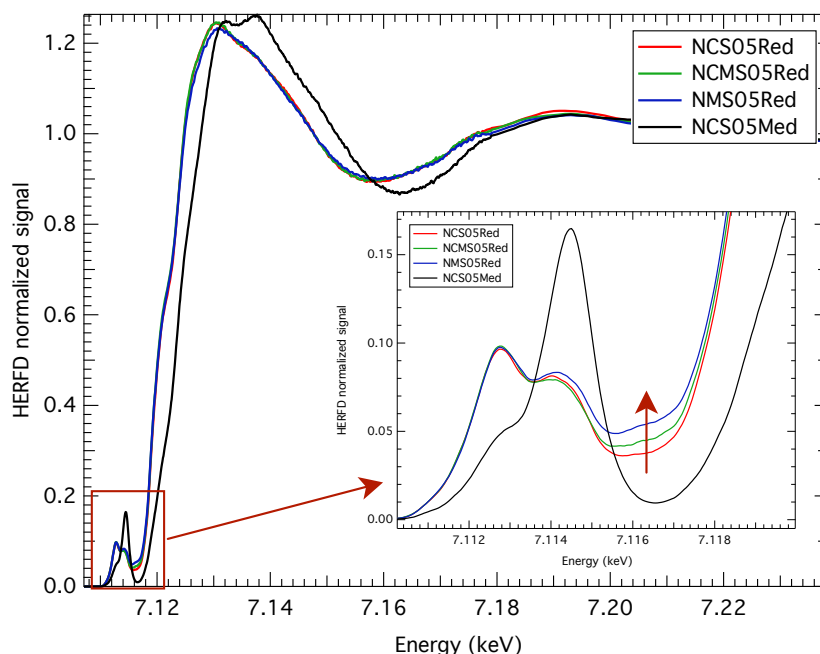


**Figure 6.17** – HERFD spectra at Fe  $K$  edge of the three reduced glasses (NCS05Red, NCMS05Red and NMS05Red) and the NCS05Med glass with an intermediate redox.

Concerning EPR, only the reduced glasses present a complete vanishing of the  $g = 2$  signal at low-temperature EPR (for Med and Ox only a decrease was observed proportionally to the  $g = 4.3$  signal).



Nevertheless, whatever the redox, the ratio  $I_{pp}(g = 4.3)/I_{pp}(g = 2)$  at 298 K decreases when Mg is added (Figure 6.18), suggesting that the NMS05 glass contains a higher proportion of  $Fe^{3+}$  clusters than the NCS05 glass.

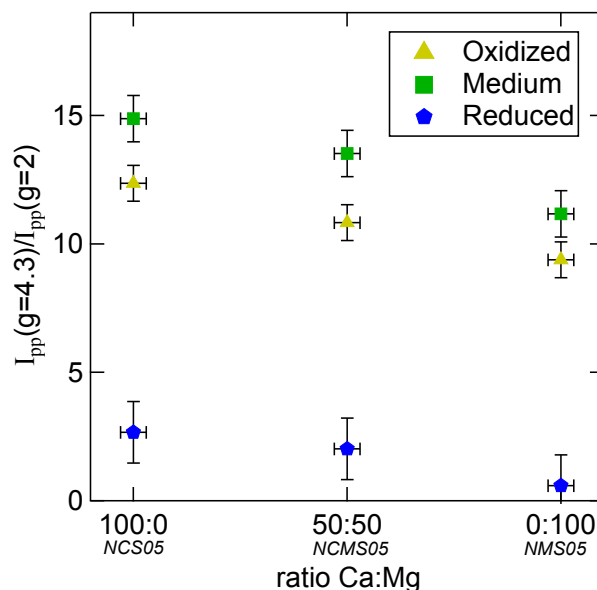


**Figure 6.18** – Ratio between the peak-to-peak intensity at  $g = 4.3$  and the peak-to-peak intensity at  $g = 2$  at 298 K as a function of the composition of the glassy matrix. The ratio  $I_{pp}(g = 4.3)/I_{pp}(g = 2)$  is correlated to the proportion of  $Fe^{3+}$  in isolated distorted sites vs  $Fe^{3+}$  in clusters.

All these results indicate that smaller alkaline-earth ions promote Fe–Fe interactions (abusively called clusters, since they are supposed to be very small), in agreement with the conclusions of Bingham et al. [2002]. Moreover, Fe–Fe interactions are maximized in the case of reduced glasses.

### 6.2.6 Calcium or magnesium who is the favorite neighbor?

Preferential coupling of transition elements with alkali or alkaline earth elements has been observed for  $Cr^{3+}$  ions in soda-lime glasses, where  $Cr^{3+}$  shows a preference for a Na-rich environment [Villain et al., 2010]. The NCMS glass has an average composition between the NCS and NMS glasses, and it always exhibits intermediate spectroscopic properties. We can wonder if the properties of the glass with an average composition (50 mol%Ca:50 mol%Mg) are the average of the 100 mol%Ca and 100 mol%Mg glasses. Or, is there a preference of iron environment for looking closer to one of the poles?

Concerning optical absorption of  $Fe^{3+}$ , when Ca is replaced by Mg, the background-subtracted spectra keep similar shapes (Figure 6.19), the NCMS05Med spectrum is lying between the NCS05Med and NMS05Med spectra. However, the intensity of this spectrum is closer to the spectrum of the calcium-rich glass rather than the magnesium-rich one. When Mg replaces Ca, the  $26\,300\text{ cm}^{-1}$  band becomes more intense while the fitted signal around  $25\,500\text{ cm}^{-1}$  becomes weaker. The total intensity is higher and the signal around  $26\,300$  is better defined for Mg-rich glass.

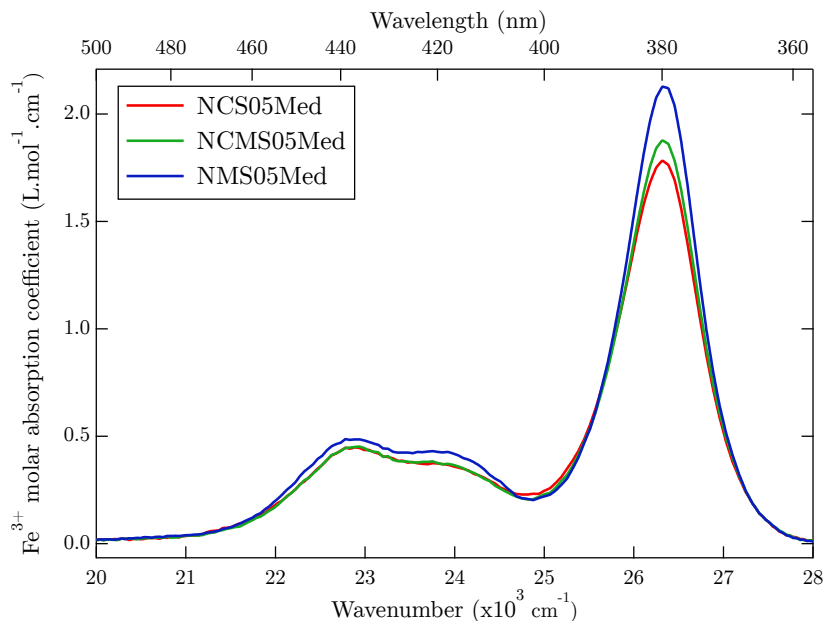


**Figure 6.19** – Optical spectra representing the extracted molar absorption coefficient of  $\text{Fe}^{3+}$ ,  $\epsilon_{\text{Fe}^{3+}}$  for the three sodium-silicate glasses NCS05Med, NCMS05Med and NMS05Med, respectively containing Ca, Ca&Mg and Mg as an alkaline earth network modifier.

The EPR results of the previous section, for  $g = 8$ ,  $g = 4.3$  and  $g = 2$  (Figure 6.12), also show a similar tendency for  $\text{Fe}^{3+}$  in NCMS to look more like  $\text{Fe}^{3+}$  in NCS than in NMS. Just as the HERFD and extracted  $K$  pre-edge (Figure 6.20), NCMS05Ox pre-edge is almost identical to the one of NCS05OX.

This situation is less clear for  $\text{Fe}^{2+}$  environment, optical absorption spectra of reduced glasses from  $4000 \text{ cm}^{-1}$  to  $18000 \text{ cm}^{-1}$  (Figures 6.14 and 6.15) suggest that ferrous iron of the 50Mg:50Ca glass is in a similar environment than in the Mg-rich glass. Concerning the XAS (Figures 6.17 and 6.20), below  $7113 \text{ eV}$  the pre-edge of NCMS is similar to NMS but above  $7113 \text{ eV}$  the situation is inverted.

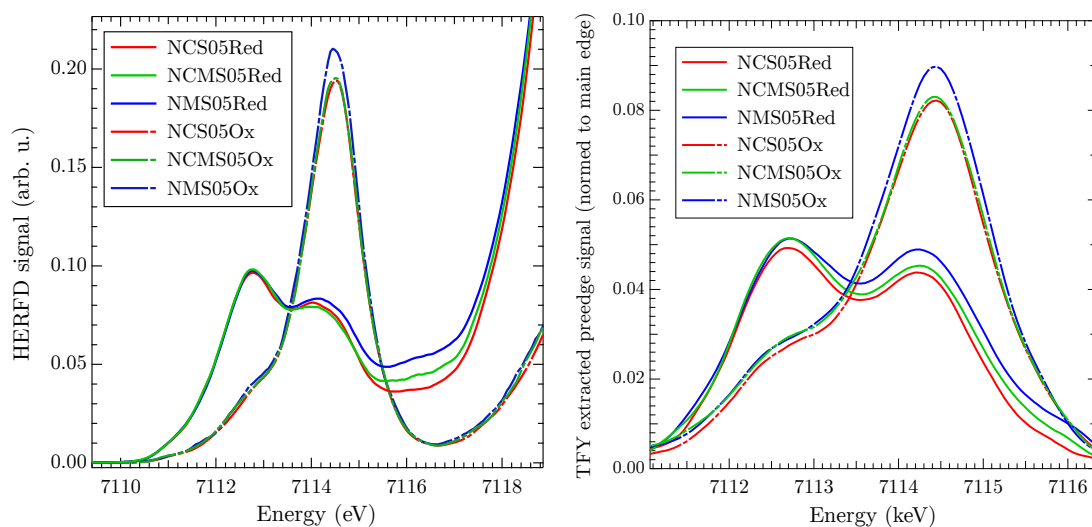


**Figure 6.20** – (Left) HERFD spectra at Fe  $K$  edge of Reduced and Oxidized glasses of the NCS, NCMS and NMS compositions. (Right) Extracted TFY pre-edge spectra at Fe  $K$  edge for the same six glasses.

To help in these comparisons, the different RIXS spectra of glasses has been fitted as a function of two other spectra. For each redox, the NCMS glass were fitted with NCS and NMS of the corresponding redox. For each composition, Med glasses were fitted with Ox and Red. The results are represented in Figure 6.21, the four corners are occupied by the extreme glasses (blue dots). The more an intermediate glass (red dots) is close to a corner, the more it looks like it.

All medium glasses are mainly oxidized, which totally agrees with their  $\text{Fe}^{2+}/\text{Fe}_{\text{tot}}$  ratio ( $R \sim 25\%$ ) closer to oxidized glasses ( $R \sim 5\%$ ) than to reduced glasses ( $R \sim 99\%$ ). Concerning NCMS glasses containing a majority of iron in the  $\text{Fe}^{3+}$  redox state (NCMS05Ox and NCMS05Med), they are both closer to the Ca-rich glasses, which confirms the observations made at the beginning of this section. On the other hand, the situation is less clear for the reduced glass NCMS05Red, containing a majority of iron in the  $\text{Fe}^{3+}$  redox state. The linear combination of RIXS suggests that  $\text{Fe}^{2+}$  environment in this glass is almost 50% of the one in NCS05Red and 50% of of the one in NMS05Red.

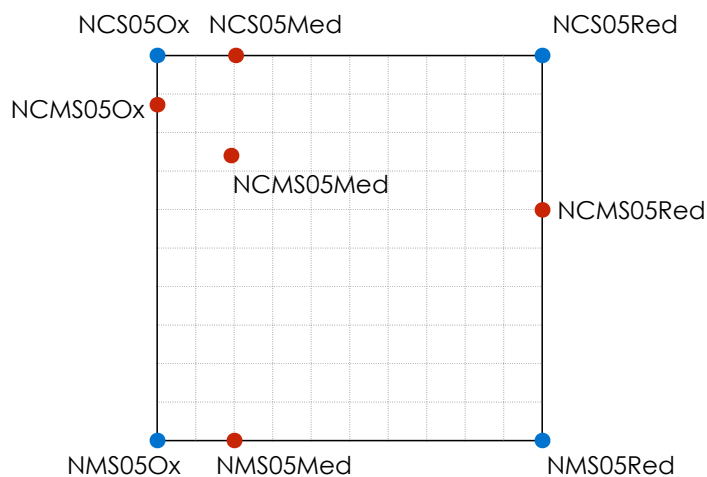


**Figure 6.21** – Linear combinations of RIXS pre-edge.

The different behavior of  $\text{Fe}^{2+}$  and  $\text{Fe}^{3+}$ , in response to the substitution of the alkaline-earth, agree with the different nature of the two iron valence ( $\text{Fe}^{2+}$  is considered as a network modifier and  $\text{Fe}^{3+}$  as network former). The environment of  $\text{Fe}^{3+}$  in NCMS looks more like  $\text{Fe}^{3+}$  in NCS than in NMS. This indicates that  $\text{Fe}^{3+}$  sites are not randomly and homogeneously distributed into the glass matrix as they are sensing a more calcic than magnesian environment. Due to its small ionic radius, Mg coordination number (CN around [4] or [5]) [Trcera et al., 2009] is smaller than Ca (CN around [7]) [Cormier and Neuville, 2004]. Because  $\text{Fe}^{3+}$  is also a small ion with lot of charge on each neighboring oxygen, the Mg–O– $\text{Fe}^{3+}$  bond is be more strained than the Ca–O– $\text{Fe}^{3+}$  bond, which could explain the preference of  $\text{Fe}^{3+}$  for Ca.

Because of the smaller valence of  $\text{Fe}^{2+}$ , each neighboring oxygen receives a smaller electric charge than for  $\text{Fe}^{3+}$ . Therefore, oxygens can manage more easily the vicinity of both Mg and  $\text{Fe}^{2+}$  ions. This can explain why the Ca/Mg substitution has a less clear effect on the environment of  $\text{Fe}^{2+}$ , which do not show a clear preference for Ca-rich or Mg-rich environments.

## Conclusions and suggestions for future work

The purpose of this thesis was to improve the comprehension of the relationships between structural and spectroscopic properties of  $\text{Fe}^{2+}$  and  $\text{Fe}^{3+}$  in silicate glasses. To do so, a multi-spectroscopic study coupling experimental methods (OAS, XAS and EPR) with ligand field multiplet calculation was achieved.

The first step consisted in the study of Fe-bearing crystalline references with iron in specific sites defined by the point group symmetries:  $O_h$ ,  $D_{4h}$ ,  $D_{3h}/C_{3v}$  and  $T_d$ . Speciation of  $\text{Fe}^{2+}$  and  $\text{Fe}^{3+}$  was characterized using ligand field theory. New developments allowed us to use one set of parameters to calculate both optical absorption spectra and total fluorescence yield at Fe  $K$  pre-edge. In light of ligand field multiplet calculations, the effect of iron local symmetry on the spectroscopic signatures was investigated through the  $p$ - $d$  hybridization. Spectroscopic signatures of [5]-fold coordinated iron in minerals confirmed the intermediate behavior of these  $\text{Fe}^{2+}$  and  $\text{Fe}^{3+}$  species between [4]-fold and [6]-fold geometries.

With this additional understanding of the relationships between local structure and spectroscopic signatures of iron in minerals, we focused on the question of iron local environment in silicate glasses. By using the multi-spectroscopic approach in the case of a simple soda-lime-silicate glass doped with iron, we looked at the dominant effect of redox. Both ferric and ferrous iron environment are modified by the redox state of the glass. For example,  $\text{Fe}^{3+}$  environment in oxidized samples is more regular on average, despite a distribution in a larger number of various sites. The study of the different calculation parameters (crystal field, Racah parameters,  $V_{pd}$  and spin-orbit coupling) on the OAS and XAS spectra of minerals contributed to interpret the evolution of the iron spectroscopic features. In particular, [5]-fold coordination of  $\text{Fe}^{2+}$  and  $\text{Fe}^{3+}$  are now better characterized in glasses. In addition, the clustering effects due to Fe-Fe interactions were evidenced to be higher in reduced glasses presenting a segregation of iron ions higher than the statistical distribution.

The last step was to project these interpretations of local structure of iron in a global scenario describing the evolution of iron environment as function of the glassy matrix composition. The effect of the absence of sodium were studied as a second order effect on spectroscopic properties compared to the first order effect of redox. Then, slight modifications of the environment were studied by replacing calcium by magnesium. This

third order effect, showed a preference for  $\text{Fe}^{3+}$  to be in a Ca-rich environment and that  $\text{Fe}^{2+}$  is sensitive to the Ca:Mg ratio but do not show any preference for either alkaline earth. Moreover, magnesium-containing glasses increase the proportion of Fe-Fe interactions compared to calcium-containing glasses.

## Perspectives for future works

### First iron population

It is known that for glasses containing large proportion of iron ( $> 1 \text{ wt}\%$ ), the Beer-Lambert law is not any more linear with iron concentration. This is due Fe-Fe interactions generating non-linear effects. However, the behavior of the first iron population is less known. I did not have time to detail results on the originality of the first populations of  $\text{Fe}^{2+}$  and  $\text{Fe}^{3+}$  in diluted glasses containing less than  $0.01 \text{ wt}\%$  ( $100 \text{ ppm}$ ) of  $\text{Fe}_2\text{O}_3$  because all the difficulty remains in the distinction of real signal from noise regarding the detection limits of spectroscopic methods. However, the high sensitivity of EPR exhibits peculiar  $\text{Fe}^{3+}$  spectroscopic signatures compared with glasses containing  $0.1$  or  $0.5 \text{ wt}\%$  of  $\text{Fe}_2\text{O}_3$ .

### Characterization of hybridization

For non-centrosymmetric geometries,  $V_{pd}$  takes non-negligible values, and  $p$ - $d$  mixing modifies the intended electronic levels, especially, the ground state. Due to transition rules, a change in the ground state symmetry leads to different relative intensities between the transitions that modifies the spectral shape. However, the physical meaning of hybridization in term of structural modification is still poorly understood. In particular, we could wonder if there is a correlation between hybridization and crystal field parameters in response to a site distortion.

### Beyond fitting an experimental spectrum with parameters

More than the possibility to reproduce experimental spectra using simulation of iron in specific sites representative of what is found in minerals, it is possible to access intermediate states that do not exist in crystals (that eventually represent an important amount of the glassy sites) by changing the calculation parameters in a realistic range considering what is found in crystals. It is therefore possible to calculate a spectrum from different spectra with any distribution of the parameters in order to take into account the amorphous nature of glasses.

LFM calculation is an interesting tool to interpret spectroscopic signatures and brings tendencies from the evolution of parameters' values but it is not a predictive tool regarding the effect of the structure. For example, we cannot predict what happens if Na is substituted by K or if the site is distorted in a specific direction.

*ab initio* calculations could be an interesting preliminary step to the LFM calculations to avoid excessive parametrization. A potential calculation protocol for simulation of glass spectra would be to use molecular dynamics (MD) to find a distribution of angles and distances for Fe-O bonds, then use DFT calculations to extract ligand field parameters, energy levels to use them as inputs for LFM calculations to calculate a large number of

spectra. To go further, *ab initio* could provide the wave functions and density of states calculated describing the electronic state in order to perform spectroscopy and electronic transitions between these levels using LFM calculation. In the end, the spectra could be averaged regarding their respective proportions estimated by MD calculations.

A similar procedure has been done for NMR by Charpentier et al. [2004] without *3d* elements. However, the presence of diluted *3d* elements necessitates large simulation boxes with lots of atoms and induces very long calculation time.

### **RIXS calculation of powders**

The application of the RIXS cross-section formula to calculate LFM spectra will improve the comparison with experimental data. Benefits are expected from the better resolution, signal to noise background and the possibility to remove perturbation from other fluorescence processes such as the overlapping signals due to manganese in the iron *K* pre-edge. The calculation of powder spectra is necessary to account for the amorphous nature of glasses. With these calculations, it will also be possible to study the angular dependence of RIXS powder spectra (dichroism).

### **Low temperature experiments on crystals**

These promising results obtained on gillespite, encourage us to complete the study of this mineral by a temperature dependence study. It could be interesting, in a further study, to measure optical transmission of a gillespite crystal at low temperature (10 K), and see what happens to the area of optical transition bands. Lower temperature decreases the effect of vibrations and therefore reduces dynamical distortions induced by thermal agitation. As a consequence, optical bands are narrowed. However, the effect on intensity is less predictable, if a decrease in the area of optical transitions is observed, then it could be interpreted as a decrease of the time spent by the site in a distorted state instead of the regular square-planar  $D_{4h}$  geometry reflecting a lower dynamical hybridization.

### **Optical Magnetic Circular Dichroism (OMCD)**

As we have seen, the main problem of  $\text{Fe}^{2+}$  optical signature in glasses is that the main band is very broad due to the overlapping of several contributions from the only spin-allowed transition of  $\text{Fe}^{2+}$  in several different sites. A promising work has been done by Jackson et al. [2005] who analyzed the  $\text{Fe}^{2+}$  bands with optical magnetic circular dichroism (MCD). The authors extracted three transitions at  $4500\text{ cm}^{-1}$ ,  $6700\text{ cm}^{-1}$  and  $8500\text{ cm}^{-1}$ , possibly corresponding to at least two different sites of coordination number between [4] and [5]. However, no correspondence between spectral signature and sites structure has been made; and this method does not explain the optical absorbance measured above  $10\,000\text{ cm}^{-1}$ .

Using the LFM simulation developments of this thesis concerning optical absorption spectroscopy, it is possible to take into account the effect of magnetic field in the calculation. For example, in **Quanty**, the Zeeman splitting, caused by the magnetic field, can be added to the Hamiltonian describing iron environment in order to analyze the evolution of optical bands with the magnetic field.



---

## References

- Abdelghany, A. M. and ElBatal, H. A. (2014). Gamma-rays interactions on optical, FTIR absorption and ESR spectra of 3d transition metals-doped sodium silicophosphate glasses. *Journal of Molecular Structure* 1067, 138–146. (see p. 216)
- Abragam, A. and Bleaney, B. (1970). *Electron paramagnetic resonance of transition ions*. Clarendon P. (see p. 50)
- Abu-Eid, R. M., Langer, K. and Seifert, F. (1978). Optical absorption and Mössbauer spectra of purple and green yoderite, a kyanite-related mineral. *Physics and Chemistry of Minerals* 3, 271–289. (see pp. 94 and 114)
- Ades, C., Toganidis, T. and Traverse, J. (1990). High temperature optical spectra of soda-lime-silica glasses and modelization in view of energetic applications. *Journal of Non-Crystalline Solids* 125, 272–279. (see p. 206)
- Aime, S., Bergamasco, B., Biglino, D., Digilio, G., Fasano, M., Giamello, E. and Lopiano, L. (1997). EPR investigations of the iron domain in neuromelanin. *Biochimica et Biophysica Acta (BBA) - Molecular Basis of Disease* 1361, 49–58. (see pp. 49 and 50)
- Altmann, S. L. and Herzog, P. (1994). *Point-group theory tables*. Clarendon Press. (see p. 27)
- Amthauer, G. and Rossman, G. R. (1984). Mixed valence of iron in minerals with cation clusters. *Physics and Chemistry of Minerals* 11, 37–51. (see p. 60)
- Ardelean, I., Peteanu, M., Filip, S., Simon, V. and Gyorffy, G. (1997). EPR and magnetic susceptibility studies of iron ions in 70TeO<sub>2</sub>-25B<sub>2</sub>O<sub>3</sub>-5PbO glass matrix. *Solid State Communications* 102, 341–346. (see p. 121)
- Ardelean, I., Pășcuță, P. and Giurgiu, L. V. (2003). EPR and Magnetic Susceptibility Investigations of Fe<sub>2</sub>O<sub>3</sub>-B<sub>2</sub>O<sub>3</sub>-KCl Glasses. *International Journal of Modern Physics B* 17, 3049–3056. (see p. 121)
- Arrio, M.-A., Rossano, S., Brouder, C., Galois, L. and Calas, G. (2000). Calculation of multipole transitions at the Fe K pre-edge through p-d hybridization in the Ligand Field Multiplet model. *Europhysics Letters* 51, 454–460. (see pp. 39, 53, 58, 61, 65 and 81)
- Bain, G. A. and Berry, J. F. (2008). Diamagnetic Corrections and Pascal's Constants. *Journal of Chemical Education* 85, 532. (see p. 212)



- Balan, E., Allard, T., Boizot, B., Morin, G. and Muller, J.-P. (1999). Structural Fe<sup>3+</sup> in natural kaolinites : new insights from electron paramagnetic resonance spectra fitting at X and Q-band frequencies. *Clays and Clay Minerals* 47, 605–616. (see pp. 46 and 242)
- Balan, E., Allard, T., Boizot, B., Morin, G. and Muller, J.-P. (2000). Quantitative measurement of paramagnetic Fe<sup>3+</sup> in kaolinite. *Clays and Clay Minerals* 48, 439–445. (see pp. 46 and 242)
- Ballhausen, C. J. (1962). Introduction to ligand field theory. McGraw-Hill. (see pp. 51, 52, 57, 60 and 237)
- Bamford, C. R. (1977). Colour generation and control in glass. Elsevier Amsterdam. (see p. 22)
- Bart, J. C. J., Burriesci, N., Cariati, F., Cavallaro, S., Giordano, N. and Petrera, M. (1982). Nature and distribution of iron in volcanic glasses: Mössbauer and ESR study of Lipari pumice. *Bull. Mineral* 105, 43–50. (see p. 121)
- Bates, T. (1962). Ligand field theory and absorption spectra of transition-metal ions in glasses. *Modern aspects of the vitreous state* 2, 195–254. (see pp. 23 and 52)
- Bauer, M. (2014). HERFD-XAS and valence-to-core-XES: new tools to push the limits in research with hard X-rays? *Physical Chemistry Chemical Physics* 16, 13827–13837. (see p. 42)
- Berger, R., Kliava, J., Yahiaoui, E.-M., Bissey, J.-C., Zinsou, P. K. and Béziade, P. (1995). Diluted and non-diluted ferric ions in borate glasses studied by electron paramagnetic resonance. *Journal of Non-Crystalline Solids* 180, 151–163. (see pp. 50, 99 and 121)
- Berthet, P., Berthon, J. and d’Yvoire, F. (1988). Xanes study of five-fold coordinated iron (III) in Fe<sub>3</sub>PO<sub>7</sub> and FeAsO<sub>4</sub>-I. *Materials Research Bulletin* 23, 1501–1508. (see p. 25)
- Berthet, P., Berthon, J. and d’Yvoire, F. (1989). EXAFS study of five-fold coordinated iron (III) in Fe<sub>3</sub>PO<sub>7</sub> and FeAsO<sub>4</sub>-I. *Materials Research Bulletin* 24, 459–465. (see p. 25)
- Bethe, H. (1929). Term splitting in crystals. *Annalen der Physik* 3, 133–208. (see p. 51)
- Bingham, P., Parker, J., Searle, T. and Smith, I. (2007). Local structure and medium range ordering of tetrahedrally coordinated Fe<sup>3+</sup> ions in alkali-alkaline earth-silica glasses. *Journal of Non-Crystalline Solids* 353, 2479–2494. (see p. 111)
- Bingham, P., Parker, J., Searle, T., Williams, J. and Fyles, K. (1999). Redox and clustering of iron in silicate glasses. *Journal of Non-Crystalline Solids* 253, 203–209. (see pp. 119, 122 and 204)
- Bingham, P. A. (2000). The Environment of Iron in Silicate Glasses. PhD thesis, University of Sheffield, Department of Engineering Materials. (see pp. 100 and 136)

- Bingham, P. A., Hannant, O. M., Reeves-McLaren, N., Stennett, M. C. and Hand, R. J. (2014). Selective behaviour of dilute  $\text{Fe}^{3+}$  ions in silicate glasses: an Fe K-edge EXAFS and XANES study. *Journal of Non-Crystalline Solids* 387, 47–56. (see pp. 25, 32, 87, 111 and 135)
- Bingham, P. A., Parker, J. M., Searle, T., Williams, J. M. and Smith, I. (2002). Novel structural behaviour of iron in alkali–alkaline-earth–silica glasses. *Comptes Rendus Chimie* 5, 787–796. (see pp. 134 and 140)
- Bogomolova, L. and Henner, E. (1980). The effects of cluster formation of the  $\text{Fe}^{3+}$  ions in silicate glasses. *Journal of Magnetic Resonance (1969)* 41, 422–431. (see pp. 99 and 121)
- Boizot, B., Petite, G., Ghaleb, D., Pellerin, N., Fayon, F., Reynard, B. and Calas, G. (2000). Migration and segregation of sodium under  $\beta$ -irradiation in nuclear glasses. *Nuclear Instruments and Methods in Physics Research Section B: Beam Interactions with Materials and Atoms* 166–167, 500–504. (see p. 215)
- Boudalis, A. K., Sanakis, Y., Dahan, F., Hendrich, M. and Tuchagues, J.-P. (2006). An Octanuclear Complex Containing the  $\{\text{Fe}_3\text{O}\}^{7+}$  Metal Core: Structural, Magnetic, Mössbauer, and Electron Paramagnetic Resonance Studies. *Inorganic Chemistry* 45, 443–453. (see p. 49)
- Boulos, E., Glebov, L. and Smirnova, T. (1997). Absorption of iron and water in the  $\text{Na}_2\text{O}$ – $\text{CaO}$ – $\text{MgO}$ – $\text{SiO}_2$  glasses. I. Separation of ferrous and hydroxyl spectra in the near IR region. *Journal of Non-Crystalline Solids* 221, 213–221. (see p. 98)
- Briois, V., dit Moulin, C. C., Sainctavit, P., Brouder, C. and Flank, A.-M. (1995). Full multiple scattering and crystal field multiplet calculations performed on the spin transition  $\text{FeII}(\text{phen})_2(\text{NCS})_2$  complex at the iron K and  $\text{L}_{2,3}$  X-ray absorption edges. *Journal of the American Chemical Society* 117, 1019–1026. (see p. 61)
- Brouder, C. (1990). Angular dependence of X-ray absorption spectra. *Journal of Physics: Condensed Matter* 2, 701–738. (see pp. 39, 59 and 242)
- Brown, G. E., Farges, F. and Calas, G. (1995). X-ray scattering and X-ray spectroscopy studies of silicate melts. *Reviews in Mineralogy and Geochemistry* 32, 317–410. (see pp. 23, 25, 101, 131 and 237)
- Burns, R. G. (1981). Intervalence Transitions in Mixed Valence Minerals of Iron and Titanium. *Annual Review of Earth and Planetary Sciences* 9, 345–383. (see p. 30)
- Burns, R. G. (1993). Mineralogical applications of crystal field theory. Cambridge University Press. (see pp. 23, 52, 53, 58, 60, 61, 66, 67, 72, 87, 92, 109, 110, 114, 124 and 236)
- Butler, P. H. (1981). Point group symmetry applications: methods and tables. Plenum Press. (see pp. 61, 64, 84 and 231)
- C14 Committee (2011). Test Methods for Chemical Analysis of Soda-Lime and Borosilicate Glass. Technical report ASTM International. (see p. 33)

- Cabaret, D., Bordage, A., Juhin, A., Arfaoui, M. and Gaudry, E. (2010). First-principles calculations of X-ray absorption spectra at the K-edge of 3d transition metals: an electronic structure analysis of the pre-edge. *Physical Chemistry Chemical Physics* 12, 5619. (see p. 40)
- Calas, G. and Petiau, J. (1983a). Coordination of iron in oxide glasses through high-resolution K-edge spectra: Information from the pre-edge. *Solid State Communications* 48, 625–629. (see pp. 23, 24, 66, 101 and 237)
- Calas, G. and Petiau, J. (1983b). Structure of oxide glasses: Spectroscopic studies of local order and crystallochemistry. Geochemical implications. *Bulletin de Minéralogie* 106, 33–55. (see pp. 29, 49, 119 and 128)
- Calvin, S. (2013). XAFS for Everyone. CRC Press. (see p. 39)
- Camara, B. (1982). ESR study of the structure of Fe (III) in silicate glasses of different basicities. *Le Journal de Physique Colloques* 43, C9–165–C9–168. (see p. 50)
- Castner, T., Newell, G. S., Holton, W. C. and Slichter, C. P. (1960). Note on the Paramagnetic Resonance of Iron in Glass. *The Journal of Chemical Physics* 32, 668–673. (see p. 46)
- Charpentier, T., Ispas, S., Profeta, M., Mauri, F. and Pickard, C. J. (2004). First-Principles Calculation of  $^{17}\text{O}$ ,  $^{29}\text{Si}$ , and  $^{23}\text{Na}$  NMR Spectra of Sodium Silicate Crystals and Glasses. *The Journal of Physical Chemistry B* 108, 4147–4161. (see p. 145)
- Chopinnet, M.-H., Lizarazu, D. and Rocanière, C. (2002). L'importance des phénomènes d'oxydo-réduction dans le verre. *Comptes Rendus Chimie* 5, 939–949. (see p. 22)
- Ciampolini, M. (1969). Spectra of 3d five-coordinate complexes. In *Structure and Bonding*, (Jørgensen, C. K., Neilands, J. B., Nyholm, R. S., Reinen, D. and Williams, R. J. P., eds), vol. 6, pp. 52–93. Springer Berlin Heidelberg Berlin, Heidelberg. (see pp. 25 and 236)
- Cochain, B. (2009). Cinétique et mécanismes d'oxydoréduction dans les silicates fondus : études expérimentales de verres nucléaires simplifiés et d'échantillons naturels. Thèse de doctorat Paris VI - UPMC Paris, France. (see p. 22)
- Cormier, L., Gaskell, P. H., Calas, G. and Soper, A. K. (1998). Medium-range order around titanium in a silicate glass studied by neutron diffraction with isotopic substitution. *Physical Review B* 58, 11322–11330. (see p. 25)
- Cormier, L. and Neuville, D. R. (2004). Ca and Na environments in  $\text{Na}_2\text{O}$ – $\text{CaO}$ – $\text{Al}_2\text{O}_3$ – $\text{SiO}_2$  glasses: influence of cation mixing and cation-network interactions. *Chemical Geology* 213, 103–113. (see p. 142)
- Cowan, R. D. (1981). *The Theory of Atomic Structure and Spectra*. University of California Press. (see pp. 52, 61, 64, 229 and 230)

- Davis, K. and Tomozawa, M. (1996). An infrared spectroscopic study of water-related species in silica glasses. *Journal of Non-Crystalline Solids* 201, 177–198. (see p. 98)
- de Groot, F. (2001). High-resolution X-ray emission and X-ray absorption spectroscopy. *Chemical Reviews* 101, 1779–1808. (see pp. 42 and 61)
- de Groot, F. M. F., Glatzel, P., Bergmann, U., van Aken, P. A., Barrea, R. A., Klemme, S., Hävecker, M., Knop-Gericke, A., Heijboer, W. M. and Weckhuysen, B. M. (2005). 1s2p resonant inelastic X-ray scattering of iron oxides. *The journal of physical chemistry. B* 109, 20751–20762. (see pp. 61 and 219)
- de Groot, F. M. F. and Kotani, A. (2008). *Core Level Spectroscopy of Solids*. CRC Press. (see p. 53)
- Delaye, J. M., Cormier, L., Ghaleb, D. and Calas, G. (2001). Investigation of multicomponent silicate glasses by coupling WAXS and molecular dynamics. *Journal of Non-Crystalline Solids* 293–295, 290–296. (see p. 124)
- Densem, N. E. and Turner, W. E. S. (1938). The equilibrium between ferrous and ferric oxides in glasses. *J. Soc. Glass Technol* 22, 372–89. (see p. 22)
- Dowsing, R. D. and Gibson, J. F. (1969). Electron Spin Resonance of High-Spin  $d^5$  Systems. *The Journal of Chemical Physics* 50, 294–303. (see p. 49)
- Duffy, J. and Ingram, M. (1976). An interpretation of glass chemistry in terms of the optical basicity concept. *Journal of Non-Crystalline Solids* 21, 373–410. (see p. 34)
- Duffy, J. A. (1996). Redox equilibria in glass. *Journal of Non-Crystalline Solids* 196, 45–50. (see p. 22)
- Dunaeva, E., Uspenskaya, I., Pokholok, K., Minin, V., Efimov, N., Ugolkova, E. and Brunet, E. (2012). Coordination and RedOx ratio of iron in sodium-silicate glasses. *Journal of Non-Crystalline Solids* 358, 3089–3095. (see pp. 49, 121 and 122)
- Duttine, M., Villeneuve, G., Poupeau, G., Rossi, A. M. and Scorzelli, R. B. (2003). Electron spin resonance of  $Fe^{3+}$  ion in obsidians from Mediterranean islands. Application to provenance studies. *Journal of Non-Crystalline Solids* 323, 193–199. (see p. 49)
- Edwards, R. J., Paul, A. and Douglas, R. W. (1972). Spectroscopy and Oxidation-Reduction of Iron in  $MO-P_2O_5$  Glasses. *Physics and Chemistry of Glasses* 13, 137–143. (see p. 99)
- Ehrt, D. (2002). UV-absorption and radiation effects in different glasses doped with iron and tin in the ppm range. *Comptes Rendus Chimie* 5, 679–692. (see p. 110)
- Ehrt, D., Leister, M. and Matthai, A. (2001). Polyvalent elements iron, tin and titanium in silicate, phosphate and fluoride glasses and melts. *Physics and Chemistry of Glasses* 42, 231–239. (see p. 99)
- Elvers, A. and Weissmann, R. (2001). ESR spectroscopy : an analytical tool for the glass industry. *Glass science and technology* 74, 32–38. (see pp. 46, 50, 135 and 136)

- Farges, F. (2001). Crystal chemistry of iron in natural grandidierites: an X-ray absorption fine-structure spectroscopy study. *Physics and Chemistry of Minerals* 28, 619–629. (see p. 103)
- Farges, F., Lefrère, Y., Rossano, S., Berthereau, A., Calas, G. and Brown Jr., G. E. (2004). The effect of redox state on the local structural environment of iron in silicate glasses: a combined XAFS spectroscopy, molecular dynamics, and bond valence study. *Journal of Non-Crystalline Solids* 344, 176–188. (see pp. 25, 100, 101, 111 and 131)
- Faye, G. H. (1969). The Optical Absorption Spectrum of Tetrahedrally Bonded  $\text{Fe}^{3+}$  in Orthoclase. *The Canadian Mineralogist* 10, 112–117. (see p. 87)
- Figgis, B. N. and Hitchman, M. A. (2000). Ligand field theory and its applications. Wiley-VCH. (see p. 52)
- Flank, A.-M., Lagarde, P., Jupille, J. and Montigaud, H. (2011). Redox profile of the glass surface. *Journal of Non-Crystalline Solids* 357, 3200–3206. (see p. 22)
- Fortune, W. B. and Mellon, M. G. (1938). Determination of Iron with o-Phenanthroline: A Spectrophotometric Study. *Industrial & Engineering Chemistry Analytical Edition* 10, 60–64. (see p. 33)
- Fox, K. E., Furukawa, T. and White, W. B. (1982). Transition-metal ions in silicate melts: II, Iron in sodium silicate glasses. *Physics and Chemistry of Glasses* 23, 169–178. (see pp. 99, 100 and 207)
- Galoisy, L. and Calas, G. (1991). Spectroscopic evidence for five-coordinated Ni in  $\text{CaNiSi}_2\text{O}_6$  glass. *American Mineralogist* 76, 1777–1780. (see p. 25)
- Galoisy, L., Calas, G. and Arrio, M. A. (2001). High-resolution XANES spectra of iron in minerals and glasses: structural information from the pre-edge region. *Chemical Geology* 174, 307–319. (see p. 101)
- Gibbs, G. V., Ross, N. L., Cox, D. F. and Rosso, K. M. (2014). Insights into the crystal chemistry of Earth materials rendered by electron density distributions: Pauling's rules revisited. *American Mineralogist* 99, 1071–1084. (see p. 51)
- Glatzel, P. and Bergmann, U. (2005). High resolution 1s core hole X-ray spectroscopy in 3d transition metal complexes—electronic and structural information. *Coordination chemistry reviews* 249, 65–95. (see pp. 42 and 240)
- Glatzel, P. and Juhin, A. (2013). X-ray Absorption and Emission Spectroscopy. In *Local Structural Characterisation*, (Bruce, D. W., O'Hare, D. and Walton, R. I., eds), pp. 89–171. John Wiley & Sons, Ltd. (see p. 40)
- Glebov, L. and Boulos, E. (1998). Absorption of iron and water in the  $\text{Na}_2\text{O}$ – $\text{CaO}$ – $\text{MgO}$ – $\text{SiO}_2$  glasses. II. Selection of intrinsic, ferric, and ferrous spectra in the visible and UV regions. *Journal of Non-Crystalline Solids* 242, 49–62. (see p. 98)

- 
- Glebov, L., Boulos, E., Glebova, L. and Smirnova, T. (1998). Intrinsic UV absorption and coloration of the Na<sub>2</sub>O-CaO-MgO-SiO<sub>2</sub> glass by different form of iron. In Proceedings of 18th International Congress on Glass pp. 71–76,, San Francisco, USA. (see p. 109)
- Goldman, D. S. and Berg, J. I. (1980). Spectral study of ferrous iron in Ca-Al-borosilicate glass at room and melt temperatures. *Journal of Non-Crystalline Solids* 38–39, Part 1, 183–188. (see pp. 23 and 100)
- Goldman, D. S. and Gupta, P. K. (1983). Diffusion-Controlled Redox Kinetics in a Glassmelt. *Journal of the American Ceramic Society* 66, 188–190. (see p. 22)
- Gonçalves Ferreira, P., de Ligny, D., Lazzari, O., Jean, A., Cintora Gonzalez, O. and Neuville, D. (2013). Photoreduction of iron by a synchrotron X-ray beam in low iron content soda-lime silicate glasses. *Chemical Geology* 346, 106–112. (see pp. 215 and 216)
- Greaves, G. (1985). EXAFS and the structure of glass. *Journal of Non-Crystalline Solids* 71, 203–217. (see p. 21)
- Griffith, J. S. (1961). *The Theory of Transition-Metal Ions*. Cambridge University Press. (see p. 53)
- Griscom, D. L. (1980). Electron spin resonance in glasses. *Journal of Non-Crystalline Solids* 40, 211–272. (see pp. 46, 47, 49, 50 and 242)
- Guillot, B. and Sator, N. (2007). A computer simulation study of natural silicate melts. Part I: Low pressure properties. *Geochimica et Cosmochimica Acta* 71, 1249–1265. (see pp. 25, 26, 111 and 237)
- Gullikson, E. M. (2010). X-ray interactions with matter, CXRO, <http://www.cxro.lbl.gov>. (see p. 65)
- Hannant, O. M., Bingham, P. A., Hand, R. J. and Forder, S. D. (2008). The structural properties of iron in vitrified toxic waste ashes. *Glass Technology - European Journal of Glass Science and Technology Part A* 49, 27–32. (see p. 107)
- Hannoyer, B., Lenglet, M., Dürr, J. and Cortes, R. (1992). Spectroscopic evidence of octahedral iron (III) in soda-lime silicate glasses. *Journal of Non-Crystalline Solids* 151, 209–216. (see p. 115)
- Haverkort, M. W., Zwierzycki, M. and Andersen, O. K. (2012). Multiplet ligand-field theory using Wannier orbitals. *Physical Review B* 85, 165113. (see p. 61)
- Henderson, G. S., de Groot, F. M. F. and Moulton, B. J. A. (2014). X-ray Absorption Near-Edge Structure (XANES) Spectroscopy. *Reviews in Mineralogy and Geochemistry* 78, 75–138. (see p. 101)
- Henderson, G. S., Fleet, M. E. and Bancroft, G. M. (1984). An X-ray scattering study of vitreous KFeSi<sub>3</sub>O<sub>8</sub> and NaFeSi<sub>3</sub>O<sub>8</sub> and reinvestigation of vitreous SiO<sub>2</sub> using quasi-crystalline modelling. *Journal of Non-Crystalline Solids* 68, 333–349. (see p. 101)

- Higgins, J. B., Ribbe, P. H. and Nakajima, Y. (1982). An ordering model for the commensurate antiphase structure of yoderite. *American Mineralogist* 67, 76–84. (see p. 93)
- Hunault, M. (2014). Rôle des éléments de transition (Co, Cu) dans la coloration des verres : application aux vitraux du moyen âge. PhD thesis, Paris 6. (see pp. 58 and 231)
- Jackson, W. E., Farges, F., Yeager, M., Mabrouk, P. A., Rossano, S., Waychunas, G. A., Solomon, E. I. and Brown Jr, G. E. (2005). Multi-spectroscopic study of Fe(II) in silicate glasses: Implications for the coordination environment of Fe(II) in silicate melts. *Geochimica et Cosmochimica Acta* 69, 4315–4332. (see pp. 23, 24, 41, 100, 101, 111 and 145)
- Jaklevic, J., Kirby, J., Klein, M., Robertson, A., Brown, G. and Eisenberger, P. (1977). Fluorescence detection of exafs: Sensitivity enhancement for dilute species and thin films. *Solid State Communications* 23, 679–682. (see p. 40)
- Johnston, W. (1964). Oxidation-Reduction Equilibria in Iron-Containing Glass. *Journal of the American Ceramic Society* 47, 198–201. (see pp. 22 and 31)
- Juhin, A., Brouder, C., Arrio, M.-A., Cabaret, D., Saintavit, P., Balan, E., Bordage, A., Seitsonen, A. P., Calas, G., Eeckhout, S. G. and Glatzel, P. (2008). X-ray linear dichroism in cubic compounds: The case of  $\text{Cr}^{3+}$  in  $\text{MgAl}_2\text{O}_4$ . *Physical Review B* 78, 195103. (see pp. 59 and 243)
- Juhin, A., Brouder, C. and de Groot, F. M. F. (2014). Angular dependence of resonant inelastic x-ray scattering: a spherical tensor expansion. *Central European Journal of Physics* 12, 323–340. (see pp. 62, 219, 220 and 223)
- Jørgensen, C. K. (1971). *Modern aspects of ligand field theory*. North-Holland Amsterdam. (see pp. 51 and 52)
- Jørgensen, C. K., de Verdier, C.-H., Glomset, J. and Sørensen, N. A. (1954). Studies of Absorption Spectra. III. Absorption Bands as Gaussian Error Curves. *Acta Chemica Scandinavica* 8, 1495–1501. (see p. 209)
- Kilcoyne, S. H. and Cywinski, R. (1995). Ferritin: a model superparamagnet. *Journal of Magnetism and Magnetic Materials* 140–144, Part 2, 1466–1467. (see p. 122)
- Kittel, C. (2004). *Introduction to Solid State Physics*. Wiley. (see pp. 44, 45 and 122)
- Koksharov, Y. A., Gubin, S. P., Kosobudsky, I. D., Beltran, M., Khodorkovsky, Y. and Tishin, A. M. (2000). Low temperature electron paramagnetic resonance anomalies in Fe-based nanoparticles. *Journal of Applied Physics* 88, 1587. (see pp. 49 and 50)
- Krause, M. O. and Oliver, J. H. (1979). Natural widths of atomic K and L levels,  $K\alpha$  X-ray lines and several KLL Auger lines. *Journal of Physical and Chemical Reference Data* 8, 329–338. (see p. 213)

- 
- Kress, V. and Carmichael, I. (1991). The compressibility of silicate liquids containing  $\text{Fe}_2\text{O}_3$  and the effect of composition, temperature, oxygen fugacity and pressure on their redox states. *Contributions to Mineralogy and Petrology* 108, 82–92. (see pp. 22 and 31)
- Kurian, R., Kunnus, K., Wernet, P., Butorin, S. M., Glatzel, P. and Groot, F. M. F. d. (2012). Intrinsic deviations in fluorescence yield detected x-ray absorption spectroscopy: the case of the transition metal L 2,3 edges. *Journal of Physics: Condensed Matter* 24, 452201. (see p. 40)
- Kurkjian, C. R. and Sigety, E. A. (1968). Co-ordination of  $\text{Fe}^{3+}$  in glass. *Physics and Chemistry of Glasses* 9, 73–83. (see pp. 49, 50, 87 and 121)
- König, E. and Kremer, S. (1977). *Ligand field energy diagrams*. Plenum Press. (see pp. 56, 89 and 231)
- Langer, K., Smith, G. and Hålenius, U. (1982). Reassignment of the absorption spectra of purple yoderite. *Physics and Chemistry of Minerals* 8, 143–145. (see pp. 94, 95, 112, 114 and 115)
- Lefrère, Y. (2002). *Propriétés d'absorption optique du  $\text{Fe}^{2+}$  et du  $\text{Fe}^{3+}$  dans des verres d'intérêt industriel : mesure, modélisation et implications structurales*. Thèse doctorat Paris VII - Diderot Paris, France. (see p. 126)
- Lever, A. B. P. (1984). *Inorganic electronic spectroscopy*. Elsevier. (see pp. 52, 53, 55, 57, 72, 75, 231, 232 and 237)
- Lin, C. (1981). Optical absorption spectra of  $\text{Fe}^{2+}$  and  $\text{Fe}^{3+}$  in garnets. *Bull Mineral* 104, 218–222. (see p. 114)
- Loeffler, B. M., Burns, R. G., Johnson, K. H., Tossell, J. A. and Vaughan, D. J. (1974). Charge transfer in lunar materials - Interpretation of ultraviolet-visible spectral properties of the moon. *Proceedings of the Fifth Lunar Conference* 5, 3007–3016. (see p. 132)
- Ludwig, W. and Falter, C. (1988). *Symmetries in Physics*, vol. 64, of Springer Series in Solid-State Sciences. Springer Berlin Heidelberg, Berlin, Heidelberg. (see p. 27)
- Manning, P. G. (1970). Racah parameters and their relationship to lengths and covalencies of  $\text{Mn}^{2+}$ - and  $\text{Fe}^{3+}$ -oxygen bonds in silicates. *The Canadian Mineralogist* 10, 677–688. (see p. 115)
- Miché, C. (1985). *Équilibres rédox du fer dans le système  $\text{Na}_2\text{O}-\text{Al}_2\text{O}_3-\text{SiO}_2$  / Iron redox equilibria in the  $\text{Na}_2\text{O}-\text{Al}_2\text{O}_3-\text{SiO}_2$  system*. PhD thesis, Paris 7 Paris, France. (see p. 87)
- Montenero, A., Friggeri, M., Giori, D. C., Belkhiria, N. and Pye, L. D. (1986). Iron-soda-silica glasses: Preparation, properties, structure. *Journal of Non-Crystalline Solids* 84, 45–60. (see pp. 49, 50, 118 and 121)
- Moon, D. W., Aitken, J. M., MacCrone, R. K. and Cieloszyk, G. S. (1975). Magnetic properties and structure of  $x\text{Fe}_2\text{O}_3, (1-x)[\text{BaO}, 4\text{B}_2\text{O}_3]$  glasses. *Physics and Chemistry of Glasses* 16, 91–102. (see p. 49)



- Morgan, G. B. and London, D. (2005). Effect of current density on the electron microprobe analysis of alkali aluminosilicate glasses. *American Mineralogist* 90, 1131–1138. (see p. 215)
- Mysen, B. O. and Richet, P. (2005). *Silicate Glasses and Melts: Properties and Structure*. Elsevier. (see p. 22)
- Nesbitt, H. W. and Bancroft, G. M. (2014). High Resolution Core- and Valence-Level XPS Studies of the Properties (Structural, Chemical and Bonding) of Silicate Minerals and Glasses. *Reviews in Mineralogy and Geochemistry* 78, 271–329. (see p. 215)
- Neuville, D. R., Cormier, L. and Caurant, D. (2013). *Du verre au cristal: Nucléation, croissance et démixtion, de la recherche aux applications*. EDP Sciences. (see p. 21)
- Nolet, D. A. (1980). Optical absorption and Mössbauer spectra of Fe, Ti silicate glasses. *Journal of Non-Crystalline Solids* 37, 99–110. (see p. 23)
- Ookawa, M., Sakurai, T., Mogi, S. and Yokokawa, T. (1997). Optical spectroscopic study of lead silicate glasses doped heavily with iron oxide. *Materials transactions-JIM* 38, 220–225. (see pp. 60 and 99)
- Paul, A. (1985). Effect of thermal stabilization on redox equilibria and colour of glass. *Journal of Non-Crystalline Solids* 71, 269–278. (see p. 32)
- Paul, A. (1990). Oxidation-reduction equilibrium in glass. *Journal of Non-Crystalline Solids* 123, 354–362. (see p. 22)
- Paul, A. and Douglas, R. W. (1965). Ferrous-ferric equilibrium in binary alkali silicate glasses. *Physics and Chemistry of Glasses* 6, 207. (see p. 22)
- Petit, P.-E., Farges, F., Wilke, M. and Solé, V. A. (2001). Determination of the iron oxidation state in Earth materials using XANES pre-edge information. *Journal of Synchrotron Radiation* 8, 952–954. (see p. 101)
- Pigeonneau, F. and Muller, S. (2013). The impact of iron content in oxidation front in soda-lime silicate glasses: An experimental and comparative study. *Journal of Non-Crystalline Solids* 380, 86–94. (see pp. 22 and 32)
- Pol'shin, E. V., Platonov, A. N., Borutzky, B. E., Taran, M. N. and Rastsvetaeva, R. K. (1991). Optical and mössbauer study of minerals of the eudialyte group. *Physics and Chemistry of Minerals* 18, 117–125. (see p. 25)
- Pyare, R. and Nath, P. (1984). Kinetics and thermodynamics of ferrous-ferric equilibrium in sodium aluminoborate glasses. *Journal of Non-Crystalline Solids* 69, 59–67. (see p. 22)
- Ravel, B. and Newville, M. (2005). *ATHENA, ARTEMIS, HEPHAESTUS*: data analysis for X-ray absorption spectroscopy using *IFEFFIT*. *Journal of Synchrotron Radiation* 12, 537–541. (see p. 41)

- 
- Reid, A. F., Perkins, H. K. and Sienko, M. J. (1968). Magnetic, electron spin resonance, optical, and structural studies of the isomorphous series  $\text{Na}(\text{Sc,Fe})\text{TiO}_4$ . *Inorganic Chemistry* *7*, 119–126. (see p. 121)
- Richet, P., Robie, R. A. and Hemingway, B. S. (1986). Low-temperature heat capacity of diopside glass ( $\text{CaMgSi}_2\text{O}_6$ ): A calorimetric test of the configurational-entropy theory applied to the viscosity of liquid silicates. *Geochimica et Cosmochimica Acta* *50*, 1521–1533. (see p. 34)
- Richet, P., Roskosz, M. and Roux, J. (2006). Glass formation in silicates: Insights from composition. *Chemical geology* *225*, 388–401. (see p. 125)
- Rossano, S., Balan, E., Morin, G., Bauer, J.-P., Calas, G. and Brouder, C. (1999).  $^{57}\text{Fe}$  Mössbauer spectroscopy of tektites. *Physics and Chemistry of Minerals* *26*, 530–538. (see pp. 23, 25 and 237)
- Rossano, S., Behrens, H. and Wilke, M. (2008). Advanced analyses of  $(^{57}\text{Fe})$  Mossbauer data of alumino-silicate glasses. *Physics and Chemistry of Minerals* *35*, 77–93. (see p. 24)
- Rossano, S., Brouder, C., Alouani, M. and Arrio, M. A. (2000a). Calculated optical absorption spectra of  $\text{Ni}^{2+}$ -bearing compounds. *Physics and Chemistry of Minerals* *27*, 170–178. (see pp. 59, 95 and 242)
- Rossano, S., Ramos, A. and Delaye, J.-M. (2000b). Environment of ferrous iron in  $\text{CaFeSi}_2\text{O}_6$  glass; contributions of EXAFS and molecular dynamics. *Journal of Non-Crystalline Solids* *273*, 48–52. (see p. 119)
- Rossano, S., Ramos, A., Delaye, J.-M., Creux, S., Filipponi, A., Brouder, C. and Calas, G. (2000c). EXAFS and Molecular Dynamics combined study of  $\text{CaO-FeO-2SiO}_2$  glass. New insight into site significance in silicate glasses. *EPL (Europhysics Letters)* *49*, 597. (see pp. 24, 25, 100 and 237)
- Rossman, G. R. (2014). Optical Spectroscopy. *Reviews in Mineralogy and Geochemistry* *78*, 371–398. (see pp. 35, 109 and 239)
- Rossman, G. R. and Taran, M. N. (2001). Spectroscopic standards for four- and fivefold-coordinated  $\text{Fe}^{2+}$  in oxygen-based minerals. *American Mineralogist* *86*, 896–903. (see pp. 25, 79, 81, 91, 92, 99 and 236)
- Rovezzi, M. and Glatzel, P. (2014). Hard x-ray emission spectroscopy: a powerful tool for the characterization of magnetic semiconductors. *Semiconductor Science and Technology* *29*, 023002. (see p. 42)
- Rueff, J. and Shukla, A. (2013). A RIXS cookbook: Five recipes for successful RIXS applications. *Journal of Electron Spectroscopy and Related Phenomena* *188*, 10–16. (see p. 42)

- Rüssel, C. (1993). Iron Oxide-Doped Alkali Lime Silica Glasses. 1. EPR Investigations. *Glastechnische Berichte-Glass Science and Technology* 66, 68–75. (see pp. 49 and 122)
- Rüssel, C. and Wiedenroth, A. (2004). The effect of glass composition on the thermodynamics of the  $\text{Fe}^{2+}/\text{Fe}^{3+}$  equilibrium and the iron diffusivity in  $\text{Na}_2\text{O}/\text{MgO}/\text{CaO}/\text{Al}_2\text{O}_3/\text{SiO}_2$  melts. *Chemical Geology* 213, 125–135. (see p. 22)
- Sakaguchi, K. and Uchino, T. (2007). Compositional dependence of infrared absorption of iron-doped silicate glasses. *Journal of Non-Crystalline Solids* 353, 4753–4761. (see pp. 22, 119, 121, 127 and 235)
- Schmetzer, K., Burford, M., Kiefert, L. and Bernhardt, H. J. (2003). The first transparent faceted grandidierite, from Sri Lanka. *Gems & Gemology* 39, 32–37. (see pp. 90 and 109)
- Schofield, P. F., Van Der Laan, G., Henderson, C. M. B. and Cressey, G. (1998). A single crystal, linearly polarized Fe 2p X-ray absorption study of gillespite. *Mineralogical Magazine* 62, 65–75. (see p. 79)
- Scholze, H. (1980). *Le Verre : nature, structure et propriétés*. Institut du Verre. (see p. 21)
- Schreiber, H. D. (1986). Redox processes in glass-forming melts. *Journal of Non-Crystalline Solids* 84, 129–141. (see p. 22)
- Schreiber, H. D., Balazs, G. B., Shaffer, A. P. and Jamison, P. L. (1982). Iron metal production in silicate melts through the direct reduction of Fe(II) by Ti(III), Cr(II), and Eu(II). *Geochimica et Cosmochimica Acta* 46, 1891–1901. (see p. 22)
- Schreiber, H. D., Kochanowski, B. K., Schreiber, C. W., Morgan, A. B., Coolbaugh, M. and Dunlap, T. G. (1994). Compositional dependence of redox equilibria in sodium silicate glasses. *Journal of Non-Crystalline Solids* 177, 340–346. (see p. 22)
- Seifert, F. and Olesch, M. (1977). Mössbauer spectroscopy of grandidierite,  $(\text{Mg,Fe})\text{Al}_3\text{BSiO}_9$ . *American Mineralogist* 62, 547–553. (see p. 25)
- Shelby, J. E. (2005). *Introduction to Glass Science and Technology*. Royal Society of Chemistry. (see p. 21)
- Sigel, G. H. and Ginther, R. J. (1968). The effect of iron on the ultraviolet absorption of high purity soda-silica glass. *Glass Technology* 9, 66–69. (see p. 110)
- Solé, V. A., Papillon, E., Cotte, M., Walter, P. and Susini, J. (2007). A multiplatform code for the analysis of energy-dispersive X-ray fluorescence spectra. *Spectrochimica Acta Part B: Atomic Spectroscopy* 62, 63–68. (see p. 41)
- Spaldin, N. A. (2010). *Magnetic Materials: Fundamentals and Applications*. Cambridge University Press. (see p. 44)
- Steele, F. N. and Douglas, R. W. (1965). Some observations on the absorption of iron in silicate and borate glasses. *Physics and Chemistry of Glasses* 6, 246. (see pp. 110 and 206)

- 
- Stephenson, D. A. and Moore, P. B. (1968). The crystal structure of grandidierite,  $(\text{Mg,Fe})\text{Al}_3\text{SiBO}_9$ . *Acta Crystallographica Section B Structural Crystallography and Crystal Chemistry* *24*, 1518–1522. (see p. 92)
- Stålhandske, C. (2000). The impact of refining agents on glass colour. *Glasteknisk Tidskrift* *55*, 65–71. (see p. 31)
- Sørensen, P. M., Pind, M., Yue, Y. Z., Rawlings, R. D., Boccaccini, A. R. and Nielsen, E. R. (2005). Effect of the redox state and concentration of iron on the crystallization behavior of iron-rich aluminosilicate glasses. *Journal of Non-Crystalline Solids* *351*, 1246–1253. (see p. 22)
- Tanabe, Y. and Sugano, S. (1954a). On the Absorption Spectra of Complex Ions II. *Journal of the Physical Society of Japan* *9*, 766. (see p. 56)
- Tanabe, Y. and Sugano, S. (1954b). On the Absorption Spectra of Complex Ions. I. *Journal of the Physical Society of Japan* *9*, 753. (see p. 56)
- Tanabe, Y. and Sugano, S. (1956). On the Absorption Spectra of Complex Ions, III The Calculation of the Crystalline Field Strength. *Journal of the Physical Society of Japan* *11*, 864–877. (see pp. 51 and 56)
- Taran, M. N., Dyar, M. D. and Matsyuk, S. S. (2007). Optical Absorption Study of Natural Garnets of Almandine-Skiagite Composition Showing Intervalence  $\text{Fe}^{2+} + \text{Fe}^{3+} \rightarrow \text{Fe}^{3+} + \text{Fe}^{2+}$  Charge-Transfer Transition. *American Mineralogist* *92*, 753–760. (see p. 138)
- Taran, M. N. and Koch-Müller, M. (2011). Optical absorption of electronic Fe–Ti charge-transfer transition in natural andalusite: the thermal stability of the charge-transfer band. *Physics and Chemistry of Minerals* *38*, 215–222. (see p. 30)
- Thole, B. T. and van der Laan, G. (1988). Linear relation between x-ray absorption branching ratio and valence-band spin-orbit expectation value. *Physical Review A* *38*, 1943–1947. (see p. 217)
- Thole, B. T., van der Laan, G., Fuggle, J. C., Sawatzky, G. A., Karnatak, R. C. and Esteva, J.-M. (1985). 3d x-ray-absorption lines and the  $3d^9 4f^{m+1}$  multiplets of the lanthanides. *Physical Review B* *32*, 5107–5118. (see pp. 61 and 64)
- Trcera, N., Cabaret, D., Rossano, S., Farges, F., Flank, A.-M. and Lagarde, P. (2009). Experimental and theoretical study of the structural environment of magnesium in minerals and silicate glasses using X-ray absorption near-edge structure. *Physics and Chemistry of Minerals* *36*, 241–257. (see p. 142)
- Tröger, L., Arvanitis, D., Baberschke, K., Michaelis, H., Grimm, U. and Zschech, E. (1992). Full correction of the self-absorption in soft-fluorescence extended x-ray-absorption fine structure. *Physical Review B* *46*, 3283–3289. (see p. 40)

- Uchino, T., Nakaguchi, K., Nagashima, Y. and Kondo, T. (2000). Prediction of optical properties of commercial soda–lime–silicate glasses containing iron. *Journal of Non-Crystalline Solids* *261*, 72–78. (see pp. 22 and 235)
- Van Vleck, J. H. and Sherman, A. (1935). The Quantum Theory of Valence. *Reviews of Modern Physics* *7*, 167–228. (see p. 51)
- Vankó, G., de Groot, F. M. F., Huotari, S., Cava, R. J., Lorenz, T. and Reuther, M. (2008). Intersite  $4p$ - $3d$  hybridization in cobalt oxides: a resonant x-ray emission spectroscopy study. arXiv:0802.2744 -. (see pp. 61 and 139)
- Varshalovich, D. A., Moskalev, A. N. and Khersonskii, V. K. (1988). Quantum theory of angular momentum. World Scientific Pub., Singapore, Teaneck, NJ, USA. (see pp. 224 and 225)
- Villain, O., Galois, L. and Calas, G. (2010). Spectroscopic and structural properties of  $\text{Cr}^{3+}$  in silicate glasses:  $\text{Cr}^{3+}$  does not probe the average glass structure. *Journal of Non-Crystalline Solids* *356*, 2228–2234. (see p. 140)
- Volotinen, T., Parker, J. and Bingham, P. (2008). Concentrations and site partitioning of  $\text{Fe}^{2+}$  and  $\text{Fe}^{3+}$  ions in a sodalimesilica glass obtained by optical absorbance spectroscopy. *Physics and Chemistry of Glasses - European Journal of Glass Science and Technology Part B* *49*, 258–270. (see pp. 87, 114 and 209)
- Watanabe, S., Sasaki, T., Taniguchi, R., Ishii, T. and Ogasawara, K. (2009). First-principles calculation of ground and excited-state absorption spectra of ruby and alexandrite considering lattice relaxation. *Physical Review B* *79*, 075109. (see p. 59)
- Waychunas, G. A., Apter, M. J. and Jr, G. E. B. (1983). X-ray K-edge absorption spectra of Fe minerals and model compounds: Near-edge structure. *Physics and Chemistry of Minerals* *10*, 1–9. (see p. 101)
- Weigel, C., Cormier, L., Calas, G., Galois, L. and Bowron, D. T. (2008a). Intermediate-range order in the silicate network glasses  $\text{NaFe}_x\text{Al}_{1-x}\text{Si}_2\text{O}_6$  ( $x=0, 0.5, 0.8, 1$ ): A neutron diffraction and empirical potential structure refinement modeling investigation. *Physical Review B* *78*. (see pp. 23, 25, 96 and 111)
- Weigel, C., Cormier, L., Calas, G., Galois, L. and Bowron, D. T. (2008b). Nature and distribution of iron sites in a sodium silicate glass investigated by neutron diffraction and EPSR simulation. *Journal of Non-Crystalline Solids* *354*, 5378–5385. (see pp. 24, 100, 119, 122 and 237)
- Weigel, C., Cormier, L., Galois, L., Calas, G., Bowron, D. and Beuneu, B. (2006). Determination of  $\text{Fe}^{3+}$  sites in a  $\text{NaFeSi}_2\text{O}_6$  glass by neutron diffraction with isotopic substitution coupled with numerical simulation. *Applied Physics Letters* *89*. (see p. 96)
- Weil, M. (2004).  $\text{Fe}^{\text{II}}_3\text{Fe}^{\text{III}}_4(\text{AsO}_4)_6$ , the first arsenate adopting the  $\text{Fe}_7(\text{PO}_4)_6$  structure type. *Acta Crystallographica Section E Structure Reports Online* *60*, i139–i141. (see p. 25)

- 
- Westre, T. E., Kennepohl, P., DeWitt, J. G., Hedman, B., Hodgson, K. O. and Solomon, E. I. (1997). A Multiplet Analysis of Fe K-Edge  $1s \rightarrow 3d$  Pre-Edge Features of Iron Complexes. *Journal of the American Chemical Society* *119*, 6297–6314. (see pp. 39, 53, 61, 66, 72 and 78)
- Wilke, M., Farges, F., Petit, P.-E., Brown, G. E. and Martin, F. (2001). Oxidation state and coordination of Fe in minerals: An Fe K-XANES spectroscopic study. *American Mineralogist* *86*, 714–730. (see pp. 25, 41, 93, 94, 96 and 120)
- Wright, A. C., Clarke, S. J., Howard, C. K., Bingham, P. A., Forder, S. D., Holland, D., Martlew, D. and Fischer, H. E. (2014). The environment of  $Fe^{2+}/Fe^{3+}$  cations in a soda–lime–silica glass. *Physics and Chemistry of Glasses* *55*, 243–252. (see p. 24)
- Yahiaoui, E., Berger, R., Servant, Y., Kliava, J., Dugunov, L. and Mednis, A. (1994). Electron-Paramagnetic-Resonance of  $Fe^{3+}$  Ions in Borate Glass - Computer-Simulations. *Journal of Physics-Condensed Matter* *6*, 9415–9428. (see pp. 118 and 121)
- Yamashita, M., Akai, T., Sawa, R., Abe, J. and Matsumura, M. (2008). Effect of preparation procedure on redox states of iron in soda-lime silicate glass. *Journal of Non-Crystalline Solids* *354*, 4534–4538. (see p. 22)
- Zachariasen, W. H. (1932). The atomic arrangement in glass. *Journal of the American Chemical Society* *54*, 3841–3851. (see p. 21)
- Zhang, J. and Sheng, J. (2013). Metastable defects induced by X-ray irradiation in Fe-doped soda-lime silicate glass. *Optical Materials* *35*, 1138–1140. (see p. 216)

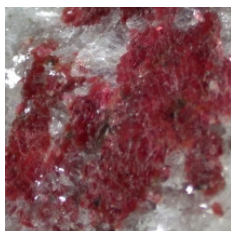


## Appendix A

# Crystalline references data

This section presents a brief overview of the 14 crystalline reference compounds used to interpret the spectroscopic signatures of glasses. The spectroscopic methods were presented in Chapter 2, for each reference, there are additional data from literature (site geometry, distances, redox, cell setting...). In the wide possibility of minerals, few iron crystalline references representative of the studied glasses were selected. When it was possible, silicate minerals with iron in one valence state were favored in order to simplify the interpretation of spectroscopic signatures due to their close compositions and similar signatures for iron environments. Some references present Fe-clusters (corner-sharing, edge-sharing...) with potential Fe–Fe magnetic interactions.

### Gillespite ( $[4,SP]Fe^{2+}$ )



Pink phyllosilicate mineral ( $BaFeSi_4O_{10}$ ) from Incline, California, with 15.43 wt% FeO. Iron is present as  $[4]Fe^{2+}$  with a square-planar geometry. There are no Fe–O–Fe clusters ( $Fe^{2+}$  are isolated). The pink color suggests that this environment is not present in glasses, nevertheless, gillespite composition and environment is simple and interesting to compare with glasses.

### Staurolite ( $[4,Td]Fe^{2+}$ )



Dark orthosilicate mineral ( $Fe_4Al_{18}Si_8O_{46}(OH)_2$ ) from Brittany, France, with 12.4 wt% FeO. Iron is present as  $[4]Fe^{2+}$  in a distorted tetrahedral site T2 due to different ligands (2 O and 2 OH). Tetrahedra share a face with an empty octahedral site (occupancy of the M4 site <1%), thus tetrahedral site containing iron are considered isolated.

### Chromite ( $[4,Td]Fe^{2+}$ )



Black chromium based spinel ( $Fe^{2+}Cr_2^{3+}O_4$ ) from an unknown locality, our natural sample had Fe substituted by Mg and Cr substituted by Al (EMPA:  $Fe_{0.3}Mg_{0.7}Cr_{0.8}Al_{1.2}O_4$  and 12.87 wt% FeO). Stoichiometry gives a redox of 97%. Iron is mainly present as  $[4]Fe^{2+}$  in isolated tetrahedral sites, but impurities of  $Fe^{3+}$  in octahedral sites may exist.



**Grandidierite ( $[^5]\text{Fe}^{2+}$ )**

Blue-green orthosilicate mineral  $((\text{Mg}, \text{Fe})\text{Al}_3(\text{BO}_4)(\text{SiO}_4)\text{O})$  from Ampamatoa, Madagascar, with 5.0 wt% FeO and an exceptional redox close to 99%. One of the rare minerals with ferrous iron substituting  $\text{Mg}^{2+}$  in [5]-fold coordinated isolated distorted triangular bipyramid. We kept only the blue-green crystals (grandidierite) and removed mica (black) and quartz (white).

**Siderite- $\text{FeCO}_3$  ( $[^6]\text{Fe}^{2+}$ )**

Yellow-brown carbonate mineral  $(\text{FeCO}_3)$  from an unknown locality, with 62 wt% FeO. Iron is present as  $[^6]\text{Fe}^{2+}$  in a slightly distorted, almost regular octahedral site sharing all corners with other octahedra.

**Hypersthene ( $[^6]\text{Fe}^{2+}$ )**

Orthopyroxene silicate  $((\text{Fe}^{2+}, \text{Mg})_2\text{Si}_2\text{O}_6)$ , similar to bronzite, from an unknown locality contains 31 wt% FeO. Fe substitutes Al in the enstatite mineral, iron is present as  $[^6]\text{Fe}^{2+}$  in an isolated distorted octahedron site (M2). Despite the high amount of iron there is no cluster.

**Diopside ( $[^6]\text{Fe}^{2+}$ )**

Silicate mineral  $(\text{CaMg}_{0.9}\text{Fe}_{0.1}\text{Si}_2\text{O}_6)$  from Pakistan, with 1.66 wt% FeO that gave a pale green color. Iron is present as  $[^6]\text{Fe}^{2+}$  in an isolated almost regular octahedron.

 **$\text{FePO}_4$  ( $[^4]\text{Fe}^{3+}$ )**

Yellow-brown synthetic phosphate  $(\text{FePO}_4)$  also named Fe-berlinite has several polymorphs such as rodolicoite, heterosite. Iron is present with 53 wt%  $\text{Fe}_2\text{O}_3$  as  $[^4]\text{Fe}^{3+}$  in slightly distorted tetrahedra. Despite the high amount of iron, iron is considered isolated because Fe-tetrahedra do not share oxygen atoms.

**Ferriorthoclase ( $[^4]\text{Fe}^{3+}$ )**

Transparent yellow silicate feldspar  $(\text{Fe} : \text{KAlSi}_3\text{O}_8)$  from Itrongay, Madagascar,  $\text{Fe}^{3+}$  is an impurity substituting  $\text{Al}^{3+}$ . Iron is present with 0.5~1 wt%  $\text{Fe}_2\text{O}_3$  as  $[^4]\text{Fe}^{3+}$  in slightly distorted tetrahedron without Fe-Fe interactions.

**Yoderite ( $^{[5]}\text{Fe}^{3+}$ )**

Purple orthosilicate mineral  $((\text{Mg}, \text{Al}, ^{[5]}\text{Fe})_8\text{Si}_4(\text{O}, \text{OH})_{20})$  probably from Mautia Hills, Tanzania, with 6.1 wt%  $\text{Fe}_2\text{O}_3$ . The purple color is due to Mn impurities. Yoderite also exists in green (not studied here). One of the rare samples containing [5]-fold coordinated ferric iron in isolated distorted triangular bipyramid (crystallographic site M3).

 **$\text{Fe}_3\text{PO}_7$** 

Red-brown synthetic phosphate with 77 wt%  $\text{Fe}_2\text{O}_3$ . Iron is present as  $^{[5]}\text{Fe}^{3+}$  in groups of 3 edge-sharing distorted trigonal bipyramids ([5]-fold) linked to other Fe by corners.

**Andradite ( $^{[6]}\text{Fe}^{3+}$ )**

Transparent green silicate  $(\text{Ca}_3\text{Fe}_2\text{Si}_3\text{O}_{12})$ , this garnet from Val Malenco, Italy, contains 31 wt%  $\text{Fe}_2\text{O}_3$  where iron is present as  $^{[6]}\text{Fe}^{3+}$  in an almost regular isolated octahedron distorted along the  $C_3$  axis. Samples contain some Cr impurity resulting in this shiny green color.

**Acmite ( $^{[6]}\text{Fe}^{3+}$ )**

This black silicate mineral is a pyroxen also named aegirine  $(\text{NaFeSi}_2\text{O}_6)$  from Mont Saint Hilaire, Quebec, with 34.6 wt%  $\text{Fe}_2\text{O}_3$ . Iron is present as  $^{[6]}\text{Fe}^{3+}$  in edge-sharing distorted octahedron.

**Maghemite  $\gamma\text{-Fe}_2\text{O}_3$  ( $^{[4,6]}\text{Fe}^{3+}$ )**

This polymorph of iron (III) oxide  $\text{Fe}_2\text{O}_3$  with a red-brown color has a spinel structure where iron is present in both  $^{[4]}\text{Fe}^{3+}$  and  $^{[6]}\text{Fe}^{3+}$ . The formula is:  $(\text{Fe}_8^{\text{III}})_{\text{T}_d}[\text{Fe}_{40/3}^{\text{III}}\square_{8/3}]_{\text{O}_h}\text{O}_{32}$ .  $\square$  represents a vacancy,  $\text{T}_d$  a tetrahedral site and  $\text{O}_h$  an octahedral site. Octahedra are linked to each other by the edges and to tetrahedra by corners.

Table A.1 compiles the studied crystalline references presented below. They are detailed with structural representations, spectroscopic data and bibliographic references in Appendix A .

**Table A.1** – Summary of studied crystalline references. Densities are expressed in  $10^3 \cdot \text{kg}/\text{m}^3$ .

name	iron site	site geometry (point group)	concentration	density	clusters
gillespite	$^{[4]}\text{Fe}^{2+}$	square planar ( $D_{4h}$ )	15.4 wt% FeO	3.33	no
staurolite	$^{[4]}\text{Fe}^{2+}$	distorted tetrahedron ( $C_{2v}$ )	12.4 wt% FeO	3.71	no
chromite	$^{[4]}\text{Fe}^{2+}$	regular tetrahedron ( $T_d$ )	12.9 wt% FeO	4.6	no
grandidierite	$^{[5]}\text{Fe}^{2+}$	distorted triangular bipyramid ( $C_s$ )	5.0 wt% FeO	2.99	no
siderite	$^{[6]}\text{Fe}^{2+}$	regular octahedron ( $O_h$ )	62 wt% FeO	3.96	corner-sharing
hypersthene	$^{[6]}\text{Fe}^{2+}$	distorted octahedron ( $C_{2v}$ )	31 wt% FeO	3.55	no
diopside	$^{[6]}\text{Fe}^{2+}$	almost regular octahedron ( $O_h$ )	1.7 wt% FeO	3.3	no
$\text{FePO}_4$	$^{[4]}\text{Fe}^{3+}$	slightly distorted tetrahedron ( $T_d$ )	53 wt% $\text{Fe}_2\text{O}_3$	3.07	no
ferriorthoclase	$^{[4]}\text{Fe}^{3+}$	tetrahedron ( $T_d$ )	1 wt% $\text{Fe}_2\text{O}_3$	2.56	no
yoderite	$^{[5]}\text{Fe}^{3+}$	distorted triangular bipyramid ( $C_{3v}$ )	6.1 wt% $\text{Fe}_2\text{O}_3$	3.39	no
$\text{Fe}_3\text{PO}_7$	$^{[5]}\text{Fe}^{3+}$	distorted triangular bipyramid ( $C_s$ )	77 wt% $\text{Fe}_2\text{O}_3$	4.07	groups of 3 edge-sharing sites, groups are linked to each-other by corners
andradite	$^{[6]}\text{Fe}^{3+}$	almost regular octahedron ( $C_{3i} = S_6$ )	31 wt% $\text{Fe}_2\text{O}_3$	3.9	no
acmite	$^{[6]}\text{Fe}^{3+}$	distorted octahedron ( $C_2$ )	34.6 wt% $\text{Fe}_2\text{O}_3$	3.52	edge-sharing
maghemite	$^{[4,6]}\text{Fe}^{3+}$	almost regular octahedron ( $T_d$ and $O_h$ )	100 wt% $\text{Fe}_2\text{O}_3$	4.9	edge-sharing octahedra linked to tetrahedra by corners

For each crystalline reference, the following data from XES  $K\beta$  main, XES  $K\beta$  satellite (i.e. V2C: Valence to Core), RIXS  $K\alpha$ , HERFD and TFY are experimental results.

X-ray emission spectroscopy (XES) is a 2-step process obtained by (1) putting an electron of the core shell  $1s$  into the continuum with the X-ray beam, (2) measuring the fluorescence photon resulting of the decay of the iron atom.  $K\alpha$  lines result of the transition  $2p \rightarrow 1s$ ,  $K\beta$  main lines result of the transition  $3p \rightarrow 1s$ ,  $K\beta$  satellite lines result of the transition valence electron to  $1s$  level.

The isotropic optical absorption spectra are calculated from  $\frac{\varepsilon_x + \varepsilon_y + \varepsilon_z}{3}$ , with x, y and z are any perpendicular directions. In this document, we approximate  $\alpha$ ,  $\beta$  and  $\gamma$  (lattice system) as perpendicular axis (but is not necessary the case). True for: orthorhombique, tetragonal, cubic systems. False for: triclinic, monoclinic, rhombohedral, hexagonal systems.

Geometry, distances and the 2 figures of the sites are taken from mineral databases (XRD references at the bottom of each page)

For more details, see <http://rruff.geo.arizona.edu/AMS/amcsd.php>

**Table of contents**

Gillespite ( $^{[4]}\text{Fe}^{2+}$ )	2
Staurolite ( $^{[4]}\text{Fe}^{2+}$ )	4
Chromite ( $^{[4]}\text{Fe}^{2+}$ )	6
Grandidierite ( $^{[5]}\text{Fe}^{2+}$ )	8
Siderite- $\text{FeCO}_3$ ( $^{[6]}\text{Fe}^{2+}$ )	10
Hypersthene ( $^{[6]}\text{Fe}^{2+}$ )	12
Diopside ( $^{[6]}\text{Fe}^{2+}$ )	14
$\text{FePO}_4$ ( $^{[4]}\text{Fe}^{3+}$ )	16
Ferriorthoclase ( $^{[4]}\text{Fe}^{3+}$ )	18
Yoderite ( $^{[5]}\text{Fe}^{3+}$ )	20
$\text{Fe}_3\text{PO}_7$ ( $^{[5]}\text{Fe}^{3+}$ )	22
Andradite ( $^{[6]}\text{Fe}^{3+}$ )	24
Acmite ( $^{[6]}\text{Fe}^{3+}$ )	26
Maghemite- $\gamma$ - $\text{Fe}_2\text{O}_3$ ( $^{[4,6]}\text{Fe}^{3+}$ )	28
RIXS $K\alpha$ $\text{Fe}^{2+}$	30
RIXS $K\alpha$ $\text{Fe}^{3+}$	31
all HERFD spectra	32
all TFY spectra	33
all TFY spectra - pre-edge without main edge	34
all XES $K\beta_{\text{sat}}$ spectra	35
all optical sticks	36

## Gillespite ( $^{4}Fe^{2+}$ )

$BaFeSi_4O_{10}$

$\sim 15.43$  wt% FeO

**Redox  $Fe^{2+}/Fe_{tot}$ : 96.7%**

**Cell setting:** Tetragonal

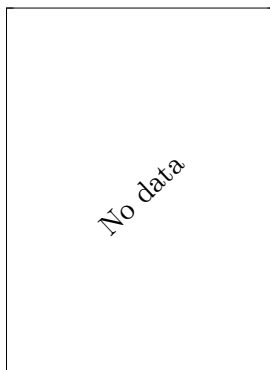
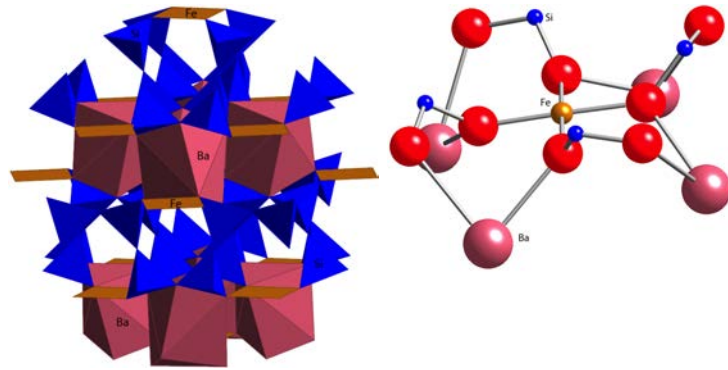
**Fe site geometry ( $\text{\AA}$ ):**

$D_{4h}$ , square-plane

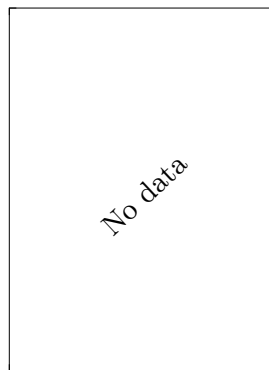
Fe–O:  $4 \times 1.9843$

Fe–Si: 3.2745

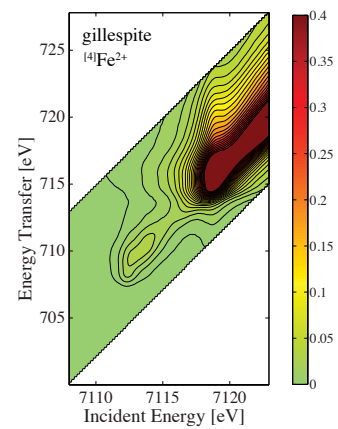
Fe–Fe: 6.0806



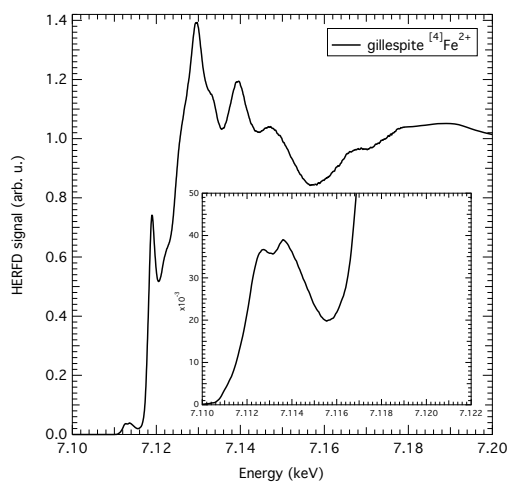
XES  $K\beta$  main



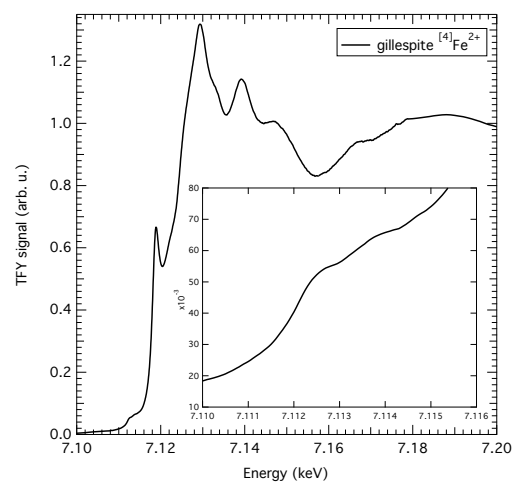
XES  $K\beta$  sat



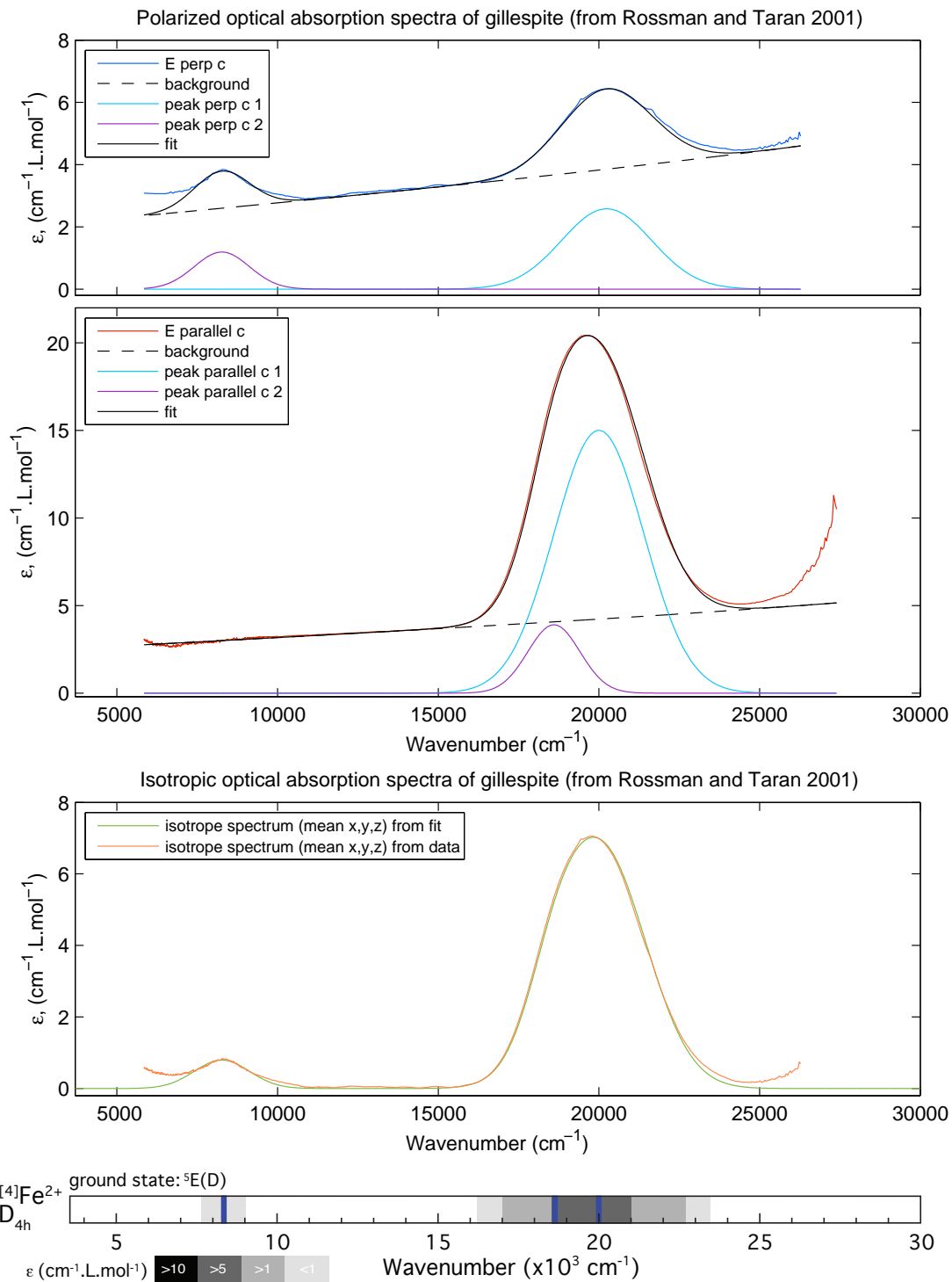
RIXS map, Fe  $K\alpha$



HERFD spectra, Fe  $K$  edge



TFY spectra, Fe  $K$  edge



**References**

R. H. Hazen, L. W. Finger, *American Mineralogist*, 68 (1983) 595-603  
 G. A. Waychunas, and G. E. Brown Jr. *Physics and Chemistry of Minerals*, 17 (1990) 420-430. (EXAFS)  
 G.R. Rossman, M.N. Taran, *American Mineralogist*, 86 (2001) 896-903 (optical absorption spectroscopy)

## Staurolite ( $^{44}\text{Fe}^{2+}$ )

$\text{Fe}_4\text{Al}_{18}\text{Si}_8\text{O}_{46}(\text{OH})_2$

$\sim 12.4$  wt% FeO

Redox  $\text{Fe}^{2+}/\text{Fe}_{\text{tot}}$ : 97%

Cell setting: Monoclinic

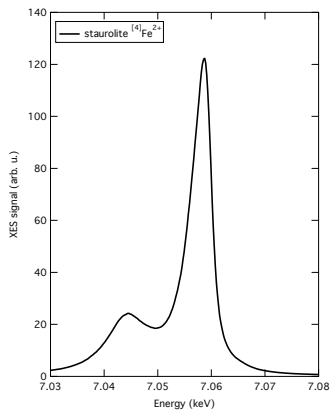
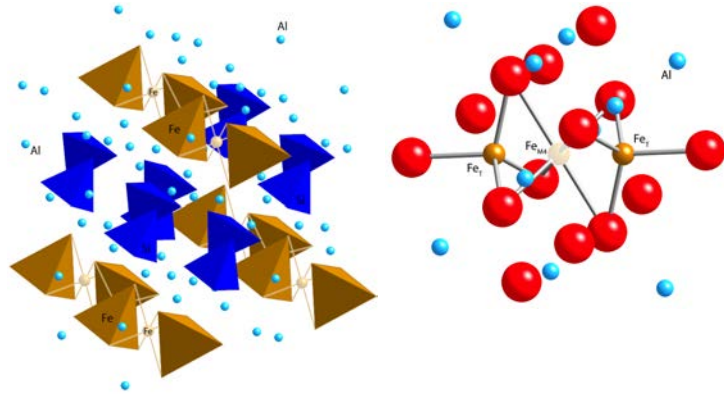
Fe site geometry ( $\text{\AA}$ ):

$T_d$  (and  $M4$ ), two face-sharing tetrahedra linked by an empty octahedral site ( $M4$ ) (occupancy  $< 1\%$ )

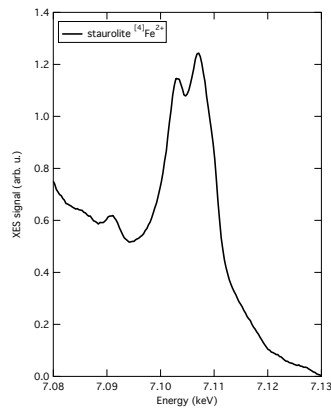
Fe– $\text{Fe}_{M4}$ :  $1 \times 1.6100$

Fe–Fe:  $1 \times 3.2201$

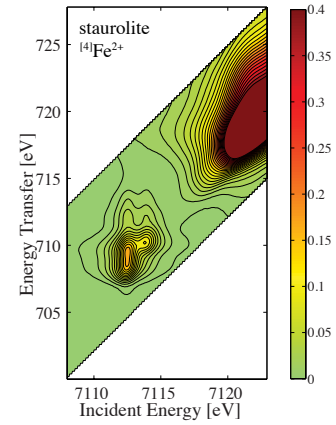
Fe–O:  $2 \times 1.9679, 1 \times 1.9956, 1 \times 2.0227$



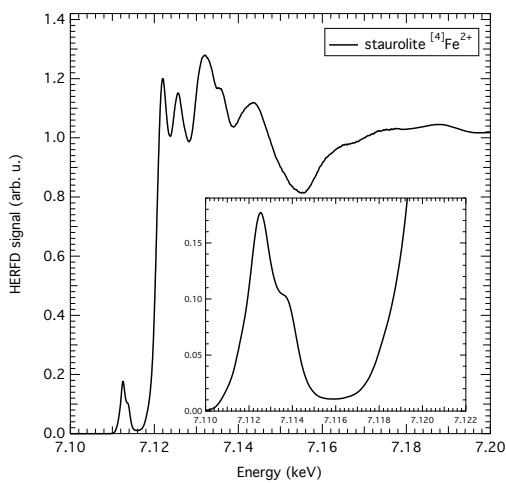
XES  $K\beta$  main



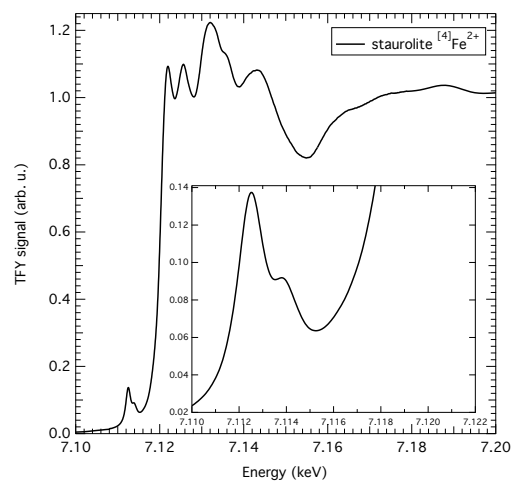
XES  $K\beta$  sat



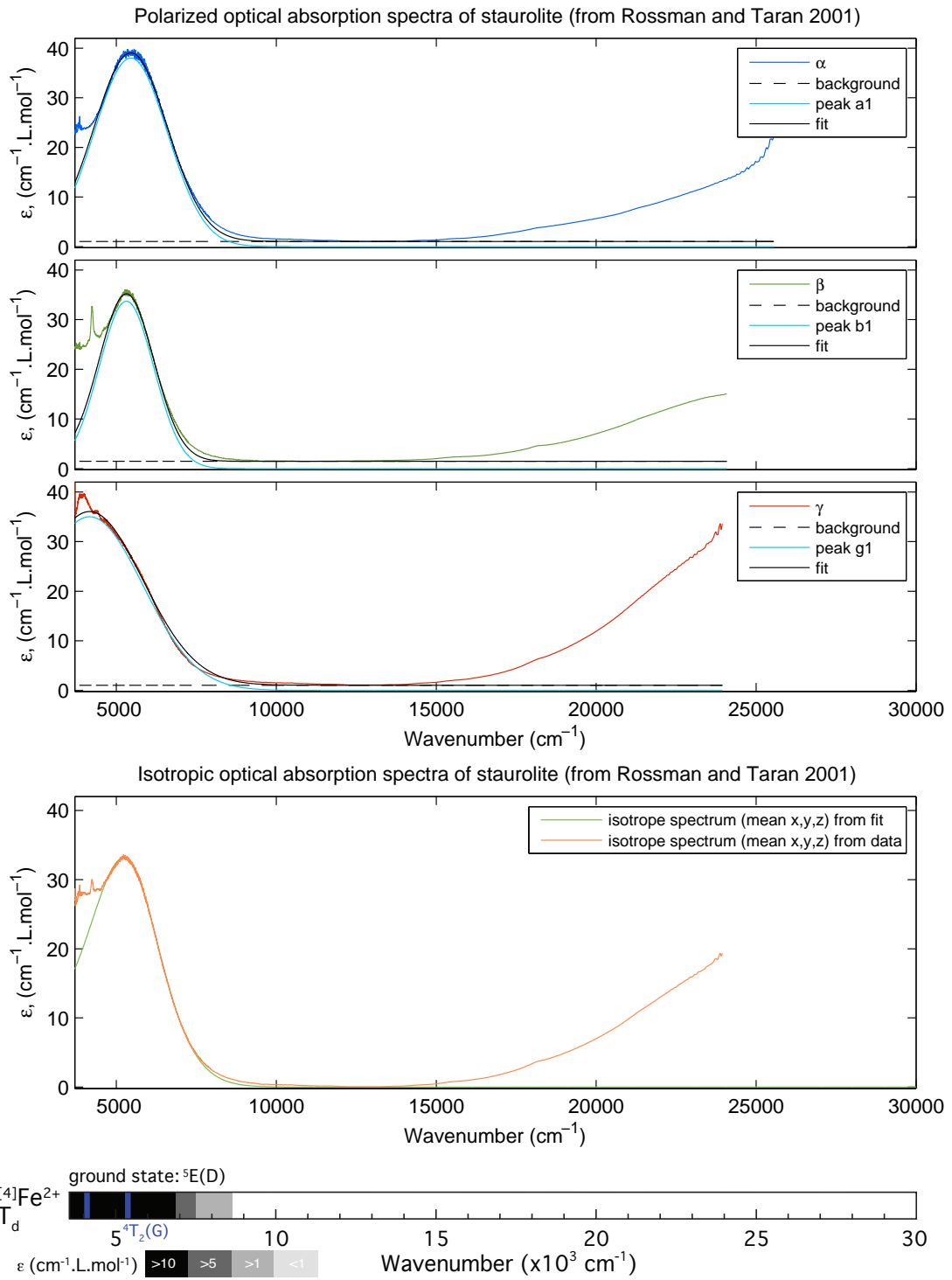
RIXS map, Fe  $K\alpha$



HERFD spectra, Fe  $K$  edge



TFY spectra, Fe  $K$  edge



**References**

R. Oberti, F.C. Hawthorne, A. Zanetti, L. Ottolini, *The Canadian Mineralogist*, 34 (1996) 1051-1057  
 G.R. Rossman, M.N. Taran, *American Mineralogist*, 86 (2001) 896-903 (optical absorption spectroscopy)  
 R. G. Burns, *Mineralogical applications of crystal field theory*, Cambridge University Press, 1993, p100 (optical absorption spectroscopy)



## Chromite ( $^{44}\text{Fe}^{2+}$ )

$\text{Fe}^{2+}\text{Cr}_2^{3+}\text{O}_4$

$\sim 12.87$  wt% FeO

Redox  $\text{Fe}^{2+}/\text{Fe}_{\text{tot}}$ : 97%

Cell setting: cubic

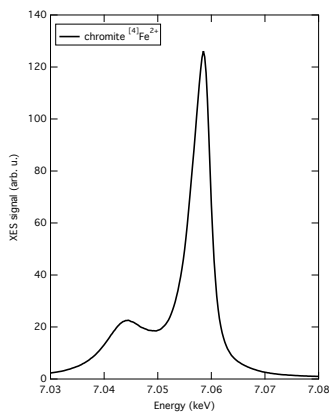
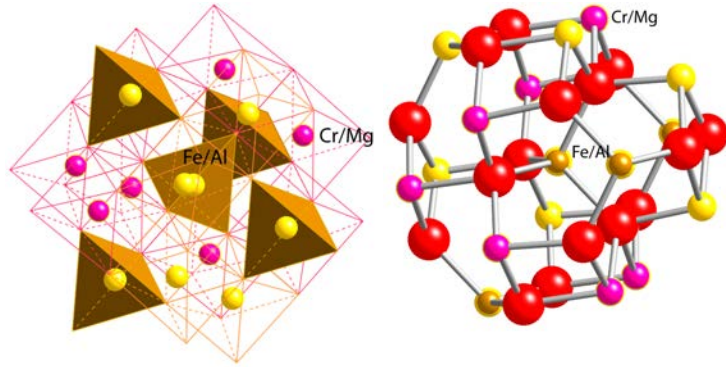
Fe site geometry ( $\text{\AA}$ ):

$T_d$ , isolated regular tetrahedron, possible presence of octahedral sites

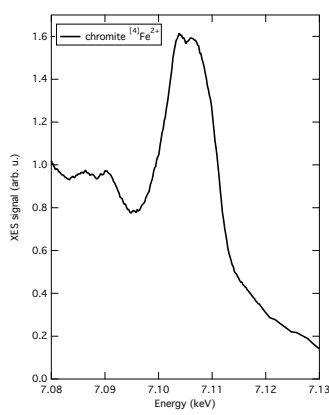
Fe–O:  $4 \times 1.9722$

Fe–Cr, Fe–Mg: 3.4519

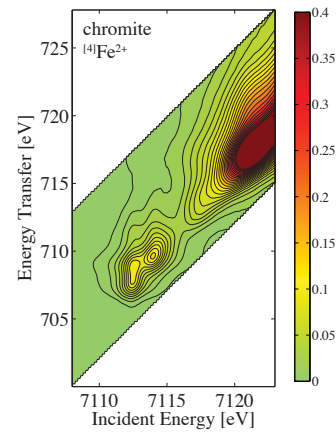
Fe–Fe: 3.6054



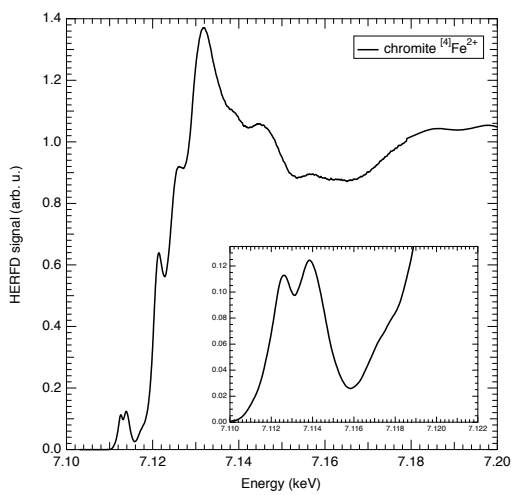
XES  $K\beta$  main



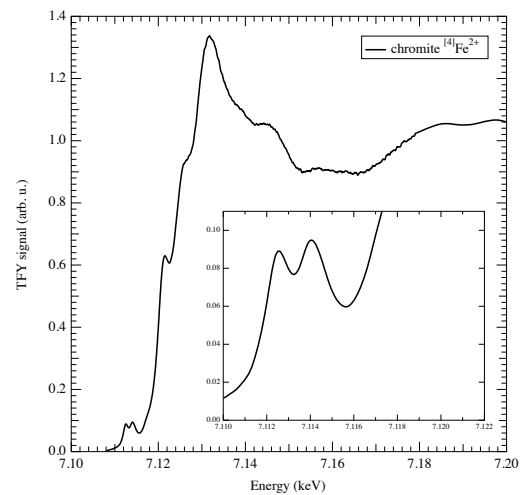
XES  $K\beta$  sat



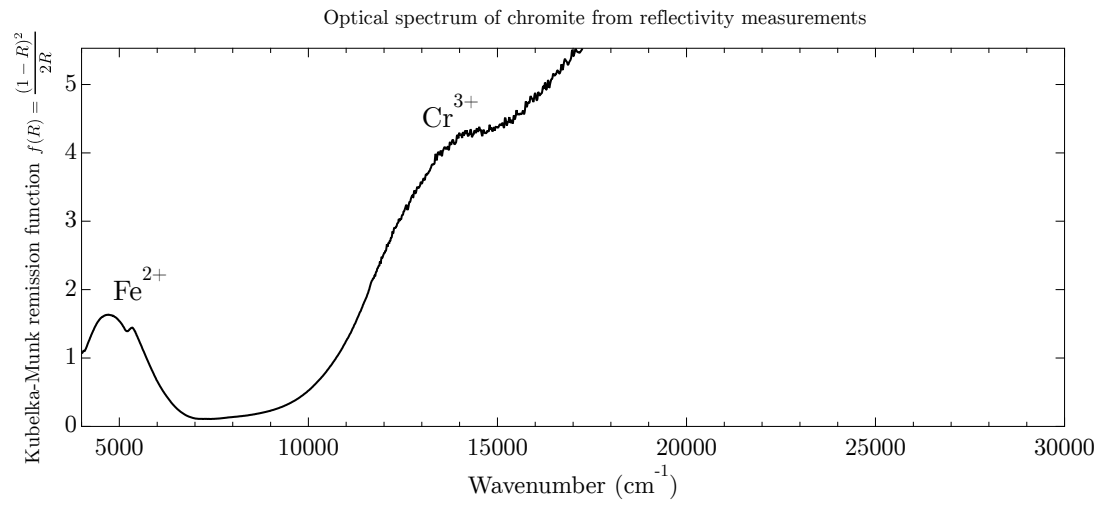
RIXS map, Fe  $K\alpha$



HERFD spectra, Fe  $K$  edge



TFY spectra, Fe  $K$  edge



## References

- D. Lenaz, A.M. Logvinova, F. Princivalle, N.V. Sobolev, *American Mineralogist*, 94 (2009) 1067-1070 (XRD)  
H.K. Mao, P.M. Bell, *Geochimica et Cosmochimica Acta*, 39 (1975) 865-866 (optical absorption spectroscopy)

## Grandierite ( $^{[5]}\text{Fe}^{2+}$ )

$(\text{Mg}, \text{Fe})\text{Al}_3(\text{BO}_4)(\text{SiO}_4)\text{O}$

$\sim 5.0$  wt% FeO

Redox  $\text{Fe}^{2+}/\text{Fe}_{\text{tot}}$ : 99%

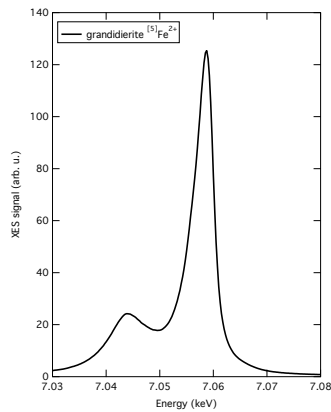
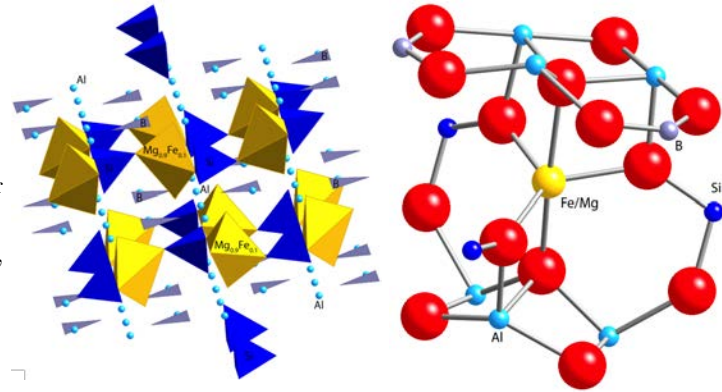
Cell setting: Orthorhombic

Fe site geometry ( $\text{\AA}$ ):

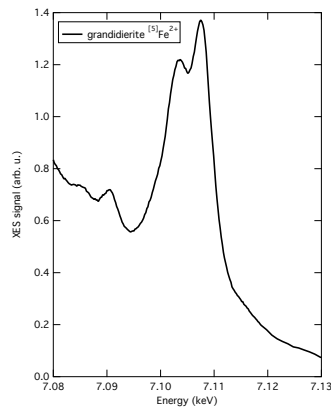
$C_{3v}, D_{3h}$ , Isolated distorted triangular bipyramid, substitution of Mg

Fe–O:  $2 \times 1.9651$ ,  $1 \times 2.0356$ ,  $1 \times 2.0568$ ,  $1 \times 2.1784$

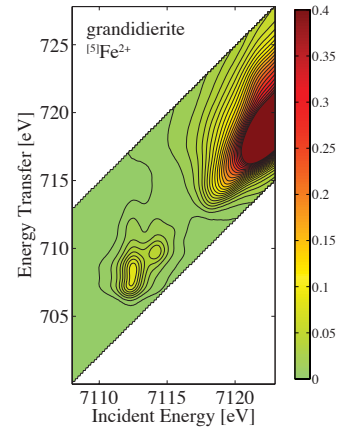
Fe–Al:  $1 \times 2.8645, 2 \times 2.9617$



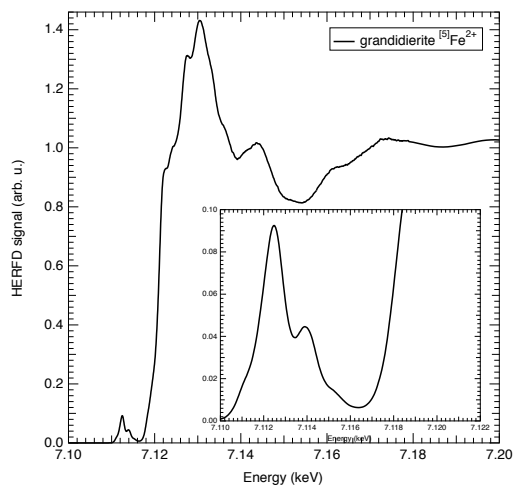
XES  $K\beta$  main



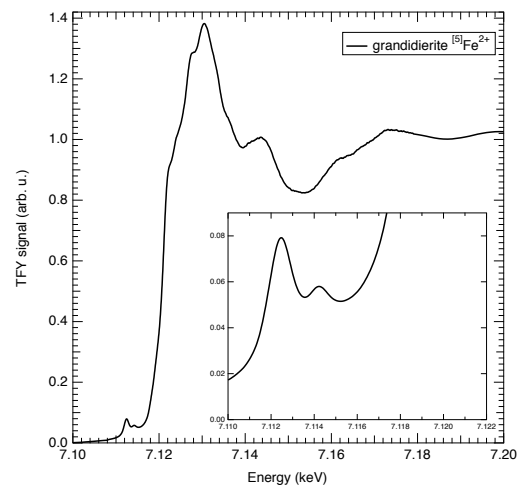
XES  $K\beta$  sat



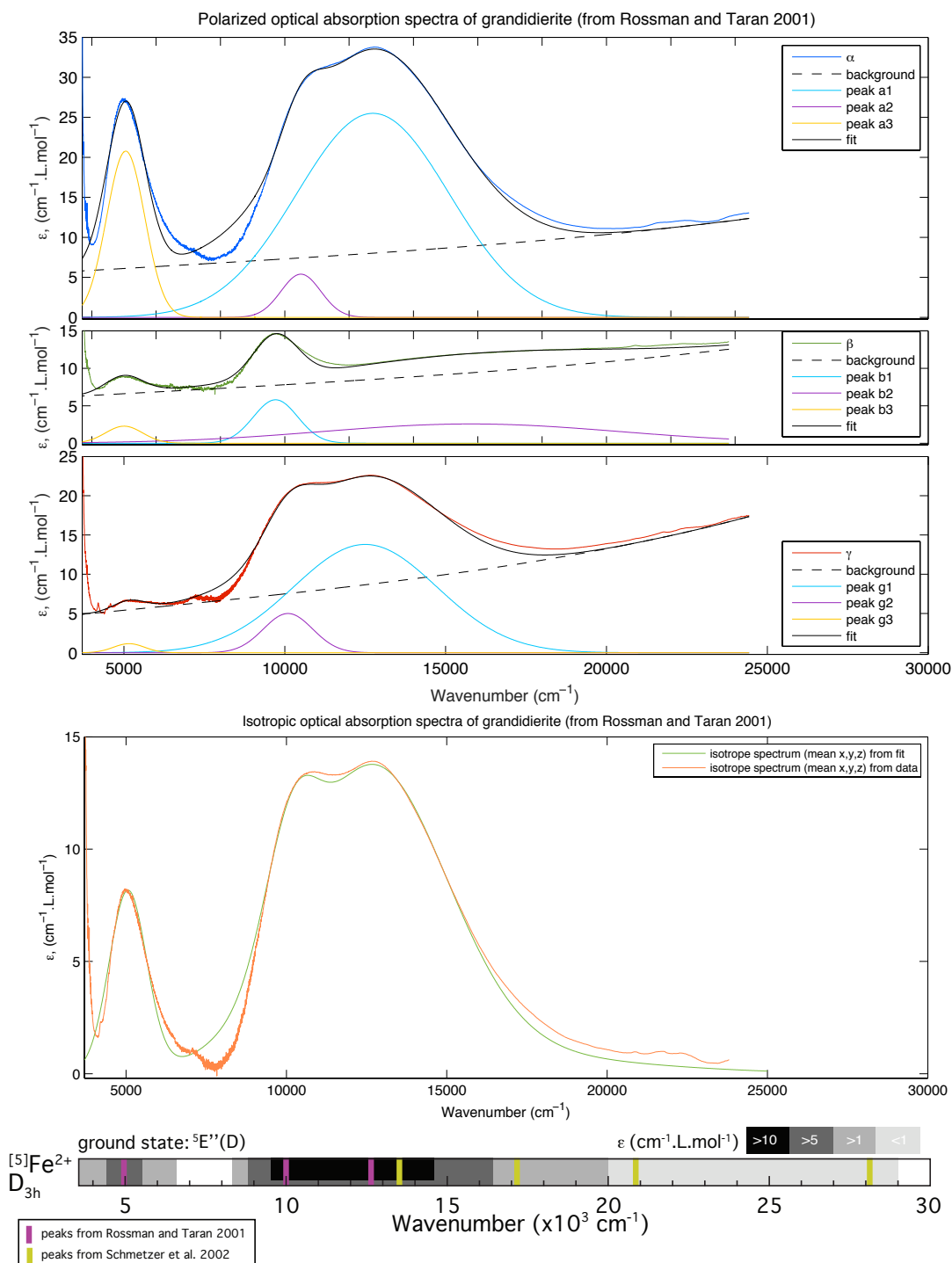
RIXS map, Fe  $K\alpha$



HERFD spectra, Fe  $K$  edge



TFY spectra, Fe  $K$  edge



**References**

D.A. Stephenson, P.B. Moore, *Acta Crystallographica Section B*, 24 (1968) 1518-1522 (XRD)  
 G.R. Rossman, M.N. Taran, *American Mineralogist*, 86 (2001) 896-903 (optical absorption spectroscopy)

## Siderite-FeCO<sub>3</sub> (<sup>6</sup>Fe<sup>2+</sup>)

FeCO<sub>3</sub>

~62 wt% FeO

Redox Fe<sup>2+</sup>/Fe<sub>tot</sub>: 100%

Cell setting: Hexagonal

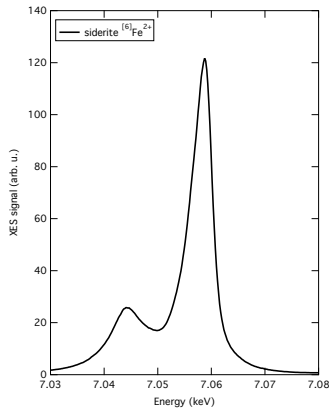
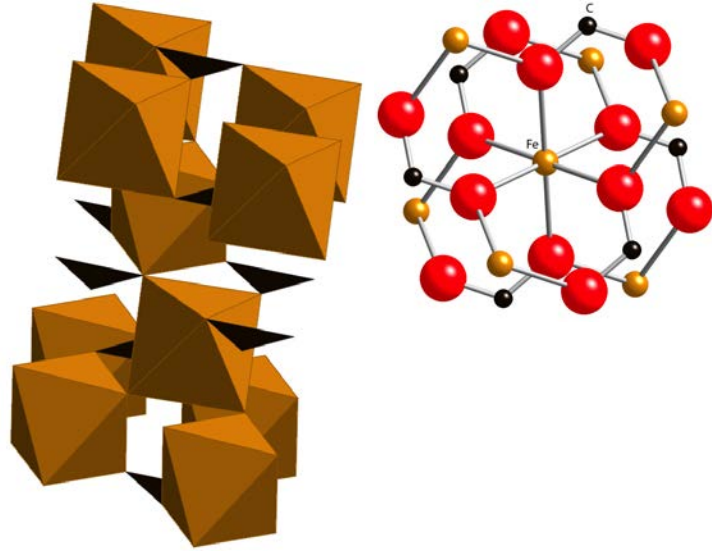
Fe site geometry (Å):

O<sub>h</sub>, corner-sharing regular octahedron

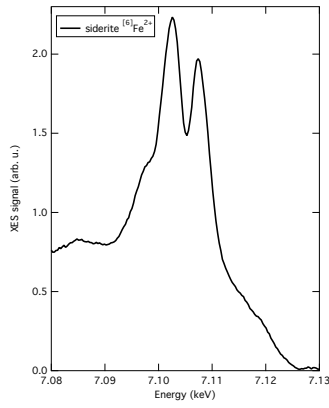
Fe–O: 6x2.1431, 6x3.2593

Fe–C: 6x2.9948

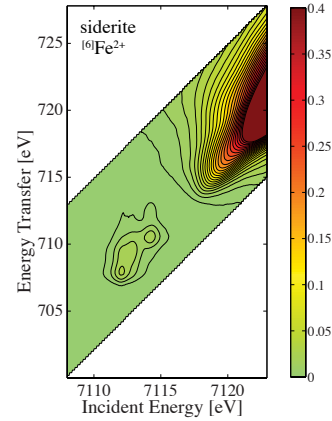
Fe–Fe: 6x3.7273



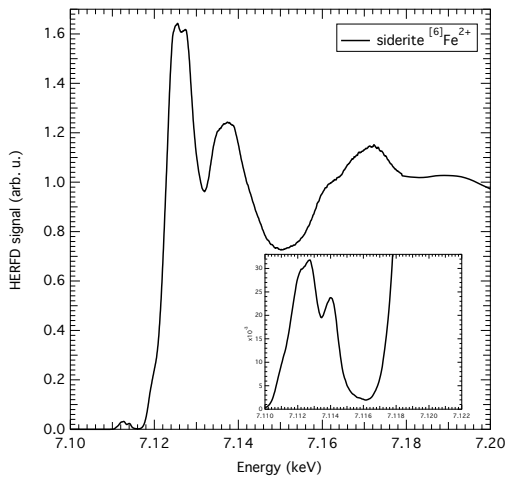
XES  $K\beta$  main



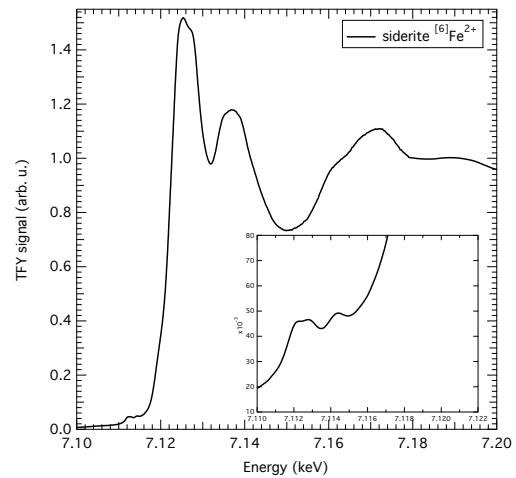
XES  $K\beta$  sat



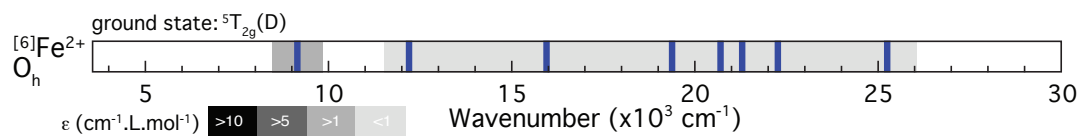
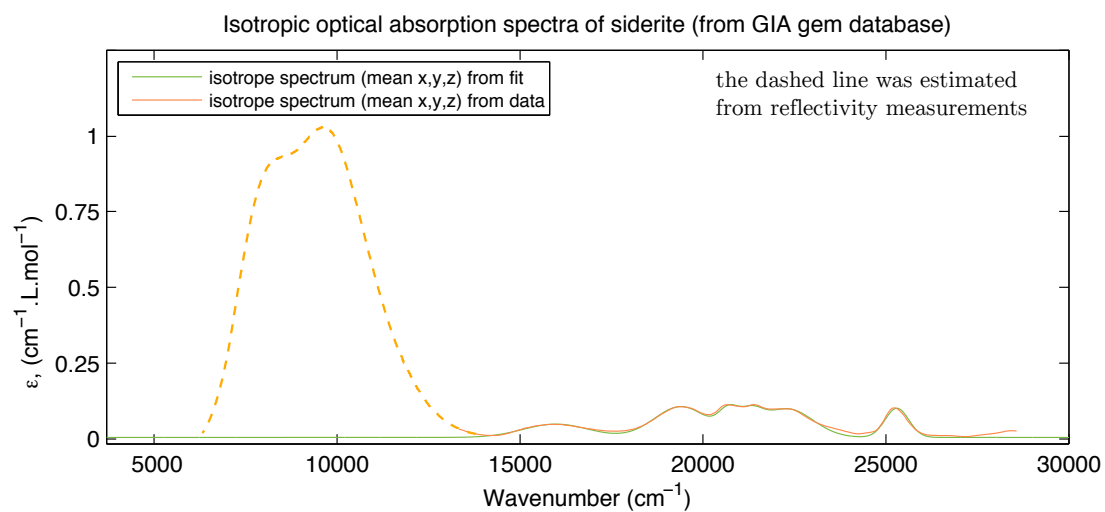
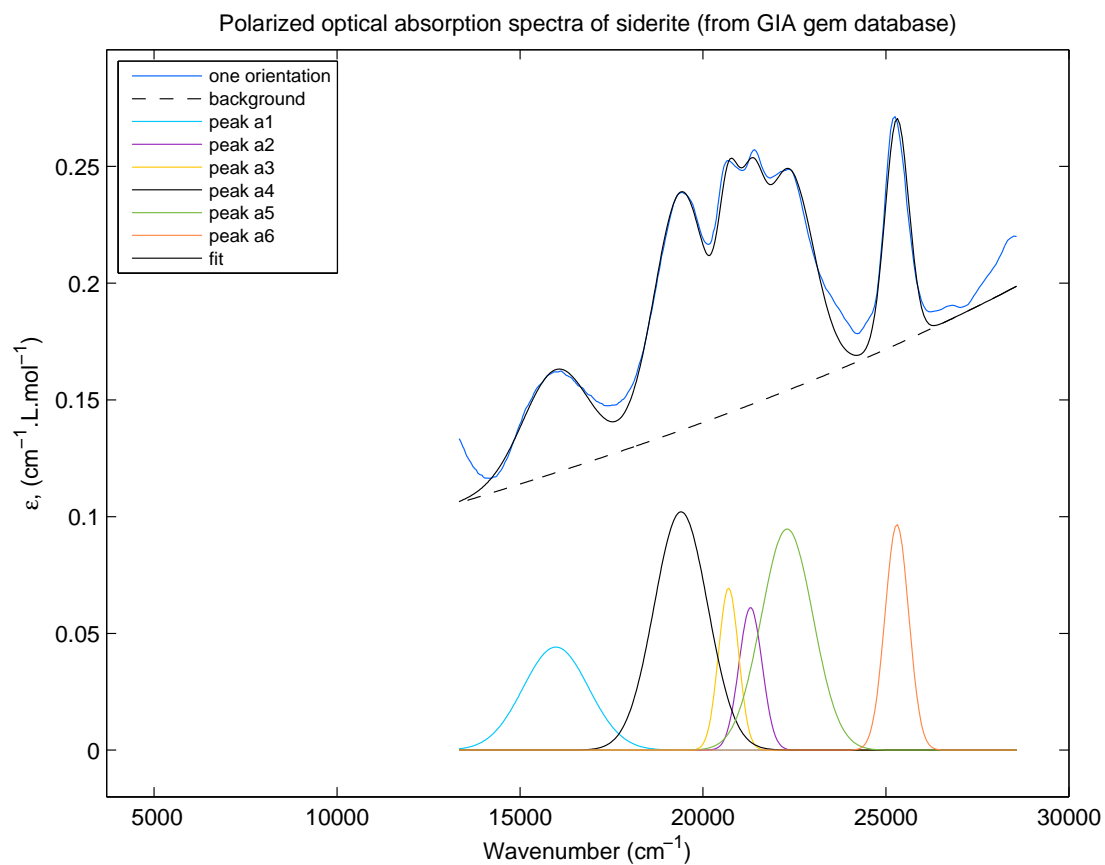
RIXS map, Fe  $K\alpha$



HERFD spectra, Fe  $K$  edge



TFY spectra, Fe  $K$  edge



References

D.L. Graf, *American Mineralogist*, 46 (1961) 1283-1316

## Hypersthene ( $^{6}\text{Fe}^{2+}$ )

$(\text{Fe}^{2+}, \text{Mg})_2\text{Si}_2\text{O}_6$

$\sim 31$  wt% FeO

Redox  $\text{Fe}^{2+}/\text{Fe}_{\text{tot}}$ : 100%

Cell setting: Orthorhombic

Fe site geometry ( $\text{\AA}$ ):

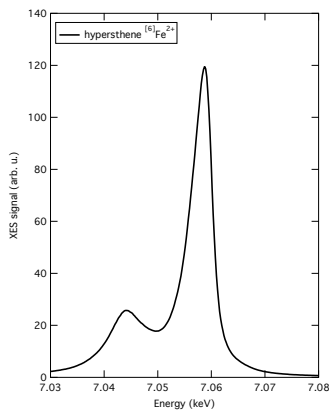
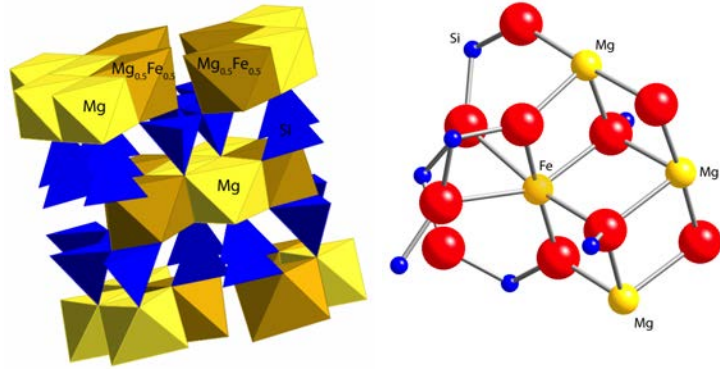
$\text{O}_h, \text{M2} (\text{C}_{2v})$ , isolated distorted octahedron, orthopyroxene, substitution of Al in the enstatite mineral

Fe–O: 1x1.9899, 1x2.0405, 1x2.0845, 1x2.1336, 1x2.3294, 1x2.4874

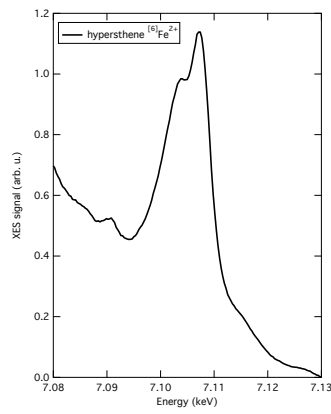
Fe–Si: 1x2.8295, 1x3.1391, 1x3.2535, 1x3.2854, 1x3.3676

Fe–Mg: 1x2.9753, 1x3.0311, 1x3.2023

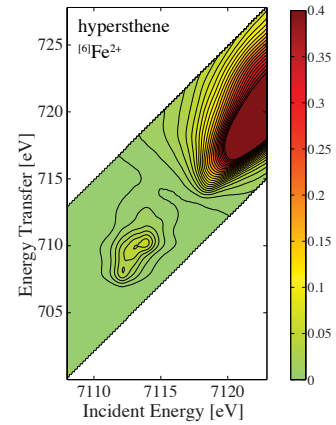
Fe–Fe:  $> 4.6992$



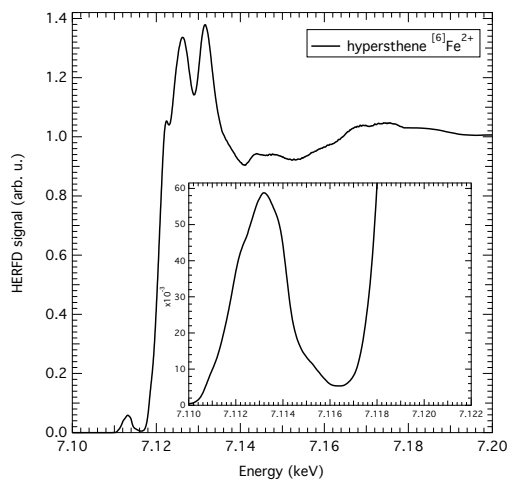
XES  $K\beta$  main



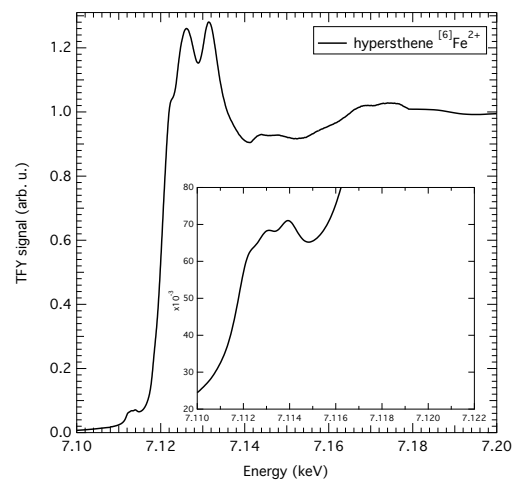
XES  $K\beta$  sat



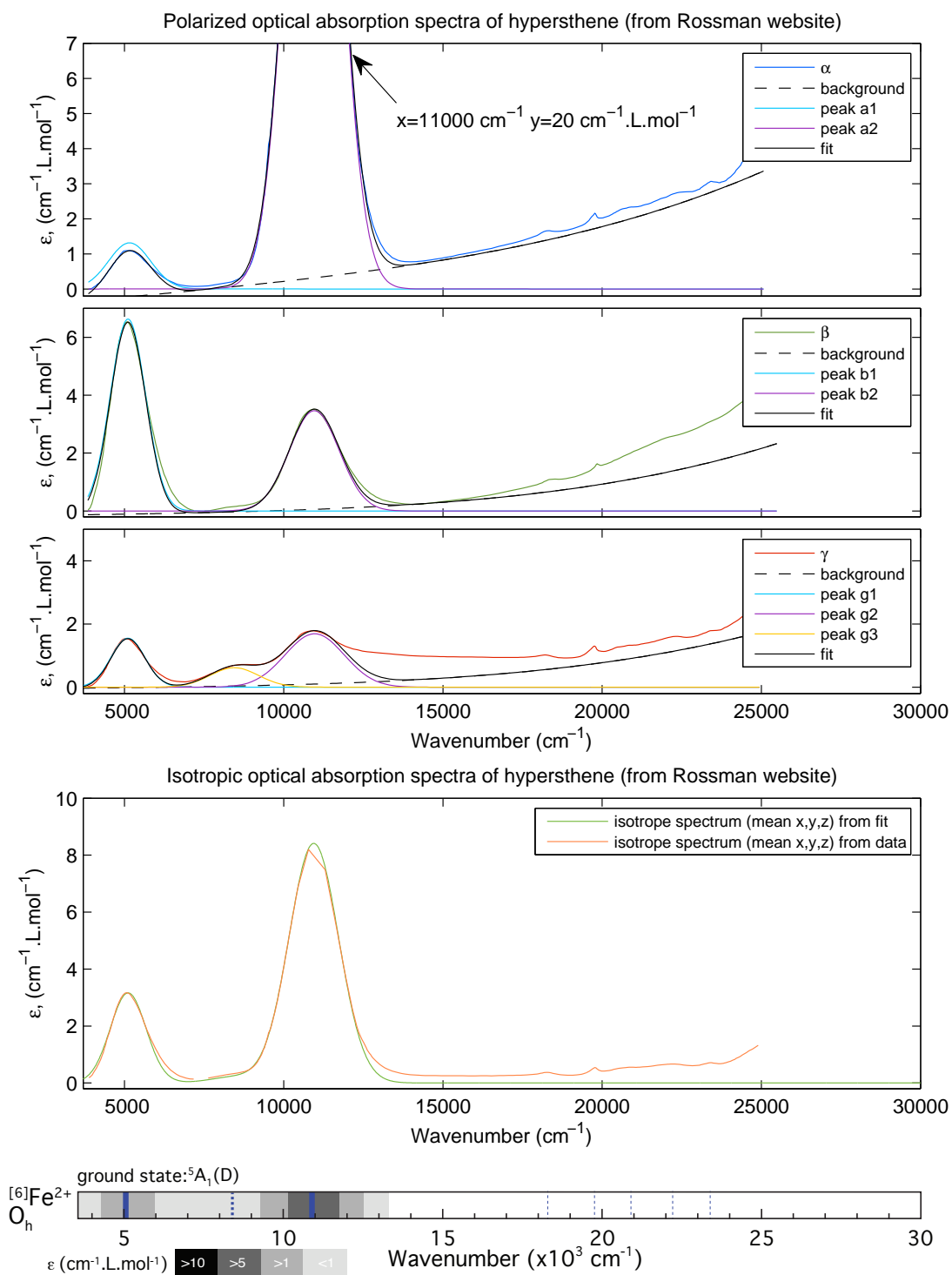
RIXS map, Fe  $K\alpha$



HERFD spectra, Fe  $K$  edge



TFY spectra, Fe  $K$  edge



## References

- D.S. Goldman, G.R. Rossman, *American Mineralogist*, 62 (1977) 151-157 (Optical absorption)  
 H. Yang, S. Ghose, *American Mineralogist*, 80 (1995) 9-20 (XRD)  
 G.Y.V. Victor, D. Ghosh, S. Ghose, *Physical Review B*, 64 (2001) (Correlation of magnetic susceptibility, mössbauer, and optical absorption spectroscopy)



## Diopside ( $^{61}\text{Fe}^{2+}$ )

$\text{CaMg}_{0.9}\text{Fe}_{0.1}\text{Si}_2\text{O}_6$

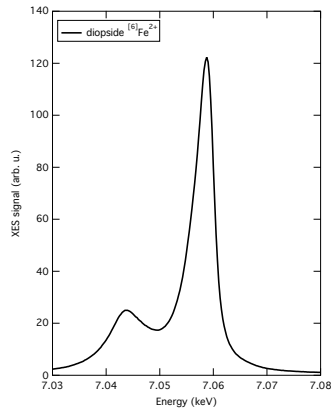
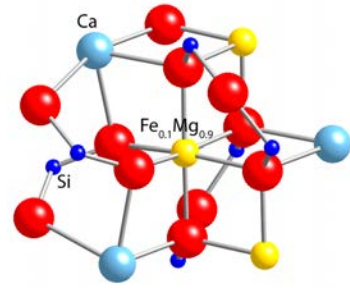
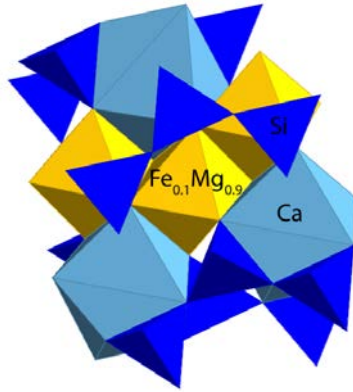
$\sim 1.66$  wt% FeO

Redox  $\text{Fe}^{2+}/\text{Fe}_{\text{tot}}$ : 100%

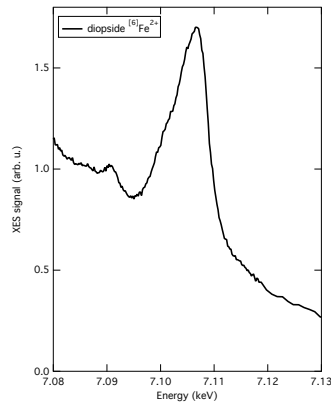
Cell setting: Monoclinic

Fe site geometry ( $\text{\AA}$ ):

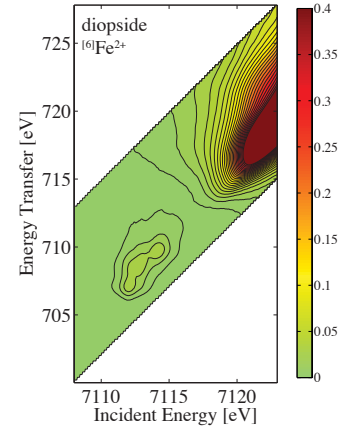
Oh, isolated almost regular octahedron



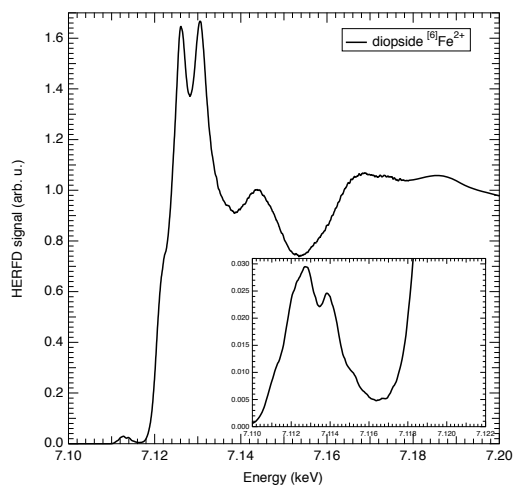
XES  $K\beta$  main



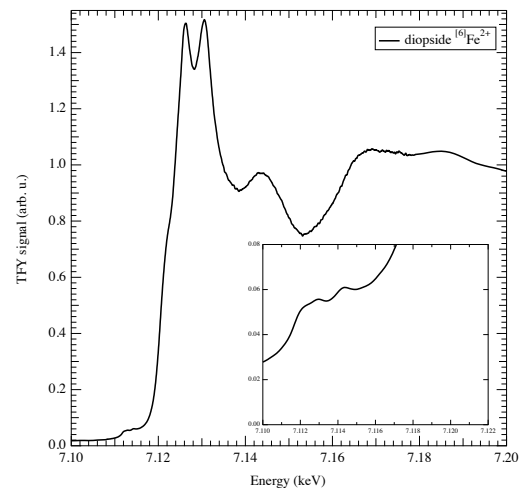
XES  $K\beta$  sat



RIXS map, Fe  $K\alpha$



HERFD spectra, Fe  $K$  edge



TFY spectra, Fe  $K$  edge

no optical absorption spectra

### References

- S. Carbonin, G. Salviulol, R. Munno, M. Desiderio, A.D. Negro, *Mineralogy and Petrology*, 41 (1989) 1-10 (XRD)  
W.B. White, K.L. Keester, *American Mineralogist*, 51 (1966) 774-791 (optical absorption spectroscopy)  
M. Wilke, F. Farges, P.-E. Petit, G.E. Brown, F. Martin, *American Mineralogist*, 86 (2001) 714-730 (XANES)

## FePO<sub>4</sub> (<sup>4</sup>Fe<sup>3+</sup>)

FePO<sub>4</sub>

~53 wt% Fe<sub>2</sub>O<sub>3</sub>

Redox Fe<sup>2+</sup>/Fe<sub>tot</sub>: 0%

Cell setting: Hexagonal

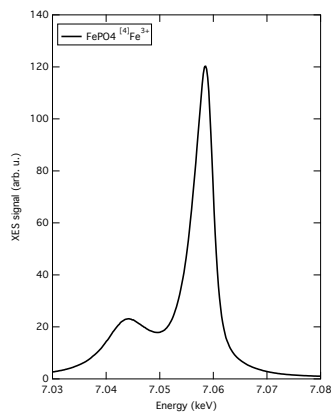
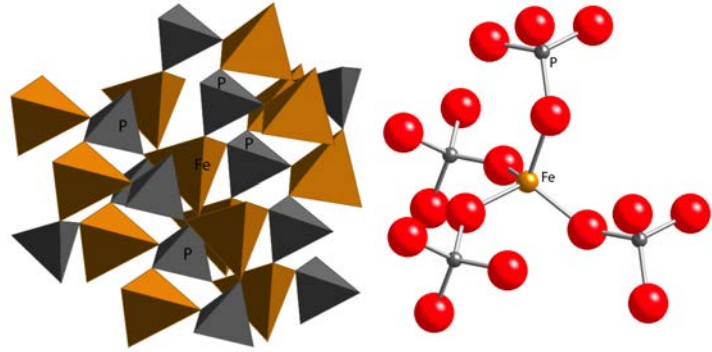
Fe site geometry (Å):

T<sub>d</sub>, isolated slightly distorted tetrahedron

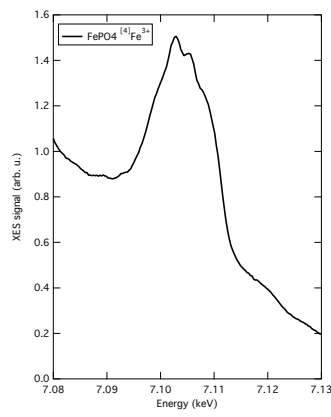
Fe–O: 2x 1.8246, 2x 1.8664

Fe–P: 2x 3.1481, 2x 3.1738

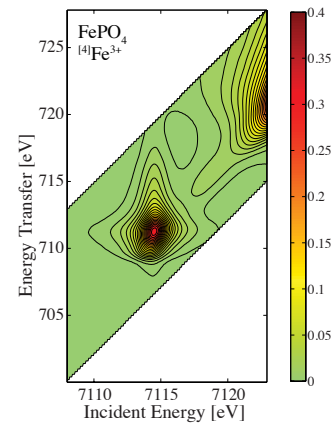
Fe–Fe: 4x 4.5353



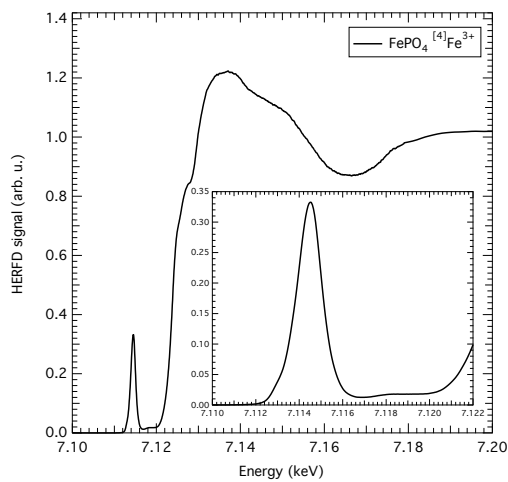
XES  $K\beta$  main



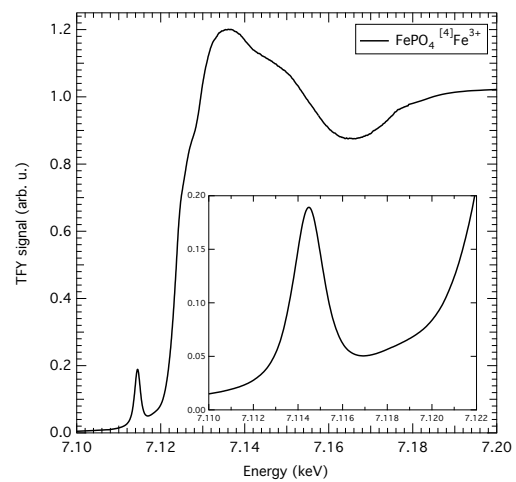
XES  $K\beta$  sat



RIXS map, Fe  $K\alpha$



HERFD spectra, Fe  $K$  edge



TFY spectra, Fe  $K$  edge

no optical absorption spectra

### References

- G.J. Long, A.K. Cheetham, P.D. Battle, *Inorganic Chemistry*, 22 (1983) 3012-3016
- Combes, J.M., A. Manceau, G. Calas, et J.Y. Bottero. *Geochimica et Cosmochimica Acta*, 53 (1989) 583-94 (X-ray absorption spectroscopy)

## Ferriorthoclase ( $[^4\text{Fe}^{3+}]$ )

$\text{Fe}:\text{KAlSi}_3\text{O}_8$

$\sim 0.5$  wt%  $\text{Fe}_2\text{O}_3$

Redox  $\text{Fe}^{2+}/\text{Fe}_{\text{tot}}$ : 0%

Cell setting: Monoclinic

Fe site geometry ( $\text{\AA}$ ):

$T_d$ , slightly distorted tetrahedron, substitution of Al (feldspar)

Fe–O:  $4 \times 1.83^a$  or  $1.87^b$ ,

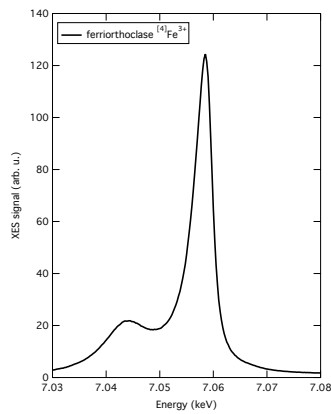
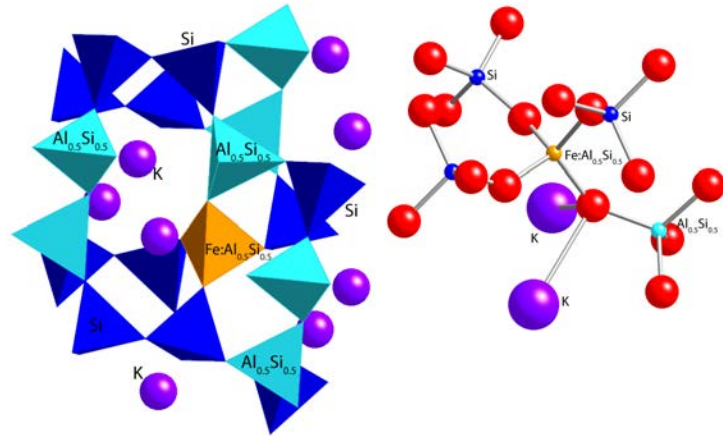
(Si,Al)–O:  $2 \times 1.6630$ ,  $2 \times 1.6720$ ,

Al–Si:  $1 \times 2.9929$ ,  $1 \times 3.1029$ ,  $1 \times 3.1720$ ,  
 $1 \times 3.1773$

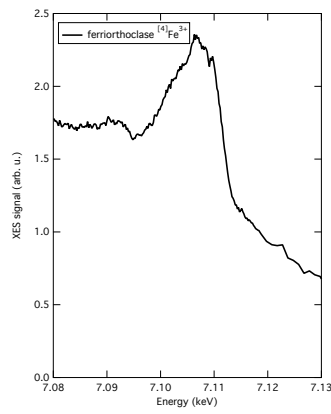
Al–K:  $1 \times 3.5903$ ,  $1 \times 3.6189$

<sup>a</sup>Cochain unpublished EXAFS data

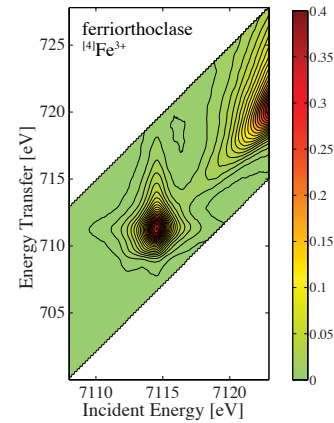
<sup>b</sup>Brown 1978 Prog Abstr Ann Mtg Geol Soc Am p 373 (Abstract)



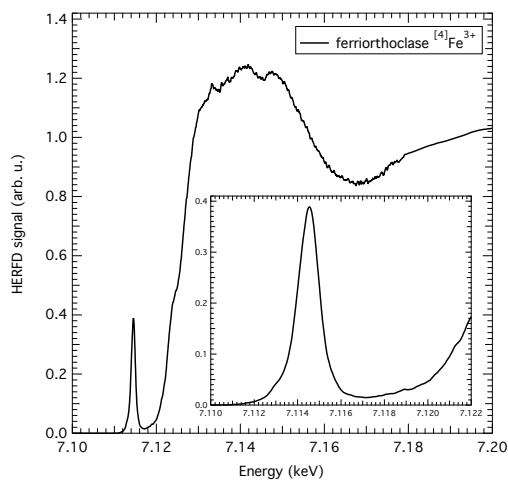
XES  $K\beta$  main



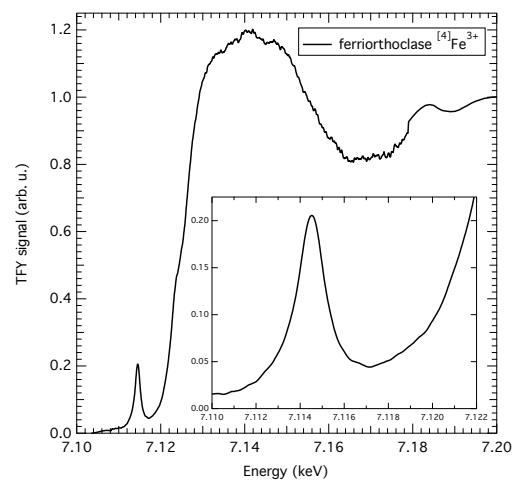
XES  $K\beta$  sat



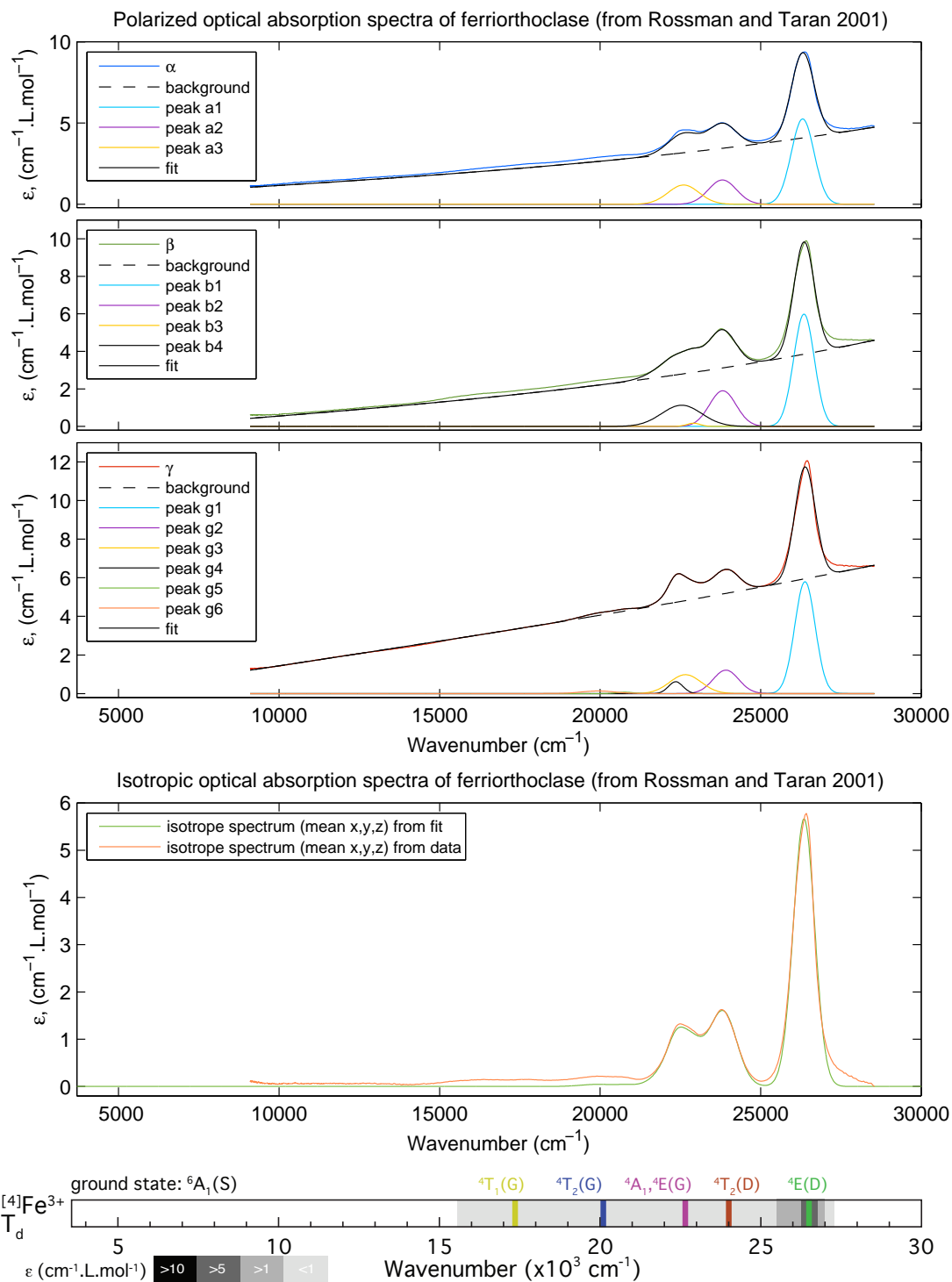
RIXS map,  $\text{Fe } K\alpha$



HERFD spectra,  $\text{Fe } K$  edge



TFY spectra,  $\text{Fe } K$  edge



## References

- D.S. Coombs, *Mineralogical Magazine* 30 (1954) 409-427 (chemistry, refractive index, XRD)
- F.F. Brown, A.M. Pritchard, *Earth and Planetary Science Letters*, 5 (1968) 259-260 (mössbauer)
- G.H. Faye, *The Canadian Mineralogist*, 10 (1969) 112-117 (optical absorption spectroscopy)
- E. Prince, G. Donnay, R.F. Martin, *American Mineralogist*, 58 (1973) 500-507 (Neutron crystal-structure refinement)
- A.M. Hofmeister, G.R. Rossman, *Physics and Chemistry of Minerals* 11 (1984) 213-224 (redox, EPR and optical absorption spectroscopy)
- W.B. White, M. Matsumura, D.G. Linnehan, T. Furukawa, B.K. Chandrasekhar, *American Mineralogist*, 71 (1986) 1415-1419 (Optical absorption and luminescence of  $Fe^{3+}$ )

## Yoderite ( $^{55}\text{Fe}^{3+}$ )

$(\text{Mg}, \text{Al}, ^{55}\text{Fe})_8\text{Si}_4(\text{O}, \text{OH})_{20}$

$\sim 6.1$  wt%  $\text{Fe}_2\text{O}_3$

Redox  $\text{Fe}^{2+}/\text{Fe}_{\text{tot}}$ : 0%

Cell setting: Monoclinic

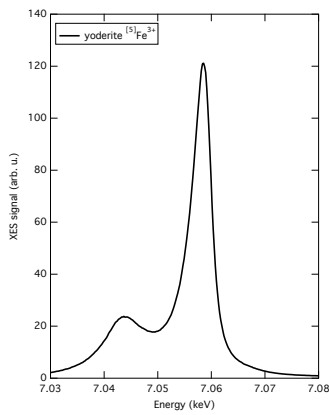
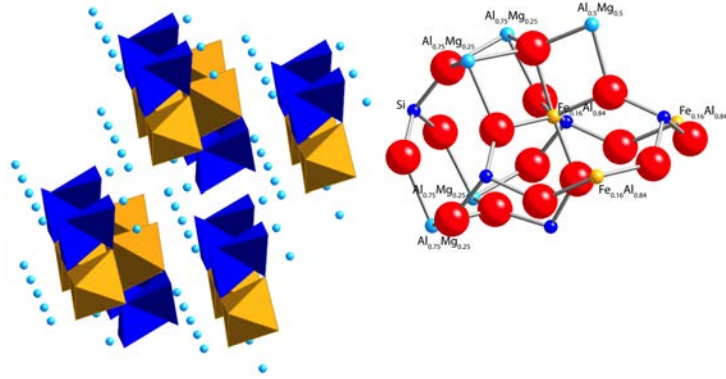
Fe site geometry ( $\text{\AA}$ ):

$\text{M3} \simeq \text{C}_{3v}$  ( $= \text{C}_s$ ), Isolated distorted triangular bipyramid

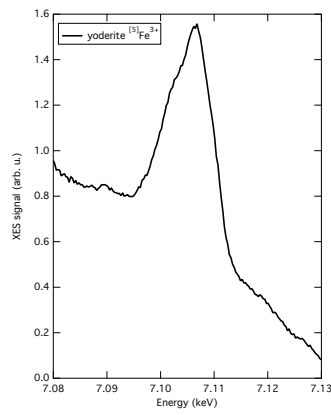
Fe–O: 1.8006, 1.8432,  $2 \times 1.8680$ , 1.9295

Fe–Al/Mg:  $1 \times 2.8980$ ,  $2 \times 2.9354$

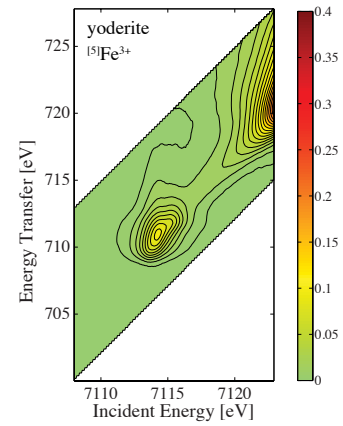
Fe–Si:  $1 \times 3.0809$ ,  $2 \times 3.1700$ ,  $1 \times 3.2067$



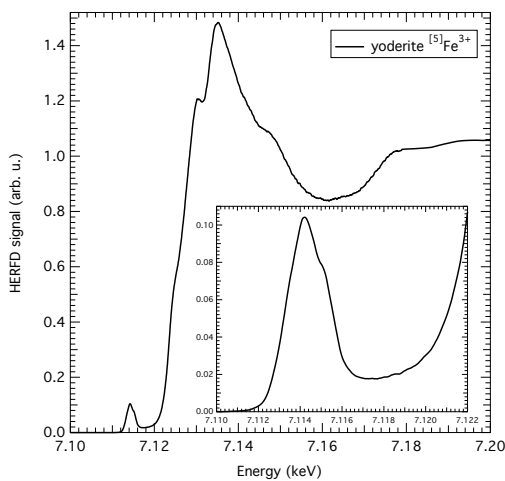
XES  $K\beta$  main



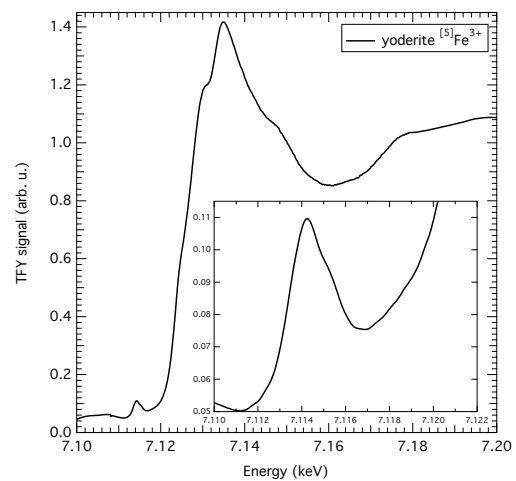
XES  $K\beta$  sat



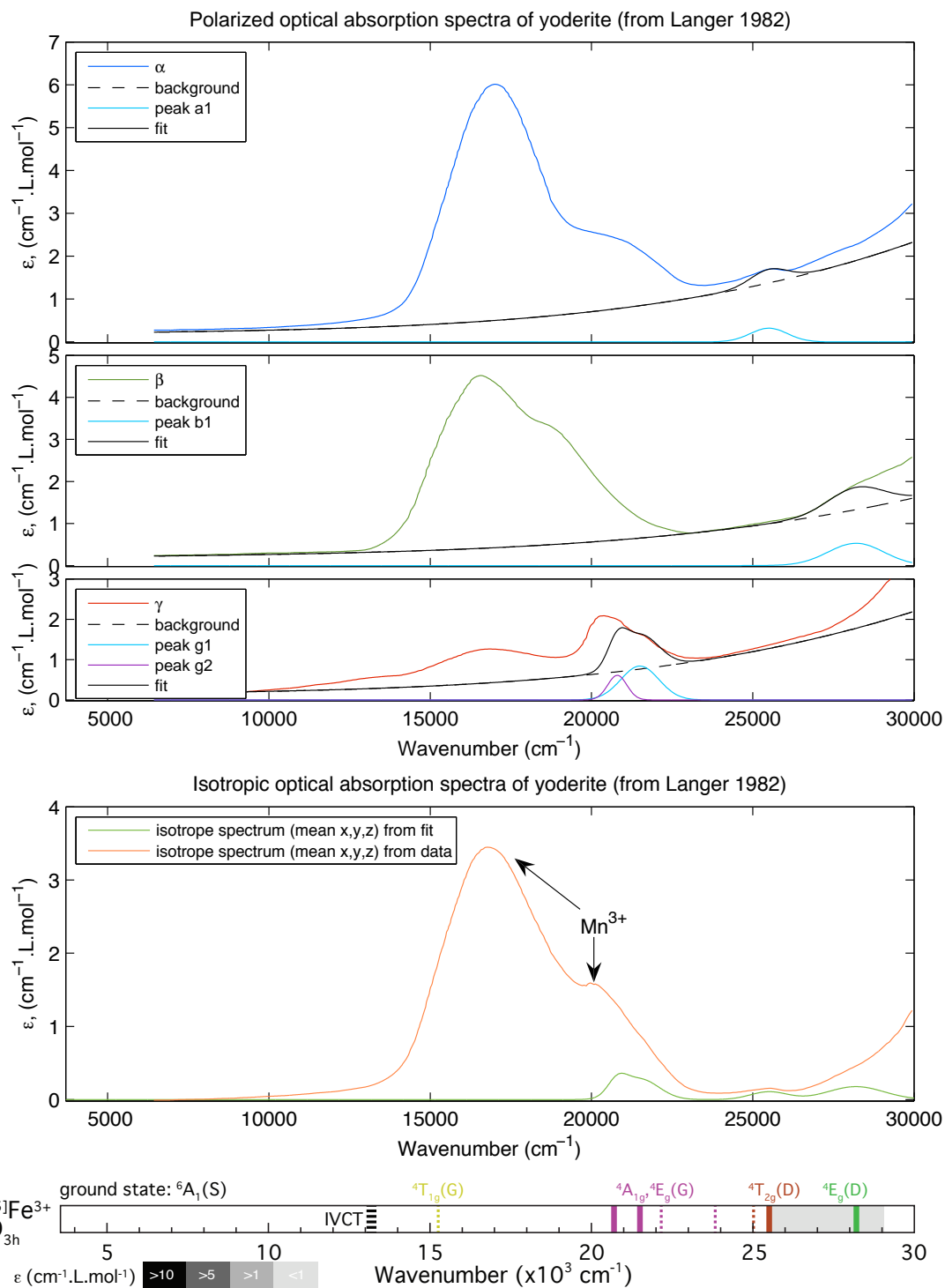
RIXS map, Fe  $K\alpha$



HERFD spectra, Fe  $K$  edge



TFY spectra, Fe  $K$  edge



## References

- J.B. Higgins, P.H. Ribbe, Y. Nakajima, *American Mineralogist*, 67 (1982) 76-84 (XRD)
- R.M. Abu-Eid, K. Langer, F. Seifert, *Physics and Chemistry of Minerals*, 3 (1978) 271-289 (mössbauer and optical absorption spectroscopy)
- K. Langer, G. Smith, U. Hålenius, *Phys Chem Minerals* 8 (1982) 143-145 (optical absorption spectroscopy)
- C. McCammon, in: T.J. Ahrens (Ed.), *AGU Reference Shelf*, American Geophysical Union, Washington, D. C., 1995: pp. 332-347 (mössbauer)



## Fe<sub>3</sub>PO<sub>7</sub> ([<sup>5</sup>]Fe<sup>3+</sup>)

Fe<sub>3</sub>PO<sub>7</sub>

~77 wt% Fe<sub>2</sub>O<sub>3</sub>

Redox Fe<sup>2+</sup>/Fe<sub>tot</sub>: 0%

Cell setting: Trigonal

Fe site geometry (Å):

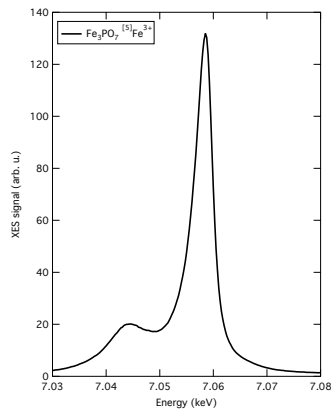
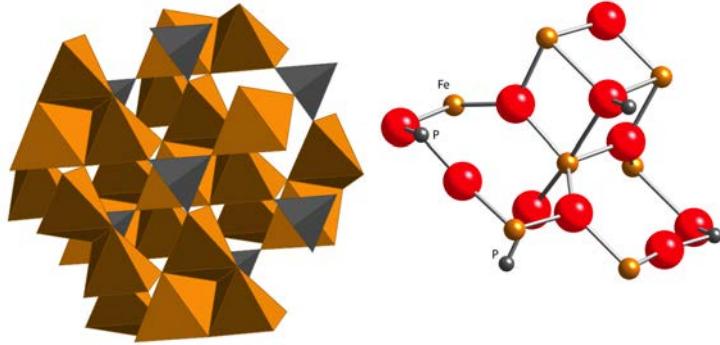
C<sub>s</sub> (C<sub>3v</sub>, D<sub>3h</sub>), groups of 3 edge-sharing distorted trigonal bipyramids (5-fold)

linked to other Fe by corners

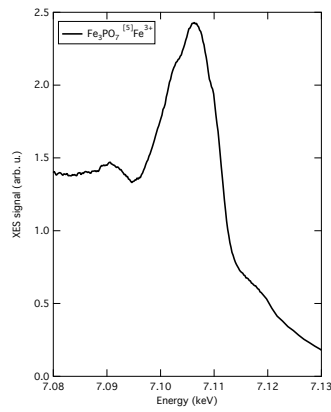
Fe–O: 1x1.8917, 1x1.9164, 2x1.9198, 1x2.1901, 2x3.1645

Fe–Fe: 2x3.1302

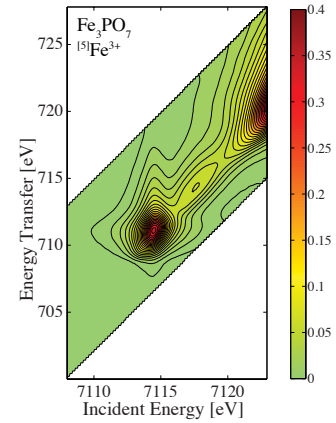
Fe–P: 1x3.3235, 1x3.3393



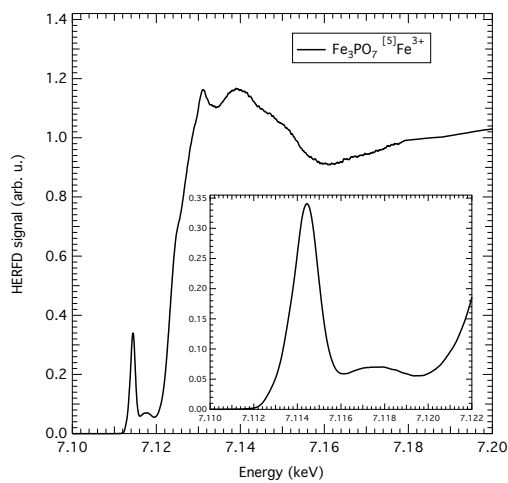
XES  $K\beta$  main



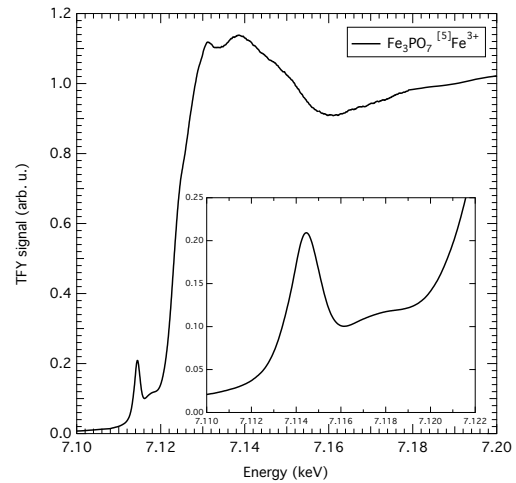
XES  $K\beta$  sat



RIXS map, Fe  $K\alpha$



HERFD spectra, Fe  $K$  edge



TFY spectra, Fe  $K$  edge

no optical absorption spectra

## References

- A. Modaressi, A. Courtois, R. Gerardin, B. Malaman, C. Gleitzer, *Journal of Solid State Chemistry*, 47 (1983) 245-255 (XRD and magnetism)
- P. Berthet, J. Berthon, F. d'Yvoire, *Materials Research Bulletin*, 23 (1988) 1501-1508 (XANES)
- P. Berthet, J. Berthon, F. d'Yvoire, *Materials Research Bulletin*, 24 (1989) 459-465 (EXAFS)
- Q. Shi, L. Zhang, M.E. Schlesinger, J. Boerio-Goates, B.F. Woodfield, *The Journal of Chemical Thermodynamics*, 62 (2013) 86-91 (heat capacity)

## Andradite ( $^{61}\text{Fe}^{3+}$ )

$\text{Ca}_3\text{Fe}_2\text{Si}_3\text{O}_{12}$

$\sim 31$  wt%  $\text{Fe}_2\text{O}_3$

Redox  $\text{Fe}^{2+}/\text{Fe}_{\text{tot}}$ : 0%

Cell setting: Cubic

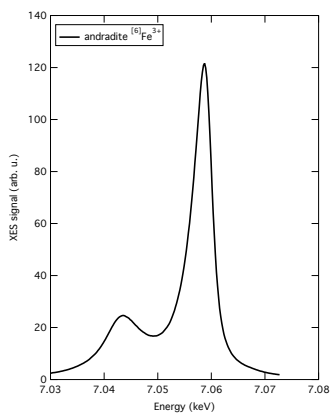
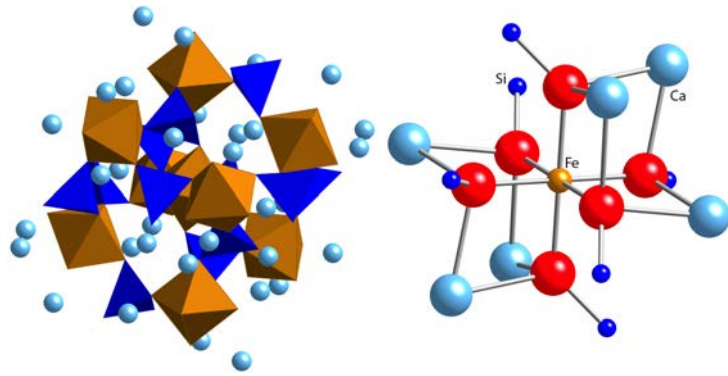
Fe site geometry ( $\text{\AA}$ ):

$C_{3i}$  ( $S_6$ ), almost regular isolated octahedron (garnet)

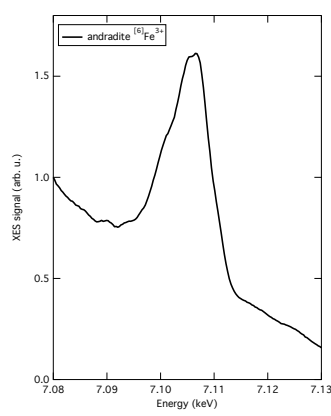
Fe–O:  $6 \times 2.0206$

Fe–Si:  $6 \times 3.3720$

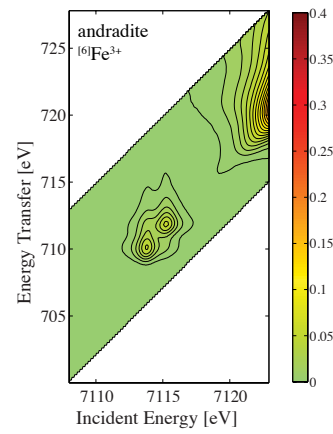
Fe–Ca:  $6 \times 3.3720$



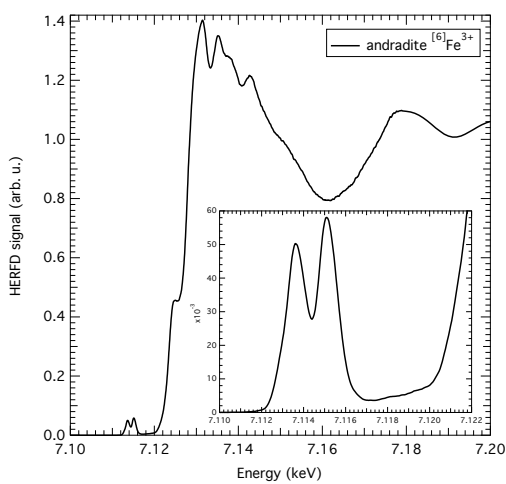
XES  $K\beta$  main



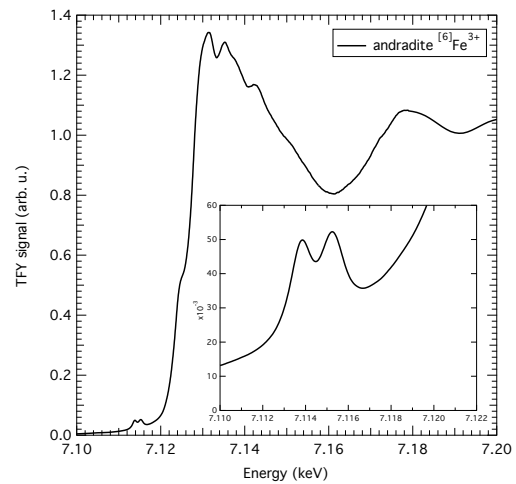
XES  $K\beta$  sat



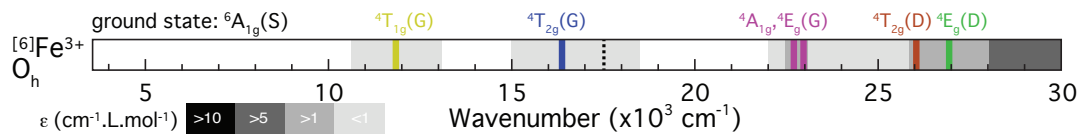
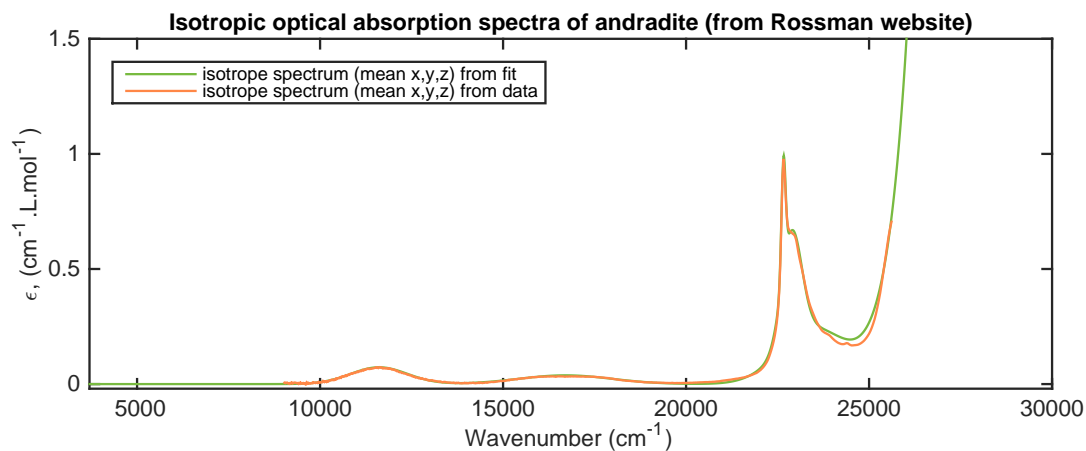
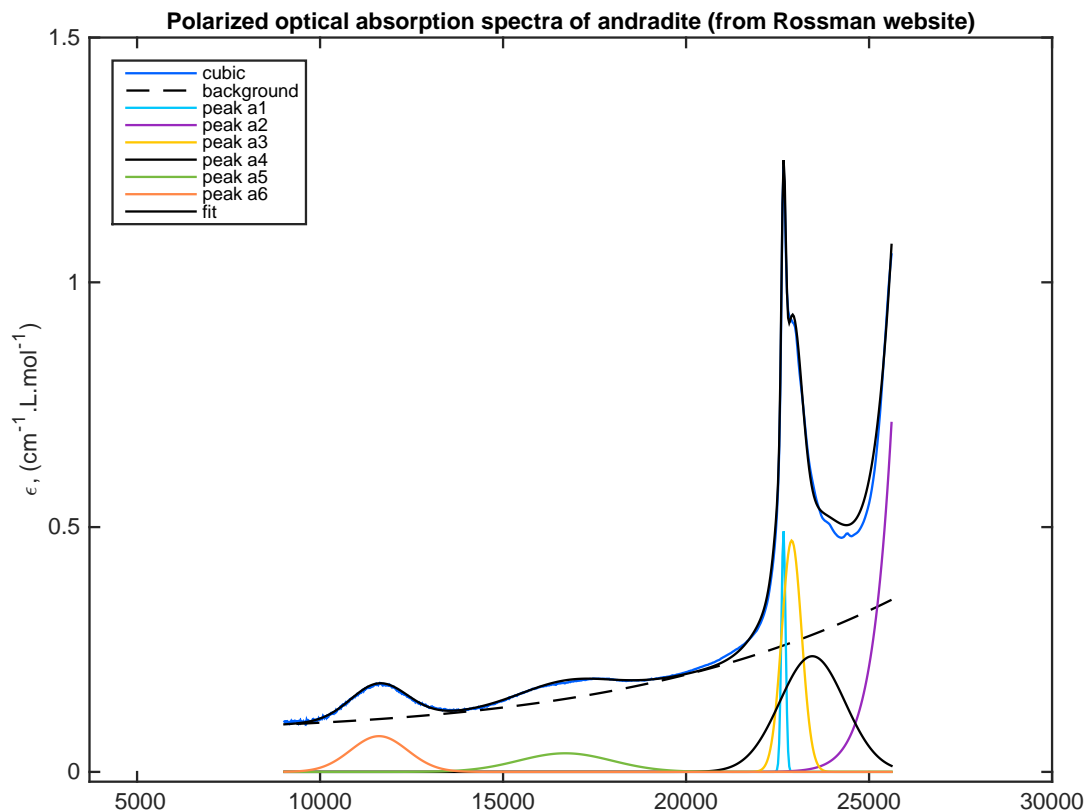
RIXS map, Fe  $K\alpha$



HERFD spectra, Fe  $K$  edge



TFY spectra, Fe  $K$  edge



**References**

T. Pilati, F. Demartin, C.M. Gramaccioli, *Acta Crystallographica*, B52 (1996) 239-250

## Acmite ( $[^6\text{Fe}^{3+}]$ )

$\text{NaFeSi}_2\text{O}_6$

$\sim 34.6$  wt%  $\text{Fe}_2\text{O}_3$

Redox  $\text{Fe}^{2+}/\text{Fe}_{\text{tot}}$ : 8%

Cell setting: Monoclinic

Fe site geometry ( $\text{\AA}$ ):

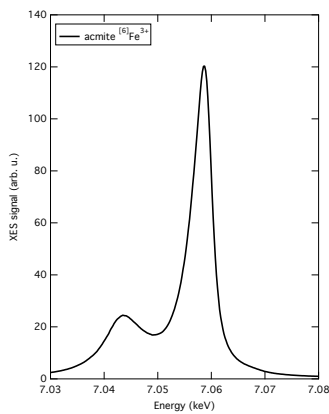
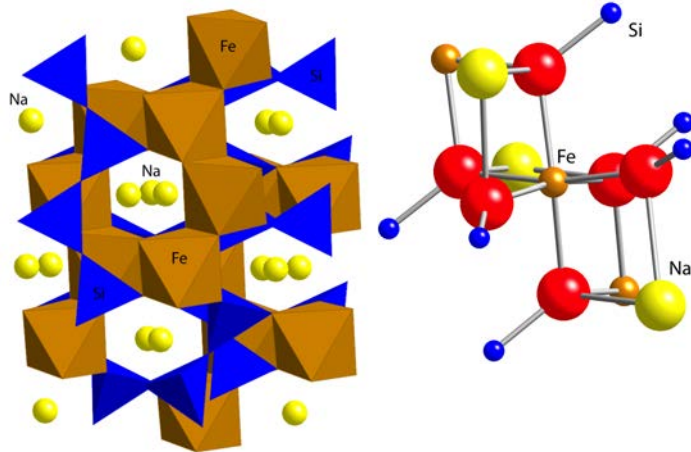
M1, edge-sharing distorted octahedron  
(a piroxene also called aegirine)

Fe–O:  $2 \times 1.9358$ ,  $2 \times 2.0293$ ,  $2 \times 2.1093$

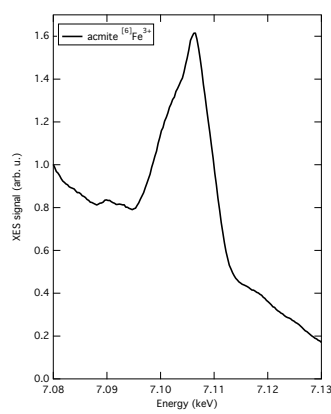
Fe–Na:  $2 \times 3.1723$ ,  $1 \times 3.5267$

Fe–Si:  $2 \times 3.1879$ ,  $2 \times 3.2889$

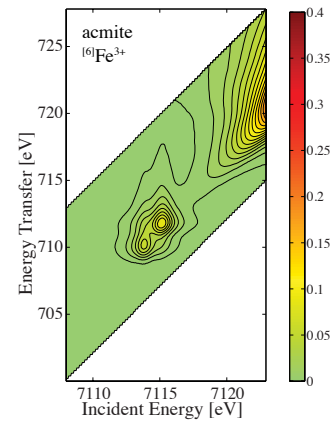
Fe–Fe:  $2 \times 3.1889$



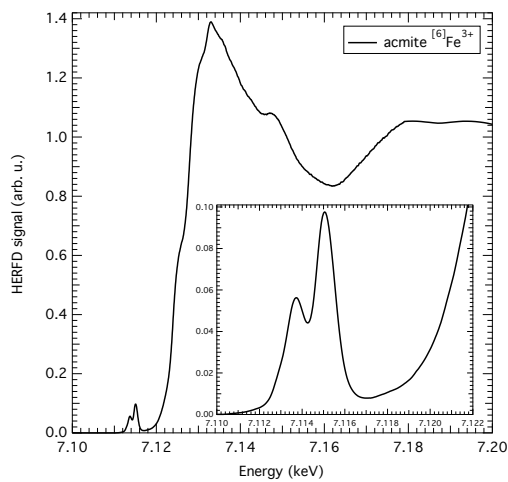
XES  $K\beta$  main



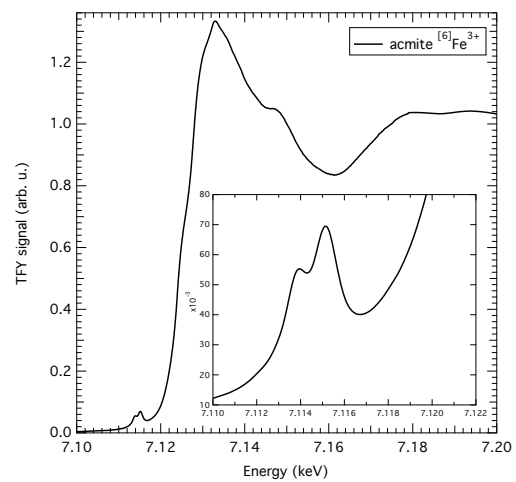
XES  $K\beta$  sat



RIXS map, Fe  $K\alpha$

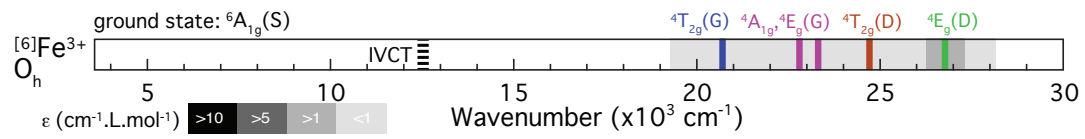


HERFD spectra, Fe  $K$  edge



TFY spectra, Fe  $K$  edge

no optical absorption spectra



## References

- M. Cameron, S. Sueno, C.T. Prewitt, J.J. Papike, *American Mineralogist*, 58 (1973) 594-618 (XRD)
- K. Langer, R.M. Abu-Eid, *Phys Chem Minerals*, 1 (1977) 273-299 (optical absorption spectroscopy)
- G. Amthauer, G.R. Rossman, *Physics and Chemistry of Minerals*, 11 (1984) 37-51 (optical absorption spectroscopy)

## Maghemite- $\gamma$ -Fe<sub>2</sub>O<sub>3</sub> (<sup>[4,6]</sup>Fe<sup>3+</sup>)

$\gamma$ -Fe<sub>2</sub>O<sub>3</sub>

~100 wt% Fe<sub>2</sub>O<sub>3</sub>

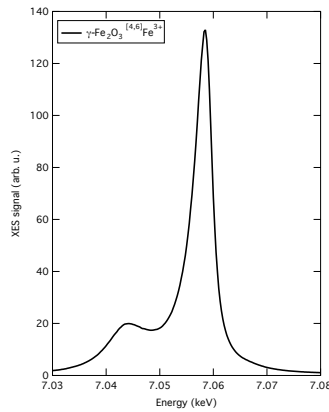
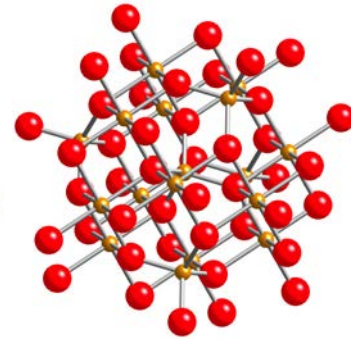
Redox Fe<sup>2+</sup>/Fe<sub>tot</sub>: 0%

Cell setting: Cubic

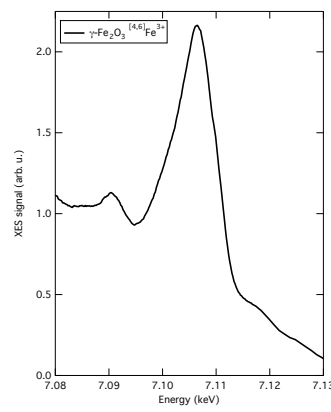
Fe site geometry (Å):

T<sub>d</sub> and O<sub>h</sub>, (Fe<sub>8</sub>)<sub>T<sub>d</sub></sub>[Fe<sub>40/3</sub>□<sub>8/3</sub>]<sub>O<sub>h</sub></sub>O<sub>32</sub>

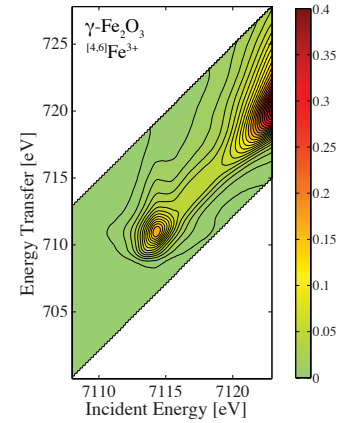
(spinel). □ represents a vacancy, T<sub>d</sub> a tetrahedral site and O<sub>h</sub> an octahedral site. Octahedra are linked each other by the edges and to tetrahedra by corners



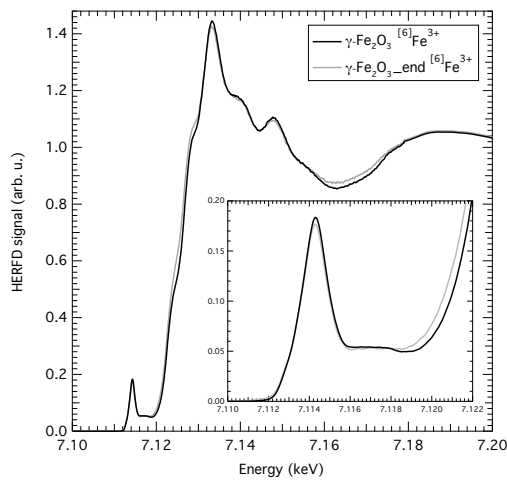
XES  $K\beta$  main



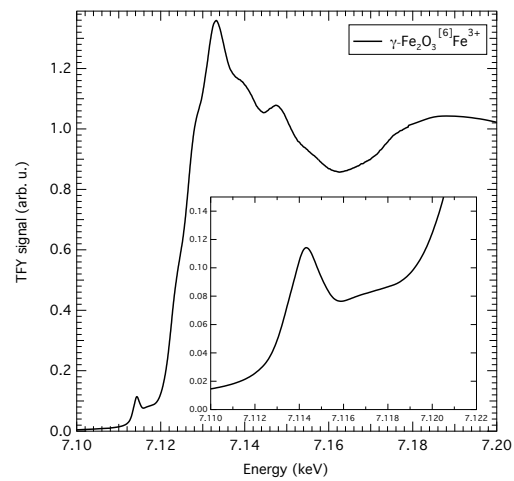
XES  $K\beta$  sat



RIXS map, Fe  $K\alpha$



HERFD spectra, Fe  $K$  edge



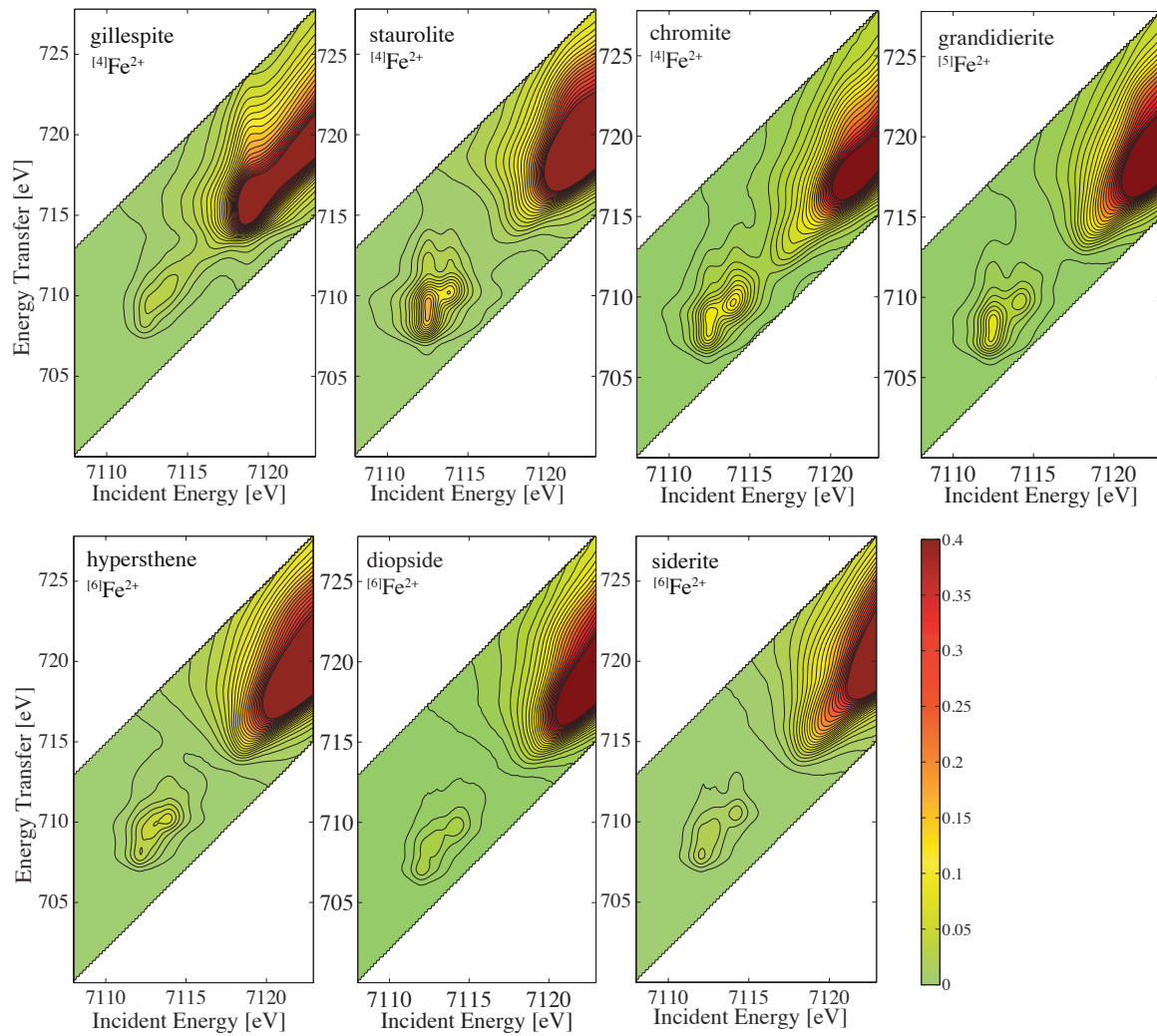
TFY spectra, Fe  $K$  edge

no optical absorption spectra

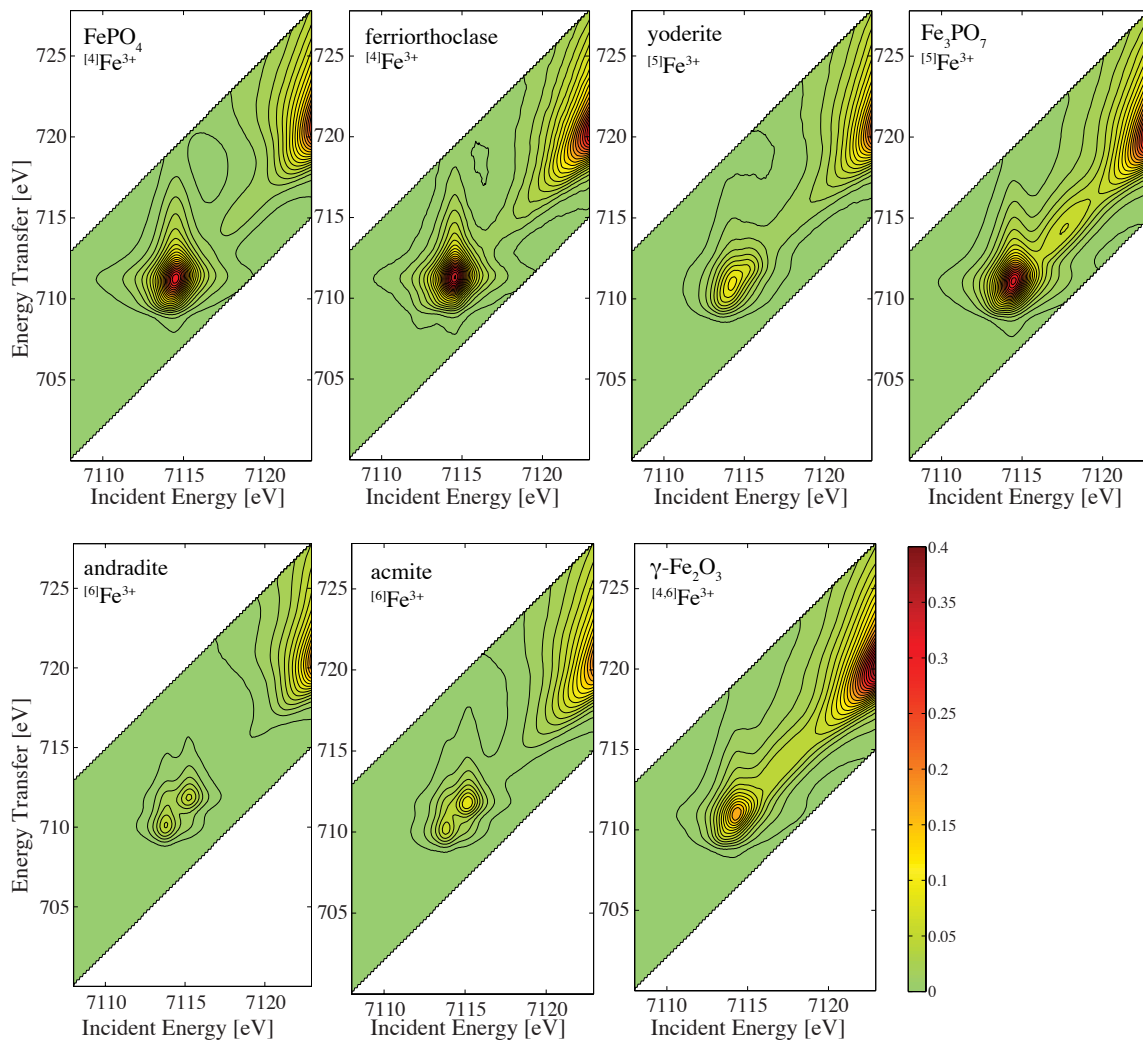
### References

- C. Pecharroman, T. Gonzalez-Carreno, J.E. Iglesias, *Physics and Chemistry of Minerals*, 22 (1995) 21-29 (XRD, IR)  
Nadeem, K., L. Ali, I. Gul, S. Rizwan, et M. Mumtaz. *Journal of Non-Crystalline Solids* 404 (2014): 72-77 (XRD, optical absorption spectroscopy, magnetic)

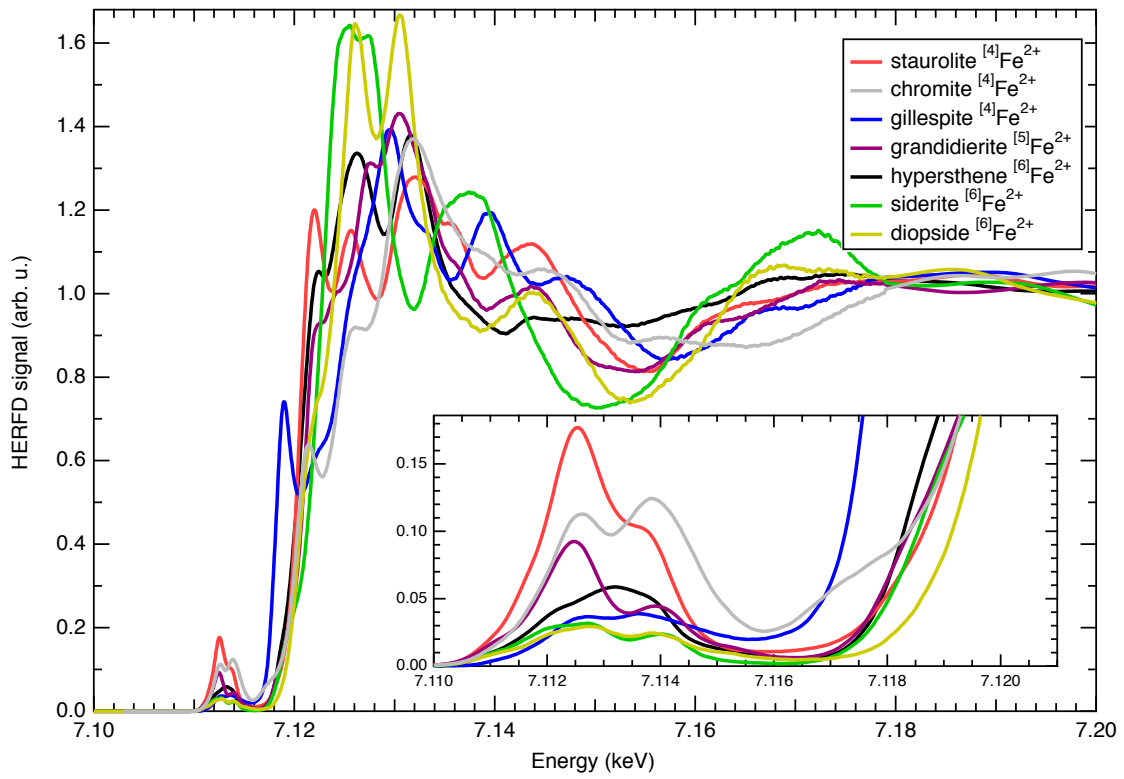
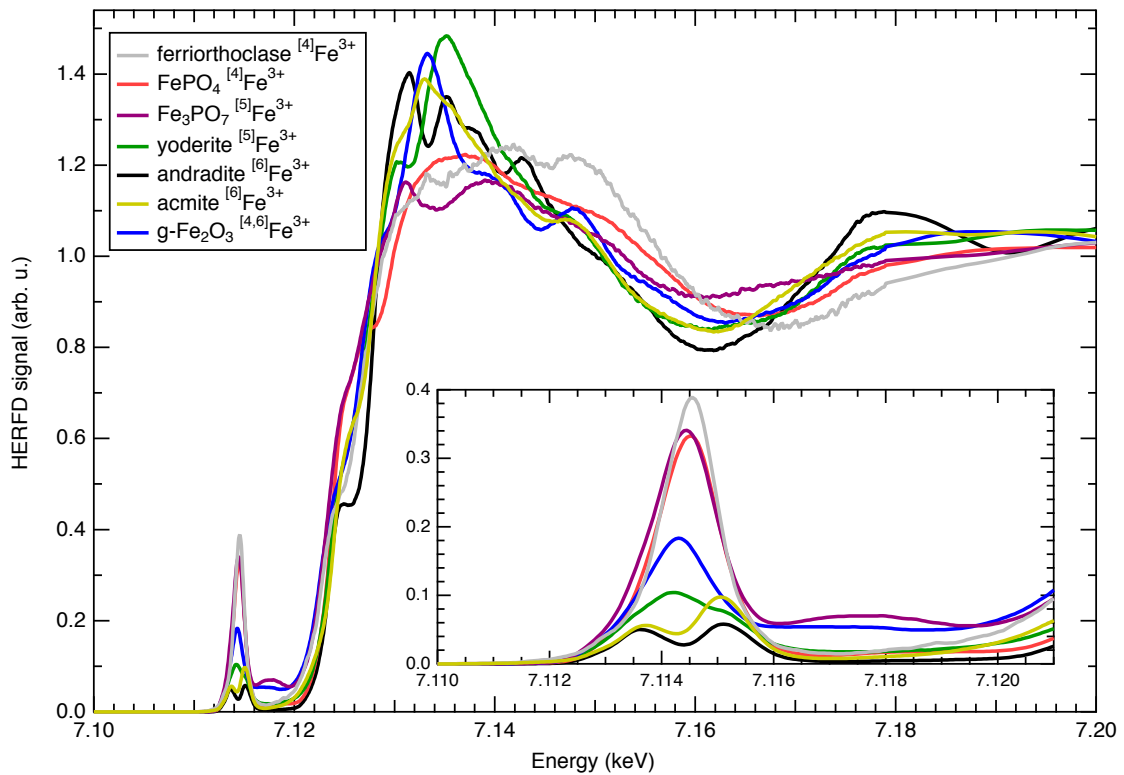


RIXS  $K\alpha$   $\text{Fe}^{2+}$ 

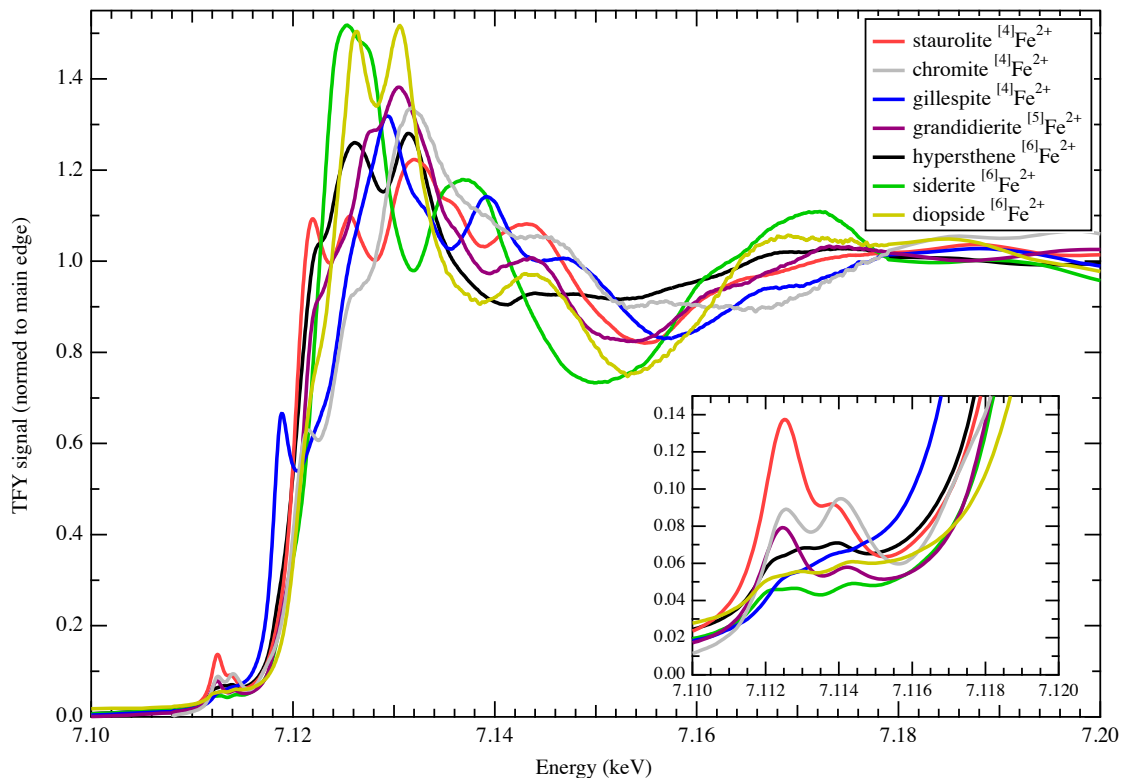
RIXS  $K\alpha$  of  $\text{Fe}^{2+}$ -bearing crystals normed with HERFD spectra and printed with the same scale

RIXS  $K\alpha$   $\text{Fe}^{3+}$ RIXS  $K\alpha$  of  $\text{Fe}^{3+}$ -bearing crystals normed with HERFD spectra and printed with the same scale

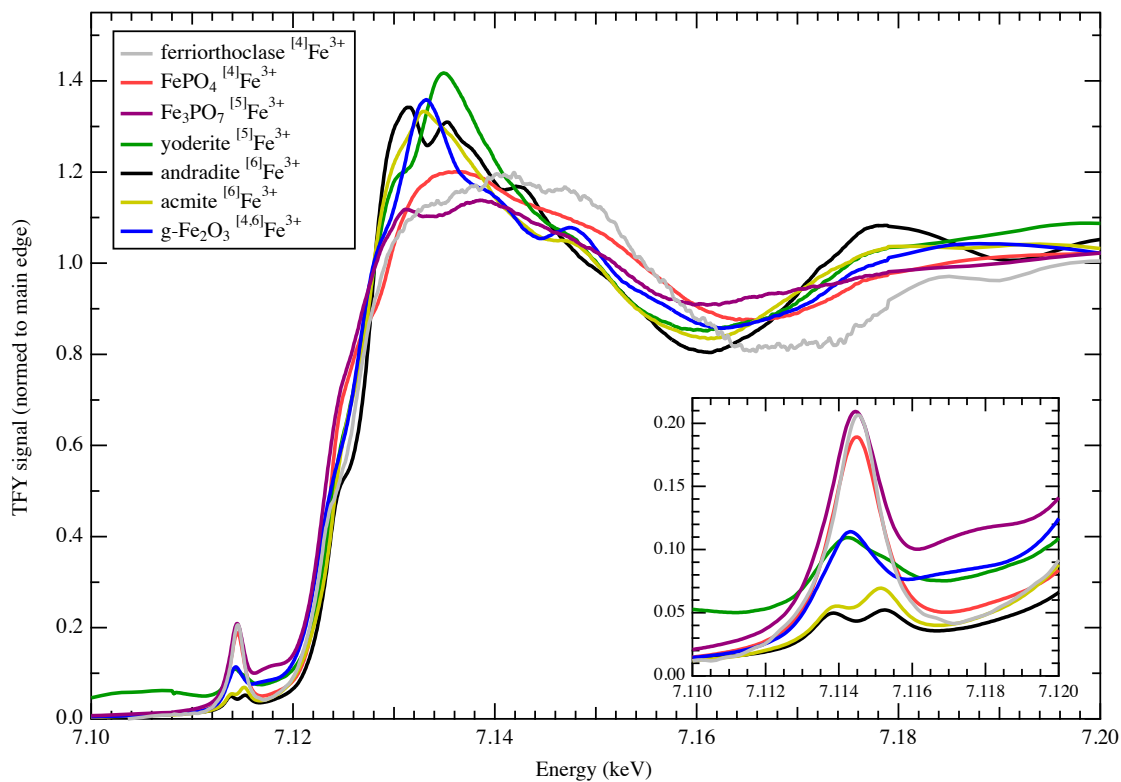
## all HERFD spectra

HERFD spectra of ferrous iron crystalline references ( $\text{Fe}^{2+}$ )HERFD spectra of ferric iron crystalline references ( $\text{Fe}^{3+}$ )

all TFY spectra

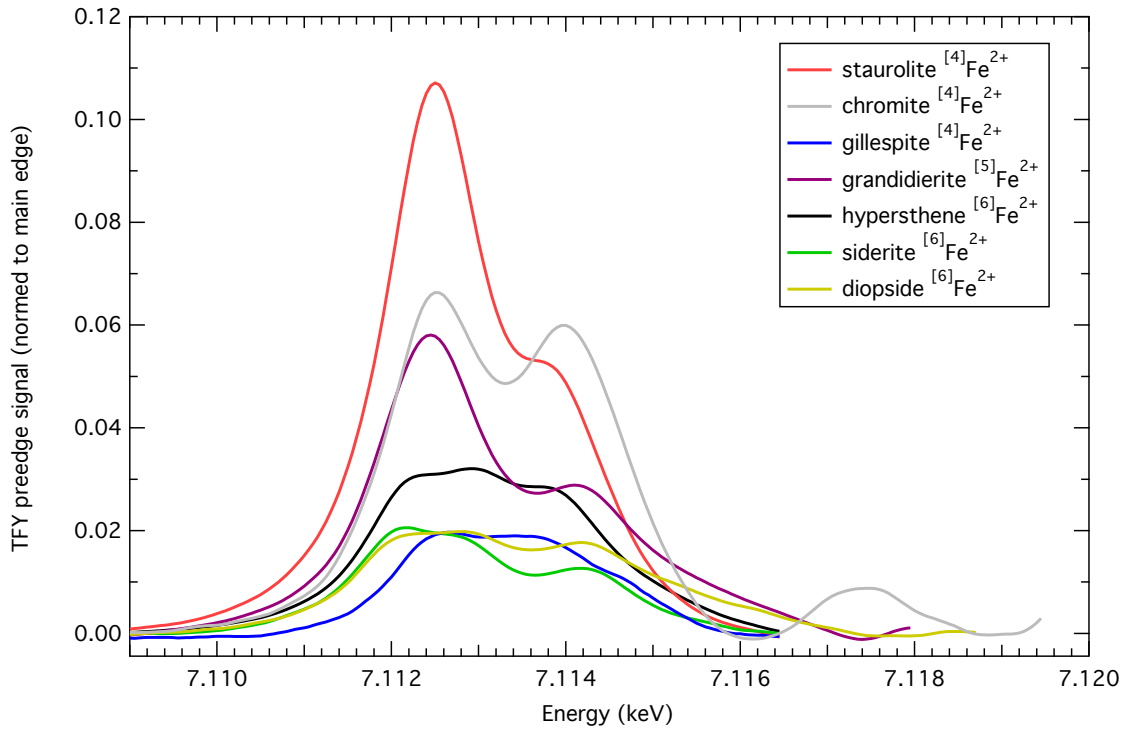


TFY spectra of ferrous iron crystalline references ( $\text{Fe}^{2+}$ )



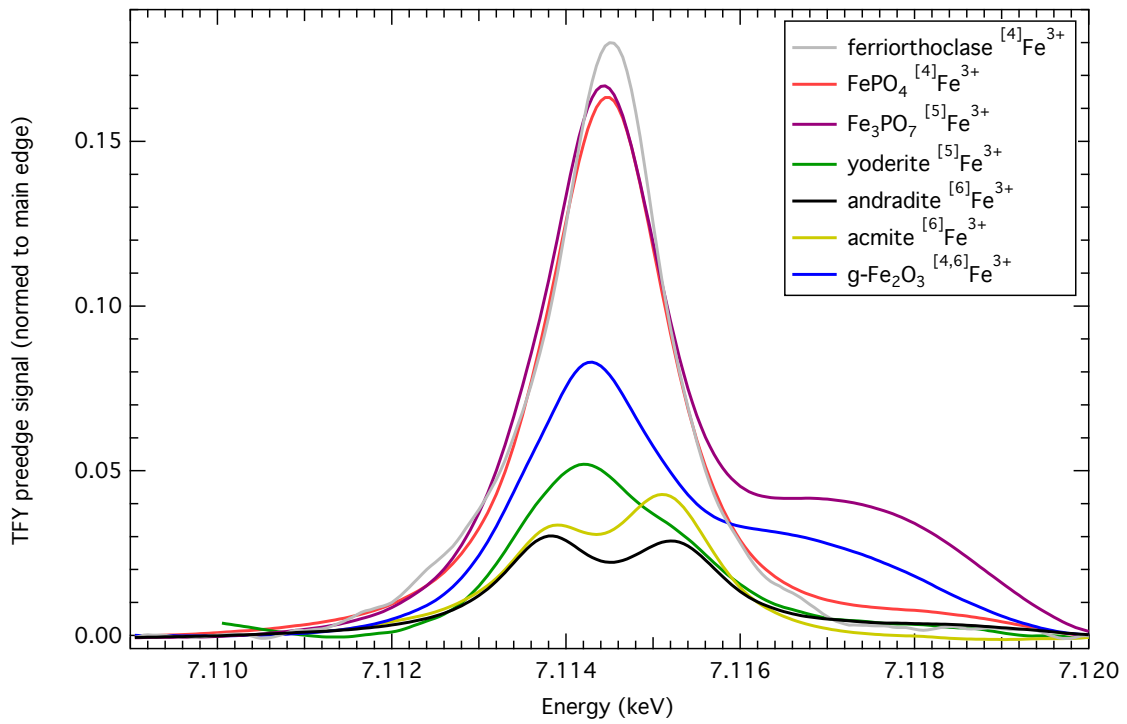
TFY spectra of ferric iron crystalline references ( $\text{Fe}^{3+}$ )

## all TFY spectra - pre-edge without main edge



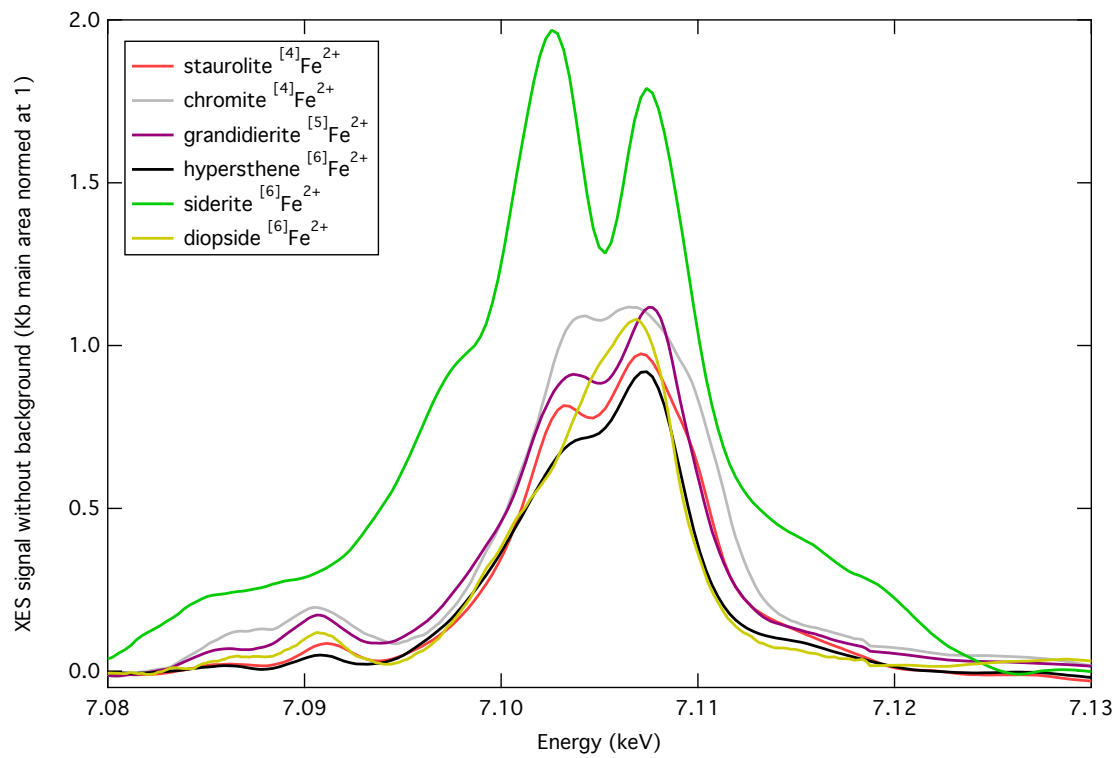
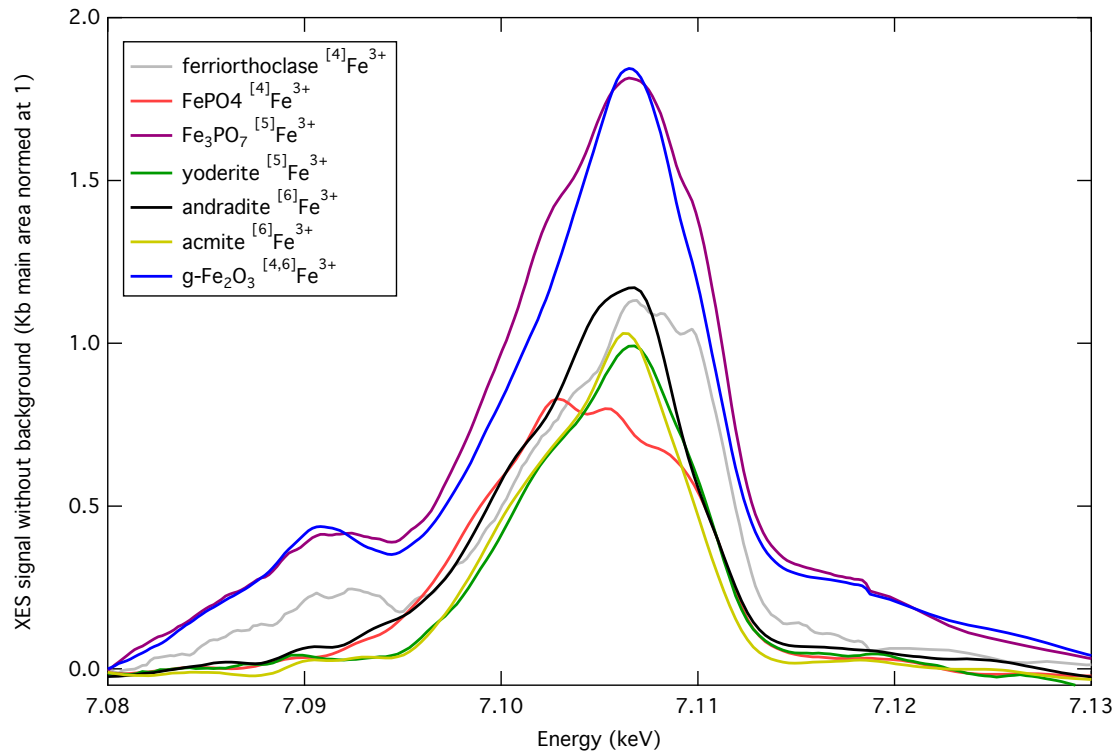
TFY pre-edge without main edge of ferrous iron crystalline references ( $\text{Fe}^{2+}$ )

Area ( $\times 10^5$ ): chromite  $^{[4]}\text{Fe}^{2+}$ : 18.8, staurolite  $^{[4]}\text{Fe}^{2+}$ : 23.3, gillespite  $^{[4]}\text{Fe}^{2+}$ : 5.6, grandidierite  $^{[5]}\text{Fe}^{2+}$ : 15.4, hypersthene  $^{[6]}\text{Fe}^{2+}$ : 10.3, siderite  $^{[6]}\text{Fe}^{2+}$ : 5.9, diopside  $^{[6]}\text{Fe}^{2+}$ : 7.7

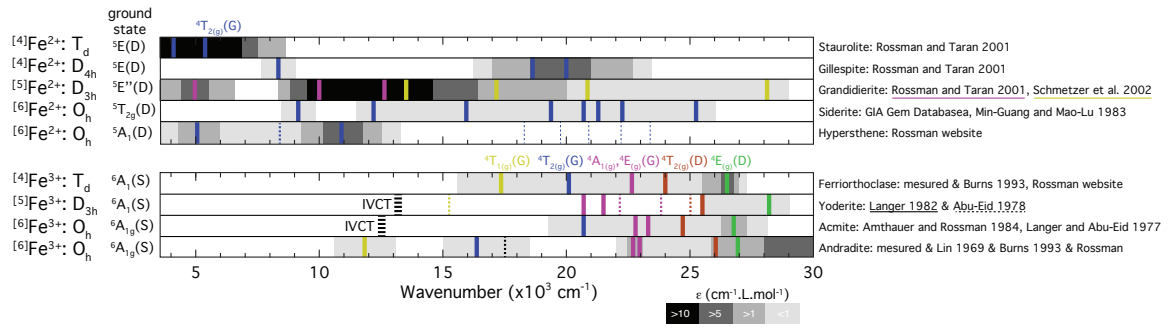


TFY pre-edge without main edge of ferric iron crystalline references ( $\text{Fe}^{3+}$ )

Area ( $\times 10^5$ ): ferriorthoclase  $^{[4]}\text{Fe}^{3+}$ : 34.3,  $\text{FePO}_4$   $^{[4]}\text{Fe}^{3+}$ : 34.2,  $\text{Fe}_3\text{PO}_7$   $^{[5]}\text{Fe}^{3+}$ : 44.1, yoderite  $^{[5]}\text{Fe}^{3+}$ : 12.0, andradite  $^{[6]}\text{Fe}^{3+}$ : 9.7, acmite  $^{[6]}\text{Fe}^{3+}$ : 10.9,  $\gamma\text{-Fe}_2\text{O}_3$   $^{[4,6]}\text{Fe}^{3+}$ : 24.9

all XES  $K\beta_{\text{sat}}$  spectraXES  $K\beta_{\text{sat}}$  spectra of ferrous iron crystalline references ( $\text{Fe}^{2+}$ )XES  $K\beta_{\text{sat}}$  spectra of ferric iron crystalline references ( $\text{Fe}^{3+}$ )

## all optical sticks



Sticks form optical spectra iron crystalline references

## Appendix B

# Optical absorption spectroscopy

### B.1 Perkin-Elmer<sup>®</sup> Lambda 1050

The spectral range covered by this instrument spans from ultraviolet (180 nm) to near-infrared (3300 nm). For transparent materials, like glasses, absorption is measured by transmission of a normal incident light beam on polished sample (to avoid surface scattering caused by roughness) with parallel faces (to avoid beam deviation).

Optical measurements presented here have been performed with a Perkin-Elmer<sup>®</sup> Lambda 1050 UV-Visible-NIR spectrophotometer in transmission mode using three detectors and two lamps to cover a wide wavelength ( $\lambda$ ) range with 1 nm step.

**Lamps** Lambda 1050 spectrometer has two light sources:

- A deuterium lamp for UV wavelength range ( $\lambda$  from 200 to 319.2 nm), a low-pressure gas-discharge light source.
- A tungsten-halogen for Visible-NIR range (from 319.2 to 3300 nm), an incandescent lamp.

**Detectors** Lambda 1050 spectrometer has three detectors:

- A photomultiplier R6872 for high energies in the entire UV/Vis wavelength range (from 200 to 860.8 nm), the gain is auto and the response is 0.2 s.
- A high-performance Peltier-cooled InGaAs detector (from 860.8 to 2500 nm), the gain is 6.75 and the response is 0.2 s.
- A Peltier-cooled PbS detector (from 2500 to np[nm]3300), the gain is 0.2 and the response is 0.2 s.

### B.2 How to convert $\alpha$ to $\varepsilon$

For  $m_{\text{glass}} = 1$  g of glass doped 0.5 wt% of  $\text{Fe}_2\text{O}_3$  there is 0.005 g of  $\text{Fe}_2\text{O}_3$ , that leads to the amount of iron  $n_{\text{Fe}}$ :

$$n_{\text{Fe}} = 2 \frac{m_{\text{Fe}_2\text{O}_3}}{M_{\text{Fe}_2\text{O}_3}} = 2 \frac{m_{\text{glass}} \times \text{wt}\%_{\text{Fe}_2\text{O}_3}}{M_{\text{Fe}_2\text{O}_3}} \quad (\text{B.1})$$

where  $M_{\text{Fe}_2\text{O}_3} = 159.69$  g/mol, is the molar mass of  $\text{Fe}_2\text{O}_3$ .



The concentration in mol/L of the total iron in glass is given by:

$$c = [\text{Fe}] = \frac{n_{\text{Fe}}}{V_{\text{glass}}} = \frac{n_{\text{Fe}} \times \rho}{m_{\text{glass}}} \quad (\text{B.2})$$

where  $\rho$  is the density in g/L (for soda-lime glasses  $\rho \sim 2500$  g/L)

With Equation B.1, the concentration can be written as:

$$c = \frac{2 \times \text{wt}\%_{\text{Fe}_2\text{O}_3} \times \rho}{M_{\text{Fe}_2\text{O}_3}} \quad (\text{B.3})$$

Depending on the species we are looking at, the molar absorption coefficient can be defined with the following relations:

$$\varepsilon_{\text{Fe}} = \frac{\alpha}{[\text{Fe}]} = \frac{\alpha}{c} ; \varepsilon_{\text{Fe}^{2+}} = \frac{\alpha}{[\text{Fe}^{2+}]} = \frac{\alpha}{c \times R} ; \varepsilon_{\text{Fe}^{3+}} = \frac{\alpha}{[\text{Fe}^{3+}]} = \frac{\alpha}{c \times (1 - R)} \quad (\text{B.4})$$

### B.3 Beer lambert verification for reduced glasses

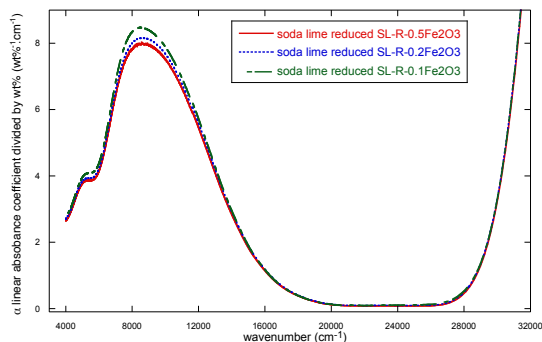
Despite its simple expression ( $A = \alpha \cdot l = \varepsilon \cdot c \cdot l$ , cf. Equation 2.3), Beer-Lambert law is not trivial. When the amount of a coloring element is increased, the linearity with concentration is not necessarily verified. It is especially the case for iron above an approximate limit of 1 wt%  $\text{Fe}_2\text{O}_3$ , the non-linear evolution proves a change in the local environment around iron. For higher iron content glasses, clusters could not be neglected because they are leading to strong optical absorption bands due to intervalence charge transfer (IVCT) [Bingham et al., 1999].

Due to their special synthesis conditions, the reduced glasses presented in this thesis have not been widely studied in the literature. To check Beer-Lambert law for  $\text{Fe}^{2+}$ , three soda-lime glasses base on the composition  $16\text{Na}_2\text{O}-10\text{CaO}-74\text{SiO}_w$  were synthesized under the same reducing conditions. They have the same matrix composition and  $\text{Fe}^{2+}/\text{Fe}_{\text{tot}}$   $R \sim 99\%$ , but different total iron content: 0.1 wt%, 0.2 wt% and 0.5 wt%  $\text{Fe}_2\text{O}_3$ . Samples were polished at a 4 mm-thickness under the same conditions.

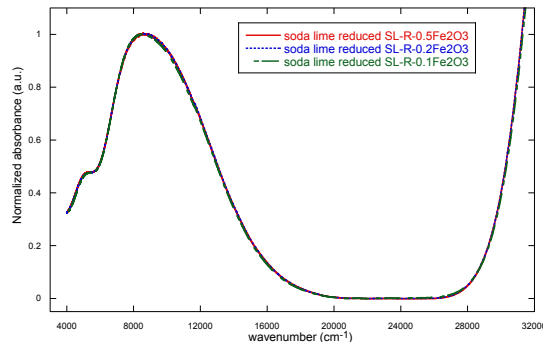
Figure B.1 shows the three absorption spectra after reflection background and normalization by the thickness and weight percent of iron (III) oxide. With the hypothesis that the density is the same for all samples, the spectra have to be equal to each other and proportional to the molar absorption coefficient  $\varepsilon$ . However, they do not overlap perfectly because the real iron amount is different from the theoretical amount. This can be caused by iron diffusion in the crucible or other process inducing a bias with the nominal composition, such as weighting uncertainties or volatilization (especially of sodium) during glass melting. Another possibility is that the geometries of iron sites slightly differ between the samples, some Fe ions thereby occupy sites with a weaker  $\varepsilon$  and became silent species.

Figure B.2 shows the normalized spectra from the minimum at  $22\,000\text{ cm}^{-1}$  to the maximum of the ferrous iron peak about  $10\,000\text{ cm}^{-1}$ . The spectral overlap means that iron ions are located in the same sites with the same proportions of each sites. There is a 3% error on iron concentration between estimated and theoretical iron amount from figures B.1

and B.2. For glasses with 0.1 wt%  $\text{Fe}_2\text{O}_3$  (1000 ppm) that means a 30 ppm error, which corresponds to electron microprobe analysis (EMPA) resolution.



**Figure B.1** – Corrected optical absorption spectra divided by the iron content of three reduced soda-lime silicate glasses with different iron content (0.1; 0.2 and 0.5 wt%)



**Figure B.2** – Normalized absorption spectra by the maximum of the ferrous iron peak of three reduced soda-lime silicate (SL) glasses with different iron content (0.1; 0.2 and 0.5 wt%)

Figure B.3 shows linear regression of the absorbance (in  $\text{cm}^{-1}$ ) at few fixed wavelengths without reflection background subtraction. The regression coefficients are close to 1, thus, the proportionality of the absorbance versus concentration in Beer-Lambert law is verified.

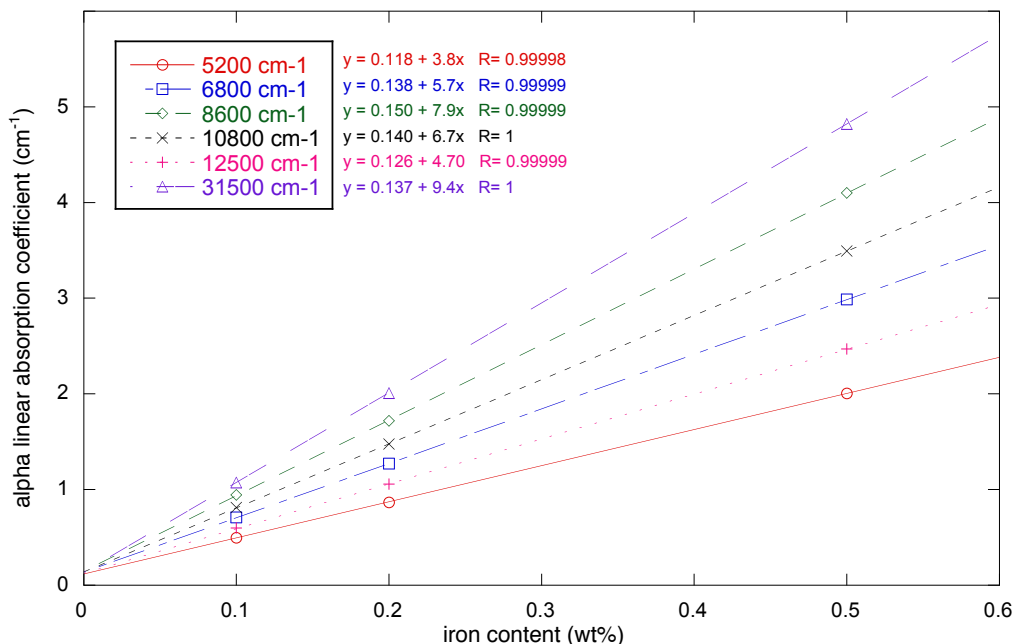


**Figure B.3** – Evolution of linear absorption coefficient with the iron content for several arbitrary wavenumbers in the UV-visible-NIR range

## B.4 Data processing of weak $\text{Fe}^{3+}$ signals

As we have seen before, the weak  $\text{Fe}^{3+}$  “*d-d* transitions” are weak and overlapped by OMCT and  $\text{Fe}^{2+}$  signals. Further data processing is therefore needed to analyze the effect of composition on  $\text{Fe}^{3+}$  spectra.

### B.4.1 Removing the UV-edge to extract $\text{Fe}^{3+}$ $d-d$ transitions

The necessity to remove the UV-edge, especially for alkali-free glasses is illustrated in Figure B.4. The position of the alkali-free UV-edge is lower than for soda-lime glasses and the weak  $\text{Fe}^{3+}$   $d-d$  bands are overlapped by the intense OMCT.

Using results from the study of the UV-range (see Section 5.3.1), the UV-edge was fitted with two Gaussian curves, then subtracted to the spectrum. Up to  $32\,000\text{ cm}^{-1}$ , Urbach law or Gaussian curve give similar results [Ades et al., 1990]. However, the fitting range can be wider when a Gaussian curve is used, the Gaussian function is parabolic in logarithmic scale while the exponential function is linear in logarithmic scale. Therefore, in Figure B.6, plotted in logarithmic scale, the tail respects Urbach law up to  $32\,000\text{ cm}^{-1}$ , as observed by Steele and Douglas [1965], but above  $32\,000\text{ cm}^{-1}$  the band has a parabolic shape confirming the preference for a Gaussian model.

After the UV-edge subtraction, the  $\text{Fe}^{3+}$  signals in the alkali-free glass are clearly visible in Figure B.5 and can be compared with the soda-lime. The contrast between these two kinds of glass and interpretation of the broader DIO peaks is detailed in Section 6.1.1.

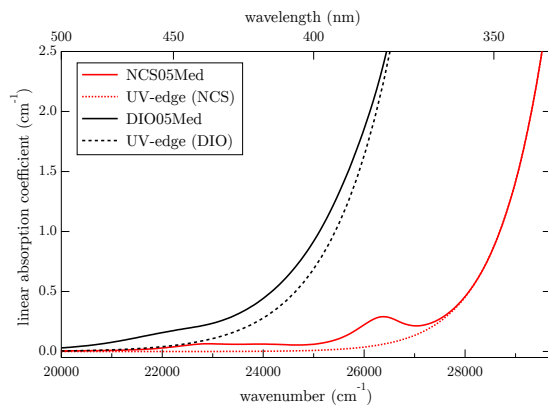


**Figure B.4** – UV edge fitting of the NCS05Med glass with one Gaussian

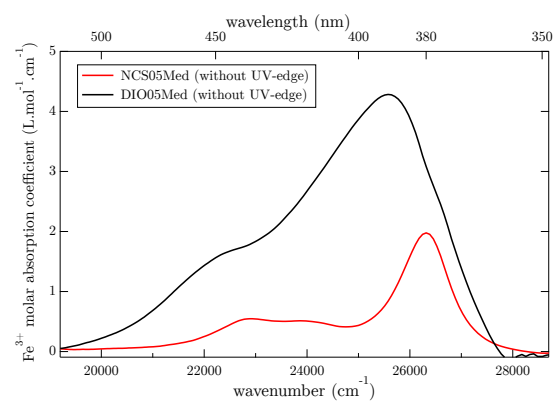


**Figure B.5** – main  $\text{Fe}^{3+}$  peak fitting with one Gaussian

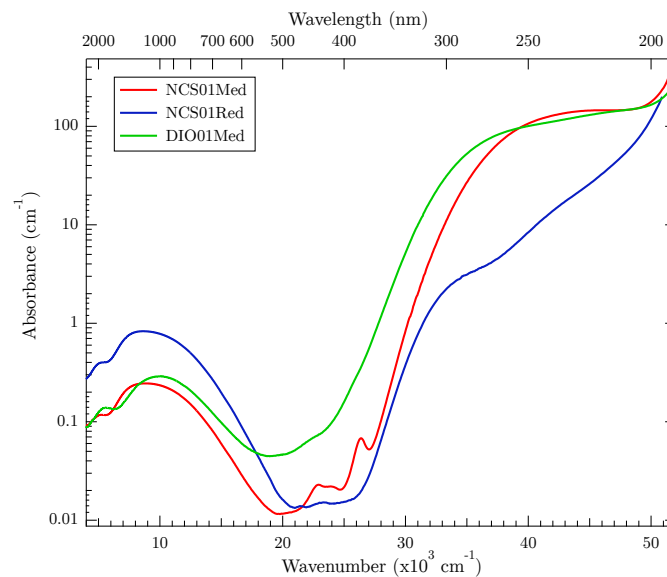


**Figure B.6** – Optical absorption spectra of for the Med and Red soda-lime silicate and Med diopside glasses. The absorbance is in logarithmic scale.

### B.4.2 Separation of Fe<sup>2+</sup>/Fe<sup>3+</sup>

Optical signals of Fe<sup>2+</sup> and Fe<sup>3+</sup> overlapped each other in the UV-Vis-NIR spectra. Nevertheless, Fe<sup>2+</sup> predominates in the range 4000 cm<sup>-1</sup> to 19 000 cm<sup>-1</sup> and Fe<sup>3+</sup> in the range 19 000 cm<sup>-1</sup> to 30 000 cm<sup>-1</sup> [Fox et al., 1982]. In order to separate the two contributions, the following method needs at least two glasses of the same composition with different redox.

In this example three soda-lime (NCS) samples with different redox are considered: NCS05Red, NCS05Med and NCS05Ox (same protocol is applied for NCMS and NMS glasses).

After subtraction of background and UV-edge (fitted from 27 500 cm<sup>-1</sup> to 30 000 cm<sup>-1</sup>), the energy range is limited from 4048.6 cm<sup>-1</sup> (2470 nm) to 30 303 cm<sup>-1</sup> (330 nm). 4048.6 cm<sup>-1</sup> to ignore OH bands and 30 303 cm<sup>-1</sup> because only artifacts remain in the UV after charge transfer removal.

Fe<sup>2+</sup> and Fe<sup>3+</sup> spectra are extracted using linear combinations of two of the 3 spectra. This system of 3 equations with 2 unknowns functions:  $\varepsilon_{Fe^{2+}}(\lambda)$  and  $\varepsilon_{Fe^{3+}}(\lambda)$  is resolved 3 times using Cramer's rule for every wavelength and the 3 couples of 2 equations: (Red,Med), (Red,Ox) and (Med,Ox).

$$\begin{cases} \varepsilon_{Red}(\lambda) = a\varepsilon_{Fe^{2+}}(\lambda) + (1-a)\varepsilon_{Fe^{3+}}(\lambda) & (Red) \\ \varepsilon_{Med}(\lambda) = b\varepsilon_{Fe^{2+}}(\lambda) + (1-b)\varepsilon_{Fe^{3+}}(\lambda) & (Med) \\ \varepsilon_{Ox}(\lambda) = c\varepsilon_{Fe^{2+}}(\lambda) + (1-c)\varepsilon_{Fe^{3+}}(\lambda) & (Ox) \end{cases}$$

with  $a$  the redox of Red glass,  $b$  the redox of Med glass,  $c$  the redox of Ox glass. The redox parameters  $a$ ,  $b$  and  $c$  of the three samples are automatically adjusted (using excel solver and GRG method) with the following restrictions:

- Minimization of  $\sum \varepsilon_{Fe^{3+}}^2$  in the range 4050 cm<sup>-1</sup> to 19 000 cm<sup>-1</sup>
- Minimization of  $\sum \varepsilon_{Fe^{2+}}^2$  in the range 19 000 cm<sup>-1</sup> to 30 000 cm<sup>-1</sup>

This adaptation of least squares method, by minimizing  $\varepsilon^2$  in the range where they are not predominant, gives the possibility to extract redox instead of using fixed redox, guessed from another method such as wet chemistry. However, in this model, molar absorption coefficients are supposed to be independent of the glass redox state.

Table B.1 shows the results of estimated redox compared to redox from wet chemistry listed in Table B.2. The calculated values are within the wet chemistry error. Thus, the small errors on estimated redox values confirm the validity of this methodology.

**Table B.1** – Calculated redox in % deduced from the optimization of the linear combination of optical spectra

name	Ox	Med	Red
NCS05	7.3	29.2	98.4
NCMS05	7.2	24.7	99.9
NMS05	9.7	25.2	99.9

**Table B.2** – Experimental redox in % obtained with wet chemistry ( $\pm 3\%$ )

name	Ox	Med	Red
NCS05	6.4	27.8	96.8
NCMS05	4.9	25.3	96.1
NMS05	6.5	23.9	96.4

Results are shown in Figures B.7(a), B.7(b) and B.8. As expected regarding the selection rules, spin-allowed transitions of  $\text{Fe}^{2+}$  are 10 times higher than  $\text{Fe}^{3+}$  spin-forbidden ones. It explains that for oxidized glasses, since  $\text{Fe}^{3+}$  is the major redox species ( $\sim 5\% \text{Fe}^{2+}$ ), the  $\text{Fe}^{3+}$  signal has the same order of magnitude than the small amount of remaining  $\text{Fe}^{2+}$ .

$\text{Fe}^{2+}$  is dominating the range from  $4000$  to  $19000 \text{cm}^{-1}$ , and there is no  $\text{Fe}^{3+}$  band able to significantly influence the optical spectrum of  $\text{Fe}^{2+}$  in this range. On the  $\text{Fe}^{2+}$  spectrum, signals from  $20000$  to  $28000 \text{cm}^{-1}$  (Figure B.7(b)) are 2 times weaker than  $\text{Fe}^{3+}$  bands. These bands could have been neglected at first in oxidized and medium glasses with redox inferior to  $\sim 25\%$ , but become be a major issue for the study of  $\text{Fe}^{3+}$  bands in glasses with  $R > 70\%$ . The interpretation of these weak signals apparently related to  $\text{Fe}^{2+}$  are discussed in Section 5.2.5.

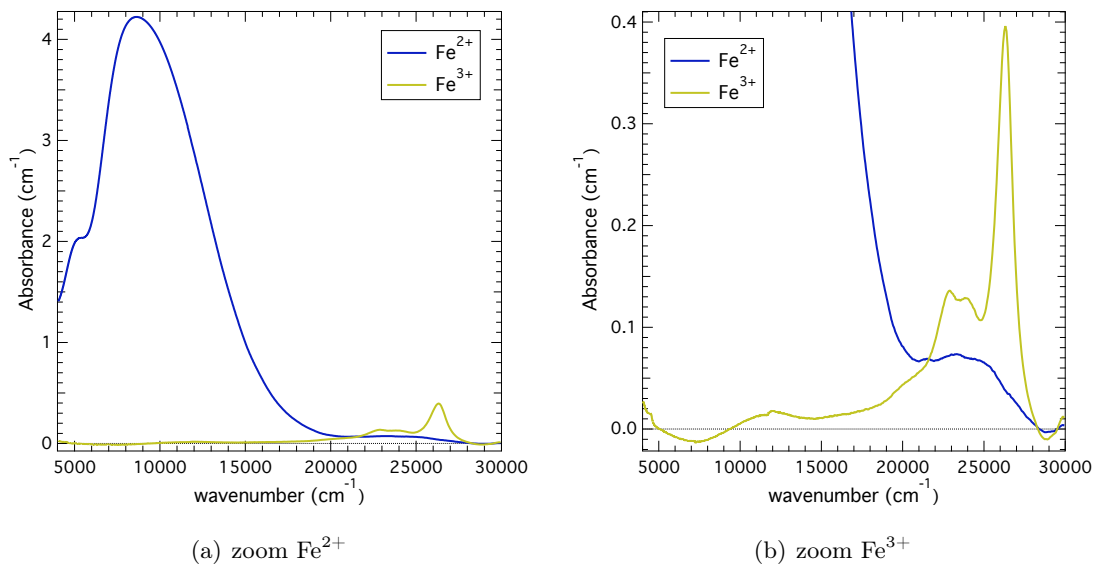


**Figure B.7** – Extracted linear absorption coefficient  $\alpha_{\text{Fe}^{2+}}$  and  $\alpha_{\text{Fe}^{3+}}$

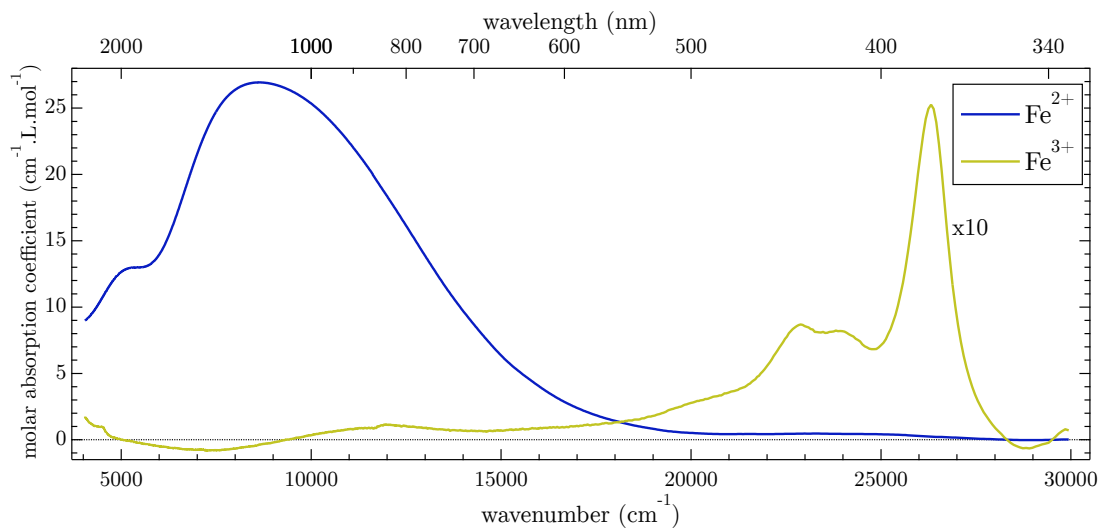


**Figure B.8** – Estimated molar absorption coefficient  $\varepsilon_{\text{Fe}^{2+}}$  and  $\varepsilon_{\text{Fe}^{3+}}$  in NCS05 glasses.  $\text{Fe}^{3+}$  has been magnified by a factor 10.

When extracting the  $\text{Fe}^{3+}$  optical signature, the spectrum takes negative values from 5000 to 9000  $\text{cm}^{-1}$  (see Figure B.7-b). This artifact in the  $\text{Fe}^{2+}$  range due to a shift of the main  $\text{Fe}^{2+}$  band with the redox. These changes of shape and position of  $\text{Fe}^{2+}$  bands with redox is related to the evolution of  $\text{Fe}^{2+}$  environment and could be a limiting issue to this deconvolution method.

The removing of the  $\text{Fe}^{2+}$  tail could be useful for the analysis of weak bands from 17 000 to 21 000  $\text{cm}^{-1}$ . For example, the weak signal around 17 000  $\text{cm}^{-1}$  on  $\text{Fe}^{3+}$  spectrum could corresponds to the transition  ${}^6A_1 \rightarrow {}^4T_1$  observed in minerals (Figure 4.24). However, this band is in the transition zone between  $\text{Fe}^{2+}$  and  $\text{Fe}^{3+}$  ranges, and its extraction could be influenced by the shift of the main  $\text{Fe}^{2+}$  with redox.

In conclusion, this separation of overlapping  $\text{Fe}^{2+}$  and  $\text{Fe}^{3+}$  optical signatures using linear combination of spectra gives a coherent estimation (without a priori) of the redox values, and is especially useful for the study of  $\text{Fe}^{3+}$  environment. In addition, for the highly oxidized ( $R \sim 5\%$ ) or reduced ( $R \sim 95\%$ ) glasses studied in this thesis, the overlap can be neglected in the regions of interest.

### B.4.3 Gaussian fit of the $\text{Fe}^{3+}$ bands

In order to extract the different  $\text{Fe}^{3+}$  contributions from the glass spectra, a Gaussian fit has been performed, based on the work of Volotinen et al. [2008] and references therein. Jørgensen et al. [1954] showed that optical absorption bands of transition metals can be approximated by Gaussian functions of the wavenumber as independent variable with good results on the residual error. For a fit with three Gaussian functions, the fitting range was restricted to 22 400–24 500  $\text{cm}^{-1}$  and 26 000–26 700  $\text{cm}^{-1}$ , nearby the three main bands of  $\text{Fe}^{3+}$  at 22 900, 24 000 and 26 300  $\text{cm}^{-1}$ . For a fit with six Gaussian functions the fitting range 20 000–28 000  $\text{cm}^{-1}$  was considered.

### B.4.4 Low-iron glasses

Glasses of the same matrix composition without added iron were synthesized in order to know the properties of the matrix such as refractive index, reflection coefficient, diamagnetism. Because EMPA precision is not adapted to this threshold, this part explains how to estimate the iron content in these glasses using optical spectroscopy: For the example, two glasses were considered, NCS00Med, a thick sample without added-iron and synthesized in the same conditions than the medium glass, NCS01Med, containing 0.1 wt% of  $\text{Fe}_2\text{O}_3$ , in both samples the  $\text{Fe}^{2+}/\text{Fe}_{\text{tot}}$  ratio is approximately  $R \sim 25\%$ .

Optical spectra are plotted in logarithmic scale for the y-axis (Figure B.9). The two glasses synthesized under air atmosphere, NCS01Med and NCS00Med, exhibit the same shape except that NCS00Med signal is about 13 times weaker. This vertical translation confirms the previous Beer-Lambert law results. This proportionality of the linear absorption coefficient (in  $\text{cm}^{-1}$ ) gives an estimation of the remaining iron content in these “iron-free” glasses. Results for the four studied composition of this thesis are compared in Table B.3 with experimental values of EMPA. Both analyses agree with a remaining iron content around 70~100 ppm of  $\text{Fe}_2\text{O}_3$ .

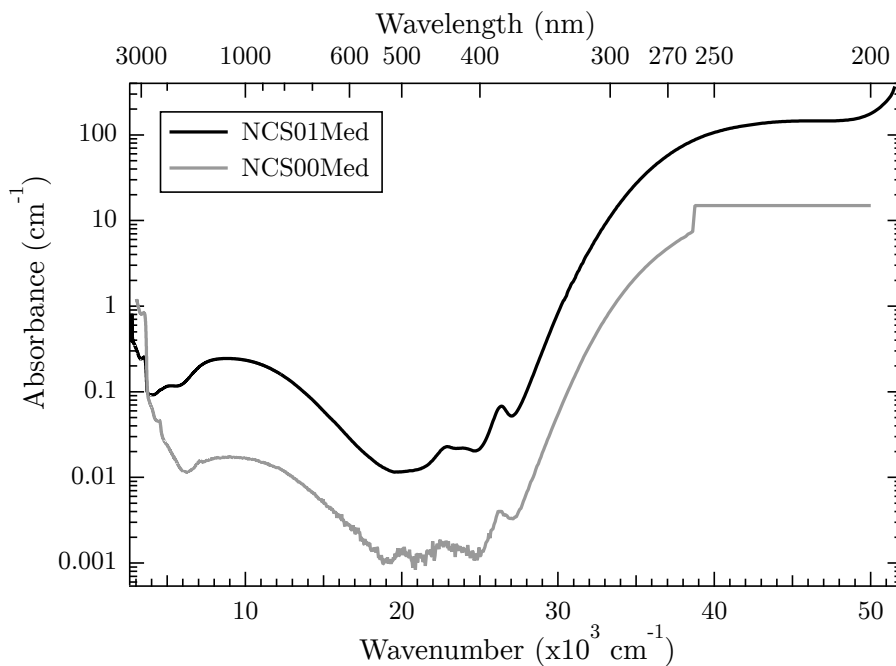


**Figure B.9** – logarithmic representation of the optical absorption spectra for the soda-lime silicate medium glasses with no added iron (NCS00Med) and 0.1 wt% of  $\text{Fe}_2\text{O}_3$  (NCS01Med).

**Table B.3** – Iron content (in ppm  $\text{Fe}_2\text{O}_3$ ) of the no added-iron glasses: estimated by EMPA and by optical absorption (comparison of UV range with 0.5 wt% glasses)

sample	iron content (ppm)	
	EMPA	OPT
NCS00Med	76	70
NCSM00Med	100	96
NMS00Med	70	80
DIO00Med	77	73

## Appendix C

# SQUID-VSM

### C.1 Magnetic units

**Table C.1** – Units in magnetism

Quantity	symbol	SI unit	cgs unit
Magnetic moment	$\mu$	$10^{-3} \text{ A.m}^2$	=1 emu
Magnetization (= moment per volume)	$M$	$10^3 \text{ A.m}^{-1}$	=1 Oe or emu.cm <sup>-3</sup>
Magnetic susceptibility	$\chi$	$4\pi \times 1$	=1 emu.cm <sup>-3</sup> .Oe <sup>-1</sup>
Molar susceptibility	$\chi_{\text{mol}}$	$4\pi \times 10^{-6} \text{ m}^3.\text{mol}^{-1}$	=1 emu.mol <sup>-1</sup> .Oe <sup>-1</sup>
Mass susceptibility	$\chi_{\text{wt}}$	$4\pi \times 10^{-3} \text{ m}^3.\text{kg}^{-1}$	=1 emu.g <sup>-1</sup> .Oe <sup>-1</sup>

Adapted from Stephen Blundell 2005

$\chi$  is the (volume) magnetic susceptibility (dimensionless),  $\chi_{\text{mol}}$  is the molar magnetic susceptibility ( $\text{m}^3.\text{mol}^{-1}$ ) and  $\chi_{\text{wt}}$  is the mass magnetic susceptibility ( $\text{m}^3.\text{kg}^{-1}$ ). These three quantities are related by:

$$\chi_{\text{mol}} = M\chi_{\text{wt}} = \frac{M}{\rho}\chi \quad (\text{C.1})$$

$M$  is the molar mass, and  $\rho$  is the density ( $\text{kg}/\text{m}^3$ )

*emu*, is short for ‘electromagnetic unit’ and is not a unit in the conventional sense. It is sometime used as a magnetic moment ( $1 \text{ emu} = 1 \text{ erg.G}^{-1}$ ) and sometime takes the dimension of a volume ( $1 \text{ emu} = 1 \text{ cm}^3$ ).

$$\chi_{\text{mol}} = \frac{\mu}{n_{\text{Fe}}H} \quad (\text{C.2})$$

For a paramagnet, the molar susceptibility  $\chi_{\text{mol}}$  is related to the effective moment  $\mu_{\text{eff}}$  in Bohr magnetron per atom with the formula:

$$\mu_{\text{eff}} = 2.827\sqrt{\chi_{\text{mol}}^{\text{cgs}}T} = 797.8\sqrt{\chi_{\text{mol}}^{\text{SI}}T} \quad (\text{C.3})$$

If the material follows a Curie’s law then  $\chi_{\text{mol}}^{\text{SI}}T$  is proportional to the Curie’s constant.



## C.2 Correction for the diamagnetism of the glassy matrix

Due to the low amount of paramagnetic species (Fe) in the studied glasses, the diamagnetic effect of the matrix (principally oxygen and silicon atoms) is not negligible. Figure C.1 shows the product of  $\chi_{wt}$  with the temperature. In this kind of very diluted glasses, we can assume that there is only diamagnetism of the matrix and paramagnetism of the iron traces. Then, due to the additivity of the magnetization, we can fit the curve with a linear function:  $y = \chi_{wt}T = C + \chi_{dia}T$

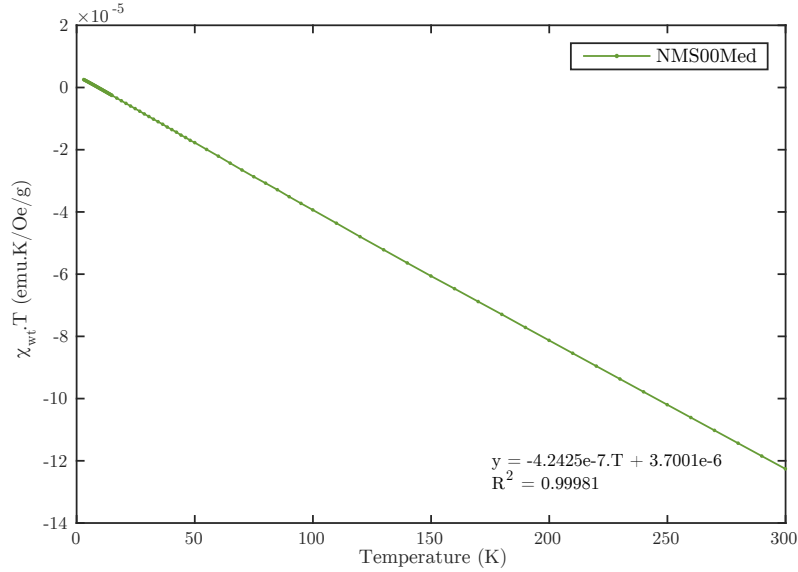


**Figure C.1** – Contribution to the susceptibility by dielectric and paramagnetic species in very low iron-content glass NMS00Med (< 100 ppm).

For NMS00Med glass  $\chi_{wt,dia}^{cgs}$ :  $-4.243 \cdot 10^{-7}$  emu/Oe/g and  $C = 3.700 \cdot 10^{-6}$  emu.K/Oe/g. According to Bain and Berry [2008], soda-magnesium matrix:  $-3.69 \cdot 10^{-7}$  emu/Oe/g. The correction for the diamagnetic contribution clearly appears in Figure C.2.

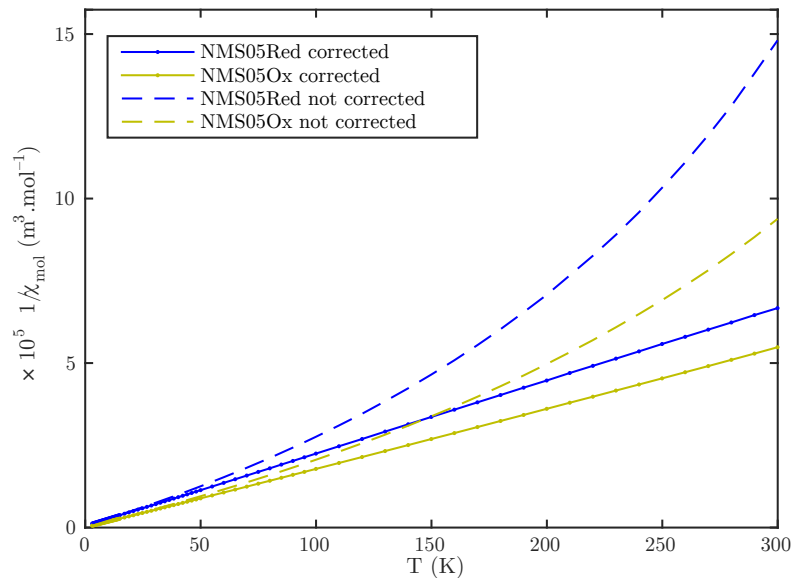


**Figure C.2** – Inverse susceptibility measured at  $H = 10$  mT.

## Appendix D

# X-ray absorption spectroscopy

### D.1 Temperature effect - Boltzmann distribution

The population  $P$  of the different multiplet levels depends on the temperature,  $T > 0$  K, following a Boltzmann distribution:

$$P \propto e^{-\frac{\Delta E}{kT}}, \text{ with } \Delta E = E_i - E_{\text{ground}} \quad (\text{D.1})$$

If the temperature is equal to the absolute zero,  $T = 0$  K, then, only the ground state (the one with the lowest energy) is filled and involved in the electronic transitions. This ground state can be degenerated, thus several levels have the same energy and are equally filled.

At room temperature,  $T = 300$  K,  $kT = 4.14 \cdot 10^{-21}$  J = 26 meV = 210 cm<sup>-1</sup>. Therefore, if  $\Delta E \geq 0.12$  eV then  $e^{-\frac{\Delta E}{kT}} < 0.01$ , the filling of the higher state is only 1% of the ground state. Likewise, if  $\Delta E \geq 0.24$  eV then  $e^{-\frac{\Delta E}{kT}} < 0.001$ , the weight of the  $i$ -th state is only 1‰ of the ground state.

### D.2 Spectral broadening

The width of spectral bands are broaden by two kinds of spectral broadenings: one is a Lorentzian (Equation D.2) broadening due to the material and related to core-hole lifetime, the second is a Gaussian (Equation D.3) broadening due to the experimental setup and related to monochromators and analyzers. They are characterized by their full width at half maximum (FWHM).

$$L(x, \gamma) = \frac{\gamma}{\pi(\gamma^2 + x^2)} = \frac{\Gamma/2}{\pi((\Gamma/2)^2 + x^2)} \quad (\text{D.2})$$

$$G(x, \sigma) = \frac{1}{\sigma\sqrt{2\pi}} e^{-\frac{x^2}{2\sigma^2}} \quad (\text{D.3})$$

The Lorentzian broadening is estimated with the core-hole lifetime calculated in Krause and Oliver [1979] (for iron: FWHM =  $\Gamma = 2\gamma = 1.25$  eV), in this thesis  $\Gamma$  was reduced to 1.12 eV because the value from Krause gave larger spectra than the experiment.

The Gaussian broadening is experimentally estimated by measuring the elastic peak. For XAS measurements at the Fe  $K$  edge at ID26, the elastic peak is at 6506.25 eV with a FWHM = 0.60 eV ( $\sigma = \frac{\text{FWHM}}{2\sqrt{2\ln 2}} = 0.255$  eV).

Note: Whatever the broadening, the area under the pre-edge is constant. The successive convolution of a spectra by two Lorentzian functions with  $\Gamma_1$  and  $\Gamma_2$  width, is equivalent to the convolution of one Lorentzian function with  $\Gamma = \Gamma_1 + \Gamma_2$ . On the other hand, the successive convolution of a spectra by two Gaussian functions with  $\sigma_1$  and  $\sigma_2$  standard deviation, is equivalent to the convolution of one Gaussian function with  $\sigma = \sqrt{\sigma_1^2 + \sigma_2^2}$ .

### D.3 Beam damage

X-ray are made of energetic photons that can disturb or damage the nature of the studied material leading to false interpretations. Therefore, an estimation of the beam-damage and its effects on the local environment of iron is a necessary step to go further in the interpretations of the experiment. Among all samples, only glasses were sensitive to the X-ray beam, we did not see any variation of the spectra of crystals with exposure time.

During a run on 13-ID-E at the Advanced Photon Source (APS) in April 2014, I measured the Fe  $K$  edge of an oxidized and a reduced glass with two different measurement protocols. For the first one, the sample was moved between each point to measure an unexposed part of the glass, while the second one was static. A Si(311) monochromator and two mirrors were used to focus the X-ray micro-beam that locally increasing the energy concentration of photons.

With time exposure (static spectra), the edge-position of oxidized samples is moving ( $-0.3$  eV) to lower energy while the edge-position of reduced samples is moving ( $+0.8$  to  $1.4$  eV) to higher energy (Figure D.1). The pre-edge exhibits the same tendency, with an increase of  $\text{Fe}^{3+}$  signature in reduced glasses and an increase of  $\text{Fe}^{2+}$  signature in oxidized glass (inset of Figure D.1). Oxidized glasses are lightly reduced, while reduced glasses are partially photooxidized.

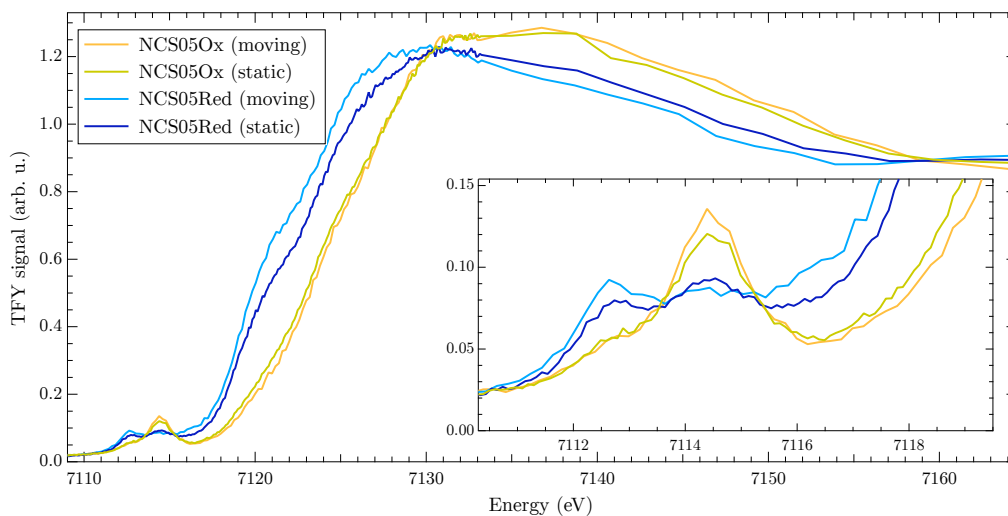


**Figure D.1** – Total Fluorescence Yield of NCS05Ox and NCS05Red glasses in static and moving measurement. Data acquired with a micro-beam at 13-IDE, APS synchrotron.

To estimate the kinetic of these effects on the sample, the beam was moved, at  $t = 0$ , to a sample zone that has not been previously exposed, the intensity of the fluorescence at a given incident and emitted energy (here 7123 eV and 6403.9 eV) was measured as a function of time (Figure D.2-b). It is also possible to measure XAS spectra in a fast acquisition mode (every 10 seconds) to see if there is a spectral shape evolution. However, this last method gives data with a poor signal to noise ratio.

In Figure D.2-a, spectra are measured after 400 s under the X-ray beam. The  $K$  edge position of the oxidized glass is at about +2.5 to +3.3 eV compared to the reduced sample. Using the kinetic curve (Figure D.2-b) with the assumption that the shape of the edge do not significantly change between  $t = 0$  and  $t = 7$  min it is possible to estimate the shift of the edge during the first minutes of exposure: +0.44 eV for NCS05Red and  $-0.33$  eV for NCS05Ox. A quick evolution is observed during the first 2 minutes, then the evolution is slower and seems to be linear with the time (observation up to 1 h). The time constant is approximately the same for both samples (about 30 s). Interestingly, we observe that reduced glasses were photooxidized, while oxidized glasses were photoreduced. The estimated redox are  $R = 80\text{--}87\%$  for NCS05Red instead of 99%,  $R = 13\text{--}17\%$  for NCS05Ox instead of 5%. NCS05Med was also photoreduced with  $R \simeq 38\%$  instead of 28%.

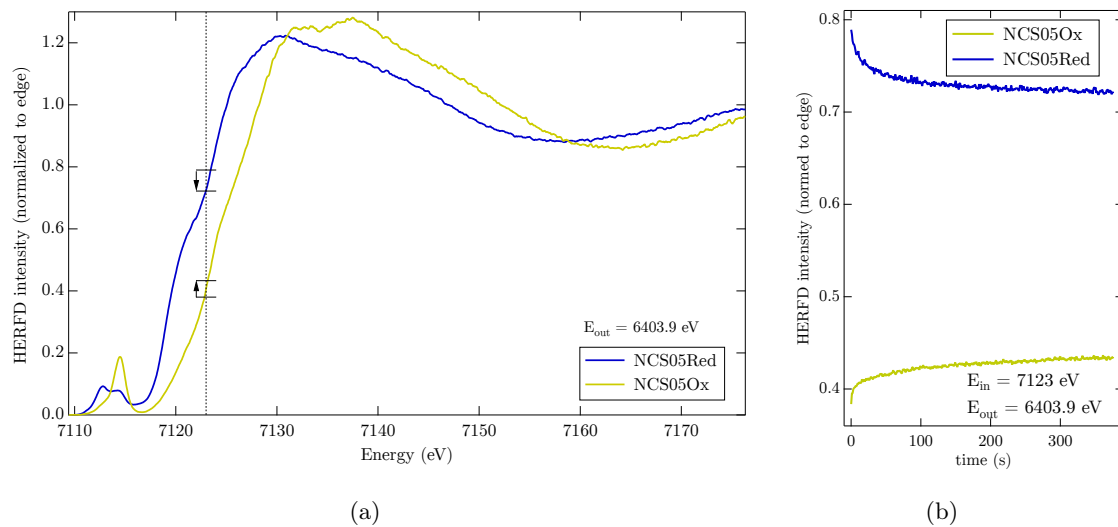


**Figure D.2** – NCS05Red and NCS05Ox glasses. a: HERFD spectra with  $E_{out} = 6403.9$  eV. b: kinetic curve, intensity at  $E_{in} = 7123$  eV and  $E_{out} = 6403.9$  eV as a function of time. Measured at ID26, ESRF synchrotron.

Photoreduction of similar Fe-doped oxidized silicate glasses have been observed by Gonçalves Ferreira et al. [2013]. In this paper, the authors argued that the coordination number does not change during the photoreduction process that has been interpreted as ionic vacancy created by the interaction of the X-ray beam with the matrix associated with cationic displacement (see also Nesbitt and Bancroft [2014, p. 305]). This phenomenon is similar to the sodium migration observed under the electron beam of the microprobe [Morgan and London, 2005] or with  $\beta$ -irradiation [Boizot et al., 2000]. The excess of electrons created by the lack of sodium cations is captured by  $\text{Fe}^{3+}$ , which is reduced to  $\text{Fe}^{2+}$ . However, this interpretation do not explain the photooxidation of reduced glasses.

One has to remember that our glasses were synthesized under specific redox conditions, and that they are frozen in a thermodynamically unstable but kinetically blocked state. The release of Auger electrons (in particular for low atomic number such as Na, Ca, Mg, Si and O) or photoelectrons by the material, due to the interaction with X-ray, can damage the chemical bonds. These broken bonds can be reformed differently, especially in view of the amorphous structure of glass, which is not ideal. This phenomenon can be considered as a local relaxation of the strains, or photoannealing, of the creation of new defects, or photoalteration, that could both generate a redox reaction explaining the photooxidation.

However, electronic defects or free radicals remain in the matrix several weeks after the experiments and can be observed with EPR (Figure D.3). The difference (bottom spectrum) shows a slight change at  $g = 4.3$  and principally a modification at  $g = 2$ , which is a typical of irradiation defects that have already been observed in silicate glasses using EPR and optical absorption spectroscopy [Abdelghany and ElBatal, 2014; Zhang and Sheng, 2013]. The beam mark is visible with the eye and is smaller than 2 by 0.3 mm and probably less than  $100\ \mu\text{m}$  in depth (penetration of the beam). It represents about 1‰ or less of the sample volume (15 mm height and 2 mm diameter). An interesting thing to note, is that even though the small irradiated volume compared to the size of the total sample used for EPR measurement, defects induced by the X-ray beam clearly appear on EPR spectra. After 2 years, the defects are still visible with EPR, but after an annealing of 1 hour at  $450^\circ\text{C}$ , the EPR spectrum is identical to the one before X-ray exposure, confirming the observation of Gonçalves Ferreira et al. [2013] that defect are not stable at high-temperature.

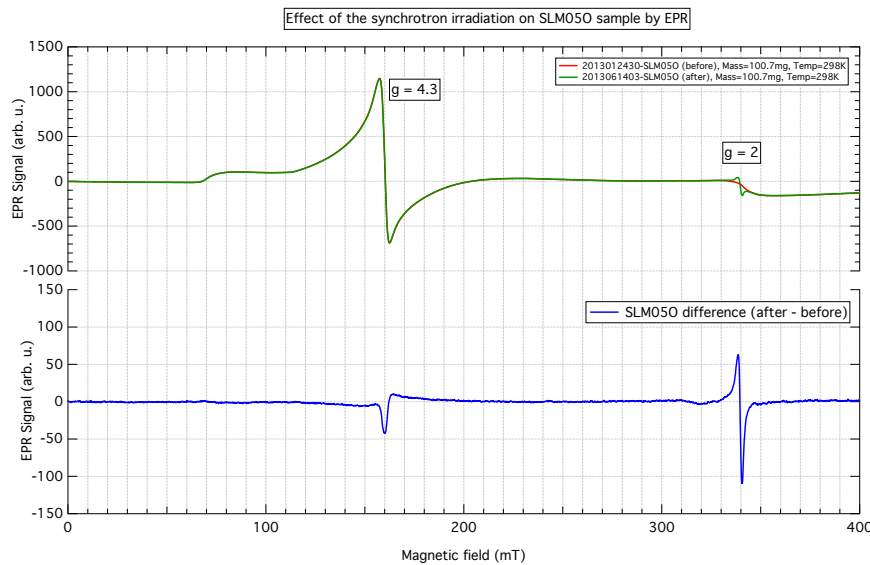


**Figure D.3** – EPR spectra of NCMS05Med glass before and after synchrotron measurement.

The good homogeneity of glass at the size of the beam spot allow measuring the sample in movement, thereby limiting the photo damage of the glass. This cannot be done with powders, due to the granularity, any beam displacement during the measurement change the intensity.

## D.4 Sum rules

Sum rules refer to theoretical estimation of the spectral area related to the nature of the transition operator (electric dipole et quadrupole) and the electron configuration of the initial state [Thole and van der Laan, 1988]. They are useful to check absorption spectrum area of an element at a given edge with initially  $n$  electrons in the destination shell regarding the considered transition. The interesting thing is that sum rules do not depend on crystal field parameters, Slater integrals, nephelauxetic ratio  $\beta$  or broadening.

For X-ray absorption spectroscopy at  $K$  and  $L_{2,3}$  edge, the useful sum rules are:

$$K \text{ pre-edge due to electric quadrupole transition } (1s \rightarrow 3d): \frac{4\ell + 2 - n_d}{15(2\ell + 1)} = \frac{10 - n_d}{75}$$

$K$  pre-edge due to electric dipole transition ( $1s \rightarrow 4p$ ):

$$\sum_{i,f} |\langle f | \hat{T} | i \rangle|^2 \delta(E_f - E_i - \hbar\omega) = \frac{4\ell + 2 - n_p}{3(2\ell + 1)} = \frac{6 - n_p}{9}$$

$$L_{2,3} \text{ electric dipole transition } (2p \rightarrow 3d): \frac{4\ell + 2 - n_d}{3(2\ell + 1)} = \frac{10 - n_d}{15}$$

with  $\ell$ , the orbital momentum of the destination shell for the transition. For example,  $\ell = 1$  for  $1s \rightarrow 4p$  and  $\ell = 2$   $1s \rightarrow 3d$ .

For a transition metal in a centrosymmetric site, there is no  $3d$ - $4p$  mixing, the  $K$  pre-edge area is only due to electric quadrupole transition. Moreover, the total intensity of the spectrum is proportional to the number of valence holes. It is possible to compare the normalized absorption of an experimental spectrum with the sum rule value  $A(\text{Fe}^{2+}) = 6.79 \cdot 10^{-2}$  and  $A(\text{Fe}^{3+}) = 9.66 \cdot 10^{-2}$  (with energy is in eV for spectral integration).



## Appendix E

# Theoretical developments with LFMT

This appendix details some theoretical developments necessary to the calculation of experimental spectra with ligand field multiplet theory.

### E.1 Isotropic resonant inelastic X-ray scattering – the powder formula

Considering a powder, with one iron site but oriented in a random direction, what is calculated spectra averaged over all directions, for a given experimental setup (polarization and wave vector of the incident beam)? Usually, the RIXS spectrum is calculated by averaging on the different absorption and emission polarizations (or branchings) [de Groot et al., 2005]. However, this approximation omits the interference terms between electric dipole and quadrupole contributions when coupling each photon to itself. The Kramers-Heisenberg formula has been recently developed in Juhin et al. [2014] in order to calculate the real powder RIXS spectrum, and that I have implemented with `Matlab`<sup>®</sup> for  $C_1$  and  $C_3$  geometries. Further developments are needed to calculate the spectrum in geometry where not all of the branching are of dimension 1 (e.g.  $T_d$  or  $O_h$ ).

The scattering of light by a quantum system is described by an equation derived by Kramers and Heisenberg before the advent of quantum theory. The multipole scattering cross-section is [Juhin et al., 2014, Equation 1]:

$$\sigma_{scat}(\hbar\omega_i, \hbar\omega_s) = r_e^2 \frac{\omega_s}{\omega_i} \sum_f \left| \varepsilon_s^* \cdot \varepsilon \langle f | e^{i(\mathbf{k}_i - \mathbf{k}_s) \cdot \mathbf{r}} | i \rangle \right. \quad (\text{E.1})$$

$$+ \frac{1}{m_e} \sum_n \frac{\langle f | \vec{\varepsilon}_s^* \cdot \mathbf{P} e^{-i\mathbf{k}_s \cdot \mathbf{r}} | n \rangle \langle n | \vec{\varepsilon}_i \cdot \mathbf{P} e^{i\mathbf{k}_i \cdot \mathbf{r}} | i \rangle}{E_i - E_n + \hbar\omega_i + i\Gamma_n} \quad (\text{E.2})$$

$$+ \frac{1}{m_e} \sum_n \frac{\langle f | \vec{\varepsilon}_i \cdot \mathbf{P} e^{i\mathbf{k}_i \cdot \mathbf{r}} | n \rangle \langle n | \vec{\varepsilon}_s^* \cdot \mathbf{P} e^{-i\mathbf{k}_s \cdot \mathbf{r}} | i \rangle}{E_i - E_n - \hbar\omega_s + i\Gamma_n} \left| \right. \quad (\text{E.3})$$

$$\delta(E_f + \hbar\omega_s - E_i - \hbar\omega_i) \quad (\text{E.4})$$



with  $m_e$  the electron mass and  $r_e = e^2/4\pi\epsilon_0 mc^2$  the classical electron radius;  $|i\rangle$ ,  $|n\rangle$  and  $|f\rangle$  are respectively the initial, intermediate and final states;  $\Gamma_N$  is the total width of the intermediate state  $|n\rangle$ ;  $\mathbf{P}$  and  $\mathbf{r}$  are the momentum and position operators.

E.1 describes Thomson scattering  $\simeq 0$ ; E.2 is the resonant term; E.3 is the non-resonant term  $\simeq 0$  in the vicinity of an absorption edge.

Using the resonant term E.2, the absorption cross-section of an isotropic RIXS spectrum for an electric dipole absorption and an electric dipole emission is [Juhin et al., 2014, Equation 17]:

$$\langle\sigma_{scat}^{E_1 E_1}\rangle = \sum_{g=0}^2 \left( (-1)^g \frac{\sqrt{2g+1}}{9} - \frac{2\sqrt{2g+1}}{(2-g)!(3+g)!} (|\vec{k}_s \cdot \vec{\epsilon}_i|^2 - \frac{1}{3}) \right) S_{L_0}^{gg0} \quad (\text{E.5})$$

Respectively, for an electric quadrupole absorption and an electric dipole emission the absorption cross-section is [Juhin et al., 2014, Equation 20]:

$$\langle\sigma_{scat}^{E_2 E_1}\rangle = \sum_{g=1}^3 \left( (-1)^g \frac{\sqrt{2g+1}}{120} + \frac{\sqrt{3}}{4\sqrt{7}} \sqrt{2g+1} \begin{Bmatrix} 1 & 2 & g \\ 2 & 1 & 2 \end{Bmatrix} \left( -\frac{1}{6} + \frac{1}{4} |\vec{k}_i \cdot \vec{k}_s|^2 + \frac{1}{4} |\vec{k}_s \cdot \vec{\epsilon}_i|^2 \right) \right) S_{L_1}^{gg0} \quad (\text{E.6})$$

with  $\begin{Bmatrix} 1 & 2 & g \\ 2 & 1 & 2 \end{Bmatrix}$  a 6- $j$  symbol;  $S_{L_0}^{gg0}$  and  $S_{L_1}^{gg0}$  are the spectral parts that do not depend on the experimental setup; the terms before are geometrical factors that only depend on the experimental setup and not on the sample (see Appendix E.2).

Equation 11 of Juhin et al. [2014] detailing the matter tensor can be simplified for  $g_1 = g_2 = g$  and  $a = 0$  (powder) by:

$$S_L^{gg0} = \frac{r_e^2 \omega_s}{\hbar^2 \omega_i} \sum_f \sum_{\gamma=-g}^g (-1)^g \frac{|A_{fi,\gamma}^{(g)}(\omega_i)|^2}{\sqrt{2g+1}} \delta(E_f + \hbar\omega_s - E_i - \hbar\omega_i) \quad (\text{E.7})$$

where:

$$|A_{fi,\gamma}^{(g)}(\omega_i)|^2 = \sum_n \frac{(E_i - E_n)(E_n - E_f)}{E_i - E_n + \hbar\omega_i + i\Gamma_n} \sum_{\lambda'=-\ell'-1}^{\ell'+1} \sum_{\lambda=-\ell-1}^{\ell+1} (\ell'+1, \lambda', \ell+1, \lambda | g\gamma) \langle f | r_{\lambda'}^{(\ell'+1)} | n \rangle \langle n | r_{\lambda}^{(\ell+1)} | i \rangle \quad (\text{E.8})$$

with  $r_{\lambda'}^{(\ell'+1)} = |\ell'+1, \lambda'\rangle$ , the  $JM$  partners:  $|1, m\rangle$  with  $m = -1, 0, 1$  for dipole and  $|2, m\rangle$  with  $m = -2, -1, 0, 1, 2$  for quadrupole transitions);  $(\ell'+1, \lambda', \ell+1, \lambda | g\gamma)$  is a Clebsch-Gordan coefficient.

## E.2 Geometrical factor of the Kramers-Heisenberg formula

The geometrical factors are the terms that only depend on the experimental setup, in contrast to  $S_L^{gg0}$  describing the sample in Equations E.5 and E.6. They describe the direction and polarization of the incident and scattered beams. Their study can suggest experimental setups that cancel some terms in the sum of the KH formula. In the case of our experiment, the incident light is taken linearly polarized with  $\vec{\varepsilon}_i$  fixed along the y-axis and the propagation vector  $\vec{k}_i$  fixed along the x-axis; the observation direction relative to  $\vec{k}_s$  can take any angle (Figure E.1). In the case of plane waves in a homogeneous isotropic non-attenuating medium (air or helium), the polarization is perpendicular to the wave vector:  $\vec{\varepsilon}_i \cdot \vec{k}_i = 0$  and  $\vec{\varepsilon}_s \cdot \vec{k}_s = 0$ ; all vectors are unit vectors:  $|\vec{\varepsilon}_i| = |\vec{k}_i| = |\vec{\varepsilon}_s| = |\vec{k}_s| = 1$ . The following figures are plotted for a varying observation direction  $\vec{k}_s$ .

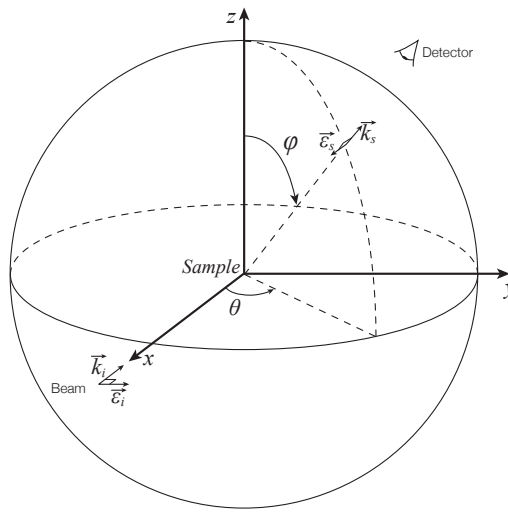


**Figure E.1** – Experimental setup of fluorescence measurement with a linearly polarized x-ray beam. The incident beam is directed by  $\vec{k}_i$  along the x-axis and the scattered beam is directed by  $\vec{k}_s$ .

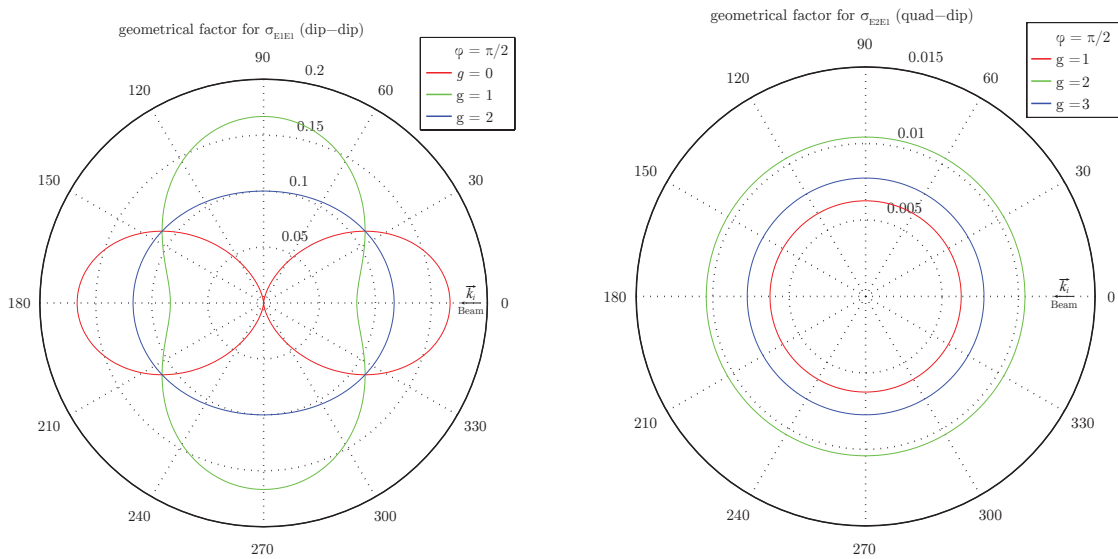


**Figure E.2** – Magnitude of the geometrical factors of the Kramers-Heisenberg formula (Equations E.6 and E.6) in the horizontal plane of the experiment ( $\phi = \pi/2$ ).

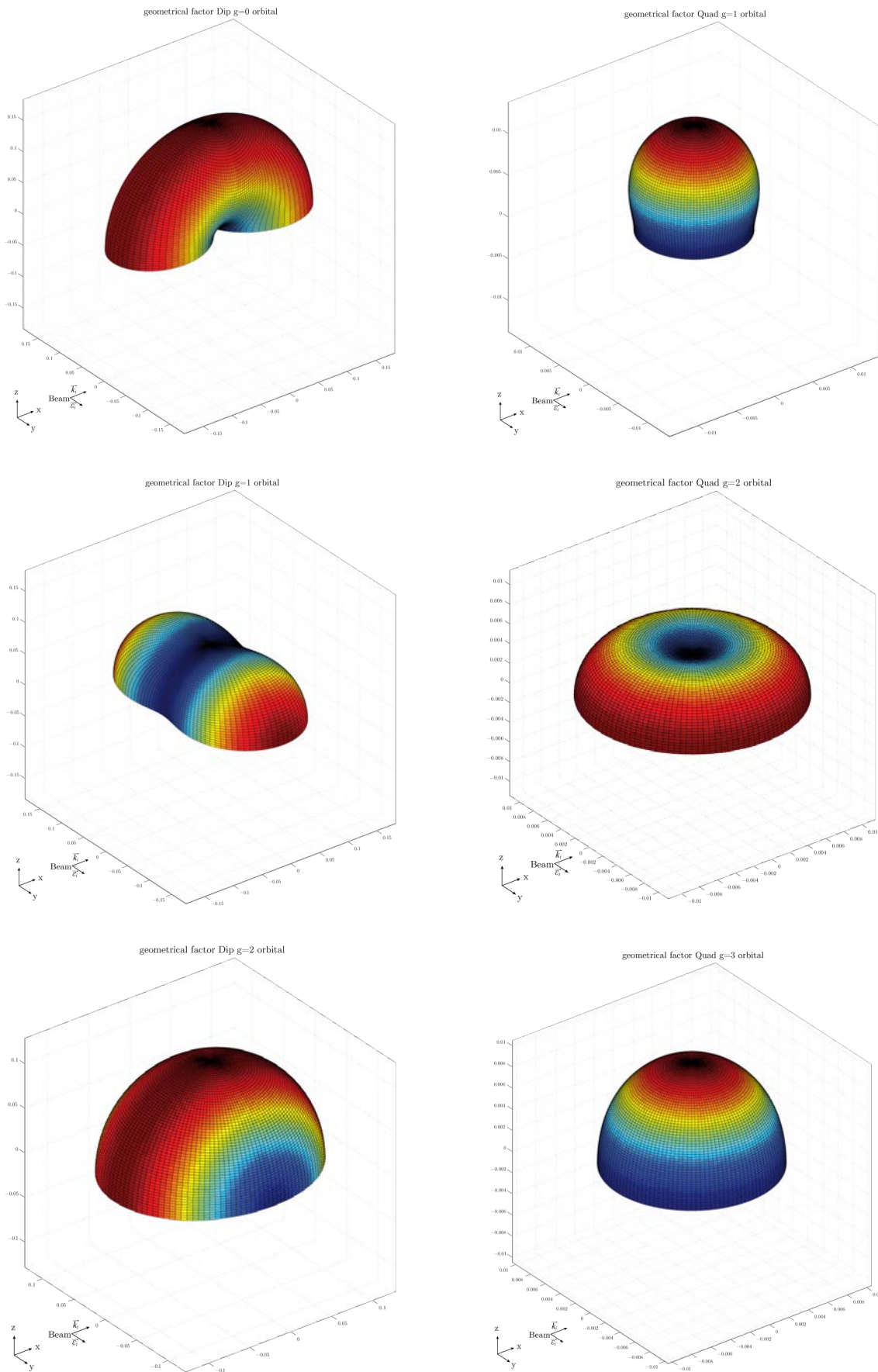


**Figure E.3** – 3D representations of the magnitude of geometrical factors for dipolar and quadrupolar contributions of the Kramers-Heisenberg formula.

### E.3 Angular dependence of RIXS. E1-E2 interference term

The matrix element describing the amplitude of the absorption is the sum of terms from electric dipole and electric quadrupole transitions. Because the absorption cross-section is expressed as the square module of the matrix element. There are interference terms between dipole and quadrupole transitions. The case of this interference term is not developed in Juhin et al. [2014]. Thanks to C. Brouder and M. Hunault, we developed it.

#### E.3.1 General expression

According to Eq. (7) of Juhin et al. [2014], the general formula of the absorption cross-section is:

$$\sigma_{\text{RIXS}} = \sum_{g_1, g_2, \ell_1, \ell_2, \ell'_1, \ell'_2} \sum_{a, b, c, u, u', v, v'} (-1)^{a+\ell_2+\ell'_2-g_2} h_{\ell_1} h_{\ell'_1}^* h_{\ell_2}^* h_{\ell'_2} \Pi_{g_1, g_2, b, c, u, v, u', v'} \begin{pmatrix} \ell'_1 + 1 & \ell_1 + 1 & g_1 \\ \ell'_2 + 1 & \ell_2 + 1 & g_2 \\ b & c & a \end{pmatrix} \begin{pmatrix} 1 & \ell_1 & \ell_1 + 1 \\ 1 & \ell_2 & \ell_2 + 1 \\ u & v & c \end{pmatrix} \begin{pmatrix} 1 & \ell'_1 & \ell'_1 + 1 \\ 1 & \ell'_2 & \ell'_2 + 1 \\ u' & v' & b \end{pmatrix} \gamma_{UL}^{bca} \cdot S_L^{g_1 g_2 a}, \quad (\text{E.9})$$

where  $\ell = 0$  for a dipole transition and  $\ell = 1$  for a quadrupole transition,  $g$  runs from  $\ell - \ell'$  to  $(\ell + \ell' + 2)$ , i.e.  $[0, 2]$  or  $[1, 3]$ , the  $h_\ell$  factors are defined by  $h_0 = -\sqrt{3}$ ,  $h_1 = \frac{i}{2}\sqrt{5}$ ,  $U = (u, v, u', v')$  and  $L = (\ell_1, \ell_2, \ell'_1, \ell'_2)$ .

For readability, the calculation is divided in four parts. Section E.3.2 details the calculation of the tensors  $\gamma_{UL}^{bca}$  which describes the incident and scattered x-rays. The tensor  $S_L^{g_1 g_2 a}$ , which describes the sample is developed in Section E.3.3. All the  $9-j$  symbols are calculated in Section E.3.4. Finally, results from these three parts are merged in Section E.3.5.

#### E.3.2 Angular terms $\gamma_{UL}^{bb0}$

$\gamma_{UL}^{bca}$  is defined by:

$$\gamma_{UL}^{bca} = \left\{ \text{Out}_{UL}^{(b)} \otimes \text{In}_{UL}^{(c)} \right\}^{(a)}, \quad (\text{E.10})$$

which is obtained by coupling the tensors  $\text{In}_{UL}^{(c)}$  of the incident beam and the tensors  $\text{Out}_{UL}^{(b)}$  of the scattered (outgoing) beam, where

$$\text{In}_{UL}^{(c)} = \left\{ \{ \varepsilon \otimes \varepsilon^* \}^{(u)} \otimes \{ \mathbf{k}^{\ell_1} \otimes \mathbf{k}^{\ell_2} \}^{(v)} \right\}^{(c)}, \quad (\text{E.11})$$

$$\text{Out}_{UL}^{(b)} = \left\{ \{ \varepsilon_s^* \otimes \varepsilon_s \}^{(u')} \otimes \{ \mathbf{k}_s^{\ell'_1} \otimes \mathbf{k}_s^{\ell'_2} \}^{(v')} \right\}^{(b)}. \quad (\text{E.12})$$

In the case of a powder, isotropy implies that  $a = 0$ ,  $g_1 = g_2$  and  $b = c = u'$ , the expression of the interference term is given by  $L_2 = (\ell_1, \ell_2, \ell'_1, \ell'_2) = (0, 1, 0, 0)$  and  $L_1 = (1, 0, 0, 0)$ . For both values of  $L$  we have  $v = 1$ ,  $v' = 0$ ,  $0 \leq b \leq 2$ ,  $g_1 = g_2 = g$  (see Section 2.3, 2.4 and D.3 in Juhin et al. [2014]) and thus:

$$\text{In}_{UL}^{(b)} = \{ \{ \varepsilon \otimes \varepsilon^* \}^{(u)} \otimes \mathbf{k} \}^{(b)}, \quad (\text{E.13})$$

$$\text{Out}_{UL}^{(b)} = \{ \varepsilon_s^* \otimes \varepsilon_s \}^{(b)}, \quad (\text{E.14})$$

$$\gamma_{UL}^{bb0} = \left\{ \left\{ \{ \varepsilon \otimes \varepsilon^* \}^{(u)} \otimes \mathbf{k} \right\}^{(b)} \otimes \{ \varepsilon_s^* \otimes \varepsilon_s \}^{(b)} \right\}^{(0)}. \quad (\text{E.15})$$

We calculated  $\gamma_{UL}^{bb0}$  for all relevant values of  $u$  and  $b$ .

### Case $b = 0$

In the case  $b = 0$ , the first factor of Equation E.15 implies  $u = 1$ , because  $\{ \varepsilon \otimes \varepsilon^* \}$  has to be of the same rank than  $\mathbf{k}$ , i.e. 1, to get a tensor of rank  $b = 0$ . Then,

$$\begin{aligned} \gamma_{UL}^{000} &= \left\{ \left\{ \{ \varepsilon \otimes \varepsilon^* \}^{(1)} \otimes \mathbf{k} \right\}^{(0)} \otimes \{ \varepsilon_s^* \otimes \varepsilon_s \}^{(0)} \right\}^{(0)} = \frac{i}{3\sqrt{2}} \varepsilon_s \cdot \varepsilon_s^* (\varepsilon \times \varepsilon^*) \cdot \mathbf{k} \\ &= -\frac{P_c}{3\sqrt{2}}, \end{aligned} \quad (\text{E.16})$$

where we used Eq. (2) of [Varshalovich et al., 1988, p. 65] and Eq. (9) of [Varshalovich et al., 1988, p. 66].

### Case $b = 1$

Three values of  $u$  are possible:

–  $u = 0$ :

$$\begin{aligned} \gamma_{UL}^{110} &= \left\{ \left\{ \{ \varepsilon \otimes \varepsilon^* \}^{(0)} \otimes \mathbf{k} \right\}^{(1)} \otimes \{ \varepsilon_s^* \otimes \varepsilon_s \}^{(1)} \right\}^{(0)} \\ &= -\frac{1}{\sqrt{3}} \varepsilon \cdot \varepsilon^* \{ \mathbf{k} \otimes \{ \varepsilon_s^* \otimes \varepsilon_s \}^{(1)} \}^{(0)} \\ &= \frac{i}{3\sqrt{2}} (\varepsilon_s^* \times \varepsilon_s) \cdot \mathbf{k} = \frac{P_{cs}}{3\sqrt{2}} \mathbf{k} \cdot \mathbf{k}_s \end{aligned} \quad (\text{E.17})$$

–  $u = 1$ :

$$\begin{aligned} \gamma_{UL}^{110} &= \left\{ \left\{ \{ \varepsilon \otimes \varepsilon^* \}^{(1)} \otimes \mathbf{k} \right\}^{(1)} \otimes \{ \varepsilon_s^* \otimes \varepsilon_s \}^{(1)} \right\}^{(0)} \\ &= -\frac{1}{\sqrt{3}} \{ \{ \varepsilon \otimes \varepsilon^* \}^{(1)} \otimes \mathbf{k} \}^{(1)} \cdot \{ \varepsilon_s^* \otimes \varepsilon_s \}^{(1)} \\ &= -\frac{i}{2\sqrt{6}} \left( (\varepsilon^* \cdot \mathbf{k}) \varepsilon \cdot (\varepsilon_s^* \times \varepsilon_s) - (\varepsilon \cdot \mathbf{k}) \varepsilon^* \cdot (\varepsilon_s^* \times \varepsilon_s) \right) \\ &= 0 \end{aligned} \quad (\text{E.18})$$

–  $u = 2$ :

$$\begin{aligned} \gamma_{UL}^{110} &= \left\{ \left\{ \{ \varepsilon \otimes \varepsilon^* \}^{(2)} \otimes \mathbf{k} \right\}^{(1)} \otimes \{ \varepsilon_s^* \otimes \varepsilon_s \}^{(1)} \right\}^{(0)} \\ &= -\frac{1}{\sqrt{3}} \{ \{ \varepsilon \otimes \varepsilon^* \}^{(2)} \otimes \mathbf{k} \}^{(1)} \cdot \{ \varepsilon_s^* \otimes \varepsilon_s \}^{(1)} \\ &= -\frac{i}{\sqrt{10}} \left( \frac{1}{3} (\varepsilon \cdot \varepsilon^*) \mathbf{k} \cdot (\varepsilon_s^* \times \varepsilon_s) - \frac{1}{2} (\varepsilon^* \cdot \mathbf{k}) \varepsilon \cdot (\varepsilon_s^* \times \varepsilon_s) - \frac{1}{2} (\varepsilon \cdot \mathbf{k}) \varepsilon^* \cdot (\varepsilon_s^* \times \varepsilon_s) \right) \\ &= -\frac{i}{3\sqrt{10}} \mathbf{k} \cdot (\varepsilon_s^* \times \varepsilon_s) = -\frac{P_{cs}}{3\sqrt{10}} \mathbf{k} \cdot \mathbf{k}_s \end{aligned} \quad (\text{E.19})$$

Where we used Eq. (2) of [Varshalovich et al., 1988, p. 65] and Eq. (9) of [Varshalovich et al., 1988, p. 66] for  $u = 0$ ; Eqs. (4) and (10) of [Varshalovich et al., 1988, p. 66] and  $\varepsilon \cdot \mathbf{k} = 0$  for  $u = 1$ ; Eqs. (4) and (11) of [Varshalovich et al., 1988, p. 66] and  $\varepsilon \cdot \mathbf{k} = 0$  for  $u = 2$ .

### Case $b = 2$

Two values of  $u$  are possible:

–  $u = 1$ :

$$\begin{aligned} \gamma_{UL}^{220} &= \left\{ \left\{ \{\varepsilon \otimes \varepsilon^*\}^{(1)} \otimes \mathbf{k} \right\}^{(2)} \otimes \{\varepsilon_s^* \otimes \varepsilon_s\}^{(2)} \right\}^{(0)} \\ &= \frac{i}{\sqrt{2}} \left\{ \{(\varepsilon \times \varepsilon^*) \otimes \mathbf{k}\}^{(2)} \otimes \{\varepsilon_s^* \otimes \varepsilon_s\}^{(2)} \right\}^{(0)} \\ &= \frac{i}{\sqrt{10}} \left( \frac{1}{2} (\varepsilon \times \varepsilon^*) \cdot \varepsilon_s^* \mathbf{k} \cdot \varepsilon_s + \frac{1}{2} (\varepsilon \times \varepsilon^*) \cdot \varepsilon_s \mathbf{k} \cdot \varepsilon_s^* - \frac{1}{3} (\varepsilon \times \varepsilon^*) \cdot \mathbf{k} \varepsilon_s \cdot \varepsilon_s^* \right) \\ &= \frac{P_c}{\sqrt{10}} \left( \frac{1}{3} - |\mathbf{k} \cdot \varepsilon_s|^2 \right) \end{aligned} \quad (\text{E.20})$$

–  $u = 2$ :

$$\gamma_{UL}^{220} = \left\{ \left\{ \{\varepsilon \otimes \varepsilon^*\}^{(2)} \otimes \mathbf{k} \right\}^{(2)} \otimes \{\varepsilon_s^* \otimes \varepsilon_s\}^{(2)} \right\}^{(0)} \quad (\text{E.21})$$

where we used Eq. (18) of [Varshalovich et al., 1988, p. 67] for  $u = 1$ .

Then,

$$\gamma_{UL}^{220} = \left\{ \{\varepsilon_s^* \otimes \varepsilon_s\}^{(2)} \otimes \left\{ \{\varepsilon \otimes \varepsilon^*\}^{(2)} \otimes \mathbf{k} \right\}^{(2)} \right\}^{(0)}. \quad (\text{E.22})$$

By using Eq. (35) of [Varshalovich et al., 1988, p. 65] and Eq. (27) of [Varshalovich et al., 1988, p. 64] we find

$$\gamma_{UL}^{220} = -\frac{1}{\sqrt{5}} \left\{ \mathbf{k} \otimes \{\varepsilon \otimes \varepsilon^*\}^{(2)} \right\}^{(2)} \cdot \{\varepsilon_s^* \otimes \varepsilon_s\}^{(2)}. \quad (\text{E.23})$$

Then, by Eq. (2) of [Varshalovich et al., 1988, p. 69],

$$\gamma_{UL}^{220} = \frac{1}{\sqrt{3}} \mathbf{k} \cdot \left\{ \{\varepsilon \otimes \varepsilon^*\}^{(2)} \otimes \{\varepsilon_s^* \otimes \varepsilon_s\}^{(2)} \right\}^{(1)}. \quad (\text{E.24})$$

Then, by Eq. (20) of [Varshalovich et al., 1988, p. 67],

$$\begin{aligned} \gamma_{UL}^{220} &= -\frac{i}{2\sqrt{30}} \left( \varepsilon \cdot \varepsilon_s^* (\varepsilon^* \times \varepsilon_s) \cdot \mathbf{k} + \varepsilon \cdot \varepsilon_s (\varepsilon^* \times \varepsilon_s^*) \cdot \mathbf{k} + \varepsilon^* \cdot \varepsilon_s^* (\varepsilon \times \varepsilon_s) \cdot \mathbf{k} \right. \\ &\quad \left. + \varepsilon^* \cdot \varepsilon_s (\varepsilon \times \varepsilon_s^*) \cdot \mathbf{k} \right). \end{aligned} \quad (\text{E.25})$$

If the polarization of the scattered beam is not measured we use the relation  $\langle \{\varepsilon_s^* \otimes \varepsilon_s\}^{(2)} \rangle = -\mathbf{k}^{(2)}/2$ . This gives us:

$$\langle \gamma_{UL}^{220} \rangle = \frac{i}{2\sqrt{30}} \left( \varepsilon \cdot \mathbf{k}_s (\varepsilon^* \times \mathbf{k}_s) \cdot \mathbf{k} + \varepsilon^* \cdot \mathbf{k}_s (\varepsilon \times \mathbf{k}_s) \cdot \mathbf{k} \right). \quad (\text{E.26})$$

### E.3.3 Matter tensors $S_L^{gg0}$

The matter tensors are, for  $L_2 = (\ell_1, \ell_2, \ell'_1, \ell'_2) = (0, 1, 0, 0)$

$$S_{L_2}^{gg0} = \frac{r_{\varepsilon}^2 \omega_s}{\hbar^2 \omega} \sum_F \left\{ A_{FI}^{(g)}(0, 0) \otimes \bar{A}_{IF}^{(g)}(1, 0) \right\}^{(0)} \delta(E_F + \hbar\omega_s - E_I - \hbar\omega), \quad (\text{E.27})$$

and for the matter tensors are, for  $L_1 = (\ell_1, \ell_2, \ell'_1, \ell'_2) = (1, 0, 0, 0)$

$$S_{L_1}^{gg0} = \frac{r_{\varepsilon}^2 \omega_s}{\hbar^2 \omega} \sum_F \left\{ A_{FI}^{(g)}(1, 0) \otimes \bar{A}_{IF}^{(g)}(0, 0) \right\}^{(0)} \delta(E_F + \hbar\omega_s - E_I - \hbar\omega). \quad (\text{E.28})$$

To derive a relation between  $S_{L_1}^{gg0}$  and  $S_{L_2}^{gg0}$ , we define  $X = \left\{ A_{FI}^{(g)}(1, 0) \otimes \bar{A}_{IF}^{(g)}(0, 0) \right\}^{(0)}$  and calculate its complex conjugate:

$$\begin{aligned} X^* &= \sum_{\gamma} (g\gamma g - \gamma|00) \left( A_{FI,\gamma}^{(g)}(1, 0) \bar{A}_{IF,-\gamma}^{(g)}(0, 0) \right)^* \\ &= \sum_{\gamma} (g\gamma g - \gamma|00) \bar{A}_{IF,-\gamma}^{(g)}(1, 0) A_{FI,\gamma}^{(g)}(0, 0) \\ &= \left\{ A_{FI}^{(g)}(0, 0) \otimes \bar{A}_{IF}^{(g)}(1, 0) \right\}^{(0)} \end{aligned} \quad (\text{E.29})$$

In other words,

$$(S_{L_1}^{gg0})^* = S_{L_2}^{gg0}. \quad (\text{E.30})$$

### E.3.4 $9j$ -symbols

For  $a = 0$

$$\begin{Bmatrix} 1 & \ell_1 + 1 & g \\ 1 & \ell_2 + 1 & g \\ b & b & 0 \end{Bmatrix} = \frac{(-1)^{\ell_1 + b + g}}{\sqrt{(2b+1)(2g+1)}} \begin{Bmatrix} 1 & \ell_1 + 1 & g \\ \ell_2 + 1 & 1 & b \end{Bmatrix}. \quad (\text{E.31})$$

$\ell_1 = 0$  and  $\ell_2 = 1$ ,  $v = 1$ ,  $c = b$

$$\begin{Bmatrix} 1 & \ell_1 & \ell_1 + 1 \\ 1 & \ell_2 & \ell_2 + 1 \\ u & v & c \end{Bmatrix} = \begin{Bmatrix} 1 & 0 & 1 \\ 1 & 1 & 2 \\ u & 1 & b \end{Bmatrix} = \frac{(-1)^{b+1}}{3} \begin{Bmatrix} 2 & b & 1 \\ u & 1 & 1 \end{Bmatrix}. \quad (\text{E.32})$$

$\ell_1 = 1$  and  $\ell_2 = 0$ ,  $v = 1$ ,  $c = b$

$$\begin{Bmatrix} 1 & \ell_1 & \ell_1 + 1 \\ 1 & \ell_2 & \ell_2 + 1 \\ u & v & c \end{Bmatrix} = \begin{Bmatrix} 1 & 1 & 2 \\ 1 & 0 & 1 \\ u & 1 & b \end{Bmatrix} = \frac{(-1)^u}{3} \begin{Bmatrix} 2 & b & 1 \\ u & 1 & 1 \end{Bmatrix}. \quad (\text{E.33})$$

$\ell'_1 = \ell'_2 = 0$ ,  $u' = b$ ,  $v' = 0$

$$\begin{Bmatrix} 1 & \ell'_1 & \ell'_1 + 1 \\ 1 & \ell'_2 & \ell'_2 + 1 \\ u' & v' & b \end{Bmatrix} = \begin{Bmatrix} 1 & 0 & 1 \\ 1 & 0 & 1 \\ b & 0 & b \end{Bmatrix} = \frac{1}{3\sqrt{2b+1}}. \quad (\text{E.34})$$

Therefore, the product of factors gives us, for  $L_1$ :

$$\frac{i\sqrt{5}}{2} (-1)^{b+u} \sqrt{(2b+1)(2g+1)(2u+1)} \begin{Bmatrix} 1 & 1 & g \\ 2 & 1 & b \end{Bmatrix} \begin{Bmatrix} 2 & b & 1 \\ u & 1 & 1 \end{Bmatrix}. \quad (\text{E.35})$$

For  $L_2$  we have the same expression, up to a factor of  $(-1)^{b+u}$ .

### E.3.5 Final formulas

Using the results of Sections E.3.2, E.3.3 and E.3.4, the isotropic term is

$$\sigma_{KH} = \sum_{u,b,g} \frac{i\sqrt{5}}{2} \sqrt{(2b+1)(2g+1)(2u+1)} \begin{Bmatrix} 1 & 1 & g \\ 2 & 1 & b \end{Bmatrix} \begin{Bmatrix} 2 & b & 1 \\ u & 1 & 1 \end{Bmatrix} \gamma_{UL_1}^{bb0} ((S_{L_1}^{gg0})^* + (-1)^{b+u} S_{L_1}^{gg0}). \quad (\text{E.36})$$

We write now the cross-section as a sum of contributions  $\sigma_{KH} = \sum_{b,u} \sigma_{KH}(b, u)$  and we give their explicit expressions. If  $b + u$  is odd, we have

$$\sigma_{KH}^{\text{odd}} = \sum_{u,b,g} \sqrt{5(2b+1)(2g+1)(2u+1)} \begin{Bmatrix} 1 & 1 & g \\ 2 & 1 & b \end{Bmatrix} \begin{Bmatrix} 2 & b & 1 \\ u & 1 & 1 \end{Bmatrix} \gamma_{UL_1}^{bb0} \text{Im}(S_{L_1}^{gg0}). \quad (\text{E.37})$$

If  $b + u$  is even, we have

$$\sigma_{KH}^{\text{even}} = \sum_{u,b,g} i\sqrt{5(2b+1)(2g+1)(2u+1)} \begin{Bmatrix} 1 & 1 & g \\ 2 & 1 & b \end{Bmatrix} \begin{Bmatrix} 2 & b & 1 \\ u & 1 & 1 \end{Bmatrix} \gamma_{UL_1}^{bb0} \text{Re}(S_{L_1}^{gg0}). \quad (\text{E.38})$$

### Time-reversal even term (non magnetic)

Only  $u = 2$  and  $b = 2$  gives a time-reversal even contribution, i.e. for which the sign is unchanged by the time-reversal transformation ( $t \mapsto -t$ ):

$$\begin{aligned} \sigma_{KH}(2, 2) &= \frac{1}{8\sqrt{30}} \text{Re} \left( \sqrt{3} S_{L_1}^{110} + S_{L_1}^{220} \right) \\ &\left( \varepsilon \cdot \varepsilon_s^* (\varepsilon^* \times \varepsilon_s) \cdot \mathbf{k} + \varepsilon \cdot \varepsilon_s (\varepsilon^* \times \varepsilon_s^*) \cdot \mathbf{k} + \varepsilon^* \cdot \varepsilon_s^* (\varepsilon \times \varepsilon_s) \cdot \mathbf{k} + \varepsilon^* \cdot \varepsilon_s (\varepsilon \times \varepsilon_s^*) \cdot \mathbf{k} \right). \quad (\text{E.39}) \end{aligned}$$



### Time-reversal odd terms

The time-reversal odd terms take the opposite sign by the time-reversal transformation ( $t \mapsto -t$ ). They depend on  $P_{cs}$ : the rate of circular polarization of the scattered beam.

In the case  $b = 1$  and  $u = 0$ :

$$\sigma_{KH}(1, 0) = -P_{cs} \mathbf{k} \cdot \mathbf{k}_s \frac{\sqrt{5}}{6\sqrt{6}} \text{Im}(S_{L_1}^{220} - \frac{1}{\sqrt{3}} S_{L_1}^{110}). \quad (\text{E.40})$$

In the case  $b = 1$  and  $u = 2$ :

$$\sigma_{KH}(1, 2) = +P_{cs} \mathbf{k} \cdot \mathbf{k}_s \frac{1}{12\sqrt{30}} \text{Im}(S_{L_1}^{220} - \frac{1}{\sqrt{3}} S_{L_1}^{110}). \quad (\text{E.41})$$

Their sum is

$$\sigma_{KH}(1, 0) + \sigma_{KH}(1, 2) = P_{cs} \mathbf{k} \cdot \mathbf{k}_s \frac{\sqrt{3}}{4\sqrt{10}} \text{Im}(S_{L_1}^{220} - \frac{1}{\sqrt{3}} S_{L_1}^{110}). \quad (\text{E.42})$$

In the case  $b = 2$  and  $u = 1$ :

$$\sigma_{KH}(2, 1) = P_c (|\mathbf{k} \cdot \boldsymbol{\varepsilon}_s|^2 - \frac{1}{3}) \frac{\sqrt{3}}{4\sqrt{10}} \text{Im}(S_{L_1}^{220} + \frac{1}{\sqrt{3}} S_{L_1}^{110}). \quad (\text{E.43})$$

### Average over the scattered beam

If the polarization of the scattered beam is not measured, we have only two non-zero terms. A time-reversal odd term depends on the rate of polarization of the incident beam and therefore vanishes with linearly polarized incident x-rays:

$$\langle \sigma_{KH}(2, 1) \rangle = P_c \left( \frac{1}{3} - |\mathbf{k} \cdot \mathbf{k}_s|^2 \right) \frac{\sqrt{3}}{8\sqrt{10}} \text{Im}(S_{L_1}^{220} + \frac{1}{\sqrt{3}} S_{L_1}^{110}), \quad (\text{E.44})$$

and a time-reversal even term that can be observed with linearly polarized x-rays:

$$\langle \sigma_{KH}(2, 2) \rangle = - \left( \boldsymbol{\varepsilon} \cdot \mathbf{k}_s (\boldsymbol{\varepsilon}^* \times \mathbf{k}_s) \cdot \mathbf{k} + \boldsymbol{\varepsilon}^* \cdot \mathbf{k}_s (\boldsymbol{\varepsilon} \times \mathbf{k}_s) \cdot \mathbf{k} \right) \frac{1}{8\sqrt{30}} \text{Re} \left( \sqrt{3} S_{L_1}^{110} + S_{L_1}^{220} \right). \quad (\text{E.45})$$

### E.3.6 Conclusion

With the experimental setup described in Section 2.4.2, the polarization is linear and  $\mathbf{k}_s$  is collinear to  $\boldsymbol{\varepsilon}$ , therefore  $\langle \sigma_{KH}(2, 2) \rangle$  is null. The interference term calculated here does not influence the experimental measurement with this setup.

## E.4 The absolute absorption cross-section $\sigma(\omega)$ in $\text{\AA}^2$

In **Quanty**, spectra are implemented by calculating the Green's function. The complex energy dependent quantity is calculated for the  $i$ -th initial state using the formula:

$$G_i(\omega) = \langle \psi_i | \hat{T}^\dagger \frac{1}{\omega - \hat{H} + i\Gamma/2} \hat{T} | \psi_i \rangle \quad (\text{E.46})$$

with  $\hat{T}$  and  $\hat{H}$  operators given in second quantization and  $\psi_i$  a many-particle wavefunction.  $\hat{T}$  is the transition operator,  $\hat{H}$  is the Hamiltonian of the final state system and  $\psi_i$  are the eigenstates of the Hamiltonian of the initial state. There is no degeneracy in **Quanty**, it the ground state is 5 times degenerated, there are 5 wave function with the ground state energy. To include at the same time the degeneracy and the effect of temperature, we sum over the  $i$ -th states (see Appendix D.1):

$$G(\omega) = \frac{1}{Z} \sum_i G_i(\omega) \cdot e^{-\frac{\Delta E}{kT}} \quad (\text{E.47})$$

with  $Z$ , the canonical partition function:

$$Z = \sum_i e^{-\frac{\Delta E}{kT}} \quad (\text{E.48})$$

For linear polarization, the angular part of the isotropic spectrum:

$$\mathcal{S} = \frac{-\text{Im}(G(\omega))}{\pi} \quad (\text{E.49})$$

For electric dipole, the isotropic spectrum from the different polarization is:

$$\mathcal{S}_{iso}^D = \frac{1}{3} (\mathcal{S}_x + \mathcal{S}_y + \mathcal{S}_z) \quad (\text{E.50})$$

For electric quadrupole:

$$\mathcal{S}_{iso}^Q = \frac{1}{15} (\mathcal{S}_{xy} + \mathcal{S}_{yz} + \mathcal{S}_{xz} + \mathcal{S}_{x^2-y^2} + \mathcal{S}_{z^2}) \quad (\text{E.51})$$

The electric dipole absorption cross-section for  $K$  pre-edge in  $\text{\AA}^2$  is:

$$\sigma_{dip}(\omega) = 4\pi^2 \hbar \omega \alpha \cdot a_0^2 (P_{1s,4p}^{(1)})^2 \cdot \mathcal{S}_{iso}^D \quad (\text{E.52})$$

with  $P_{\ell,\ell'}^{(k)} = \langle n\ell || r^{(k)} || n\ell' \rangle$  the mono-electronic radial matrix element (unitless),  $k = 1$  for dipole operator and  $k = 2$  for quadrupole operator [Cowan, 1981].  $P_{1s,4p}^{(1)}$  is replaced by  $P_{2p,3d}^{(1)}$  for  $L_{2,3}$  edge, and by  $P_{3d,4p}^{(1)}$  for optical transitions. The electric quadrupole absorption cross-section for  $K$  pre-edge in  $\text{\AA}^2$  is:

$$\sigma_{quad}(\omega) = 4\pi^2 \hbar \omega \alpha \cdot \left( \frac{a_0^2 \hbar \omega}{2\hbar c} \right)^2 (P_{1s,3d}^{(2)})^2 \cdot \mathcal{S}_{iso}^Q \quad (\text{E.53})$$

where  $a_0 = 0.529\,177\,1\text{ \AA}$ , the Bohr radius;  $\alpha = 0.007\,297\,351$ , the fine structure constant (dimensionless);  $\hbar_3 d6.582\,173 \cdot 10^{-16}\text{ eV}\cdot\text{s}$ , the Planck constant and  $c = 2.997\,924\,58 \cdot 10^{18}\text{ \AA}/\text{s}$ , the light speed.

Note: For optical absorption spectroscopy  $\sigma$  is in  $\text{\AA}^2$  and can be converted to molar absorption coefficient  $\varepsilon$  in  $\text{L}\cdot\text{mol}^{-1}\cdot\text{cm}^{-1}$  with the following relationship:

$$\varepsilon = \sigma \cdot \frac{10^{-19}}{\ln 10} \cdot \mathcal{N}_A \simeq \sigma \cdot 2.615 \cdot 10^4 \quad (\text{E.54})$$

where  $\mathcal{N}_A = 6.022 \cdot 10^{23}\text{ mol}^{-1}$ , the Avogadro's number.

## E.5 Crystal field Hamiltonian in $D_{3h}$ geometry

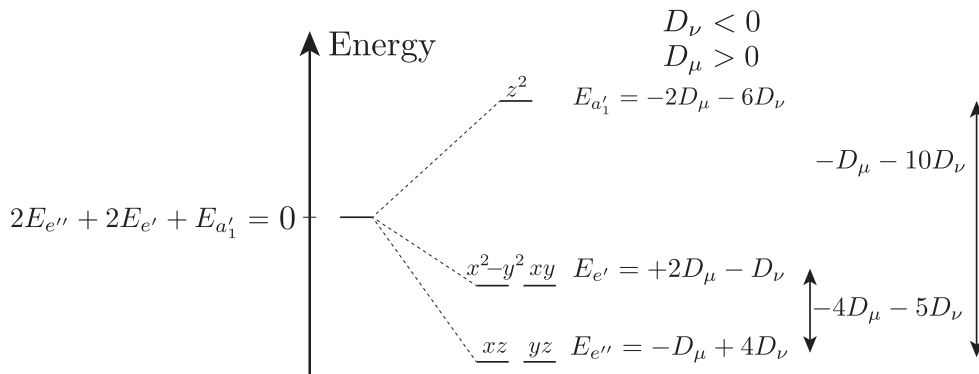


**Figure E.4** – Energy level diagram for  $D_{3h}$

The crystal field is decomposed as:

$$V(r, \theta, \varphi) = \sum_{k=0}^{\infty} \sum_{m=-k}^{m=k} B_k^m r^k Y_k^m(\theta, \varphi) = \sum_{k=0}^{\infty} \sum_{m=-k}^{m=k} A_{k,m} r^k C_k^m(\theta, \varphi) \quad (\text{E.55})$$

Where  $Y_k^m$  are spherical harmonics,  $C_k^m$  are normalized spherical harmonics and  $B_k^m$ ,  $A_k^m$  are coefficients. According to Cowan [1981, p. 146]:

$$C_k^m(\theta, \varphi) = \sqrt{\frac{4\pi}{2k+1}} Y_k^m(\theta, \varphi) \quad (\text{E.56})$$

then we can take the expectation value over the radial equations to get

$$\langle R(r) | V | R(r) \rangle = \sum_{k,m} A_{k,m} C_k^m(\theta, \varphi) \quad (\text{E.57})$$

For crystal field in  $D_{3h}$ ,  $A_k^m$  for  $V_{CF}$  are:

$$A_0^0 = \frac{1}{5}(E_{A_1'} + 2E_{E'} + 2E_{E''}) \quad (\text{E.58a})$$

$$A_2^0 = E_{A_1'} - 2E_{E'} + E_{E''} \quad (\text{E.58b})$$

$$A_4^0 = \frac{3}{5}(3E_{A_1'} + E_{E'} - 4E_{E''}) \quad (\text{E.58c})$$

They can be found with in the Mathematica<sup>®</sup> version of **Quanty** using:

```
Needs["SolidStatePhysics`PointGroupSymmetry`"]
VD3h = PotentialExpansion["D3h", 2]
```

The relationship between the energy of the orbitals and the ligand field parameters can be found in the literature (such as Lever [1984, p. 22 eqn(1.35)] or König and Kremer [1977, p. 21 eqn(3.86)]):

$$E_{A_1'} = -2D\mu - 6D\nu \quad (\text{E.59a})$$

$$E_{E'} = +2D\mu - D\nu \quad (\text{E.59b})$$

$$E_{E''} = -D\mu + 4D\nu \quad (\text{E.59c})$$

after replacing in the previous equations we get:

$$A_0^0 = 0 \quad (\text{E.60a})$$

$$A_2^0 = -7D\mu \quad (\text{E.60b})$$

$$A_4^0 = -21D\nu \quad (\text{E.60c})$$

With the formalism of Butler [1981], Hunault [2014] calculated:

$$X^{2000} = \sqrt{70}D\mu \quad (\text{E.61a})$$

$$X^{4000} = -3\sqrt{70}D\nu \quad (\text{E.61b})$$

With these  $A_k^m$  we can defined in **sap** the crystal field operators for  $D\mu$  and  $D\nu$

— Dmu

```
— Akm = ssp.PotentialExpandedOnYlm("D3h", 2, {-2, 2, -1});
```

```
Akm = {{0, 0, 0}, {2, 0, -7}, {4, 0, 0}};
```

```
OppDmu = ssp.NewOperator("CF", NFermion, dIndexUp, dIndexDn, Akm);
```

— Dnu

```
— Akm = ssp.PotentialExpandedOnYlm("D3h", 2, {-6, 1, 4});
```

```
Akm = {{0, 0, 0}, {2, 0, 0}, {4, 0, -21}};
```

```
OppDnu = ssp.NewOperator("CF", NFermion, dIndexUp, dIndexDn, Akm);
```

To count  $N_{A_1'}$ , the number of electrons in the level  $A_1'$  we take  $E_{A_1'} = 1$ ,  $E_{E'} = 0$  and

$E_{E''} = 0$  to calculate the following  $A_k^m$ :

$$A_0^0 = \frac{1}{5} \quad (\text{E.62a})$$

$$A_2^0 = 1 \quad (\text{E.62b})$$

$$A_4^0 = \frac{9}{5} \quad (\text{E.62c})$$

Finally, we found:

**Table E.1** –  $A_k^m$  coefficients for  $D_{3h}$

$A_k^m$	$V_{D\mu}$	$V_{D\nu}$	$V_{N_{A'_1}}$	$V_{N_{E'}}$	$V_{N_{E''}}$
$A_0^0$	0	0	$\frac{1}{5}$	$\frac{2}{5}$	$\frac{2}{5}$
$A_2^0$	-7	0	1	-2	1
$A_4^0$	0	-21	$\frac{9}{5}$	$\frac{3}{5}$	$-\frac{12}{5}$

For a trigonal bipyramid, with principal axis along z, the expected order of the orbitals is  $E_{e''} < E_{e'} < E_{a'_1}$  Lever [1984, p. 25] then  $3D_\mu > 5D_\nu$  and  $4D_\mu < -5D_\nu$  (see Figure E.5)

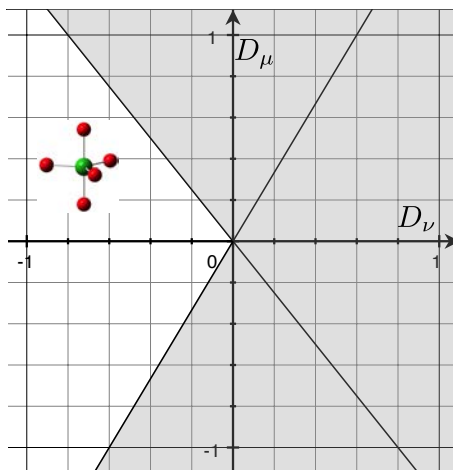


**Figure E.5** – Values of crystal field parameters representing a trigonal bipyramid

## Appendix F

# Curriculum Vitae

## EMPLOYMENT

---

- 2012-2015 **Research Engineer**, CIFRE PhD at IMPMC–UPMC (Paris) sponsored by Asahi Glass Company (**AGC**)  
*“Spectroscopic and structural properties of iron in silicate glasses”*, PhD manuscript & all intermediary reports in English
- Deep knowledge of glass material: synthesis, polishing, properties
  - Multi-technique analysis, crossing experimental and simulated results from advanced scientific methods
  - Measurement & processing of glasses: optical absorption spectroscopy, EPR/ESR, microprobe (EMPA), synchrotron XANES
  - Computer calculation and multi electronic numerical resolution of Schrödinger equation
- 2012 **Master’s internship** (6 months) at IMPMC–UPMC, Paris, France +1 month at AGC Research Center, Japan  
*“Analysis of iron-doped silicate glass structure using optical spectroscopy”*, dissertation & all intermediary reports in English
- 2011 **Research project** (3 months), LEG–ESPCI Paris  
*“Super-resolution infrared camera”*
- Development of a photolithography process in clean room
  - Surface ultrasound generation using a SAW (Surface Acoustic Wave) filter.
  - Far field infrared imaging
- 2010 **R&D Internship** (5 months) at EOS-imaging, Paris  
*“Reducing the vibration sensitivity of a gas detector for radiology”*
- Improvement of a multi-wire proportional chamber designed by Georges Charpak
  - Selection of suitable mechanical and electrical insulators
  - Digital radiography signal processing
- 2009 **Optional internship** (1 month) at LPEM–ESPCI Paris  
*“Li-ion battery studied by X-ray absorption and Mössbauer spectrometry”*
- Mössbauer measurements with radioactive sources, radiation protection
  - Development of automatic processing of experimental data
- 

## COMPUTER SCIENCE EXPERTISE

---

**Programming:** C/C++, Matlab and LaTeX; notion of Python, Fortran, PHP, Labview and Mathematica

**Multimedia:** Graphic design, photo, video (FinalCut, Photoshop, Illustrator)

**Websites:** Creation of four web sites (IMPMC intranet, professional artist, 2 associations)

**Operating systems:** OS X, Linux (Debian), Windows

**Server:** Apache2, LDAP/Kerberos, mail, wiki, forum, CMS, MySQL

---

## EDUCATION

---

- 2012-2015 **PhD** in Physics and Chemistry of Materials, Université Pierre et Marie Curie (**UPMC**), Paris
- 2011-2012 **Master of Science** in sensors, instrumentation and measurements, **ESPCI Paris** & **UPMC** (Paris 6)
- 2008-2011 **Engineering diploma** in Physics, Chemistry and Biology, **ESPCI Paris**
- 

## LANGUAGES

---

**French** : native

**English** : fluent

**Spanish** : basics

**Japanese** : basics

---

## DISTINCTIONS

---

- 2014 **“Poster award”** at the plenary session of the French glass community (USTV), Baccarat
- 2013 **“Best-poster award”** at the 12<sup>th</sup> International Conference on Non-Crystalline Materials (NCM12)
- 2012 member of the winning team of ICG Summer School for “a mobile app for glass technologists”
- 2011 **“Excellence grant”** by X–ESPCI–Saint-Gobain
- 

## INTERNATIONAL CONFERENCES

---

- 2015 **Oral presentation** at the 14<sup>th</sup> International Conference on Physics of Non-Crystalline Solids (PNCS14), USA
- 2014 **Oral presentation** at the 21<sup>st</sup> International Mineralogical Association (IMA2014), South Africa
- 2013 **Oral presentation** at the 23<sup>rd</sup> International Congress on Glass (ICG23), Czech Republic
- 2013 **Poster** at the 12<sup>th</sup> International Conference on Non-Crystalline Materials (NCM12), Italy
-

---

# Résumé de la thèse en français

## 1 Introduction à la problématique du fer dans les verres : un ion hétérovalent dans un milieu complexe

### 1.1 Contexte

L'objectif de cette thèse est d'étudier les propriétés spectroscopiques du fer dans des verres silicatés d'intérêt industriel ainsi que le lien entre ces propriétés et l'environnement local autour du fer. Le fer est de loin l'élément de transitions le plus abondant dans la croûte terrestre. Il se retrouve donc systématiquement dans les matières premières utilisées par l'industrie pour la fabrication des millions de tonnes de verres produites chaque année. Le fer en impureté est entre autres utilisé pour contrôler les propriétés optiques (coloration, isolation thermique, transmission énergétique, etc.) du verre dans de nombreuses applications industrielles (par exemple l'automobile, le bâtiment ou les panneaux solaires). Une compréhension de l'influence du fer sur les propriétés optiques permettrait de maîtriser et d'améliorer les caractéristiques techniques des verres.

### 1.2 Redox

Dans les matériaux amorphes comme le verre, ou encore les minéraux et les complexes de coordinations, le fer est le plus souvent présent sous forme de fer ferreux ( $\text{Fe}^{2+}$ ) ou de fer ferrique ( $\text{Fe}^{3+}$ ), dont les proportions relatives définissent le redox :

$$R = \frac{[\text{Fe}^{2+}]}{[\text{Fe}^{2+}] + [\text{Fe}^{3+}]}$$

Le redox dépend des conditions de synthèse comme la composition chimique, la température ou les conditions atmosphériques (pression partielle en oxygène). Les ions ferreux et ferriques donnent aux verres une coloration bleue ( $\text{Fe}^{2+}$ ), jaune ( $\text{Fe}^{3+}$ ) ou verte (présence d'ions des deux degrés d'oxydation). Ils influencent aussi les propriétés thermiques en raison de l'impact sur l'absorption de la lumière dans le proche infrarouge [Sakaguchi and Uchino, 2007] ou l'ultraviolet [Uchino et al., 2000].

### 1.3 Le verre

Les verres sont des matériaux amorphes qui ne possèdent pas d'ordre à longue distance. Néanmoins, un ordre local est observé à courte distance, la répartition des atomes dans les premières sphères de coordinences n'est pas aléatoire. Par exemple, les atomes de fer



sont localisés dans des environnements spécifiques, dépendant, entre autres, du redox. Les atomes de fer d'un même degré d'oxydation se répartissent statistiquement entre plusieurs sites possibles, ayant chacun des caractéristiques et une influence sur les propriétés finales (moyenne de la distribution dans les différents sites) du verre différentes. Le caractère amorphe des verres et la nature hétérovalente du fer sont deux raisons expliquant les difficultés de compréhension de l'environnement du fer dans les verres malgré l'intense recherche scientifique des 80 dernières années dans ce domaine.

#### 1.4 Relation structure-propriétés

L'étude de l'environnement local du fer est une question cruciale car la structure est reliée aux propriétés chimiques et spectroscopiques (Figure 1). L'interprétation des relations entre l'environnement local du fer et les propriétés spectroscopiques permet de relier les différentes méthodes d'analyse à la structure atomique et électronique dans le matériau considéré. L'utilisation de la spectroscopie, au travers des interactions rayonnement-matière, sonde les relations structure-propriétés dans le verre. Elle permet entre autres de suivre l'effet d'un changement de la composition chimique d'un verre sur l'environnement local du fer par l'impact observé sur les propriétés spectroscopiques. Par exemple, l'utilisation de la spectroscopie d'absorption optique UV-Visible-proche infrarouge permet de corréler les propriétés colorimétriques des verres contenant des métaux de transitions avec l'état redox et l'environnement structural de ces éléments de transitions. Des méthodes complémentaires de la spectroscopie d'absorption optique, comme l'absorption des rayons X ou la résonance paramagnétique électronique (RPE), peuvent être utilisées.

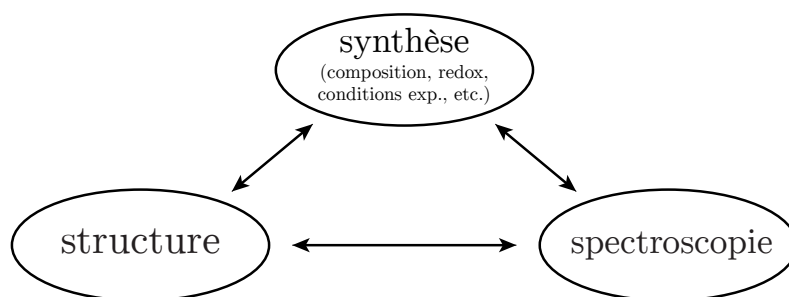


**Figure 1** – Schéma des relations entre propriétés structurales, chimiques et spectroscopiques.

#### 1.5 Intérêt des cristaux pour l'étude des verres

Dans le but de déterminer les propriétés structurales à partir de l'analyse spectroscopique, les composés cristallins sont des références utiles. En effet, leur composition structurale est connue, et les signatures spectroscopiques observées sont très sensibles à la géométrie locale et à la coordinence. Les signatures spectroscopiques de différents environnements tétraédriques ou octaédriques dans les minéraux ont été largement étudiées et caractérisées [Burns, 1993]. Dans une moindre mesure, la présence de fer dans des sites de coordinence [5] (comme la bipyramide trigonale ou la pyramide à base carrée) a été étudiée dans des complexes [Ciampolini, 1969] ou des minéraux [Rossman and Taran, 2001].

## 1.6 L'environnement du fer dans les verres

L'information structurale, comme les distances Fe–O ou la coordination, peut être obtenue par la diffraction de neutrons ou la spectroscopie EXAFS (extended X-ray absorption fine structure). D'autres méthodes expérimentales, comme les spectroscopies d'absorption optique, absorption des rayons X ou RPE, permettent d'obtenir de l'information structurale de façon indirecte en comparant, par exemple, les signatures obtenue dans des minéraux pour des sites bien définis. Toutes ces méthodes peuvent aussi être couplées avec des simulations numériques (e.g. reverse Monte Carlo (RMC), empirical potential structure refinement (EPSR) or molecular dynamics (MD)).

Il est montré que la coordination du fer dans les verres est majoritairement comprise entre [4] et [6] [Calas and Petiau, 1983a]. La présence de  $\text{Fe}^{2+}$  en coordination [5] a été mise en évidence dans les verres silicatés par Brown et al. [1995] et confirmé par plusieurs études Guillot and Sator [2007]; Rossano et al. [1999, 2000c]; Weigel et al. [2008b]. Cependant, les sites de coordination [5] ne sont pas systématiquement considérés par les auteurs lors de l'interprétation des signatures spectroscopiques du fer dans les verres.

## 1.7 La théorie des groupes pour décrire l'environnement local

Le nombre de coordination est un paramètre intéressant mais sa simplicité ne tient pas compte de la complexité des environnements locaux. En effet, la position des ligands et la géométrie locale du site formé par le fer et ses premiers voisins oxygène influencent les propriétés spectroscopiques [Ballhausen, 1962; Lever, 1984].

En général, des coordinences différentes signifient des groupes ponctuels de symétrie différents. Néanmoins, il n'y pas de relation univoque entre ces deux notions. Cette notion est illustrée par la Figure 2 sur laquelle sont tracé plusieurs polyèdres de coordination correspondant à un même groupe de symétrie. En revanche, la coordination d'un site peut être déterminée par la connaissance du groupe ponctuel de symétrie et des valeurs des paramètres de champ cristallin utilisés pour le décrire.

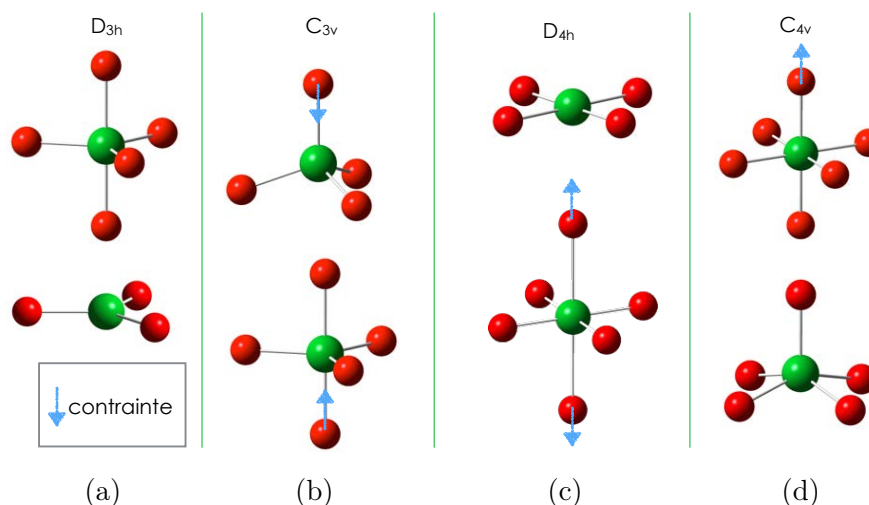


**Figure 2** – Polyèdres de coordination et leurs groupes ponctuels de symétrie associés. Les flèches bleues représente des contraintes liées à des déplacements atomiques.

## 1.8 Problématique

La distorsion et la distribution du fer dans une large variété de sites compliquent la détermination de l'environnement. De plus, cette complexité est accentuée par la présence de deux degrés d'oxydation du fer ( $\text{Fe}^{2+}$  et  $\text{Fe}^{3+}$ ), chacun avec sa propre distribution dans des sites plus ou moins distordus de coordinence [4], [5] ou [6]. Ces sites peuvent aussi s'agréger au lieu d'être uniformément distribué dans la matrice verrière, ils forment alors des clusters de fer présentant des propriétés différentes des sites isolés.

L'objectif de cette thèse est de croiser les résultats de différentes méthodes expérimentales et numériques afin d'obtenir de nouvelles informations sur l'environnement local du fer dans les verres silicatés. Une attention particulière sera portée l'étude des orbitales de valences  $3d$  du fer qui sont impliquées dans la liaison chimique avec ses voisins, reflétant son environnement local.

## 2 Échantillons et méthodes expérimentales

### 2.1 Compositions et synthèses

Deux types de verres silicatés ont été étudiés. L'un avec la composition  $74\text{SiO}_2-16\text{Na}_2\text{O}-10\text{RO}$  où R est un ion alcalino-terreux ( $\text{Mg}^{2+}$ ,  $\text{Ca}^{2+}$  ou un mélange des deux). L'autre est un verre sans alcalins basé sur la composition du diopside, un minéral de composition  $50\text{SiO}_2-25\text{CaO}-25\text{MgO}$ . Ces verres ont été dopés au fer en ajoutant 0.5 %pds de  $\text{Fe}_2\text{O}_3$  (Table 1).

**Table 1** – Compositions nominales des verres synthétisés.

Composition de la matrice vitreuse (%mol)	$\text{Fe}_2\text{O}_3$ (%pds)	Nom de code
$74\text{SiO}_2-16\text{Na}_2\text{O}-10\text{CaO}$	0.5	NCS
$74\text{SiO}_2-16\text{Na}_2\text{O}-10\text{MgO}$	0.5	NMS
$74\text{SiO}_2-16\text{Na}_2\text{O}-5\text{CaO}-5\text{MgO}$	0.5	NCMS
$50\text{SiO}_2-25\text{CaO}-25\text{MgO}$	0.5	DIO

Ces compositions ont été synthétisées sous trois conditions atmosphériques avec différentes pressions partielles en oxygène (Figure 3) :

- oxydantes, sous oxygène, pour faire des verres oxydés (Ox) avec un redox  $R \sim 5\%$ ,
- ambiantes, sous air, pour faire des verres intermédiaires (Med) avec un redox  $R \sim 25\%$ ,
- réductrices, sous azote, pour faire des verres réduits (Red) avec un redox  $R \sim 99\%$ .



**Figure 3** – Soda-lime silicate glasses (NCS) at three different redox states (oxidized, air synthesized, reduced), sample thickness: 2.5 mm.

## 2.2 Spectroscopie d'absorption optique

La spectroscopie d'absorption optique est une méthode très utilisée qui a l'avantage d'être simple à mettre en œuvre et d'être particulièrement adaptée à l'étude de la couleur et des propriétés optiques dans l'infrarouge et l'ultraviolet. Sa bonne résolution énergétique permet de distinguer de faible levée de dégénérescence des niveaux  $3d$  de l'ordre du centième d'eV [Rossman, 2014]. Cette levée de dégénérescence causée par l'effet du champ de ligands créé par les voisins justifie que cette spectroscopie est particulièrement sensible à la géométrie locale des atomes absorbeurs.

Les mesures d'absorption optiques ont été réalisées en transmission sur des échantillons polis et plans d'épaisseur 2,5 mm et 5,5 mm. L'énergie des photons utilisés est comprise dans la gamme 0,5–6 eV (i.e. 4000–50 000  $\text{cm}^{-1}$  ou 2500–200 nm)

## 2.3 Spectroscopie d'absorption des rayons X (XAS)

La spectroscopie d'absorption des rayons X est un outil puissant pour l'étude de la structure électronique et cristallographique d'une impureté dans une structure-hôte. Elle a le double avantage d'être sélective chimiquement et orbitalement. On peut en effet sélectionner l'élément étudié grâce à l'énergie des rayons X incidents, chaque élément ayant une énergie bien définie. De même, on peut choisir dans quelle couche l'électron est excité et donc quels états vides sont sondés. On parle de seuils K si l'électron excité provient de la couche 1s. Toutes les expériences réalisées au cours de cette thèse ont été faites au seuil K du fer (situé à 7112 eV). En fonction de l'énergie incidente, différents événements peuvent se produire (Figure 4).

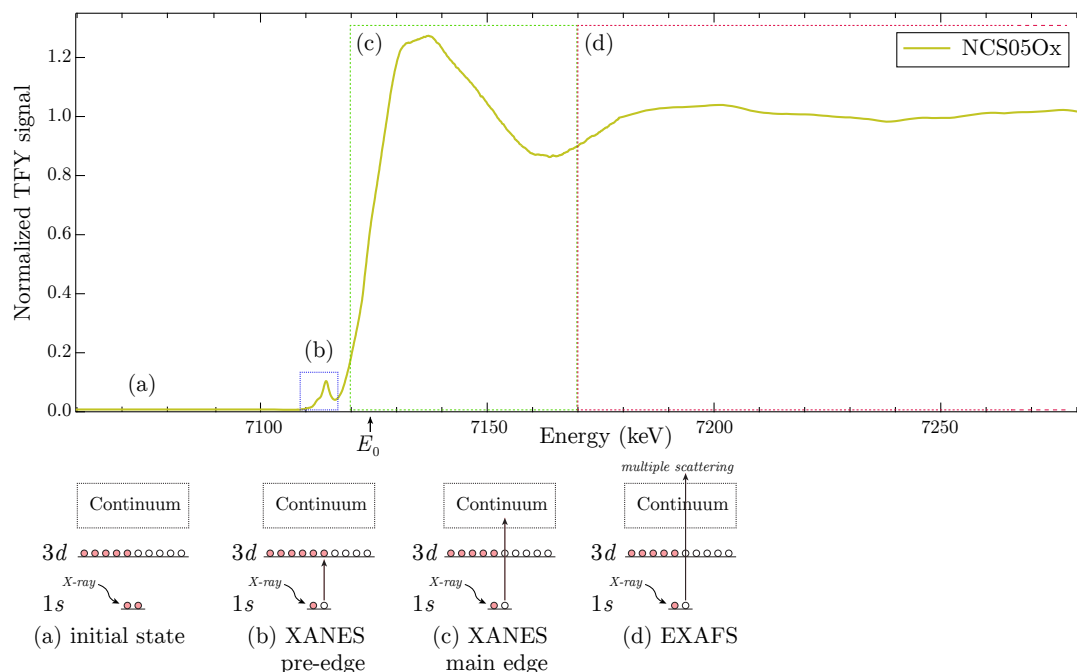


**Figure 4** – Les différentes régions du spectre XAS (ici, le seuil  $K$  du fer pour l'échantillon de verre NCS05Ox).

Cette thèse s'intéresse particulièrement au préseuil  $K$  (Figure 4-b), pour lequel l'énergie incidente est plus faible que l'énergie du seuil mais reste suffisante pour transférer un électron  $1s$  dans la première orbitale non pleine. Il permet de sonder les niveaux  $3d$  localisés sur l'atome absorbeur. Le préseuil est essentiellement décrit par deux phénomènes : (i) une transition locale quadrupolaire électrique  $1s \rightarrow 3d$ ; une transition locale dipolaire électrique  $1s \rightarrow 4p$ . Dans le cas d'un site centrosymétrique seules les transitions quadrupolaires électriques sont à l'origine du signal du préseuil.

Les mesures de XAS ont été réalisées sur la ligne de lumière ID26 de l'ESRF à Grenoble (France). Toutes les données ont été collectées en utilisant un monochromateur Si(311) et une détection en fluorescence avec un angle de  $90^\circ$  entre le faisceau incident et le faisceau diffusé (Figure 5). La polarisation du faisceau incident est prise horizontale et linéaire.

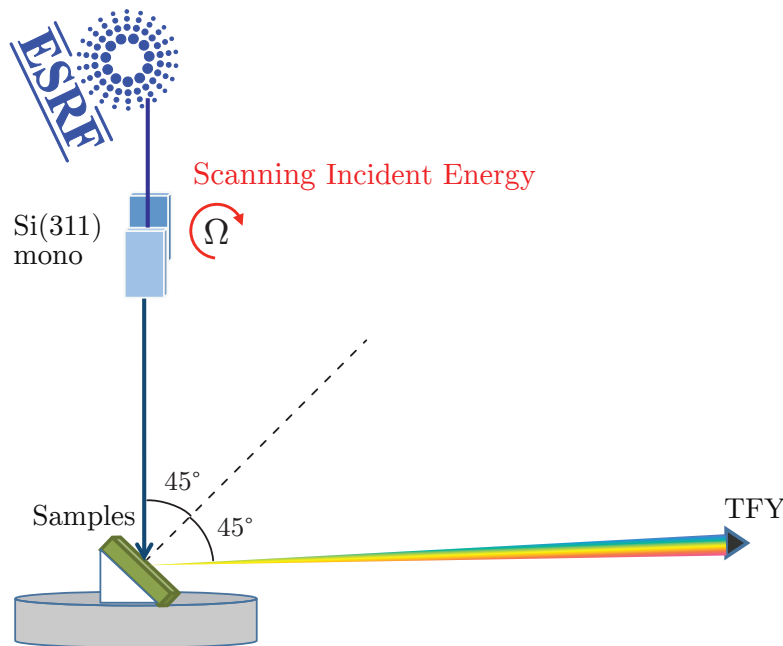
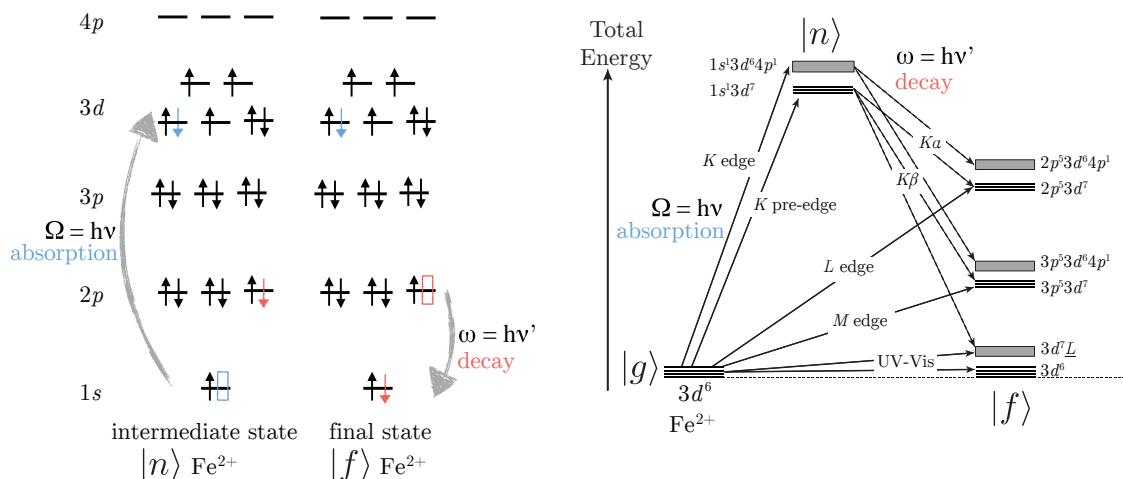


Figure 5 – Principe de la mesure de XAS.

## 2.4 Spectroscopie RIXS et HERFD

Afin d'améliorer les résultats obtenus avec la méthode XAS, décrite au paragraphe précédent, des mesures hautes-résolution utilisant les techniques Résonant Inelastic X-ray Scattering (RIXS) et High-Energy Resolution Fluorescence Detected X-ray Absorption Spectroscopy (HERFD-XAS ou simplement HERFD).

Le principe de cette méthode qui met en jeu un processus à deux photons, illustré sur la Figure 6. Les mesures sont tracées sur un graph 3D (appelé "plan RIXS") en fonction de  $(\Omega, \omega)$  ou  $(\Omega, \Omega - \omega)$  pour les axes  $(x, y)$  et l'intensité relative au nombre de photons émis est tracée selon l'axe  $z$  [Glatzel and Bergmann, 2005].



**Figure 6** – Vision monoélectronique (gauche) et vision multiélectronique (droite) des transitions électroniques du  $\text{Fe}^{2+}$  impliquées en RIXS spectroscopy.  $\Omega$  est l'énergie d'absorption incidente,  $\omega$  l'énergie de fluorescence émise et  $\Omega - \omega$  l'énergie de transfert.

Ces mesures ont été réalisées simultanément aux mesures XAS sur la ligne ID26 de l'ESRF. La Figure 5 illustre le montage expérimental, dont le principe consiste à analyser la fluorescence de l'échantillon en utilisant des cristaux analyseurs. Dans le cas présent la fluorescence  $K\alpha$  (6404 eV) a été analysée avec quatre cristaux de Ge(440) pour diffracter les rayons X émis. Pour une énergie de fluorescence fixée la méthode est appelée HERFD.

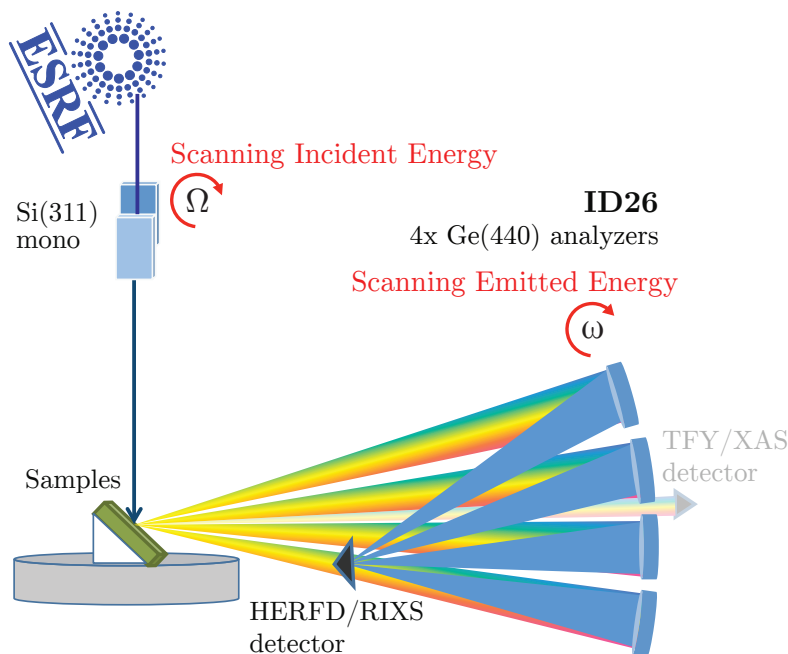


**Figure 7** – Principe de la mesure de RIXS.

## 2.5 SQUID

Des mesures de susceptibilité magnétique ont été réalisées afin de vérifier que le comportement paramagnétique des échantillons de verres dopé au fer. Le comportement attendu est paramagnétique (avec une matrice de verre légèrement diamagnétique) mais un écart pourrait suggérer des interactions Fe-Fe dus à un effet de *clustering*. Ces mesures de ont été

faite avec un système MPMS<sup>®</sup>3 (Magnetic Property Measurement System) de Quantum Design. Il s'agit d'un système SQUID-VSM (Superconducting Quantum Interference Device avec Vibrating Sample Magnetometer) dans lequel un échantillon d'environ 150 mg est fixé dans une paille oscillant selon l'axe vertical dans une cavité à des températures entre 2.5 K et 300 K et un champ magnétique entre  $-7$  T et  $7$  T. Des mesures de l'aimantation  $M$  ont été réalisées en fonction du champ magnétique  $H$  et de la température  $T$ .

## 2.6 Résonance Paramagnétique Électronique (RPE)

La Résonance Paramagnétique Électronique (RPE) est une méthode très utilisée pour l'étude du clustering, de la distorsion de site et de la quantification du  $\text{Fe}^{3+}$  [Balan et al., 1999, 2000; Griscom, 1980]. En pratique, aux fréquences utilisées (bande X et bande Q) et aux températures utilisées (supérieures à 4 K) seul le  $\text{Fe}^{3+}$  produit un signal RPE ; les autres ions ( $\text{Fe}^{2+}$  et de la matrice vitreuse) étant "silencieux".

Les mesures ont été réalisées avec un spectromètre Bruker ESP300 en bande X (9,5 GHz) et en bande Q (34 GHz) la fréquence de modulation utilisée est de 100 kHz et l'amplitude de modulation de 1 mT. Des mesures basses températures ont été réalisées entre 300 K et jusqu'à 4 K avec un cryostat Oxford.

## 3 La théorie des multiplets en champ de ligands appliquée au calcul des spectres d'absorption X et d'absorption optique

L'approche théorique utilisée dans cette thèse afin de reproduire les spectres expérimentaux est une approche multiélectronique basée sur la théorie des multiplets en champ de ligands (Ligand Field Multiplet, LFM). Cette approche semi-empirique, dédiée aux systèmes avec de fortes interaction électroniques. Elle consiste à calculer la section efficace d'absorption :

$$\sigma(\hbar\omega) = 4\pi^2 \alpha \hbar\omega \sum_{i,f} \frac{1}{d_i} |\langle f | \hat{O} | i \rangle|^2 \delta(E_f - E_i - \hbar\omega)$$

où  $\hbar\omega$  est l'énergie des photons incidents,  $\alpha = e^2/4\pi\epsilon_0\hbar c$  la constante de structure fine ( $\alpha \simeq 7.297 \cdot 10^{-3}$ ) et  $d_i$  la dégénérescence de l'état initial  $|i\rangle$ . La fonction de Dirac  $\delta(E_f - E_i - \hbar\omega)$  permet d'assurer la conservation de l'énergie. L'opérateur de transition  $\hat{O}$  permet de relier l'état initial  $|i\rangle$  d'énergie  $E_i$  à l'état final  $\langle f|$  d'énergie  $E_f$ . Cet Hamiltonien est relié à la nature de la transition. Par exemple, les opérateurs de transition dipolaire et quadrupolaire sont respectivement défini par  $\hat{O}_{dip} = \hat{\epsilon} \cdot \mathbf{r}$  et  $\hat{O}_{quad} = \frac{1}{2}(\hat{\epsilon} \cdot \mathbf{r})(\hat{\mathbf{k}} \cdot \mathbf{r})$ , avec  $\hat{\epsilon}$  et  $\hat{\mathbf{k}}$ , qui sont respectivement le vecteur unitaire de polarisation et le vecteur d'onde de la lumière [Brouder, 1990].

Dans le cas d'une transition optique seules les transitions dipolaires sont considérées Rossano et al. [2000a]. Dans le cas de l'absorption X il est possible de calculer les préseuils  $K$  en réalisant la somme des contributions dipolaire et quadrupolaires, la section efficace d'absorption totale est alors :

$$\sigma(\hbar\omega) = \sigma_{dip}(\hbar\omega) + \sigma_{quad}(\hbar\omega)$$

Cette somme reste valable tant que le site est centrosymétrique ou que le matériau est non-magnétique et que la polarisation utilisée est linéaire Juhin et al. [2008]. Pour un site centrosymétrique la contribution dipolaire est théoriquement nulle et seule la contribution quadrupolaire (plus faible que la dipolaire) participe au signal. Lorsque le site est centrosymétrique, les orbitales  $4p$  et  $3d$  peuvent s'hybrider et doit être pris en compte dans le calcul des spectres.

La caractéristique de cette méthode est que l'ion est considéré avec tous ses électrons comme isolé dans un champ de ligands. Les calculs multiplets ne prennent pas en compte la structure complète du cristal mais uniquement la symétrie autour de l'atome absorbeur. En fonction du nombre de ligands et de leur position (Figure 8) le groupe ponctuel de symétrie varie. Ceci a pour conséquence une levée de dégénérescence différente et des transitions qui n'ont pas les mêmes positions, ni intensités.

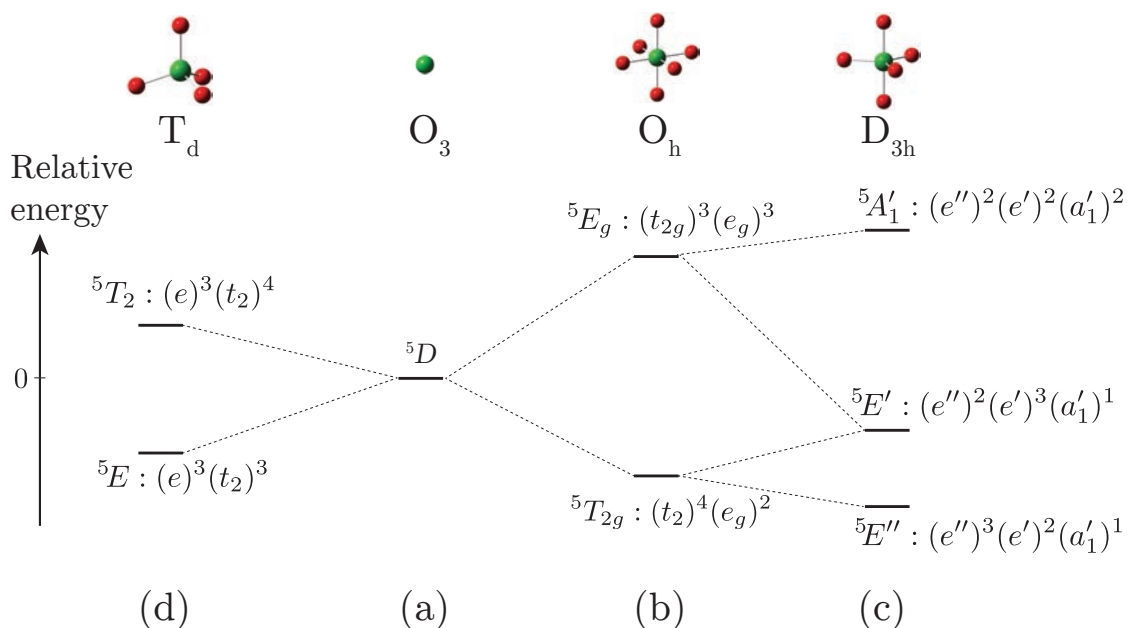


**Figure 8** – Évolution du terme spectroscopique fondamental  $5D$  (multiélectronique) d'un ion  $Fe^{2+}$  ( $d^6$ ) haut-spin en fonction de la géométrie locale.

Dans le cadre de cette thèse, les calculs multiélectroniques ont été réalisés pour l'étude du préseuil  $K$  et des spectres d'absorption optique en utilisant le logiciel **Quanty** développé par Maurits Haverkort et coll. Le formalisme utilisé est basé sur la seconde quantification et les fonctions de Green. Il est possible de calculer les spectres de poudre pour différentes géométries de site et de comparer ces spectres avec les expériences d'absorption optique et des rayons X.






## 4 Étude d'un jeu de références cristallines : détermination et interprétation des signatures spectrales

Afin d'étudier les verres, une étape préliminaire est de mieux comprendre les signatures spectrales de chaque site. Pour cela, différents minéraux contenant du fer présent dans un seul environnement bien caractérisé ont été utilisés.



La description de l'effet des ligands et des niveaux électroniques dépendent de la géométrie locale. Le groupe ponctuel de symétrie et le nombre de paramètres nécessaires associé à chaque groupe étudié sont résumés dans la Table 2.

**Table 2** – Liste des paramètres de champ cristallin et d'hybridation en fonction du groupe ponctuel de symétrie étudiée. L'état fondamental pour des ions  $\text{Fe}^{2+}$  et  $\text{Fe}^{3+}$  haut-spin sont donnés avec leur dégénérescence entre parenthèses.

Point group symmetry	Crystal field parameters	$p-d$ hybridization parameters	Ground state (dim)	
			$d^6-\text{Fe}^{2+}$	$d^5-\text{Fe}^{3+}$
$\text{O}_h$ 	$10Dq$	–	${}^5T_{2g}$ (15)	${}^6A_{1g}$ (6)
$\text{D}_{4h}$ 	$Dq$ $Dt$ $Ds$	–	${}^5A_{1g}$ (5)	${}^6A_{1g}$ (6)
$\text{T}_d$ 	$10Dq$	$V_{pd}$	${}^5E$ (10)	${}^6A_1$ (6)
$\text{C}_{4v}$ 	$Dq$ $Dt$ $Ds$	$V_{pd}^e$ $V_{pd}^a$	${}^5E$ (10)	${}^6A_1$ (6)
$\text{D}_{3h}$ 	$D\mu$ $D\nu$	$V_{pd}$	${}^5E''$ (10)	${}^6A_1'$ (6)

L'Hamiltonien d'hybridation  $p-d$  dépend, pour l'état initial, de la différence d'énergie  $\Delta$  entre les configurations électroniques  $3d^n 4p^0$  et  $3d^{n-1} 4p^1$  (Figure 9). Pour l'état final, la situation est analogue et la différence d'énergie est nommée  $\Delta'$ . En plus de cette différence d'énergie, l'intensité de l'hybridation est paramétrée par le coefficient  $V_{pd}$  (en eV).

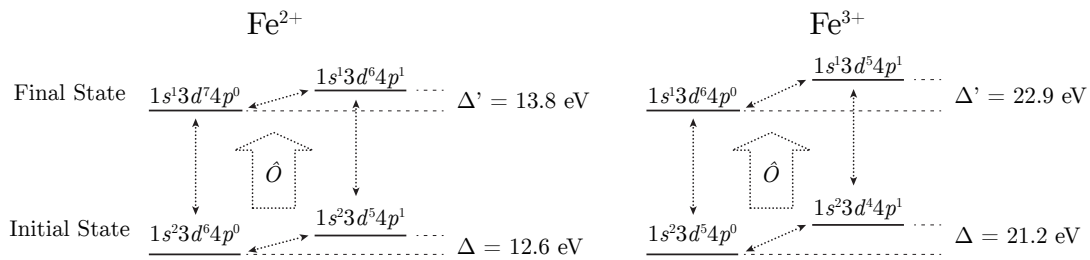


**Figure 9** – Schéma de l'interaction de configuration pour le  $\text{Fe}^{2+}$  et le  $\text{Fe}^{3+}$  tenant compte de l'hybridation  $p-d$  dans le cadre de la théorie des multiplets en champ de ligands LFMT).

Dans le cadre de cette thèse, les références cristallines suivantes ont été étudiées : siderite ( $[6, \text{O}_h]\text{Fe}^{3+}$ ), andradite ( $[6, \text{C}_{3i}]\text{Fe}^{2+}$ ), gillespite ( $[4, \text{D}_{4h}]\text{Fe}^{2+}$ ), staurolite ( $[4, \text{T}_d]\text{Fe}^{2+}$ ), ferriorthoclase ( $[4, \text{T}_d]\text{Fe}^{3+}$ ), grandidierite ( $[5, \text{C}_{3v}]\text{Fe}^{2+}$ ) et yoderite ( $[5, \text{C}_{3v}]\text{Fe}^{3+}$ ). Dans chacun des cas, les paramètres des spectres d'absorption optique et des rayons X ont été reproduits, en ajustant au mieux les paramètres du calcul. L'effet des différents paramètres a été étudié

afin d'obtenir des tendances permettant d'extrapoler les résultats obtenus sur les cristaux ne contenant qu'un site du fer aux verres contenant une distribution de sites.

Les spectres optiques obtenus n'ont jamais été calculé par de précédentes études. Le bon accord entre les données calculés et l'expérience est très prometteur.

Les contributions dipolaires et quadrupolaires au préseuil  $K$  du fer sont résumées dans la Table 3. Les calculs confirment que la proportion de dipolaire est plus importante dans le cas d'un site non-centrosymétrique alors qu'elle est nulle lorsqu'un centre de symétrie est présent.

**Table 3** – Valeur de l'intégrale de l'intensité normalisée du préseuil  $K$  des spectres XAS issue des absorptions dipolaires et quadrupolaires en fonction de la géométrie. Les aires sont multipliées par 100 et correspondent à l'intégrale du préseuil normalisé avec une énergie en eV.

Géométrie	Minéral	Calcul LFM			Expérience Total
		Quad	Dip	Total	
$[6]Fe^{2+} (O_h)$	siderite	6.1	0.1	6.2	5.9
		(98%)	(2%)	(100%)	
$[4]Fe^{2+} (D_{4h})$	gillespite	6.2	0.4	6.6	5.6
		(94%)	(6%)	(100%)	
$[5]Fe^{2+} (D_{3h})$	grandidierite	6.0	5.2	11.2	11.8
		(54%)	(46%)	(100%)	
$[4]Fe^{2+} (T_d)$	staurolite	5.8	23.6	29.4	23.3
		(20%)	(80%)	(100%)	
$[6]Fe^{3+} (O_h)$	andradite	8.6	0.2	8.8	9.7
		(98%)	(2%)	(100%)	
$[5]Fe^{3+} (C_{3v})$	yoderite	8.8	2.4	11.2	12.0
		(79%)	(21%)	(100%)	
$[4]Fe^{3+} (T_d)$	ferriorthoclase	8.3	26.2	34.5	34.3
		(24%)	(76%)	(100%)	

En plus de la possibilité de calculer et reproduire les spectres d'absorption optique et des rayons X expérimentaux du fer dans des minéraux, les calculs mettent en évidence l'importance de la géométrie de site considéré et de la valeur des paramètres de champ cristallin utilisé pour décrire la structure locale. La complémentarité des deux méthodes expérimentales permet d'améliorer la description des signatures spectrales du fer.

## 5 Environnement local du fer dans un verre sodocalcique

L'utilisation d'une approche multi-spectroscopique est une des clés de la compréhension des relations entre la structure du fer dans les verres et des propriétés spectroscopiques du  $Fe^{2+}$  et du  $Fe^{3+}$ .

### 5.1 Analyse structure-spectroscopie du $Fe^{2+}$

L'utilisation des spectre optique de référence cristalline donne une idée des positions et des intensités attendues pour les transitions optiques du fer dans les verres. La corrélation

avec ces références a aussi été réalisé en comparant les spectres d'absorption X des verres et minéraux. Les données confirment l'importance de considérer la coordinence [5] du  $\text{Fe}^{2+}$ .

Afin de mieux comprendre cette influence de la coordinence [5], plusieurs spectres optiques du  $\text{Fe}^{2+}$  en  $C_{3v}$  ont été calculés afin de représenter différents environnement de coordinence [5] possibles. Ces spectres optiques calculés sont tracés sur la Figure 10. L'information principale apportée par ce calcul est la possibilité de reproduire l'ensemble du signal optique expérimental en ne modifiant que les paramètres de champ cristallin d'une coordinence [5] en géométrie  $C_{3v}$ . Il est donc important de considérer ce type de géométrie en plus des géométrie tétraédriques (coordinence 4) et octaédriques (coordinence 6) habituellement considérées.

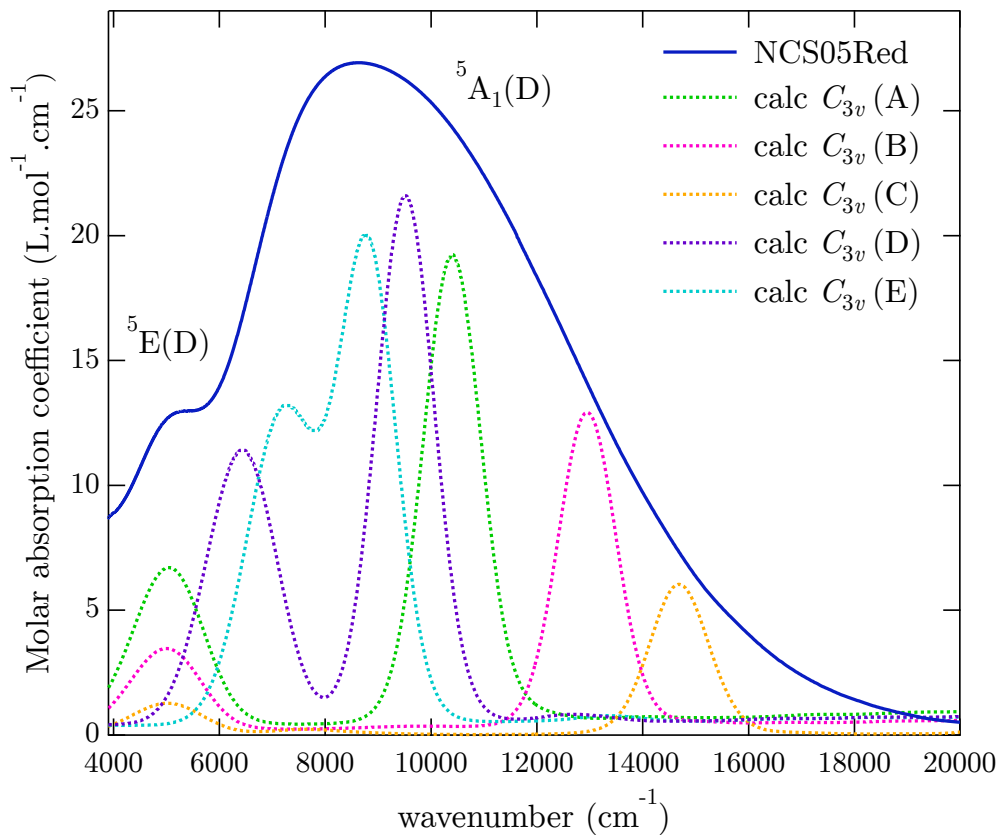


**Figure 10** – Spectres d'absorption optique du fer dans le verre NCS05Red, ainsi que les spectres calculés pour du  $\text{Fe}^{2+}$  en géométrie  $C_3$  (A,B, C D et E).

## 5.2 Analyse structure-spectroscopie du $\text{Fe}^{3+}$

L'étude croisée des différentes spectroscopies a permis de mettre en évidence la présence de  $\text{Fe}^{3+}$  en coordinence 5. L'utilisation de la RPE donne aussi une information sur la distortion et la distribution des sites du  $\text{Fe}^{3+}$  dans la matrice verrière. La Figure 11 permet ainsi de montrer que malgré la diminution du nombre de  $\text{Fe}^{3+}$  lorsqu'un verre est réduit les  $\text{Fe}^{3+}$  restant sont plus distordus. En revanche, les  $\text{Fe}^{3+}$  restant sont moins distribués et sont donc présents dans des sites plus semblables les uns aux autres. Par comparaison, les verres oxydés présente une plus grandes variétés de sites du  $\text{Fe}^{3+}$  qui sont globalement plus réguliers que dans les verres réduits.

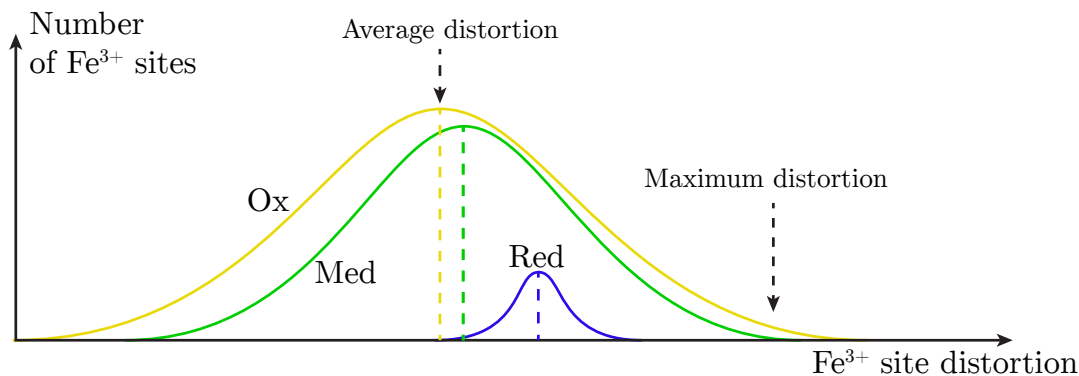


**Figure 11** – Représentation schématique de la distribution et de la distorsion du Fe<sup>3+</sup> dans les verres NCS en fonction du redox.

### 5.3 Fer en cluster vs. fer isolés

Les mesures de SQUID-VSM et de RPE croisées avec les données d'absorption optique et des rayons X montrent que des effets de clustering dues à des interactions Fe–Fe sont visible dans les verres contenant seulement 0.5 %pds de Fe<sub>2</sub>O<sub>3</sub>. Ces interactions sont plus importantes dans le cas des verres réduits dans lesquels il est montré que les Fe<sup>3+</sup> résiduels ont tendance à se trouver dans le voisinage d'autres ions fer. Cependant, les mesures de SQUID ont démontré l'absence de nanoparticules de fer. Ainsi, même si des effets de clustering sont visible en RPE et absorption X, ils restent minoritaires dans le signal et leur effet sur les propriétés optiques sont limités.

## 6 Conclusions et perspectives

L'objectif de cette thèse était d'améliorer la compréhension des relations structure-propriétés du Fe<sup>2+</sup> et du Fe<sup>3+</sup> dans les verres silicatés. Pour ce faire une étude multi-spectroscopique a été réalisée en couplant les méthodes d'absorption optique, absorption des rayons X (XAS, RIXS et HERFD) et la résonance paramagnétique électronique (RPE). Les données expérimentales ont été comparées avec des résultats de calculs multiplet permettant de reproduire les signaux des préseuil *K* du fer et les spectres d'absorption optique.

L'étude de plusieurs références cristallines contenant du fer dans différentes géométries a permis de caractériser l'environnement du fer dans des sites spécifiques en utilisant la théorie du champ de ligand. Les nouveaux développements ont permis de reproduire les spectres d'absorption optique et des rayons X. Les effets de la géométrie locale ont été pris compte à travers les paramètres de champ cristallin et les paramètres d'hybridation, qui ont permis de reproduire les positions et intensités des spectres.

L'utilisation de ces signatures spectroscopiques couplées aux tendances obtenues en faisant varier les paramètres de calculs permet d'extrapoler les résultats aux verres. En particulier, l'étude de références cristallines avec du fer en coordinence [5] permet de mieux caractériser ce type d'environnement dans les verres. D'autre part, des modifications de la composition des verres a permis d'étudier les variations spectroscopiques associées au redox du verre, à la présence ou absence de sodium et au ratio calcium/magnésium.



# Résumé

Parmi l'infinité de compositions verrières, les silicates représentent 90 % de la production mondiale de verre et sont utilisés pour de nombreuses applications industrielles (par exemple l'automobile, le bâtiment ou les panneaux solaires). Des verres silicatés dopés avec 0.5 %pds de  $\text{Fe}_2\text{O}_3$  ont été spécifiquement synthétisés dans des conditions d'oxydoréduction extrêmes, réductrices ou oxydantes. L'objectif étant d'isoler les signatures spectroscopiques respectives du  $\text{Fe}^{2+}$  et du  $\text{Fe}^{3+}$  qui sont habituellement mélangés en raison de la nature hétérovalente du fer.

Cependant, les conditions de synthèse ne permettent pas d'isoler des environnements spécifiques du fer qui reste distribué dans les verres. Par conséquent, des minéraux contenant du  $\text{Fe}^{2+}$  et du  $\text{Fe}^{3+}$  dans des environnements bien définis ont été sélectionnés. La compréhension des relations structure-spectroscopie dans ces références cristallines est donc une étape préliminaire à l'interprétation des signatures spectroscopiques du fer dans les verres.

Une étude multi-spectroscopique a été réalisée sur les verres et minéraux en combinant des méthodes expérimentales (absorption optique, absorption des rayons X au seuil  $K$  du fer, résonance paramagnétique électronique) et théoriques (calculs multiélectroniques dans l'approche en champ de ligand pour reproduire les spectres de pré-seuils  $K$  et de spectres optiques) pour mieux comprendre l'environnement local du fer dans les verres.

L'étude des références cristallines a permis de montrer l'influence de la symétrie locale ( $O_h$ ,  $T_d$ ,  $D_{4h}/C_{4v}$  et  $D_{3h}/C_{3v}$ ) du site du fer et de l'hybridation  $p-d$  sur sa signature spectroscopique. Concernant l'étude des verres silicatés réduits, une majorité du  $\text{Fe}^{2+}$  est présent en coordinance 5, il est montré que cette dernière permet de reproduire et d'expliquer la signature du fer par une distribution des paramètres de champ cristallin rendant compte de la nature amorphe du verre. L'analyse des verres oxydés a permis d'appuyer l'existence de  $\text{Fe}^{3+}$  en coordinance 5 dans les verres sodo-calciques, dont la prise en compte est nécessaire pour l'interprétation des spectres optiques en complément des coordinances tétraédriques. Cette étude apporte un éclairage nouveau sur les variations structurales et spectroscopiques du fer en réaction à une substitution du calcium par du magnésium ou à l'absence d'alcalin dans la composition de la matrice verrière.

## Mots-clés:

impureté, absorption optique, XANES, RPE, redox du fer, silicates, champ cristallin.

# Abstract

Among the infinite possibilities of glass compositions, soda-lime silicates represent of 90% of the glass production and are widely used for many industrial applications (e.g. automotive, solar panels, construction). Specific glasses silicate containing 0.5 wt% of  $\text{Fe}_2\text{O}_3$  were synthesized with extreme redox. The use of reducing and oxidizing conditions allows to isolate the respective  $\text{Fe}^{2+}$  and  $\text{Fe}^{3+}$  spectroscopic signatures that are usually mixed due to the heterovalent nature of iron.

However, synthesis conditions do not allow to isolate specific iron environment that remains distributed in glasses. Thus,  $\text{Fe}^{2+}$ - and  $\text{Fe}^{3+}$ -bearing minerals containing iron in well defined environments were selected. The comprehension of structure-spectroscopy relationships in these crystalline references is a preliminary step to the interpretation of iron spectroscopic signature in glasses.

A multi-spectroscopic study was performed on glasses and minerals by combining experimental (optical absorption, X-ray absorption at the iron  $K$  edge, and electron paramagnetic resonance) and theoretical (multielectronic calculations using ligand field multiplet approach to reproduce the  $K$  pre-edge and optical absorption spectra) methods.

The study of crystalline references evidenced the influence of local symmetry ( $O_h$ ,  $T_d$ ,  $D_{4h}/C_{4v}$  et  $D_{3h}/C_{3v}$ ) on iron sites and of  $p$ - $d$  hybridization on iron spectroscopic signatures. Concerning the study of reduced silicate glasses, the majority of  $\text{Fe}^{2+}$  is present in [5]-fold coordination, this speciation can reproduce and explain the iron signature by using a distribution of the crystal field parameters to take into account the amorphous nature of glass. The analysis of oxidized glasses supports the existence of  $\text{Fe}^{3+}$  in [5]-fold coordination. These species need to be considered, in addition to tetrahedral geometries, for the interpretation of optical spectra. This study shed light on structural and spectroscopic variations of iron due to the substitution of calcium by magnesium or by the absence of alkali in the composition of the glass matrix.

**Keywords:**

impurity, optical absorption, XANES, EPR, iron redox, silicates, crystal field.